DEVELOPMENT OF PULSE-WIDTH-MODULATION TECHNIQUES FOR MULTI-PHASE AND MULTI-LEG VOLTAGE SOURCE INVERTERS

DRAŽEN DUJIĆ

A thesis submitted in partial fulfilment of the requirements of Liverpool John Moores University for the degree of Doctor of Philosophy

September 2008

ABSTRACT

A huge body of work has been published in recent times in the area of multi-phase machines and drives. Many aspects of these drives have been analysed, such as reduction of torque pulsations, increased reliability and fault tolerance, improved power sharing capabilities and possibilities for realisation of series-connected multi-motor drives with supply coming from a single multi-phase voltage source inverter (VSI). Various pulse width modulation (PWM) schemes have been developed for multi-phase machines with concentrated and distributed windings, utilising both carrier-based PWM and space vector PWM (SVPWM) approaches. However, no systematic analysis has been performed in order to determine basic properties of multi-phase PWM in general, and to establish close correlation between carrier-based PWM and space vector PWM, for multi-phase VSIs.

This thesis presents an analysis and development of multi-phase PWM schemes for sinusoidal output voltage generation with two-level multi-phase VSIs, which are suitable for multi-phase machines with distributed windings. Therefore, attention is paid to the elimination of low order harmonics. The scope of the thesis has been narrowed down to the continuous PWM schemes and operation in the linear region of the modulation only. Both multi-phase carrier-based PWM and SVPWM schemes are considered, and, in particular, five-phase, seven-phase and nine-phase systems are addressed in detail. Thus, a strong link between these two different approaches is established, allowing for an easier comparison of the features offered by each method. All PWM schemes are practically implemented in a DSP and experimentally verified through extensive experimentation on the custom-built multi-phase VSI.

In addition to the methods of sinusoidal output voltage generation, achieved by means of the synthesis of the reference in only the first plane of the multi-phase system with simultaneous zeroing of voltages in all the other planes, the impact of the various PWM schemes on the output current ripple is analysed as well. Two different approaches are presented, based on the extension of the commonly used analytical tools for three-phase systems. Both approaches yield the same results for a particular PWM scheme and certain phase number. Yet, the results, obtained during these analyses, are completely different from those well known for three-phase PWM schemes, and suggest that current ripple optimisation is not possible in multi-phase drives by means of harmonic injection.

Since all the developed PWM schemes are aimed for multi-phase machines with distributed windings, a further analysis is undertaken for multi-motor drives, realised by an appropriate connection of $(n-1)/2$ n-phase machines to a single n-phase VSI. A simple analytical method for analysis of voltage limits is developed, together with multi-frequency output voltage PWM schemes, which are suitable for these type of drives. An arbitrary allocation of the available dc bus voltage is made possible among machines in series connection, within the operational boundaries that define linear region of modulation. Experimental verification is performed on the series-connected five-phase two-motor drive.

Finally, PWM schemes for the reduced switch-count multi-motor drives are developed. An n-leg VSI is used to supply $(n-1)/2$ three-phase machines, connected in such a way that all machines share one inverter leg. Operational area for the linear modulation is determined by considering the voltage requirement of each machine, and the developed modulation schemes are experimentally verified on several multi-leg VSI fed multi-motor drives. Both operation in the open-loop and closed-loop control mode are investigated, confirming the feasibility of the developed PWM schemes.

ACKNOWLEDGEMENT

to
Nikola
and
Małgorzata

CONTENTS

8. ANALYTICAL ANALYSIS OF CURRENT RIPPLE RMS OF MULTI-PHASE DRIVES – POLYGON APPROACH

9. PWM METHODS FOR MULTI-FREQUENCY OUTPUT VOLTAGE GENERATION WITH MULTI-PHASE VOLTAGE SOURCE INVERTERS

LIST OF PRINCIPAL SYMBOLS

n	Number of phases
$A, B, C, \ldots$	Inverter legs in general or used in sub-script to associate the principal symbol with a certain leg
$a, b, c, \ldots$	Phases of the machine/load or used in sub-script to associate the principal symbol with a certain phase
v	Voltage
i	Current
m_k	Switching functions where sub-script denotes the corresponding inverter leg
V_{dc}	Dc bus voltage
α	Characteristics angle; takes values of either $\alpha = 2\pi/n$ or $\alpha = P\pi/n$
$\underline{C}_n$	Decoupling transformation matrix for an n-phase system
d-q	2-D plane in general; sub-scripts identify a particular plane
N	Neutral point of the machine/load; a sub-script identifies a particular machine/load
P	Denotes polygon/plane number
K_P, L_P	Trigonometric constants defined with $K_P = \sin(P\frac{\pi}{n})$ and $L_P = \cos(P\frac{\pi}{n})$; use of sub-script is omitted for $P = 1$
M	Modulation index; an added sub-script defines closer meaning or association with a particular machine
G	Modulator gain
ϑ	Instantaneous reference space vector position
T_s	Switching period
f_s	Switching frequency

T	Times of application of space vectors, where sub-script defines a particular space vector
δ	Duty cycle where sub-script defines a particular space vector
s	Sector in the d-q plane; super-script (if present) defines particular plane
μ	Control variable that alters the zero space vector duty cycle distribution
b	Relative ratio of the magnitude of the n-th harmonic to the fundamental
$\varDelta$	Deviation of a certain variable
d	Differential operator
t	Time in general, or with sub-script that defines a particular instant
L	Inductance, where sub-script can be used for more precise definition
R	Resistance where sub-script can be used for more precise definition
λ	Harmonic flux

GENERAL

$^{-}$	Line above the symbol identifies space vector
*	When in super-script, denotes the reference value
N	In sub-script defines normalisation value

LIST OF USED ABBREVIATIONS

ac	Alternating Current
2-D	Two-Dimensional
3-D	Three-Dimensional
CPWM	Continuous Pulse Width Modulation
CMV	Common Mode Voltage
dc	Direct Current
emf	Electro Motive Force
DPWM	Discontinuous Pulse Width Modulation
DSP	Digital Signal Processor
IGBT	Insulated Gate Bipolar Transistor
FFT	Fast Fourier Transformation
HDF	Harmonic Distortion Factor
mmf	Magneto Motive Force
p.u.	per-unit
PWM	Pulse Width Modulation
RFOC	Rotor Flux Oriented Control
rms	Root Mean Square (value)
SVPWM	Space Vector Pulse Width Modulation
VSD	Vector Space Decomposition
VSI	Voltage Source Inverter

Chapter 1

INTRODUCTION

1.1 PRELIMINARY CONSIDERATIONS

Numerous industry applications, such as for example textile and paper industry, steel mills, electric and hybrid electric vehicles, ship propulsion, railway traction, 'more-electric' aircraft, etc., require utilisation of variable speed electric drives. Depending on the actual application, different types of electric machines can be used, such as induction motors, permanent magnet synchronous motors, switched reluctance motors, dc motors, etc. The trend in the industry, in retrofitting and design of new plants, is to dispense with dc motors wherever possible and to utilise ac machines instead. Reasons for this are a simpler structure of ac machines, better robustness, lower cost and virtually maintenance-free operation.

As far as the variable speed operation of electric drives is concerned, this is nowadays invariably achieved by supplying the machine, regardless of the type, from a power electronic converter. This has been enabled by rapid developments in the areas of ac machine control algorithms, power semiconductors and microprocessors/digital signal processors (DSPs) during the last four decades. Combining fast-switching power semiconductors with computationally powerful DSPs provides a convenient way to realise the complex control algorithms for ac machines, so that excellent quality of speed/position control is achieved. The standard variable speed electric drive architecture nowadays consists of a three-phase ac machine, three-phase power electronic converter, and a microprocessor/DSP-based controller. By far the most frequently utilised power electronic converter is the three-phase two-level voltage source inverter (VSI), which is controlled using an appropriate algorithm of pulse width modulation (PWM). The output of such a PWM VSI is a train of pulses, of constant amplitude, which correspond to the fundamental voltage of a certain magnitude, frequency and phase that is applied to the machine, as required by the specific control algorithm used in a particular variable speed ac drive.

With regard to the number of phases that ac machine has (and therefore VSI as well), the standard solution nowadays is utilisation of a three-phase machine and inverter. This is so since these machines/inverters are readily available, off-the-shelf products and is a consequence of the fact that in the past, in vast majority of cases, the machines were directly connected to three-phase power grid. Low cost and mass production have therefore established three-phase machines as the standard solution in the industry. However, in the variable speed drives, since the machine is supplied from a power electronic converter rather than directly from the three-phase grid, the requirement to have three phases does not exist any more since the power electronic converters can be built with an arbitrary number of phases. Therefore, the number of phases appears as a new design variable that can be used to improve characteristics of a drive and to satisfy certain requirements that are not achievable with three-phase drives, as will be discussed shortly.

Selection of a multi-phase variable speed drive for an application requires three basic changes compared to the standard solution with a three-phase drive: design and manufacturing of a multi-phase machine, modification of the power electronic converter topology and the development of appropriate control algorithms (from the machine point of view, as well as with regard to the power electronic converter control strategy). The research results presented in this thesis are focused on the analysis, development, implementation and experimental evaluation of novel control strategies for multi-phase power electronic converters. More specifically, the focus is on PWM strategies applicable in conjunction with multi-phase VSIs feeding a single multi-phase machine or several multi-phase machines in an appropriate connection to a multi-phase VSI. Thus, various PWM strategies for five-phase, seven-phase and nine-phase VSIs are analysed. The decision to concentrate on PWM techniques for VSIs with odd number of phases is predominantly related to the fact that most of the existing body of work applies to the PWM methods for six-phase VSIs. This is so since the six-phase motor drive has been the most frequently investigated candidate for various applications, and stems from the fact that a six-phase inverter can be realised by using two three-phase, readily available off-the-shelf, inverters. The author has himself conducted in the past research on PWM methods for control of a six-phase VSI for the purposes of completion of the Master of Science thesis [Dujić (2005), Dujić et al (2006), Dujić et al (2007a)].

The research conducted in the area of the PWM techniques for multi-phase VSIs also includes utilisation of a single inverter as the supply for a multi-motor drive system, based on utilisation of multi-phase machines. The existing alternative is to use three-phase machines, in which case they are customarily supplied from their own three-phase VSIs. A significant

effort has been put in recent times into the development of so called reduced switch-count inverter topologies applicable in conjunction with three-phase multi-motor drive systems. The second research track in this thesis therefore explores PWM techniques for the one specific reduced switch-count two-level VSI topology, aimed at supplying a multitude of three-phase variable speed drives.

1.2 AN OVERVIEW OF MULTI-MOTOR AND MULTI-PHASE DRIVES

As noted, numerous industrial applications require more than one variable speed drive for successful operation [Belhadj et al (2001), Pena-Eguiluz et al (2001), Matsumoto et al (2001)]. Such multi-motor drives are commonly realised by connecting several three-phase converter-machine units to a common dc link thus allowing independent vector (or direct torque) control of each machine with ability to directly utilise energy during regenerative braking of one machine by other machines. A different approach used in traction is based on one three-phase inverter supplying parallel-connected three-phase motors [Matsumoto et al (2001)]. This does not allow independent control of individual machines and assumes equal loading conditions on each machine and the same shaft speeds. If these conditions are not satisfied unstable operation may result. While parallel connection does offer a reduction in the overall cost of a multi-motor drive, this is obtained at the expense of the lack of independent control of machines, making independent inverter-machine units connected to the same dc bus the standard industry choice whenever independent control is required.

Multi-phase machines (machines with the number of phases n greater than three) are characterised with a number of advantages when compared to their three-phase counterparts. To start with, the stator excitation in a multi-phase machine produces a field with a lower space-harmonic content, so that the efficiency can be higher than in a three-phase machine [Williamson and Smith (2003)]. This also leads to a lower acoustic noise emitted from the machine [Golubev and Ignatenko (2000)]. Next, multi-phase machines have a greater fault tolerance then their three-phase counterparts. If one phase of a three-phase machine becomes open-circuited the machine becomes single-phase. In contrast to this, a multi-phase machine can continue to develop a rotating field as long as the number of open-circuited phases is no more than n-3. Multi-phase machines are less susceptible than their three-phase counterparts to time-harmonic components in the stator current, which produce torque ripple. Last but not least, for a given motor power, utilisation of multi-phase machines enables a reduction in the

voltage/current rating of power semiconductors of the power electronic converter. Ever since the inception of the first variable speed multi-phase (five-phase induction) motor drive in 1969 [Ward and Härer (1969)], multi-phase machines and drives have been attracting steady but limited attention. The situation has changed dramatically during the last ten years or so, which have seen multi-phase motor drives becoming a focal point of the research activities worldwide. Such a situation has arisen predominantly due to some very specific variable speed drive applications, where the afore-mentioned advantages of multi-phase machines are of paramount interest. These include electric ship propulsion, electric and hybrid electric vehicles, locomotive traction and the concept of the 'more-electric' aircraft. Thus, significant new research results in this area have been published in recent times [Levi et al (2007b)].

Selection of multi-phase machines for a multi-motor drive results in new topologies that can provide independent control of several multi-phase machines supplied from a single multi-phase VSI. Several multi-phase machines can be connected in series or parallel with the use of an appropriate phase transposition which enables independent control of all the machines [Jones (2005), Iqbal (2005)]. This configuration simultaneously offers a great reduction in the number of semiconductors used. Such topologies are not possible with three-phase drives. The idea stems from the fact that flux and torque control of a multi-phase machine with near-sinusoidal magnetomotive force (mmf) distribution requires only two currents regardless of the number of phases. Remaining degrees of freedom are usually used to enhance torque production by means of low order harmonic injection when the multi-phase machine is designed with concentrated windings (quasi-rectangular mmf distribution) or for fault tolerant operation [Levi et al (2007b)]. An entirely different utilisation of the remaining degrees of freedom is possible with multi-phase machines having distributed windings (near-sinusoidal mmf distribution). A certain number of multi-phase machines can be connected in series/parallel, in such a manner that flux/torque producing currents of one machine appear as non-flux/torque producing currents for all other machines and vice versa. Principal layout of the concept of series/parallel connected multi-phase multi-motor drives is shown in Fig. 1.1 and Fig 1.2, respectively. A multi-phase multi-motor drive, comprising two five-phase series-connected machines, has been proposed for the first time on a conceptual level by Gatarić (2000). This concept was further explored in detail and verified by extensive theoretical and experimental investigation in research undertaken by Jones (2005) and Iqbal (2005).

The research of Jones (2005) carried out a comprehensive analytical study covering all possible supply phase numbers for series-connected multi-phase multi-motor drives (both odd and even) and investigated the numbers and different types of the machines that can be

connected. All the simulation studies were performed under assumption of idealised sinusoidal supply condition and the vector control, assuming current control in either stationary or rotating reference frame. Experimental investigations were carried out on a six-phase drive in single machine configuration (symmetrical six-phase machine) as well as in two-motor configuration (series-connected symmetrical six-phase and a three-phase machine). The research of Iqbal (2005) covered aspects of modelling and control of series-connected five-phase and six-phase two-motor drives. Additionally, attention was also paid to the modelling aspects of five-phase and six-phase VSIs. Several PWM schemes, mostly based on the space vector approach, and suitable for these drive configurations, were analysed but none of them was experimentally implemented. Complete experimental investigation on actual multi-phase drives was based on the current control in the stationary reference frame using ramp-comparison method, so that there was no requirement to develop adequate PWM algorithms for the multi-phase VSIs. However, if current control is executed in the rotating reference frame, it is mandatory to have appropriate PWM schemes for VSI control. It is for this reason that one specific objective of this thesis is the analysis, development and implementation of PWM techniques for multi-phase VSI supplying multi-phase machines both in single-motor drive and in multi-motor drive configurations (series/parallel connection to multi-phase VSI).

As the first step towards development of novel PWM schemes that can effectively satisfy voltage requirements of several machines in series/parallel connection, PWM schemes aimed at control of a multi-phase VSI supplying only one multi-phase machine are investigated. The analysis includes continuous carrier-based PWM and space vector PWM (SVPWM) methods in the linear modulation region of operation. Characteristics of the modulators in overmodulation are beyond the scope of research presented here. PWM methods for five-phase, seven-phase and nine-phase VSIs are investigated in great depth establishing a link between carrier-based PWM and SVPWM, as well as generalising the development of the latter approach. Next, based on these findings, a novel PWM scheme for multi-phase VSI is developed, which is able to generate multi-frequency output voltage in accordance with the requirements of each machine in series/parallel connection, while still keeping optimized switching pattern with minimal number of commutations per switching period (from the point of view of PWM methods there is no difference if multi-phase machines are in series or parallel connection to the multi-phase VSI). Since parallel topology suffers from some serious drawbacks [Jones et al (2006a), Jones et al (2006b)], PWM development in the thesis is primarily aimed at series-connected multi-motor drives.
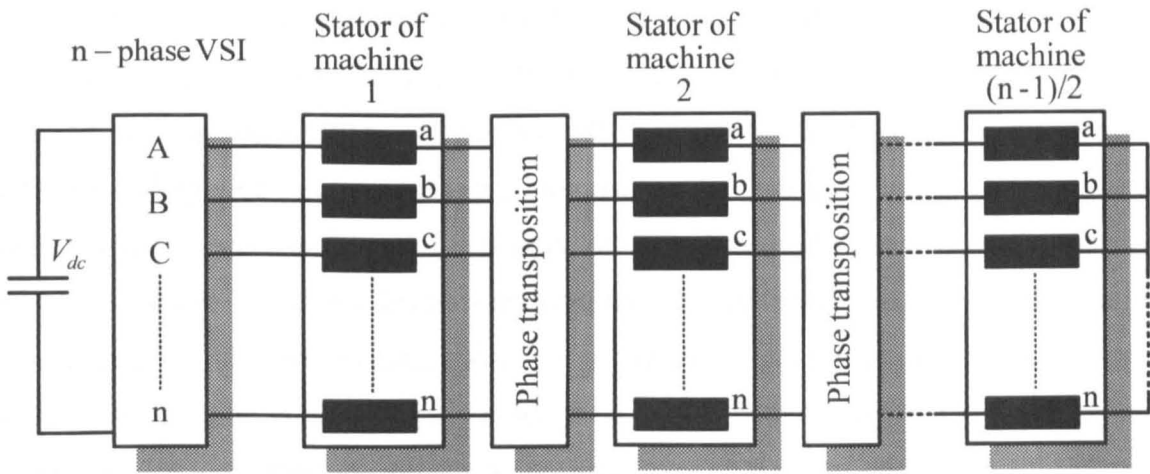
Fig. 1.1: Concept of multi-phase multi-motor drive system – series connection.
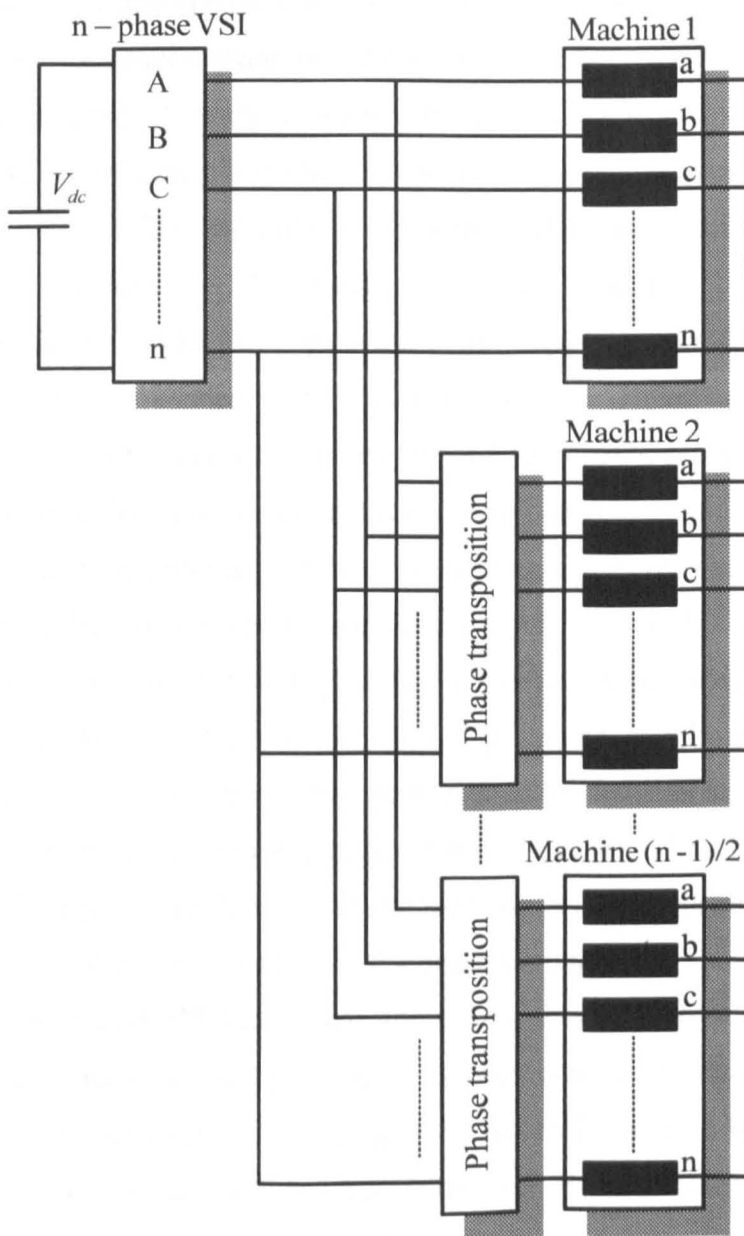
Fig. 1.2: Concept of multi-phase multi-motor drive system – parallel connection.

In order to reduce the overall cost of the system by reducing the number of power semiconductors used, various alternative drive topologies for three-phase machines have been suggested. A comparative study of these so called reduced switch-count drive structures was conducted and applied to a mobile robot motorisation by Bouscayrol et al (1996). Use of a four-leg inverter was considered for supply of two three-phase machines [Barnard et al (1994)], where two legs of the inverter are common for both machines, while remaining legs are connected to only one machine each. Due to the nature of connection of machines to the inverter, the operation is possible only at identical speeds with the same or opposite direction of rotation. Another structure utilises a four-leg inverter with an additional split-capacitor bank as the fifth common leg [Francois and Bouscayrol (1999)]. A multi-motor drive topology comprising two three-phase machines supplied via a single five-leg VSI has been proposed, where two machines share one of the inverter legs [Francois and Bouscayrol (1999), Delarue et al (2001)]. Such a two-motor drive offers a saving in the number of semiconductors used, while enabling independent control of both machines under certain limitations, which will be addressed later. Various reduced switch-count drive systems have also been reported in Jacobina et al (2002) and Jacobina et al (2005).

In addition to the PWM techniques for multi-phase single-motor and multi-motor drives, PWM schemes for reduced switch-count multi-motor drives based on three-phase machines are analysed. The concept is based on utilisation of a multi-leg VSI to supply several three-phase machines connected in such a way that one phase of each machine is connected to the common inverter leg, while the remaining phases of machines are connected to their own inverter legs (alternatively, common inverter leg can be replaced with split-capacitor leg, thus offering further savings in the number of semiconductors [Francois and Bouscayrol (1999)], however features of such a topology are beyond the scope of the thesis). Since characteristics of the VSI are not any more related to characteristics of a multi-phase system, VSI is further termed as multi-leg rather than multi-phase. Thus, having an n-leg VSI allows for $(n-1)/2$ three-phase machines to be supplied, while still being able to independently control each of them, under some restrictions that are elaborated later on. Focus of research is again narrowed to the area of PWM methods and a novel PWM method is developed (using both carrier-based and space vector approaches) that overcomes disadvantages of the existing PWM techniques. Principal layout of a multi-leg VSI fed multi-motor drive system is shown in Fig. 1.3. For illustration purposes, it is assumed that n-th leg of an n-leg VSI is common to all $(n-1)/2$ three-phase machines. In general, which particular leg is selected as the common leg does not have any impact on the developed PWM scheme.
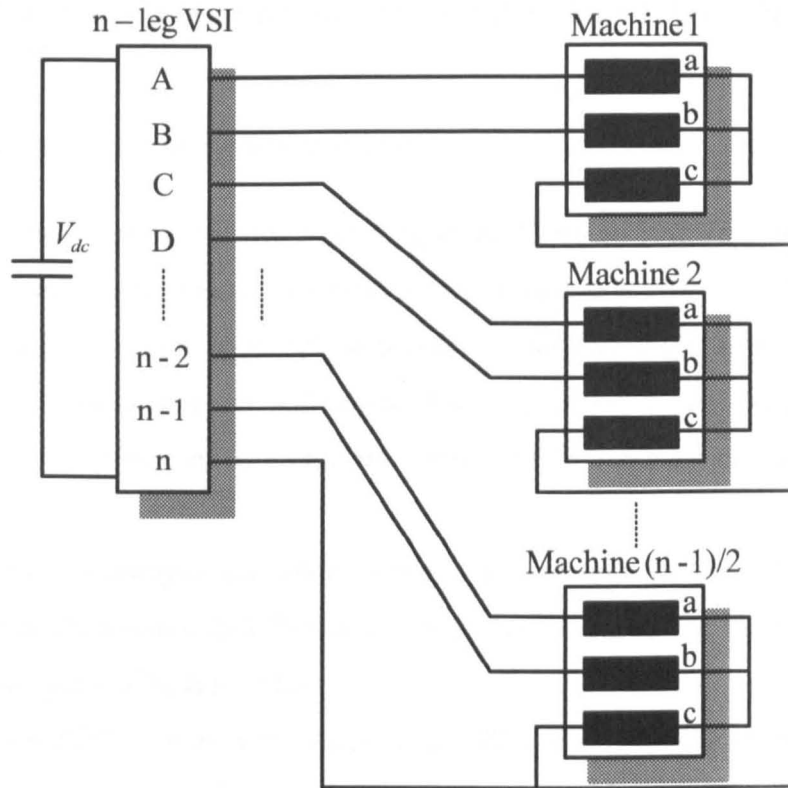
Fig. 1.3: Concept of multi-leg VSI fed multi-motor drive system.

The two analysed multi-motor drive systems have some common features, although the machines are different with respect to the number of phases:

- Having an n-phase/n-leg VSI allows for $(n-1)/2$ machines to be supplied.

- Independent control of each machine within a multi-motor drive is possible.

- Operational range of each machine within a multi-motor drive is greatly affected by the available dc bus voltage (a feature that is investigated in detail in the thesis).

- The PWM scheme must be able to generate multi-frequency output voltage to satisfy requirements of all machines.

- Ac machines of different types can be freely mixed: induction motors, permanent magnet synchronous motors, synchronous reluctance motors, wound rotor synchronous motors.

- Both topologies enable reduction in the number of power semiconductors and accompanied electronics.

For the purposes of the experimental investigations and verification of the developed theoretical concepts a custom designed nine-phase two-level VSI has been manufactured together with an accompanying TMS320F2812 DSP-based control system (Appendix A). Thus, great flexibility has been achieved, allowing fast and easy reconfiguration of the experimental rig in accordance with the requirements of the research.

1.3 RESEARCH OBJECTIVES AND ORIGINALITY OF THE RESEARCH

The principal objectives of the research were:

1. *To carry out a comprehensive modelling of multi-phase voltage source inverters, with emphasis on five-phase, seven-phase and nine-phase VSIs.*

2. *To investigate characteristics of continuous carrier-based and space vector based pulse width modulators for multi-phase VSIs, operating in the linear modulation region, and supplying multi-phase machines with the numbers of phases as stated in 1.*

3. *To examine advantages and shortcomings of both approaches defined in 2 and establish bi-directional link between carrier-based and space vector pulse width modulators for multi-phase VSIs.*

4. *To develop PWM schemes for multi-phase VSIs (using carrier-based and space vector approach), which are able to produce multi-frequency output voltage applicable to control of multi-phase series-connected multi-motor drives.*

5. *To develop PWM schemes for multi-leg VSIs (using carrier-based and space vector approach), which are able to produce multi-frequency output voltage applicable to control of several three-phase machines in accordance with the multi-leg VSI fed multi-motor drive structure.*

6. *To explore and develop analytical tools for characterisation of the dc bus utilisation in multi-phase/multi-leg drives.*

7. *To investigate output harmonic current ripple in multi-phase drives caused by the application of various PWM schemes.*

8. *To design and build nine-phase two-level VSI with accompanying DSP control system for the purpose of experimental verification of results obtained by theoretical and simulation studies.*

By achieving the objectives listed above, a significant body of new knowledge has been produced. This is partially evidenced by the already published research papers that have resulted from the thesis (and are appended to the thesis in Appendix D). Chapters 4 to 10 contain the original results from the research and therefore represent the main contributions of this thesis.

1.4   ORGANISATION OF THE THESIS

This thesis is organised in 12 chapters, followed by 4 appendices.

Chapter 1 contains an overview of multi-motor and multi-phase drive systems. Existing three-phase multi-machine drive systems are introduced and recently developed multi-motor drives with multi-phase machines in series/parallel connection to a single multi-phase VSI are briefly surveyed. A reduced switch-count topology based on the use of several three-phase machines supplied from a single multi-leg VSI is identified as a potentially viable solution for reduction of the overall cost of the multi-motor drives. The need for the research conducted within the scope of this thesis is thus established and objectives of the research are finally set forth.

Chapter 2 presents a literature survey in the area of PWM techniques for multi-phase variable speed drives. Due to the differences in PWM for two-level VSIs with an odd and with an even phase number and having in mind that the emphasis in this thesis is on VSIs with an odd number of phases, PWM methods applicable to inverters with odd and even number of phases are reviewed separately. Further, the existing PWM strategies suitable for multi-frequency output voltage generation, of the type required for the drive configurations of Figs. 1.1 and 1.2, are addressed. The chapter also includes a survey of existing PWM methods for the multi-leg inverter supply topology of Fig. 1.3.

The modelling and space vector representation of multi-phase VSIs are addressed in chapter 3. The voltage space vectors, represented in multiple two-dimensional (2-D) planes, are obtained with the use of a decoupling transformation applied to a five-phase, seven-phase and nine-phase VSI. The mapping of harmonics of different order after transformation is explained for every analysed number of phases. This foundation is therefore necessary for development of the PWM methods based on the space vector approach. Additionally, modelling aspects of a multi-leg VSI are covered, emphasising similarities with a three-phase VSI that are used later on for development of the PWM scheme.

Chapter 4 deals with development of continuous SVPWM schemes for a five-phase VSI for sinusoidal output voltage generation. Three different schemes are presented based on the utilisation of different sets of active space vectors. It is demonstrated at first that simple extension of well known principles of a three-phase SVPWM does not yield sinusoidal output voltage. Therefore, two SVPWM schemes are introduced, based on the use of four active space vectors, which are able to generate sinusoidal harmonic-free output voltage.

Experimental results that are collected from a five-phase star-connected *R-L* load show excellent match with predicted theoretical results obtained by means of simulations.

Development of SVPWM schemes for a seven-phase and nine-phase VSI, based on vector space decomposition (VSD) approach, is presented in chapter 5. Sinusoidal output voltage is obtained for both considered topologies based on application of six and eight active space vectors, respectively. Obtained simulation and experimental results from seven-phase and nine-phase *R-L* loads are in excellent agreement, confirming the feasibility of developed schemes. Theoretical development presented in chapter 4 and chapter 5 is further extended and general structure of a multi-phase SVPWM modulator for sinusoidal output voltage generation with odd phase number VSIs is derived.

Carrier-based PWM schemes for multi-phase VSIs are analysed in chapter 6. Based on the simple extensions of well known principles for three-phase drives, general structure of multi-phase carrier-based modulator is established. Principle of zero-sequence injection is adapted to multi-phase VSIs, and influence of various selections of zero-sequence signal is analysed. Main properties of carrier-based PWM schemes are identified and a link with characteristics of SVPWM is established, thus correlating these two different approaches. Experimental results are presented, confirming theoretical findings.

In chapter 7 an analytical analysis of current ripple in five-phase drives caused by application of different PWM schemes is presented. Theoretical analysis is based on the space vector theory and is termed 'complex approach'. Characteristics of current ripple are analysed using the concept of harmonic flux in order to simplify analysis placed in two 2-D planes. Obtained theoretical results are experimentally verified on a five-phase drive.

Chapter 8 presents an alternative method to analyse current ripple in multi-phase drives and is termed 'polygon approach'. The method relies on the use of multiple polygon connections that exists in multi-phase systems, and offers generic solutions applicable to all multi-phase topologies. Thus, results from the chapter 7 are confirmed once more in an alternative fashion. Additionally, output current ripple characteristics of other multi-phase systems (including three-phase one) are determined and verified by means of simulations.

Chapter 9 contains complete development of a PWM scheme able to provide multi-frequency output voltage necessary for control of multi-phase series-connected multi-motor drives. Both carrier-based and space vector approach are elaborated in great depth, and verified experimentally on a five-phase two-motor drive. Finally, problem of voltage limits is addressed and a simple analytical method is devised for characterisation of the linear modulation operational range of various multi-phase multi-motor drives.

Multi-leg VSI fed multi-motor drives are analysed in chapter 10. A novel PWM method is developed, by effectively utilising existing knowledge related to three-phase PWM methods. Voltage limits are also explored and behaviour of a five-leg VSI fed two-motor, seven-leg VSI fed three-motor and nine-leg VSI fed four-motor drives is experimentally investigated, proving the effectiveness of the PWM scheme.

Chapter 11 provides conclusions and a summary of the thesis, highlighting the most important findings from each chapter. Guidelines for future research are also given.

References are listed in chapter 12.

Chapter 2

STATE OF THE ART IN PULSE WIDTH MODULATION FOR MULTI-PHASE/MULTI-LEG VOLTAGE SOURCE INVERTERS

2.1   PRELIMINARY REMARKS

The literature review given here is aimed to present the latest developments in the area of PWM strategies for multi-phase/multi-leg VSIs used in variable speed drives. However, an attempt is made to provide the survey with some kind of historical chronology in order to provide a better understanding of the recent developments in this area. Research efforts in the past have been focused on various aspects of multi-phase drives and attention is here paid to what is believed to be the most important issues relevant for the scope of this thesis. Thus, references are classified according to their content and are discussed in separate sub-sections for clarity reasons. Attention given to reduced switch-count drives or multi-leg VSI fed multi-motor drives (the term that will be used in the thesis) is focused on topologies that utilise more than one three-phase machine. An effort is made to make this review complementary to those reported already in Jones (2005) and Iqbal (2005), and also up-to-date by covering the latest results, published in the area of research up to the end of the year 2007. Several survey papers are currently available covering many aspects of multi-phase drives and offering extensive bibliography for further reading [Singh (2002), Jones and Levi (2002), Bojoi et al (2006a), Levi et al (2007b)].

In what follows, multi-phase drives in pre-PWM era with the inverter switching at fundamental frequency are addressed first. With proliferation of use of PWM in modern variable speed drives, focus of research has gradually shifted to PWM for multi-phase machines with various phase numbers. Thus, PWM methods for multi-phase drives with even phase number are addressed next, predominantly covering six-phase drives. Drives with odd phase numbers are further discussed, separately for each of the winding arrangements that may be used. Finally, existing PWM methods for multi-leg VSI fed drives are surveyed.

2.2 THE EARLY DAYS – 180° CONDUCTION MODE

There are three main reasons why multi-phase machines/drives were considered as an alternative to the well established three-phase drives, in the early days of development [Ward and Härer (1969), Nelson and Krause (1974), Ferraris and Lazzari (1983)].

The first one is the ability to achieve operation with better (lower) torque ripple. Due to the square-wave (six-step) mode of operation, used at that time for three-phase inverters, such a control was inevitably producing low frequency torque ripple. The lowest frequency torque ripple harmonic in an n-phase machine is caused by the time harmonics of the supply of the order $2n\pm1$ with ripple frequency $2n$ times higher than the supply frequency. Thus, it has been observed that an increase in the number of phases of a machine is a potential solution for this problem, since frequency of the torque ripple can be effectively increased, with a corresponding decrease of the ripple magnitude at the same time [Apsley et al (2006)].

Probably the first variable speed multi-phase machine drive was reported by Ward and Härer (1969). Ten-step mode of operation was investigated utilising a five-phase thyristor based inverter supplying a five-phase induction motor. It was suggested at the time that it is preferable to use multi-phase machines with an odd number of phases since in the case of even phase numbers, with spatial displacement between any two consecutive two phases equal to $2\pi/n$, the resulting torque pulsations have the same frequency and amplitude as in a machine with only half as many phases. It was also observed that increasing the number of phases leads to a reduction of the amplitude of torque pulsations with simultaneous increase in their frequency. Experimental investigation concluded that in the case of a five-phase machine, the amplitude of torque fluctuations was about three times smaller than in a corresponding three-phase machine, but it was also noticed that the level of the third harmonic in motor line current was too high, which increased the losses in the motor. The reason for this is the ten-step mode of operation of a five-phase inverter which limits the number of space vectors that can be used for output voltage generation (only 10 large space vectors from the set of 32 space vectors in total).

Another comprehensive analysis of the five-phase induction motor drive was reported by Pavithran et al (1988). The objective was to improve the waveform of the motor phase current while keeping torque pulsations as low as possible. Mathematical model, based on complex symmetrical components, was applied for theoretical analysis. A thyristor based five-phase inverter was used to carry out experiments with a 45 slot frame, six poles, 3 hp five-phase induction motor. It was noticed that there is a trade-off in the attempt to achieve

good output current waveform (low distortion) and low torque ripple. If the harmonic elimination procedure is chosen to improve the machine current waveform, it would lead to increased torque pulsations. On the other hand, harmonic elimination pattern that minimizes the torque pulsations in the drive results in poor machine current waveform. The situation was significantly improved when PWM was employed, resulting in nearly sinusoidal current waveform with the torque ripple at 30 times the fundamental frequency. Although torque ripple was still rather high, it was anticipated that due to its high frequency it would get filtered by the inertia of the drive.

A six-phase induction machine, designed with two sets of three-phase windings spatially shifted by 30 degrees and with isolated neutrals, was also extensively investigated in the early days. With this stator winding layout, spatial displacement between two consecutive phases is not constant any more, and when machines are designed with multiple three-phase windings, spatial displacement between any two consecutive three-phase windings is π/n. The net result is that the lowest torque ripple harmonic appears again at $2n$ times the fundamental frequency, as with multi-phase machines having an odd number of phases (and in contrast to the even phase numbers with uniform spatial displacement between consecutive phases of $2\pi/n$, where the lowest torque ripple harmonic is of the order n). Supply was provided from a six-phase voltage source inverter [Abbas et al (1984)] or a six-phase current source inverter [Andersen and Bienek (1981), Gopakumar et al (1984), Dente and Labrique (1985)]. The obvious gain of using multi-phase machines with two (or more) three-phase windings is that the supply can be easily obtained by means of two (or more) three-phase inverters.

Nowadays, this advantage of multi-phase machines has become less important since with the use of PWM methods harmonic content of the inverter output voltage can be effectively controlled. This is especially true for low and medium power applications. However, in very high power applications, due to the limitations of the present power semiconductors related to the relatively low switching frequencies required to maintain low switching losses, this advantage offered by multi-phase machines, is still relevant.

The second reason that initiated early development is the fact that for a given machine's output power, utilisation of more than three phases enables splitting of the power across a larger number of inverter legs, thus reducing per-leg (per-switch) ratings of power semiconductors [Ferraris and Lazzari (1983)]. This is important in high power applications, where limited ratings of power semiconductors can make realisation of three-phase converters rather difficult. Nowadays, electric ship propulsion systems are one of the main areas where multi-phase machines are seriously considered and used in practice. Thus, a fifteen-phase 19

MW drive system has been developed for military applications [McCoy and Benatmane (1998), Benatmane and McCoy (1998)]. Survey papers on marine electric propulsion systems and recent developments have been presented by Hodge et al (2002) and Hodge et al (2004).

Finally, the third advantage common to all multi-phase drives is an increased fault tolerance when compared to their three-phase counterparts [Jahns (1980)]. If one phase of a three-phase machine becomes open-circuited the machine becomes single-phase. In contrast to this, a multi-phase machine can continue to develop rotating field as long as the number of open-circuited phases is no more than n-3. Continued post-fault tolerant operation requires addition of some kind of post-fault control strategy to the drive control system. Selection of the strategy will depend on several parameters such as: type of the machine, type of power converter, or some other control criteria specified in advance. For example, fifteen-phase ship propulsion system described by Benatmane and McCoy (1998), is implemented with independent H-bridge inverters for each phase of the machine, while the machine itself is designed with three sets of isolated five-phase windings.

While, as stated already, increase in the torque ripple frequency enabled by an increase in the number of phases is of relatively little importance in modern PWM variable speed drives, distribution of power over a higher number of phases and fault tolerance are still as relevant as they were in the past. They are the main reasons for an increased interest in multi-phase machines and drives in recent times.

2.3   PWM TECHNIQUES FOR TWO-LEVEL MULTI-PHASE VOLTAGE SOURCE INVERTERS

By and large, the existing research in connection with PWM control of multi-phase drives is related to the two-level VSI and is mostly based on the SVPWM approach. While carrier-based PWM methods are simpler to implement, SVPWM methods offer better insight into properties of multi-phase drives and have therefore been analysed more frequently. It should be noted here that utilisation of multi-phase multi-level inverters has also been considered for high-power applications such as electric ship propulsion [Corzine et al (1998), Lu and Corzine (2005), Gritter et al (2005)] or locomotive traction [Steiner et al (2000)]. Control of multi-phase multi-level inverters is however beyond the scope of this thesis.

As already noted stator windings of an n-phase machine can be designed in such a way that the spatial displacement between any two consecutive stator phases equals $\alpha = 2\pi/n$, in which case a symmetrical multi-phase machine results. This will always be the situation if the

number of phases is a prime number (for example, five-phase or seven-phase machines) and machine will have a single neutral point. However, if the number of phases is an even number or an odd number that is not a prime number, stator windings may be realised in a different manner, as k sets of a-phase windings, resulting in a machine with k neutral points (which can form a single neutral point or may be mutually isolated), since $n = k \cdot a$. Typically, $a = 3$ and $k = 2,3,4,5...$, resulting in a machine with multiple sets of three-phase windings. However, a fifteen-phase machine can be realised with multiple sets of three-phase windings or five-phase windings [Benatmane and McCoy (1998)], and thus a can be three or five. In this kind of arrangement of windings, spatial displacement between first phases of the two consecutive sets of a-phase windings is $\alpha = \pi/n$ leading to an asymmetrical multi-phase machine. It is important to emphasize here that the notions of asymmetrical and symmetrical windings are used in conjunction with the disposition of phase magnetic axes in the cross-section of the machine.

An important property of multi-phase machines is the fact that flux and torque control of a multi-phase machine requires only two currents regardless of the number of phases. Taking as an example an n-phase machine (where n is a prime number) in star connection with single neutral point, there are therefore n-3 additional degrees of freedom (currents) that can be utilised for other purposes. If a machine is with concentrated winding, thus having quasi-rectangular mmf distribution, injection of a certain amount of low order harmonic into stator supply voltage can be used to enhance torque production. For a machine with distributed windings (near-sinusoidal mmf distribution) additional degrees of freedom can be used for realisation of multi-motor drives with several multi-phase machines in series/parallel-connection, with supply coming from a single multi-phase VSI. Alternatively, additional degrees of freedom can be used to design fault tolerant control strategies. Arrangement of the windings on stator has a great impact on what kind of output voltage multi-phase inverter should generate and therefore a variety of PWM methods have been reported in literature, which are suitable for particular types of machines. It is important to note that an n-phase machine (where n is a prime number), in addition to star connection, can also be connected in $(n$-1$)/2$ different polygon connections. Ferraris and Lazzari (1983) analysed such a possibility for various phase numbers. However, to this date, feasibility of using polygon connections in practice has never been demonstrated.

With regard to the modulation methods used, the emphasis in research has been placed on SVPWM methods. Since an n-phase system corresponds to an $(n-1)$-dimensional space

(n is regarded here as a prime number and the star-connected load is with single isolated neutral point), the customary approach towards designing a SVPWM scheme consists in decomposing the (n-1)-dimensional space into (n-1)/2 2-D sub-spaces (planes), using either real decoupling transformations or the symmetrical component approach [Zhao and Lipo (1995), Grandi et al (2006a)]. Each of the available 2^n voltage space vectors of an n-phase VSI appears simultaneously in all such 2-D planes (d_1-q_1, d_2-q_2, etc.). Development of the SVPWM schemes in almost all of the available studies follows the principle of the vector space decomposition (VSD) introduced by Zhao and Lipo (1995). Selection of the active VSI voltage vectors must be performed considering all (n–1)/2 2-D planes, if the fundamental and harmonic components are to be correctly controlled. In order to generate sinusoidal output voltages, the number of used active space vectors depends on the number of 2-D planes that need to be considered. The general rule can be established that one needs to apply n-1 active space vectors over a switching period in order to generate sinusoidal output voltages. These are selected as the active space vectors neighbouring the reference space vector in the given sector of the first d_1-q_1 plane. Since all space vectors map simultaneously into all (n-1)/2 planes, each of the (n-1)/2 planes will contain certain low-order harmonics and further development of the SVPWM depends on the type of the multi-phase machine and/or on the number of machines controlled from a single VSI supply. Although both carrier-based PWM and SVPWM methods have been analysed in the past for multi-phase VSIs, no link between basic properties of two approaches has been established, such as the one reported for three-phase PWM methods by Zhou and Wang (2002).

2.3.1 PWM METHODS FOR AC DRIVES WITH EVEN PHASE NUMBERS

Among all even phase numbers, six-phase drives are the most frequently analysed ones. The origins can be tracked all the way back to the beginning of the twentieth century [Alger et al (1930)] when this configuration was introduced to increase the total power capability of large synchronous generators. There are two possible six-phase machine structures. In the most common one, asymmetrical six-phase machine, stator winding consists of two three-phase windings shifted in space by 30°. In the other structure, symmetrical six-phase machine, there are two sets of three-phase windings that are spatially shifted by 60°, giving rise to uniform spatial displacement between any two consecutive phases of 60°. Most of the existing work is related to asymmetrical six-phase machines with two isolated neutral

points (this type of machine comes under various names including dual three-phase machine or split-phase machine).

Modelling of asymmetrical six-phase machines is elaborated in works of Lipo (1980), Hadiouche et al (2000) and Razik et al (2005). Field oriented control for dual three-phase drives and their characteristics are presented in works of Bojoi et al (2002a), Bojoi et al (2003) and Bojoi et al (2006b). Bojoi et al (2006c) have also demonstrated that such a drive can be controlled using only two current sensors placed in phases belonging to different three-phase sets, without any significant deterioration of the drive performance. Since the asymmetrical six-phase machine is the common choice, most of the available work regarding PWM techniques applies to this type of the machine. If an asymmetrical six-phase machine is supplied from a VSI controlled using 180° conduction mode or the simplest SVPWM, large harmonic non-flux/torque producing currents appear in the machine [Gopakumar et al (1993a)]. Zhao and Lipo (1995) have therefore proposed an improved SVPWM, based on VSD approach, with the aim of eliminating harmonics of the order $6k\pm1$ ($k = 1, 3, 5...$). These harmonics do not contribute to the torque production but lead to large stator current harmonics of the low order, restricted only by the stator leakage impedance. Implemented SVPWM scheme uses four adjacent active space vectors with the largest magnitude from the first plane. Times of application are calculated in such a way to zero above mentioned harmonic components from the second plane. Compared with other digital PWM strategies for an asymmetrical six-phase machine, VSD approach to SVPWM gives much better results from the point of view of harmonic minimisation than other methods, however with an increased computational demand in implementation, as reported by Bojoi et al (2002b). Significant improvement with regard to the implementation complexity has been recently reported by Hadiouche et al (2006), where both continuous and discontinuous space vector PWM methods have been elaborated. Some other strategies for PWM signal generation in conjunction with asymmetrical six-phase machines have also been proposed by Gopakumar et al (1993b) and Bakhshai et al (1998).

A different control scheme for asymmetrical six-phase machine, which requires modification of the PWM, has been reported by Lyra and Lipo (2002). They have shown that by connecting two neutral connections into a single one and by further connecting the neutrals to the mid-point of the split-capacitor dc bus, structure becomes feasible for injection of the third harmonic (zero sequence) current components in the phase currents, which greatly improves the machine's torque density.

PWM control aimed at feeding a symmetrical six-phase machine has been investigated to a much lesser extent. Performance of vector controlled symmetrical six-phase drive has been investigated by Vukosavić et al (2005) without detailed considerations of the PWM method. Due to the different phase shift between VSI output voltage space vectors, the difference between the SVPWM control of asymmetrical and symmetrical six-phase VSIs is considerable. Currently available works, related to the SVPWM of symmetrical six-phase VSIs, are those of Correa et al (2003a), Correa et al (2003b) and Correa et al (2003c). These have considered a system with isolated neutral points of the two three-phase windings and have developed symmetrical PWM schemes with commutation in a single inverter leg in transition from one space vector to the other, so that the minimum number of commutations takes place and the switching frequency of all inverter legs is the same (and equal to the inverter switching frequency). It is also possible to devise space vector PWM schemes where switching frequency varies from one inverter leg to the other. Kianinezhad et al (2005) have demonstrated development of such a SVPWM scheme for a symmetrical six-phase VSI. Although it also yields sinusoidal output, uneven switching frequency in different inverter legs makes it inferior when compared to the other schemes for sinusoidal output voltage generation. SVPWM scheme for a symmetrical six-phase machine with single neutral point has been developed using VSD approach and verified experimentally for various selections of active space vectors within the switching period [Dujić et al (2006)]. Dujić et al (2007a) have presented scheme aimed at producing sinusoidal or near-sinusoidal voltages across the entire range of possible fundamental output voltage for a symmetrical six-phase VSI.

Among other drives with even phase number, twelve-phase synchronous machine in configuration with four sets of three-phase windings spatially shifted by 15° has been analysed by Hua et al (2006). Yet, supply for such a machine has been provided from four three-phase cycloconverters with 15° phase shifted output, and not from a multi-phase VSI.

2.3.2 PWM METHODS FOR AC DRIVES WITH ODD PHASE NUMBERS (MACHINES WITH DISTRIBUTED WINDINGS)

When the windings of the machine are distributed on the stator core, so that near-sinusoidal mmf distribution results, output voltage coming from the inverter, must contain only fundamental component without any low order harmonic components. This is of special importance, since any low order harmonic voltage components are restricted only by the stator leakage impedance and their existence can therefore cause large unwanted harmonic currents, thus increasing losses in the machine.

Silva et al (2004) have reported development of a SVPWM scheme for a five-phase VSI aimed at sinusoidal output voltage generation. Phase voltages of a five-phase system are transformed into two 2-D spaces (two planes). A simple extension of the three-phase SVPWM (use of only two adjacent large active space vectors per switching period) does not produce sinusoidal voltage output in a five-phase system and therefore more than two active vectors must be used. Use of four active space vectors (two large and two medium) is proposed with appropriate calculation of active space vector application times in order to obtain cancellation of activated space vectors in the second plane. The state durations are weighted by the factor 1.6180 which is the ratio between the large and medium active space vectors in the first plane. To decrease the number of switching events per cycle and hence switching losses as well, dead banding of one inverter leg is proposed, thus leading to discontinuous PWM (DPWM).

SVPWM schemes, reported by Iqbal and Levi (2005) and Iqbal and Levi (2006a), yield the same sinusoidal output voltage, achieved again by using four active space vectors per switching period. The same dwell times are obtained, although in a different way compared to Silva et al (2004). As long as pure sinusoidal output voltage is considered, SVPWM offers an increase in the dc bus utilisation of 5.15%, compared to the simplest sinusoidal modulation. In order to further extend the operational range and thus improve dc bus utilisation, a scheme based on use of only two large vectors is considered. This inevitably leads to introduction of low order harmonics into inverter output voltage since the second plane is not any more considered during implementation. A gradual transition is suggested from the use of four active space vectors per switching period to use of only two large space vectors per switching period, once when the maximum dc bus utilisation is reached for the former method. Thus, operation in the higher range of modulation index is accompanied by the introduction of an amount of low order harmonics.

Xue and Wen (2005) have presented simulation results for two SVPWM strategies for sinusoidal output voltage generation. The first method is identical as those already elaborated [Silva et al (2004), Iqbal and Levi (2005), Iqbal and Levi (2006a)] and is based on use of two medium and two large space vectors per switching period. The second method also uses four active space vectors, but this time four adjacent large active space vectors are selected per switching period, the same as in the work of Zhao and Lipo (1995) for an asymmetrical six-phase VSI. This selection of space vectors leads to increased and uneven number of commutations per inverter leg, making the method suboptimal from the point of view of switching losses, as well as from the point of view of easiness of implementation. However,

synthesis of sinusoidal output voltage is possible, since cancellation of harmonic components can be achieved in the second plane by introducing proper dwell times. Another implementation of the SVPWM for five-phase drives has been reported by Xue et al (2006). The same switching pattern is used with four active space vectors per switching period. Theoretical findings are verified with experimental results.

Carrier-based PWM methods for a five-phase VSI were analysed in Iqbal et al (2006a), Ojo and Dong (2005), and Casadei et al (2005). By extending the well known third harmonic injection principle for three-phase VSIs, it has been shown that in the case of a five-phase VSI injection of the fifth harmonic leads to an increase in the dc bus utilisation in the linear modulation region by 5.15% [Iqbal et al (2006a)]. This principle can be applied to any odd n-phase number machine, where injection of the n-th harmonic can be used, although the improvement in dc bus utilisation rapidly decreases as the number of phases increases. A generalised continuous carrier-based approach that allows control of both the fundamental and the third harmonic, with emphasis on voltage limit problems, has been presented in Casadei et al (2005), while discontinuous carrier-based modulation schemes have been elaborated by Ojo and Dong (2005). Several DPWM schemes for a five-phase VSI, obtained by direct extension from the well known DPWM schemes for three-phase drives, have been compared by means of simulation by Zhang et al (2006). It was observed that the total harmonic distortion (THD) of DPWM methods decreases with increasing modulation index, thus suggesting use of DPWM in drives that usually operate with high value of the modulation index. However, other relevant figures of merit were not used to compare continuous PWM (CPWM) and DPWM methods.

The only analysis of SVPWM for a seven-phase VSI has been conducted by Grandi et al (2006b). Space vectors of a seven-phase system were analysed in three planes, and zero reference space vector in the second and the third plane was imposed in order to prevent generation of the fifth and the third harmonic, respectively. To achieve sinusoidal output voltage six active space vectors are used per switching period, thus following the general rule that in an n-phase system n-1 active space vector must be applied. Switching pattern is organized so as to have the minimal number of commutations and verification of the modulator performance has been done by means of simulation. Seven-phase SVPWM provides an increase of 2.57% in the dc bus utilisation when compared to the sinusoidal modulation.

A nine-phase machine's windings can be connected in two ways, with a single neutral point and with three isolated neutral points. Development of PWM schemes for a machine

with windings in star connection with single neutral has been investigated by Kelly et al (2003) and Grandi et al (2007a). Kelly et al (2003) have investigated pole-phase modulation and used symmetrical nine-phase machine as an example. Main characteristics of nine-phase VSI are analysed, considering eighteen-step mode of operation and PWM as well. Space vectors of a nine-phase VSI are derived and further classified into sub-sets, based on the equivalent load configuration, when these space vectors are applied. It is recognised that for implementation of a SVPWM, only those space vectors with largest magnitude from every sub-set should be used. Due to the increased number of space vectors of a nine-phase VSI, implementation of the PWM method was performed based on carrier-based offset injection PWM (basically injection of the ninth harmonic and its odd multiples), which is the equivalent of the SVPWM based on use of eight active space vectors per switching period. This is justified with simplicity in implementation, compared to the SVPWM, where time consuming calculations need to be performed to obtain dwell times. An increase in the dc bus utilisation of only 1.54% is obtained compared to the simplest sinusoidal modulation. Another discussion of the SVPWM for a nine-phase VSI, based on the consideration of four 2-D planes and aimed at sinusoidal output voltage has been reported by Grandi et al (2007a). It was demonstrated, by means of simulations, that in order to cancel harmonic components in all planes other than the first one, eight active space vectors must be used with properly determined dwell times. Nine-phase windings can also be connected as three sets of three-phase windings on the same stator core, with three isolated neutrals. Development of a PWM scheme for such a drive was reported in Grandi et al (2007b). Such a configuration of windings enables improvement in the dc bus utilisation that is the same as for three-phase drives, which is 15.47%.

Finally, development of a PWM scheme for a fifteen-phase VSI with load connected as five sets of three-phase windings was described in Wang et al (2007). Presented development is based on the orthogonal vector space concept, thus being very similar to most of the work related to SVPWM methods for multi-phase inverters. However, only four active space vectors are selected per switching period, since developed SVPWM scheme is based on consideration of only two planes: the fundamental plane and the fifth harmonic plane. Other planes corresponding to harmonics of orders $30k \pm 7$, $30k \pm 11$ and $30k \pm 13$ ($k = 0, 1, 2, 3...$), are ignored in order to reduce the number of calculations and make the SVPWM scheme computationally efficient. When implemented, such a SVPWM utilises only 30 active space vectors out of the total of $2^{15}=32768$ space vectors offered by the fifteen-phase two-level VSI, at the expense of generation of the above mentioned low order harmonics.

On the basis of the presented survey it can be concluded that in most of the cases SVPWM schemes for *n*-phase VSIs aimed at pure sinusoidal output voltage generation are based on the utilisation of *n*-1 active space vectors per switching period. Such a selection appears as a very natural one when the carrier-based PWM methods are analysed in a greater depth, as it will be shown in the thesis, and makes it easier to understand similarities and connections among two approaches.

2.3.3 PWM METHODS FOR AC DRIVES WITH ODD PHASE NUMBERS (MACHINES WITH CONCENTRATED WINDINGS)

As explained already, machines with a prime number of phases are always considered as being star connected with a single neutral. In contrast to three-phase machines. which are normally designed with a distributed stator winding (with exception of a brushless dc motor), multi-phase machines are more versatile with regard to this design aspect. An increase of the number of phases makes it more difficult to realise a distributed winding machine and multi-phase machines with concentrated windings are therefore very common. Such a machine offers a possibility to enhance torque production by injection of stator current harmonics. For an *n*-phase machine, all odd harmonics in between 1 and *n* can be used to couple with the corresponding spatial mmf harmonic in order to increase the total average torque. Thus for a five-phase machine the third harmonic can be used [Ryu et al (2005), Xu et al (2001)], for a seven-phase machine the third and the fifth [Toliyat et al (1991), Locment et al (2006)], for a nine-phase machine the third, the fifth and the seventh [Coates et al (2001)], etc.

In order to achieve this, the PWM method must generate multi-frequency output voltage from the VSI as a supply to the machine, while controlling simultaneously magnitudes of both fundamental and the harmonic component(s). However, such a multi-frequency output voltage is in this case with a well known relation between the fundamental and the harmonic components regarding frequencies, magnitudes and phase shifts. The amount of injected harmonic components usually represents around 10%-20% of the fundamental. Ryu et al (2005) have demonstrated development of a SVPWM method based on the multiple *d-q* space concept for multi-phase machines with concentrated windings, where non-sinusoidal air gap flux density distribution is preferable to increase the torque per-ampere ratio. A five-phase inverter is used as a practical example and the devised method uses pre-selected (using only the first plane) four active space vectors per sector (two large and two medium space vectors neighbouring the reference). Injection of the third harmonic with a phase equal to 180° at the same time enhances torque and increases dc bus utilisation.

Ojo et al (2006) have presented a PWM method for control of a five-phase VSI that can generate inverter output voltage with or without the third harmonic component. Thus, the method can be utilised for machines with both types of the stator winding. The method uses pre-selected four active space vectors from the first plane (where fundamental component is) and the principle of superposition to calculate duration of active space vectors in each plane, before creating the final switching pattern. Although classified by authors as a carrier-based method, due to the nature how durations of active space vector application are obtained, the method is closer to the SVPWM. A similar PWM method of mixed nature, termed 'duty cycle space vector' approach (DCSV), is elaborated in Casadei et al (2005) and Casadei et al (2007). The method combines multiple space vector representation of multi-phase systems with traditional carrier-based modulation providing directly per-leg duty cycles over the switching period. Additional zero-sequence is added to modulation signals in order to centre them. The results, presented for a five-phase VSI with injection of the third harmonic, are in accordance with findings of Ryu et al (2005).

A synchronous reluctance machine with concentrated windings was investigated by Toliyat et al (1992), Toliyat et al (1998), Xu and Fu (2002) and Shi and Toliyat (2002). A 10% increase in the developed torque was reported. PWM methods, used in Toliyat et al (2000) and Shi and Toliyat (2002), were based on a direct extension of the SVPWM principle for a three-phase system. Thus only two large space vectors per switching period were used, which inevitably leads to development of both the fundamental and the low-order harmonic components. However, since the machine is with concentrated windings the impedance for the low-order harmonics is considerably larger than in the case of a machine with near-sinusoidal mmf, so that generated low-order stator current harmonics are rather small.

During implementation of methods based on the SVPWM approach, sequence of space vectors inside the switching period is determined in advance, at the development stage of a modulation scheme. Once when the sequence is known, durations of used vectors are calculated and duty cycles ('on' time over the switching period) per inverter legs are obtained. Additionally, in order to simplify analysis and development, SVPWM methods are almost exclusively based on VSD approach. A rather different approach, inspired by Gatarić (2000), is taken in Duran and Levi (2006) in order to develop a multi-dimensional SVPWM and avoid the use of VSD. Thus development of a PWM scheme for an n-phase system is done in the $(n\text{-}1)$-dimensional space, rather than in the $(n\text{-}1)/2$ 2-D spaces. The idea is to avoid pre-selection of the active space vectors, using the first plane only for the given reference space vector, which may have up to $n\text{-}1$ non-zero components. Instead, a criterion is defined that

promotes use of active space vectors that are the closest to the reference space vector in the (n-1)-dimensional space. If two space vectors are spatially at the same distance from the reference space vector in the (n-1)-dimensional space, the smaller space vector will be used for the output voltage generation. Simulations have confirmed feasibility of such an approach for both sinusoidal output voltage generation and generation of sinusoidal voltage with low order harmonic injection. Although it has been verified that the multi-dimensional SVPWM method can be implemented in real-time using look-up tables [Duran et al (2007a)], additional memory resources are required, compared to the other SVPWM methods. While theoretical value of the multi-dimensional PWM approach is high, the method is computationally very demanding and does not guarantee equal number of commutations per inverter legs. It is therefore of little practical importance at present.

2.3.4 PWM METHODS FOR MULTI-FREQUENCY OUTPUT VOLTAGE GENERATION

As already emphasised, irrespectively of the number of phases, only two currents are sufficient for independent flux and torque control of a multi-phase machine. The remaining degrees of freedom are usually used for enhancement of torque production (machines with concentrated windings) or design of post-fault control strategies. However, if a machine is with distributed windings, an entirely different possibility arises. Several multi-phase machines can be connected in series/parallel using an appropriate phase transposition. In such a connection flux/torque producing currents of one machine appear as non-flux/torque producing currents for all other machines and vice versa. While this idea, based on utilisation of a five-phase VSI to control two five-phase machines in series connections, was introduced by Gatarić (2000), the origins of the concept can be traced back to the work of Osama and Lipo (1999). They considered a symmetrical six-phase machine and supplied phases with two current components. One of these was generating flux and torque, while the second one was creating forces required for bearing relief, without impacting on the machine's flux and torque production.

Assuming that the VSI phase number is a prime number, (n-1)/2 n-phase machines can be connected in series using an appropriate phase transposition [Levi et al (2004a)]. The supply comes from a single n-phase VSI and the independent control of the machines is made possible thanks to the phase transposition introduced in the series connection [Levi et al (2004b)]. A corresponding analysis, covering multi-phase multi-motor drives with even numbers of phases, where (n-2)/2 machines can be connected, is described in Levi et al

(2003a). In this case all machines are not with the same number of phases. Investigation of a vector controlled six-phase two-motor drive, comprising a symmetrical six-phase machine and a three-phase machine in series connection, concluded that the current control in stationary reference frame is better suited to these drives [Jones et al (2004b), Jones et al (2005a)]. It is also pointed out that a six-phase machine should be with higher ratings than a three-phase machine since the six-phase machine's stator winding losses increase due to the series connection with the three-phase machine. However the three-phase machine is not affected in any way by the series connection with the six-phase machine. The concept is independent of the machine type and six-phase two-motor drive with induction and permanent magnet machine in series connection has been reported by Levi et al (2006a). A nine-phase multi-motor drive (similar to a six-phase two-motor drive) does not utilise machines with the same number of phases and it consists of three nine-phase machines and a single three-phase machine as the last one in the series-connection [Jones et al (2003b)]. Fully decoupled control is demonstrated by means of simulations. Performance of a five-phase two-motor drive, of the type proposed by Gatarić (2000), has been investigated using current control in the stationary reference frame [Levi et al (2003b)] and current control in the rotating reference frame [Jones et al (2004a), Jones et al (2005b)], using simulations. It has been shown that control in the rotating reference frame requires a modification of the vector controller structure in order to compensate additional voltage drops that appear due to the flow of currents of the other machine in the series connection. A seven-phase multi-motor drive utilises three seven-phase machines and the control scheme can be implemented in the same manner as for a five-phase two-motor drive [Jones et al (2003a)].

From the point of view of the PWM, a series-connected multi-phase multi-motor drive requires that multi-frequency output voltage is generated by the multi-phase VSI. While this is exactly the same requirement as for a multi-phase single motor drive with concentrated windings, there is a huge difference with regard to the required magnitudes and frequencies of the output voltage components. This corresponds to the situation where there is one reference voltage space vector in each of the planes (number of the planes is in the principle equal to the number of machines in the series connection). Magnitudes and frequencies of these $(n\text{-}1)/2$ reference voltage space vectors are now completely independent one from the other, in contrast to the harmonic injection case discussed earlier. Taking two-motor five-phase drive system [Levi et al (2007a)] as an example, the situation may arise where magnitude of the reference in the $d_2\text{-}q_2$ plane (reference voltage of the second machine) is considerably larger than the reference in the $d_1\text{-}q_1$ plane (reference voltage of the first machine). The existing

space vector PWM methods, with vector selection based on the reference in the first d_1-q_1 plane, are unable to cope with such a situation. Hence the experimental studies on two-motor series-connected five-phase and six-phase drive systems with a single VSI supply [Iqbal et al (2005), Levi et al (2007a), Mohapatra et al (2005), Levi et al (2005)] have all utilised carrier-based PWM, where desired inverter modulating signals are generated in a straightforward manner. By means of an appropriate summation of sets of references for two five-phase motors in series-connection, carrier-based multi-frequency PWM scheme is obtained [Iqbal et al (2006b)]. An additional zero-sequence component is added to centre peaks of modulating signals at equal distance from zero (assuming that they are bipolar). The only known attempt to develop a SVPWM method for the five-phase two-motor structure, using the concept of multiple 2-D sub-spaces, has been described in Iqbal and Levi (2006b). It was suggested to select in each of the two planes, completely independently, a set of four active space vectors neighbouring the corresponding reference. Then it becomes possible to create two voltage space vector references independently, using the same approach and the same analytical expressions as for the case of purely sinusoidal output voltage generation. However, the application of the selected vectors was done in such a way that d_1-q_1 plane reference voltage was generated in the first switching period, while the d_2-q_2 plane voltage reference was generated in the next switching period. Such an approach to realisation of the two space vector voltage references has automatically restricted the available fundamental for each of the two machines to only 50% of its maximum value for the given dc bus voltage (since only every second period is used for application of the voltage to any of the two machines). With such a method, even when one of the machines is at standstill and thus does not require voltage (except for magnetisation), the whole dc bus voltage is actually not available to the other machine. Therefore, such a SVPWM method is not good enough since it essentially requires doubling of the dc bus voltage (compared to a single-motor drive), while simultaneously disregarding actual operating states of the machines (and therefore effectively underutilising the available dc bus voltage).

A different possibility, which overcomes this problem of the dc bus voltage underutilisation, has been examined in Duran et al (2007b). It has been shown by simulation that the multi-dimensional SVPWM method can create multi-frequency output voltage effectively within the limitations of the available dc bus voltage. However, the method yields uneven switching frequencies in inverter legs, thus leading to increased switching losses, and is far too complicated for the real-world on-line implementation.

2.4   PWM TECHNIQUES FOR MULTI-LEG INVERTER FED MULTI-MOTOR DRIVES

Many industrial manufacturing processes in the textile, paper and steel industries require high-performance control of a number of converter-fed induction or synchronous machines. The motors frequently operate with different loads and speeds and it is therefore a requirement that the motors are independently controlled. One widely accepted alternative for reducing the cost of such multi-motor drive systems is to use a common dc bus while each three-phase motor has its own three-phase VSI as the supply. Further reductions in the complexity and capital cost can be achieved by employing converter topologies with a reduced number of power semiconductors.

Solutions proposed for single motor drives are mostly based on replacement of one of the three inverter legs with a split-capacitor leg. An important property of the resulting four-switch topology is that the PWM control can generate only two line voltages while the third one is obtained by means of the Kirchhoff's law from the split-capacitor bank in the dc link. Van der Broeck and van Wyk (1984) discussed the harmonic effects of the reduction of the number of switching devices at the output stage from six to four and the method of generating three-phase waveforms with two dc link voltages [Van der Broeck and Skudelny (1988)]. The modulation strategy suggested can produce three-phase balanced sinusoidal waveforms at a reduced output voltage of 86.6% compared to the conventional six switch inverter. In another topology proposed by Enjeti and Rahman (1993) and Enjeti et al (1993) the diode bridge rectifier is replaced by a single-phase current controlled rectifier, employing two switches and two capacitors, and thus enabling input current and input power factor control. Thus, only six switches are required to provide single-phase to three-phase power conversion with the capability of bidirectional power flow. Kim and Lipo (1996) proposed three-phase to three-phase VSI-PWM rectifier/inverter with eight switches. Two identical four-switch (H-bridge) inverters are used, for both rectifier and the inverter, with split-capacitor dc high voltage link. A SVPWM method, which minimises torque ripple for a four-switch inverter has been developed by Blaabjerg et al (1995), where it has been observed that such a topology is very sensitive due to the nonlinearities, especially at low modulation indices. An overview of reduced switch-count converter topologies for three-phase drives is given in Lee et al (2001). Some of the drawbacks of the reduced switch-count topologies include increased voltage stress on both the power semiconductors and the machine, increased switching losses due to a

higher dc link voltage, and single-phase circulating currents through the dc link split-capacitors.

Further analysis of reduced switch-count single motor drives is beyond the scope of the thesis. Only multi-motor three-phase drives are therefore addressed in what follows, and are termed further on multi-leg inverter fed multi-motor drives. As noted already, Bouscayrol et al (1996) have reported a comparative study of reduced switch-count drive structures including a four-leg inverter for supply of two three-phase machines (two legs of the inverter are common for both machines, while the remaining legs are connected to only one machine each). This structure however does not allow independent control of both machines. An alternative is to utilise a four-leg inverter with an additional split-capacitor bank as the fifth leg, in which case independent control of the machines becomes possible, although the topology suffers from problems associated with current flow through capacitors of the common leg. The same drive structure was analysed by Ledezma et al (2001) where connection of either two two-phase machines or two three-phase machines was considered. Use of two-phase machines offers advantages since switch utilisation ratio is the same as in the case of the standard six-switch inverter. Also, circulating current through the split-capacitors can be regulated towards zero value by controlling line current in each inverter to be 180° out of phase. This is however not possible to achieve when three-phase motors are used. The need for precise control of fluctuations of the mid-point potential of the split-capacitor has been analysed also by Oka and Matsuse (2006), who suggested that phase difference of 180° in the machine currents can suppress these fluctuations; this is however hard to satisfy with three-phase machines.

Another possible topology that reduces the number of inverter legs has been analysed by Francois and Bouscayrol (1999). Here a five-leg inverter (ten power semiconductor switches) is used to supply two three-phase induction machines. One phase of each motor is connected to the same leg of the five-leg inverter. The remaining inverter legs are connected to the other phases of motors. Thus, split-capacitor leg from topology analysed by Bouscayrol et al (1996) has been replaced with the fifth inverter leg. Developed PWM method is termed 'pulse position width modulation' (PPWM) and is based on separate modulation of voltages of each of the machines over two consecutive switching periods. To allow for operation over the full speed range for both machines, dc bus voltage has to be doubled, which in practice may not be allowable since it may cause problems related to insulation of the machine windings and ratings of the inverter power semiconductors. The PWM method utilises only 14 of the 32 available switching states of the five-leg inverter and effectiveness of the PWM

method was verified by simulations. Further development of the same concept, and confirmation that this configuration enables fully independent control of two machines, has been reported by Delarue et al (2001) and Delarue et al (2003a). The five-leg converter is again controlled in such a way that the voltage available to each machine is automatically restricted to half of the dc bus voltage. This is the result of the PWM technique, where two consecutive switching periods are once more used to apply required voltages to the two motors in an alternating manner. In essence, one machine is short-circuited by means of zero space vector application while voltage reference is imposed to the other machine, and vice versa. Hence only 50% of the dc bus voltage is available for one machine, regardless of the operating conditions of the other machine. This PWM scheme leads also to a harmonic side-band around one half of the switching frequency, thus increasing switching losses. The complete PWM scheme has been developed based on the fact that inverter is with five legs, thus resulting in a complicated control structure for a five-leg VSI fed two-motor drive.

A generic control method for multi-leg VSIs has been reported by Delarue et al (2003b). The method is based on the analysis of line voltages of the inverter and it requires large conversion tables to be determined for every multi-leg topology in advance. The method has been verified experimentally for two-leg, three-leg, four-leg and five-leg VSI supplying balanced and unbalanced loads. The problem of only 50% dc bus voltage availability for each of the two machines in five-leg VSI topology has been overcome here by using 31 instead of 14 switching states. This has enabled an arbitrary distribution of the dc bus voltage between the two machines.

A comparison of two reduced switch-count topologies against the standard industrial solution, based on utilisation of independent converter-machine units connected to the same dc bus voltage, has been presented by Jacobina et al (2002). The first topology uses multiple two-leg inverters to supply three-phase machines, where the third phases of each machine share the additional inverter leg. The second topology has a split-capacitor leg instead of the additional inverter leg. Both topologies represent generalisation and extension of the concepts explained earlier. Thus to control n three-phase machines, the first topology would require $2n+1$ inverter legs, while the second topology would require $2n$ inverter legs and an additional split-capacitor leg. Standard industrial solution requires $3n$ inverter legs to control n three-phase machines. Analysis has been carried out on a conceptual level, and requirements for increased ratings of the common inverter leg have been recognised. The additional inverter leg is the preferred solution over the split-capacitor leg since such a topology exhibits lower harmonic distortion (although it is still higher compared to the standard solution).

Various connections of two two-phase machines, two three-phase machines and three-phase and two-phase machine to the five-leg VSI are elaborated and main characteristics of each topology are addressed in Jacobina et al (2005). Here, considerations regarding the PWM scheme are given for every analysed topology, and two modulation schemes are suggested for multi-leg VSI fed multi-motor drives. Both PWM schemes prioritise one of the three-phase machines during development of the PWM scheme and adapt voltage requirements of other machines in the multi-motor drive. Injection of zero-sequence signals is used to extend operation in the linear region, while in the case of the second PWM scheme injection is used to improve THD of currents of only one of the three-phase machines. Operation of two permanent magnet motors fed from the five-leg inverter and controlled by PWM method named "expanded two arm modulations" (ETAM), has been reported by Kimura et al (2005). Additionally, problems of driving in parallel two permanent magnet synchronous motors with a five-leg inverter were analysed by Nozawa et al (2006). Attempts to improve the dc bus utilisation with the five-leg topology have been reported by Oka et al (2006). The improvement is obtained at the expense of prescribing the operating conditions of the two motors (speed and loading) as identical, and thus eliminating the possibility of independent control of the two motors.

Su et al (2006) have considered use of a five-leg inverter for control of two permanent magnet machines for automotive applications. The integrated drive system employs a five-leg inverter as the supply for a three-phase traction permanent magnet motor and a two-phase compressor motor by connecting the common terminal connection of the two-phase motor to the neutral point of the three-phase motor. Thus, in this topology, each phase of two machines has its own associated inverter leg, in contrast to the previously examined topologies. Independent control is achieved by implementing rotor flux oriented control (RFOC) for a three-phase motor and a similar RFOC and position sensorless control for the two-phase motor. Due to the nature of the connection it is suggested that two-phase compressor motor should be of smaller ratings compared to the three-phase traction motor in order to avoid high fluctuation in the currents of the traction motor due to the zero-sequence components caused by the two-phase motor.

A five-leg inverter requires ten power semiconductor switches and offers already saving of two switches compared to the standard industrial solution with one three-phase inverter per machine. Possibility for further reduction in the number of semiconductors of a reduced switch-count inverter, able to control two three-phase motors, is reported by Kominami and Fujimoto (2007). A nine-switch inverter, realised as three legs with three

series-connected power switches in each, has been developed for control of two three-phase machines. Machines are connected in the same fashion as with a standard three-phase VSI, to the existing mid-points of each leg. However, since there are three switches per leg, there are two sets of mid-points, the upper and lower, to which the two three-phase machines are connected. Such topology utilises separate modulation, since either all upper or all lower switches alternatively have to conduct at the same time, depending on which machine's voltage is modulated. However, the method allows for arbitrary allocation of the available dc bus voltage among the two machines, by adding an offset signal calculated based on the voltage requirements, to the reference signals of machines. It is observed that although independent control is possible, there are small mutual interferences in currents of the machines. Shibata and Hoshi (2007) have considered further reduction in the number of semiconductors of such a topology by replacing one of the legs with a split-capacitor leg (three series-connected capacitors). Such a reduction in the switch-count introduces an increase in the current ripple, as well as an increase in interference between currents of two loads.

A common characteristic for all PWM schemes developed so far for multi-leg VSI fed drives is an absence of the link with existing PWM strategies for three-phase drives. Developed schemes mostly use the multi-leg inverter as a starting point, thus ignoring the fact that machines are three-phase ones. This leads to rather complicated control structures, which are hard to generalise to an n-leg inverter. This is the reason why the multi-leg PWM scheme, developed in this thesis, is based on the principles well known for three-phase drives, thus allowing the complete drive control structure to be based on the same building-blocks (including modulator) as in the case of three-phase single-motor drives.

2.5 SUMMARY

The literature review, provided in this chapter, has surveyed the state of the art in the areas relevant for the research undertaken in the thesis. Some of the advantages of the multi-phase machines over their three-phase counterparts have been reviewed, and it was shown how these advantages can be utilised in multi-motor drives. Various existing PWM schemes for multi-phase VSIs have been addressed, aimed at control of multi-phase machines with either concentrated or distributed windings, as well as for series-connected multi-phase multi-motor drives. Various topologies for reduced switch-count single motor and multi-motor drives have been also surveyed. These are predominantly aimed at supply of a multitude of

three-phase or two-phase motors. Corresponding PWM techniques for such supply systems have been reviewed as well with a particular emphasis on their shortcomings.

As the first step towards the development of PWM schemes for multi-phase machines, mathematical modelling and space vector representation of an n-phase VSI is elaborated next.

Chapter 3

MULTI-PHASE AND MULTI-LEG VOLTAGE SOURCE INVERTERS

3.1   INTRODUCTION

This chapter introduces the basic sets of equations and notions that are necessary for the analysis of SVPWM techniques for multi-phase VSIs in subsequent chapters. Therefore, the principles of modelling and space vector representation of a multi-phase VSI are briefly reviewed. Starting from the general *n*-phase VSI topology, space vector representation based on multiple *d-q* planes is presented.

The chapter is organised as follows. In section 3.2 the basic notions and notation are defined which are used throughout the thesis irrespectively of the number of phases. The concept of the switching function is introduced first, based on which expressions for leg voltages, phase voltages, line voltages and common mode voltage (CMV) can be derived next. Section 3.3 introduces the general space vector transformation for multi-phase systems and, using the VSD approach, defines voltage space vectors of a multi-phase VSI in transformed 2-D planes (sub-spaces). In particular, voltage space vectors of a five-phase, seven-phase and nine-phase VSI are covered. Voltage space vectors in corresponding planes are defined for each considered phase number, thus providing a starting point for subsequent development of PWM modulation schemes based upon space vector theory. The emphasis is placed on explaining important issues related to harmonic mapping into new planes, which is of paramount importance during design and implementation of various SVPWM strategies. This is so since, in order to properly synthesise inverter output voltages, all *d-q* planes must be considered. Section 3.4 deals with basic modelling aspects of a multi-leg VSI, by considering the way in which three-phase machines are connected to the multi-leg VSI. While some properties of a multi-leg VSI are the same as for a multi-phase VSI, multi-phase space vector theory is not applicable since features of a multi-leg VSI fed drive are in essence related to three-phase systems. Summary of the chapter is given in section 3.5.

3.2   MODELLING OF MULTI-PHASE VOLTAGE SOURCE INVERTERS

General topology of a two-level *n*-phase VSI supplying balanced star-connected load is shown in Fig. 3.1. Arrangement of *2n* power semiconductor switches in pairs creates *n* inverter legs. These form an *n*-phase VSI that can provide leg output voltage, referenced to mid-point of dc bus, with only two levels: $\pm V_{dc}/2$. Analysis and developments of all PWM schemes in subsequent chapters apply to this kind of the multi-phase VSIs (a different topology, considered often for fault-tolerant applications, utilises independent H-bridges for each phase of the load, in contrast to the topology considered here where load is in star-connection [Ertugrul et al (2002)]). For the sake of simplicity, it is assumed that constant ripple-free dc voltage is provided at the inverter input. Dc bus voltage is equally shared by two capacitors and therefore dc bus mid-point can be used as a reference point in subsequent analysis although in practice this point normally does not exist. All the power semiconductor switches are assumed to be ideal in order to simplify theoretical analysis.

To determine expressions for the output phase voltages of the inverter it is necessary at first to examine behaviour of switches in each inverter leg. Since the inverter is supplied from the voltage source, two switches in the same inverter leg cannot be turned 'on' at the same time because this would short-circuit the voltage source. In the same way they cannot be turned 'off' simultaneously because this will result in undetermined voltage to the load connected to the inverter leg. Thus, the states of two switches in the same inverter leg are complementary. This leads to the conclusion that during operation of an *n*-phase two-level VSI there are 2^n possible switching configurations. It is therefore possible to define logic-type switching functions which express the state of the switches for each inverter leg.
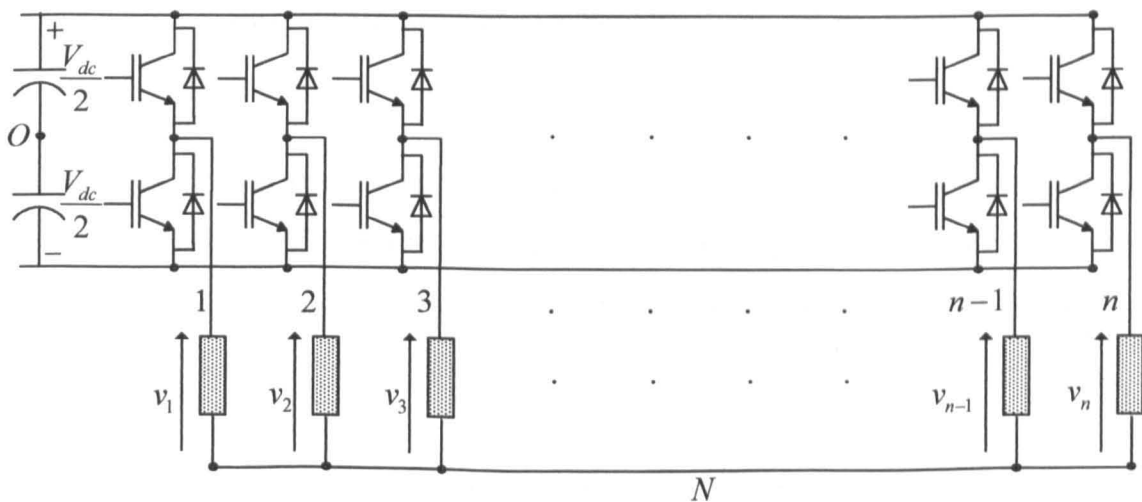
Fig. 3.1: Multi-phase (*n*-phase) VSI supplying a star-connected load.

36

Inverter legs/phases are identified at this stage with numbers that are in the range from 1 to n, where n represents number of inverter legs/phases. Later on, for specified phase numbers (e.g. five-phase, seven-phase, nine-phase...), a different notation is used, where phases are labelled with the lower case letters (a, b, c,...), while the upper case letters ($A, B, C,...$) are used for the inverter legs.

Switching functions can be defined for upper and lower switch in every inverter leg as having the value '1' when the switch is closed ('on' state) and '0' when the switch is open ('off' state), respectively. Since the switching functions for two switches in each inverter leg are dependant (complementary), use of only one switching function is enough to define state of both switches in a leg, and it is common to use only switching function of the upper switch. Thus, one can define switching function m_k ($k = 1, 2, 3...n$) as having the value '1' when upper switch is closed, and '0' when it is open. Switching function for lower switch can easily be obtained as $1-m_k$, for every leg. The k-th leg output voltage referenced to the dc bus mid-point can be expressed as:

$$v_k^{leg} = \frac{V_{dc}}{2}(2m_k - 1) = v_{NO} + v_k \tag{3.1}$$

where v_k^{leg} are the leg voltages, v_k are the phase voltages, and v_{NO} is the voltage between the load neutral point and the dc bus mid-point (common-mode voltage (CMV)). Thus, the inverter leg voltages can take only two values ($+V_{dc}/2$ or $-V_{dc}/2$). In the case of a star-connected balanced load, sum of the phase voltages (v_k) must be zero and summation of equations (3.1) developed for all k in the case of an n-phase system yields the expression for common-mode voltage:

$$v_{NO} = \frac{1}{n}\sum_{k=1}^{n} v_k^{leg} \tag{3.2}$$

The same equation, expressed in terms of switching functions, has the form:

$$v_{NO} = \frac{V_{dc}}{n}\sum_{k=1}^{n} m_k - \frac{V_{dc}}{2} \tag{3.3}$$

It follows from (3.3) that the CMV of an n-phase VSI feeding star-connected symmetrical n-phase load takes $n+1$ different voltage levels, between $\pm V_{dc}/2$, with steps of V_{dc}/n. Phase voltages of the n-phase star-connected load are obtained by substitution of (3.3) into (3.1):

$$v_k = V_{dc}\left[m_k - \frac{1}{n}\sum_{k=1}^{n} m_k\right] \tag{3.4}$$

It can be seen from Fig. 3.1 that, with respect to the first phase of an n-phase system (where n is an odd number), there are a total of n-1 different sets of line voltages that can be identified.

However, because of the symmetry in the system, there are actually only $(n-1)/2$ different sets. In general, based on switching functions, instantaneous values of these sets of line voltages can be expressed in a similar way to the phase voltages. Thus each set of line voltages with respect to the first phase ($k = 1$) can be found as:

$$v_{k,k+l} = V_{dc}(m_k - m_{k+l})$$ (3.5)

where $l = 1, 2, 3...(n-1)/2$.

A more specific definition of different groups of line voltages will be given in detail for particular phase number topologies, when appropriate. The set of expressions introduced until now is sufficient to describe all the relevant voltages of the n-phase VSI.

3.3 SPACE VECTOR REPRESENTATION OF MULTI-PHASE VOLTAGE SOURCE INVERTERS

By considering n homogeneous and time-dependant real quantities $x_k(t)$ related to an n-phase system, the generalised space vector transformation is defined as:

$$\bar{x}_{S_h} = \frac{1}{n}\sum_{k=1}^{n} x_k \alpha^{h(k-1)}, \qquad h = 0,1,2,...,n-1$$ (3.6)

where $\alpha = e^{j2\pi/n}$, [Grandi et al (2006a)]. Quantities denoted as $\bar{x}_{S_h}$ are complex numbers, and they represent space vector components of sequence h. An exception is the zero-sequence component $\bar{x}_{S_0}$, which is a real quantity (obtained for $h = 0$; the second zero-sequence component occurs when $h = n/2$ in the case of a system with an even number of phases). The inverse transformation is given by [Grandi et al (2006a)]:

$$x_k = \sum_{h=0}^{n-1} \bar{x}_{S_h} \alpha^{-h(k-1)}, \qquad k = 1,2,3,...,n$$ (3.7)

It appears that there are $n-1$ space vectors that must be used to describe an n-phase system. However, inspection of the general space vector transformation given by (3.6) shows that there is a redundancy due to:

$$\bar{x}_{S_{n-h}} = \frac{1}{n}\sum_{k=1}^{n} x_k \alpha^{(n-h)(k-1)} = \frac{1}{n}\sum_{k=1}^{n} x_k \alpha^{-h(k-1)} = \bar{x}_{S_h}^*, \qquad h = 1,2,...,n-1$$ (3.8)

Hence it is enough to use $(n-1)/2$ space vectors plus zero-space vector to fully describe an n-phase system (n is an odd number). Before generating space vectors using (3.6), it is necessary to change normalisation factor that comes before summation in order to maintain similarity with the space vector transformation used in the case of a three-phase system. Power variant form of the transformation is more suitable for analysis of SVPWM methods

since it makes the magnitude of the reference voltage space vector equal to the peak value of the desired sinusoidal phase voltage. Therefore, an additional multiplication by 2 is performed for all space vector components of (3.6). Thus, for an *n*-phase system space vectors are defined with:

$$\bar{x}_h = 2\bar{x}_{S_h} = \frac{2}{n}\sum_{k=1}^{n} x_k \alpha^{h(k-1)}, \qquad h = 0,1,2,...,n-1 \tag{3.9}$$

By analysing these sequences one finds that sequences $\bar{x}_h$ and $\bar{x}_{n-h}$ are actually the same sequences with opposite phase sign and the redundancy explained with (3.8) becomes clear. Thus, in the case of an *n*-phase system, zero-sequence component and $(n-1)/2$ space vectors are sufficient to fully describe the system. Selection of these space vectors sequences can be done in several ways. Thus in the case of a five-phase system, selected sequence is $(\bar{x}_0,\bar{x}_1,\bar{x}_2)$ in the works of Iqbal and Levi (2005) and Ojo and Dong (2005), while another sequence $(\bar{x}_0,\bar{x}_1,\bar{x}_3)$ has been assumed in the works of Ryu et al (2005) and Silva et al (2004).

From this point onwards the sequence $(\bar{x}_0,\bar{x}_1,\bar{x}_2,...\bar{x}_{(n-1)/2})$ will be used to describe an *n*-phase system. Since the following analysis is related to PWM methods, time-dependant real quantities $x_k(t)$ that are of interest are actually phase voltages $v_k(t)$. Hence, instead of using the general notation $(\bar{x}_0,\bar{x}_1,\bar{x}_2,...)$, voltage space vectors are denoted as $(v_{zs},\bar{v}_{d_1-q_1},\bar{v}_{d_2-q_2},...)$, respectively. Correspondingly, the 2-D planes where the vectors $(\bar{v}_{d_1-q_1},\bar{v}_{d_2-q_2},\bar{v}_{d_3-q_3}...)$ belong are denoted as d_1-q_1, d_2-q_2, d_3-q_3, etc., respectively, and v_{zs} represents zero-sequence component (and is of course a real number). Thus the voltage space vectors for an *n*-phase system can be written as:

$$v_{zs} = \frac{2}{n}\sum_{k=1}^{n} v_k \tag{3.10}$$

$$\bar{v}_{d_h-q_h} = \frac{2}{n}\sum_{k=1}^{n} v_k \alpha^{h(k-1)}, \qquad h = 1,2,...,(n-1)/2 \tag{3.11}$$

Representation of an *n*-phase VSI's *n*-dimensional space vector is replaced in this way by representation in $(n-1)/2$ 2-D planes d_1-q_1, d_2-q_2, d_3-q_3, etc., and one single-dimensional plane (zero-sequence; since the load is balanced star-connected with isolated neutral point, zero-sequence space vector is zero so that the final system for analysis is in essence $(n-1)$-dimensional). By resolving every space vector into real and imaginary part with $\bar{v}_{d_h-q_h} = v_{d_h} + jv_{q_h}$ each component of the corresponding 2-D plane can be identified. In order to simplify further analysis of PWM methods for a multi-phase VSI, expressions (3.10) and

(3.11) are developed for each k and h and organized into a real matrix. Thus, the generalised space vector transformation in power-variant form for a multi-phase system (where n is an odd number), shown as a real matrix, becomes:

$$\underline{C}_n = \frac{2}{n}\begin{bmatrix} 1 & \cos(\alpha) & \cos(2\alpha) & \cos(3\alpha) & \dots & \cos(n-1)\alpha \\ 0 & \sin(\alpha) & \sin(2\alpha) & \sin(3\alpha) & \dots & \sin(n-1)\alpha \\ 1 & \cos(2\alpha) & \cos(4\alpha) & \cos(6\alpha) & \dots & \cos 2(n-1)\alpha \\ 0 & \sin(2\alpha) & \sin(4\alpha) & \sin(6\alpha) & \dots & \sin 2(n-1)\alpha \\ 1 & \cos(3\alpha) & \cos(6\alpha) & \cos(9\alpha) & \dots & \cos 3(n-1)\alpha \\ 0 & \sin(3\alpha) & \sin(6\alpha) & \sin(9\alpha) & \dots & \sin 3(n-1)\alpha \\ 1 & \cos(4\alpha) & \cos(8\alpha) & \cos(12\alpha) & \dots & \cos 4(n-1)\alpha \\ 0 & \sin(4\alpha) & \sin(8\alpha) & \sin(12\alpha) & \dots & \sin 4(n-1)\alpha \\ \vdots & \vdots & \vdots & \vdots & \vdots & \vdots \\ 1 & \cos(\frac{n-1}{2})\alpha & \cos 2(\frac{n-1}{2})\alpha & \cos 3(\frac{n-1}{2})\alpha & \dots & \cos(n-1)(\frac{n-1}{2})\alpha \\ 0 & \sin(\frac{n-1}{2})\alpha & \sin 2(\frac{n-1}{2})\alpha & \sin 3(\frac{n-1}{2})\alpha & \dots & \sin(n-1)(\frac{n-1}{2})\alpha \\ 1/2 & 1/2 & 1/2 & 1/2 & \dots & 1/2 \end{bmatrix} \quad (3.12)$$

where now $\alpha = 2\pi/n$, and n represents the number of phases. This is so-called real decoupling transformation (Clarke's transformation) [White and Woodson (1959)], which in essence decomposes an n-dimensional vector space into $(n-1)/2$ 2-D and mutually decoupled planes. Hence, by applying (3.12) to a multi-phase system, the original n-phase system is decomposed into $(n-1)/2$ 2-D and mutually orthogonal planes. New $(n-1)/2$ 2-D planes are defined with the first $(n-1)/2$ pairs of rows in (3.12), d_1-q_1, d_2-q_2, d_3-q_3, etc. The last row defines a single-dimensional zero-sequence sub-space that can not be excited in the case of an isolated neutral point of a star-connected n-phase load.

An important consequence of the application of (3.12) is that the families of odd harmonics are effectively mapped into different planes, which simplifies further implementation of a particular PWM scheme. Thus, the fundamental components are mapped into d_1-q_1 (the first two rows in (3.12)) while all the other harmonic components appear in other planes in a manner that depends on the number of phases. The mapping principles are explained in subsequent sub-sections for five-phase, seven-phase and nine-phase topologies, respectively. Knowledge of the plane where each particular harmonic component appears makes it easier to devise a proper modulation scheme that will either neutralise these harmonic components or allow injection of a certain amount of selected harmonics in a controllable fashion.

Each phase of the inverter will be further on identified with a letter ($k = a, b, c,...$) rather than with a number as before. Similarly, corresponding inverter leg voltages will be

denoted with capital letters A, B, C,...etc in sub-script. Additionally, the following constants are found to be useful and are introduced and used throughout the subsequent chapters:

$$K_P = \sin(P\frac{\pi}{n})$$
$$L_P = \cos(P\frac{\pi}{n})$$

(3.13)

Here, $P = 1,2,3,...(n\text{-}1)/2$ (equal to the number of 2-D planes for a given n) and, in particular case when $P = 1$, use of the sub-script will be omitted. The same symbols K and L are used for all considered phase numbers, although the values are different in accordance with (3.13).

Equations (3.1)-(3.5) are functions of the dc bus voltage and, for simplicity, various inverter voltages are further on normalised with respect to $V_{dc}/2$. If normalisation is not applied this is noted.

3.3.1 VOLTAGE SPACE VECTORS OF A FIVE-PHASE VOLTAGE SOURCE INVERTER

The topology of a five-phase VSI supplying a five-phase star-connected load is shown in Fig. 3.2. Inverter legs are identified (A to E) and all phase voltages and two characteristic line voltages are shown. During the operation of a five-phase VSI there are $2^5 = 32$ possible switching configurations determined by the values of the switching functions m_k. Considering all 32 switching configurations, instantaneous values of phase voltages of a five-phase load ($k = a, b, c, d, e$ for v_k; $k = A, B, C, D, E$ for m_k), can be calculated based on (3.4) as:

$$v_k = V_{dc}\left[m_k - \frac{1}{5}(m_A + m_B + m_C + m_D + m_E)\right]$$

(3.14)
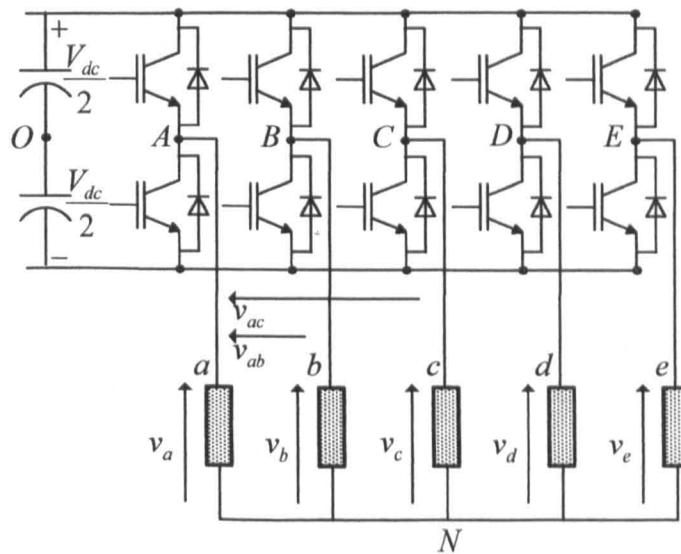
Fig. 3.2: A five-phase VSI supplying a five-phase star-connected load.

Decoupling transformation matrix for a five-phase system is from (3.12) given with
($\alpha = 2\pi/5$):

$$\underline{C}_5 = \frac{2}{5}\begin{bmatrix} 1 & \cos(\alpha) & \cos(2\alpha) & \cos(3\alpha) & \cos(4\alpha) \\ 0 & \sin(\alpha) & \sin(2\alpha) & \sin(3\alpha) & \sin(4\alpha) \\ 1 & \cos(2\alpha) & \cos(4\alpha) & \cos(\alpha) & \cos(3\alpha) \\ 0 & \sin(2\alpha) & \sin(4\alpha) & \sin(\alpha) & \sin(3\alpha) \\ 1/2 & 1/2 & 1/2 & 1/2 & 1/2 \end{bmatrix} \qquad (3.15)$$

A program was written using MATLAB software in order to calculate and visualise all 32 voltage space vectors. At first all phase voltages for all 32 switching configurations are determined based on (3.14). By applying (3.15) to these phase voltages in accordance with

$$\begin{bmatrix} v_{d1} \\ v_{q1} \\ v_{d2} \\ v_{q2} \\ v_{zs} \end{bmatrix} = \underline{C}_5 \begin{bmatrix} v_a \\ v_b \\ v_c \\ v_d \\ v_e \end{bmatrix} \qquad (3.16)$$

one obtains voltage space vectors in the d_1-q_1 and d_2-q_2 planes. The result of plotting the space vectors in the d_1-q_1 and d_2-q_2 planes is shown in Figs. 3.3 and 3.4 (not normalised with $V_{dc}/2$). The tip of each space vector is shown and it is identified with a decimal number. By converting each decimal number into a five-digit binary number, switching functions that define particular space vectors (switching states) are obtained. The most significant bit (MSB) of the binary number matches the value of the switching function m_A, the second MSB that of m_B etc. Out of 32 space vectors, two are zero space vectors and the rest are the active space vectors. The active vectors can be classified into three groups based on their magnitudes and each plane can be divided into 10 sectors (each spanning $\pi/5$).

Different groups of active space vectors are labelled with G_k^n, where n is the number of phases and k stands for the group number. Thus for the case when $n = 5$ one has $k = 0, 1, 2$ or 3. Zero space vector group is governed with $k = 0$. Due to the existence of only three different active space vector groups in a five-phase system, with respect to the plane d_1-q_1, these groups will be termed: small space vectors (G_1^5), medium space vectors (G_2^5) and large space vectors (G_3^5). Each group consists of ten active space vectors. By connecting tips of these vectors in the d_1-q_1 and d_2-q_2 planes, three decagons (with zero mutual phase shifts, and not shown because of clarity) appear and they clearly identify each group. The magnitude of zero space vectors is zero, small space vectors are of magnitude $|\bar{v}_s| \approx 0.2472 V_{dc}$, medium of $|\bar{v}_m| \approx 0.4 V_{dc}$ and large are with a magnitude of $|\bar{v}_l| \approx 0.6472 V_{dc}$ [Iqbal (2005)].
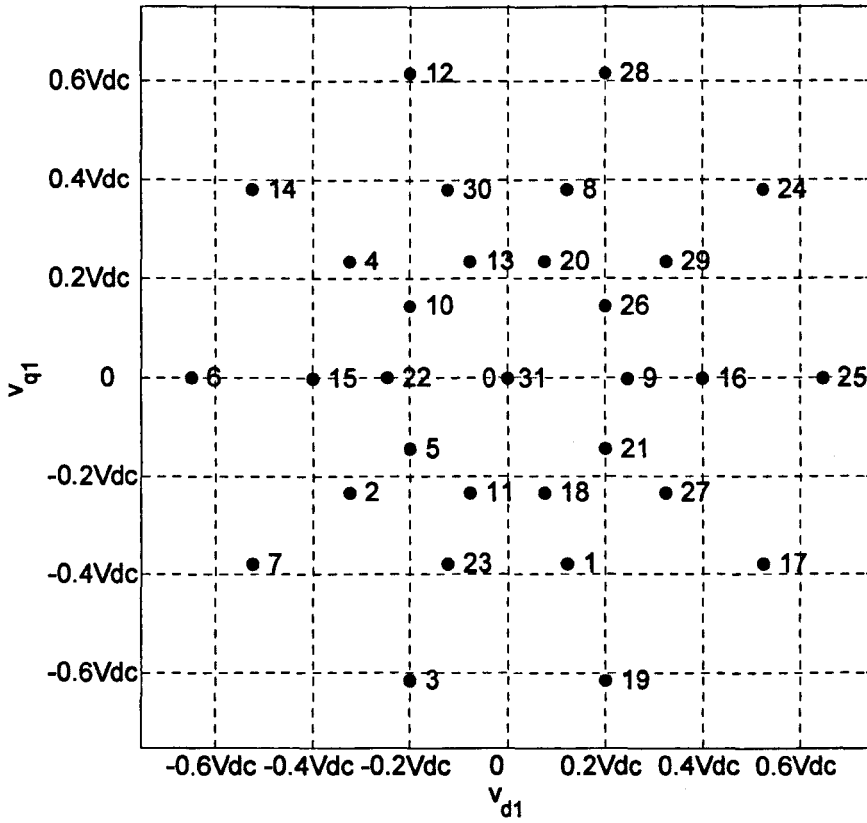
Fig. 3.3: Space vectors of a five-phase VSI in the d_1-q_1 plane.
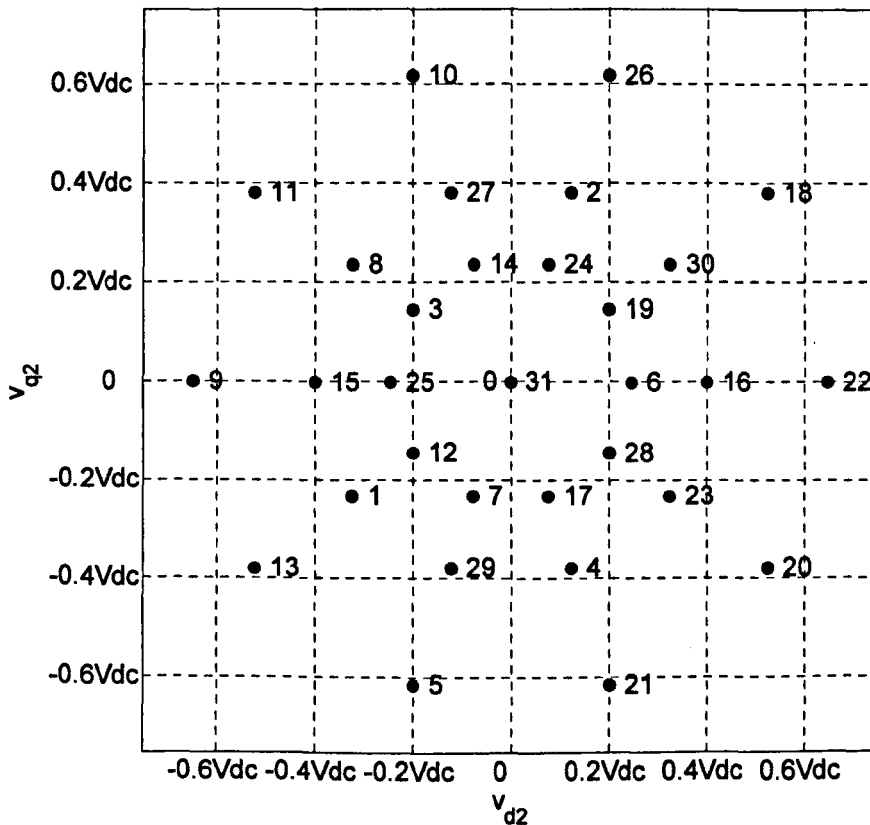
Fig. 3.4: Space vectors of a five-phase VSI in the d_2-q_2 plane.

By considering positions of the space vectors in the d_1-q_1 and d_2-q_2 planes it can be concluded from Figs. 3.3 and 3.4 that [Iqbal (2005)]:

- Space vectors that create the inner-most decagon in the d_1-q_1 plane map into the outer-most decagon in the d_2-q_2 plane; thus the small space vectors from the d_1-q_1 plane are actually the large space vectors in the d_2-q_2 plane.

- Space vectors that create the outer-most decagon in the d_1-q_1 plane map into the inner-most decagon in the d_2-q_2 plane; thus the large space vectors from the d_1-q_1 plane are actually the small space vectors in the d_2-q_2 plane.

- The middle decagon in both planes is created by the same (medium) space vectors. However, the mapping reveals that the phase sequence a, b, c, d, e of the d_1-q_1 plane corresponds to a, c, e, b, d sequence in the d_2-q_2 plane, which are basically the third-harmonic voltages.

- Zero space vectors are the same in both planes.

By analysing the load configurations that can be formed depending on the switching function values, one finds that there are six different configurations. Load configurations are denoted with {0-5}, {1-4}, {2-3}, {3-2}, {4-1}, {5-0}, where the first/second number in brackets specifies how many upper/lower switches is in the 'on' state, respectively. These load configurations are shown in Fig. 3.5 from where instantaneous values of phase voltages that are used as an input in (3.16) can be identified for each particular load configuration. Alternatively, these six load configurations can be considered as three pairs of different load configurations since configurations {2-3} and {3-2}, {1-4} and {4-1}, and {0-5} and {5-0} lead to the same instantaneous phase voltages but with an opposite sign. All four different groups of space vectors (referenced to the magnitudes of the space vectors in the first plane) are classified in Table 3.1. Magnitudes of each group are shown using constants introduced in (3.13), $K = \sin(\pi/5)$ and $K_2 = \sin(2\pi/5)$, and scaling with $V_{dc}/2$ is performed.

Table 3.1: Five-phase VSI space vector groups and their relation with load configurations.

Group	Magnitude in the d_1-q_1 plane	Magnitude in the d_2-q_2 plane	Load configurations	Alternative name
G_0^5	0	0	{0-5},{5-0}	Zero - $\bar{v}_o$
G_1^5	$\dfrac{4}{5}\dfrac{K}{K_2}$	$\dfrac{4}{5}\dfrac{K_2}{K}$	{2-3},{3-2}	Small - $\bar{v}_s$
G_2^5	$\dfrac{4}{5}$	$\dfrac{4}{5}$	{1-4},{4-1}	Medium - $\bar{v}_m$
G_3^5	$\dfrac{4}{5}\dfrac{K_2}{K}$	$\dfrac{4}{5}\dfrac{K}{K_2}$	{2-3},{3-2}	Large - $\bar{v}_l$
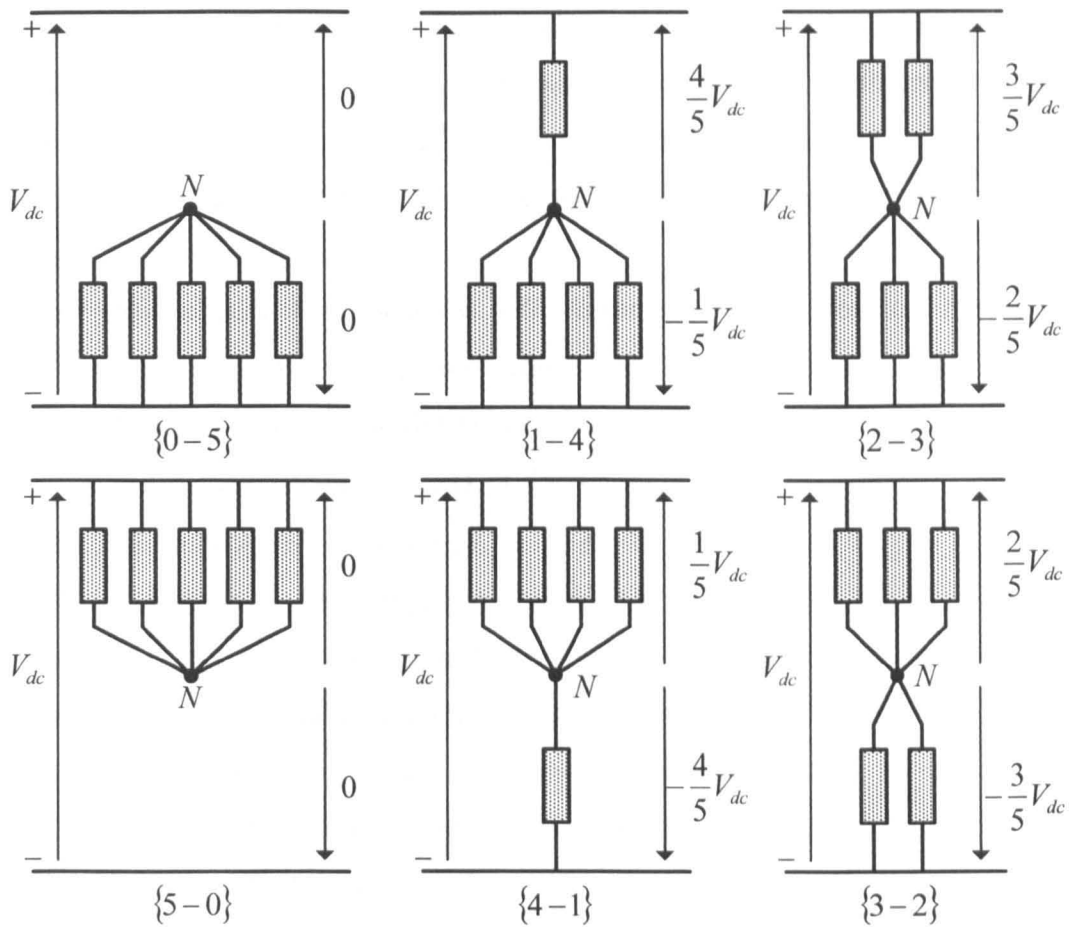
Fig. 3.5: Characteristic configurations of a five-phase load.

It can be noted that when either small or large space vectors are applied, the load appears in {2-3} or {3-2} configurations, while the use of medium vectors brings the load into {1-4} or {4-1} configurations. When zero space vectors are applied, the five-phase load is effectively short circuited ({0-5} or {5-0} configuration). Although any small or large space vector will bring the load into {2-3} or {3-2} configuration, one can establish that only large active space vectors have adjacent relation of '1' in switching states [Kelly et al (2003), Xue and Wen (2005)]. This means that appearance of a five-digit binary number whose bits correspond to m_A m_B m_C m_D m_E is such that all switching functions of value '1' appear next to each other. Note that for a star connected load, leg E is next to the leg A in the same way as is leg B. For example, the large space vector $\bar{v}_{28}$ from the first plane (Fig 3.3) has the combination of the switching functions (11100), while the small space vector $\bar{v}_{26}$ has (11010). In both cases the load will appear in {3-2} configuration. However, as a consequence of the different ordering of '1' in switching states, magnitudes of these two groups of active space vector are different. It is easy to see that switching functions of space vector $\bar{v}_{26}$ that are with value of '1' are not grouped together. In general, among all the space vectors that lead to the

same load configuration, those with adjacent relation of '1' in switching states will have the largest magnitude [Kelly et al (2003), Xue and Wen (2005)]. This observation is of high importance during selection of active space vectors involved in output voltage generation, since it is directly related to the achievable modulation index and generated number of commutations per switching period.

An additional advantage, obtained with vector space decomposition, is related to the harmonic mapping into different planes [Iqbal (2005)]. Families of odd harmonics are effectively mapped according to the following rules ($k = 0, 1, 2, 3...$):

- $10k \pm 1$ harmonics $\rightarrow d_1$-q_1 plane (**1**, **9**, **11**, **19**, **21**,...).
- $10k \pm 3$ harmonics $\rightarrow d_2$-q_2 plane (**3**, **7**, **13**, **17**, **23**,...).
- $10k \pm 5$ harmonics $\rightarrow$ zero-sequence plane (**5**, **15**, **25**,...).

Harmonics that are characteristic for zero-sequence plane are non-existent due to the star connection of a load. In a five-phase system the third harmonic is the lowest order harmonic that can be used for torque enhancement when a machine is with concentrated windings. However, if sinusoidal output voltage is to be generated, the third harmonic must be zeroed, which means that the design of a PWM scheme must consider simultaneously both planes.

3.3.2 VOLTAGE SPACE VECTORS OF A SEVEN-PHASE VOLTAGE SOURCE INVERTER

Voltage space vectors of a seven-phase VSI (shown with seven-phase load in Fig. 3.6) can be defined in a similar fashion as for a five-phase VSI.
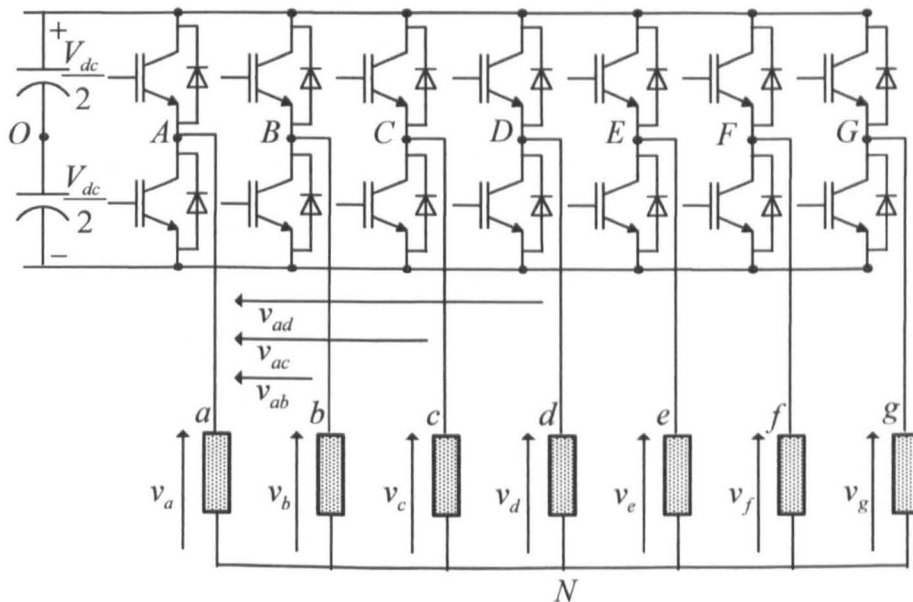

Fig. 3.6: A seven-phase VSI supplying a seven-phase star-connected load.

There are $2^7 = 128$ possible switching configurations depending on values of the switching functions m_k. Instantaneous values of phase voltages of a seven-phase load can be calculated as:

$$v_k = V_{dc}\left[m_k - \frac{1}{5}(m_A + m_B + m_C + m_D + m_E + m_F + m_G)\right]$$ (3.17)

where now $k = a, b, ...g$ for v_k and $k = A, B, ...G$ for m_k. Decoupling transformation matrix for a seven-phase system is from (3.12):

$$\underline{C}_7 = \frac{2}{7}\begin{bmatrix} 1 & \cos(\alpha) & \cos(2\alpha) & \cos(3\alpha) & \cos(4\alpha) & \cos(5\alpha) & \cos(6\alpha) \\ 0 & \sin(\alpha) & \sin(2\alpha) & \sin(3\alpha) & \sin(4\alpha) & \sin(5\alpha) & \sin(6\alpha) \\ 1 & \cos(2\alpha) & \cos(4\alpha) & \cos(6\alpha) & \cos(\alpha) & \cos(3\alpha) & \cos(5\alpha) \\ 0 & \sin(2\alpha) & \sin(4\alpha) & \sin(6\alpha) & \sin(\alpha) & \sin(3\alpha) & \sin(5\alpha) \\ 1 & \cos(3\alpha) & \cos(6\alpha) & \cos(2\alpha) & \cos(5\alpha) & \cos(\alpha) & \cos(4\alpha) \\ 0 & \sin(3\alpha) & \sin(6\alpha) & \sin(2\alpha) & \sin(5\alpha) & \sin(\alpha) & \sin(4\alpha) \\ 1/2 & 1/2 & 1/2 & 1/2 & 1/2 & 1/2 & 1/2 \end{bmatrix}$$ (3.18)

where $\alpha = 2\pi/7$. In the same way as in the preceding section, using MATLAB, all phase voltages for all 128 switching configurations are determined at first using (3.17). Transforming these phase voltages by means of

$$\begin{bmatrix} v_{d1} & v_{q1} & v_{d2} & v_{q2} & v_{d3} & v_{q3} & v_{zs} \end{bmatrix}^T = \underline{C}_7\begin{bmatrix} v_a & v_b & v_c & v_d & v_e & v_f & v_g \end{bmatrix}^T$$ (3.19)

one obtains voltage space vectors in the d_1-q_1, d_2-q_2 and d_3-q_3 planes.

Space vectors, obtained in three 2-D planes, are shown in Figs. 3.7-3.9 (without normalisation with $V_{dc}/2$). Each dot represents a tip of the space vector. Similar to the five-phase system, it can be seen from these figures that there is no switching state redundancy (i.e. there are not any two or more switching states that produce the same active space vector) and each space vector has a unique appearance in all three planes (except for two zero space vectors that appear in the origin in all planes).

Each plane can be divided into fourteen sectors, each of which spans $\pi/7$. Space vectors are labelled again with a decimal number that, when converted to the binary representation, reveals values of the switching functions for each inverter leg. There are two zero space vectors and the rest are the active space vectors that can be classified in different groups, based on their magnitudes. By connecting tips of the active space vectors that belong to the same group, 14-sided polygons (not shown, for clarity) are obtained for each group, with the exception of the vectors that belong to the group having the third largest magnitude, where a 28-sided polygon appears. This group is easily recognised, since these space vectors are not aligned with the remaining space vectors, along the 'fictional' lines that separate the sectors.
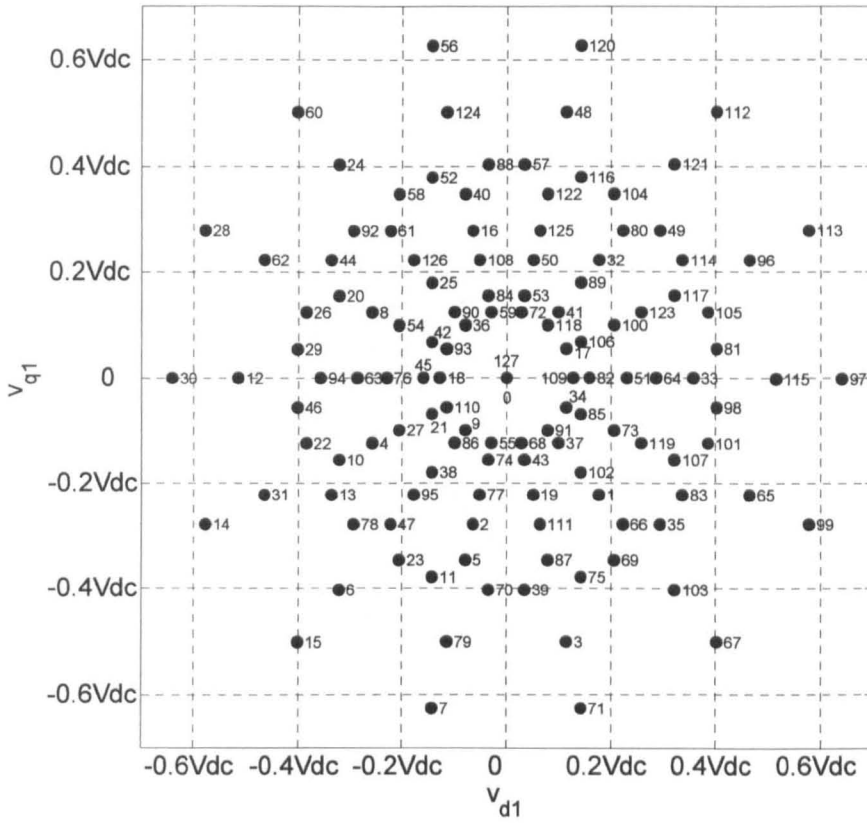
Fig. 3.7: Space vectors of a seven-phase VSI in the d_1-q_1 plane.
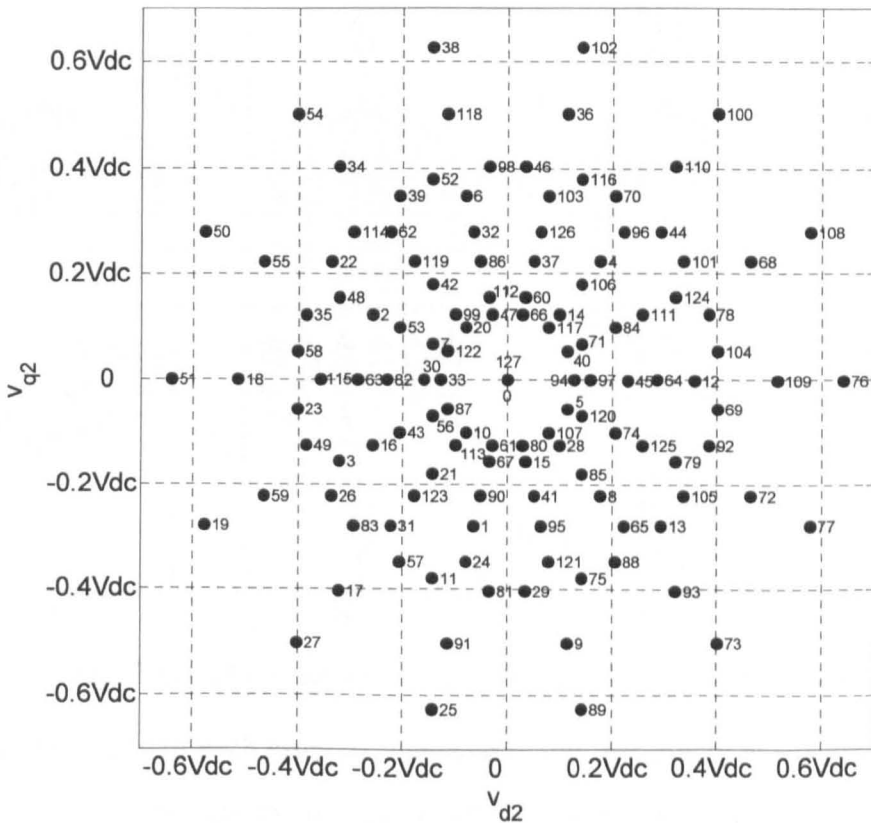
Fig. 3.8: Space vectors of a seven-phase VSI in the d_2-q_2 plane.
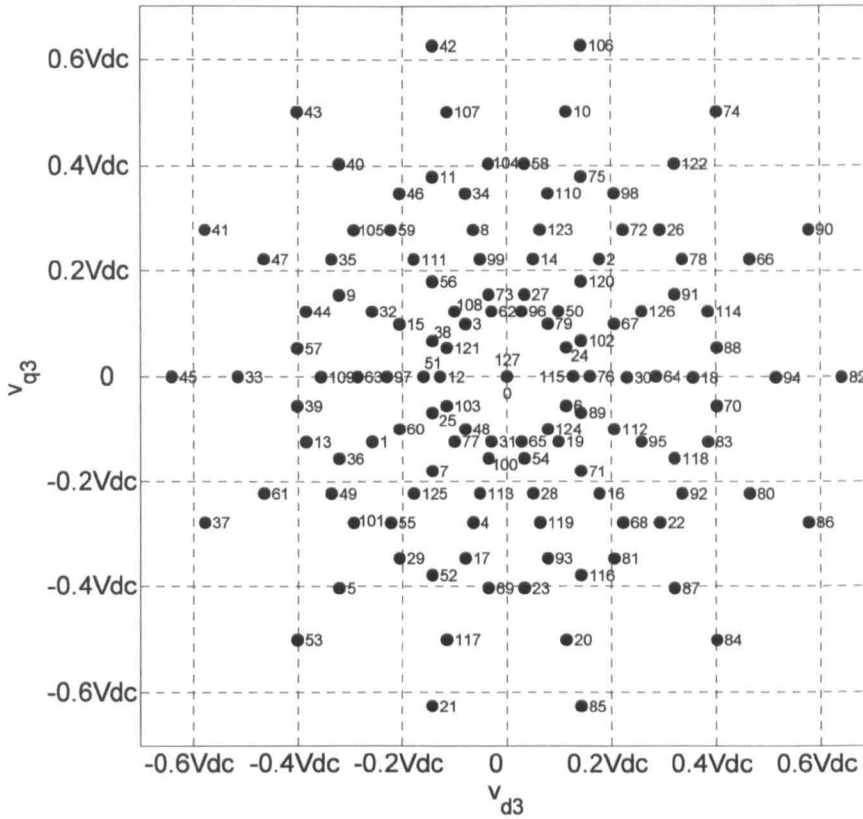
Fig. 3.9: Space vectors of a seven-phase VSI in the d_3-q_3 plane.
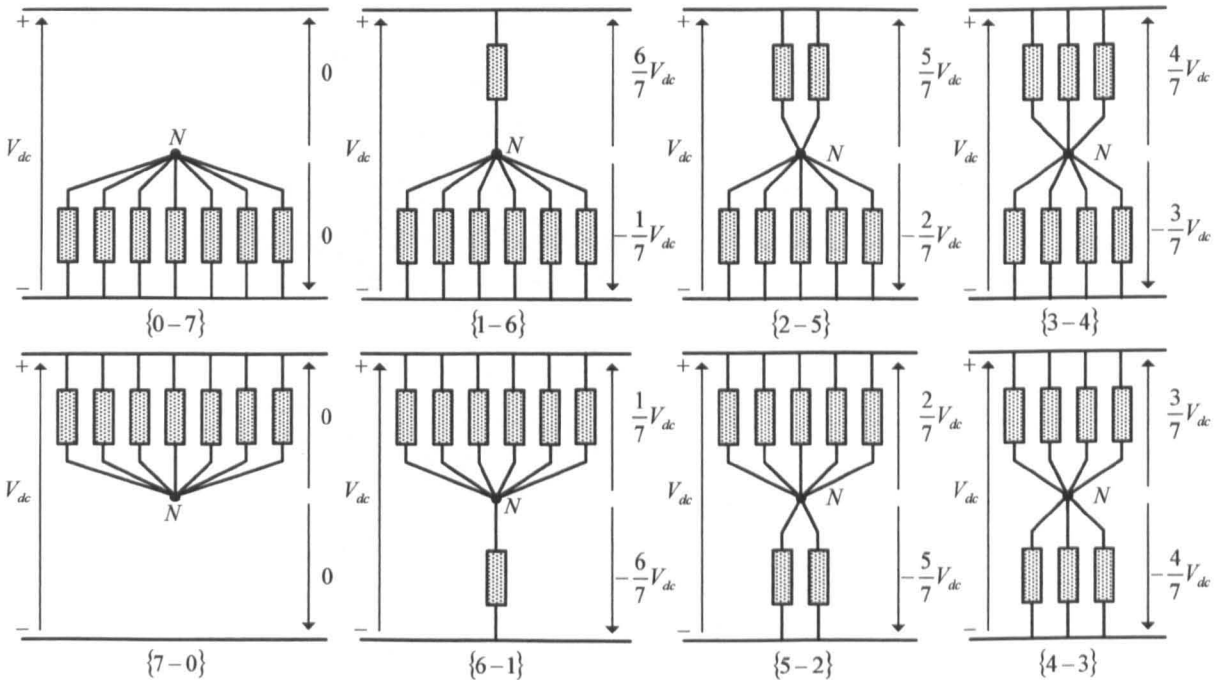
Fig. 3.10: Characteristic configurations of a seven-phase load.

The magnitude of each group (referenced to the first plane) is labelled with G_k^n, where $n = 7$, and k stands for the group number (0 to 8). There are eight different load configurations of a seven-phase load, as shown in Fig. 3.10, {0-7}, {1-6}, {2-5}, {3-4}, {4-3}, {5-2}, {6-1}

and {7-0}. Instantaneous non-normalised values of phase voltages, characteristic for each load topology, are also given in Fig. 3.10 and are used as the input into (3.19). Normalised magnitudes of space vectors in each plane and relations between different space vector groups and load configurations are summarised in Table 3.2, where the constants of (3.13) are: $K = \sin(\pi/7)$, $K_2 = \sin(2\pi/7)$ and $K_3 = \sin(3\pi/7)$. The magnitude of the group of space vectors (G_6^7) that form the 28-sided polygon is given as a numerical value without the use of trigonometric constants. It will be demonstrated later on that, for a development of SVPWM schemes for a sinusoidal output voltage generation, this group of space vectors is not utilised.

It is important to note that, once more, the same load configurations occur as a result of application of active space vectors belonging to the different groups. For example (Fig. 3.7), load configuration {3-4} appears as a result of application of active space vectors belonging to the following groups: $G_2^7 \to \bar{v}_{82}(1010010)$, $G_3^7 \to \bar{v}_{100}(1100100)$, $G_6^7 \to \bar{v}_{81}(1010001)$ or $G_8^7 \to \bar{v}_{97}(1100001)$. Although every space vector from any of these groups will bring the load into {3-4} or {4-3} configuration, one can find that only active space vectors from G_8^7 group posses adjacent relation of '1' in switching states. As a consequence, the magnitude of these active space vectors is the largest among the vectors that lead to {3-4} or {4-3} load configurations. A similar conclusion results by analysing relations of switching functions with regard to the load configurations {2-5}, {5-2} where an adjacent relation of '1' in switching states exists only for the vectors from group G_7^7. Therefore, vectors belonging to the group G_7^7

Table 3.2: Seven-phase VSI space vector groups and their relation with load configurations.

| Group	Magnitude in the d_1-q_1 plane	Magnitude in the d_2-q_2 plane	Magnitude in the d_3-q_3 plane	Load configurations
G_0^7	0	0	0	{0-7},{7-0}
G_1^7	$\dfrac{4}{7}\dfrac{K}{K_3}$	$\dfrac{4}{7}\dfrac{K_2}{K}$	$\dfrac{4}{7}\dfrac{K_3}{K_2}$	{2-5},{5-2}
G_2^7	$\dfrac{4}{7}\dfrac{K}{K_2}$	$\dfrac{4}{7}\dfrac{K_2}{K_3}$	$\dfrac{4}{7}\dfrac{K_3}{K}$	{3-4},{4-3}
G_3^7	$\dfrac{4}{7}\dfrac{K_2}{K_3}$	$\dfrac{4}{7}\dfrac{K_3}{K}$	$\dfrac{4}{7}\dfrac{K}{K_2}$	{3-4},{4-3}
G_4^7	$\dfrac{4}{7}$	$\dfrac{4}{7}$	$\dfrac{4}{7}$	{1-6},{6-1}
G_5^7	$\dfrac{4}{7}\dfrac{K_3}{K_2}$	$\dfrac{4}{7}\dfrac{K}{K_3}$	$\dfrac{4}{7}\dfrac{K_2}{K}$	{2-5},{5-2}
G_6^7	≈ 0.8081	≈ 0.8081	≈ 0.8081	{3-4},{4-3}
G_7^7	$\dfrac{4}{7}\dfrac{K_2}{K}$	$\dfrac{4}{7}\dfrac{K_3}{K_2}$	$\dfrac{4}{7}\dfrac{K}{K_3}$	{2-5},{5-2}
G_8^7	$\dfrac{4}{7}\dfrac{K_3}{K}$	$\dfrac{4}{7}\dfrac{K}{K_2}$	$\dfrac{4}{7}\dfrac{K_2}{K_3}$	{3-4},{4-3}

have the largest magnitude from all the space vectors that lead to {2-5} or {5-2} configurations. On the other hand, all the space vectors associated with {1-6} or {6-1} configuration belong to the same group G_4^7. Further discussion of this issue and its importance during implementation of a SVPWM aimed for sinusoidal output voltage generation will be given in chapter 5.

Finally, mapping of the families of odd harmonics into different planes in the case of a seven-phase VSI follows the rules ($k = 0, 1, 2, 3...$)[Grandi et al (2006b]:

- $14k \pm 1$ harmonics $\rightarrow d_1$-q_1 plane (**1**, 13, 15, 27, 29...).
- $14k \pm 5$ harmonics $\rightarrow d_2$-q_2 plane (**5**, 9, 19, 23, 32...).
- $14k \pm 3$ harmonics $\rightarrow d_3$-q_3 plane (**3**, 11, 17, 25, 31...).
- $14k \pm 7$ harmonics $\rightarrow$ zero-sequence plane (7, 21, 35,...).

Once more, zero-sequence harmonics are non-existent. The lowest order harmonics that can be injected for torque enhancement when the machine is with concentrated windings are the third and the fifth harmonic. These harmonics are mapped into the d_3-q_3 and d_2-q_2 plane, respectively. However, for a sinusoidal output voltage, a PWM scheme must zero all of the harmonics in the d_2-q_2 and d_3-q_3 planes and synthesise only the fundamental component in the first plane. Development of such a PWM scheme is detailed in chapter 5.

3.3.3 VOLTAGE SPACE VECTORS OF A NINE-PHASE VOLTAGE SOURCE INVERTER

In contrast to five-phase and seven-phase topologies, there is more than one nine-phase topology since nine is not a prime number. A nine-phase machine (load) can be realised with three sets of three-phase windings on the same stator core, mutually displaced by $20°$ and having usually three isolated neutral points. This kind of topology, for which development of corresponding SVPWM scheme has been analysed by Grandi et al (2007b), is beyond the scope of the thesis. Alternatively, the nine-phase windings can be distributed symmetrically, with $40°$ spatial displacement between any two consecutive phases, and with a single neutral point (three separate neutral points can also be used). Such a topology is considered further on and is shown in Fig. 3.11. The number of possible switching states, determined with the values of the switching functions m_k is $2^9 = 512$. Instantaneous values of phase voltages of a nine-phase load can be calculated using (3.4) as ($k = a$ to i for v_k; $k = A$ to I for m_k):

$$v_k = V_{dc}\left[m_k - \frac{1}{5}(m_A + m_B + m_C + m_D + m_E + m_F + m_G + m_H + m_I) \right]$$ (3.20)
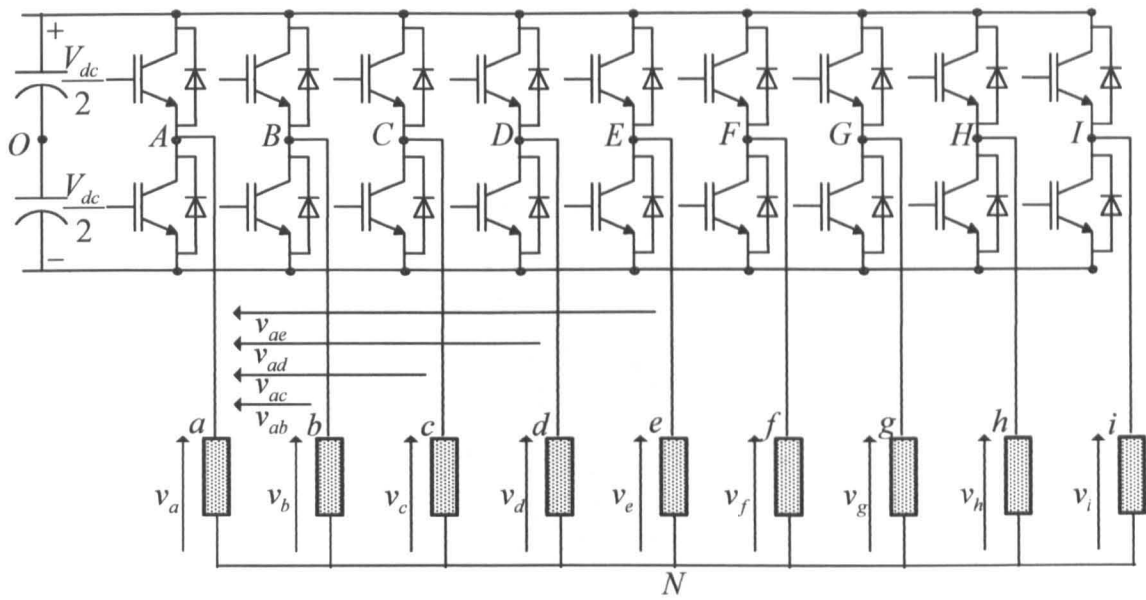
Fig. 3.11: A nine-phase VSI supplying a nine-phase star-connected load.

Decoupling transformation matrix (3.12) has the form ($\alpha = 2\pi/9$):

$$
\underline{C}_9 = \frac{2}{9}
\begin{bmatrix}
1 & \cos(\alpha) & \cos(2\alpha) & \cos(3\alpha) & \cos(4\alpha) & \cos(5\alpha) & \cos(6\alpha) & \cos(7\alpha) & \cos(8\alpha) \\
0 & \sin(\alpha) & \sin(2\alpha) & \sin(3\alpha) & \sin(4\alpha) & \sin(5\alpha) & \sin(6\alpha) & \sin(7\alpha) & \sin(8\alpha) \\
1 & \cos(2\alpha) & \cos(4\alpha) & \cos(6\alpha) & \cos(8\alpha) & \cos(\alpha) & \cos(3\alpha) & \cos(5\alpha) & \cos(7\alpha) \\
0 & \sin(2\alpha) & \sin(4\alpha) & \sin(6\alpha) & \sin(8\alpha) & \sin(\alpha) & \sin(3\alpha) & \sin(5\alpha) & \sin(7\alpha) \\
1 & \cos(3\alpha) & \cos(6\alpha) & 1 & \cos(3\alpha) & \cos(6\alpha) & 1 & \cos(3\alpha) & \cos(6\alpha) \\
0 & \sin(3\alpha) & \sin(6\alpha) & 0 & \sin(3\alpha) & \sin(6\alpha) & 0 & \sin(3\alpha) & \sin(6\alpha) \\
1 & \cos(4\alpha) & \cos(8\alpha) & \cos(3\alpha) & \cos(7\alpha) & \cos(2\alpha) & \cos(6\alpha) & \cos(\alpha) & \cos(5\alpha) \\
0 & \sin(4\alpha) & \sin(8\alpha) & \sin(3\alpha) & \sin(7\alpha) & \sin(2\alpha) & \sin(6\alpha) & \sin(\alpha) & \sin(5\alpha) \\
1/2 & 1/2 & 1/2 & 1/2 & 1/2 & 1/2 & 1/2 & 1/2 & 1/2
\end{bmatrix}
\tag{3.21}
$$

It should be noted that the third pair of rows of (3.21) is different in nature from the other pairs. This is a consequence of the number nine not being a prime number and being a multiple of three. Using MATLAB and combining (3.20) with (3.21) into

$$
\begin{bmatrix} v_{d1} & v_{q1} & v_{d2} & v_{q2} & v_{d3} & v_{q3} & v_{d4} & v_{q4} & v_{zs} \end{bmatrix}^T =
$$
$$
\underline{C}_9 \begin{bmatrix} v_a & v_b & v_c & v_d & v_e & v_f & v_g & v_h & v_i \end{bmatrix}^T
\tag{3.22}
$$

voltage space vectors of a nine-phase system in the d_1-q_1, d_2-q_2, d_3-q_3 and d_4-q_4 planes are obtained.

There are now four 2-D planes to be considered [Grandi et al (2007a)]. In contrast to the previous two cases, there is now a big redundancy in appearance of voltage space vectors caused by the form of the decoupling transformation matrix. Due to the high number of space vectors, only tips of the space vectors are shown in Figs. 3.12 and 3.13 (the same notation with decimal numbers could be used; due to the large number of vectors, numbers are omitted). Since the disposition of the voltage space vectors is the same in all planes other than d_3-q_3, Fig. 3.12 is simultaneously valid for the planes d_1-q_1, d_2-q_2 and d_4-q_4.
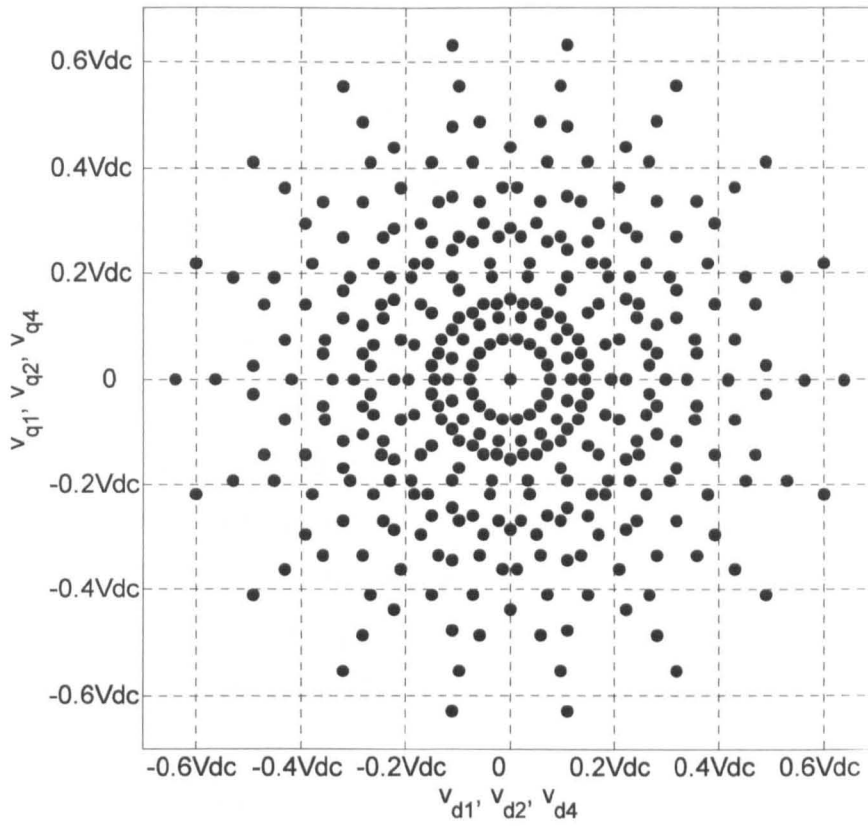
Fig. 3.12: Space vectors of a nine-phase VSI in the d_1-q_1, d_2-q_2 and d_4-q_4 planes.
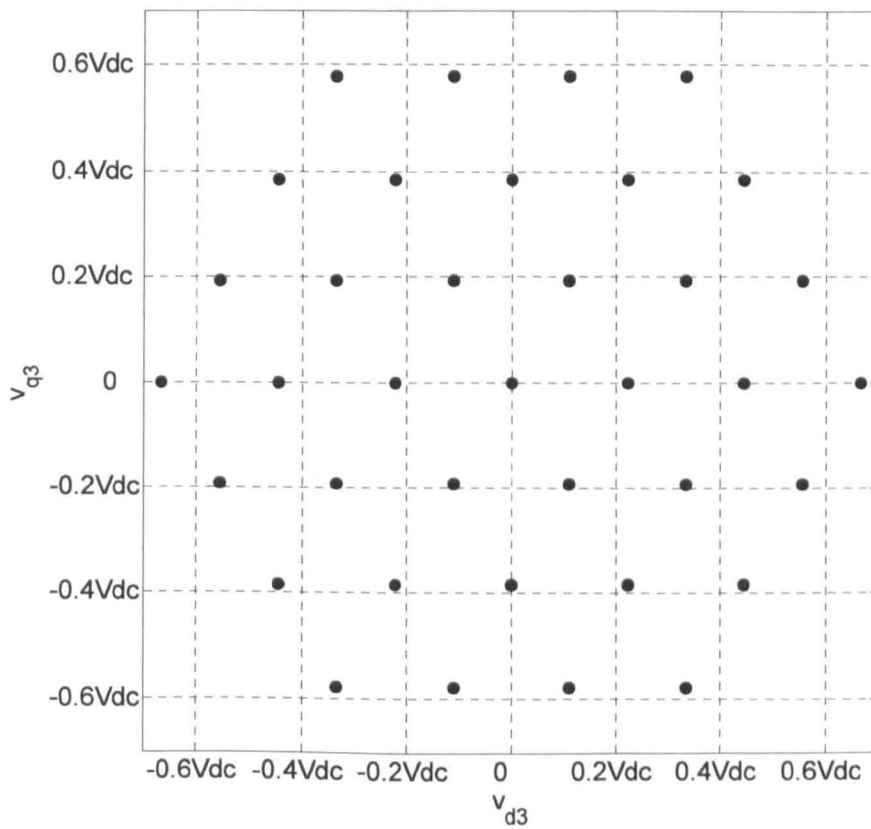
Fig. 3.13: Space vectors of a nine-phase VSI in the d_3-q_3 plane.

It is important to note however that any given space vector appears in different locations in these three planes, although the same locations are occupied by 512 different space vectors in all three planes. The redundancy is especially pronounced in the plane d_3-q_3 where all 512 space vectors appear in only 37 different locations. The number of sectors is eighteen and each sector spans $\pi/9$. The number of zero space vectors is also increased and there are 8 of them in the d_1-q_1, d_2-q_2 and d_4-q_4 planes, while 56 vectors appear as zero space vectors in the d_3-q_3 plane. The same zero space vectors appear in all three planes other than d_3-q_3, and they are $\bar{v}_0, \bar{v}_{73}, \bar{v}_{146}, \bar{v}_{219}, \bar{v}_{292}, \bar{v}_{365}, \bar{v}_{438}$ and $\bar{v}_{511}$.

The rest are the active space vectors, which with respect to the plane d_1-q_1, can be classified into 16 different groups based on their magnitudes. The same labelling is used with $n = 9$ now. Ten different load configurations (Fig. 3.14) can take place, {0-9}, {1-8}, {2-7}, {3-6}, {4-5}, {5-4}, {6-3}, {7-2}, {8-1} and {9-0}. Table 3.3 summarises relations between different space vector groups and load configurations. Magnitudes of all space vector groups, that are important for the development of the SVPWM scheme, are expressed using constants of (3.13) that are now $K = \sin(\pi/9)$, $K_2 = \sin(2\pi/9)$, $K_3 = \sin(3\pi/9)$ and $K_4 = \sin(4\pi/9)$. All of these space vector groups consist of space vectors located at angular positions equal to $k\pi/9$ ($k = 0$ to 17), which define borders between different sectors. The magnitudes of remaining active space vectors are given only with numerical values. Among all the space vectors that lead to configuration {4-5} or {5-4}, those that are with adjacent relation of '1' in switching states will have the largest magnitude. Hence they appear as space vectors in the outer-most polygon in the d_1-q_1 plane (Fig. 3.12) and belong to the G_{16}^9 group. The same is valid for all the other load configurations with respect to different space vectors groups, with the exception of configuration {1-8} or {8-1} that is exclusively associated with group G_6^9.
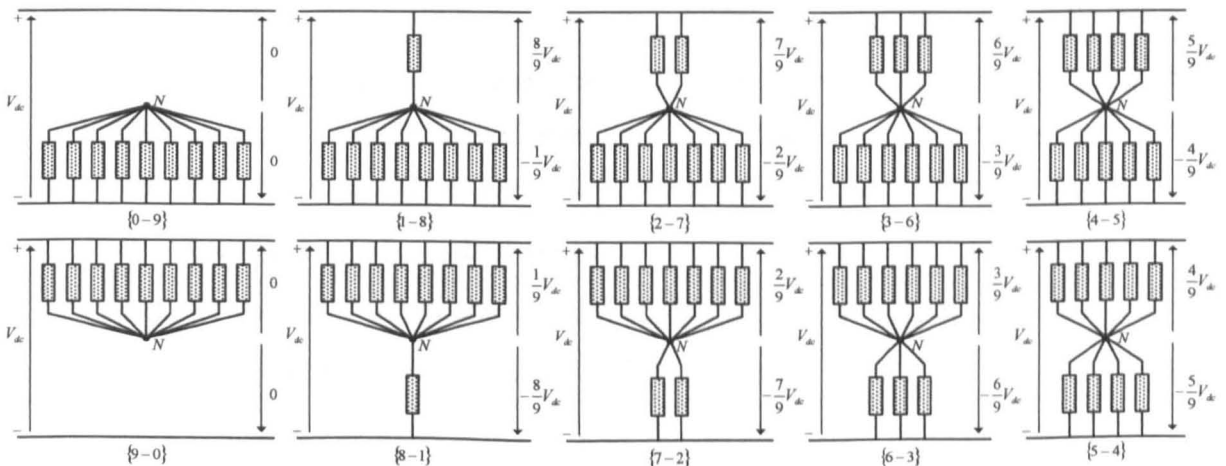
Fig. 3.14: Characteristic configurations of a nine-phase load.

Table 3.3: Nine-phase VSI space vector groups and their relations with load configurations.

Group	Magnitude in the d_1-q_1 plane	Magnitude in the d_2-q_2 plane	Magnitude in the d_3-q_3 plane	Magnitude in the d_4-q_4 plane	Load configurations
G_0^9	0	0	$0,\frac{4}{3}$	0	{0-9},{9-0} {3-6},{6-3}
G_1^9	$\frac{4}{9}\frac{K}{K_4}$	$\frac{4}{9}\frac{K_2}{K}$	$\frac{4}{9},\frac{8}{9}$	$\frac{4}{9}\frac{K_4}{K_2}$	{2-7},{7-2} {4-5},{5-4}
G_2^9	$\frac{4}{9}\frac{K}{K_2}$	$\frac{4}{9}\frac{K_2}{K_4}$	$\frac{4}{9}$	$\frac{4}{9}\frac{K_4}{K}$	{4-5},{5-4}
G_3^9	$\frac{4}{9}\frac{K_2}{K_4}$	$\frac{4}{9}\frac{K_4}{K}$	$\frac{4}{9}$	$\frac{4}{9}\frac{K}{K_2}$	{4-5},{5-4}
G_4^9	≈0.3040	≈0.5714	≈0.7698	≈0.8754	{3-6},{6-3}
G_5^9	$\frac{4}{9}\frac{K_3}{K_4}$	$\frac{4}{9}\frac{K_3}{K}$	0	$\frac{4}{9}\frac{K_3}{K_2}$	{3-6},{6-3}
G_6^9	$\frac{4}{9}$	$\frac{4}{9}$	$\frac{4}{9},\frac{8}{9},≈1.1759$	$\frac{4}{9}$	{1-8},{8-1} {2-7},{7-2} {4-5},{5-4}
G_7^9	≈0.5385	≈0.7239	$\frac{4}{9}$	≈0.9817	{4-5},{5-4}
G_8^9	≈0.5714	≈0.8754	≈0.7698	≈0.3040	{3-6},{6-3}
G_9^9	$\frac{4}{9}\frac{K_3}{K_2}$	$\frac{4}{9}\frac{K_3}{K_4}$	0	$\frac{4}{9}\frac{K_3}{K}$	{3-6},{6-3}
G_{10}^9	$\frac{4}{9}\frac{K_4}{K_2}$	$\frac{4}{9}\frac{K}{K_4}$	$\frac{4}{9},\frac{8}{9}$	$\frac{4}{9}\frac{K_2}{K}$	{2-7},{7-2} {4-5},{5-4}
G_{11}^9	≈0.7239	≈0.9817	$\frac{4}{9}$	≈0.5385	{4-5},{5-4}
G_{12}^9	$\frac{4}{9}\frac{K_2}{K}$	$\frac{4}{9}\frac{K_4}{K_2}$	$\frac{4}{9},\frac{8}{9}$	$\frac{4}{9}\frac{K}{K_4}$	{2-7},{7-2} {4-5},{5-4}
G_{13}^9	≈0.8754	≈0.3040	≈0.7698	≈0.5714	{3-6},{6-3}
G_{14}^9	≈0.9817	≈0.5385	$\frac{4}{9}$	≈0.7239	{4-5},{5-4}
G_{15}^9	$\frac{4}{9}\frac{K_3}{K}$	$\frac{4}{9}\frac{K_3}{K_2}$	0	$\frac{4}{9}\frac{K_3}{K_4}$	{3-6},{6-3}
G_{16}^9	$\frac{4}{9}\frac{K_4}{K}$	$\frac{4}{9}\frac{K}{K_2}$	$\frac{4}{9}$	$\frac{4}{9}\frac{K_2}{K_4}$	{4-5},{5-4}

Similar to the previous two analysed cases, it is possible to determine rules which govern the mapping of families of odd harmonic into different planes [Coates et al (2001), Grandi et al (2007a)]. In the case of a nine-phase system one has (k = 0, 1, 2, 3...):

- $18k\pm1$ harmonics → d_1-q_1 plane (1, 17, 19, 35, 37...).
- $18k\pm7$ harmonics → d_2-q_2 plane (7, 11, 25, 31, 43...).
- $18k\pm3$ harmonics → d_3-q_3 plane (3, 15, 21, 32, 39...).
- $18k\pm5$ harmonics → d_4-q_4 plane (5, 13, 23, 31, 41...).
- $18k\pm9$ harmonics → zero-sequence plane (9, 27, 45,...).

As with five-phase and seven-phase systems, zero-sequence harmonics are non-existent. There is an option now to inject the third, the fifth and the seventh harmonic in addition to the fundamental component for torque enhancement in concentrated winding machines [Coates et al (2001)]. Development of a SVPWM scheme, presented in chapter 5 is however based on neutralisation of all low-order harmonic components in order to generate sinusoidal output voltage. Such a solution is required whenever a machine is designed with distributed windings.

3.4 MODELLING OF MULTI-LEG VOLTAGE SOURCE INVERTERS

Topology of a multi-leg VSI fed multi-motor drive is shown in Fig. 3.15 for a particular configuration, based on a nine-leg VSI supplied four-motor drive. It can be seen that the first leg of the inverter is shared by one of the phases of each machine, while remaining legs are connected in the standard manner to the remaining phases of the three-phase machines. From control point of view, which leg of a multi-leg inverter is selected as a common does not matter, and leg *A* is selected here for purely illustration purposes. Based on Fig. 3.15 it is easy to establish a general rule for an *n*-leg inverter supplying (*n*-1)/2 three-phase machines. Thus, a five-leg VSI can be used for control of two machines, a seven-leg VSI for three machines, etc. Theory of vector space representation for multi-phase systems cannot be applied any more since loads connected to the inverter are now basically three-phase ones.
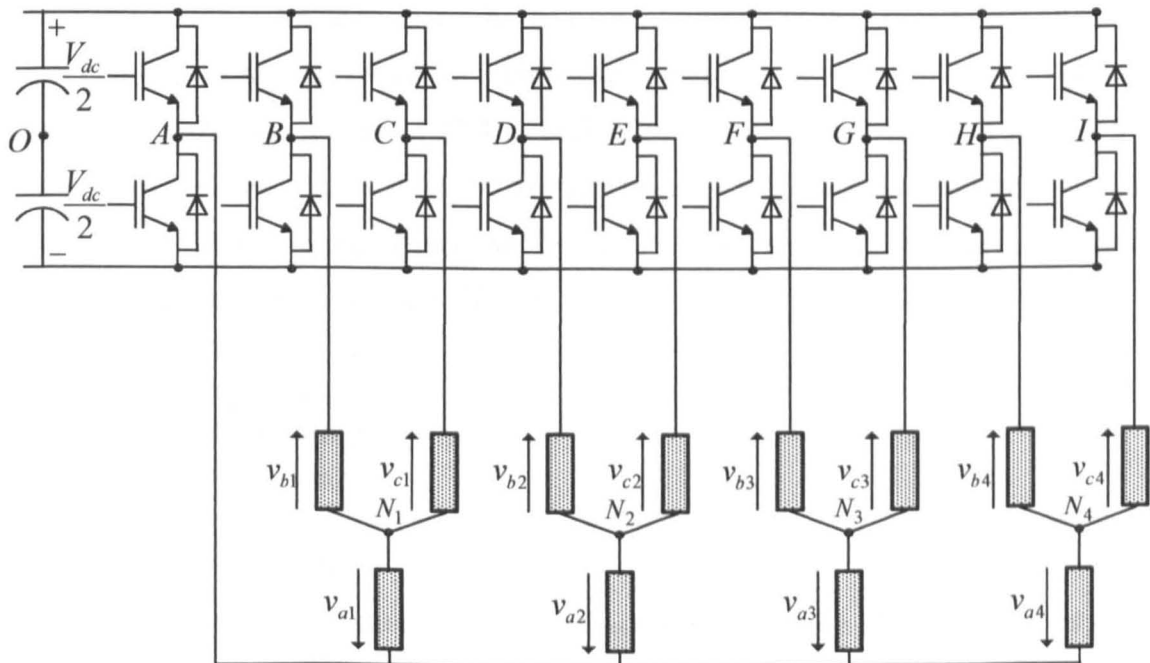
Fig. 3.15: A nine-leg VSI fed four-motor drive.

From the point of view of the multi-leg inverter and control issues, situation is however very similar to the multi-phase case. There are still 2^n available switching configurations for an n-leg inverter. Each three-phase load is connected to only three legs, thus restricting the number of switching configurations visible by that load to only $2^3 = 8$. This is the same number of switching configurations (space vectors) that would normally be used in a standard three-phase VSI. Switching functions can still be defined as in the first part of this chapter for a multi-phase VSI and leg voltages can be expressed based on that. However, since leg A is the common leg, its leg voltage is impacting on all machines, while leg voltages of the remaining legs are only influencing the machine connected to the particular leg.

The leg voltages of a multi-leg VSI, in accordance with the topology shown in Fig. 3.15, can be expressed as:

$$v_A = \frac{V_{dc}}{2}(2m_A - 1) = v_{N_1O} + v_{a1} = v_{N_2O} + v_{a2} = v_{N_3O} + v_{a3} = v_{N_4O} + v_{a4}$$

$$v_B = \frac{V_{dc}}{2}(2m_B - 1) = v_{N_1O} + v_{b1}$$

$$v_C = \frac{V_{dc}}{2}(2m_C - 1) = v_{N_1O} + v_{c1} \tag{3.23}$$

$$v_D = \frac{V_{dc}}{2}(2m_D - 1) = v_{N_2O} + v_{b2}$$

$$\vdots$$

$$v_I = \frac{V_{dc}}{2}(2m_I - 1) = v_{N_4O} + v_{c4}$$

For balanced star-connected three-phase loads, sum of the phase voltages of each load will be zero and therefore the same expression for CMV given with (3.2) or (3.3) can be used, provided that CMV is defined separately for each machine and the leg voltages of the three inverter legs supplying that particular machine are used. Phase voltages of the three-phase loads are obtainable by means of (3.4), considering the switching function related to the common leg A and the other two switching functions of legs associated with the particular machine. Finally, line voltages of each machine can be referenced with respect to the common leg A and thus effectively controlled. That is:

$$v_{AB} = v_{ab1} = V_{dc}(m_A - m_B)$$
$$v_{AC} = v_{ac1} = V_{dc}(m_A - m_C)$$
$$v_{AD} = v_{ab2} = V_{dc}(m_A - m_D)$$
$$v_{AE} = v_{ac2} = V_{dc}(m_A - m_E) \tag{3.24}$$
$$\vdots$$
$$v_{AI} = v_{ac3} = V_{dc}(m_A - m_I)$$

As it can be seen, the set of equations necessary to analyse a multi-leg VSI supplied drive is rather simple and is mostly based on the well known relations for a three-phase VSI. This fact

is used later on in the development of a modulation scheme able to satisfy voltage requirements of all three-phase machines. In particular, the PWM method, developed and presented in chapter 10, is based on utilisation of the well known principles of three-phase modulation methods. Both carrier-based and space vector PWM strategies are elaborated, and are characterised with simplicity in implementation and excellent performance.

3.5 SUMMARY

Basic sets of equations are introduced in this chapter, which are necessary for the description of multi-phase and multi-leg VSIs. Logic type switching functions are defined for each leg of the inverter, and they are used to express different voltages of a multi-phase and a multi-leg system. General space vector transformation is introduced and power variant form of the decoupling transformation matrix is defined. This enables vector space decomposition of an n-phase system into $(n$-1$)/2$ 2-D and mutually orthogonal planes that are labelled throughout the thesis as d_1-q_1, d_2-q_2, d_3-q_3, etc. By applying this transformation to phase voltages of an n-phase star-connected load connected to an n-phase VSI, voltage space vectors in all $(n$-1$)/2$ planes are obtained. Single dimensional zero-sequence plane is not excited in the case of a star-connected n-phase load with isolated neutral. Mapping of families of odd harmonics is explained for all three topologies (five-phase, seven-phase and nine-phase) considered in the thesis. Additionally, basic considerations with regard to multi-leg inverter modelling are given and similarities with three-phase drives are identified. The material presented in this chapter creates foundation necessary for development of PWM schemes for multi-phase and multi-leg inverters.

Development of such continuous SVPWM schemes for sinusoidal output voltage generation with a five-phase VSI is elaborated in the next chapter.

Chapter 4

SPACE VECTOR PWM METHODS FOR SINUSOIDAL OUTPUT VOLTAGE GENERATION WITH A FIVE-PHASE VOLTAGE SOURCE INVERTER

4.1   INTRODUCTION

Analysis, development, implementation and experimental verification of various PWM techniques for a five-phase VSI, based on space vector approach, are presented in this chapter. Techniques, covered in the thesis, can be classified in broad terms as carrier-based PWM methods and space vector based PWM methods. Carrier-based PWM methods utilise low frequency reference signal comparison with high-frequency carrier signal in order to generate a train of pulses that follows the volt-second principle over the carrier period. Historically speaking, these methods are older and have been developed for three-phase systems during the era of analogue electronics. All of them however have been adapted to the digital form with the subsequent development of microcontrollers and DSPs. Space vector PWM methods are on the other hand direct digital methods. Volt-second principle is utilised by averaging the reference space vector (that normally corresponds to the fundamental signal) with pre-selected set of active space vectors over the switching period. Time of application of different vectors is calculated from a set of equations and, using software/hardware units of a DSP, switching pulse patterns are generated.

From the point of view of the switching characteristics, PWM schemes can be divided into continuous PWM (CPWM) and discontinuous PWM (DPWM). For CPWM schemes, in each carrier signal period (switching period), every inverter leg switches between the positive and negative rail of the dc bus. In DPWM strategies, in every switching period, one of the inverter legs, is clamped either to the negative or positive rail of the dc bus. Non-switching action in an inverter leg during some switching periods of the DPWM schemes leads to the reduction in the average switching frequency and to lowering of switching losses in the DPWM schemes [Holmes and Lipo (2003)]. At the same time this allows for an increase in

the switching frequency of a DPWM compared to CPWM, if the switching losses are to be kept at the same level as with the CPWM schemes [Kolar et al (1991a)]. Regimes of operation of modulators, regardless of the type, can be classified as: linear mode and non-linear mode (overmodulation). Operation in the linear region is characterised with unity modulator gain value while operation in the overmodulation region is followed with a significant decrease in the modulator gain value [Hava et al (1998)]. When in overmodulation, all methods (both CPWM and DPWM) have a discontinuous nature regarding the PWM switching pattern [Holmes and Lipo (2003)]. In what follows, characteristics of modulation strategies for multi-phase VSIs are investigated under the following restrictions: only CPWM schemes (carrier-based PWM and SVPWM), operating in the linear modulation region, are encompassed by the study. DPWM schemes and the operation in overmodulation are therefore beyond the scope of this thesis.

SVPWM schemes for a five-phase VSI are elaborated in this chapter, while the carrier-based PWM methods are analysed in chapter 6. In both cases, generation of purely sinusoidal output voltage is the aim with zeroing of all low order harmonic components. Some of the PWM methods presented in the thesis are based on existing modulation schemes for a three-phase VSI and, when possible, a simple extension to the multi-phase case is done. This is mostly the situation with carrier-based PWM schemes analysed later on in the thesis. SVPWM schemes for multi-phase VSIs require a more detailed analysis and correlation with the three-phase case is not always straightforward as it will be demonstrated. Therefore, special attention is paid to the similarities and differences between the multi-phase carrier-based PWM and SVPWM strategies, in order to establish a better link between the two, at the first sight, different approaches.

The chapter is organised as follows. Section 4.2 defines basic terms necessary for analysis and development of SVPWM schemes and, later on, carrier-based PWM schemes. Characteristics of SVPWM methods common to all multi-phase topologies, covered in the thesis, are addressed and performance criteria are defined for the purposes of analysis and comparison of obtained results. In section 4.3, three different SVPWM schemes for a five-phase VSI are investigated and experimental results are collected from a five-phase VSI fed balanced star-connected static *R-L* load. Effects and impacts of various selections of active space vector sets are analysed and different modulation schemes are developed. It is shown that a simple extension of the three-phase SVPWM cannot provide sinusoidal output voltage since it is accompanied with low order harmonic components from the second plane, in accordance with the mapping presented in chapter 3. Therefore, use of four active space

vectors is mandatory for sinusoidal output voltage generation. Two SVPWM schemes, based on utilisation of four active space vectors, are presented and compared. Summary of the chapter is given in section 4.4.

SVPWM methods for sinusoidal output voltage generation with a five-phase VSI have been analysed already by Silva et al (2004), Iqbal and Levi (2005), Iqbal and Levi (2006a), Xue and Wen (2005) and Xue et al (2006). These methods are reviewed in this chapter, in order to establish a benchmark for further generalisation of SVPWM schemes for sinusoidal output voltage generation with multi-phase VSIs. Also, development of a multi-frequency PWM scheme reported in chapter 9 will heavily rely on the results presented in this chapter. An effort is made to obtain results in a form that will enable a simple comparison with the carrier-based PWM methods later on. The main original results of this chapter have been presented in Dujić et al (2007c) and partially in Dujić et al (2008a).

4.2 PRELIMINARY CONSIDERATIONS

It is necessary to at first define basic terms and establish some performance criteria that are required for analysis and comparison of different PWM methods. Square-wave or $2n$-step mode of operation of a multi-phase VSI is omitted from the analysis since this type of control is nowadays rarely of interest. This mode of operation is obtained by setting the conduction time of each inverter switch to $180°$ with $2\pi/n$ phase delay between firing of two switches in any two consecutive phases. One complete cycle of operation of the inverter can be divided into $2n$ distinct modes thus leading to well known terms: six-step mode for three-phase VSI, ten-step mode for five-phase VSI, etc. It can be easily shown that these $2n$ modes of operation correspond to the application of only $2n$ space vectors defined in the previous chapter as the space vectors with the largest magnitudes in the d_1-q_1 plane. Thus, these space vectors belong to the groups G_3^5, G_8^7 and G_{16}^9, respectively. More details regarding ten-step mode of operation of a five-phase VSI are available in Iqbal (2005).

In order to define modulation index for PWM modulators properly, some results obtained from the square-wave mode of operation must be considered. Fundamental component magnitude of the square-wave mode phase voltage has the value of $V_{2n-step} = 2V_{dc}/\pi$ for a given dc bus voltage. The ratio of the magnitude of the fundamental phase voltage V_m to the fundamental component magnitude of the square-wave mode voltage is termed the modulation index M:

$$M = \frac{V_m}{V_{2n-step}} \qquad\qquad\qquad (4.1)$$

Using this definition, very often found in literature (for example, van der Broeck et al (1988), Hava et al (1998b)), maximum modulation index (or the full dc bus voltage utilisation) can be achieved only in the 2*n*-step mode of operation and then it is by definition unity, $M_{2n-step} = 1$. In order to simplify further analysis, a different definition of the modulation index will be used here. Modulation index is defined as the ratio of the fundamental output phase voltage magnitude (peak value) and half of the dc bus voltage:

$$M = \frac{V_m}{V_{dc}/2} \qquad\qquad\qquad (4.2)$$

Based on (4.2), fundamental inverter output phase voltage magnitude is determined with $V_m = M V_{dc}/2$. Thus, when 2*n*-step mode of operation is reached, modulation index is of the value $M_{2n-step} = 4/\pi \approx 1.2731$. Additionally, in order to cover the complete possible range of operation of a modulator, it is essential to define reference modulation index M^* as:

$$M^* = \frac{V_m^*}{V_{dc}/2} \qquad\qquad\qquad (4.3)$$

where V_m^* is the peak value of the fundamental reference (sinusoidal) modulating signal [Hava (1998)]. From this definition, it follows that both modulation indices (4.2) and (4.3) have a value of unity when the numerator equals $V_{dc}/2$. For each of the PWM modulation schemes it is possible to find a modulation index value that separates linear region and overmodulation region of operation. While operating in the linear region, modulation index and reference modulation index are equal. As emphasised already, overmodulation region is characterised with a significant decrease in the fundamental voltage component gain and characteristics are different for each type of the modulator [Hava (1998)]. Modulator gain G is defined as the ratio of the output voltage fundamental component peak value V_m to the reference modulation wave fundamental component peak value V_m^*:

$$G = \frac{V_m}{V_m^*} = \frac{M}{M^*} \qquad\qquad\qquad (4.4)$$

Thus, in the linear region of operation modulator gain has unity value while a decrease occurs in the overmodulation. Since overmodulation is beyond the scope of research in this thesis, only one modulation index based on (4.2) is used further on. In the linear region, having a unity gain implies that both modulation indices are actually equal, and therefore use of only one suffices.

Next, for the purpose of comparison of the performance obtained with different types of PWM modulators, several performance criteria can be introduced. In most cases, selected criteria will heavily depend on the application, design of the drive, machine type, power level, type of power semiconductors used, etc. It is thus possible to use harmonic distortion of the machine currents or voltages, torque ripple, switching losses or overall dynamic performance as the figure of merit. Demands such as minimisation of acoustic noise generated during operation of a motor drive [Accardo et al (2006)] or CMV elimination for prolonging the life of machine bearings [Oriti et al (1997a), Oriti et al (1997b)] can lead to the development of special PWM schemes with superior performance regarding the selected criterion, although performance with regard to some other criteria can be not so good. In this thesis, spectrum content of VSI output voltage/current will be used as the figure of merit for comparison of performance of the different PWM schemes. Since all PWM schemes are at this stage aimed at sinusoidal output voltage generation, such a figure of merit is sufficient for comparative evaluation of the developed PWM strategies. In addition, the PWM schemes are analytically and experimentally compared with respect to their current ripple characteristics responsible for switching harmonic losses in chapters 7 and 8.

Finally, the common constraints imposed to all PWM schemes analysed and presented in the thesis are related to the easiness of implementation. The principle of operation of the PWM dedicated hardware units of modern DSPs is basically identical to the principle of generation of the PWM pulses with the analogue carrier-based PWM methods. In analogue implementation, pulses per inverter legs are generated by means of comparison of the appropriate fundamental reference signals with a high frequency carrier signal. Switching period/frequency in such an implementation is defined with the carrier frequency, which is in low/medium drives sufficiently higher than the fundamental frequency. In the digital world of a DSP, PWM pulses are obtained in a very similar fashion. Reference signals are sampled and loaded into dedicated registers. The content (digital word of a certain number of bits, e.g. 8, 16, 32) is then compared against values of up/down running counters/timers with a predefined period that corresponds to the switching period. Thus, the high frequency carrier signal is replaced with dedicated digital counters/timers whose operation is precisely controlled with the clock signal (usually in the range of hundreds of MHz and pre-scalable to the lower clock rate). Analogue carrier signals are usually of saw-tooth or triangular shape. Setting the counters/timers in the continuous up/down mode of operation corresponds to the triangular carrier signal in analogue world and leads to generation of symmetrical switching patterns. This means that each of the inverter legs, considering operation in the linear region only, will

have two commutations per switching period and appearance of the switching pattern will be symmetrical with respect to the middle of the switching period. This imposed restriction greatly affects the switching pattern as long as SVPWM methods are concerned. At the same time it can be used as a guideline for selection of active space vectors, as it will be shown.

4.3 CONTINUOUS SPACE VECTOR PWM FOR A FIVE-PHASE VOLTAGE SOURCE INVERTER

Although SVPWM schemes for sinusoidal output voltage generation have already been analysed by Silva et al (2004), Iqbal and Levi (2005), Iqbal and Levi (2006a) and Xue and Wen (2005), with the exception of the work of Silva et al (2004), the analyses were purely theoretical. A comprehensive and systematic analysis of three particular SVPWM schemes is therefore undertaken in this section, based on selection of the different active space vectors and accompanied with a thorough experimental evaluation. At first, it is shown that simple extension of the well known three-phase SVPWM does not yield sinusoidal output voltage and results in the presence of the third harmonic in voltage/current waveforms. Increasing the number of active space vectors per switching period makes it possible to generate pure sinusoidal output voltages. Two PWM schemes, based on the application of four active space vectors per switching period, are analysed and compared. The first one utilises two medium and two large active space vectors per switching period, while the second scheme is based on the use of four large active space vectors. Although both schemes yield a sinusoidal output voltage with the same level of dc bus utilisation, method based on the use of four large active space vectors leads to difficulties in implementation based on standard DSP PWM hardware units, as it will be explained. Therefore, only the SVPWM scheme based on the use of two medium and two large active space vectors is experimentally investigated together with the scheme based on the extension of the three-phase SVPWM.

4.3.1 SPACE VECTOR PWM BASED ON THE USE OF TWO LARGE ACTIVE SPACE VECTORS

A simple extension of the three-phase SVPWM can be easily applied to a five phase VSI. Such a scheme is based on the use of two adjacent large active space vectors per switching period. Since in a three-phase system there is only one plane to be considered, the same approach will be followed for the five-phase case. This will illustrate the effects of neglecting the existence of multiple *d-q* planes in multi-phase systems.

Having only large active space vectors from the d_1-q_1 plane involved in the switching pattern reduces the number of used active space vectors from 30 to only 10. Large active space vectors of the d_1-q_1 plane are shown in Fig. 4.1 together with their mapping into small space vectors in the d_2-q_2 plane. However, the d_2-q_2 plane is not used during synthesis of the SVPWM scheme and its impact on the output voltages is analysed after simulation/experimental results are given. Two zero space vectors are used in addition to the active space vectors in the same way as for a three-phase SVPWM. Since only large and zero space vectors are utilised, the five-phase load will never appear in {1-4} and {4-1} configurations that result for medium space vectors.

There is only one reference space vector in the d_1-q_1 plane that, when normalised with $V_{dc}/2$ in order to be in the agreement with the contents of Table 3.1, can be expressed using the modulation index as:

$$\bar{v}^* = Me^{j\vartheta} \tag{4.5}$$

where ϑ is the instantaneous reference space vector position in the d_1-q_1 plane.

It is enough to consider in the analysis the situation when the reference space vector is in sector 1, as shown in Fig. 4.2. To simplify the analysis, the active space vectors are labelled with additional sub-scripts 'a' and 'b', associated with fictional lines that separate sectors. Thus, regardless of the sector being considered, when rotating anti-clockwise in the d_1-q_1 plane, each sector starts with a certain 'a' large space vector and ends with a certain 'b' large space vector.
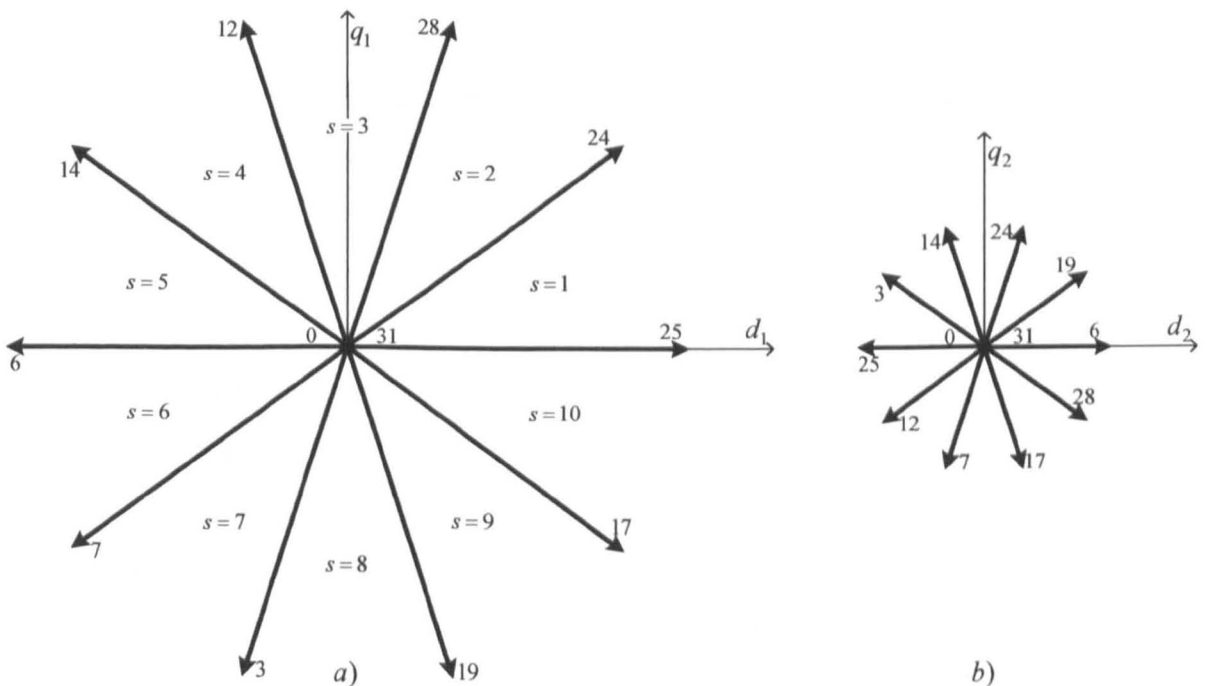
Fig. 4.1: Large space vectors of the d_1-q_1 plane and their mapping into the d_2-q_2 plane.
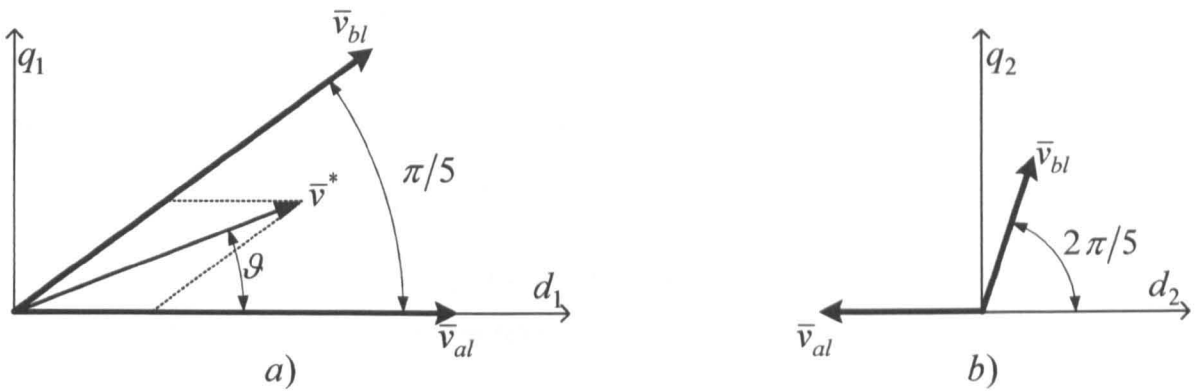
Fig. 4.2: Principle of averaging of the reference space vector with two large space vectors in the d_1-q_1 plane (a)), and two activated small space vectors in the d_2-q_2 plane (b)).

The reference space vector is realised in the d_1-q_1 plane by means of averaging over the switching period (T_s) with two adjacent large active space vectors applied during properly calculated times of applications:

$$\bar{v}^* T_s = \bar{v}_{al} T_{al} + \bar{v}_{bl} T_{bl} \tag{4.6}$$

Equation (4.6) does not consider the d_2-q_2 plane where two small space vectors that correspond to two selected large space vectors from the d_1-q_1 plane are activated (Fig. 4.2b). Taking into consideration the situation shown in Fig. 4.2 and using simple trigonometry, complex equation (4.6) can be decomposed into two real equations:

$$M \cos(\vartheta) T_s = \frac{4}{5} \frac{K_2}{K} T_{al} + \frac{4}{5} \frac{K_2}{K} L T_{bl}$$
$$M \sin(\vartheta) T_s = \frac{4}{5} \frac{K_2}{K} K T_{bl} \tag{4.7}$$

In (4.7), values for the magnitudes of large space vectors are taken from Table 3.1 and constants introduced in (3.13) are used to express projections of the active space vectors onto two axes. After some manipulation, times of application of active space vectors over the switching period are obtained as:

$$T_{al} = \frac{M}{\frac{4}{5} K_2} \sin(\frac{\pi}{5} - \vartheta) T_s; \qquad T_{bl} = \frac{M}{\frac{4}{5} K_2} \sin(\vartheta) T_s \tag{4.8}$$

The remaining time within a switching period belongs to the two zero space vectors and its total value can be found as:

$$T_O = T_0 + T_{31} = T_s - T_{al} - T_{bl} \tag{4.9}$$

By replacing (4.8) into (4.9), the total time of application of zero space vectors in the first sector, as a function of the modulation index, can be calculated as:

$$T_O = T_0 + T_{31} = [1 - M \frac{5L_2}{2K_2} \cos(\frac{\pi}{10} - \vartheta)] T_s \tag{4.10}$$

Distribution of (4.10) among two zero space vectors represents a degree of freedom that can be used to produce different PWM methods. SVPWM, analysed here, shares this total time of application in a classical way, equally among two zero space vectors:

$$T_0 = T_{31} = \frac{1}{2}[1 - M\frac{5L_2}{2K_2}\cos(\frac{\pi}{10} - \vartheta)]T_s \tag{4.11}$$

To simplify further writing, duty cycles are introduced as a relative time of application of each space vector over the switching period:

$$\delta_{al} = \frac{T_{al}}{T_s}; \qquad \delta_{bl} = \frac{T_{bl}}{T_s}; \qquad \delta_0 = \frac{T_0}{T_s}; \qquad \delta_{31} = \frac{T_{31}}{T_s}; \qquad \delta_s = \frac{T_s}{T_s} = 1 \tag{4.12}$$

All results presented until now are based on the analysis in the first sector of the d_1-q_1 plane. A general solution, applicable for every sector s ($s = 1$ to 10) and expressed by means of introduced duty cycles, has the form:

$$\delta_{al} = \frac{M}{\frac{4}{5}K_2}\sin(s\frac{\pi}{5} - \vartheta); \qquad \delta_{bl} = \frac{M}{\frac{4}{5}K_2}\sin(\vartheta - (s-1)\frac{\pi}{5})$$

$$\delta_0 = \delta_{31} = \frac{1}{2}\delta_O = \frac{1}{2}[1 - M\frac{5L_2}{2K_2}\cos((2s-1)\frac{\pi}{10} - \vartheta)] \tag{4.13}$$

Once when the duty cycle of each space vector is obtained for a given reference space vector, the switching pattern can be synthesised based on the pre-selected set of space vectors. For the SVPWM analysed here, the set contains only ten active large space vectors (group G_3^5) and two zero space vectors (group G_0^5) that need to be organised in a certain order inside the switching period. An illustration of the switching pattern for the first two sectors is given in Fig. 4.3. A symmetrical switching pattern is obtained and the sequence of the applied vectors in all odd sectors is $\bar{v}_0, \bar{v}_{bl}, \bar{v}_{al}, \bar{v}_{31}, \bar{v}_{al}, \bar{v}_{bl}, \bar{v}_0$, while in even sectors the sequence is different, $\bar{v}_0, \bar{v}_{al}, \bar{v}_{bl}, \bar{v}_{31}, \bar{v}_{bl}, \bar{v}_{al}, \bar{v}_0$. Such an arrangement provides an equal and minimal (for the continuous modulation) number of commutations per inverter leg.
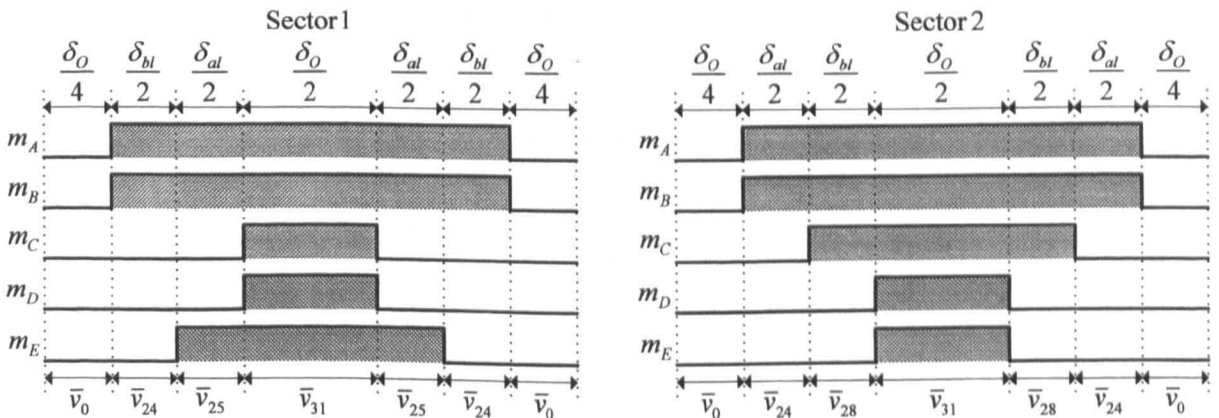

Fig. 4.3: Switching pattern in the first two sectors.

For implementation, knowledge of the switching pattern in all sectors is necessary together with the total values of duty cycles per inverter legs. This is obtained by simple summation of the calculated duty cycles of each space vector for every leg in accordance with the predefined switching pattern in every sector. Thus, duty cycles, from the one having the smallest value to the one having the largest value, are defined with:

$$\delta_1 = \frac{\delta_0}{2}$$
$$\delta_2^O = \delta_1 + \delta_{al}; \qquad\qquad \delta_2^E = \delta_1 + \delta_{bl} \qquad\qquad (4.14)$$
$$\delta_3 = \delta_1 + \delta_{al} + \delta_{bl}$$

where superscripts '*O*' and '*E*' stand for 'odd' and 'even' sector, respectively. This is easy to identify in Fig. 4.3, based on illustration for the first two sectors. Disposition of duty cycles for all five legs of a VSI in all ten sectors is summarised in Table 4.1. These values are the actual values that will be loaded in the dedicated compare registers of a DSP PWM unit during final implementation. The SVPWM generated switching functions (m_A to m_E) can be identified from Fig. 4.3.

The maximum achievable fundamental output voltage defines dc bus utilisation of the PWM method. It can be determined in two ways based on the presented analysis: i) graphically, from Fig. 4.2, by considering the reference space vector as being in the middle of the sector and finding the projection of one of the adjacent large space vectors on the reference space vector; ii) it can be determined from (4.10) as the value of the modulation index at which the total time of application of the zero space vectors becomes equal to zero, again, for the reference space vector in the middle of the first sector ($\vartheta = \pi/10$). One thus finds that the maximum achievable value of the modulation index of this SVPWM is:

$$M_{\max} = \frac{2K_2}{5L_2} \approx 1.2311 \qquad\qquad (4.15)$$

This value is high and it represents 96.7% of the magnitude of the fundamental obtainable in the ten-step mode ($M_{2n\text{-}step} \approx 1.2731$). It is also higher than the value obtainable with the three-phase SVPWM which is $M_{max} \approx 1.1547$.

Table 4.1: Duty cycle disposition through sectors.

Leg | Sector	1	2	3	4	5	6	7	8	9	10
A	δ_3	δ_3	δ_2^O	δ_1	δ_1	δ_1	δ_1	δ_2^E	δ_3	δ_3
B	δ_3	δ_3	δ_3	δ_3	δ_2^O	δ_1	δ_1	δ_1	δ_1	δ_2^E
C	δ_1	δ_2^E	δ_3	δ_3	δ_3	δ_3	δ_2^O	δ_1	δ_1	δ_1
D	δ_1	δ_1	δ_1	δ_2^E	δ_3	δ_3	δ_3	δ_3	δ_2^O	δ_1
E	δ_2^O	δ_1	δ_1	δ_1	δ_1	δ_2^E	δ_3	δ_3	δ_3	δ_3

Simulations were further carried out, using MATLAB/Simulink. Dc bus voltage is set to 1 per unit (p.u.), the switching frequency is 5 kHz, and all phase voltages are low-pass filtered with a time constant of 0.8 ms. The inverter switches are assumed to be ideal and thus no dead-time is introduced in the model. Simulations were performed for three different values of the modulation index (a low value, a value close to 50% of the maximum achievable and the maximum value of the modulation index) with fundamental frequency set to 50 Hz.
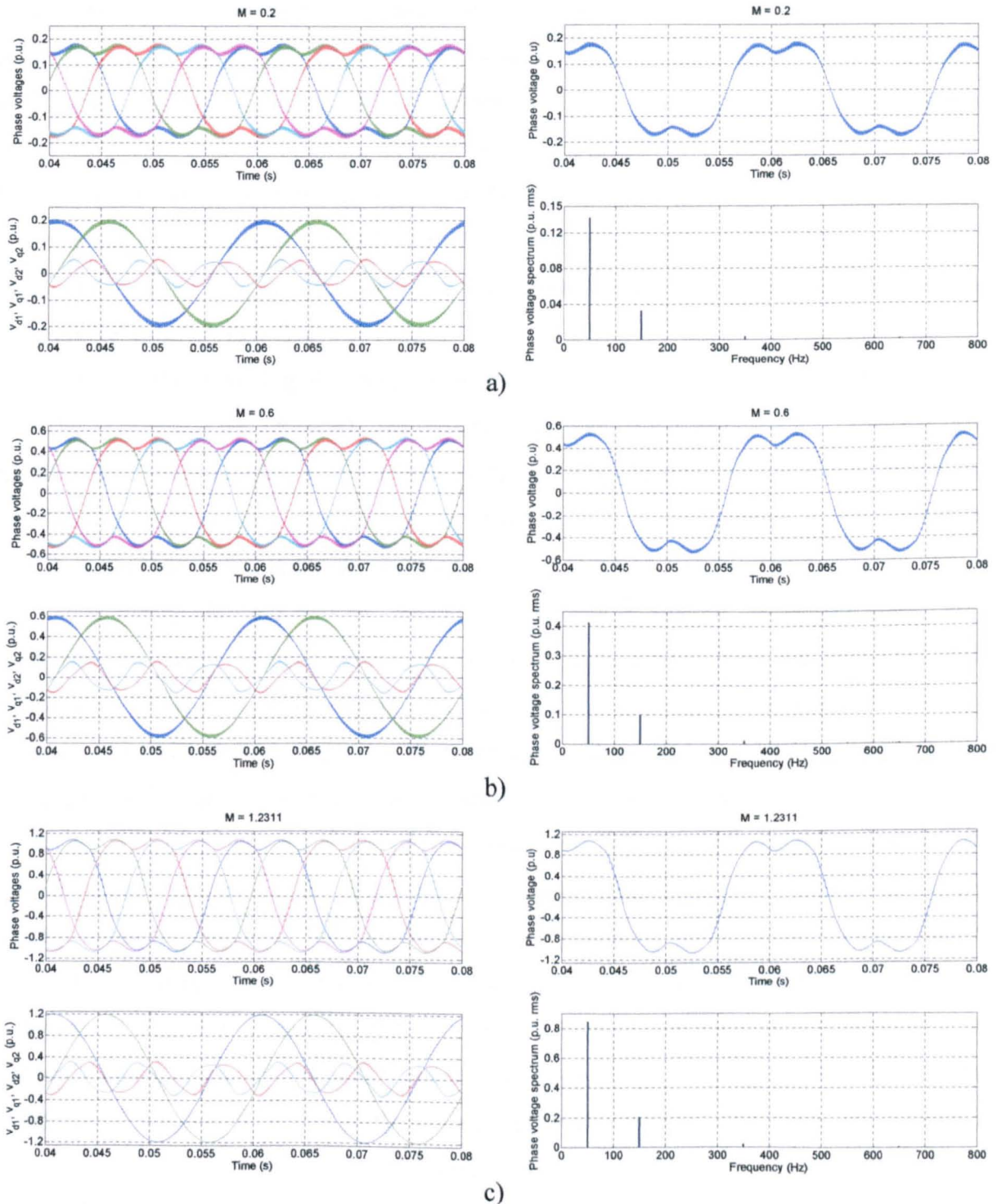
Fig. 4.4: Simulation results - phase voltages and their axis components in two planes (left) and phase voltage with its spectrum (right) at: a) $M = 0.2$, b) $M = 0.6$, and c) $M = 1.2311$.

Although the reference (4.5) at the input of the modulator is purely sinusoidal, the output phase voltages are not. It can be seen from the simulation results (left upper parts of Fig. 4.4), phase voltages are non-sinusoidal and contain harmonic components in addition to the fundamental. When the transformation given with (3.15) is applied to the generated phase voltages, their representation in the planes d_1-q_1 and d_2-q_2 is obtained (left lower parts of Fig. 4.4). It can be seen that, in addition to the fundamental component generated in the d_1-q_1 plane in accordance with the modulator input reference space vector, there are components of higher frequencies in the second plane. This is further demonstrated by taking the FFT of one of the phase voltages (right part of Fig. 4.4) where these components are clearly visible (rms values are shown in the spectrum). In addition to the fundamental, spectrum shows presence of the third harmonic (around 23.8%) and the seventh harmonic (around 2.5%). Thus, a simple extension of the three-phase SVPWM cannot produce a sinusoidal output voltage. As a consequence of the second plane not being considered, harmonics characteristic for the d_2-q_2 plane are generated ($10k \pm 3$, $k = 0, 1, 2...$).

It is visible from Fig. 4.1 that, regardless of the sector, when two large space vectors from the d_1-q_1 plane are activated, their mapped pair (two small space vectors from the d_2-q_2 plane) is activated simultaneously. However, times of application for the active vectors are calculated considering only the first plane, resulting in non-zero average voltage generated over the switching period in the second plane.

To verify the simulations results, the SVPWM scheme is implemented in a TMS320F2812 DSP and experiments were carried out on a five-phase star-connected static *R-L* load. A description of the experimental set-up and parameters of the static *R-L* load are given in Appendix A and Appendix B, respectively. Switching frequency is set to 5 kHz (dead-time is 3.25 μs and it is not compensated for) and the fundamental frequency is kept constant, at 50 Hz. Only the value of the modulation index is varied, taking readings for several values over the whole achievable range. One phase voltage of a five-phase load is directly measured using the HP35665A dynamic signal analyser and it is low pass filtered with a cut-off frequency of 1.6 kHz. Dc bus voltage was around 600 V. Based on the results presented in Fig. 4.5, it can be seen that both waveforms of the phase voltage and the harmonic contents are in accordance with results obtained by simulations. Harmonics of the second plane are clearly visible in the voltage spectrum (the third at 150 Hz, the seventh at 350 Hz and the thirteenth at 650 Hz) and their rms values are in constant ratio to the fundamental over the whole range of the modulation index.
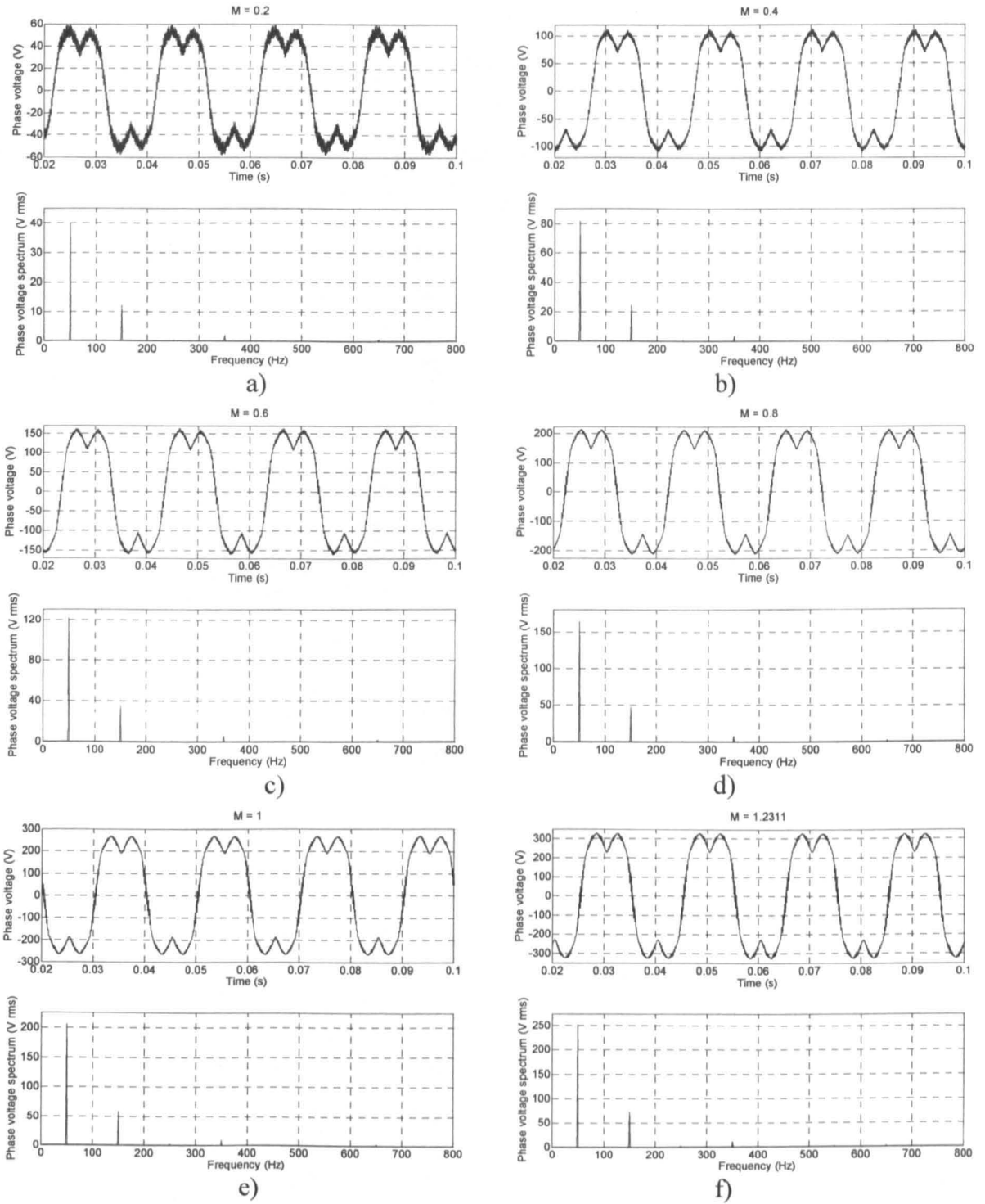
Fig. 4.5: Experimental results - phase voltage and its spectrum at: a) $M = 0.2$, b) $M = 0.4$, c) $M = 0.6$, d) $M = 0.8$, e) $M = 1$, and f) $M = 1.2311$.

In addition to the phase voltage, CMV has been measured between the neutral connection of the star-connected load and the mid-point of the dc bus capacitors. For this, a Tektronix TDS1012 scope was used with a voltage probe with 50X attenuation. The results are shown in Fig. 4.6, from where characteristic voltage levels can be identified. In a five-phase system, CMV can appear with six different voltage levels: $\pm V_{dc}/2$, $\pm 3V_{dc}/10$, $\pm V_{dc}/10$.

The largest magnitude level is a result of the load being in {0-5} and {5-0} configurations, which correspond to zero space vectors. Voltage level of $\pm 3V_{dc}/10$ appears when load is in configurations {1-4} and {4-1}, thus being linked to the use of medium active space vectors, while the remaining $\pm V_{dc}/10$ voltage level appears when load is in {2-3} and {3-2} configurations, e.g. when small or large active space vectors are used.
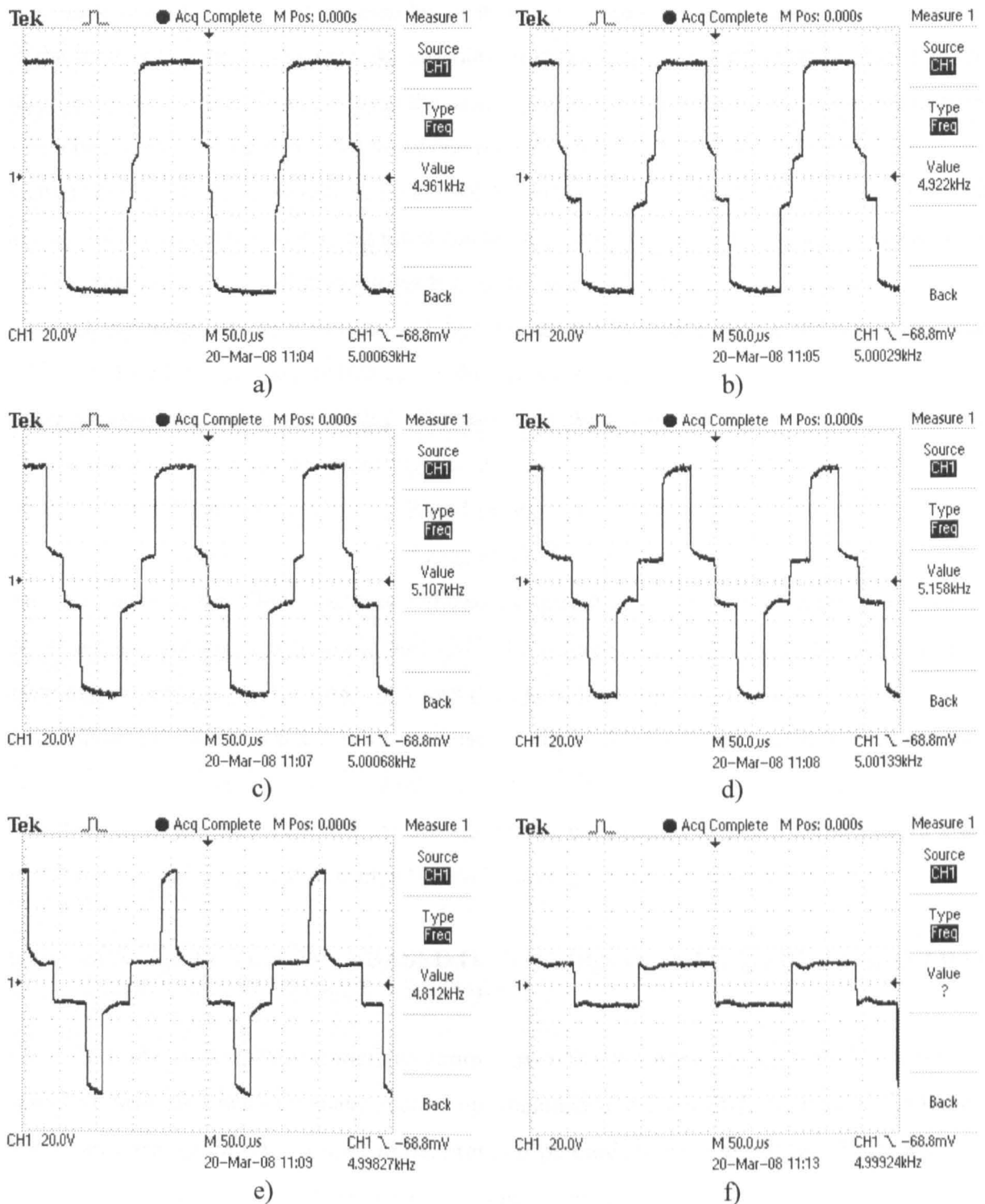
Fig. 4.6: Experimentally measured common-mode voltage at: a) $M = 0.2$, b) $M = 0.4$, c) $M = 0.6$, d) $M = 0.8$, e) $M = 1$, and f) $M = 1.2311$ (Scale: 100V/div).

Since the analysed SVPWM scheme does not utilise medium space vectors, this is reflected in the appearance of the CMV. This can be clearly identified from Fig. 4.6 considering that the real scaling is actually 100V/div (used scope does not support 50X probe and was set to 10X input probe). For low values of the modulation index, zero space vector duty cycles are bigger than duty cycles of the active space vectors, resulting in voltage levels at ±300 V lasting longer than voltage levels at ±60 V (which are the result of the application of the large active space vectors). As modulation index increases, a decrease is visible in the zero vector duty cycles. Finally, when the maximum achievable value of the modulation index is reached, they become equal to zero (when the reference space vector is in the middle of any sector) resulting in disappearance of the ±300 V voltage levels in the CMV. This is illustrated in Fig. 4.6f, where the CMV is captured for the maximum value of the modulation index. A further increase of modulation index leads into the overmodulation.

Knowledge of the CMV caused by various PWM schemes is important, since the CMV produced by the fast switching of the power semiconductors is often the reason for bearing damages [Oriti et al (1997a)]. Three-phase PWM schemes, aimed at reduction of the CMV, are mostly based on removing the zero space vectors from the switching pattern [Hofmann and Zitzelsberger (2006)]. Based on Figs. 4.6, it is visible that this kind of action would lead to a reduction of the CMV magnitude for a five-phase system too. Additionally, rate of change of the CMV could be reduced by introducing the medium space vectors into the switching pattern, which would add $\pm 3V_{dc}/10$ voltage levels into the CMV waveform. A more detailed analysis of the CMV is however beyond the scope of the thesis.

Based on the presented results, the use of only two large space vectors cannot produce sinusoidal output voltages and the number of active space vectors must be increased [Silva et al (2004), Iqbal and Levi (2005)]. At the same time, both planes of a five-phase system must be considered. Development of such a SVPWM strategy is presented next.

4.3.2 SPACE VECTOR PWM BASED ON THE USE OF TWO MEDIUM AND TWO LARGE ACTIVE SPACE VECTORS

In order to establish complete control over the harmonic content of the generated output voltage, two medium space vectors are included into the switching pattern in addition to the two large space vectors used in the previous method [Silva et al (2004)]. There are now twenty active space vectors involved in the output voltage generation, which appear in Fig. 4.7 as medium and large space vectors in the d_1-q_1 plane, and medium and small space vectors in the d_2-q_2 plane, respectively.
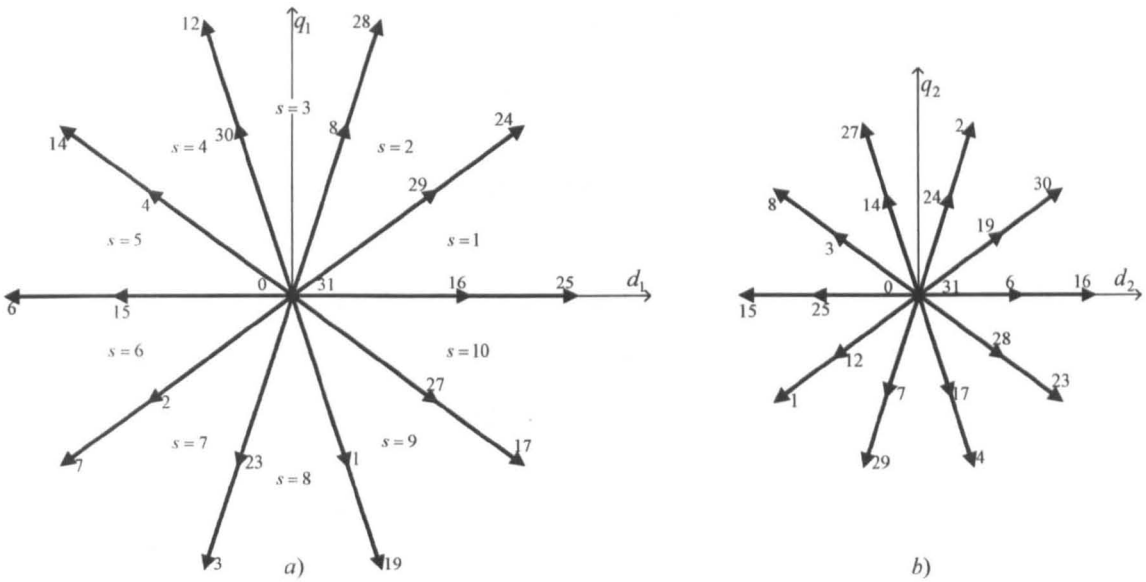
Fig. 4.7: Large and medium space vectors of the d_1-q_1 plane, and their mapping in the d_2-q_2 plane.

Pairs of medium and large space vectors from the d_1-q_1 plane that are colinear appear in the d_2-q_2 plane as medium and small space vectors with a $180°$ phase shift. By using these four vectors it is possible to zero the average voltage in the d_2-q_2 plane, if the times of application are properly determined [Silva et al (2004), Iqbal and Levi (2005), Iqbal and Levi (2006a), Xue and Wen (2005)].

The reference space vector is realised again in the d_1-q_1 plane by means of averaging over the switching period, but this time with two medium and two large active space vectors. However, the second plane is now included by setting the reference voltage to zero over the switching period as the requirement. This is illustrated in Fig. 4.8a, where it is visible that there is only one reference space vector in the first plane.
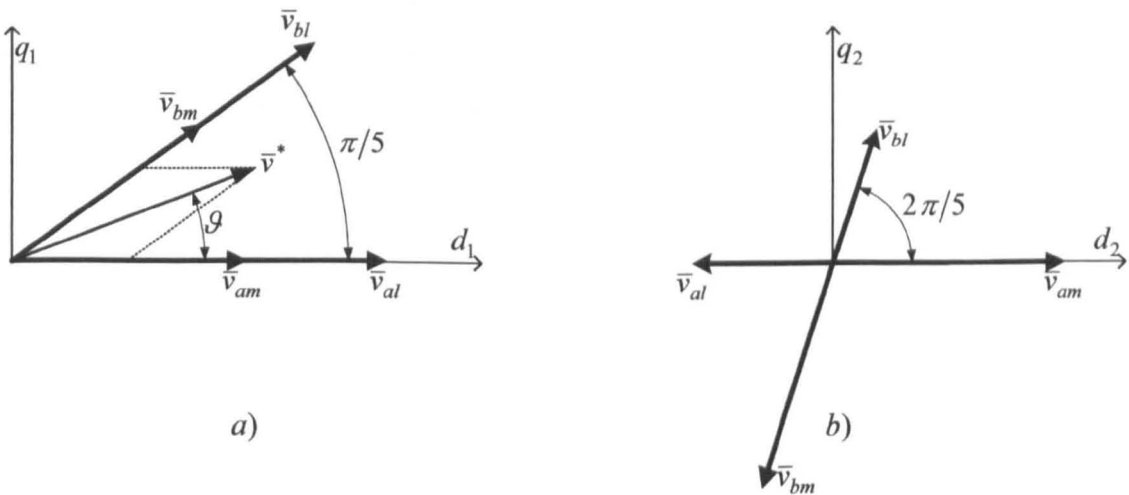
Fig. 4.8: Principle of calculation of times of application of the active space vectors.

Thus one has, by considering the situation shown in Fig. 4.8, the following:

$$\vec{v}^* T_s = \vec{v}_{am} T_{am} + \vec{v}_{al} T_{al} + \vec{v}_{bm} T_{bm} + \vec{v}_{bl} T_{bl}$$
$$0 = \vec{v}_{am} T_{am} + \vec{v}_{al} T_{al} + \vec{v}_{bm} T_{bm} + \vec{v}_{bl} T_{bl}$$
(4.16)

The first equation corresponds to the d_1-q_1 plane, while the second is for the d_2-q_2 plane and the active vector input is referenced to the first plane. Thus, space vectors with index 'l' in the second equation are actually the small space vectors from the second plane. Magnitudes of all space vectors are in Table 3.1. Two complex equations of (4.16) can be decomposed into real and imaginary parts, using Fig. 4.8 and data of Table 3.1, as follows.

$$M\cos(\vartheta)T_s = \frac{4}{5}T_{am} + \frac{4}{5}\frac{K_2}{K}T_{al} + \frac{4}{5}LT_{bm} + \frac{4}{5}\frac{K_2}{K}LT_{bl}$$

$$M\sin(\vartheta)T_s = \frac{4}{5}KT_{bm} + \frac{4}{5}\frac{K_2}{K}KT_{bl}$$

$$0 = \frac{4}{5}T_{am} - \frac{4}{5}\frac{K}{K_2}T_{al} - \frac{4}{5}L_2T_{bm} + \frac{4}{5}\frac{K}{K_2}L_2T_{bl}$$

$$0 = -\frac{4}{5}K_2T_{bm} + \frac{4}{5}\frac{K}{K_2}K_2T_{bl}$$
(4.17)

In addition to the times of application of the active space vectors, total time of application of zero space vectors is now determined with:

$$T_O = T_0 + T_{31} = T_s - T_{am} - T_{al} - T_{bm} - T_{bl}$$
(4.18)

By selecting again equal distribution of (4.18) among two zero space vectors, after some manipulations, solution of (4.17) and (4.18) in the first sector, expressed by means of previously introduced duty cycles, is:

$$\delta_{am} = KM\sin(\frac{\pi}{5}-\vartheta); \qquad \delta_{bm} = KM\sin(\vartheta)$$

$$\delta_{al} = K_2M\sin(\frac{\pi}{5}-\vartheta); \qquad \delta_{bl} = K_2M\sin(\vartheta)$$
(4.19)

$$\delta_0 = \delta_{31} = \frac{1}{2}\delta_O = \frac{1}{2}[1 - K_2M\cos(\frac{\pi}{10}-\vartheta)]$$

Set of expressions (4.19) can be easily generalised for any sector s ($s = 1$ to 10), thus providing complete solution in the form:

$$\delta_{am} = KM\sin(s\frac{\pi}{5}-\vartheta); \qquad \delta_{bm} = KM\sin(\vartheta-(s-1)\frac{\pi}{5})$$

$$\delta_{al} = K_2M\sin(s\frac{\pi}{5}-\vartheta); \qquad \delta_{bl} = K_2M\sin(\vartheta-(s-1)\frac{\pi}{5})$$
(4.20)

$$\delta_0 = \delta_{31} = \frac{1}{2}\delta_O = \frac{1}{2}[1 - K_2M\cos((2s-1)\frac{\pi}{10}-\vartheta)]$$

It should be noted here that the ratio of duty cycles of large and medium space vectors is the same as the ratio of magnitudes of large to medium, and medium to small space vectors:

$$\frac{\delta_{al}}{\delta_{am}} = \frac{\delta_{bl}}{\delta_{bm}} = 2L \approx 1.618; \qquad \frac{|\vec{v}_l|}{|\vec{v}_m|} = \frac{8L/5}{4/5} = 2L; \qquad \frac{|\vec{v}_m|}{|\vec{v}_s|} = \frac{4/5}{8L_2/5} = 2L$$
(4.21)
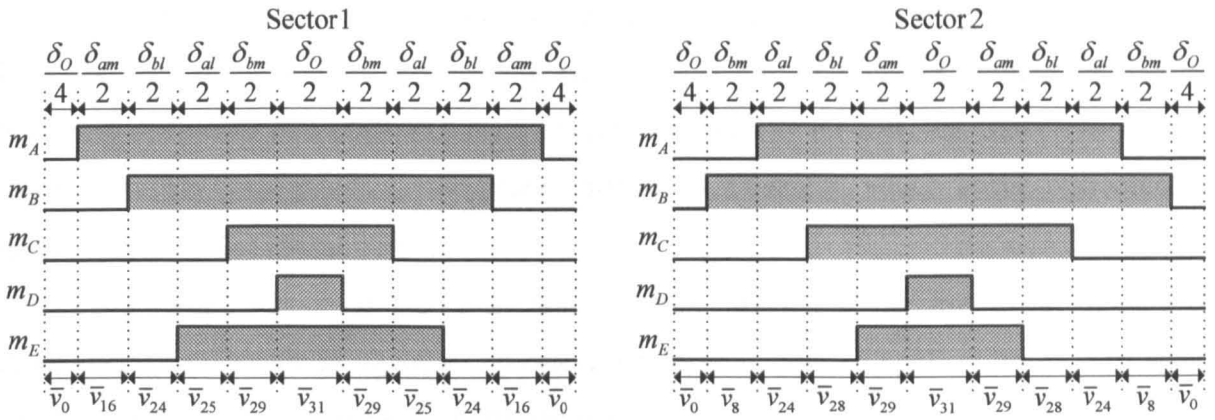
Fig. 4.9: Switching pattern in the first two sectors.

This makes it possible to obtain zero average value in the second plane since activated pairs of space vectors in the second plane are acting in opposition. Although with different magnitudes, they will cancel each other due to the mutual relation of the corresponding duty cycles (Fig. 4.8b).

Switching pattern for the first two sectors is shown in Fig. 4.9. It is symmetrical and the sequence of applied space vectors in all odd sectors is $\bar{v}_0, \bar{v}_{am}, \bar{v}_{bl}, \bar{v}_{al}, \bar{v}_{bm}, \bar{v}_{31}, \bar{v}_{bm}, \bar{v}_{al}, \bar{v}_{bl}, \bar{v}_{am}, \bar{v}_0$, while in even sectors the sequence is different and follows the rule $\bar{v}_0, \bar{v}_{bm}, \bar{v}_{al}, \bar{v}_{bl}, \bar{v}_{am}, \bar{v}_{31}, \bar{v}_{am}, \bar{v}_{bl}, \bar{v}_{al}, \bar{v}_{bm}, \bar{v}_0$. Each inverter leg is characterised with two commutations per switching period. The sequence of space vectors is arranged in such a way that in the first half of the switching period the load appears in configurations {0-5}, {1-4}, {2-3}, {3-2}, {4-1}, {5-0} and then in reversed order during the second half of the switching period. Thus, a sequential transition of the switching states is obtained from one zero space vector to another, by switching one by one inverter upper switch 'on' during the first half of the switching period, and 'off' during the second half. One can easily establish that all active space vectors used in the switching pattern are with adjacent relation of '1', as discussed in the previous chapter. Duty cycles for each inverter leg, necessary for final implementation, are obtained by summation of results of (4.20) in accordance with the predetermined switching pattern, and are given with:

$$\delta_1 = \frac{\delta_O}{2}$$
$$\delta_2^O = \delta_1 + \delta_{bm}; \qquad \delta_2^E = \delta_1 + \delta_{am}$$
$$\delta_3^O = \delta_2^O + \delta_{al}; \qquad \delta_3^E = \delta_2^E + \delta_{bl} \qquad (4.22)$$
$$\delta_4^O = \delta_3^O + \delta_{bl}; \qquad \delta_4^E = \delta_3^E + \delta_{al}$$
$$\delta_5 = \delta_1 + \delta_{am} + \delta_{al} + \delta_{bm} + \delta_{bl}$$

Table 4.2 summarises distribution of duty cycles for all inverter legs in all ten sectors. It can be seen that every leg receives the same sequence of duty cycles through ten sectors, with only difference that sequences are shifted by two sectors for each leg. Since every sector spans $\pi/5$, this corresponds to the phase shift of $2\pi/5$ degrees, which is the characteristic phase shift for a five-phase system.

Maximum value of the modulation index, obtainable in the linear region of modulation, can be found again as the value when total time of application of zero space vectors becomes zero. Thus from (4.19) one gets:

$$M_{\max} = \frac{1}{K_2} \approx 1.0515 \tag{4.23}$$

This value is considerably smaller than the maximum achievable value of the previous method, but, as shown next, purely sinusoidal output voltage is generated thanks to the use of four active space vectors and properly determined duty cycles. A similar set of simulations is carried out under the same conditions as in the previous sub-section. Behaviour of the modulator with low, medium and maximum value of modulation index is examined, and results are shown in Fig. 4.10.

As can be seen, purely sinusoidal output phase voltages are generated without any low order harmonics characteristic for the second plane. This is evident by exploring the spectrum of the phase voltage and/or the phase voltage axes components. It is clear that only the fundamental component from the first plane is present. Neglecting the switching harmonics, the average value obtained in the second plane is zero, in accordance with requirements set by equations (4.16).

The same results are obtained experimentally and can be seen in Fig. 4.11 for several values of the modulation index. This time the spectrum shows no signs of low order harmonics from the second plane and only the fundamental component is visible, of a value which is in accordance with the settings of the modulation index. Thus purely sinusoidal output voltage is generated, although of a lower maximum achievable value for the fundamental component, compared to the previous method.

Table 4.2: Duty cycle disposition through sectors.

Leg | Sector	1	2	3	4	5	6	7	8	9	10
A	δ_5	δ_4^E	δ_3^O	δ_2^E	δ_1	δ_1	δ_2^O	δ_3^E	δ_4^O	δ_5
B	δ_4^O	δ_5	δ_5	δ_4^E	δ_3^O	δ_2^E	δ_1	δ_1	δ_2^O	δ_3^E
C	δ_2^O	δ_3^E	δ_4^O	δ_5	δ_5	δ_4^E	δ_3^O	δ_2^E	δ_1	δ_1
D	δ_1	δ_1	δ_2^O	δ_3^E	δ_4^O	δ_5	δ_5	δ_4^E	δ_3^O	δ_2^E
E	δ_3^O	δ_2^E	δ_1	δ_1	δ_2^O	δ_3^E	δ_4^O	δ_5	δ_5	δ_4^E

Fig. 4.10: Simulation results - phase voltages and their axis components in two planes (left) and phase voltage with its spectrum (right) at: a) $M = 0.2$, b) $M = 0.5$, and c) $M = 1.0515$.

Use of both medium and large space vectors leads to appearance of all six characteristic voltage levels in the CMV. This is shown in Fig. 4.12 where it can be seen that the CMV appears with voltage levels of: ±300 V, ±180 V and ±60 V (dc bus voltage is 600 V). A difference in the shape of CMV with regard to the previous method (Fig. 4.6) is the presence of voltage levels of ±180 V that are the result of the application of medium space

vectors, when load is in configurations {1-4} and {4-1}. It can be observed that, with an increase of the modulation index, duration of voltage levels characteristic for the zero space vectors decreases, and vanishes once when the maximum value of the modulation index is reached. Instant captured in Fig. 4.12f demonstrates this. When compared with the CMV of the previous method (Fig. 4.6), steps of the CMV, generated every time the activated space vector changes, are now equal, resulting in generally lower overall dv/dt.
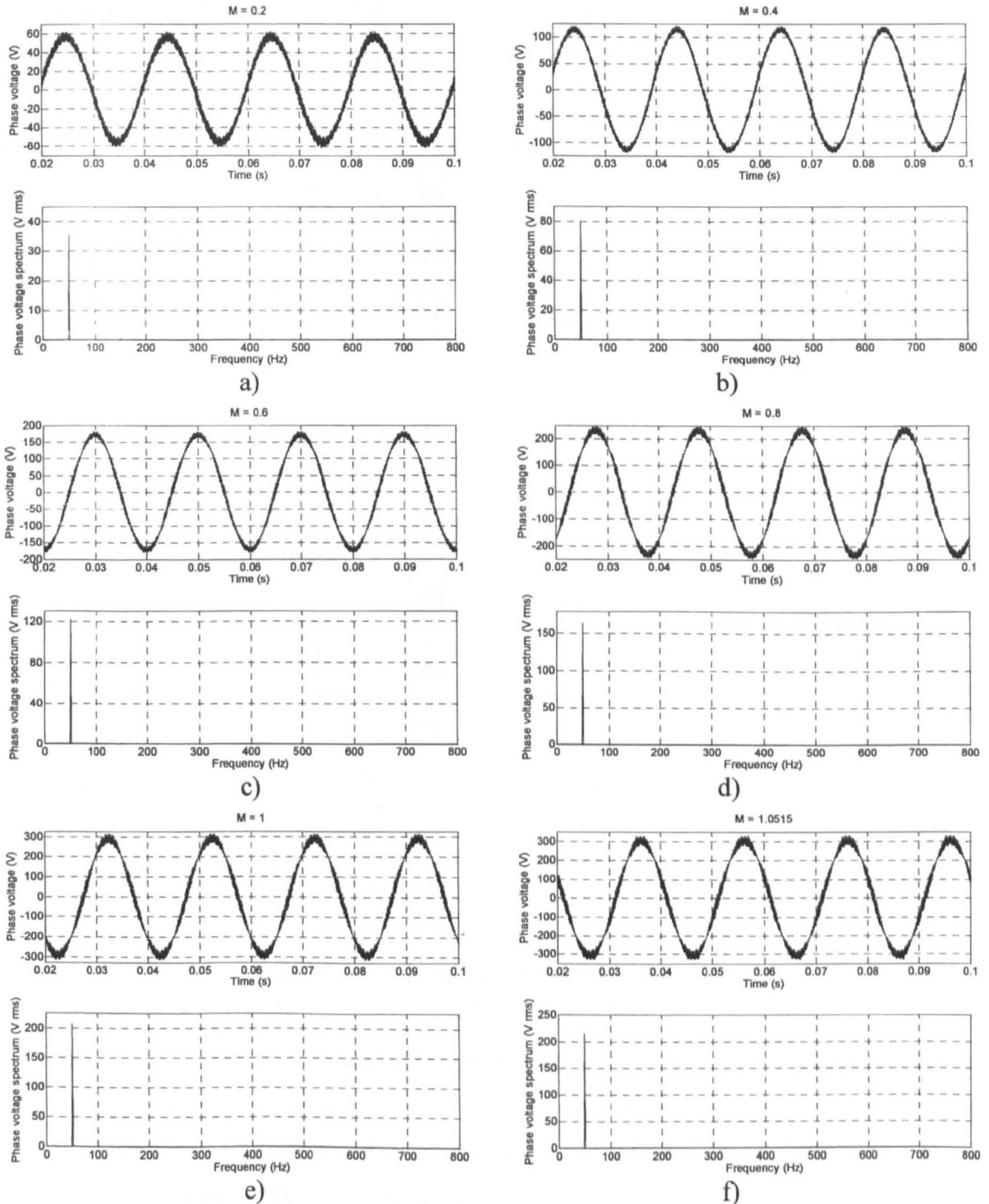
Fig. 4.11: Experimental results - phase voltage and its spectrum at: a) $M = 0.2$, b) $M = 0.4$, c) $M = 0.6$, d) $M = 0.8$, e) $M = 1$, and f) $M = 1.0515$.
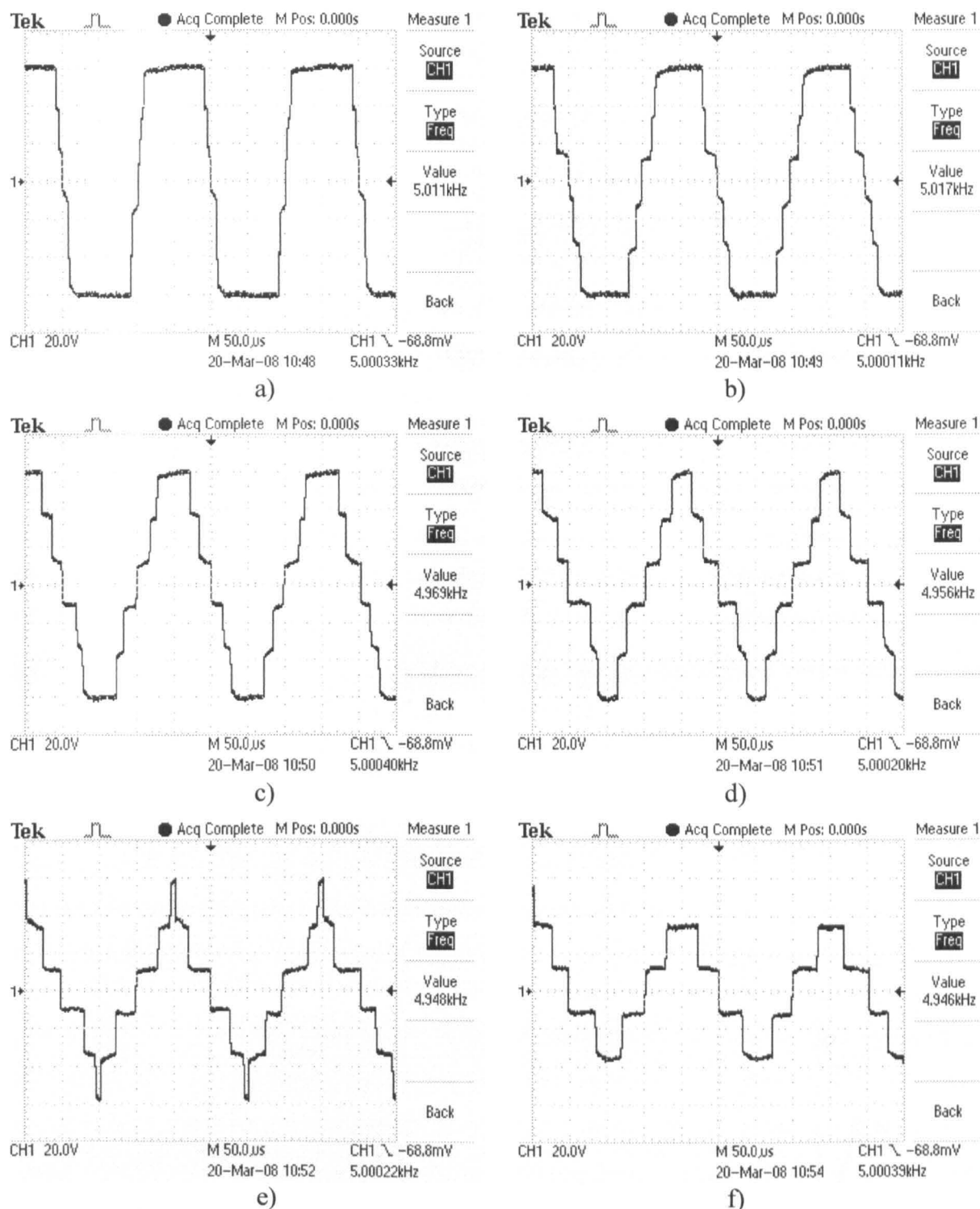
Fig. 4.12: Experimentally measured common-mode voltage at: a) $M = 0.2$, b) $M = 0.4$, c) $M = 0.6$, d) $M = 0.8$, e) $M = 1$, and f) $M = 1.0515$ (Scale: 100V/div).

The results, presented so far, demonstrated the effects of different selection of active space vectors involved in the SVPWM scheme. In both cases selected set of active space vectors allowed for minimal number of commutations per switching period. A different selection [Xue and Wen (2005)] is reviewed next, to show that sinusoidal output voltage can be obtained by means of an alternative selection of the set of active space vectors.

4.3.3 SPACE VECTOR PWM BASED ON THE USE OF FOUR LARGE ACTIVE SPACE VECTORS

As an alternative to the use of two medium and two large space vectors, sinusoidal output voltage can be also generated by means of four adjacent large space vectors, as it has been demonstrated by Xue and Wen (2005). In addition to adjacent large space vectors (denoted earlier with '*a*' and '*b*'), two more large space vectors are selected for synthesis of the reference space vectors (denoted with '*c*' and '*d*'), as shown in Fig. 4.13. Thus, four adjacent large space vectors are used, similar to work of Zhao and Lipo (1995) (although for an asymmetrical six-phase system with two isolated neutral points). Sector definition in the d_1-q_1 plane remains as for the previous two schemes. There are now four small space vectors included into development of a scheme in the d_2-q_2 plane that correspond to the selected large space vectors from the plane d_1-q_1. Positions of all space vectors in both planes are shown in Fig. 4.13, when the reference space vector is in the first sector of the d_1-q_1 plane.

By setting the reference for the second plane to zero, one can write the following set of equations that must be satisfied in order to average the reference space vector with the four large space vectors:

$$\bar{v}^* T_s = \bar{v}_{al} T_{al} + \bar{v}_{bl} T_{bl} + \bar{v}_{cl} T_{cl} + \bar{v}_{dl} T_{dl}$$
$$0 = \bar{v}_{al} T_{al} + \bar{v}_{bl} T_{bl} + \bar{v}_{cl} T_{cl} + \bar{v}_{dl} T_{dl}$$

(4.24)

As in the previous two cases, each equation of (4.14) corresponds to one plane.
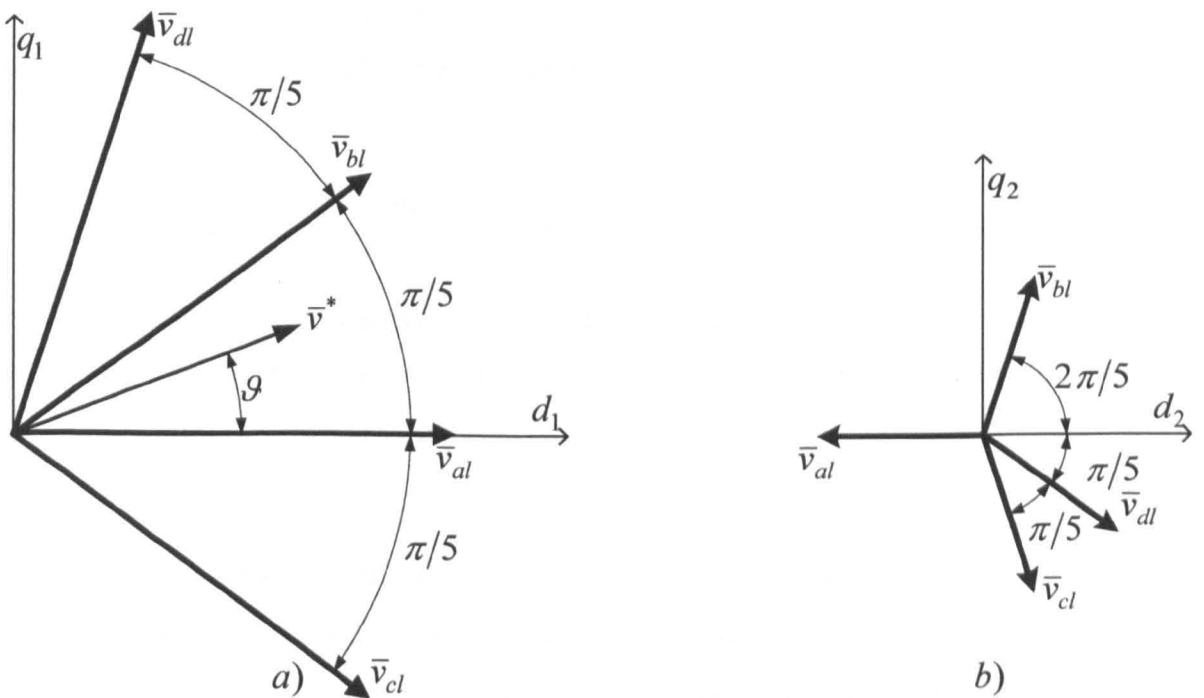
Fig. 4.13: Principle of calculation of times of application of active space vectors.

Decomposing (4.24), based on situation illustrated in Fig. 4.13, and using constants defined with (3.13) yields:

$$M\cos(\vartheta)T_s = \frac{4}{5}\frac{K_2}{K}T_{al} + \frac{4}{5}\frac{K_2}{K}LT_{bl} + \frac{4}{5}\frac{K_2}{K}LT_{cl} + \frac{4}{5}\frac{K_2}{K}L_2T_{dl}$$

$$M\sin(\vartheta)T_s = \frac{4}{5}\frac{K_2}{K}KT_{bl} - \frac{4}{5}\frac{K_2}{K}KT_{cl} + \frac{4}{5}\frac{K_2}{K}K_2T_{dl}$$

$$0 = -\frac{4}{5}\frac{K}{K_2}T_{al} + \frac{4}{5}\frac{K}{K_2}L_2T_{bl} + \frac{4}{5}\frac{K}{K_2}L_2T_{cl} + \frac{4}{5}\frac{K}{K_2}LT_{dl}$$

$$0 = \frac{4}{5}\frac{K}{K_2}K_2T_{bl} - \frac{4}{5}\frac{K}{K_2}K_2T_{cl} - \frac{4}{5}\frac{K}{K_2}KT_{dl}$$

(4.25)

After some manipulations, solution in the first sector for duty cycles of four active large space vectors is determined as:

$$\delta_{al} = \frac{M}{\frac{8}{5}L}\left[\frac{L_2}{L+L_2}\cos(\vartheta) + K_2\frac{L-L_2}{K^2+K_2^2}\sin(\vartheta)\right]$$

$$\delta_{bl} = \frac{M}{\frac{8}{5}L}\left[\frac{1}{2[L+L_2]}\cos(\vartheta) + \frac{K-K_2}{2[K^2+K_2^2]}\sin(\vartheta)\right]$$

(4.26)

$$\delta_{cl} = \frac{M}{\frac{8}{5}L}\left[\frac{1}{2[L+L_2]}\cos(\vartheta) - \frac{K+K_2}{2[K^2+K_2^2]}\sin(\vartheta)\right]$$

$$\delta_{dl} = \frac{M}{\frac{8}{5}L}\frac{K_2}{K^2+K_2^2}\sin(\vartheta)$$

Total duty cycle of the zero space vectors can be found as:

$$\delta_O = \delta_0 + \delta_{31} = 1 - \delta_{al} - \delta_{bl} - \delta_{cl} - \delta_{dl}$$

(4.27)

By substituting (4.26) in (4.27), the expression for total zero space vector duty cycle is found as:

$$\delta_O = 1 - \frac{1}{\frac{8}{5}L}M\left[\frac{L_2+1}{L+L_2}\cos(\vartheta) + K_2\frac{L-L_2}{K^2+K_2^2}\sin(\vartheta)\right]$$

(4.28)

This expression, although it appears complicated, is actually the same as the one obtained for the SVPWM based on the use of two medium and two large space vectors, and thus after some manipulation (4.28) can be reduced to:

$$\delta_O = 1 - K_2M\cos(\frac{\pi}{10} - \vartheta)$$

(4.29)

This duty cycle is equally distributed among two zero space vectors.

The generalised solution for all duty cycles, applicable to all sectors s ($s = 1$ to 10), and considering equal distribution of the total zero space vector duty cycle among two zero vectors can be written in the form:

$$\delta_{al} = \frac{M}{\frac{8}{5}L}\left[\frac{L_2}{L+L_2}\cos(\vartheta-(s-1)\frac{\pi}{5})+K_2\frac{L-L_2}{K^2+K_2^{\ 2}}\sin(\vartheta-(s-1)\frac{\pi}{5})\right]$$

$$\delta_{bl} = \frac{M}{\frac{8}{5}L}\left[\frac{1}{2[L+L_2]}\cos(\vartheta-(s-1)\frac{\pi}{5})+\frac{K-K_2}{2[K^2+K_2^{\ 2}]}\sin(\vartheta-(s-1)\frac{\pi}{5})\right]$$

$$\delta_{cl} = \frac{M}{\frac{8}{5}L}\left[\frac{1}{2[L+L_2]}\cos(\vartheta-(s-1)\frac{\pi}{5})-\frac{K+K_2}{2[K^2+K_2^{\ 2}]}\sin(\vartheta-(s-1)\frac{\pi}{5})\right] \qquad (4.30)$$

$$\delta_{dl} = \frac{M}{\frac{8}{5}L}\frac{K_2}{K^2+K_2^{\ 2}}\sin(\vartheta-(s-1)\frac{\pi}{5})$$

$$\delta_0 = \delta_{31} = \frac{1}{2}\delta_O = \frac{1}{2}[1-K_2 M\cos((2s-1)\frac{\pi}{10}-\vartheta)]$$

Dc bus utilisation is the same as with the previous method, so that the maximum modulation index is:

$$M_{max} = \frac{1}{K_2} \approx 1.0515 \qquad (4.31)$$

Switching pattern for the first two sectors is shown in Fig. 4.14. Sequence of the space vectors in all odd sectors is $\bar{v}_0, \bar{v}_{cl}, \bar{v}_{al}, \bar{v}_{bl}, \bar{v}_{dl}, \bar{v}_{31}, \bar{v}_{dl}, \bar{v}_{bl}, \bar{v}_{al}, \bar{v}_{cl}, \bar{v}_0$, while in even sectors the sequence is different and follows the rule $\bar{v}_0, \bar{v}_{dl}, \bar{v}_{bl}, \bar{v}_{al}, \bar{v}_{cl}, \bar{v}_{31}, \bar{v}_{cl}, \bar{v}_{al}, \bar{v}_{bl}, \bar{v}_{dl}, \bar{v}_0$. Although the sequence is symmetrical, it has an uneven number of commutations per inverter leg. It can be seen that in every sector one of the inverter legs needs to change its state six times, while all the other legs have two commutations per switching period. This kind of switching pattern is hard to implement with the standard DSP PWM units and this method is therefore analysed only by means of simulations. The results are presented in Fig. 4.15. Since only large and zero space vectors are used, during the first half of the switching period the load appears in configurations {0-5} {2-3}, {3-2}, {2-3}, {3-2}, {5-0} and in reversed order during the second half of the switching period.
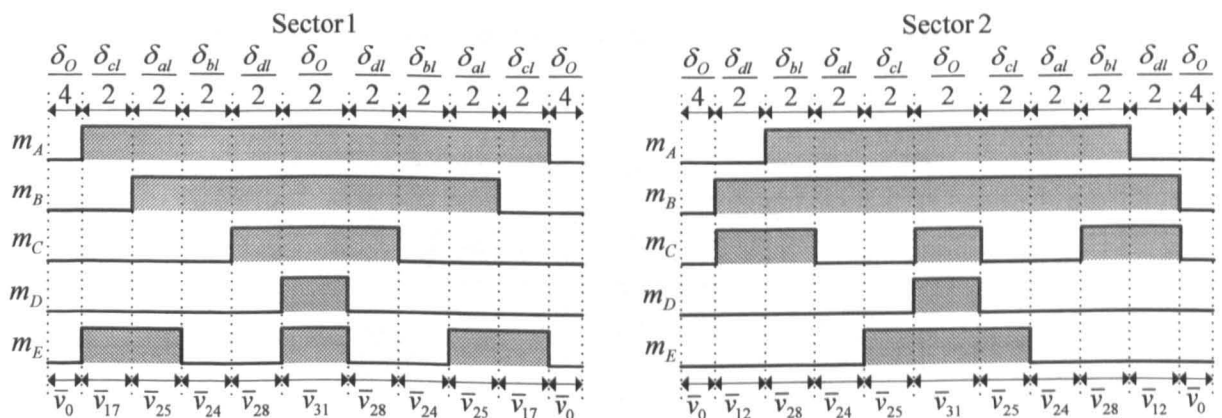

Fig. 4.14: Switching pattern in the first two sectors.

Duty cycles for each leg are obtained by summation of the results of calculations (4.30) in accordance with the predetermined switching pattern:

$$
\begin{aligned}
\delta_1 &= \frac{\delta_O}{2} \\
\delta_2^O &= \delta_1 + \delta_{dl}; & \delta_2^E &= \delta_1 + \delta_{cl} \\
\delta_3^O &= \delta_1 + \delta_{al} + \delta_{cl}; & \delta_3^E &= \delta_1 + \delta_{bl} + \delta_{dl} \\
\delta_4^O &= \delta_2^O + \delta_{bl} + \delta_{al}; & \delta_4^E &= \delta_2^E + \delta_{al} + \delta_{bl} \\
\delta_5 &= \delta_1 + \delta_{al} + \delta_{bl} + \delta_{cl} + \delta_{dl}
\end{aligned}
\tag{4.32}
$$

Distribution of the final duty cycles through all ten sectors for each inverter leg is summarised in Table 4.3. The duty cycle δ_3 which leads to six commutations in the corresponding inverter leg, is highlighted. The arrangement of duty cycles is identical as for the previous SVPWM method (Table 4.2), but with calculations now being based on (4.32). The main difference is the need for six commutations in order to realise duty cycle δ_3 which is hard to implement in standard DSP PWM units, without significantly increasing the complexity of the modulator or an addition of peripheral electronic circuits.

Results of simulations, given in Fig. 4.15, show that purely sinusoidal output voltages are generated, with no presence of any low order harmonics from the second plane. Spectrum shows only fundamental component of the same value as in the previous method, in accordance with the set modulation index values. Although the set of used active space vectors is different, zero average value is obtained in the second plane due to the properly determined duty cycles. At the same time, activation of small space vectors from the second plane leads to lower switching harmonic magnitudes in the second plane than with the method of sub-section 4.3.2 (this cannot be seen in Fig 4.15 but has been established in the course of simulation work). However, the switching pattern is not optimal from the point of view of the number of commutations, since it yields increased switching losses compared to the previous method. Thus the only advantage, lower switching harmonics in the second plane, is significantly outweighted by these shortcomings and no attempt has been made to test this SVPWM experimentally.

Table 4.3: Duty cycle disposition through sectors.

Leg | Sector	1	2	3	4	5	6	7	8	9	10
A	δ_5	δ_4^E	δ_3^O	δ_2^E	δ_1	δ_1	δ_2^O	δ_3^E	δ_4^O	δ_5
B	δ_4^O	δ_5	δ_5	δ_4^E	δ_3^O	δ_2^E	δ_1	δ_1	δ_2^O	δ_3^E
C	δ_2^O	δ_3^E	δ_4^O	δ_5	δ_5	δ_4^E	δ_3^O	δ_2^E	δ_1	δ_1
D	δ_1	δ_1	δ_2^O	δ_3^E	δ_4^O	δ_5	δ_5	δ_4^E	δ_3^O	δ_2^E
E	δ_3^O	δ_2^E	δ_1	δ_1	δ_2^O	δ_3^E	δ_4^O	δ_5	δ_5	δ_4^E

Fig. 4.15: Simulation results - phase voltages and their axis components in two planes (left) and phase voltage and its spectrum (right) at: a) $M = 0.2$, b) $M = 0.5$, and c) $M = 1.0515$.

4.4   SUMMARY

Three SVPWM schemes for a five-phase VSI have been presented in this chapter. A simple extension of the well known SVPWM principles for a three-phase VSI does not yield sinusoidal output voltage, since the fundamental is accompanied by the low order harmonics

from the second plane. It is therefore demonstrated that four active space vectors per switching period must be used with simultaneous consideration of both planes of a five-phase system.

Two different selections of four active space vectors are analysed further and their impact on the switching pattern is demonstrated. While it is possible to generate sinusoidal output voltages in both cases, selection of four large space vectors leads to difficulties related to the implementation with standard DSP PWM units, as well as to an increase in the average switching frequency. It is for this reason that only PWM scheme based on utilisation of both medium and large space vectors is a viable solution for real world applications. Theoretical considerations are at first examined by simulations and are further verified by means of experimental measurements. In addition to the phase voltage, common-mode voltage is also measured in order to illustrate effects of various space vectors.

Results obtained for a five-phase VSI suggest that in an n-phase system, in order to achieve sinusoidal output voltage, n-1 active space vectors should be used. At the same time, as discussed in this chapter, these space vectors should be with adjacent relation of '1' in switching states [Xue and Wen (2005), Kelly et al (2003)]. Finally, organisation of these space vectors within symmetrical switching pattern should yield sequential transition with a single commutation from the first zero space vector toward the second zero space vector. Based on these considerations, SVPWM schemes for sinusoidal output voltage generation with seven-phase and nine-phase VSIs are developed in the next chapter.

Chapter 5

SPACE VECTOR PWM METHODS FOR SINUSOIDAL OUTPUT VOLTAGE GENERATION WITH SEVEN-PHASE AND NINE-PHASE VOLTAGE SOURCE INVERTERS

5.1 INTRODUCTION

It has been demonstrated in chapter 4 that, in order to obtain sinusoidal output voltage from a five-phase VSI, both planes must be considered in the development of a SVPWM scheme. It has also been shown that the number of used active space vectors must be equal to four and two different selections have been presented. For the easiness of DSP implementation, scheme that yields sequential transition of commutations of inverter legs is selected as the most suitable one, and it has been experimentally verified. A five-phase load, during the first half of the switching period appears in the load configurations that are in the order: {0-5}, {1-4}, {2-3}, {3-2}, {4-1}, {5-0} and then in reversed order during the second half of the switching period. At the same time, all used space vectors are with adjacent relation of '1' in switching states. Based on these findings, it is possible to expand and develop SVPWM for other multi-phase VSIs assuming again multi-phase load in star connection. Thus, in this chapter, development and experimental verification of SVPWM strategies for seven-phase and nine-phase VSIs are presented.

SVPWM for a seven-phase VSI is developed in section 5.2. It is demonstrated that consideration of only the first plane does not lead to sinusoidal output voltage. Therefore, six active space vectors are used to develop the scheme, based on simultaneous consideration of all three planes that exists in a seven-phase system. A similar analysis is performed for a nine-phase VSI in section 5.3. However, only SVPWM scheme based on the use of eight active space vectors is presented and sinusoidal output voltages are generated. Balanced static R-L loads in star connection with single neutral point are used in all the experiments. Section 5.4 discusses dc bus utilisation in multi-phase VSIs depending on the number of active space vectors used, while generalised SVPWM for multi-phase VSIs is presented in section 5.5.

Summary of the chapter is given in section 5.6. The main results of this chapter have been presented in Dujić et al (2007b) and Dujić et al (2007d).

5.2 CONTINUOUS SPACE VECTOR PWM FOR A SEVEN-PHASE VOLTAGE SOURCE INVERTER

Unlike five-phase drives, seven-phase drives have not been analysed in great depth in the past. Locment et al (2006) have analysed control in fault operation of a seven-phase axial flux permanent magnet synchronous machine supplied by a seven-leg VSI. The design of machine was presented and experimental results were provided during faulted operation with two phases opened. The method for reducing torque ripple has also been suggested. However, no particular PWM method has been devised and simple triangle intersection PWM was used. The only analysis of SVPWM for a seven-phase VSI has been conducted by Grandi et al (2006b) where, in order to achieve sinusoidal output voltage, six active space vectors have been used per switching period. However, no experimental results were presented.

Development of SVPWM for a seven-phase VSI must be performed based on consideration of all three planes that exists in a seven-phase system [Grandi et al (2006b)]. Again, similar to the analysis presented in chapter 4, it is demonstrated first that simple extension of the well known three-phase SVPWM does not yield sinusoidal output voltage and results in presence of low order harmonics in the voltage/current waveforms. Therefore, the number of active space vectors is increased and the final duty cycles are calculated based on a set of equations that consider all three planes.

5.2.1 SPACE VECTOR PWM BASED ON THE USE OF TWO ACTIVE SPACE VECTORS

If a reference space vector is to be realised in the d_1-q_1 plane, with the use of only two adjacent largest active space vectors per switching period, one can find that only fourteen active space vectors that belong to the group G_8^7 are of interest. Active space vectors of the group G_8^7 are shown in Fig. 5.1, according to their mapping in the d_1-q_1, d_2-q_2 and d_3-q_3 planes. Magnitudes of these space vectors in all three planes have already been summarised in Table 3.2 and are therefore not shown in Fig. 5.1. These space vectors will bring the load into {3-4} and {4-3} load configurations. Number of sectors is equal to fourteen, as shown in Fig. 5.1a. Two zero space vectors (0 and 127) that are used (shown in Fig. 5.1a) are at the same time zero space vectors in the other two planes (not shown for the sake of clarity).
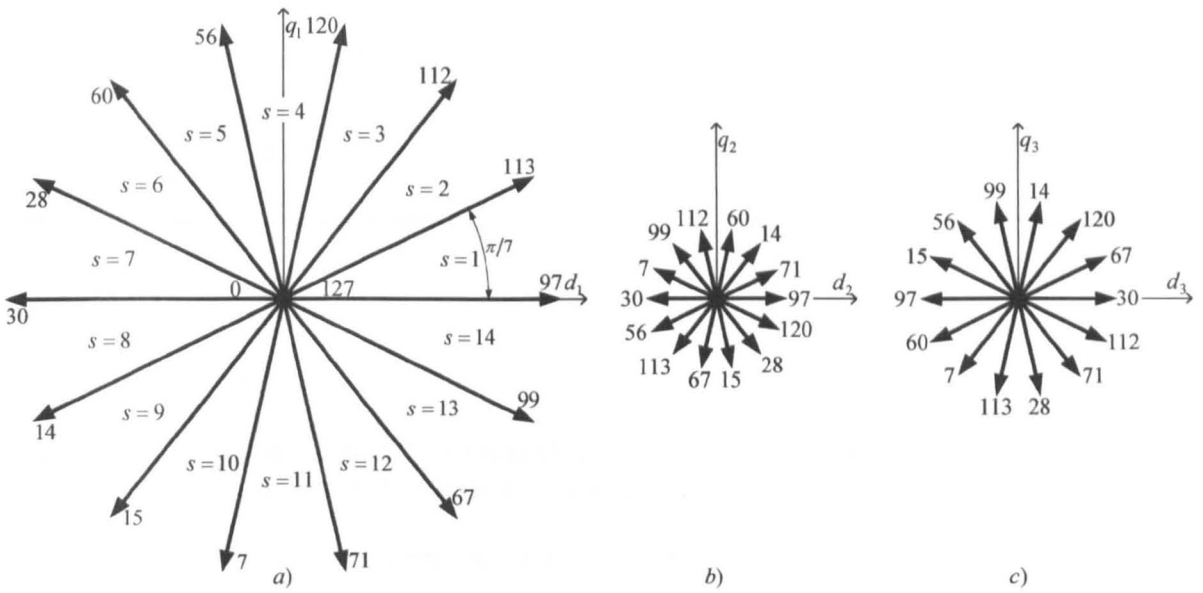
Fig. 5.1: Space vectors selected for SVPWM from the d_1-q_1 plane (a)) and their mapping in the d_2-q_2 (b)) and d_3-q_3 (c)) planes.

As in chapter 4, there is only one reference space vector in the d_1-q_1 plane that can be expressed, after normalisation, as:

$$\bar{v}^* = M e^{j\vartheta} \tag{5.1}$$

Considering the situation when the reference space vector is in the sector 1 of the d_1-q_1 plane, as shown in Fig. 5.2a, and using similar notions defined in chapter 4 (only sub-scripts 'a' and 'b', without sub-script 'l'), one has the reference space vector which is realised in the d_1-q_1 plane by means of averaging over the switching period (T_s) with two active space vectors:

$$\bar{v}^* T_s = \bar{v}_a T_a + \bar{v}_b T_b \tag{5.2}$$

Based on Fig. 5.2a, Table 3.2 (where magnitudes of the space vectors are defined), and with the use of simple trigonometry, equation (5.2) can be decomposed into two real equations:

$$
\begin{aligned}
M\cos(\vartheta)T_s &= \frac{4}{7}\frac{K_3}{K}T_a + \frac{4}{7}\frac{K_3}{K}LT_b \\
M\sin(\vartheta)T_s &= \frac{4}{7}\frac{K_3}{K}KT_b
\end{aligned}
\tag{5.3}
$$

Constants used in (5.3) are defined with (3.13), where now $n = 7$. Using directly duty cycle concept introduced earlier, and considering again equal distribution of the total duty cycle of the zero space vector among two zero space vectors, the solution in the first sector is given with:

$$
\delta_a = \frac{M}{\frac{4}{7}K_3}\sin(\frac{\pi}{7}-\vartheta); \qquad \delta_b = \frac{M}{\frac{4}{7}K_3}\sin(\vartheta)
$$

$$
\delta_0 = \delta_{127} = \frac{1}{2}\delta_O = \frac{1}{2}[1 - M\frac{7L_3}{2K_3}\cos(\frac{\pi}{14}-\vartheta)]
\tag{5.4}
$$
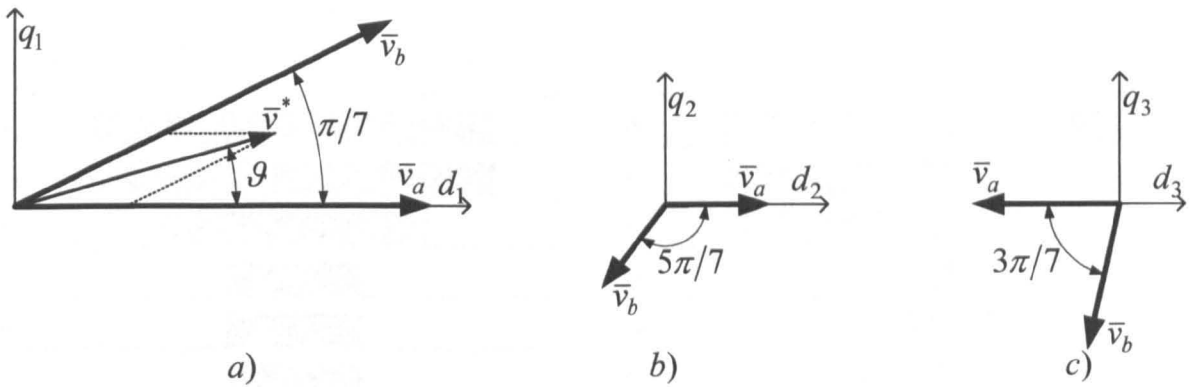
Fig. 5.2: Principle of averaging of the reference space vector with two vectors in the d_1-q_1 plane (a)), and activated vectors in the d_2-q_2 plane (b)) and d_3-q_3 plane (c)).

General solution, applicable for every sector s ($s = 1$ to 14), has the form:

$$\delta_a = \frac{M}{\frac{4}{7}K_3}\sin(s\frac{\pi}{7} - \vartheta); \qquad \delta_b = \frac{M}{\frac{4}{7}K_3}\sin(\vartheta - (s-1)\frac{\pi}{7})$$

$$\delta_0 = \delta_{127} = \frac{1}{2}\delta_O = \frac{1}{2}[1 - M\frac{7L_3}{2K_3}\cos((2s-1)\frac{\pi}{14} - \vartheta)]$$

(5.5)

Once the duty cycles have been calculated, the switching pattern can be synthesised based on the selected set of active space vectors from the group G_8^7 and two zero space vectors (group G_0^7). Symmetrical switching pattern (with two commutations per inverter leg) for the first two sectors is shown in Fig. 5.3. The sequence of the vectors in all odd sectors is $\bar{v}_0, \bar{v}_a, \bar{v}_b, \bar{v}_{127}, \bar{v}_b, \bar{v}_a, \bar{v}_0$, while in the even sectors it is $\bar{v}_0, \bar{v}_b, \bar{v}_a, \bar{v}_{127}, \bar{v}_a, \bar{v}_b, \bar{v}_0$. Per-leg duty cycles (Table 5.1) are determined for every sector by an appropriate summation of calculated duty cycles of (5.5) in accordance with the predefined switching pattern. Thus, final duty cycles are defined as (where superscripts 'O' and 'E' stand again for odd and even sector, respectively):

$$\delta_1 = \frac{\delta_O}{2}$$
$$\delta_2^O = \delta_1 + \delta_b; \qquad \delta_2^E = \delta_1 + \delta_a$$
$$\delta_3 = \delta_1 + \delta_a + \delta_b$$

(5.6)

Table 5.1: Duty cycle disposition through sectors.

Leg | Sector	1	2	3	4	5	6	7	8	9	10	11	12	13	14
A	δ_3	δ_3	δ_3	δ_2^E	δ_1	δ_1	δ_1	δ_1	δ_1	δ_1	δ_2^O	δ_3	δ_3	δ_3
B	δ_3	δ_3	δ_3	δ_3	δ_3	δ_2^E	δ_1	δ_1	δ_1	δ_1	δ_1	δ_1	δ_2^O	δ_3
C	δ_2^O	δ_3	δ_3	δ_3	δ_3	δ_3	δ_3	δ_2^E	δ_1	δ_1	δ_1	δ_1	δ_1	δ_1
D	δ_1	δ_1	δ_2^O	δ_3	δ_3	δ_3	δ_3	δ_3	δ_3	δ_2^E	δ_1	δ_1	δ_1	δ_1
E	δ_1	δ_1	δ_1	δ_1	δ_2^O	δ_3	δ_3	δ_3	δ_3	δ_3	δ_3	δ_2^E	δ_1	δ_1
F	δ_1	δ_1	δ_1	δ_1	δ_1	δ_1	δ_2^O	δ_3	δ_3	δ_3	δ_3	δ_3	δ_3	δ_2^E
G	δ_3	δ_2^E	δ_1	δ_1	δ_1	δ_1	δ_1	δ_1	δ_2^O	δ_3	δ_3	δ_3	δ_3	δ_3

Fig. 5.3: Switching pattern in the first two sectors.

Maximum achievable value of the modulation index is obtained from (5.5), for the condition when the total duty cycle of zero space vectors becomes equal to zero for the reference space vector being in the middle of the first sector ($\vartheta = \pi/14$). Thus, when only two active space vectors are used per switching period, the maximum achievable value of the modulation index is:

$$M_{max} = \frac{2K_3}{7L_3} \approx 1.2518 \tag{5.7}$$

Compared to the magnitude of the fundamental obtained in square-wave (fourteen-step) mode of operation, $M_{2n\text{-}step} \approx 1.2731$, this represents a value of 98.33%. At the same time, this is a higher value than the one obtained with the five-phase SVPWM based on the use of only two large space vectors, where maximum achievable value was $M_{max} \approx 1.2311$.

Simulations were further carried out, using MATLAB/Simulink, under the same operating conditions as in chapter 4. The input space vector is given as a sinusoidal reference and behaviour of the modulator at low, medium and maximum achievable value of the modulation index is analysed. From the set of simulation results, shown in Fig. 5.4, it can be seen that the generated output phase voltage (only one phase voltage is now shown) is not sinusoidal and contains low order harmonic components. This is the result of activated space vectors in the d_2-q_2 and d_3-q_3 planes, which were not considered during the development of the modulation scheme. Thus, phase voltages contain the fifth harmonic (around 10.36%) and the ninth harmonic (around 2.02%) from the plane d_2-q_2, as well as the third harmonic (around 25.58%) and the eleventh harmonic (around 0.72%) from the d_3-q_3 plane. This is also noticeable in the left parts of Fig. 5.4, where transformed phase voltage axes components are shown for all three planes. While the fundamental component in the d_1-q_1 plane is purely

sinusoidal, components in the other two planes are distorted, since they contain all characteristic harmonics of a particular plane, in accordance with the harmonic mapping discussed in chapter 3 (sub-section 3.3.2). Thus, a simple extension of the three-phase SVPWM, applied to a seven-phase system, cannot produce sinusoidal output voltage and it results in presence of voltage harmonics from the second and the third plane.
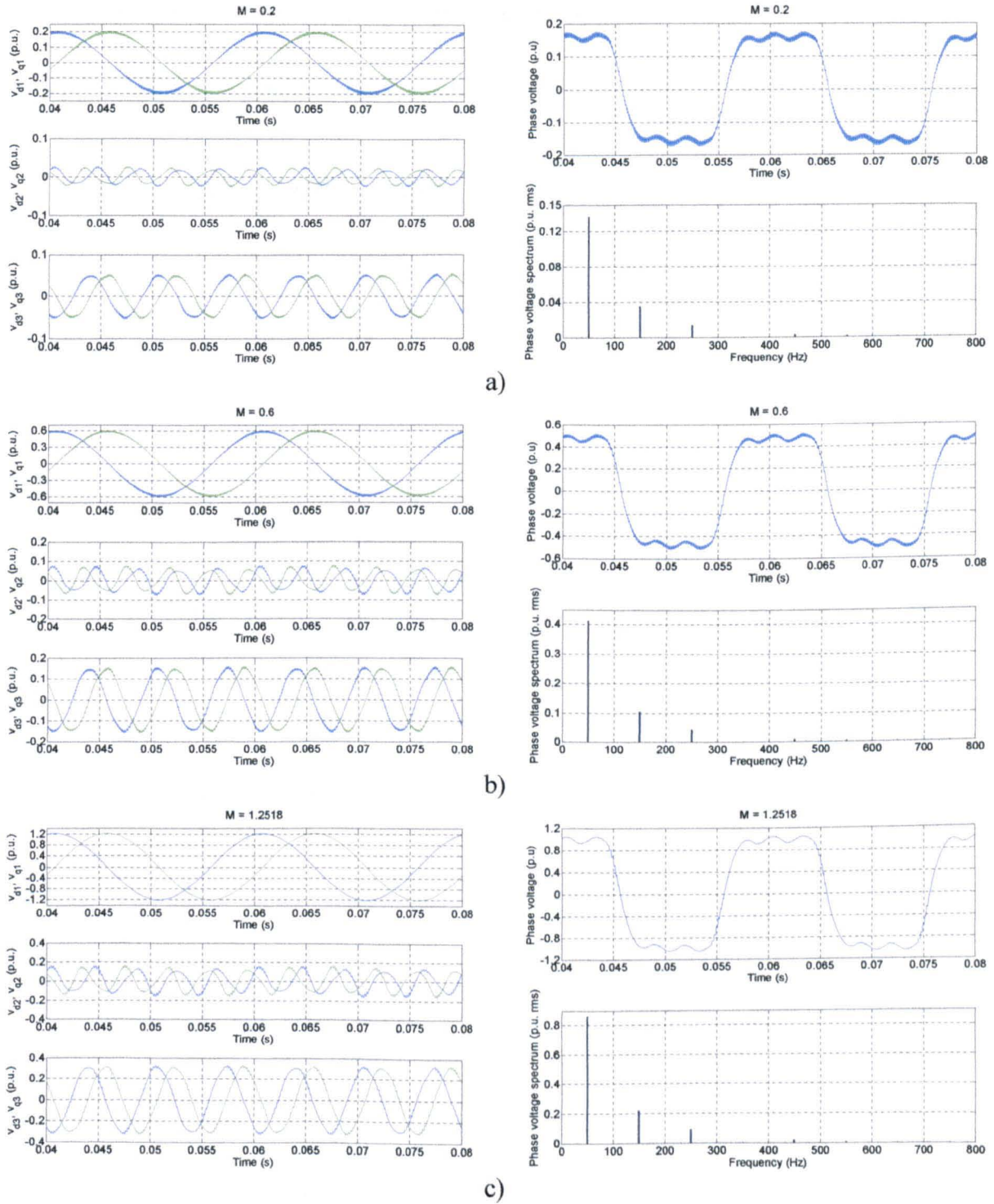
Fig. 5.4: Simulation results - phase voltage axis components after transformation in three planes (left), and phase voltage and its spectrum (right) at:
a) $M = 0.2$, b) $M = 0.6$, and c) $M = 1.2518$.

To further verify these findings, the scheme is implemented in the DSP and tested experimentally. Experimental results, collected from the seven-phase star-connected static *R-L* load, are shown in Fig. 5.5. They are in excellent agreement with the results obtained by simulations. Phase voltage spectrum clearly shows the presence of harmonic components from the second and the third planes, and their values are with fixed ratio to the value of the fundamental over the whole range of the modulation index variation.
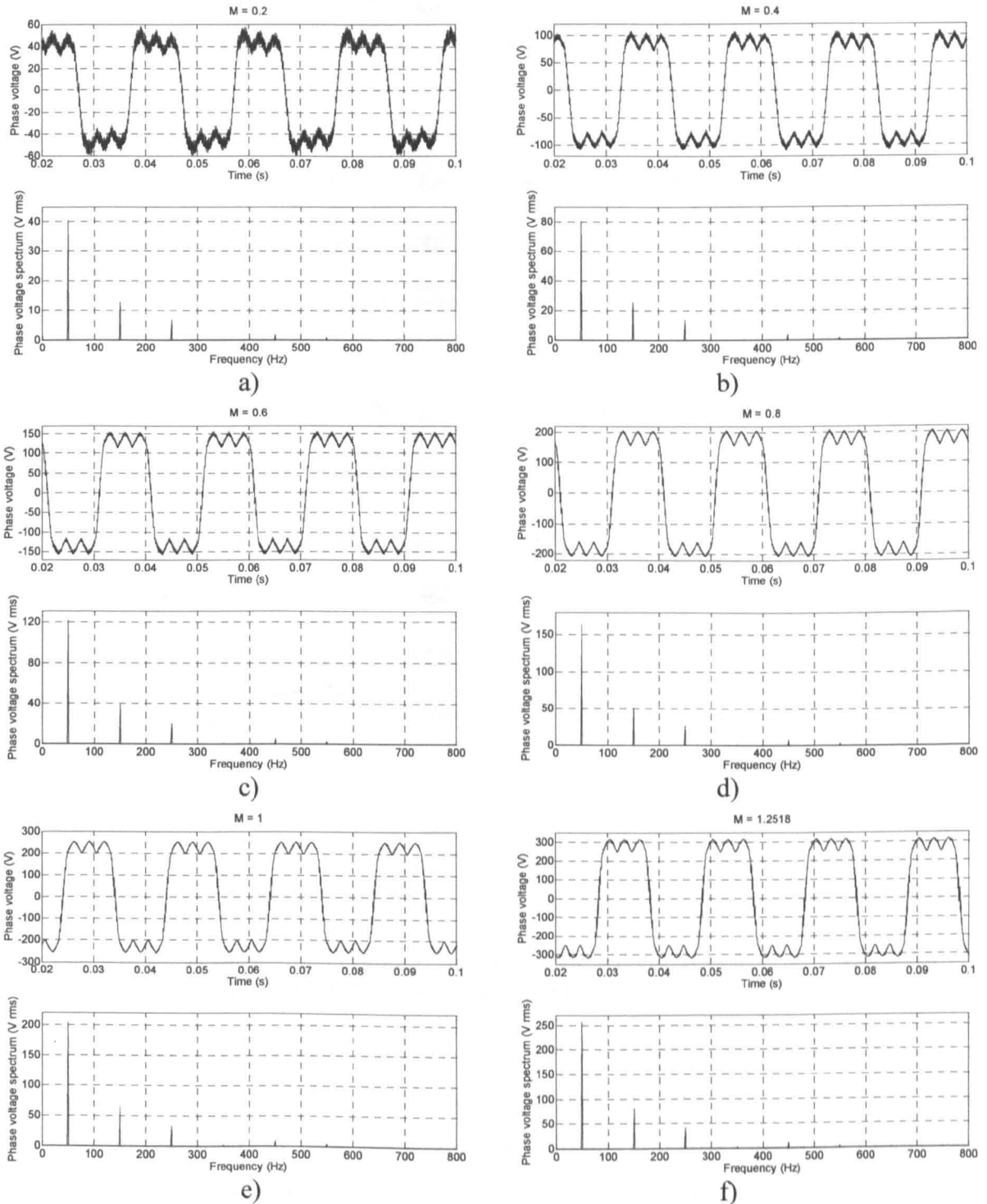
Fig. 5.5: Experimental results - phase voltage and its spectrum at: a) $M = 0.2$, b) $M = 0.4$, c) $M = 0.6$, d) $M = 0.8$, e) $M = 1$, and f) $M = 1.2518$.
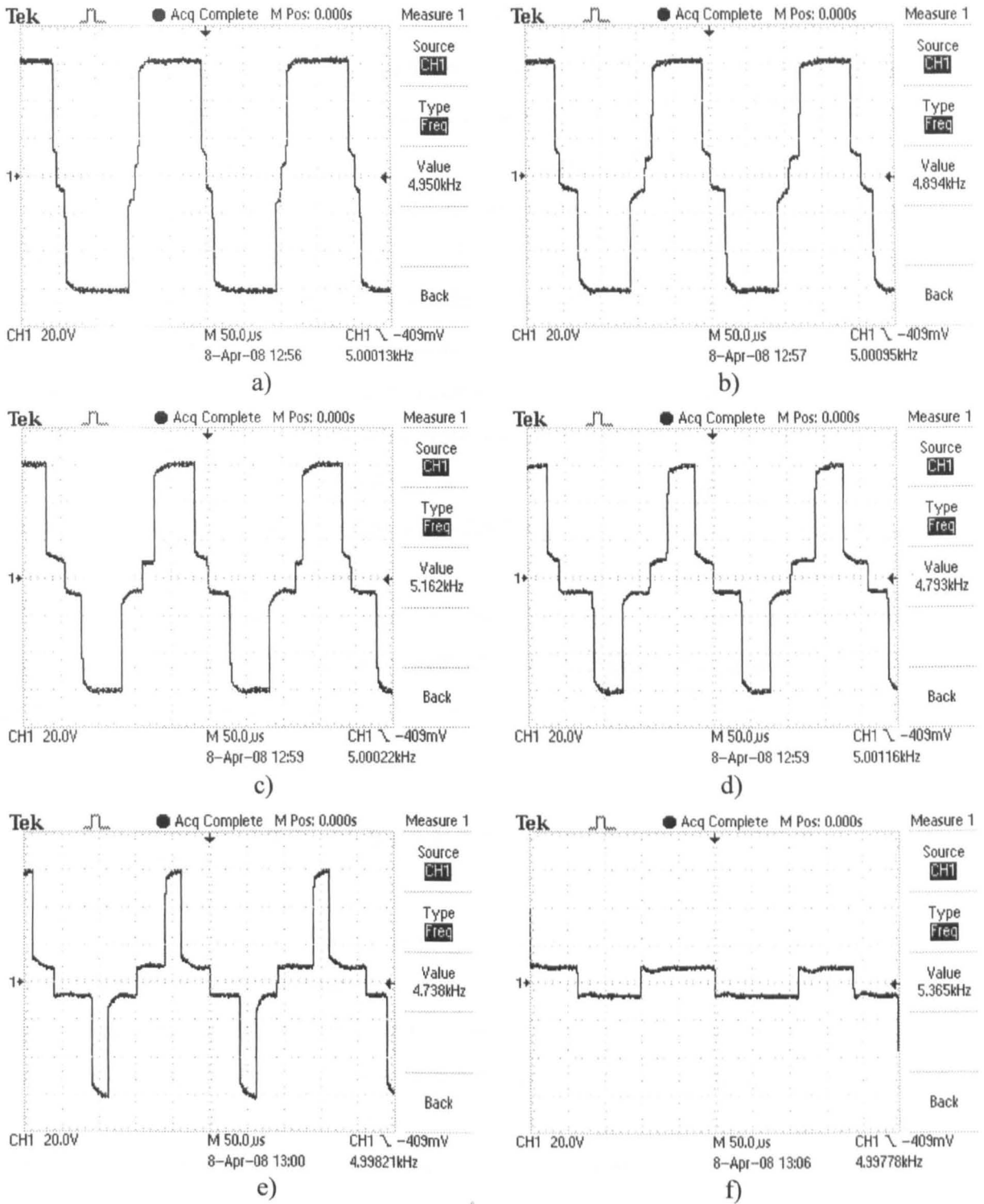
Fig. 5.6: Experimentally measured common-mode voltage at a) $M = 0.2$, b) $M = 0.4$, c) $M = 0.6$, d) $M = 0.8$, e) $M = 1$, and f) $M = 1.2518$ (Scale: 100V/div).

Measured CMV is shown in Fig 5.6, for various values of the modulation index. In general, in a seven-phase system, CMV can appear with eight different voltage levels: $\pm V_{dc}/2$, $\pm 5V_{dc}/14$, $\pm 3V_{dc}/14$, and $\pm V_{dc}/14$. For a 600 V dc bus, this effectively gives the voltage levels of approximately ± 300 V, ± 215 V, ± 129 V, ± 43 V. Voltage levels with the largest magnitude ($\pm V_{dc}/2$) are the result of the load being in {0-7} and {7-0} configurations, which corresponds

to the use of the zero space vectors. This is the same as for a five-phase system, and is in general valid for all multi-phase systems. Space vectors with the largest magnitude (group G_8^7) will bring the load into configurations {3-4} and {4-3}, resulting in the CMV with voltage levels of $\pm V_{dc}/14$ (± 43 V). Since this SVPWM scheme uses only these two groups of space vectors, appearance of CMV is in accordance with these theoretical considerations since these voltage levels can be clearly identified in Fig. 5.6. With an increase of the modulation index, duty cycles of the zero space vectors decrease, until they finally become zero for the maximum obtainable value of the modulation index. This is however valid only in the middle of each sector. As the reference space vector moves away from middle of the sector, total duty cycle of zero space vectors becomes different from zero even for the maximum value of the modulation index. Captured instant in Fig 5.6f corresponds to the situation when reference space vector is in the middle of a sector, so that the voltage levels in the CMV that correspond to the zero space vectors do not exist.

Since the use of only two active space vectors cannot produce sinusoidal output voltage, the number of active space vectors must be increased. Simultaneously, all three planes must be considered in the development of a SVPWM strategy. Such a SVPWM scheme is elaborated next.

5.2.2 SPACE VECTOR PWM BASED ON THE USE OF SIX ACTIVE SPACE VECTORS

To generate sinusoidal output voltage with a seven-phase VSI, all three planes must be considered simultaneously. This requires an increase in the number of applied active space vectors. Based on considerations given in chapter 4, the need to use six active space vectors within a switching period is easily recognised. By imposing other constraints, such as symmetrical switching pattern with two commutations per inverter leg and sequential transitions with single commutation from one to the other zero space vector, selection of active space vectors can be performed. With this in mind, the switching pattern during the first half of the switching period should use space vectors that will bring the load into sequence of load configurations {0-7}, {1-6}, {2-5}, {3-4}, {4-3}, {5-2}, {6-1} and {7-0}. Finally, by considering that among all the space vector groups which bring the load into a certain configurations, only those space vectors with adjacent relation of '1' are with the largest magnitude, the resulting set of active space vectors can be finally determined. These are the space vectors belonging to the groups G_0^7, G_4^7, G_7^7 and G_8^7, in accordance with the

selection given in Table 3.2. Thus, there are now 42 active space vectors involved in the output voltage generation, in contrast to only 14 used in the previous method, together with two zero space vectors. Locations and magnitudes of selected active space vectors can be identified from Figs. 3.7-3.9. To further simplify analysis, active space vectors are labelled with additional sub-scripts '*a*' and '*b*', followed by a number that identifies the space vector group with respect to the magnitude in the first plane and in accordance with the established classification. Considering the reference space vector in the first sector of the d_1-q_1 plane and imposing zero reference value in the other two planes, one has the situation shown in Fig. 5.7. All six active space vectors are shown in the first plane, with their mapping in the other two planes. In order to average the reference space vector over the switching period with six active space vectors and simultaneously neutralise low order harmonics from the planes other than the first one, one has to solve the following set of equations:

$$\bar{v}^*T_s = \bar{v}_{a4}T_{a4} + \bar{v}_{a7}T_{a7} + \bar{v}_{a8}T_{a8} + \bar{v}_{b4}T_{b4} + \bar{v}_{b7}T_{b7} + \bar{v}_{b8}T_{b8}$$
$$0 = \bar{v}_{a4}T_{a4} + \bar{v}_{a7}T_{a7} + \bar{v}_{a8}T_{a8} + \bar{v}_{b4}T_{b4} + \bar{v}_{b7}T_{b7} + \bar{v}_{b8}T_{b8}$$
$$0 = \bar{v}_{a4}T_{a4} + \bar{v}_{a7}T_{a7} + \bar{v}_{a8}T_{a8} + \bar{v}_{b4}T_{b4} + \bar{v}_{b7}T_{b7} + \bar{v}_{b8}T_{b8}$$

(5.8)

Each equation describes one plane. Although the same notation is used in (5.8) for all planes, magnitudes of active space vectors are actually different in every plane in accordance with Table 3.2. Decomposing (5.8) into six real equations yields:

$$M\cos(\vartheta)T_s = \frac{4}{7}T_{a4} + \frac{4}{7}\frac{K_2}{K}T_{a7} + \frac{4}{7}\frac{K_3}{K}T_{a8} + \frac{4}{7}LT_{b4} + \frac{4}{7}\frac{K_2}{K}LT_{b7} + \frac{4}{7}\frac{K_3}{K}LT_{b8}$$

$$M\sin(\vartheta)T_s = \frac{4}{7}KT_{b4} + \frac{4}{7}\frac{K_2}{K}KT_{b7} + \frac{4}{7}\frac{K_3}{K}KT_{b8}$$

$$0 = \frac{4}{7}T_{a4} - \frac{4}{7}\frac{K_3}{K_2}T_{a7} + \frac{4}{7}\frac{K}{K_2}T_{a8} - \frac{4}{7}L_2T_{b4} + \frac{4}{7}\frac{K_3}{K_2}L_2T_{b7} - \frac{4}{7}\frac{K}{K_2}L_2T_{b8}$$

$$0 = -\frac{4}{7}K_2T_{b4} + \frac{4}{7}\frac{K_3}{K_2}K_2T_{b7} - \frac{4}{7}\frac{K}{K_2}K_2T_{b8}$$

(5.9)

$$0 = \frac{4}{7}T_{a4} + \frac{4}{7}\frac{K}{K_3}T_{a7} - \frac{4}{7}\frac{K_2}{K_3}T_{a8} + \frac{4}{7}L_3T_{b4} + \frac{4}{7}\frac{K}{K_3}L_3T_{b7} - \frac{4}{7}\frac{K_2}{K_3}L_3T_{b8}$$

$$0 = \frac{4}{7}K_3T_{b4} + \frac{4}{7}\frac{K}{K_3}K_3T_{b7} - \frac{4}{7}\frac{K_2}{K_3}K_3T_{b8}$$

a)   *b)*   *c)*
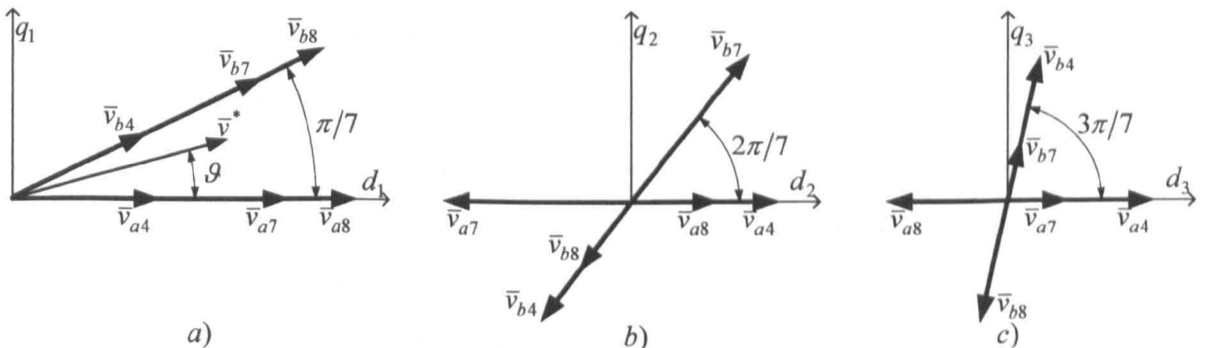
Fig. 5.7: Principle of calculation of times of application of active space vectors.

Total time of application of zero space vectors within a switching period is determined as:

$$T_O = T_0 + T_{127} = T_s - T_{a4} - T_{a7} - T_{a8} - T_{b4} - T_{b7} - T_{b8} \tag{5.10}$$

After some manipulations, solutions of (5.9) and (5.10) in the first sector, expressed by means of duty cycles and assuming equal distribution of the total duty cycle of the zero space vector among the two zero space vectors, are in the form:

$$\delta_{a4} = KM \sin(\frac{\pi}{7} - \vartheta); \qquad \delta_{b4} = KM \sin(\vartheta)$$

$$\delta_{a7} = K_2 M \sin(\frac{\pi}{7} - \vartheta); \qquad \delta_{b7} = K_2 M \sin(\vartheta)$$

$$\delta_{a8} = K_3 M \sin(\frac{\pi}{7} - \vartheta); \qquad \delta_{b8} = K_3 M \sin(\vartheta) \tag{5.11}$$

$$\delta_0 = \delta_{127} = \frac{1}{2}\delta_O = \frac{1}{2}[1 - K_3 M \cos(\frac{\pi}{14} - \vartheta)]$$

Set of equations (5.11) is very similar to the solution obtained for a five-phase SVPWM (4.19) with regard to the use of characteristic trigonometric constants and applied active space vectors. Thus, simple expressions, which are easy to implement in a DSP, are generated, based on trigonometric constants defined with (3.13). Solution applicable to every sector s ($s = 1$ to 14) is in the form:

$$\delta_{a4} = KM \sin(s\frac{\pi}{7} - \vartheta); \qquad \delta_{b4} = KM \sin(\vartheta - (s-1)\frac{\pi}{7})$$

$$\delta_{a7} = K_2 M \sin(s\frac{\pi}{7} - \vartheta); \qquad \delta_{b7} = K_2 M \sin(\vartheta - (s-1)\frac{\pi}{7})$$

$$\delta_{a8} = K_3 M \sin(s\frac{\pi}{7} - \vartheta); \qquad \delta_{b8} = K_3 M \sin(\vartheta - (s-1)\frac{\pi}{7}) \tag{5.12}$$

$$\delta_0 = \delta_{127} = \frac{1}{2}\delta_O = \frac{1}{2}[1 - K_3 M \cos((2s-1)\frac{\pi}{14} - \vartheta)]$$

It is easy to verify that the ratio of calculated duty cycles of different active space vectors is at the same time the ratio of the magnitudes of different groups of active space vectors:

$$\frac{\delta_{a7}}{\delta_{a4}} = \frac{|\overline{v}_{a7}|}{|\overline{v}_{a4}|} = \frac{K_2}{K}; \qquad \frac{\delta_{a8}}{\delta_{a4}} = \frac{|\overline{v}_{a8}|}{|\overline{v}_{a4}|} = \frac{K_3}{K}; \qquad \frac{\delta_{a8}}{\delta_{a7}} = \frac{|\overline{v}_{a8}|}{|\overline{v}_{a7}|} = \frac{K_3}{K_2}$$

$$\frac{\delta_{b7}}{\delta_{b4}} = \frac{|\overline{v}_{b7}|}{|\overline{v}_{b4}|} = \frac{K_2}{K}; \qquad \frac{\delta_{b8}}{\delta_{b4}} = \frac{|\overline{v}_{b8}|}{|\overline{v}_{b4}|} = \frac{K_3}{K}; \qquad \frac{\delta_{b8}}{\delta_{b7}} = \frac{|\overline{v}_{b8}|}{|\overline{v}_{b7}|} = \frac{K_3}{K_2} \tag{5.13}$$

Switching pattern for the first two sectors is shown in Fig. 5.8. The sequence of space vectors in all odd sectors is $\overline{v}_0, \overline{v}_{a4}, \overline{v}_{b7}, \overline{v}_{a8}, \overline{v}_{b8}, \overline{v}_{a7}, \overline{v}_{b4}, \overline{v}_{127}, \overline{v}_{b4}, \overline{v}_{a7}, \overline{v}_{b8}, \overline{v}_{a8}, \overline{v}_{b7}, \overline{v}_{a4}, \overline{v}_0$, while in all even sectors the sequence is $\overline{v}_0, \overline{v}_{b4}, \overline{v}_{a7}, \overline{v}_{b8}, \overline{v}_{a8}, \overline{v}_{b7}, \overline{v}_{a4}, \overline{v}_{127}, \overline{v}_{a4}, \overline{v}_{b7}, \overline{v}_{a8}, \overline{v}_{b8}, \overline{v}_{a7}, \overline{v}_{b4}, \overline{v}_0$. Thus, the sequence is arranged in such a way that during the first half of the switching period load appears in load configurations {0-7}, {1-6}, {2-5}, {3-4}, {4-3}, {5-2}, {6-1}, {7-0}, and in reversed order during the second half of the switching period. All active space vectors that are used in the switching pattern are with an adjacent relation of '1', as discussed earlier.
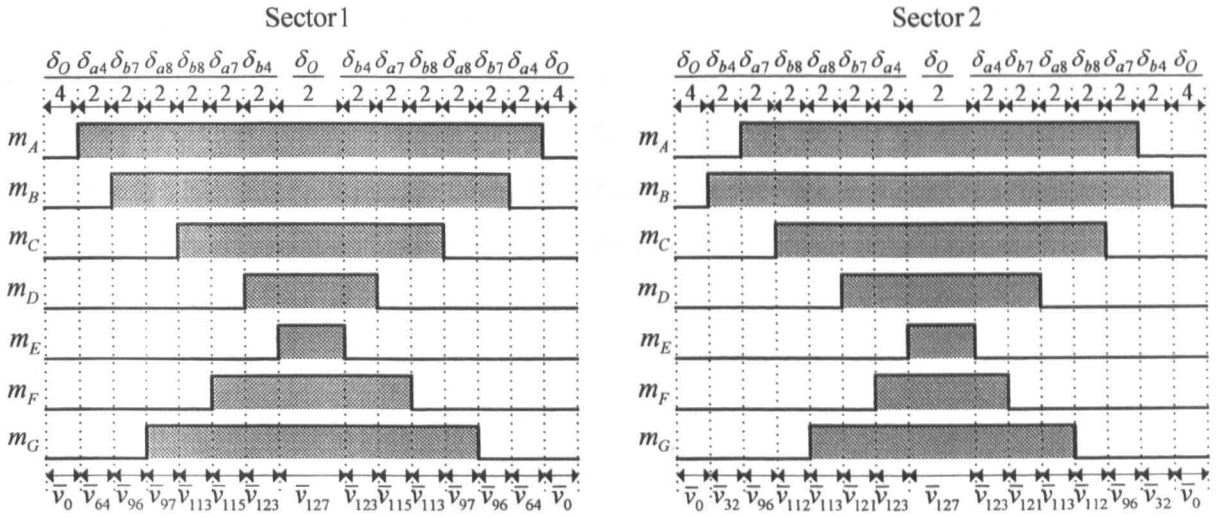
Fig. 5.8: Switching pattern in the first two sectors.

Final duty cycles, used during DSP implementation, are determined as:

$$\delta_1 = \frac{\delta_O}{2}$$
$$\delta_2^O = \delta_1 + \delta_{b4}; \qquad \delta_2^E = \delta_1 + \delta_{a4}$$
$$\delta_3^O = \delta_2^O + \delta_{a7}; \qquad \delta_3^E = \delta_2^E + \delta_{b7}$$
$$\delta_4^O = \delta_3^O + \delta_{b8}; \qquad \delta_4^E = \delta_3^E + \delta_{a8} \tag{5.14}$$
$$\delta_5^O = \delta_4^O + \delta_{a8}; \qquad \delta_5^E = \delta_4^E + \delta_{b8}$$
$$\delta_6^O = \delta_5^O + \delta_{b7}; \qquad \delta_6^E = \delta_5^E + \delta_{a7}$$
$$\delta_7 = \delta_1 + \delta_{a4} + \delta_{a7} + \delta_{a8} + \delta_{b4} + \delta_{b7} + \delta_{b8}$$

Duty cycle disposition through all fourteen sectors and for every inverter leg is summarized in Table 5.2. Maximum value of the modulation index, obtainable in the linear region of modulation, is:

$$M_{max} = \frac{1}{K_3} \approx 1.0257 \tag{5.15}$$

This value is significantly smaller than the maximum value obtained in the sub-section 5.2. However, use of six active space vectors yields purely sinusoidal output voltage.

Table 5.2: Duty cycle disposition through sectors.

Leg \ Sector	1	2	3	4	5	6	7	8	9	10	11	12	13	14
A	δ_7	δ_6^E	δ_5^O	δ_4^E	δ_3^O	δ_2^E	δ_1	δ_1	δ_2^O	δ_3^E	δ_4^O	δ_5^E	δ_6^O	δ_7
B	δ_6^O	δ_7	δ_7	δ_6^E	δ_5^O	δ_4^E	δ_3^O	δ_2^E	δ_1	δ_1	δ_2^O	δ_3^E	δ_4^O	δ_5^E
C	δ_4^O	δ_5^E	δ_6^O	δ_7	δ_7	δ_6^E	δ_5^O	δ_4^E	δ_3^O	δ_2^E	δ_1	δ_1	δ_2^O	δ_3^E
D	δ_2^O	δ_3^E	δ_4^O	δ_5^E	δ_6^O	δ_7	δ_7	δ_6^E	δ_5^O	δ_4^E	δ_3^O	δ_2^E	δ_1	δ_1
E	δ_1	δ_1	δ_2^O	δ_3^E	δ_4^O	δ_5^E	δ_6^O	δ_7	δ_7	δ_6^E	δ_5^O	δ_4^E	δ_3^O	δ_2^E
F	δ_3^O	δ_2^E	δ_1	δ_1	δ_2^O	δ_3^E	δ_4^O	δ_5^E	δ_6^O	δ_7	δ_7	δ_6^E	δ_5^O	δ_4^E
G	δ_5^O	δ_4^E	δ_3^O	δ_2^E	δ_1	δ_1	δ_2^O	δ_3^E	δ_4^O	δ_5^E	δ_6^O	δ_7	δ_7	δ_6^E

A set of simulations has been carried out and the behaviour of the modulator has been investigated for different values of the modulation index. The results are shown in Fig. 5.9. One phase voltage is illustrated together with its spectrum (right part of Fig. 5.9). It can be seen that the spectrum shows no signs of harmonic components other than the fundamental, which is 50 Hz and with an rms value that corresponds to the set value of *M*.
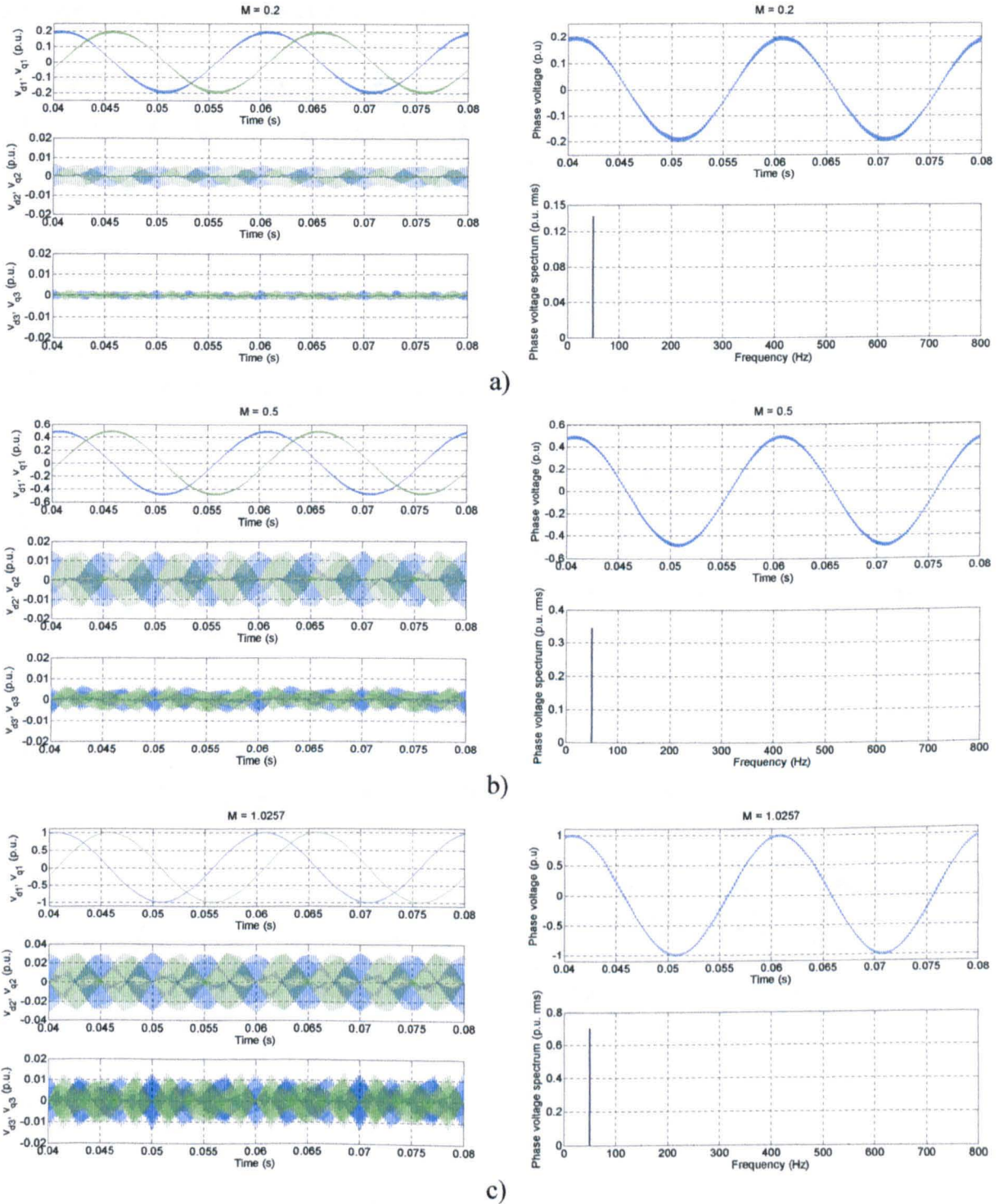
Fig. 5.9: Simulation results - phase voltage axis components after transformation in three planes (left), and phase voltage and its spectrum (right) at:
a) $M = 0.2$, b) $M = 0.5$, and c) $M = 1.0257$.

After transformation of phase voltages into all three planes, using (3.18), it can be seen (left part of Fig. 5.9) that only the d_1-q_1 plane contains fundamental components, while other two planes are with the zero average value. The scales have been adjusted in Fig. 5.9 to illustrate that the d_2-q_2 and d_3-q_3 planes contain only the switching harmonics, and not any low order harmonics, in contrast to the method in sub-section 5.2. However, the maximum achievable value of the fundamental is now lower.
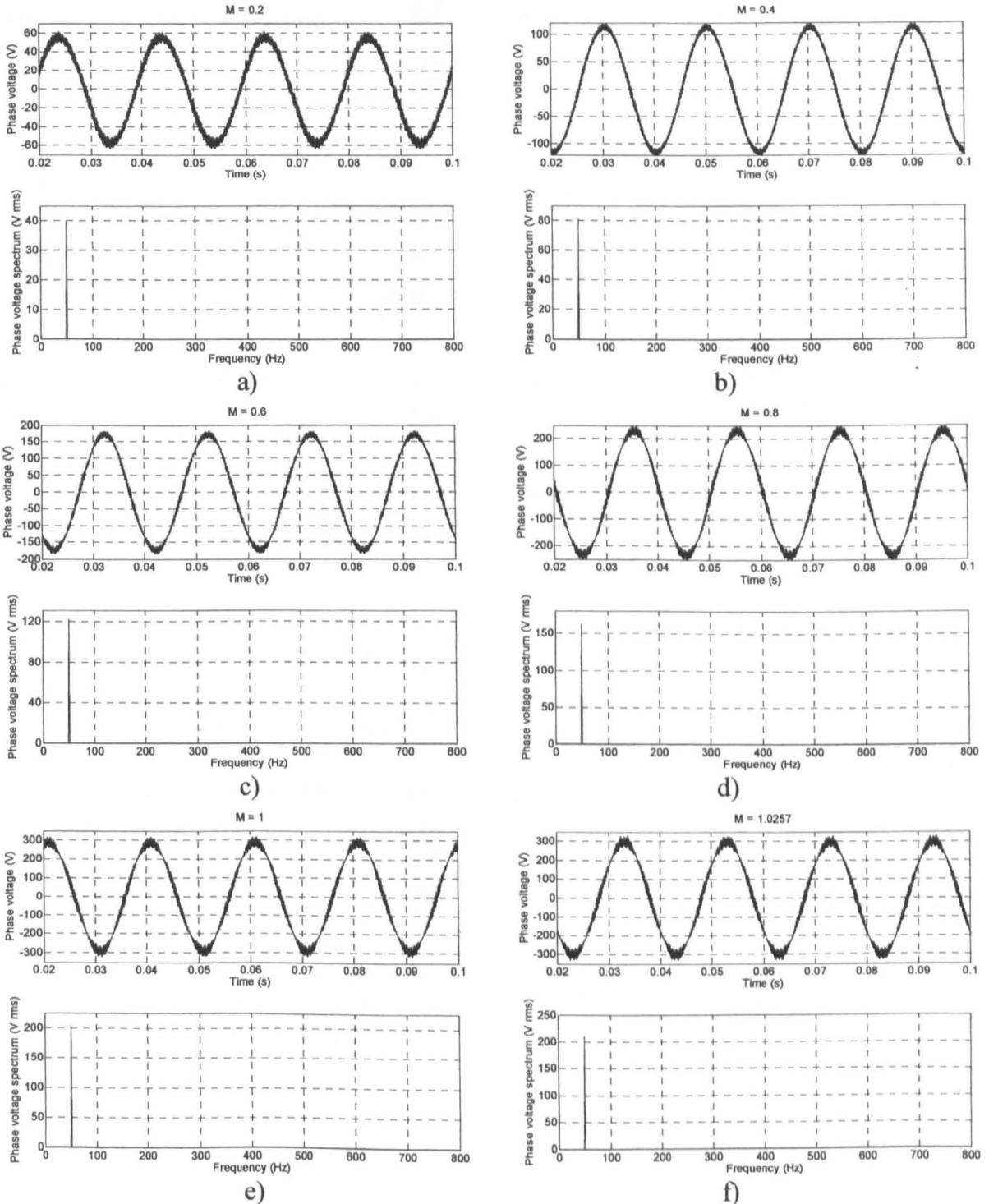
Fig. 5.10: Experimental results - phase voltage and its spectrum at: a) $M = 0.2$, b) $M = 0.4$, c) $M = 0.6$, d) $M = 0.8$, e) $M = 1$, and f) $M = 1.0257$.

The same seven-phase star-connected static *R-L* load is used for experimental investigation and the results are shown in Fig. 5.10. Again, an excellent agreement between simulation and experimental results is achieved. Purely sinusoidal phase voltages are generated and there is not any trace of the low order harmonics in the phase voltage spectrum. CMV is measured next and the results are shown in Fig. 5.11.
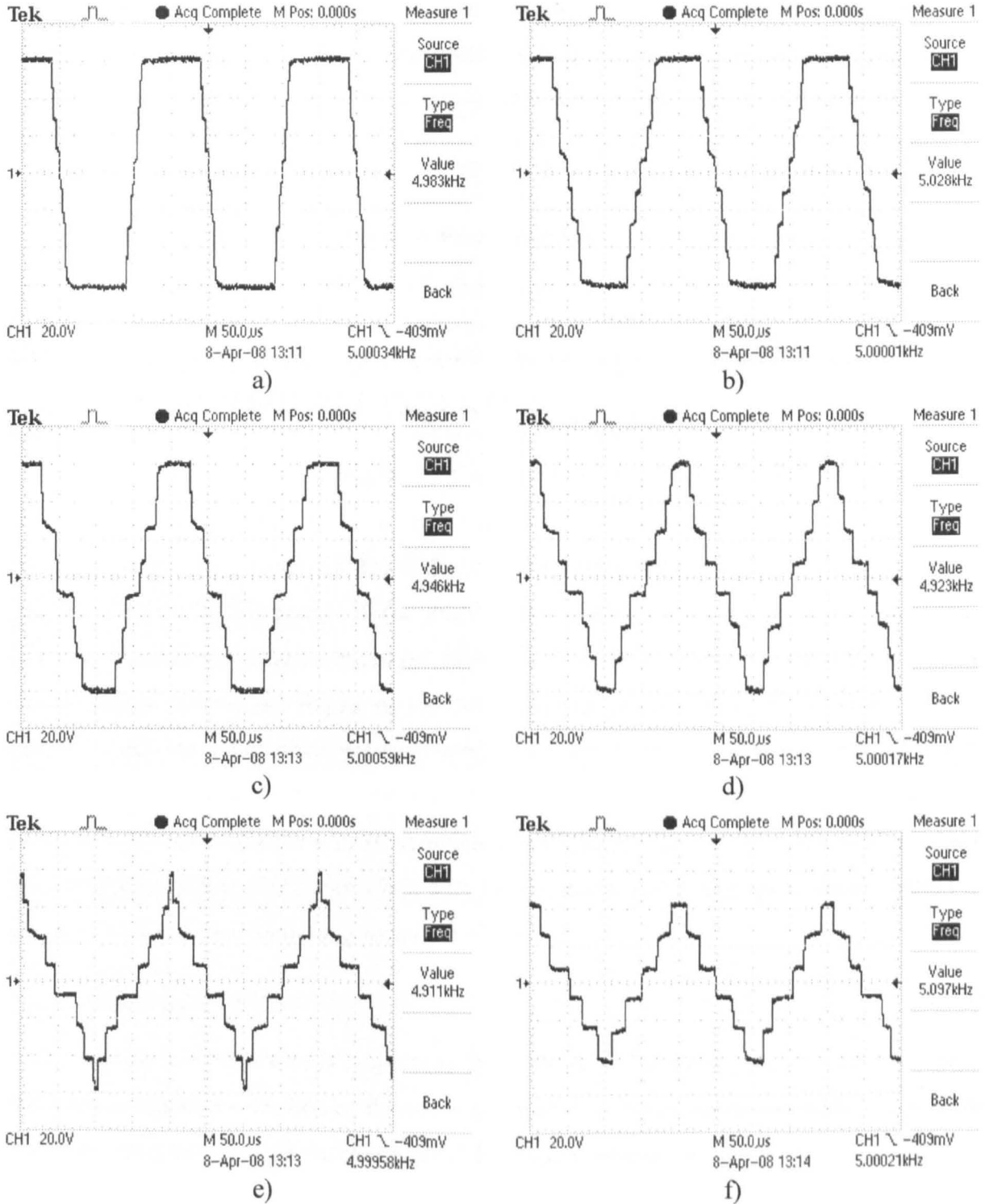
Fig. 5.11: Experimentally measured common-mode voltage at a) $M = 0.2$, b) $M = 0.4$, c) $M = 0.6$, d) $M = 0.8$, e) $M = 1$, and f) $M = 1.0257$ (Scale: 100V/div).

Since the SVPWM method uses six active space vectors together with two zero space vectors per switching period, all load configurations are present during the operation. Therefore, the CMV now contains all voltage levels characteristic for a seven-phase system. This is demonstrated in Fig. 5.11 for the various values of the modulation index. In general, the magnitude of the activated space vector (with respect to the first plane), and the absolute value of the magnitude of the resulting CMV are in the inverse proportion. This is easy to check knowing the order of the space vectors within a switching period and the measured CMV. When compared to the CMV of the five-phase SVPWM (Fig. 4.12), it can be seen that steps of the generated CMV are smaller, which results in generally lower overall dv/dt in the seven-phase system.

Based on the results presented for a five-phase and seven-phase VSI, a SVPWM scheme for a nine-phase VSI, aimed at sinusoidal output voltage generation, is devised next.

5.3 CONTINUOUS SPACE VECTOR PWM FOR A NINE-PHASE VOLTAGE SOURCE INVERTER

Developed SVPWM schemes for five-phase and seven-phase VSIs, based on the use of only two active space vectors, inherently introduce low order harmonics into phase voltages. While this is beneficial for multi-phase machines with concentrated windings, it can cause large current harmonics if the multi-phase machine is designed with a distributed winding. A SVPWM scheme, based on utilisation of only two active space vectors from the largest group, can be developed in the same manner as in section 5.2.1. Since both the procedure and the conclusions are very much the same, characteristics of such a scheme for nine-phase VSIs are omitted and only scheme aimed at sinusoidal output voltage generation is developed. However, for the sake of completeness of the results presented, maximum value of the modulation index, obtainable when only two of the largest active space vectors (from the group G_{16}^9) are used per switching period, is given:

$$M_{\max} = \frac{2K_4}{9L_4} \approx 1.2603 \tag{5.16}$$

It can be seen that this value is larger than those obtained for the five-phase and seven-phase VSIs and it represents 98.99% of the value obtainable in the square-wave mode of operation. Constants used in (5.16) are defined with (3.13), where now $n = 9$.

To generate sinusoidal output voltages, eight active space vectors per switching period have to be used [Kelly et al (2003), Grandi et al (2007a)]. These active space vectors are

102

chosen again as those with an adjacent relation of '1' in the switching states. Based on the data given in Table 3.3, these space vectors belong to the groups G_6^9, G_{12}^9, G_{15}^9, and G_{16}^9. These groups are with the largest magnitude among all the other groups that bring the load into the same load configuration. Hence the active space vectors belonging to these groups are with the adjacent relation of '1'.

To derive the set of expressions needed for the implementation, it is necessary to consider the situation illustrated in Fig. 5.12. Reference space vector is shown in Fig. 5.12a as being in the first sector (there are 18 sectors in total) together with the adjacent six active space vectors. Mapping of these six active space vectors in the planes d_2-q_2, d_3-q_3, and d_4-q_4 is shown in the remaining parts of Fig. 5.12. Imposing zero reference values in all the planes other than the first one, the set of equations that must be satisfied in order to average the reference space vector with six active space vectors over the switching period, can be written as:

$$\vec{v}^* T_s = \bar{v}_{a6}T_{a6} + \bar{v}_{a12}T_{a12} + \bar{v}_{a15}T_{a15} + \bar{v}_{a16}T_{a16} + \bar{v}_{b6}T_{b6} + \bar{v}_{b12}T_{b12} + \bar{v}_{b15}T_{b15} + \bar{v}_{b16}T_{b16}$$
$$0 = \bar{v}_{a6}T_{a6} + \bar{v}_{a12}T_{a12} + \bar{v}_{a15}T_{a15} + \bar{v}_{a16}T_{a16} + \bar{v}_{b6}T_{b6} + \bar{v}_{b12}T_{b12} + \bar{v}_{b15}T_{b15} + \bar{v}_{b16}T_{b16}$$
$$0 = \bar{v}_{a6}T_{a6} + \bar{v}_{a12}T_{a12} + \bar{v}_{a15}T_{a15} + \bar{v}_{a16}T_{a16} + \bar{v}_{b6}T_{b6} + \bar{v}_{b12}T_{b12} + \bar{v}_{b15}T_{b15} + \bar{v}_{b16}T_{b16}$$
$$0 = \bar{v}_{a6}T_{a6} + \bar{v}_{a12}T_{a12} + \bar{v}_{a15}T_{a15} + \bar{v}_{a16}T_{a16} + \bar{v}_{b6}T_{b6} + \bar{v}_{b12}T_{b12} + \bar{v}_{b15}T_{b15} + \bar{v}_{b16}T_{b16}$$

(5.17)

Each row corresponds to one plane, and the reference space vector is defined in the same way as before. Magnitudes of active space vectors are available from Table 3.3. Decomposing (5.17) into eight real equations yields:

$$M\cos(\vartheta)T_s = \frac{4}{9}\left[T_{a6} + \frac{K_2}{K}T_{a12} + \frac{K_3}{K}T_{a15} + \frac{K_4}{K}T_{a16} + LT_{b6} + \frac{K_2}{K}LT_{b12} + \frac{K_3}{K}LT_{b15} + \frac{K_4}{K}LT_{b16}\right]$$

$$M\sin(\vartheta)T_s = \frac{4}{9}\left[KT_{b6} + \frac{K_2}{K}KT_{b12} + \frac{K_3}{K}KT_{b15} + \frac{K_4}{K}KT_{b16}\right]$$

$$0 = \frac{4}{9}\left[T_{a6} - \frac{K_4}{K_2}T_{a12} + \frac{K_3}{K_2}T_{a15} - \frac{K}{K_2}T_{a16} - L_2T_{b6} + \frac{K_4}{K_2}L_2T_{b12} - \frac{K_3}{K_2}L_2T_{b15} + \frac{K}{K_2}L_2T_{b16}\right]$$

$$0 = \frac{4}{9}\left[-K_2T_{b6} + \frac{K_4}{K_2}K_2T_{b12} - \frac{K_3}{K_2}K_2T_{b15} + \frac{K}{K_2}K_2T_{b16}\right]$$

(5.18)

$$0 = \frac{4}{9}\left[T_{a6} + T_{a12} - T_{a16} + L_3T_{b6} + L_3T_{b12} - L_3T_{b16}\right]$$

$$0 = \frac{4}{9}\left[K_3T_{b6} + K_3T_{b12} - K_3T_{b16}\right]$$

$$0 = \frac{4}{9}\left[T_{a6} - \frac{K}{K_4}T_{a12} - \frac{K_3}{K_4}T_{a15} + \frac{K_2}{K_4}T_{a16} - L_4T_{b6} + \frac{K}{K_4}L_4T_{b12} + \frac{K_3}{K_4}L_4T_{b15} - \frac{K_2}{K_4}L_4T_{b16}\right]$$

$$0 = \frac{4}{9}\left[-K_4T_{b6} + \frac{K}{K_4}K_4T_{b12} + \frac{K_3}{K_4}K_4T_{b15} - \frac{K_2}{K_4}K_4T_{b16}\right]$$

The total time of application of zero space vectors within a switching period is determined as:

$$T_O = T_0 + T_{S11} = T_s - T_{a6} - T_{a12} - T_{a15} - T_{a16} - T_{b6} - T_{b12} - T_{b15} - T_{b16}$$

(5.19)
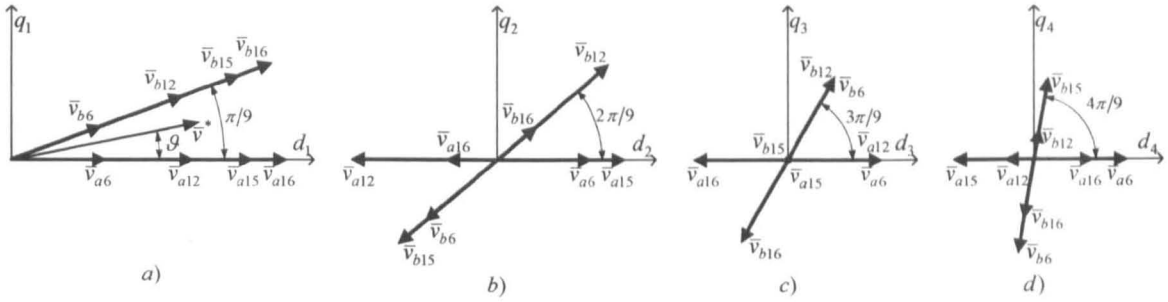
Fig. 5.12: Principle of calculation of times of application of active space vectors.

After some manipulations, duty cycles of both active and zero space vectors (selecting again equal sub-division of the total zero vector duty cycle between two zero space vectors), in the first sector, are obtained in the form:

$$\delta_{a6} = KM \sin(\frac{\pi}{9} - \vartheta); \qquad \delta_{b6} = KM \sin(\vartheta)$$

$$\delta_{a12} = K_2 M \sin(\frac{\pi}{9} - \vartheta); \qquad \delta_{b12} = K_2 M \sin(\vartheta)$$

$$\delta_{a15} = K_3 M \sin(\frac{\pi}{9} - \vartheta); \qquad \delta_{b15} = K_3 M \sin(\vartheta) \qquad (5.20)$$

$$\delta_{a16} = K_4 M \sin(\frac{\pi}{9} - \vartheta); \qquad \delta_{b16} = K_4 M \sin(\vartheta)$$

$$\delta_0 = \delta_{511} = \frac{1}{2}\delta_O = \frac{1}{2}[1 - K_4 M \cos(\frac{\pi}{18} - \vartheta)]$$

Solution applicable to every sector s ($s = 1$ to 18) is of the form:

$$\delta_{a6} = KM \sin(s\frac{\pi}{9} - \vartheta); \qquad \delta_{b6} = KM \sin(\vartheta - (s-1)\frac{\pi}{9})$$

$$\delta_{a12} = K_2 M \sin(s\frac{\pi}{9} - \vartheta); \qquad \delta_{b12} = K_2 M \sin(\vartheta - (s-1)\frac{\pi}{9})$$

$$\delta_{a15} = K_3 M \sin(s\frac{\pi}{9} - \vartheta); \qquad \delta_{b15} = K_3 M \sin(\vartheta - (s-1)\frac{\pi}{9}) \qquad (5.21)$$

$$\delta_{a16} = K_4 M \sin(s\frac{\pi}{9} - \vartheta); \qquad \delta_{b16} = K_4 M \sin(\vartheta - (s-1)\frac{\pi}{9})$$

$$\delta_0 = \delta_{511} = \frac{1}{2}\delta_O = \frac{1}{2}[1 - K_4 M \cos((2s-1)\frac{\pi}{18} - \vartheta)]$$

Again, it is simple to check based on the data given in Table 3.3 that the ratio of calculated duty cycles of different active space vectors is at the same time the ratio of the magnitudes of different groups of active space vectors:

$$\frac{\delta_{a12}}{\delta_{a6}} = \frac{|\bar{v}_{a12}|}{|\bar{v}_{a6}|} = \frac{K_2}{K}; \qquad \frac{\delta_{a15}}{\delta_{a6}} = \frac{|\bar{v}_{a15}|}{|\bar{v}_{a6}|} = \frac{K_3}{K}; \qquad \frac{\delta_{a16}}{\delta_{a6}} = \frac{|\bar{v}_{a16}|}{|\bar{v}_{a6}|} = \frac{K_4}{K}$$

$$\frac{\delta_{a15}}{\delta_{a12}} = \frac{|\bar{v}_{a15}|}{|\bar{v}_{a12}|} = \frac{K_3}{K_2}; \qquad \frac{\delta_{a16}}{\delta_{a12}} = \frac{|\bar{v}_{a16}|}{|\bar{v}_{a12}|} = \frac{K_4}{K_2}; \qquad \frac{\delta_{a16}}{\delta_{a15}} = \frac{|\bar{v}_{a16}|}{|\bar{v}_{a15}|} = \frac{K_4}{K_3} \qquad (5.22)$$

This is demonstrated in (5.22) based on the magnitudes and duty cycles of 'a' active space vectors. However, it is easy to verify that the same is valid for 'b' space vectors.

Switching pattern for the first two sectors is shown in Fig. 5.13. In all odd sectors, the sequence is $\bar{v}_0, \bar{v}_{a6}, \bar{v}_{b12}, \bar{v}_{a15}, \bar{v}_{b16}, \bar{v}_{a16}, \bar{v}_{b15}, \bar{v}_{a12}, \bar{v}_{b6}, \bar{v}_{511}, \bar{v}_{b6}, \bar{v}_{a12}, \bar{v}_{b15}, \bar{v}_{a16}, \bar{v}_{b16}, \bar{v}_{a15}, \bar{v}_{b12}, \bar{v}_{a6}, \bar{v}_0$, while in all even sectors it is $\bar{v}_0, \bar{v}_{b6}, \bar{v}_{a12}, \bar{v}_{b15}, \bar{v}_{a16}, \bar{v}_{b16}, \bar{v}_{a15}, \bar{v}_{b12}, \bar{v}_{a6}, \bar{v}_{511}, \bar{v}_{a6}, \bar{v}_{b12}, \bar{v}_{a15}, \bar{v}_{b16}, \bar{v}_{a16}, \bar{v}_{b15}, \bar{v}_{a12}, \bar{v}_{b6}, \bar{v}_0$. Therefore, during the first half of the switching period the load appears in load configurations {0-9}, {1-8}, {2-7}, {3-6}, {4-5}, {5-4}, {6-3}, {7-2}, {8-1}, {9-0} and then in reversed order during the second half of the switching period. Again, as in the case of the five-phase and seven-phase SVPWM, all active space vectors that are used for switching pattern are with adjacent relation of '1', as discussed earlier [Kelly et al (2003)].

Final duty cycles, for each inverter leg and corresponding sector, that are necessary for DSP implementation, are determined as:

$$\delta_1 = \frac{\delta_O}{2}$$

$$\delta_2^O = \delta_1 + \delta_{b6}; \qquad \delta_2^E = \delta_1 + \delta_{a6}$$
$$\delta_3^O = \delta_2^O + \delta_{a12}; \qquad \delta_3^E = \delta_2^E + \delta_{b12}$$
$$\delta_4^O = \delta_3^O + \delta_{b15}; \qquad \delta_4^E = \delta_3^E + \delta_{a15}$$
$$\delta_5^O = \delta_4^O + \delta_{a16}; \qquad \delta_5^E = \delta_4^E + \delta_{b16}$$
$$\delta_6^O = \delta_5^O + \delta_{b16}; \qquad \delta_6^E = \delta_5^E + \delta_{a16}$$
$$\delta_7^O = \delta_6^O + \delta_{a15}; \qquad \delta_7^E = \delta_6^E + \delta_{b15}$$
$$\delta_8^O = \delta_7^O + \delta_{b12}; \qquad \delta_8^E = \delta_7^E + \delta_{a12}$$
$$\delta_9 = \delta_1 + \delta_{a6} + \delta_{a12} + \delta_{a15} + \delta_{a16} + \delta_{b6} + \delta_{b12} + \delta_{b15} + \delta_{b16}$$

(5.23)

This is summarised in Table 5.3, for every inverter leg and all the sectors. Maximum value of the modulation index for the nine-phase SVPWM, obtainable in the linear region of the modulation when eight active space vectors are used per switching period, is equal to:

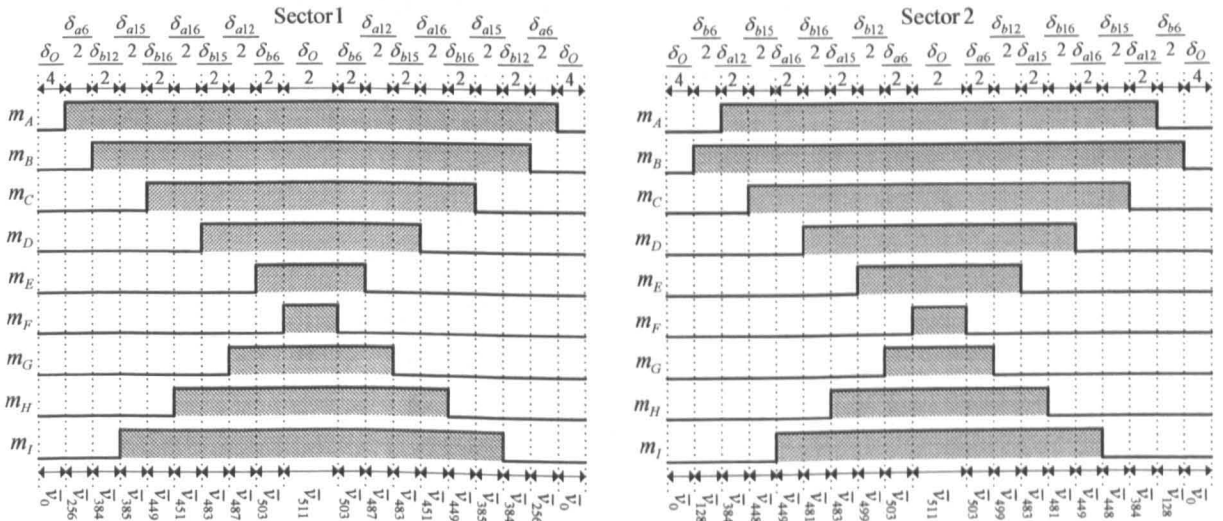$$M_{\max} = \frac{1}{K_4} \approx 1.0154$$

(5.24)

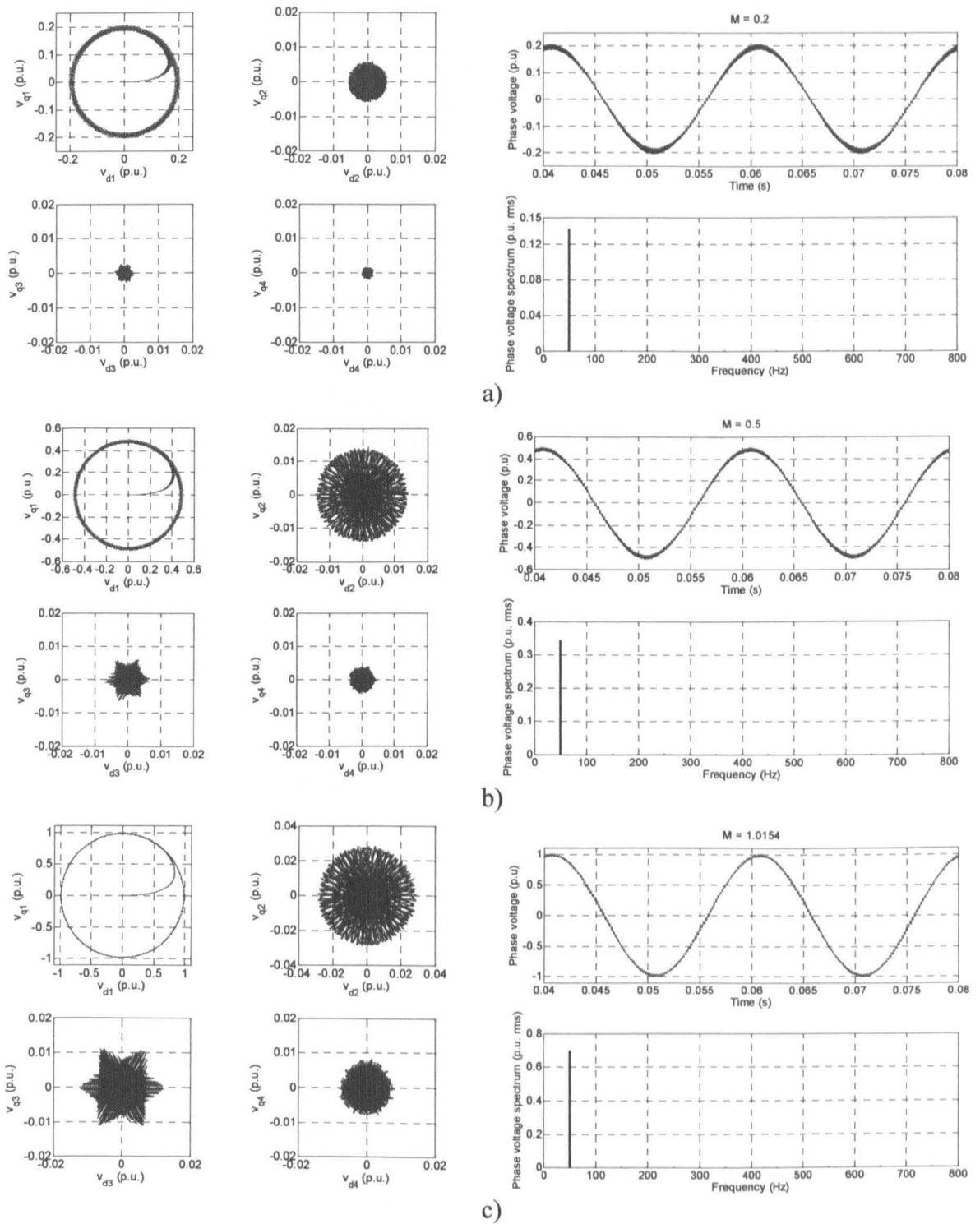**Fig. 5.13:** Switching pattern in the first two sectors.

As can be seen, maximum value of the modulation index is lower than the values obtained for the five-phase and seven phase SVPWM strategies. Although for all three topologies sinusoidal output voltage is generated, maximum achievable fundamental voltage decreases as the phase number increases.

Operation of the modulator has been simulated and the results are shown in Fig. 5.14. Only one phase voltage is shown together with its spectrum (right part of Fig. 5.14). It is visible that the spectrum shows no sign of harmonic components other than the fundamental, which is again 50 Hz. Phase voltages are transformed based on (3.22), and representation in all four planes is obtained. These results are now shown in Fig. 5.14 using X-Y plots in each plane and therefore trajectories of corresponding space vectors are obtained. Thus it can be seen that only the d_1-q_1 plane contains the fundamental components of a magnitude in accordance with the set value of the modulation index, while there are only switching harmonics present in the other three planes (zero reference space vector input). Scale on the graphs is different for planes other than the first one, in order to clearly demonstrate this. By properly determining duty cycles of active space vectors based on simultaneous consideration of all four planes, low order harmonic content in the planes d_2-q_2, d_3-q_3, and d_4-q_4 has been effectively kept at zero average value over the switching period [Grandi et al (2007a)].

Nine-phase star connected R-L load has been used for experimental verification of this SVPWM scheme. Again, phase voltage and CMV are measured, and results are shown in Fig. 5.15 and Fig. 5.16, respectively. Conditions during the experiments are the same as for the five-phase and seven-phase systems. Results obtained for the phase voltage are in accordance with simulation results, presented earlier, and phase voltage spectrum contains only the fundamental component. Measured phase voltage rms value is in agreement with the set value of the modulation index, considering that the dc bus voltage is 600 V.

Table 5.3: Duty cycle disposition through sectors.

Leg | Sector	1	2	3	4	5	6	7	8	9	10	11	12	13	14	15	16	17	18
A	δ_9	δ_8^E	δ_7^O	δ_6^E	δ_5^O	δ_4^E	δ_3^O	δ_2^E	δ_1	δ_1	δ_2^O	δ_3^E	δ_4^O	δ_5^E	δ_6^O	δ_7^E	δ_8^O	δ_9
B	δ_8^O	δ_9	δ_9	δ_8^E	δ_7^O	δ_6^E	δ_5^O	δ_4^E	δ_3^O	δ_2^E	δ_1	δ_1	δ_2^O	δ_3^E	δ_4^O	δ_5^E	δ_6^O	δ_7^E
C	δ_6^O	δ_7^E	δ_8^O	δ_9	δ_9	δ_8^E	δ_7^O	δ_6^E	δ_5^O	δ_4^E	δ_3^O	δ_2^E	δ_1	δ_1	δ_2^O	δ_3^E	δ_4^O	δ_5^E
D	δ_4^O	δ_5^E	δ_6^O	δ_7^E	δ_8^O	δ_9	δ_9	δ_8^E	δ_7^O	δ_6^E	δ_5^O	δ_4^E	δ_3^O	δ_2^E	δ_1	δ_1	δ_2^O	δ_3^E
E	δ_2^O	δ_3^E	δ_4^O	δ_5^E	δ_6^O	δ_7^E	δ_8^O	δ_9	δ_9	δ_8^E	δ_7^O	δ_6^E	δ_5^O	δ_4^E	δ_3^O	δ_2^E	δ_1	δ_1
F	δ_1	δ_1	δ_2^O	δ_3^E	δ_4^O	δ_5^E	δ_6^O	δ_7^E	δ_8^O	δ_9	δ_9	δ_8^E	δ_7^O	δ_6^E	δ_5^O	δ_4^E	δ_3^O	δ_2^E
G	δ_3^O	δ_2^E	δ_1	δ_1	δ_2^O	δ_3^E	δ_4^O	δ_5^E	δ_6^O	δ_7^E	δ_8^O	δ_9	δ_9	δ_8^E	δ_7^O	δ_6^E	δ_5^O	δ_4^E
H	δ_5^O	δ_4^E	δ_3^O	δ_2^E	δ_1	δ_1	δ_2^O	δ_3^E	δ_4^O	δ_5^E	δ_6^O	δ_7^E	δ_8^O	δ_9	δ_9	δ_8^E	δ_7^O	δ_6^E
I	δ_7^O	δ_6^E	δ_5^O	δ_4^E	δ_3^O	δ_2^E	δ_1	δ_1	δ_2^O	δ_3^E	δ_4^O	δ_5^E	δ_6^O	δ_7^E	δ_8^O	δ_9	δ_9	δ_8^E

Fig. 5.14: Simulation results - phase voltages after transformation into four planes (left), and phase voltage and its spectrum (right) at: a) $M = 0.2$, b) $M = 0.5$, and c) $M = 1.0154$.

Results of measurements of the CMV are presented in Fig. 5.16. According to (3.3), CMV can take ten different voltage levels in a nine-phase system: $\pm V_{dc}/2$, $\pm 7V_{dc}/18$, $\pm 5V_{dc}/18$, $\pm 3V_{dc}/18$, and $\pm V_{dc}/18$. Having a 600 V dc bus voltage, these voltage levels are roughly ± 300 V, ± 233 V, ± 166 V, ± 100 V, and ± 33 V. Thus, voltage steps are with a value of $V_{dc}/9$ which is effectively around 66 V. Developed SVPWM scheme uses eight active space vectors per

switching period, arranged in such an order to yield a sequential transition of switching states, with a single commutation during change of the activated space vector. Therefore, all load configurations are in use and consequently CMV takes all characteristic voltage levels. These can be clearly identified from Fig. 5.16. As the maximum value of the modulation index is approached durations of voltage levels that are the result of the zero space vectors decrease and eventually vanish completely.
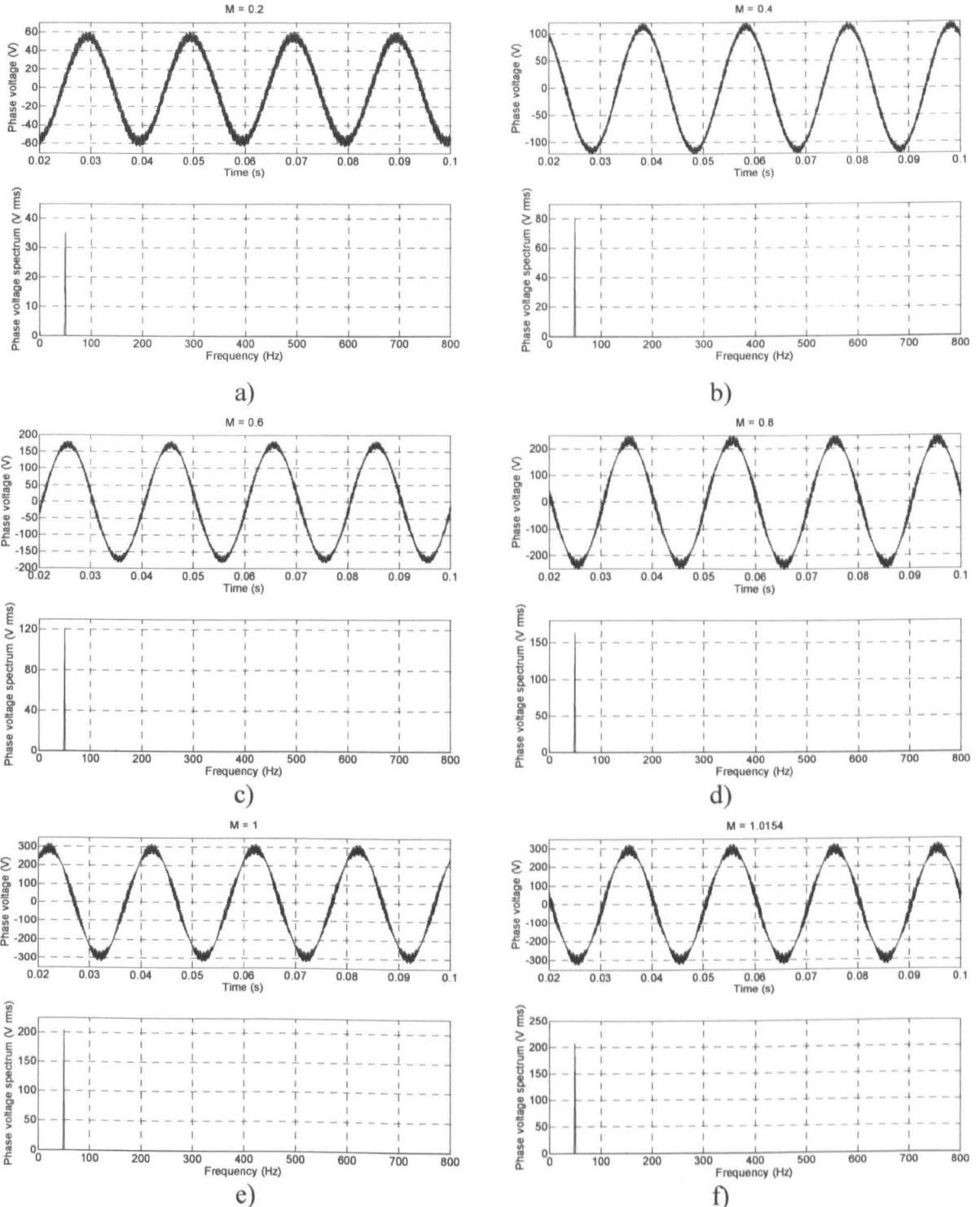
Fig. 5.15: Experimental results - phase voltage and its spectrum at: a) $M = 0.2$, b) $M = 0.4$, c) $M = 0.6$, d) $M = 0.8$, e) $M = 1$, and f) $M = 1.0154$.
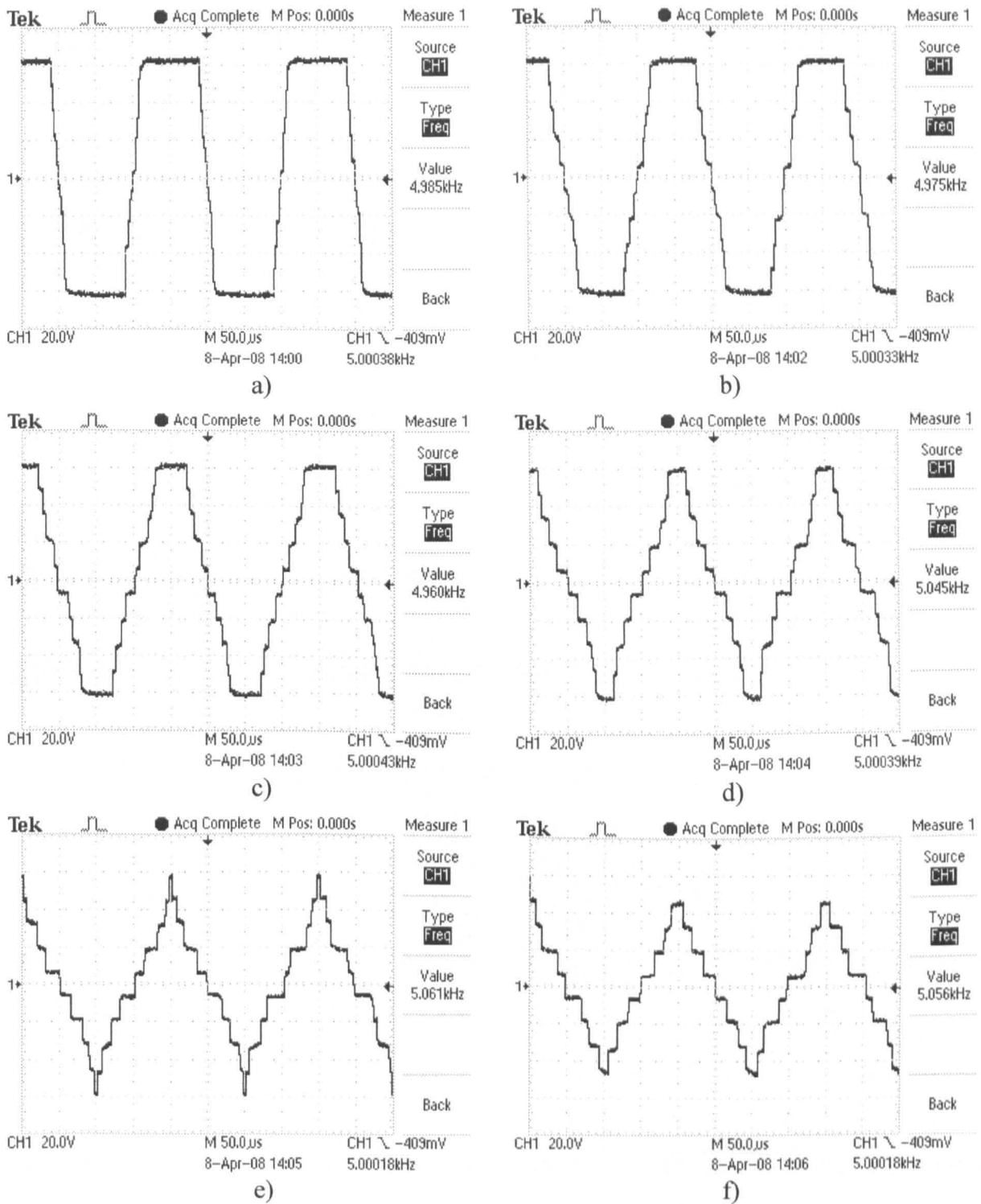
Fig. 5.16: Experimentally measured common-mode voltage at a) $M = 0.2$, b) $M = 0.4$, c) $M = 0.6$, d) $M = 0.8$, e) $M = 1$, and f) $M = 1.0154$ (Scale: 100V/div).

Great similarity in results obtained so far can be used to establish a general method, aimed at development of multi-phase SVPWM schemes for an arbitrary odd phase number. Before doing that, some common features of the developed SVPWM schemes are addressed first, primarily related to the levels of dc bus utilisation obtained with different selections of the set of active space vectors for a SVPWM.

5.4 DC BUS UTILISATION OF MULTI-PHASE VOLTAGE SOURCE INVERTERS

Based on the material presented so far, an excellent agreement of theoretical and experimental results has been achieved. It has been confirmed that, in order to achieve sinusoidal output voltage with an n-phase VSI, n-1 active space vectors must be used per switching period. In general, the number of active space vectors must equal the number of available degrees of freedom in a system [Zhao and Lipo (1995)]. These are selected for each topology as those space vectors with the adjacent relation of '1' in the switching states [Kelly et al (2003), Xue and Wen (2005)], and organised in such a manner to yield symmetrical switching pattern with two commutations per inverter leg, over the switching period. This greatly simplifies implementation using standard DSP PWM units. At the same time, it has been demonstrated that a simple extension of the three-phase SVPWM, based on the use of two adjacent largest active space vectors per switching period, does not yield sinusoidal output voltage. Low order harmonics, characteristic for the planes other than the first one, have been generated.

It is interesting to compare the dc bus utilisation of multi-phase VSIs, for these two rather different SVPWM strategies. Considering the modulation index values given with (4.15), (5.7), and (5.16) it can be seen that the maximum obtainable value of the fundamental, in the case of SVPWM scheme based on the use of only two adjacent largest active space vectors per switching period, increases with an increase of the number of phases. Thus, in general, for an n-phase system (n is an odd number) one can find that the maximum level the fundamental can reach is of the value:

$$M_{max-h}(n) = \frac{2}{n} \frac{K_{(n-1)/2}}{L_{(n-1)/2}} = \frac{2}{n} \frac{\sin(\frac{n-1}{2}\frac{\pi}{n})}{\cos(\frac{n-1}{2}\frac{\pi}{n})} \tag{5.25}$$

The additional sub-script 'h' is used to emphasise that this value of the fundamental is obtained at the expense of low order harmonic existence. The magnitudes of these harmonic components are in a fixed relation to the magnitude of the fundamental over the whole range of the modulation index. On the other hand, when purely sinusoidal output voltage is generated, based on (4.23), (5.15), and (5.24), utilisation of the dc bus voltage decreases as the number of phases increases. Thus, for an n-phase system:

$$M_{max}(n) = \frac{1}{K_{(n-1)/2}} = \frac{1}{\sin(\frac{n-1}{2}\frac{\pi}{n})} \tag{5.26}$$
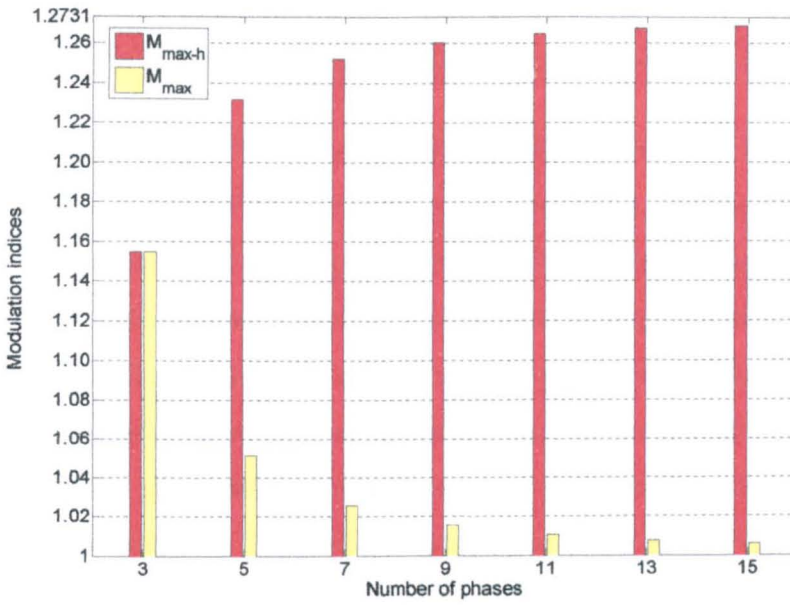
Fig. 5.17: Dc bus utilisation as the function of the number of phases.

Expressions (5.25) and (5.26) are graphically illustrated in Fig. 5.17, for the phase numbers up to fifteen. As can be seen, multi-phase SVPWM schemes based on the use of only two adjacent largest active space vectors offer an increase in the dc bus utilisation as the number of phase increases. The maximum value increases towards the maximum value obtainable during $2n$-mode of operation $M_{2n-step} = 4/\pi \approx 1.2731$. At the same time, as the number of phases increases, n-phase SVPWM schemes based on the use of n-1 active space vectors show a decrease in the value of the maximum obtainable modulation index. It can be verified that the trend of decrease is towards the value of the modulation index equal to $M = 1$.

It can be concluded that, in multi-phase machines with concentrated windings, better dc bus utilisation than for the three-phase case can be achieved. Low order harmonics, generated in addition to the fundamental, are in this case even desirable since they enable torque enhancement. This has been demonstrated in the past for five-phase drives [Ryu et al (2005)], seven-phase drives [Locment et al (2006)] and nine-phase drives [Coates et al (2001)]. In real-world applications, this means that rated operating voltage of the multi-phase machine can be reached from the lower dc bus voltage, thanks to harmonic injection that simultaneously enhances developed torque.

On the other hand, multi-phase machines with distributed windings suffer from poorer dc bus utilisation, compared to three-phase machines. As Fig. 5.17 indicates, the maximum value of the modulation index in the linear region of modulation tends towards unity as the number of phases increases.

5.5 GENERALISATION OF THE SVPWM FOR MULTI-PHASE VOLTAGE SOURCE INVERTERS

It is important to notice that there is a great similarity between sets of equations used in the implementation of the SVPWM schemes for five-phase, seven-phase and nine-phase VSIs. This offers a possibility to develop a generic SVPWM algorithm, applicable to all odd phase number VSIs, which can simplify and speed-up implementation of multi-phase SVPWM schemes aimed at sinusoidal output voltage generation. Common for all n-phase sinusoidal SVPWM schemes presented so far is the need to use n-1 active space vectors per switching period. As the phase number n increases, the number of available space vectors of an n-phase VSI also increases as 2^n. While in the case of a five-phase VSI it is still relatively easy to deal with 32 space vectors, this becomes tedious for higher phase numbers. Thus, selection of the set of n-1 active space vectors is not always a straightforward task.

As indicated earlier, the final set of space vectors must be with the adjacent relation of '1'. This at the same time means that selected space vectors belong to different groups that are with the largest magnitudes among all the groups that bring the load into the same configurations. Still, to perform such a selection, it is necessary to know the complete set of space vectors for every multi-phase topology. Once when the set of n-1 active space vectors is identified and the reference space vector magnitude and position are known, it is necessary to solve an algebraic set of n-1 equations, in order to obtain duty cycles of each active space vector. These equations (e.g. (4.17), (5.9), and (5.18)) are generated considering positions and magnitudes of the selected active space vectors in all $(n$-1$)/2$ 2-D planes. The aim is to generate the fundamental in the first plane, while zero average value is imposed as the restriction in all the other planes.

However, regardless of the phase number, the pattern of appearance of solutions is almost identical, provided that these are expressed by means of trigonometric constants defined with (3.13). This can be observed by comparing the solutions for five-phase, seven-phase and nine-phase SVPWM schemes that are given with (4.20), (5.12), and (5.21), respectively. Obviously, these solutions have been obtained using the knowledge of the selected set of active space vectors and attributes of each of the space vectors in every plane. Yet, the form of solutions allows a generalisation, since the only important variables that change with the change of the phase number are trigonometric constants. Clearly, the number of used active space vectors also changes, as well as the membership of a particular group, characteristic for a particular phase number.

Based on (4.20), (5.12), and (5.21), a generic solution for duty cycles of the active space vectors used for an *n*-phase SVPWM for sinusoidal output voltage generation can be written as:

$$
\begin{bmatrix} \delta_{a1} \\ \delta_{a2} \\ \vdots \\ \delta_{a(n-1)/2} \end{bmatrix} = \begin{bmatrix} K \\ K_2 \\ \vdots \\ K_{(n-1)/2} \end{bmatrix} M \sin(s\frac{\pi}{n} - \vartheta); \qquad \begin{bmatrix} \delta_{b1} \\ \delta_{b2} \\ \vdots \\ \delta_{b(n-1)/2} \end{bmatrix} = \begin{bmatrix} K \\ K_2 \\ \vdots \\ K_{(n-1)/2} \end{bmatrix} M \sin(\vartheta - (s-1)\frac{\pi}{n}) \qquad (5.27)
$$

It is recognised in (5.27) that applied active space vectors are with different magnitudes and that there are $(n-1)/2$ pairs of '*a*' and '*b*' active space vectors with the same magnitudes that are proportional to the calculated duty cycles. Duty cycles are now designated with an additional sub-scripts (1 to $(n-1)/2$), starting from the smallest one to the largest one, respectively. Thus, a precise knowledge of the group membership is not necessary for implementation. Duty cycles of two zero space vectors, assuming equal distribution of the total duty cycle of zero space vectors, are in the form:

$$
\delta_0 = \delta_{2^n - 1} = \frac{1}{2}\delta_O = \frac{1}{2}[1 - K_{(n-1)/2}M\cos((2s-1)\frac{\pi}{2n} - \vartheta)] \qquad (5.28)
$$

Once calculated, duty cycles need to be summed properly in order to obtain per-leg duty cycles that will be distributed in accordance with the current sector. To perform that, knowledge of the sequence of space vectors within the switching period is necessary. In all SVPWM methods presented, symmetrical switching pattern is generated by having $\bar{v}_0$ zero space vector at the beginning and at the end of the switching period, and $\bar{v}_{2^n - 1}$ zero space vector in the middle of the switching period. The ordering of active space vectors, between zero space vectors $\bar{v}_0$ and $\bar{v}_{2^n - 1}$, during the first half of the switching period in the first sector, is illustrated in Fig. 5.18, for all three analysed topologies. It can bee seen that the ordering of active space vectors follows the rule that is easy to generalise for any phase number. The sequence starts with the smallest '*a*' space vector and changes in an alternating manner, through the selected set of active space vectors, ending with the smallest '*b*' space vector.
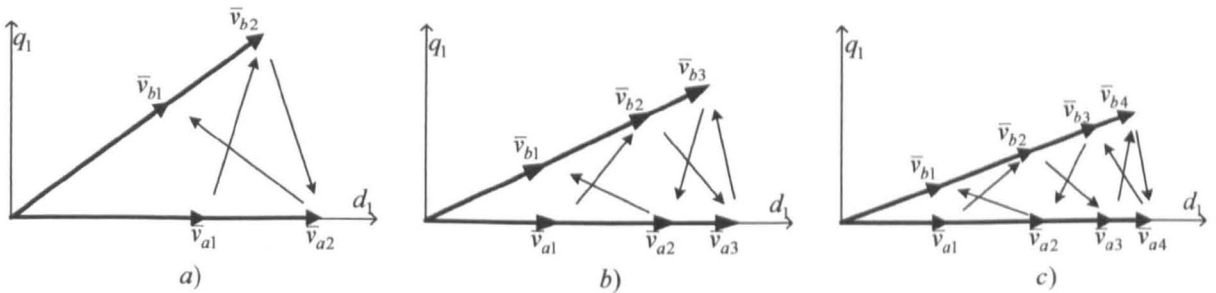
Fig. 5.18: Sequences of active space vectors during the first half of the switching period in the first sector for: a) five, b) seven, and c) nine-phase SVPWM.

113

The sequence is then reversed during the second half of the switching period between zero space vectors $\bar{v}_{2^n-1}$ and $\bar{v}_0$, thus being the mirror image of the sequence from the first half of the switching period. Although illustrations in Fig. 5.18 are for the first sector, the same applies to all the other odd sectors. With regard to the ordering of the active space vectors in the even sectors, by analysing switching patterns given earlier for each topology, it is easy to notice that the sequences of active space vectors in all even sectors are obtained by swapping the sequences of the first and the second half of the odd sector sequences. Thus, in all even sectors, during the first half of the switching period, the sequence is identical to the sequence in odd sectors applied during the second half of the switching period, and vice versa.

Based on these considerations, it is possible to generalise the set of expressions that yields the values of the final per-leg duty cycles. Thus, in all odd sectors of an n-phase SVPWM, per-leg duty cycles (n of them), in increasing order, can be calculated as:

$$\delta_1 = \frac{\delta_O}{2}$$

$$\begin{bmatrix} \delta_2^O \\ \delta_3^O \\ \delta_4^O \\ \vdots \\ \delta_{(n-1)/2+1}^O \\ \delta_{(n-1)/2+2}^O \\ \vdots \\ \delta_{n-2}^O \\ \delta_{n-1}^O \\ \delta_n \end{bmatrix} = \begin{bmatrix} 0 & 0 & 0 & \cdots & 0 & 0 & \cdots & 0 & 0 & 1 \\ 0 & 0 & 0 & \cdots & 0 & 0 & \cdots & 0 & 1 & 1 \\ 0 & 0 & 0 & \cdots & 0 & 0 & \cdots & 1 & 1 & 1 \\ \cdots & \cdots & \cdots & \cdots & \cdots & \cdots & \cdots & \cdots & \cdots & \cdots \\ 0 & 0 & 0 & \cdots & 0 & 1 & \cdots & 1 & 1 & 1 \\ 0 & 0 & 0 & \cdots & 1 & 1 & \cdots & 1 & 1 & 1 \\ \cdots & \cdots & \cdots & \cdots & \cdots & \cdots & \cdots & \cdots & \cdots & \cdots \\ 0 & 0 & 1 & \cdots & 1 & 1 & \cdots & 1 & 1 & 1 \\ 0 & 1 & 1 & \cdots & 1 & 1 & \cdots & 1 & 1 & 1 \\ 1 & 1 & 1 & \cdots & 1 & 1 & \cdots & 1 & 1 & 1 \end{bmatrix} \cdot \begin{bmatrix} \delta_{b1} \\ \delta_{a2} \\ \delta_{b3} \\ \vdots \\ \delta_{a(n-1)/2} \\ \delta_{b(n-1)/2} \\ \vdots \\ \delta_{a3} \\ \delta_{b2} \\ \delta_{a1} \end{bmatrix} + \delta_1 \qquad (5.29)$$

For even sectors, basically the same calculations can be applied, but this time with the reversed sequences of the duty cycles of active space vectors, in accordance with the reversed sequence of active space vectors. Therefore:

$$\delta_1 = \frac{\delta_O}{2}$$

$$\begin{bmatrix} \delta_2^E \\ \delta_3^E \\ \delta_4^E \\ \vdots \\ \delta_{(n-1)/2+1}^E \\ \delta_{(n-1)/2+2}^E \\ \vdots \\ \delta_{n-2}^E \\ \delta_{n-1}^E \\ \delta_n \end{bmatrix} = \begin{bmatrix} 0 & 0 & 0 & \cdots & 0 & 0 & \cdots & 0 & 0 & 1 \\ 0 & 0 & 0 & \cdots & 0 & 0 & \cdots & 0 & 1 & 1 \\ 0 & 0 & 0 & \cdots & 0 & 0 & \cdots & 1 & 1 & 1 \\ \cdots & \cdots & \cdots & \cdots & \cdots & \cdots & \cdots & \cdots & \cdots & \cdots \\ 0 & 0 & 0 & \cdots & 0 & 1 & \cdots & 1 & 1 & 1 \\ 0 & 0 & 0 & \cdots & 1 & 1 & \cdots & 1 & 1 & 1 \\ \cdots & \cdots & \cdots & \cdots & \cdots & \cdots & \cdots & \cdots & \cdots & \cdots \\ 0 & 0 & 1 & \cdots & 1 & 1 & \cdots & 1 & 1 & 1 \\ 0 & 1 & 1 & \cdots & 1 & 1 & \cdots & 1 & 1 & 1 \\ 1 & 1 & 1 & \cdots & 1 & 1 & \cdots & 1 & 1 & 1 \end{bmatrix} \cdot \begin{bmatrix} \delta_{a1} \\ \delta_{b2} \\ \delta_{a3} \\ \vdots \\ \delta_{b(n-1)/2} \\ \delta_{a(n-1)/2} \\ \vdots \\ \delta_{b3} \\ \delta_{a2} \\ \delta_{b1} \end{bmatrix} + \delta_1 \qquad (5.30)$$

It is visible from (5.29) and (5.30) that the smallest per-leg duty cycle (δ_1) corresponds to the application of the zero space vector $\bar{v}_{2^n-1}$ in the middle of the switching period, while the largest duty cycle (δ_n) is the result of summation of δ_1 and all the active space vector duty cycles.

Finally, once when per-leg duty cycles are calculated, they need to be distributed properly among inverter legs depending on the current sector. Distribution for the five-phase, seven-phase and nine-phase SVPWM has been summarised in Tables 4.2, 5.2, and 5.3, respectively. Based on these, it is possible to establish the pattern for duty cycle distribution. It is enough to consider situation with respect to the first inverter leg A. It can be observed that the first n sectors receive duty cycles in the order from the largest one to the smallest one, respecting the odd/even sector relations. Then, in the remaining n sectors, the order of duty cycles is reversed, and they are applied from the smallest one to the largest one, again respecting the odd/even sector relations. For all the other inverter legs, duty cycle disposition is obtained by simple shifting of the sequence of the previous leg by two sectors. Since sectors span π/n, this is effectively a shifting of $2\pi/n$ degrees, in accordance with the spatial shift of the machine's phase windings. Thus, disposition for leg B is obtained by shifting duty cycles of leg A by two sectors, leg C receives then resulting duty cycles of leg B shifted again by two sectors, and so on. In this way, duty cycle disposition for all n inverter legs in all $2n$ sectors is obtained. This is summarised for the general case in Table 5.4. It is easy to verify that Table 5.4 can be reduced to the previously given Tables 4.2, 5.2, and 5.3, by replacing the phase number n with the appropriate value.

Finally, general layout of an n-phase SVPWM modulator, which is in accordance with the DSP implementation used during experimental testing of the SVPWM schemes that have been presented in this chapter and chapter 4, is given in Fig. 5.19.

Table 5.4: Duty cycle disposition through sectors.

Leg | Sector	1	2	3	...	n	n+1	...	2n-2	2n-1	2n
A	δ_n	δ_{n-1}^E	δ_{n-2}^O	...	δ_1	δ_1	...	δ_{n-2}^E	δ_{n-1}^O	δ_n
B	δ_{n-1}^O	δ_n	δ_n	...	δ_3^O	δ_2^E	...	δ_{n-4}^E	δ_{n-3}^O	δ_{n-2}^E
C	δ_{n-3}^O	δ_{n-2}^E	δ_{n-1}^O	...	δ_5^O	δ_4^E	...	δ_{n-6}^E	δ_{n-5}^O	δ_{n-4}^E
⋮	⋮	⋮	⋮	...	⋮	⋮	...	⋮	⋮	⋮
(n+1)/2	δ_2^O	δ_3^E	δ_4^O	...	δ_n	δ_{n-1}^E	...	δ_2^E	δ_1	δ_1
⋮	⋮	⋮	⋮	...	⋮	⋮	...	⋮	⋮	⋮
n-2	δ_{n-6}^O	δ_{n-7}^E	δ_{n-8}^O	...	δ_6^O	δ_7^E	...	δ_{n-3}^E	δ_{n-4}^O	δ_{n-5}^E
n-1	δ_{n-4}^O	δ_{n-5}^E	δ_{n-6}^O	...	δ_4^O	δ_5^E	...	δ_{n-1}^E	δ_{n-2}^O	δ_{n-3}^E
n	δ_{n-2}^O	δ_{n-3}^E	δ_{n-4}^O	...	δ_2^O	δ_3^E	...	δ_n	δ_n	δ_{n-1}^E

In order to calculate per-leg duty cycles for the next switching period, during the current switching period, for a given reference space vector and the particular *n*-phase topology considered, at first sector *s* must be determined depending on the current position of the reference space vector. Once when the sector is determined, using current attributes of the reference space vector, duty cycles of *n*-1 active space vectors can be calculated based on (5.27). Duty cycles of the zero space vectors can be determined based on (5.28) and it is assumed here that the total zero vector duty cycle is equally shared between two zero space vectors. In a general case this distribution can be performed in some other manner and it represents the available degree of freedom that can be used to modify characteristics of the SVPWM scheme [Holmes (1996), Blasko (1997), Holmes and Lipo (2003)].

Calculated duty cycles are further summed in order to obtain the final per-leg duty cycles using (5.29) for odd sectors, and (5.30) for even sectors. Finally, calculated per-leg duty cycles are distributed to inverter legs (Table 5.4), based on the current sector value. These values are actually loaded in the corresponding 'compare' registers of the DSP PWM units, and are compared against up/down running counters/timers, before producing final PWM signals at the DSP output pins, which are further provided to the inputs of the IGBT drivers of the inverter.

It is important to note that, in order to implement multi-phase SVPWM schemes based on the proposed general structure of the modulator, the actual analysis of the space vectors of a multi-phase system in all characteristic planes can be omitted completely. The reason for this is related to the form of the generic solutions for duty cycles of the active space vectors which are based on the use of trigonometric constants. These constants are characteristic of each particular topology, and they embed proper dwell times for each active space vector. Thus, although developed SVPWM schemes are for different *n*-phase VSIs, their form is very similar and it allows for generalisation that can greatly speed up the implementation stage.
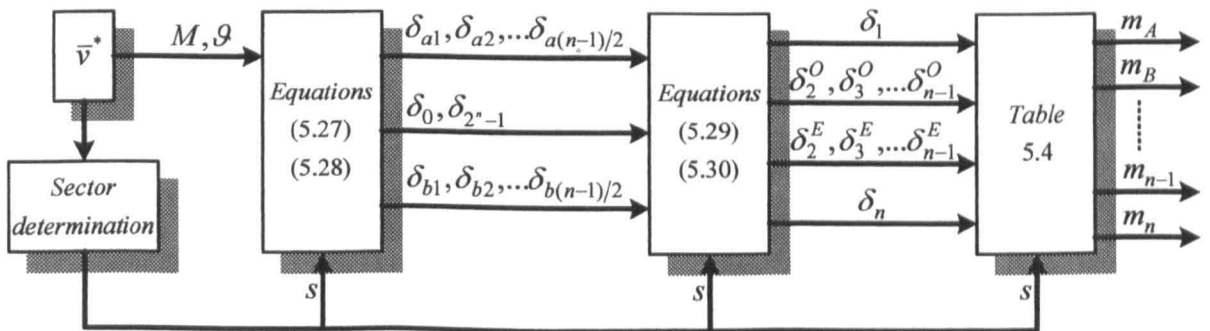
Fig. 5.19: General layout of an *n*-phase SVPWM modulator for sinusoidal output voltage generation.

A proof that this similarity is not accidental, will be given in the next chapter, where carrier-based PWM schemes are analysed. Feasibility of proposed generalisation is verified in chapter 10 for the case of three-phase SVPWM.

5.6 SUMMARY

SVPWM schemes for sinusoidal output voltage generation with seven-phase and nine-phase VSI are presented in this chapter. Similar to the five-phase case, the use of only two active space vectors does not yield sinusoidal output voltage and is accompanied with presence of low order harmonics, characteristic for planes other than the first one. Therefore, the number of used active space vector is increased and all the planes are considered during development. Thus, six active space vectors have been used for the seven-phase SVPWM, and eight for the nine-phase SVPWM. In both cases purely sinusoidal output voltage has been achieved. This is verified theoretically, by means of simulations, and experimentally, by conducting measurements on multi-phase star connected loads.

Theoretical developments enable generalisation of the implementation steps of the multi-phase SVPWM schemes aimed at sinusoidal output voltage generation. This is demonstrated by deriving a generic set of equations and steps that can be used for development of any *n*-phase SVPWM (*n* is an odd number). Validity of the proposed generalised structure of the multi-phase modulator will be confirmed by an analysis of the carrier-based schemes. This is presented in the next chapter.

Chapter 6

CARRIER-BASED PWM METHODS FOR MULTI-PHASE VOLTAGE SOURCE INVERTERS

6.1 INTRODUCTION

In this chapter, analysis of various carrier-based PWM techniques for the multi-phase VSIs is presented. In contrast to the SVPWM strategies, carrier-based PWM methods for multi-phase VSIs have been explored to a lesser extent in the past. A possible reason for this is the fact that the space vector theory, applied to multi-phase VSIs, offers a better insight into the harmonic elimination procedure, since the fundamental and various low order harmonic components are mapped into different planes. Thus, this approach has been the focus of much research, as shown by the survey in chapter 2. On the other hand, carrier-based PWM schemes, based on the comparison of a low frequency reference signal with a high-frequency carrier signal that generates a train of pulses, appear to be much simpler for implementation while being able to offer the same performance as the SVPWM [Zhou and Wang (2002)]. Thus, main characteristics of the carrier-based PWM methods for multi-phase VSIs are analysed in order to link them with the characteristics of the SVPWM schemes.

This chapter is organized as follows. In section 6.2, basic properties of carrier-based PWM schemes are elaborated by extending the well known three-phase carrier-based PWM principles to the multi-phase systems. A general layout of the carrier-based PWM modulator is presented and the significance of zero-sequence signal injection is explained. Section 6.3 deals with characteristics of the simple sinusoidal modulation, as applied in conjunction with five-phase, seven-phase and nine-phase VSIs. An extension of the well known harmonic injection principle for three-phase VSI is further applied to the above mentioned multi-phase topologies and this is elaborated in section 6.4. A different, offset-based, zero-sequence injection is discussed in section 6.5, and a clear connection with the previously analysed SVPWM strategies is thus established. Some experimental results are given in section 6.6, while the main differences between the carrier-based PWM and SVPWM with regard to the

DSP implementation are addressed in section 6.7. A summary of the chapter is given in section 6.8. The main original results of this chapter have been presented in Dujić et al (2007b) and Dujić et al (2007c).

6.2   CONTINUOUS CARRIER-BASED PWM – BASIC PROPERTIES

Carrier-based PWM techniques are the classical and most widely used methods of modulation for VSIs. Generalised structure of the carrier-based modulator including the zero-sequence signal calculator is shown in Fig. 6.1. Modulating signals are compared with the high frequency carrier signal and, as a result, switching signals are generated for each inverter leg. The principle can be easily explained considering one phase of the modulator. When the modulating signal is greater than the carrier signal, the modulator output takes the high value '1', which brings the upper switch in the inverter leg in the 'on' state. At the same time, corresponding lower switch goes in the 'off' state and the load at the output of this phase gets connected to the positive rail of the dc bus. Whenever the modulating signal is below the carrier signal, the inverse situation occurs regarding the switch states and the load gets connected to the negative rail of the dc bus. In digital implementation, the carrier signal is actually realised with the use of DSP counters/timers, as depicted in Fig. 6.1. Also, the explanation given above assumes a certain logic for polarity of the output signals, and is only for illustration purposes. Modern DSP PWM units allow for control of the polarity of generated PWM signals to be adjusted in accordance with the remaining electronics on the signal path to the IGBTs, so, for example, low value '0' at the DSP output pin may be needed to turn on the upper IGBT. Thus, by means of a simple comparison, switching functions, defined in chapter 3, are obtained for each of the inverter legs.

A universal representation of the modulating signals $v_k(t)$ for carrier-based modulators, based on Fig. 6.1, can be written as ($k = a$ to n):

$$v_k(t) = v_k^*(t) + v_{zs}(t) \tag{6.1}$$

where $v_{zs}(t)$ represents the zero-sequence signal, and $v_k^*(t)$ are the sinusoidal fundamental signals. In the case of an n-phase VSI, these fundamental signals are n sinusoidal signals displaced in time by $2\pi/n$ degrees, which, after scaling with $V_{dc}/2$, can be expressed as:

$$v_k^*(t) = M \cos(\vartheta - k\frac{2\pi}{n}) \tag{6.2}$$

Here $\vartheta = \omega t$, with $k = a$ to n when used as sub-script for fundamental signals, while on the right hand side (inside the bracket), $k = 0,1,2,\dots n\text{-}1$. Fundamental signals defined with (6.2)

are in the range (-1÷1) and, to make the comparison with the carrier signal possible, it is assumed that triangular carrier signal is also within the same range. The time dependence of signals (6.1) and (6.2) will be omitted further on for the sake of brevity.

Zero-sequence signal represents a degree of freedom that can be used to modify characteristics and design various PWM schemes [Holmes and Lipo (2003)]. This signal is usually determined based on the initial set of sinusoidal fundamental signals and an appropriate manipulation of them. In the three-phase PWM this was used to increase the dc bus utilisation [Buja and Indri (1975)], to improve the current ripple [van der Broeck and Skudelny (1988)] or to develop various generalised PWM schemes [Blasko (1997), Hava et al (1998a)]. Analysis of the carrier-based PWM schemes for multi-phase VSIs, presented in this chapter, is restricted only to CPWM schemes in the linear region, which are characterised by the constant presence of switching activities over the switching period. DPWM schemes are beyond the scope of the thesis. Thus, based on the different selections of the zero-sequence signal, three different carrier-based PWM schemes for multi-phase VSIs are analysed next. Sinusoidal PWM (SPWM), harmonic injection PWM (HIPWM) and offset (triangular) injection PWM (TIPWM) are adapted for multi-phase VSIs based on the three-phase PWM principles. The attention is paid to establishing the clear correlation between the main characteristics of the carrier-based PWM strategies and the SVPWM strategies, presented earlier. Therefore, the set of active space vectors activated by the carrier-based PWM schemes is analysed, as well as is the dc bus utilisation.
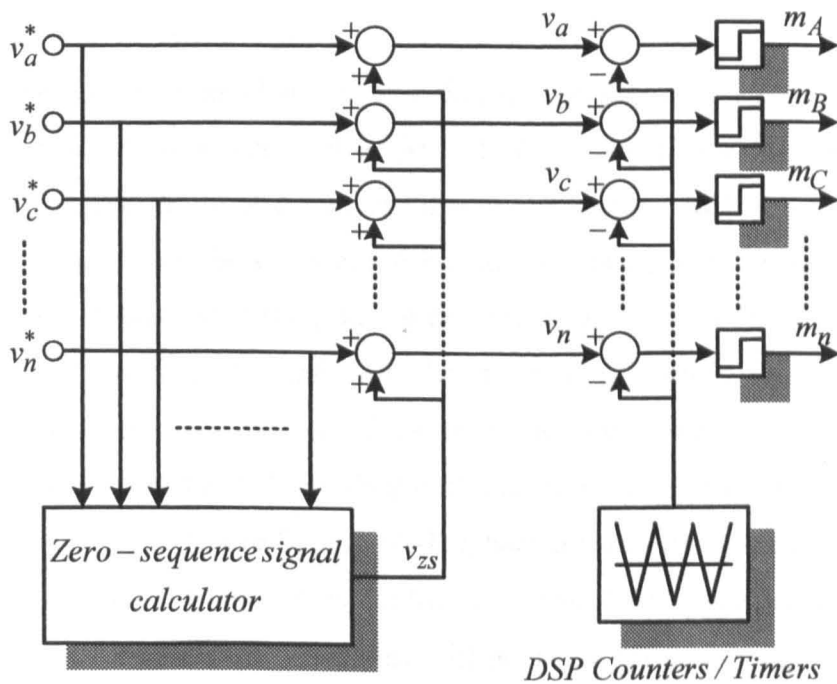

Fig. 6.1: Principle of carrier-based PWM.

6.3   SINUSOIDAL PWM – SPWM

According to the layout shown in Fig. 6.1, in order to obtain SPWM, the zero-sequence signal is selected as:

$$v_{zs} = 0 \tag{6.3}$$

The modulating signals for all *n*-phases are then equal to the sinusoidal fundamental signals (6.2). This is the simplest form of the carrier-based PWM scheme and its characteristics will be investigated for the five-phase, seven-phase and nine-phase VSIs. Same notions introduced earlier, such as duty cycles and definition of the modulation index, are used throughout this chapter, in order to ease the comparison of the results with those previously obtained for the SVPWM schemes.

6.3.1   FIVE-PHASE SPWM

On the basis of (6.1)-(6.3) the modulating signals are equal to the sinusoidal fundamental signals,

$$v_a = v_a^* = M\cos(\vartheta)$$

$$v_b = v_b^* = M\cos(\vartheta - 2\frac{\pi}{5})$$

$$v_c = v_c^* = M\cos(\vartheta - 4\frac{\pi}{5}) \tag{6.4}$$

$$v_d = v_d^* = M\cos(\vartheta + 4\frac{\pi}{5})$$

$$v_e = v_e^* = M\cos(\vartheta + 2\frac{\pi}{5})$$

Modulating signals of (6.4) are shown in Fig. 6.2, for one period of the fundamental and for the value of the modulation index set as $M = 1$. It is easy to see that the period of the fundamental signal can be divided into ten distinctive sectors, each spanning $\pi/5$ degrees. Classification of the sectors shown in Fig. 6.2 is in accordance with ten sectors identified in the d_1-q_1 plane of a five-phase system during development of the SVPWM. It is important to notice that in each sector, the order of the modulating signals with respect to their instantaneous values does not change. Thus, over the whole first sector, the sequence of modulating signals, organized in descending order, is: v_a, v_b, v_e, v_c, v_d. This is summarised for all ten sectors in Table 6.1, where fundamental signals are actually given since they are equal to the modulating signals for the SPWM. At the same time, in every sector, minimal, medium and maximal signal are identified, since they will be useful for analysis given later on in the chapter.
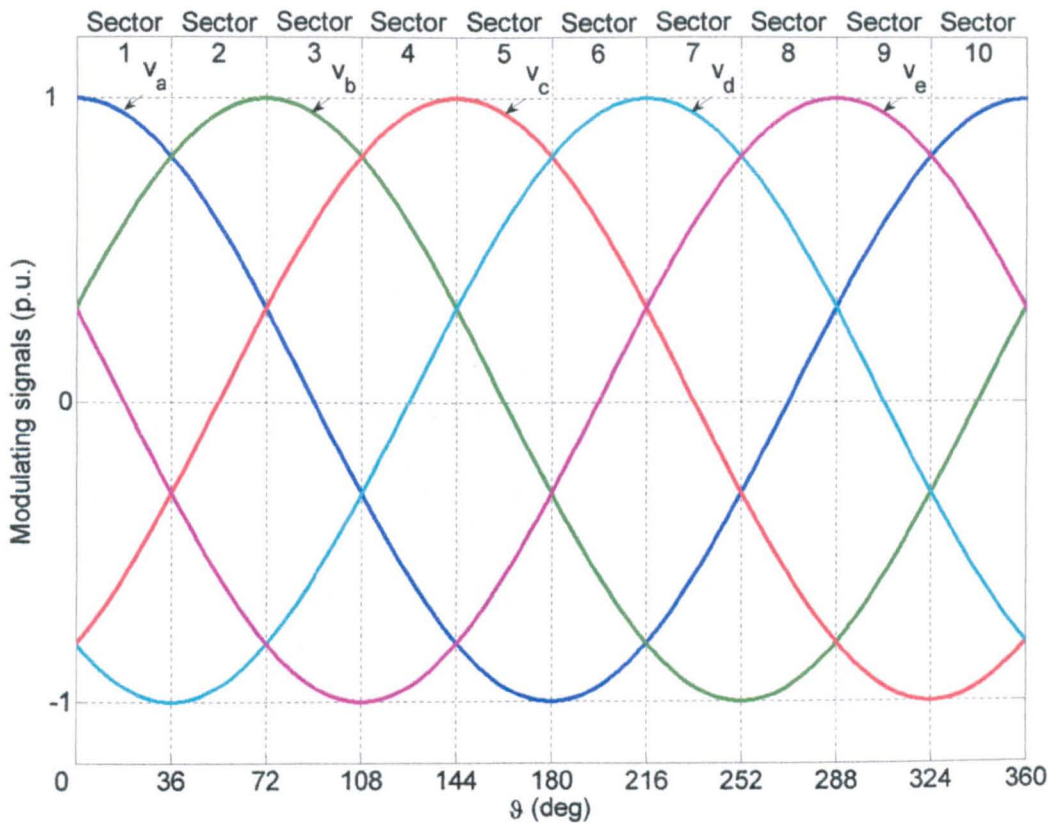
Fig. 6.2: Modulating signals of the five-phase SPWM.

Since the frequency of the carrier signal is much higher than the frequency of the modulating signals, values of modulating signals can be regarded as being constant over the period of the carrier signal (regular sampled PWM). Similar to the analysis presented during development of the SVPWM schemes, it is enough to consider the situation with respect to the first sector only. Such a situation is shown in Fig. 6.3 (not to scale), where all five modulating signals are shown together with one period of the triangular carrier signal. In the lower part of Fig. 6.3, generated switching pattern (switching functions) is shown, obtained by means of comparison of the modulating signals with the carrier signal. Period of the carrier defines switching period (T_s) and corresponds to the unity duty cycle. It is simple to establish that activated space vectors within the switching period are the same as those selected for the SVPWM, based on the use of two medium and two large active space vectors (Fig. 4.9).

Table 6.1: The order of the fundamental signals through sectors.

Order | Sector	1	2	3	4	5	6	7	8	9	10
v_{max}^*	v_a^*	v_b^*	v_b^*	v_c^*	v_c^*	v_d^*	v_d^*	v_e^*	v_e^*	v_a^*
⋮	v_b^*	v_a^*	v_c^*	v_b^*	v_d^*	v_c^*	v_e^*	v_d^*	v_a^*	v_e^*
v_{mid}^*	v_e^*	v_c^*	v_a^*	v_d^*	v_b^*	v_e^*	v_c^*	v_a^*	v_d^*	v_b^*
⋮	v_c^*	v_e^*	v_d^*	v_a^*	v_e^*	v_b^*	v_a^*	v_c^*	v_b^*	v_d^*
v_{min}^*	v_d^*	v_d^*	v_e^*	v_e^*	v_a^*	v_a^*	v_b^*	v_b^*	v_c^*	v_c^*
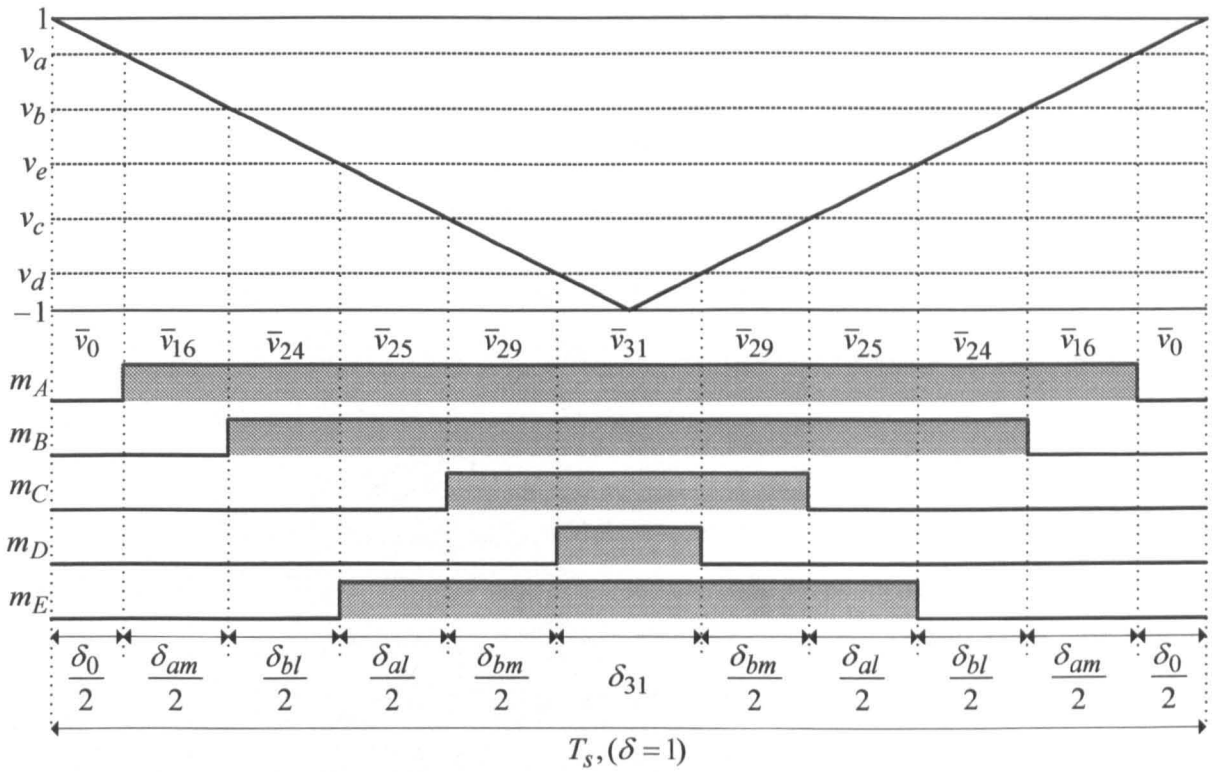
Fig. 6.3: Principle of generation of the switching pattern for a five-phase SPWM.

At first, duty cycle for each of the inverter legs can be obtained (shaded parts in Fig. 6.3). They correspond to per-leg duty cycles of the SVPWM, calculated with (4.22). Based on Fig. 6.3, these can be obtained by means of simple trigonometry. Duty cycle of each of the inverter legs can be expressed as:

$$
\begin{aligned}
\delta_A &= \frac{1}{2}[1+v_a] = \frac{1}{2}[1+M\cos(\vartheta)] \\
\delta_B &= \frac{1}{2}[1+v_b] = \frac{1}{2}[1+M\cos(\vartheta-2\frac{\pi}{5})] \\
\delta_C &= \frac{1}{2}[1+v_c] = \frac{1}{2}[1+M\cos(\vartheta-4\frac{\pi}{5})] \\
\delta_D &= \frac{1}{2}[1+v_d] = \frac{1}{2}[1+M\cos(\vartheta+4\frac{\pi}{5})] \\
\delta_E &= \frac{1}{2}[1+v_e] = \frac{1}{2}[1+M\cos(\vartheta+2\frac{\pi}{5})]
\end{aligned}
\tag{6.5}
$$

It is further possible to determine duty cycles of each space vector activated by the carrier-based PWM. One finds from Fig. 6.3 that simple subtraction of appropriate per-leg duty cycles yields:

$$
\begin{aligned}
\delta_0 &= 1 - \delta_A \\
\delta_{am} &= \delta_A - \delta_B \\
\delta_{bl} &= \delta_B - \delta_E \\
\delta_{al} &= \delta_E - \delta_C \\
\delta_{bm} &= \delta_C - \delta_D \\
\delta_{31} &= \delta_D
\end{aligned}
\tag{6.6}
$$

123

By substituting (6.5) into (6.6), duty cycles of space vectors in the first sector are determined as:

$$\delta_{am} = KM\sin(\frac{\pi}{5} - \vartheta); \qquad \delta_{bm} = KM\sin(\vartheta)$$

$$\delta_{al} = K_2M\sin(\frac{\pi}{5} - \vartheta); \qquad \delta_{bl} = K_2M\sin(\vartheta) \tag{6.7}$$

$$\delta_0 = \frac{1}{2}[1 - M\cos(\vartheta)]; \qquad \delta_{31} = \frac{1}{2}[1 + M\cos(\vartheta + 4\frac{\pi}{5})]$$

Trigonometric constants, defined with (3.13), are used again to simplify the appearance of the solution. Comparing (6.7) with (4.19), obtained for the SVPWM, it can be seen that duty cycles obtained for active space vectors are exactly the same. Thus, while in the SVPWM approach it was necessary to consider positions of the active space vectors in both planes in order to determine duty cycles that provide zero average value in the second plane, this is naturally achieved by the carrier-based PWM. It means that SPWM will yield zero average voltage value in the second plane over the switching period since the same result is obtained for the active space vector duty cycles. This means that total duty cycle of the zero space vectors is also the same. However, it can be seen from (6.7) that SPWM does not share this total duty cycle equally among two zero space vectors. The corresponding duty cycles are different and they differ from the zero vector duty cycles of the SVPWM, given with (4.19). Effects of this on output current ripple will be investigated in chapters 7 and 8.

The principle demonstrated in Fig. 6.1 is based on the three-phase carrier-based PWM and is extended to multi-phase case by a simple addition of more inputs/outputs. In the context of this chapter, where analysis has been narrowed to PWM schemes that yield sinusoidal output voltage, use of such a layout is completely valid, since fundamental component of the output voltage is always mapped into the first plane. However, as explained in chapter 3, an *n*-phase system must be analysed in (*n*-1)/2 2-D planes. Thus, development of the SVPWM schemes for *n*-phase VSIs had to deal with (*n*-1)/2 reference space vectors (one in each plane). If sinusoidal output voltage is to be generated, this is achieved by proper selection of active space vectors and by setting the references to zero in all planes other than the first one. Translated into language of the carrier-based PWM, an *n*-phase carrier-based PWM must consider (*n*-1)/2 sets of references (fundamental sinusoidal signals), where each set corresponds to one particular plane. Since references in all planes other than the first one are zero, for sinusoidal output voltage generation, this is implicitly accounted for in Fig. 6.1.

Main characteristics of a seven-phase and nine-phase SPWM are briefly addressed next, based on the analysis given for the five-phase SPWM.

6.3.2 SEVEN-PHASE SPWM

The main characteristics of seven-phase SPWM can be determined in the same way as for the five-phase SPWM. Due to the selection of zero-sequence signal (6.3), modulating signals are equal to seven fundamental sinusoidal signals defined with (6.2). These can be analysed graphically (similar to Fig. 6.2), from where the ordering of magnitude of modulating signals over every sector can be identified. This is summarised in Table 6.2 for all fourteen sectors. Restricting the analysis to the first sector, and considering only one period of the carrier signal, one has the situation shown in Fig. 6.4. The sequence of the space vectors activated by seven-phase SPWM is identical to the sequence selected for the seven-phase SVPWM when six active space vectors are used. Again, simple trigonometry yields the relation of the per-leg duty cycles and the modulating signals:

$$\delta_A = \frac{1}{2}[1+v_a]; \quad \delta_B = \frac{1}{2}[1+v_b]; \quad \ldots \quad \delta_G = \frac{1}{2}[1+v_g] \tag{6.8}$$

Duty cycles of each space vector in the first sector are obtained from Fig. 6.4, by means of subtraction of corresponding per-leg duty cycles, as:

$$
\begin{aligned}
\delta_{a4} &= \delta_A - \delta_B; & \delta_{b4} &= \delta_D - \delta_E \\
\delta_{a7} &= \delta_F - \delta_D; & \delta_{b7} &= \delta_B - \delta_G \\
\delta_{a8} &= \delta_G - \delta_C; & \delta_{b8} &= \delta_C - \delta_F \\
\delta_0 &= 1 - \delta_A; & \delta_{127} &= \delta_E
\end{aligned}
\tag{6.9}
$$

Finally, (6.9) can be expressed in a more suitable form for analysis, as:

$$
\begin{aligned}
\delta_{a4} &= KM \sin(\frac{\pi}{7} - \vartheta); & \delta_{b4} &= KM \sin(\vartheta) \\[6pt]
\delta_{a7} &= K_2 M \sin(\frac{\pi}{7} - \vartheta); & \delta_{b7} &= K_2 M \sin(\vartheta) \\[6pt]
\delta_{a8} &= K_3 M \sin(\frac{\pi}{7} - \vartheta); & \delta_{b8} &= K_3 M \sin(\vartheta) \\[6pt]
\delta_0 &= \frac{1}{2}[1 - M \cos(\vartheta)]; & \delta_{127} &= \frac{1}{2}[1 + M \cos(\vartheta + 6\frac{\pi}{7})]
\end{aligned}
\tag{6.10}
$$

Table 6.2: The order of the fundamental signals through sectors.

Order | Sector	1	2	3	4	5	6	7	8	9	10	11	12	13	14
v^*_{max}	v^*_a	v^*_b	v^*_b	v^*_c	v^*_c	v^*_d	v^*_d	v^*_e	v^*_e	v^*_f	v^*_f	v^*_g	v^*_g	v^*_a
$\vdots$	v^*_b	v^*_a	v^*_c	v^*_b	v^*_d	v^*_c	v^*_e	v^*_d	v^*_f	v^*_e	v^*_g	v^*_f	v^*_a	v^*_g
$\vdots$	v^*_g	v^*_c	v^*_a	v^*_d	v^*_b	v^*_e	v^*_c	v^*_f	v^*_d	v^*_g	v^*_e	v^*_a	v^*_f	v^*_b
v^*_{mid}	v^*_c	v^*_g	v^*_d	v^*_a	v^*_e	v^*_b	v^*_f	v^*_c	v^*_g	v^*_d	v^*_a	v^*_e	v^*_b	v^*_f
$\vdots$	v^*_f	v^*_d	v^*_g	v^*_e	v^*_a	v^*_f	v^*_b	v^*_g	v^*_c	v^*_a	v^*_d	v^*_b	v^*_e	v^*_c
$\vdots$	v^*_d	v^*_f	v^*_e	v^*_g	v^*_f	v^*_a	v^*_g	v^*_b	v^*_a	v^*_c	v^*_b	v^*_d	v^*_c	v^*_e
v^*_{min}	v^*_e	v^*_e	v^*_f	v^*_f	v^*_g	v^*_g	v^*_a	v^*_a	v^*_b	v^*_b	v^*_c	v^*_c	v^*_d	v^*_d
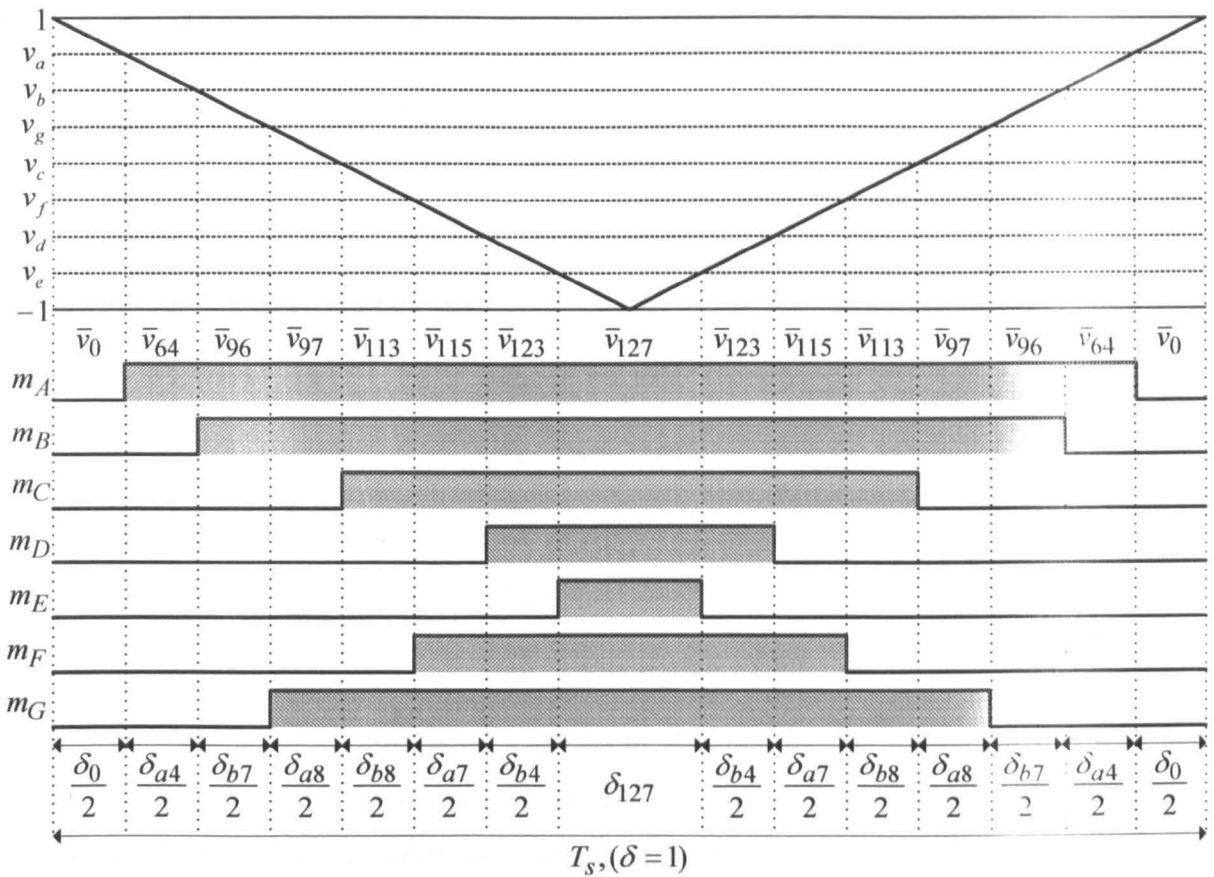
Fig. 6.4: Principle of generation of the switching pattern for seven-phase SPWM.

By analysing (6.10), one finds again that the duty cycles of the active space vectors, in the first sector, are identical to those of (5.11), obtained for the SVPWM. However, as in the five-phase case, distribution of the total duty cycle of zero space vectors is now different and is not governed with equal distribution among two zero space vectors. This impacts on the output current ripple characteristics of the seven-phase SPWM, but not on the synthesis of the sinusoidal output voltage, since duty cycles of active space vectors will zero the average voltage in the d_2-q_2 and d_3-q_3 planes. Thus, seven-phase SPWM naturally applies six active space vectors, which are the same as those selected for the SVPWM.

6.3.3 NINE-PHASE SPWM

Modulating signals are now equal to nine fundamental reference signals defined with (6.2). The ordering of the magnitudes of these signals, over all eighteen sectors, is summarized in Table 6.3. Considering again only the first sector, plots similar to those presented in Fig. 6.3 and Fig. 6.4 can be obtained, from where per-leg duty cycles can be determined as:

$$\delta_A = \frac{1}{2}[1+v_a]; \quad \delta_B = \frac{1}{2}[1+v_b]; \ . \ . \ . \ \delta_I = \frac{1}{2}[1+v_i] \tag{6.11}$$

126

Further on, duty cycles of each space vector in the first sector are determined with:

$$
\begin{aligned}
\delta_{a6} &= \delta_A - \delta_B; & \delta_{b6} &= \delta_E - \delta_F \\
\delta_{a12} &= \delta_G - \delta_E; & \delta_{b12} &= \delta_B - \delta_I \\
\delta_{a15} &= \delta_I - \delta_C; & \delta_{b15} &= \delta_D - \delta_G \\
\delta_{a16} &= \delta_H - \delta_D; & \delta_{b16} &= \delta_C - \delta_H \\
\delta_0 &= 1 - \delta_A; & \delta_{s11} &= \delta_F
\end{aligned}
\tag{6.12}
$$

Finally, (6.12) can be developed into:

$$
\begin{aligned}
\delta_{a6} &= KM \sin(\tfrac{\pi}{9} - \vartheta); & \delta_{b6} &= KM \sin(\vartheta) \\[2mm]
\delta_{a12} &= K_2 M \sin(\tfrac{\pi}{9} - \vartheta); & \delta_{b12} &= K_2 M \sin(\vartheta) \\[2mm]
\delta_{a15} &= K_3 M \sin(\tfrac{\pi}{9} - \vartheta); & \delta_{b15} &= K_3 M \sin(\vartheta) \\[2mm]
\delta_{a16} &= K_4 M \sin(\tfrac{\pi}{9} - \vartheta); & \delta_{b16} &= K_4 M \sin(\vartheta) \\[2mm]
\delta_0 &= \tfrac{1}{2}[1 - M \cos(\vartheta)]; & \delta_{s11} &= \tfrac{1}{2}[1 + M \cos(\vartheta + 8\tfrac{\pi}{9})]
\end{aligned}
\tag{6.13}
$$

Once again, this is exactly the same as the result obtained for the nine-phase SVPWM, with the exception of the duty cycles of two zero space vectors. They are with different distribution, which is not equal to the one selected for the nine-phase SVPWM. Thus, nine-phase SPWM selects naturally the set of eight active space vectors, by means of comparison with the carrier signal. This is in contrast to the nine-phase SVPWM, where tedious analysis of a large number of space vectors in four planes must be performed. The only difference is related to the distribution of duty cycles of zero space vectors, which is now different than with the SVPWM scheme.

Based on the theoretical results presented so far, some common characteristics of a multi-phase SPWM are addressed next.

Table 6.3: The order of the fundamental signals through sectors.

Order | Sector	1	2	3	4	5	6	7	8	9	10	11	12	13	14	15	16	17	18
v_{max}^*	v_a^*	v_b^*	v_b^*	v_c^*	v_c^*	v_d^*	v_d^*	v_e^*	v_e^*	v_f^*	v_f^*	v_g^*	v_g^*	v_h^*	v_h^*	v_i^*	v_i^*	v_a^*
$\vdots$	v_b^*	v_a^*	v_c^*	v_b^*	v_d^*	v_c^*	v_e^*	v_d^*	v_f^*	v_e^*	v_g^*	v_f^*	v_h^*	v_g^*	v_i^*	v_h^*	v_a^*	v_i^*
$\vdots$	v_i^*	v_c^*	v_a^*	v_d^*	v_b^*	v_e^*	v_c^*	v_f^*	v_d^*	v_g^*	v_e^*	v_h^*	v_f^*	v_i^*	v_g^*	v_a^*	v_h^*	v_b^*
$\vdots$	v_c^*	v_i^*	v_d^*	v_a^*	v_e^*	v_b^*	v_f^*	v_c^*	v_g^*	v_d^*	v_h^*	v_e^*	v_i^*	v_f^*	v_a^*	v_g^*	v_b^*	v_h^*
v_{mid}^*	v_h^*	v_d^*	v_i^*	v_e^*	v_a^*	v_f^*	v_b^*	v_g^*	v_c^*	v_h^*	v_d^*	v_i^*	v_e^*	v_a^*	v_f^*	v_b^*	v_g^*	v_c^*
$\vdots$	v_d^*	v_h^*	v_e^*	v_i^*	v_f^*	v_a^*	v_g^*	v_b^*	v_h^*	v_c^*	v_i^*	v_d^*	v_a^*	v_e^*	v_b^*	v_f^*	v_c^*	v_g^*
$\vdots$	v_g^*	v_e^*	v_h^*	v_f^*	v_i^*	v_g^*	v_a^*	v_h^*	v_b^*	v_i^*	v_c^*	v_a^*	v_d^*	v_b^*	v_e^*	v_c^*	v_f^*	v_d^*
$\vdots$	v_e^*	v_g^*	v_f^*	v_h^*	v_g^*	v_i^*	v_h^*	v_a^*	v_i^*	v_b^*	v_a^*	v_c^*	v_b^*	v_d^*	v_c^*	v_e^*	v_d^*	v_f^*
v_{min}^*	v_f^*	v_f^*	v_g^*	v_g^*	v_h^*	v_h^*	v_i^*	v_i^*	v_a^*	v_a^*	v_b^*	v_b^*	v_c^*	v_c^*	v_d^*	v_d^*	v_e^*	v_e^*

6.3.4 MULTI-PHASE SPWM – COMMON PROPERTIES

It is easy to establish that, common to all SPWM schemes regardless of the phase number, is the maximum achievable value of the modulation index [Holmes and Lipo (2003)]. All SPWM schemes are characterised with maximum value of the modulation index of:

$$M_{SPWM} = 1 \tag{6.14}$$

Any further increase of the modulation index will push the peaks of the modulating signals above the carrier signal and overmodulation will occur (clamping over the carrier period in some inverter legs). This poor dc bus utilisation is a reason why zero-sequence signal injection is introduced in three-phase carrier-based modulators, with the aim to extend the operation in the linear region [Holmes and Lipo (2003)].

What is important to emphasise here is that SPWM scheme for an n-phase VSI naturally selects n-1 active space vectors per switching period. This is so because comparison of n modulating signals with the triangular carrier signal happens sequentially, bringing the legs of the inverter one-by-one to the upper rail of dc bus during the first half of the switching period (the first half of the carrier period). Thus, n-1 active space vectors are activated, in between two zero space vectors that correspond to all n inverter legs being connected to the lower/upper dc bus rail, respectively. Mutual relation of fundamental signals provides no change in ordering of magnitudes over the sectors that are identified as being the same as those for the SVPWM. This is the same situation as the one obtained with the SVPWM, thus resulting in an n-phase load being in all possible load configurations. Based on the analytical results presented, these active space vectors are applied with such times of applications (duty cycles) that provide automatically zero average voltage in all the planes other than the first one. Duty cycles are now obtained from the set of fundamental sinusoidal signals that are firmly defined, and thus embed proper dwell times for activated different space vectors that are again expressed based on trigonometric constants (3.13). Thus, generalisation presented in section 5.5 for calculation of duty cycles of the space vectors is completely valid.

The main difference, as emphasised already, is distribution of the duty cycles of the zero space vectors. Distribution, adopted for the analysed SVPWM schemes, represents classical choice of equal sharing of the total zero space vector duty cycle between two zero space vectors [Holmes and Lipo (2003)]. This, however, is just a special case of utilisation of the available degree of freedom, since an endless number of different distributions can be realised by introducing a new control variable into the modulation scheme, which is

responsible for control of distribution of the total duty cycle of zero space vectors [Holmes (1996), Blasko (1997), Hava et al (1998a)]. On the other hand, SPWM yields a certain distribution that uniquely characterises the modulation scheme. Effects of this are analysed in the thesis only from the point of view of the impact on the inverter output current ripple and are presented in chapters 7 and 8 for multi-phase drives.

Poor utilisation of the available dc bus is the main drawback of all SPWM schemes. In three-phase drives, this problem is solved by injection of the third harmonic into modulating signals, thus making them of flat-top form, which allows for further increase of the fundamental above the carrier, without entering into overmodulation. The same principle is adopted here and presented next for multi-phase VSIs.

6.4 HARMONIC INJECTION PWM – HIPWM

It is well known that injection of the third harmonic can be used to extend linear region of operation of three-phase carrier-based modulators [Holmes and Lipo (2003)]. This leads at the same time to optimisation of the current ripple value and the reduction of the switching harmonic losses in three-phase drives [van der Broeck and Skudelny (1988), Kolar et al (1991b)]. It has been reported that injection of the third harmonic with level $b = -1/4$ (b is defined in (6.15)) is the optimal solution regarding the optimisation of the current ripple (although with slightly lower dc bus utilisation), while the injection of the third harmonic with level $b = -1/6$ maximises the dc bus utilisation (although it yields slightly higher current ripple (harmonic current rms) value) [Holmes and Lipo (2003)]. In this section, injection is performed with the aim to maximise dc bus utilisation, while the possibilities for optimisation of current ripple are analysed in the next two chapters.

Based on the work of Iqbal et al (2006a), general concept of injection of the n-th harmonic into an n-phase system can be established. Thus, the zero-sequence signal that yields the injection of the n-th harmonic into an n-phase system is of the form:

$$v_{zs} = bM \cos(n\vartheta) \qquad (6.15)$$

Parameter b defines the relative amount of the n-th harmonic with respect to the fundamental:

$$b = M_n/M \qquad (6.16)$$

To determine the amount of injection that maximises dc bus utilisation, it is enough to consider situation with respect to the modulating signal of phase 'a'. After injection of (6.16), the resulting modulating signal is defined with:

$$v_a = M \cos(\vartheta) + bM \cos(n\vartheta) \qquad (6.17)$$

In order to extend linear region of modulation, injection must make it possible for the modulation index to go above unity value. Fundamental signal, defined based on the cosine function, has the peak values at $\vartheta = l\pi$ ($l = 0,1,2,...$). To obtain extension of the linear region, the n-th harmonic has to re-position the peak values of the modulating signal. The n-th harmonic is with zero values at instants when $\vartheta = (2l+1)\pi/2n$ ($l = 0,1,2,...$) and does not have an impact on the fundamental signals after injection. However, if phase of the n-th harmonic is properly selected, it can lower the existing peak of the fundamental signal at instants $\vartheta = l\pi$ ($l = 0,1,2,...$) and create two new peaks at instants defined with $\vartheta = l\pi \pm (2l+1)\pi/2n$ ($l = 0,1,2,...$). If $l = 0$ is selected, as an illustration, one finds that new peak value (the one for positive sign) is shifted from $\vartheta = 0$ to $\vartheta = \pi/2n$. To find the optimal amount of injection that will maximise dc bus utilisation, one needs to find a maximum for the function defined as the modulating signal (6.17):

$$\frac{dv_a}{d\vartheta} = \frac{d[M\cos(\vartheta) + bM\cos(n\vartheta)]}{d\vartheta} = 0 \tag{6.18}$$

The solution is obtained in the form:

$$b = -\frac{\sin(\vartheta)}{n\sin(n\vartheta)} \tag{6.19}$$

Substituting condition $\vartheta = \pi/2n$, where new peak appears, yields the optimal amount of injection as:

$$b = -\frac{\sin(\pi/2n)}{n} \tag{6.20}$$

It is visible that the n-th harmonic is of opposite phase ($180°$ phase shift) with respect to the fundamental. Further, it is possible to find the new maximum value of the peak magnitude of the fundamental signal. If the modulator is to stay in the linear region of operation, then for the amount of injection defined with (6.20), when the value of the modulating signal reaches carrier maximum value, the following holds true:

$$v_a(\vartheta = \pi/2n) = M\cos(\vartheta) + bM\cos(n\vartheta) = 1 \tag{6.21}$$

Solving (6.21) for $\vartheta = \pi/2n$ and substituting (6.20), yields maximum achievable value as:

$$M_{HIPWM}(n) = \frac{1}{\cos(\pi/2n)} \tag{6.22}$$

Using relationship $\cos(\pi/2n) = \sin((n-1)\pi/2n) = K_{(n-1)/2}$ (valid for all n) one finds that the dc bus utilisation characteristic for the carrier-based HIPWM is the same as for the n-phase SVPWM, which applies n-1 active space vector per switching period, given with (5.26). Table 6.4 summarizes values of (6.22) and (6.20) for the harmonic phase numbers up to fifteen.

To demonstrate the effects of injection of the *n*-th harmonic into an *n*-phase system, Fig. 6.5 shows the characteristic signals, obtained by means of simulation, for the five-phase and seven-phase carrier-based HIPWM, respectively. In both cases modulation index and the level of injection are in accordance with Table 6.4. It can be seen from Fig. 6.5 that injection allows for the peak value of the fundamental signal to exceed unity value, up to the value when the peak of the modulating signal reaches saturation level (±1 in this case). Decrease in the dc bus utilisation that comes with the increase of the number of phases can be explained in a simple manner, graphically from Fig. 6.5. As already established, new peak values, after injection, appear for $\vartheta = l\pi \pm (2l+1)\pi/2n$, ($l = 0,1,2,...$). Considering the case for $l = 0$, for illustration, the peak value that was before injection at $\vartheta = 0$, is now replaced with new peak located at $\vartheta = \pi/2n$, as noted in Fig 6.5. With an increase of the phase number *n*, new peak value positions, defined with $\vartheta = \pi/2n$, appear closer to $\vartheta = 0$, leaving less room for the fundamental signal (and modulation index at the same time) to go above the unity value. Thus, dc bus utilisation rapidly approaches level of the SPWM as the number of phases increases.

It is important to note that injection of the zero-sequence signal does not change ordering of the magnitudes of modulating signals over the sectors (Tables 6.1-6.3), since the same signal is added to the fundamental signals. Thus, it is simple to verify that duty cycles of the active space vectors are the same as for the SPWM, since in calculations (6.7), (6.10) and (6.13) the zero-sequence signal gets cancelled. Therefore, all the expressions given so far remain valid and attention needs to be paid only to the distribution of duty cycles of zero space vectors, which is now different.
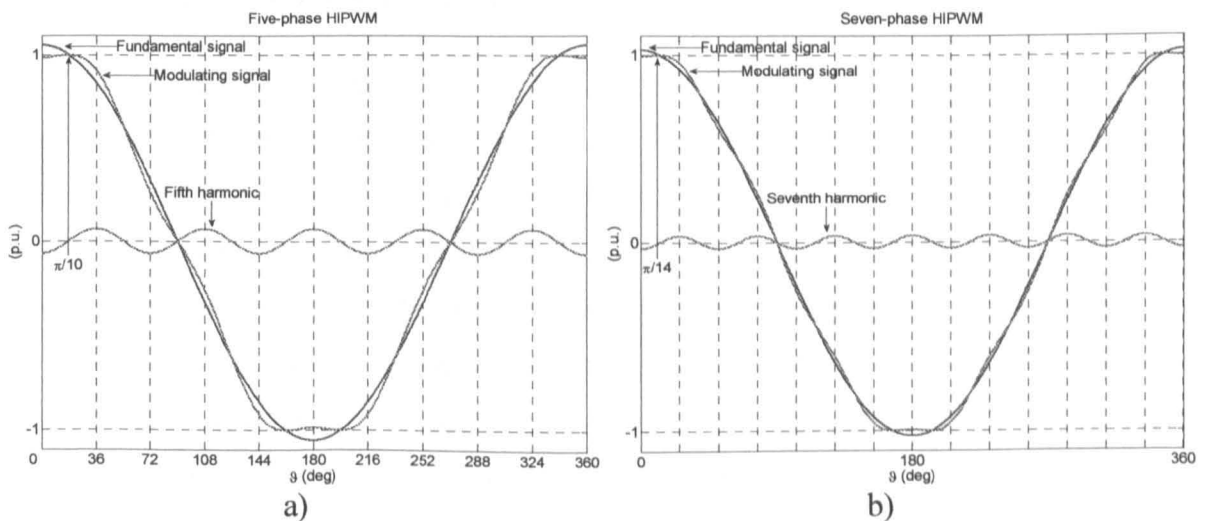
Fig. 6.5: Characteristic signals of the a) five-phase and, b) seven-phase HIPWM.

Table 6.4: Dc bus utilisation of HIPWM and the level of injection as functions of the phase number.

n	3	5	7	9	11	13	15
M_{HIPWM}	1.1547	1.0515	1.0257	1.0154	1.0103	1.0073	1.0055
$|b|$	0.1667	0.0618	0.0318	0.0193	0.0129	0.0093	0.0070

Duty cycles of zero space vectors, defined as $\delta_0 = 1 - \delta_A$ and $\delta_{31} = \delta_D$ in (6.6) for the first sector, given together with duty cycles of active space vectors in the case of five-phase HIPWM, are of the form:

$$\delta_{am} = KM \sin(\frac{\pi}{5} - \vartheta); \qquad \delta_{bm} = KM \sin(\vartheta)$$

$$\delta_{al} = K_2 M \sin(\frac{\pi}{5} - \vartheta); \qquad \delta_{bl} = K_2 M \sin(\vartheta) \qquad (6.23)$$

$$\delta_0 = \frac{1}{2}[1 - M \cos(\vartheta) - bM \cos(5\vartheta)]; \qquad \delta_{31} = \frac{1}{2}[1 + M \cos(\vartheta + 4\frac{\pi}{5}) + bM \cos(5\vartheta)]$$

Similar is obtained for the seven-phase and nine-phase HIPWM. Duty cycles of active space vectors are again identical to those obtained for the SPWM. However, duty cycles of zero space vectors are for the seven-phase HIPWM:

$$\delta_0 = \frac{1}{2}[1 - M \cos(\vartheta) - bM \cos(7\vartheta)]; \qquad \delta_{127} = \frac{1}{2}[1 + M \cos(\vartheta + 6\frac{\pi}{7}) + bM \cos(\text{-} \vartheta)] \qquad (6.24)$$

while for the nine-phase HIPWM they are:

$$\delta_0 = \frac{1}{2}[1 - M \cos(\vartheta) - bM \cos(9\vartheta)]; \qquad \delta_{511} = \frac{1}{2}[1 + M \cos(\vartheta + 8\frac{\pi}{9}) + bM \cos(9\vartheta)] \qquad (6.25)$$

The effects of this distribution of duty cycles of zero space vectors will be analysed in the next two chapters.

6.5 OFFSET (TRIANGULAR) INJECTION PWM – TIPWM

Previous two selections of the zero-sequence signal are basically performed without the use of 'zero-sequence calculator' from Fig. 6.1. While SPWM does not use any injection, HIPWM injects the n-th harmonic which is in a synchronised relation to the set of fundamental signals. A different injection, based on the consideration of the values of the fundamental signals, has been reported for the three-phase VSI by King (1974) and realised with an analogue circuit at the time. This involved the use of three-phase diode rectifier to collect envelopes (minimum and maximum values) of the modulating signals, which where then summed and scaled, before adding (injecting) to the fundamental signals. It led to an increase in dc bus utilisation of around 15.47%, compared to the SPWM. The method re-appeared in literature later in digital realisation utilising space vector theory and it is known

nowadays as SVPWM [van der Broeck et al (1988)]. However, as long as the carrier-based PWM is considered, the same zero-sequence signal is valid for the multi-phase case as the one originally developed for three-phase VSIs. Definition of this zero-sequence signal is:

$$v_{zs} = -0.5(v^*_{\max} + v^*_{\min}) \tag{6.26}$$

Signals inside the brackets are determined based on the maximum and minimum values of the input set of fundamental signals. While in the three-phase system, due to $v^*_a + v^*_b + v^*_c = 0$, (6.26) can alternatively be written as $v_{zs} = 0.5v^*_{mid}$, this is not the case for $n > 3$.

Like in the previous case, after the injection, the ordering of the modulating signals does not change and it stays as before injection (Tables 6.1-6.3). Thus it can be concluded that TIPWM will activate the same sequence of active space vectors like SPWM, HIPWM and SVPWM and, at the same time, durations of the active space vectors duty cycles will be the same as for all methods presented so far. Thus, only duty cycles of two zero space vectors need to be analysed. For the five-phase TIPWM, one finds, based on (6.6) and Table 6.1 that, in the first sector, duty cycles of two zero space vectors are:

$$
\begin{aligned}
\delta_0 &= \frac{1}{2}[1 - M\cos(\vartheta) + \frac{1}{2}(M\cos(\vartheta) + M\cos(\vartheta + 4\frac{\pi}{5}))] \\
\delta_{31} &= \frac{1}{2}[1 + M\cos(\vartheta + 4\frac{\pi}{5}) - \frac{1}{2}(M\cos(\vartheta) + M\cos(\vartheta + 4\frac{\pi}{5}))]
\end{aligned}
\tag{6.27}
$$

Simplifying (6.27), using basic trigonometric relations, yields:

$$\delta_0 = \delta_{31} = \frac{1}{2}[1 - K_2 M\cos(\frac{\pi}{10} - \vartheta)] \tag{6.28}$$

This is the same, equal, distribution of the total zero space vector duty cycle between two zero space vectors as the one selected for the five-phase SVPWM. The same can be found for the seven-phase and nine-phase TIPWM, respectively:

$$\delta_0 = \delta_{127} = \frac{1}{2}[1 - K_3 M\cos(\frac{\pi}{14} - \vartheta)] \tag{6.29}$$

$$\delta_0 = \delta_{511} = \frac{1}{2}[1 - K_4 M\cos(\frac{\pi}{18} - \vartheta)] \tag{6.30}$$

Thus, as in three-phase case [Zhou and Wang (2002)], carrier-based PWM based on the injection of the zero-sequence signal defined with (6.26) is the equivalent of the SVPWM, with equal distribution of zero space vector duty cycles. At the same time (6.26) centres modulating signals around zero, which is a feature that will be exploited later on in the thesis. The effectiveness of selection of (6.26) in multi-phase PWM methods has already been demonstrated by Casadei et al (2005) and Casadei et al (2007) for a PWM scheme termed 'duty cycle space vector' approach. The same zero-sequence has been used for a nine-phase VSI by Kelly et al (2003), where SVPWM approach has been considered computationally too

demanding for implementation and therefore the carrier-based approach has been followed. To illustrate the effects of such a zero-sequence signal injection, simulations similar to the HIPWM, have been carried out and characteristic signals are shown in Fig. 6.6.

The appearance of the zero-sequence signal is 'triangular'-like and therefore the term triangular injection PWM (TIPWM) is used here. However, based on (6.26), it is obvious that zero-sequence signal is obtained by manipulating the fundamental sinusoidal signals, and piece-wise linearity of the zero-sequence signal is therefore a valid approximation. In essence, zero-sequence signal determined with (6.26) effectively injects all the $n \cdot k$ harmonics, where k is an odd number [King (1974), Holmes and Lipo (2003)]. This can be verified by analysing the spectrum of the zero-sequence signal. Based on the results shown in Fig. 6.6, one finds that peaks of the modulating signals after injection appear again at instants $\vartheta = l\pi \pm (2l+1)\pi/2n$, $(l = 0,1,2,...)$, the same as with HIPWM. Dc bus utilisation is therefore the same as for HIPWM and SVPWM schemes, and the maximum value of the modulation index is:

$$M_{TIPWM}(n) = \frac{1}{K_{(n-1)/2}}$$

(6.31)

Generalised form of the zero-sequence injection that leads to development of a 'hybrid' PWM (HPWM) scheme with adjustable characteristics has been presented by Blasko (1997) for the three-phase VSI. This zero-sequence is defined with:

$$v_{zs} = -[(1-2\mu) + \mu v^*_{max} + (1-\mu)v^*_{min}]$$

(6.32)

Here, μ is the control variable within the range (0÷1) that can be used to alter the characteristics of the PWM scheme. Selecting $\mu = 0.5$ yields (6.26), which is therefore just a special case of the HPWM. By selecting other values for μ, both CPWM and DPWM schemes can be generated. The same principle can be applied for multi-phase PWM schemes.
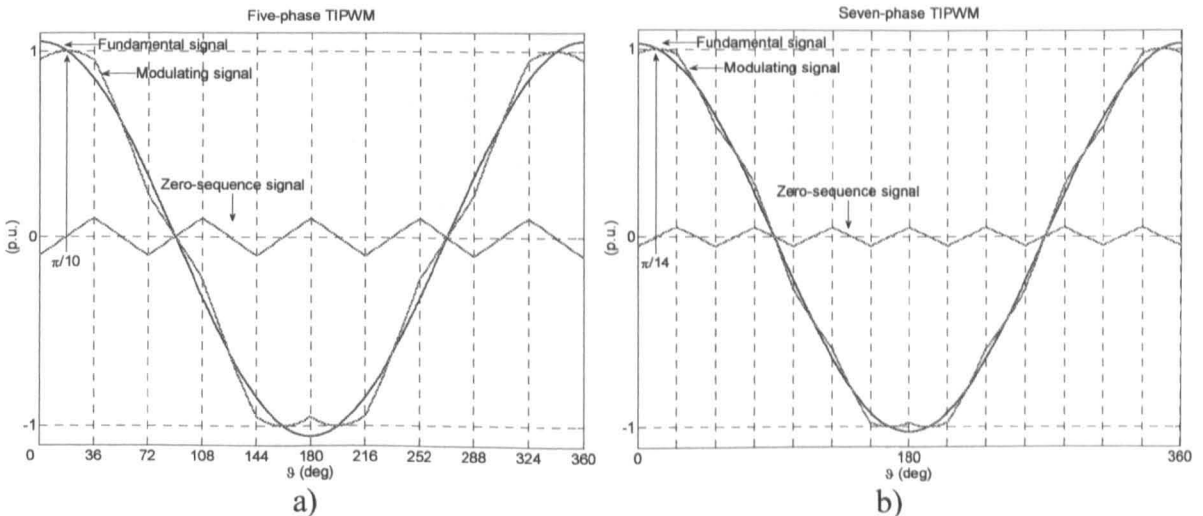

Fig. 6.6: Characteristic signals of the a) five-phase and, b) seven-phase TIPWM.
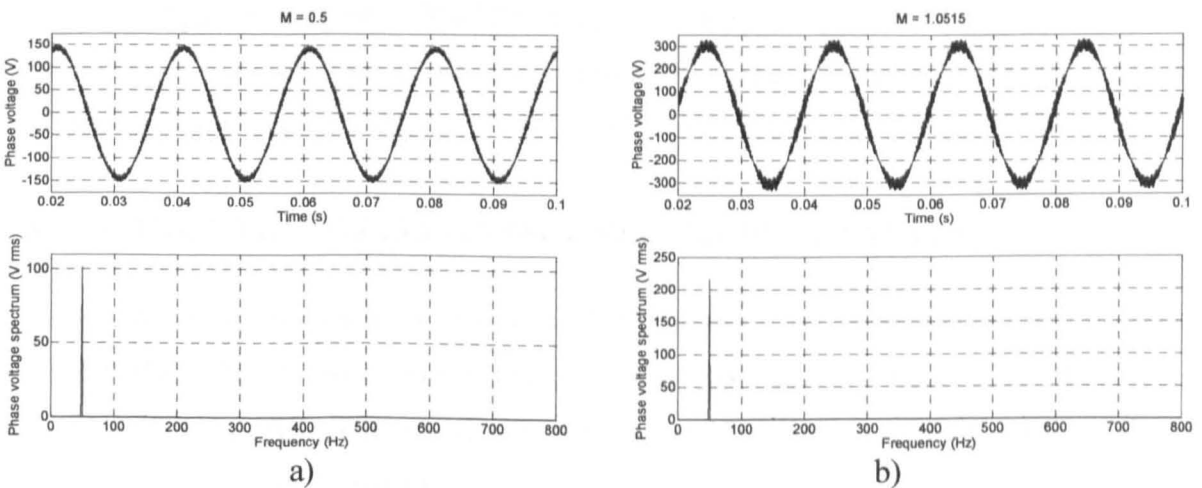
6.6   EXPERIMENTAL RESULTS

Since all PWM schemes, regardless of the number of phases, yield sinusoidal output voltage, experimental results are presented only for the five-phase case. All three carrier-based PWM schemes are implemented in the DSP and results are collected from the five-phase star-connected R-L load. The same conditions as for SVPWM schemes are set during the experiments. Operation at various values of the modulation index was investigated and results, given in Figs. 6.7-6.9, apply to $M = 0.5$ and $M = M_{max}$.

Experimentally recorded phase voltage spectrum in all three cases shows no sign of any low order harmonics from the d_2-q_2 plane. Sinusoidal voltages are generated and 5.15% increase in the output phase voltage is obtained with the fifth HIPWM (FHIPWM) and the TIPWM (equivalent of SVPWM and realised using carrier-based PWM principles), when compared to the SPWM.
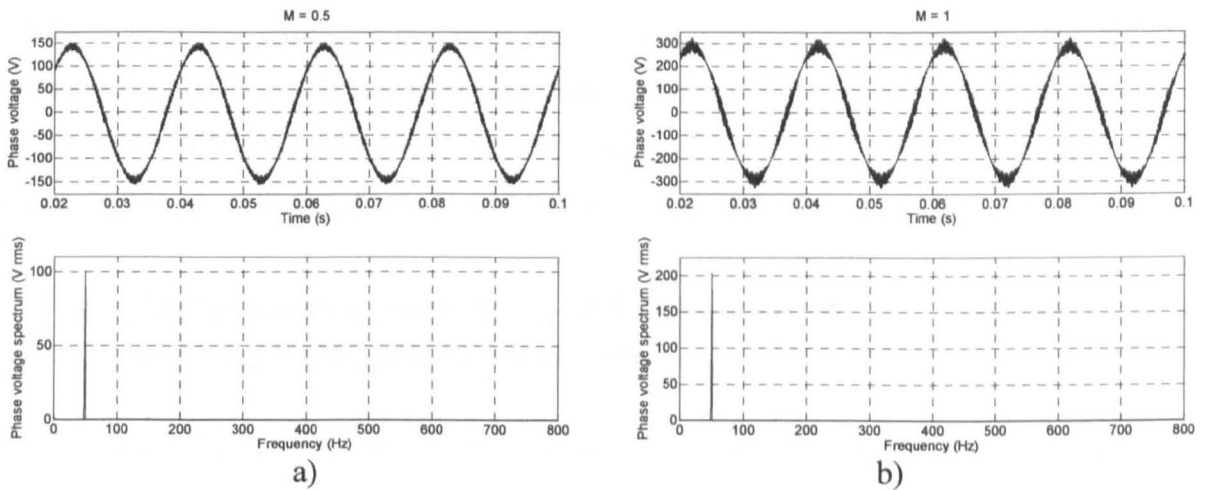
Fig. 6.7: Experimental results - phase voltage and its spectrum for five-phase SPWM at:
a) $M = 0.5$ and b) $M = 1$;

Fig. 6.8: Experimental results - phase voltage and its spectrum for five-phase FHIPWM at:
a) $M = 0.5$ and b) $M = 1.0515$.
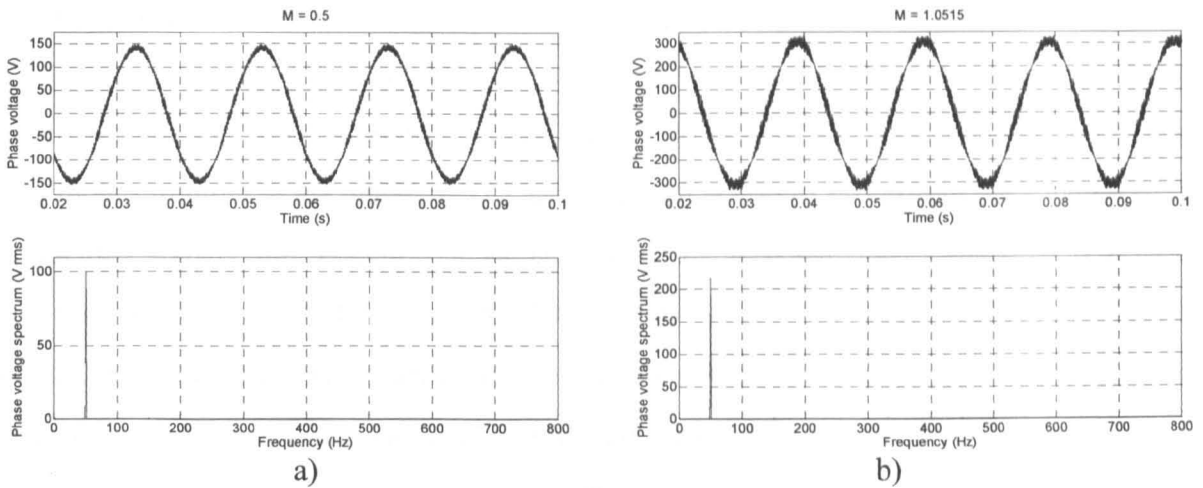
Fig. 6.9: Experimental results - phase voltage and its spectrum for five-phase TIPWM at: a) $M = 0.5$ and b) $M = 1.0515$.

CMV voltage is not measured this time, since its appearance is the same as for the five-phase SVPWM (Fig. 4.12). The only difference is related to duration of voltage levels associated with zero space vectors, since each analysed method has unique distribution of the zero space vector duty cycles. However, these differences are obvious from the analytical results presented so far while they may not be easily observable from the experimentally recorded CMV waveforms, due to short time intervals involved.

6.7   CARRIER-BASED PWM vs. SVPWM FOR MULTI-PHASE VOLTAGE SOURCE INVERTERS

Considering all the results presented so far for the carrier-based PWM and SVPWM schemes, it is obvious that, as with three-phase PWM schemes, an equivalence between these approaches can be established. Thus TIPWM, which uses offset injection to improve dc bus utilisation, is equivalent to the SVPWM as long as equal splitting of the total zero vector duty cycle is selected (various other distributions of this duty cycle between two zero space vectors result in other PWM schemes [Blasko (1997)] and are beyond the scope of the thesis).

6.7.1   DISTRIBUTION OF ZERO SPACE VECTOR DUTY CYCLES

Analytically obtained expressions for distribution of zero space vector duty cycles of all three PWM scheme can be compared graphically for various values of the modulation index. Since these distributions are similar for all considered phase number, they are shown here only for the five-phase PWM schemes and for two values of the modulation index. This is illustrated in Figs. 6.10 and 6.11, for M=0.2 and M=0.8, respectively. In all three cases,

distributions are symmetrical with regard to the middle of the sector, and when in the middle of the sector, all three PWM schemes are with the same value for the zero space vector duty cycles. At the same time, δ_0 and δ_{31} of the FHIPWM (dashed line) and SVPWM (dotted line) have their minimum in the middle of the sector, which is caused by shifting peak values of the modulating signals after injection of the corresponding zero sequence signals. SPWM (solid line) however has minimum for δ_0 always at the beginning of the sector (and at the end of the sector for δ_{31}) due to the values of the fundamental signals (v_a^* and v_d^*, respectively) that control distribution of these duty cycles. Illustrations given in Figs. 6.10 and 6.11 are for the first sector, while the same is valid for the remaining sectors.

These distributions are what distinguishes one PWM scheme from another and their significance will be clarified later on, when analysis of the output current ripple of multi-phase drives is presented.

a)   b)
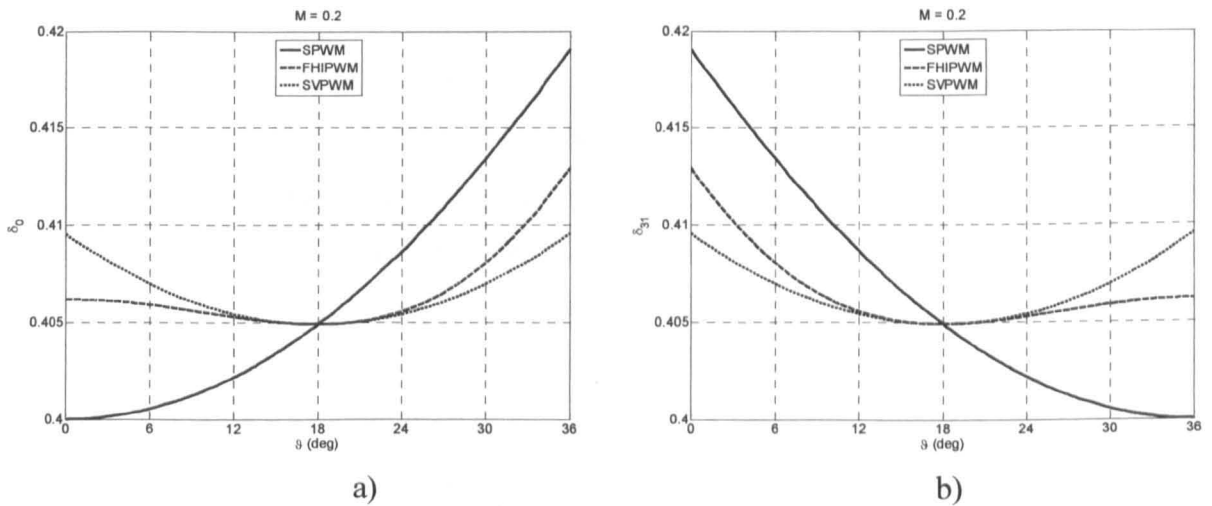
Fig. 6.10: Variations of zero space vector duty cycles over the first sector for all three PWM schemes with *M*=0.2; a) δ_0 and b) δ_{31}.

a)   b)
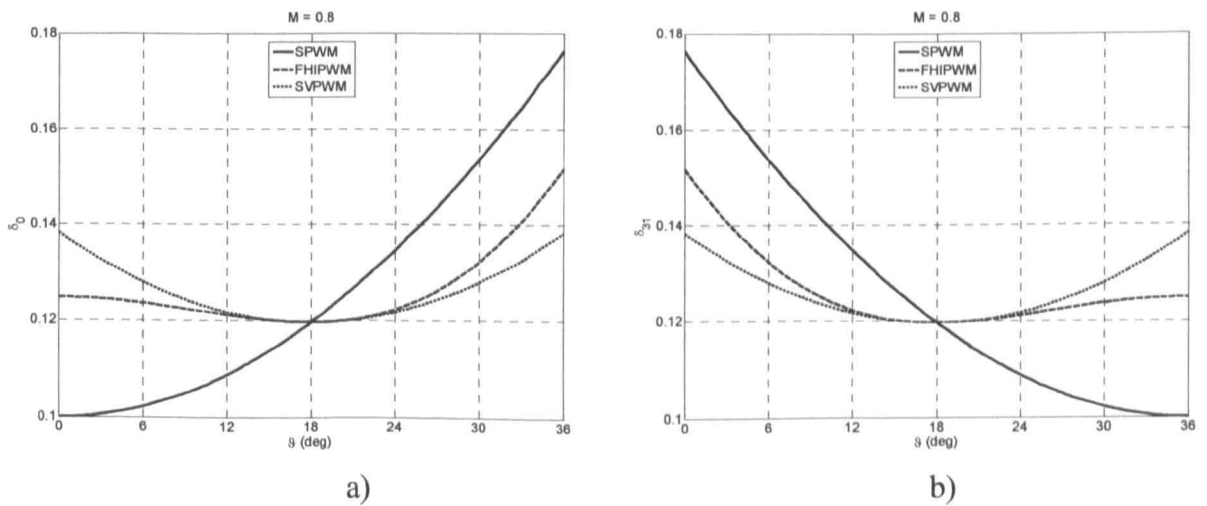
Fig. 6.11: Variations of zero space vector duty cycles over the first sector for all three PWM schemes with *M*=0.8; a) δ_0 and b) δ_{31}.

6.7.2 DSP IMPLEMENTATION

Nowadays, when control algorithms of every electric motor drive are implemented in digital domain with the use of some kind of a DSP, it is interesting to compare what kind of requirements different PWM modulators impose on the digital system. DSPs optimised for motor control mostly come with hardware PWM units that utilise high-speed counters/timers with accompanying compare registers in order to generate train of pulses at the output. Principle of operation of these hardware units can be understood as being based on carrier-based PWM (Fig. 6.1). It is up to the user to initialise PWM unit properly by defining parameters such as shape of the carrier signal (saw-tooth or triangular), switching frequency, PWM polarity, dead time, and to provide modulating signals for the compare registers. Assuming that modulating signals are sampled and sampled values are already loaded into compare registers and that switching frequency is 5 kHz, a DSP has 200 μs to perform control algorithm that includes the PWM modulator in the last stage in order to produce modulation signals for the next switching period (it is assumed that symmetrical switching pattern is to be generated and DSP unit is updated once per switching period; double update is very often used to produce asymmetrical pattern, by loading compare registers twice per switching period). All that time, the hardware PWM unit works in the background, taking care that the modulating signals from the previous calculation are transformed into appropriate pulses for the gate driver circuits. Since machine's control algorithms can be very complicated, it is desirable that the PWM modulator does not load DSP too much. Hence it should be simple, fast and should not occupy a lot of memory space. Structure of a carrier-based PWM modulator is very simple and requires only a few mathematical calculations in order to provide modulating signals. Assuming that field-oriented control is utilised, phase voltage references are available and the most time-consuming operation may be calculation of the appropriate zero-sequence component (if one is added). After adding zero-sequence signal to the fundamental signals, modulating signals are ready to be loaded into compare registers of the DSP PWM unit. Even with an increase of the number of phases, the principle of operation is the same and potential problems can only arise from the hardware incapability to provide enough independent PWM channels, since the existing DSPs are optimized for three-phase motor drives.

On the other hand, a space vector PWM modulator (Fig. 5.19), after receiving input reference space vector, has to go through several stages. At first, sector where the reference space vector is, has to be determined. Once when the correct sector number is available,

calculation of times of application of active space vector can take place. Very often this calculation requires some constants that can be pre-stored in the memory (e.g. a lookup table) and use of trigonometric functions. Time of application of zero space vectors must be calculated in accordance with the type of the modulation selected. Finally, calculated times of application of space vectors must be distributed in accordance with the predefined switching pattern for each sector, which may require another lookup table, to create modulation signals that are ready to load into compare registers. From these few steps it is obvious that the SVPWM is computationally much more demanding approach than the carrier-based PWM. With an increase in the number of phases, complexity of the modulator increases, although structure may stay the same (Fig. 5.19). Although similarities in implementation do exist, the number of applied active space vectors increases as the number of phases increases, thus making the implementation more and more complex.

6.8 SUMMARY

Carrier-based PWM schemes for sinusoidal output voltage generation with multi-phase VSIs have been presented in this chapter. The simplest multi-phase SPWM scheme is analysed and the main characteristics are determined. It is shown that injection of the zero-sequence signal does not change the mutual relation between resulting modulating signals (order over the sectors) and therefore all schemes apply the same set of space vectors over the switching period. Poor dc bus utilisation of a SPWM is improved with injection of the n-th harmonic (HIPWM), or the injection of all odd $n \cdot k$ harmonics (TIPWM). The latter method is the multi-phase carrier-based equivalent of the multi-phase SVPWM, the same as for three-phase case. Experimental results are presented for the five-phase carrier-based methods and implementation issues are addressed for both carrier-based and SVPWM.

Leaving aside implementation issues, the only major difference between carrier-based PWM methods is the distribution of zero space vector duty cycles (SVPWM, as noted, is equivalent to the carrier-based TIPWM). The effects of this on current ripple rms value are investigated next for all the methods considered so far, at first using the five-phase system as an example. Later on, general analysis is presented that covers all multi-phase systems.

Chapter 7

ANALYTICAL ANALYSIS OF CURRENT RIPPLE RMS OF FIVE-PHASE DRIVES – COMPLEX APPROACH

7.1 INTRODUCTION

Results, presented so far with regard to the main characteristics of various PWM schemes for multi-phase VSIs, are closely related to those already known for three-phase PWM. There is a full equivalence between carrier-based PWM and SVPWM, which has been clearly established by proper selection of the zero-sequence signal. The same space vectors are applied over the switching period (with the same duty cycle values) regardless of the PWM method used, as long as purely sinusoidal output voltage is the goal. Disregarding the need to analyse multi-phase systems in more than one d-q plane and implementation dissimilarities between carrier-based PWM and SVPWM, the main difference is related to the distribution of zero space vector duty cycles over the switching period. This distribution is controlled with injection of an appropriate zero-sequence signal and is a PWM degree of freedom that is used to increase dc bus utilisation over the level achievable with SPWM. It is well known that in three-phase drives, output current ripple (actually current ripple rms, since it defines harmonic losses) can be optimised simultaneously with dc bus utilisation [Holmes and Lipo (2003)]. There are no such results reported so far for multi-phase PWM methods and it is for this reason that detailed analysis is carried out in this chapter for a five-phase VSI. The analysis is based here on the space vector theory and is termed 'complex approach'. In chapter 8 a more general approach is presented, based on the use of polygon connections of multi-phase systems and is thus termed 'polygon approach'.

This chapter is organised as follows. In section 7.2, the importance of current ripple rms analysis is elaborated by surveying the existing literature related to the three-phase PWM methods. Based on these results, some analytical tools are adopted for multi-phase systems. Section 7.3 introduces notion of 'harmonic flux' that is used throughout the chapter to evaluate current ripple rms (use of harmonic flux notion is more suitable for analysis of multi-

phase systems due to the existence of multiple *d-q* planes and the difference among inductances associated with each plane, as it will be explained). Harmonic flux trajectories in each of 2-D planes are investigated in section 7.4. In section 7.5 squared harmonic flux over the switching period is numerically evaluated (microscopic analysis) in each plane, while section 7.6 presents final harmonic distortion factors obtained analytically (macroscopic analysis) for each of the analysed PWM schemes. Discussion of the analytical results and simulation/experimental verification is given in sections 7.7 and 7.8, respectively. Summary of the chapter is given in section 7.9.

7.2 SIGNIFICANCE OF CURRENT RIPPLE RMS AND COMMONLY USED ANALYTICAL TOOLS

With proliferation of the use of PWM controlled three-phase VSIs, it has been gradually recognised that, in order to optimise inverter/drive design, characteristics of various PWM schemes and their impact on overall drive performance must be carefully analysed. This is necessary for proper dimensioning of active and passive components within the converter, as well as for determination of the impact of PWM operation on the mains harmonics, dc link harmonics and output harmonics.

The use of computer-aided design has been proposed by many authors in order to obtain input/output harmonic contents caused by PWM operation of power converters [Bowes and Clements (1982), Ziogas and Photiadis (1983), Ziogas et al (1985)]. However, this approach suffers from some disadvantages such as: a need to perform a multitude of simulations in order to cover broad range of operating conditions since every single simulation gives the results for a single set of input parameters; obtained results are in numerical form and it is not easy to apply them to a slightly different system and therefore every new system requires new analysis; sensitivity to quality of utilised models, etc. Therefore, analytical approach to analysis has been developed, with the aim to enable generation of results that allow relative comparison of various characteristics of different PWM methods, while not necessarily providing exact numerical results.

Van der Broeck and Skudelny (1988) have presented analytical analysis of the harmonic content of current, torque pulsation, and harmonic copper losses of a three-phase reduced switch-count drive system. Polynomial closed-form solutions are obtained, which allow for easy graphical comparison, assuming relatively high switching frequency during PWM operation (at least nine times the fundamental frequency). This assumption is

reasonable as long as low and medium power drives are under consideration, where relatively high switching frequencies are used in practice. A complete analysis of PWM converter system has been presented in Kolar et al (1989) and Kolar et al (1991a), addressing switching losses, dc link harmonics and inverter input/output harmonics. It has been shown that reduction of the output current harmonics in the case of CPWM can be achieved by proper zero-sequence signal injection or by the development of DPWM schemes, and by increasing the switching frequency. More detailed analysis, based on space vector theory, has demonstrated that optimisation of output current ripple rms in a three-phase system can be achieved at the expense of a slightly lower dc bus utilisation compared to the maximum achievable level [Kolar et al (1990a), Kolar et al (1990b)]. Thus injection of the third harmonic with a level of $b = -1/6$ optimises dc bus utilisation with slightly poorer current ripple rms characteristic, while injection with a level of $b = -1/4$ minimises current ripple rms value at the expense of around 3% lower dc bus utilisation [Buja and Indri (1975)]. A further reduction of the rms value of the current ripple is possible by development of DPWM schemes, which allow for further increase of the switching frequency while maintaining the switching losses at the same level as with CPWM [Kolar et al (1991b)]. Influence of different sequences of space vectors of a SVPWM on the output current ripple has been investigated by Stefanović and Vukosavić (1992), suggesting different organisations of the switching pattern depending on the type of load connected to the inverter. To analyse the output current ripple, analytical approach has been used with the analysis conducted in the complex plane.

While the inverter output current ripple can be minimised by a properly devised PWM scheme, this is not the case with the inverter input current ripple [Dahono et al (1996), Kolar et al (1999)]. Analytically obtained characteristic for inverter input current ripple shows no dependency on the selected PWM scheme and is a function of only modulation index and load power factor. An optimisation is possible regarding the input voltage ripple (dc link voltage ripple) in the same way as the optimisation of the output current ripple, with a difference that dependency on the load power factor is present again. Harmonic evaluation of output current rms of two-level and three-level VSIs has been performed by Fukuda and Suzuki (1997), by defining 'Harmonic Distortion Determining Factor' (HDDF) as a figure of merit. This is in essence an analytical closed-form polynomial solution that describes output current ripple rms value, already used in papers by Van der Broeck and Skudelny (1988), Kolar et al (1990a) and Kolar et al (1990b). Hybrid PWM (HPWM) scheme developed by Blasko (1997), as well as the generalised DPWM (GDPWM) scheme of Hava et al (1998a), offered adjustable characteristics over the whole range of modulation by introduction of selectable distribution

of the zero space vectors duty cycles. Thus, both schemes yield better (lower) current ripple rms characteristics, especially at higher values of modulation index than classical SVPWM (although GDPWM requires doubling of the switching frequency to offer reductions).

An analytical analysis of the main properties of carrier-based PWM methods for three-phase drives, based on space vector theory, has been conducted by Hava et al (1999). Current ripple rms value (waveform quality) has been analysed using concept of 'harmonic flux', which represents time integral of harmonic voltage vector (which is basically voltage error vector caused by the discrete nature of operation of the PWM VSI during generation of the output voltage reference vector). Various three-phase PWM schemes were analysed and superiority of injection with the level of $b = -1/4$ in the third HIPWM regarding the current ripple rms characteristic was confirmed again. Exactly the same methodology has been applied by Qiang et al (2005) in order to evaluate switching frequency harmonics of the developed common mode voltage reduction modulator. A similar notion, termed 'stator flux ripple', has been used to evaluate various possible sequences of active space vectors of the three-phase SVPWM [Narayanan and Ranganathan (2005)] by analysing components of the stator flux ripple along d-q axes, thus allowing for independent torque pulsation evaluation based on the q-axis characteristics. Optimisation of SVPWM switching pattern [Casadei et al (2004)] resulted in slightly lower current ripple rms value compared to the conventional SVPWM, with a reduced number of commutations for high values of the modulation index.

The approach, followed in analysis of the current ripple rms in the most of cases, has been based on the use of space vector theory [Kolar et al (1990a), Kolar et al (1990b), Hava et al (1999)]. A different approach, where analysis is placed in the original domain and based on delta connection of the three-phase load, has also been used [Van der Broeck and Skudelny (1988), Dahono et al (1996), Blasko (1997), Holmes and Lipo (2003)]. Whatever approach is used, the same final results were obtained, with the difference that the space vector approach offers a better insight into development of the solution. An important result of all of these analyses is the fact that in three-phase drives injection of the proper zero-sequence signal at the same time increases dc bus utilisation and reduces current ripple rms, compared to the characteristics offered by the SPWM. However, both can not be optimised simultaneously as discussed in Kolar et al (1990a) and Kolar et al (1990b), and already emphasised before.

The only attempt to perform a similar analysis for multi-phase systems has been carried out by Dahono (2006), Dahono and Deni (2006) and Deni et al (2007). Analysis of Dahono (2006) dealt with a multi-phase machine in polygon connection, thus effectively simplifying the analysis to the case of H-bridge inverter supply (the same kind of analysis is

used for three-phase PWM schemes, with machine windings in delta connection). However, the existence of two different polygon connections in a five-phase system has not been recognised and injection of the third harmonic with levels characteristic for three-phase systems (−1/4 and −1/6) has been considered for the improvement of output current ripple. The analysis is incomplete and flawed in many aspects, although, interestingly, obtained results suggest that injection of the third harmonic cannot optimise current ripple rms value in the case of a five-phase drive. A similar analysis, based again on only one polygon connection of a five-phase load, has been carried out by Dahono and Deni (2006). The fifth harmonic zero-sequence signal injections have been analysed and compared with well known solutions for three-phase systems and it is concluded again that SPWM yields the best current ripple rms characteristic. Finally, Deni et al (2007) have considered injection of both the third and the fifth harmonic in polygon connected five-phase system with the aim to reduce current ripple rms value. Problems with this analysis are again related to the fact that multi-phase systems have more than one possible polygon connection. More precisely, the number of different polygon connections equals the number of 2-D planes in which a multi-phase system needs to be analysed. While in the three-phase case there is a unique transformation from star into delta connection, this is not the case with multi-phase systems, as discussed by Ferraris and Lazzari (1983). In the particular case of Deni et al (2007), the third harmonic belongs to the d_2-q_2 plane while the fifth harmonic is from the zero-sequence plane. Yet, authors suggested that injection of both mentioned harmonic can reduce current ripple rms, when compared to the injection of only the third harmonic.

Based on this short survey regarding the analysis of output current ripple rms characteristic of VSIs, a lack of any detailed analysis, related to multi-phase drives in order to characterise various PWM schemes, is obvious. For the sake of completeness of the analysis, two different approaches are developed in this thesis. The first one is applied to the five-phase case and is based on the space vector theory. Therefore, it is termed 'complex approach' since analysis of current ripple rms is placed in two 2-D planes of a five-phase system. This is presented in this chapter. The second approach explores, as an alternative, the use of available polygon connections of a multi-phase system in order to obtain current ripple rms characteristics and is termed 'polygon approach'. Such an approach is presented in chapter 8. Feasibility of these approaches is verified by direct comparison of the obtained results. In addition, analytically obtained results are verified experimentally for the five-phase PWM schemes. The analysis covers all three PWM schemes, presented in chapters 4 and 6 for the five-phase VSI, namely SPWM, FHIPWM (with $b = -\sin(\pi/10)/5$) and SVPWM (TIPWM).

7.3 FIVE-PHASE HARMONIC FLUX RMS ANALYSIS – COMPLEX APPROACH

Before proceeding with the analysis of output current ripple, several assumptions must be adopted in order to obtain valid results [Holmes and Lipo (2003)]:

- High switching frequency is assumed.

- Average internal electromotive force (emf) of the load is assumed to be constant over the switching period and equal to the reference space vector.

- Impact of the equivalent resistance on current waveform over a switching period can be neglected and linear change of current can be assumed.

The mechanism of creation of the output current ripple is explained by considering the situation illustrated in Fig. 7.1. For the purposes of analysis it is enough to consider only the first sector again [Kolar et al (1990a), Kolar et al (1990b), Hava et al (1999)]. This is illustrated in Fig. 7.1a, where the reference space vector is given together with adjacent four active space vectors from the d_1-q_1 plane and their mapped equivalents in the d_2-q_2 plane (Fig. 7.1b). The reference space vector in the second plane is zero in order to zero low order harmonic components. Discrete nature of operation of the inverter generates reference space vector by means of averaging with selected active space vectors over the switching period. Thus, whenever any of the space vectors is applied at the output of the inverter, error voltage vectors are generated as shown in Fig. 7.1c for the first plane and in Fig. 7.1d for the second plane. This error voltage (deviation of output voltage), when applied over the load inductance, will cause current ripple (deviation of output current $\bar{\imath}$ from the reference value $\bar{\imath}^*$),

$$\Delta \bar{\imath} = \bar{\imath} - \bar{\imath}^* \tag{7.1}$$

Durations of application of each space vector are determined with the values of corresponding duty cycles over the switching period, which at the same time define the shape of generated output current ripple. Due to the assumed high switching frequency, impact of the equivalent resistance can be neglected and instantaneous current ripple can be approximated with straight line segments. Thus, a simple equivalent circuit suitable for the analysis is defined with:

$$L\frac{d\bar{\imath}}{dt} \approx L\frac{\Delta \bar{\imath}}{\Delta t} = (\bar{v} - \bar{v}^*) \tag{7.2}$$

Here $\bar{v}$ represents the space vectors activated over the time interval Δt within a switching period. From (7.2) one has that deviation of the current can be expressed as:

$$\Delta \bar{\imath} = \frac{\bar{v} - \bar{v}^*}{L}\Delta t \tag{7.3}$$
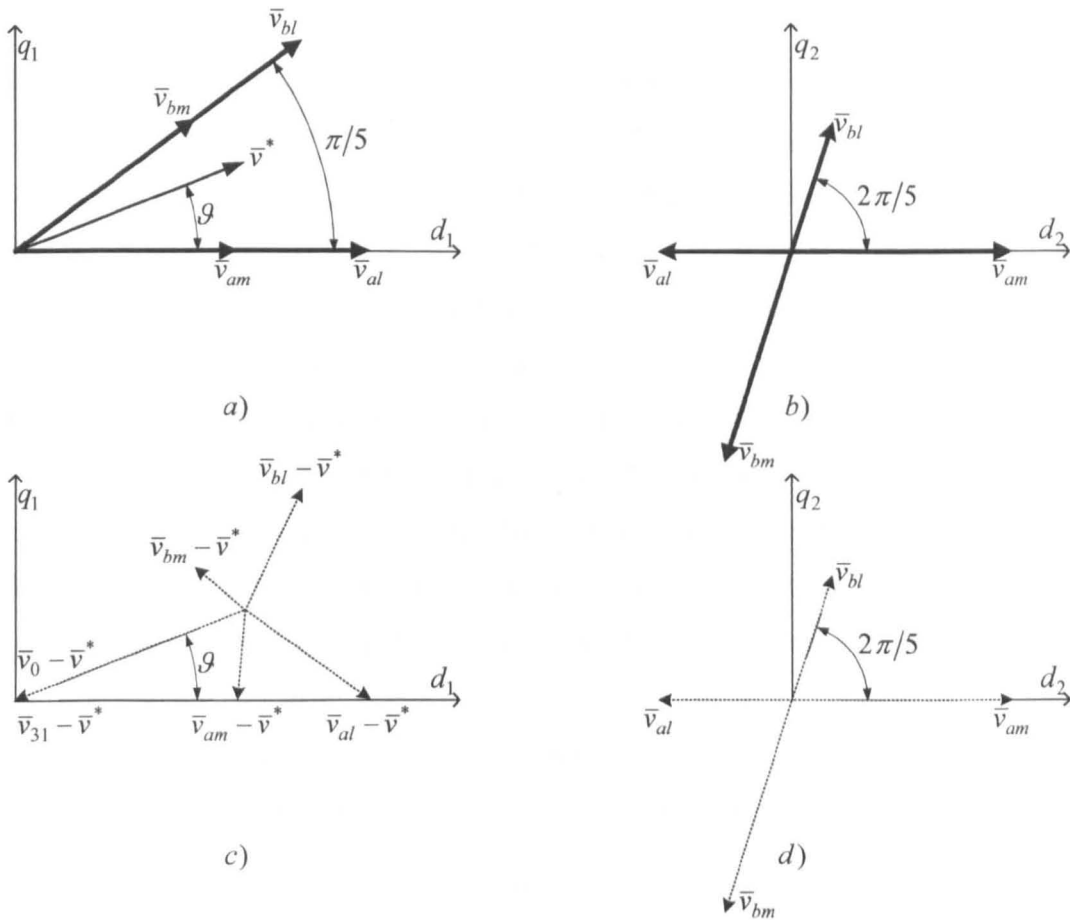
Fig. 7.1: Space vectors used for considered PWM schemes in the d_1-q_1 and d_2-q_2 planes (a) and b)) and generated error voltage vectors in each plane (c) and d)).

Deviation of current expressed with (7.3) is suitable for an analysis in three-phase systems since the equivalent inductance, necessary for the analysis, can easily be obtained for an induction motor as:

$$L = L_\sigma = L_{\gamma s} + \frac{L'_{\gamma r} L_m}{L'_{\gamma r} + L_m} \tag{7.4}$$

where $L_{\gamma s}$, $L_{\gamma r}$ and L_m are stator leakage, rotor leakage and magnetising inductance, respectively [Holmes and Lipo (2003)]. However, in the case of multi-phase systems, situation is slightly more complicated. Any voltage deviations in the d_1-q_1 plane are responsible for current ripple appearing on the equivalent inductance in the d_1-q_1 plane, while deviations of voltage in the d_2-q_2 plane are restricted only by the stator leakage inductance [Levi et al (2007b)]. Therefore, use of (7.3) represents an obstacle and can lead to difficulties when applied to multi-phase systems. A simple solution is obtained if the notion of 'harmonic flux' ($\bar{\lambda}$) is introduced, where harmonic flux is actually the time integral of the error voltage vectors [Hava et al (1999), Narayanan and Ranganathan (2005)]. With this definition, (7.3) now takes an alternative form of:

146

$$\Delta \overline{\lambda} = L \Delta \overline{i} = (\overline{v} - \overline{v}^*) \Delta t \tag{7.5}$$

Thus, the analysis of current ripple (harmonic current) is now replaced by the analysis of harmonic flux, which can be performed independently in each plane. It is obvious from (7.5) that harmonic current and harmonic flux are only different in scale, and if necessary, current harmonic characteristic can be easily obtained later on by scaling of the obtained results for harmonic flux by the corresponding inductances.

The complex approach, based on the harmonic flux concept, allows for the analysis to be performed at several different levels. This offers a great insight into the mechanism of creation of the output current ripple, as it will be demonstrated. The analysis will further be done for SVPWM, FHIPWM (the fifth HIPWM) and SVPWM (the equivalent of TIPWM). All these schemes are characterised with the same set of active vectors applied over the switching period, with the only difference being in the distribution of the zero space vector duty cycles. Since the switching pattern is symmetrical, it is enough to consider for the analysis only the first half of the switching period, as shown in Fig. 7.2. Space vectors are denoted in accordance with Fig. 7.1a and duty cycles, necessary for analysis, are indicated.
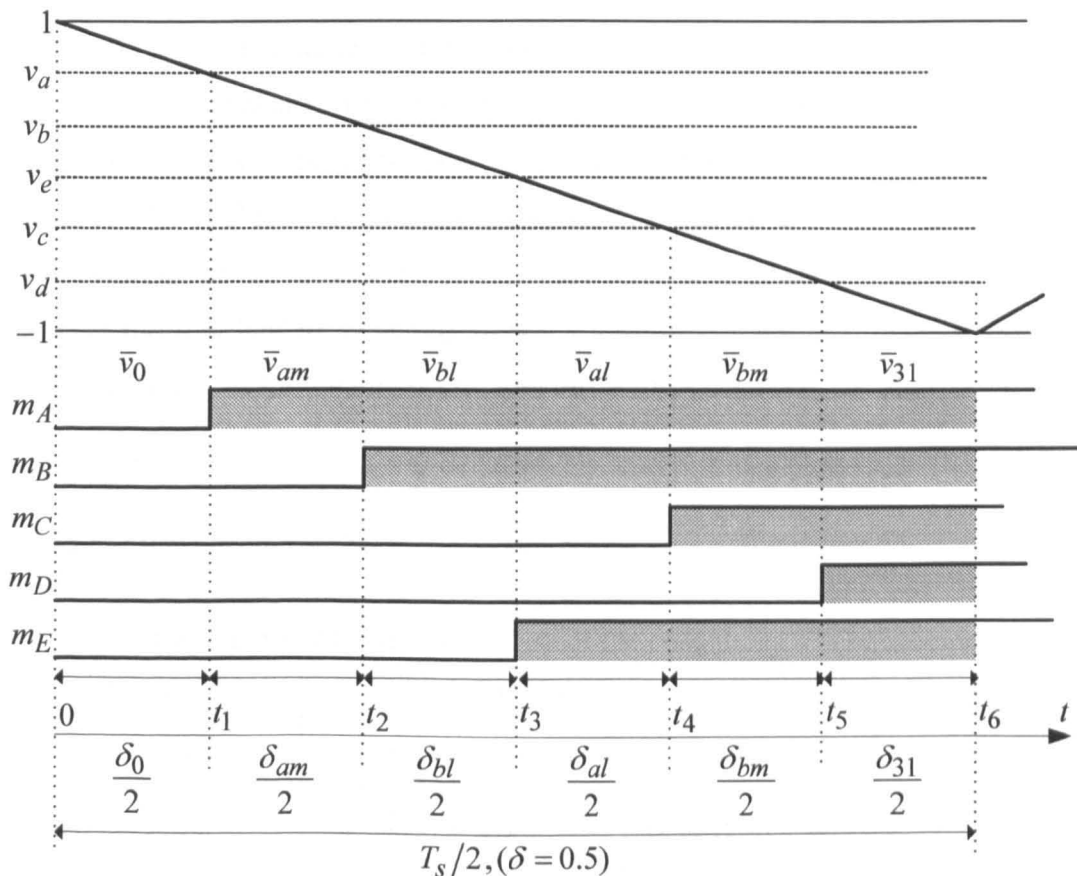
Fig. 7.2: Switching pattern, characteristic for the analysed five-phase PWM schemes, during the first half of the switching period.

The time axis is shown in Fig. 7.2 and characteristic time instants (0 to t_6) are denoted to distinguish different sub-intervals determined with different duty cycles. For a given reference space vector in the first sector, duty cycles of all three methods are summarised again in Table 7.1, since they will be used during the analysis. All previously introduced definitions, such as the modulation index (4.2) and trigonometric constants (3.13), are still valid and will be used throughout the chapter. Harmonic flux trajectories are analysed first.

7.4 HARMONIC FLUX TRAJECTORIES

As the first step, it is possible to generate harmonic flux trajectories (trajectories of error voltage vector) in both planes over the switching period, for all three PWM schemes considered. This can be done by performing the following calculation over the first half of the switching period (as noted, due to the symmetry, only the first half of the switching period is sufficient for analysis) [Hava et al (1999)]:

$$\bar{\lambda} = \int_0^{\frac{T_s}{2}} (\bar{v} - \bar{v}^*) dt \qquad (7.6)$$

Since linear change is assumed for the harmonic flux, a precise knowledge of the time dependence is not necessary. The approach adopted in this thesis therefore does not require knowledge of the time dependence and it can be regarded as an extension of Kolar et al (1990a) and Kolar et al (1990b) to a five-phase system. Instead of evaluating the time integral of (7.6), deviations of the harmonic flux ($\Delta\bar{\lambda}$) are calculated directly at the end of every sub-interval over the first half of switching period (sub-intervals are effectively defined by duty cycles of used space vectors). Duty cycles and sub-intervals are related with:

$$\delta_0 = \frac{2}{T_s}t_1; \qquad \delta_{am} = \frac{2}{T_s}(t_2 - t_1); \qquad \delta_{bl} = \frac{2}{T_s}(t_3 - t_2)$$

$$\delta_{al} = \frac{2}{T_s}(t_4 - t_3); \qquad \delta_{bm} = \frac{2}{T_s}(t_5 - t_4); \qquad \delta_{31} = \frac{2}{T_s}(t_6 - t_5) \qquad (7.7)$$

Table 7.1: Duty cycle distribution of the considered PWM schemes.

SPWM	FHIPWM	SVPWM
$\delta_0 = \frac{1}{2}[1 - M\cos(\vartheta)]$	$\delta_0 = \frac{1}{2}[1 - M\cos(\vartheta) - bM\cos(5\vartheta)]$	$\delta_0 = \frac{1}{2}[1 - K_2 M\cos(\frac{\pi}{10} - \vartheta)]$
$\delta_{31} = \frac{1}{2}[1 + M\cos(\vartheta + 4\frac{\pi}{5})]$	$\delta_{31} = \frac{1}{2}[1 + M\cos(\vartheta + 4\frac{\pi}{5}) + bM\cos(5\vartheta)]$	$\delta_{31} = \frac{1}{2}[1 - K_2 M\cos(\frac{\pi}{10} - \vartheta)]$
$\delta_{am} = KM\sin(\frac{\pi}{5} - \vartheta);$ $\qquad \delta_{bm} = KM\sin(\vartheta)$		
$\delta_{al} = K_2 M\sin(\frac{\pi}{5} - \vartheta);$ $\qquad \delta_{bl} = K_2 M\sin(\vartheta)$		

Assuming initial zero value for the deviation of harmonic flux [Hava et al (1999)] one can calculate values of the harmonic flux (space vector $\Delta\bar{\lambda}$) in the d_1-q_1 plane directly, at the end of every sub-interval over the first half of the switching period as:

$$\Delta\bar{\lambda}_{dq1}(0) = 0$$
$$\Delta\bar{\lambda}_{dq1}(t_1) = -\bar{v}^*\delta_0\,T_s/2$$
$$\Delta\bar{\lambda}_{dq1}(t_2) = \Delta\bar{\lambda}_{dq1}(t_1) + \delta_{am}(\bar{v}_{am} - \bar{v}^*)T_s/2$$
$$\Delta\bar{\lambda}_{dq1}(t_3) = \Delta\bar{\lambda}_{dq1}(t_2) + \delta_{bl}(\bar{v}_{bl} - \bar{v}^*)T_s/2 \qquad (7.8)$$
$$\Delta\bar{\lambda}_{dq1}(t_4) = \Delta\bar{\lambda}_{dq1}(t_3) + \delta_{al}(\bar{v}_{al} - \bar{v}^*)T_s/2$$
$$\Delta\bar{\lambda}_{dq1}(t_5) = \Delta\bar{\lambda}_{dq1}(t_4) + \delta_{bm}(\bar{v}_{bm} - \bar{v}^*)T_s/2$$
$$\Delta\bar{\lambda}_{dq1}(t_6) = \Delta\bar{\lambda}_{dq1}(t_5) - \delta_{31}\bar{v}^*v$$

Normalisation factor for the harmonic flux is selected the same as in [Kolar et al (1990b), Blasko (1997)] and is related to the current ripple analysis of the half-bridge inverter:

$$\Delta\lambda_N = L\Delta i_N = \frac{V_{dc}T_s}{8} \qquad (7.9)$$

With (7.9), the previously introduced normalisation for the magnitude of active space vectors is also encompassed and after some manipulations (7.8) can be expressed in a simplified form as:

$$\Delta\bar{\lambda}_{dq1}(0) = 0$$
$$\Delta\bar{\lambda}_{dq1}(t_1) = -2\bar{v}^*\delta_0$$
$$\Delta\bar{\lambda}_{dq1}(t_2) = 2\left[\bar{v}_{am}\delta_{am} - \bar{v}^*[\delta_0 + \delta_{am}]\right]$$
$$\Delta\bar{\lambda}_{dq1}(t_3) = 2\left[\bar{v}_{am}\delta_{am} + \bar{v}_{bl}\delta_{bl} - \bar{v}^*[\delta_0 + \delta_{am} + \delta_{bl}]\right] \qquad (7.10)$$
$$\Delta\bar{\lambda}_{dq1}(t_4) = 2\left[\bar{v}_{am}\delta_{am} + \bar{v}_{bl}\delta_{bl} + \bar{v}_{al}\delta_{al} - \bar{v}^*[\delta_0 + \delta_{am} + \delta_{bl} + \delta_{al}]\right]$$
$$\Delta\bar{\lambda}_{dq1}(t_5) = 2\bar{v}^*\delta_{31}$$
$$\Delta\bar{\lambda}_{dq1}(t_6) = 0$$

The left-hand side of (7.10) is now in per-unit (p.u.), although the same symbols are used as in (7.8). The same procedure can be repeated for the d_2-q_2 plane, which initially yields:

$$\Delta\bar{\lambda}_{dq2}(0) = 0$$
$$\Delta\bar{\lambda}_{dq2}(t_1) = 0$$
$$\Delta\bar{\lambda}_{dq2}(t_2) = \Delta\bar{\lambda}_{dq2}(t_1) + \delta_{am}\bar{v}_{am}\,T_s/2$$
$$\Delta\bar{\lambda}_{dq2}(t_3) = \Delta\bar{\lambda}_{dq2}(t_2) + \delta_{bl}\bar{v}_{bl}\,T_s/2 \qquad (7.11)$$
$$\Delta\bar{\lambda}_{dq2}(t_4) = \Delta\bar{\lambda}_{dq2}(t_3) + \delta_{al}\bar{v}_{al}\,T_s/2$$
$$\Delta\bar{\lambda}_{dq2}(t_5) = \Delta\bar{\lambda}_{dq2}(t_4) + \delta_{bm}\bar{v}_{bm}\,T_s/2$$
$$\Delta\bar{\lambda}_{dq2}(t_6) = \Delta\bar{\lambda}_{dq2}(t_5)$$

After development and normalisation of (7.11) with (7.9) one has for the harmonic flux trajectories in the d_2-q_2 plane, when expressed in per-unit:

$$\Delta\overline{\lambda}_{dq2}(0) = 0$$

$$\Delta\overline{\lambda}_{dq2}(t_1) = 0$$

$$\Delta\overline{\lambda}_{dq2}(t_2) = 2\overline{v}_{am}\delta_{am}$$

$$\Delta\overline{\lambda}_{dq2}(t_3) = 2\left[\overline{v}_{am}\delta_{am} + \overline{v}_{bl}\delta_{bl}\right] \qquad (7.12)$$

$$\Delta\overline{\lambda}_{dq2}(t_4) = 2\left[\overline{v}_{am}\delta_{am} + \overline{v}_{bl}\delta_{bl} + \overline{v}_{al}\delta_{al}\right]$$

$$\Delta\overline{\lambda}_{dq2}(t_5) = 0$$

$$\Delta\overline{\lambda}_{dq2}(t_6) = 0$$

It is important to note here that harmonic flux values over the first half of the switching period in the d_2-q_2 plane are not the functions of the zero space vector duty cycles, in contrast to the situation in the d_1-q_1 plane. Thus only active space vector duty cycles are of interest during analysis of harmonic flux trajectories in the d_2-q_2 plane. As a consequence, all three analysed PWM schemes are with exactly the same characteristic regarding the harmonic flux in the second plane. However, zero space vector duty cycles are included in (7.10), resulting in different harmonic flux trajectories for every PWM scheme in the first plane. To obtain the plots, normalised (with $V_{dc}/2$) complex values of applied space vectors in the first sector of the d_1-q_1 plane are necessary, which are defined in Table 7.2 (together with complex values of the vectors in the second plane and real and imaginary parts for both planes as well).

Based on the values of the harmonic flux at the end of every sub-interval, given with (7.10) and (7.12), it is possible to obtain harmonic flux trajectories in both planes for various values of the input reference space vector. Since trajectories in the second plane are the same for all three PWM schemes, this plane is analysed first. Although the analysis is analytical, harmonic flux trajectories are generated by means of numerical evaluation of (7.10) and (7.12) using MATLAB, in order to present them graphically in each of the planes.

Table 7.2: Applied active space vectors and their real and imaginary parts in both planes.

|	$\overline{v}_{am}$	$\overline{v}_{bm}$	$\overline{v}_{al}$	$\overline{v}_{bl}$
d_1-q_1	$\dfrac{4}{5}$	$\dfrac{4}{5}e^{j\frac{\pi}{5}}$	$\dfrac{8}{5}L$	$\dfrac{8}{5}Le^{j\frac{\pi}{5}}$
d_1	$\dfrac{4}{5}$	$\dfrac{4}{5}L$	$\dfrac{8}{5}L$	$\dfrac{8}{5}L^2$
q_1	0	$\dfrac{4}{5}K$	0	$\dfrac{8}{5}KL$
d_2-q_2	$\dfrac{4}{5}$	$\dfrac{4}{5}e^{-j3\frac{\pi}{5}}$	$-\dfrac{8}{5}L_2$	$\dfrac{8}{5}L_2e^{j2\frac{\pi}{5}}$
d_2	$\dfrac{4}{5}$	$-\dfrac{4}{5}L_2$	$-\dfrac{8}{5}L_2$	$\dfrac{8}{5}L_2^2$
q_2	0	$-\dfrac{4}{5}K_2$	0	$\dfrac{8}{5}K_2L_2$

7.4.1   HARMONIC FLUX TRAJECTORIES IN THE SECOND PLANE

Harmonic flux trajectories in the first sector of the d_2-q_2 plane are investigated for several values of the input reference space vector. Trajectories are shown only for the first half of the switching period, which is sufficient for the analysis. During the second half of the switching period, harmonic flux trajectories can be easily obtained by evaluating (7.12) in the reversed order, due to the symmetry of the switching pattern. At first, generated harmonic flux trajectories are illustrated in Fig. 7.3 for one particular value of the reference space vector defined in the d_1-q_1 plane with $\bar{v}^* = 0.5e^{j\pi/15}$. Although reference space vector for the d_2-q_2 plane is set to zero (to zero the unwanted low order harmonics), activated space vectors from the second plane generate harmonic flux trajectories. Based on Fig. 7.1d and order of the space vectors during the first half of the switching period (Fig. 7.2), generated trajectories can be easily understood. During the sub-interval (0 - t_1), since there is zero reference space vector in the d_2-q_2 plane and zero space vector ($\bar{v}_0$) is applied, there is not any error voltage created in the second plane, and harmonic flux stays in the origin. In the next sub-interval (t_1 - t_2) medium space vector ($\bar{v}_{am}$) is applied and due to the zero reference space vector, error voltage is present and trajectory is generated which pulls the harmonic flux in the direction of the activated active space vector. By analysing remaining sub-intervals (t_2 - t_6) and the applied space vectors one establishes the rest of the trajectory in Fig. 7.3. It can be seen that by the middle of the switching period (t_6) harmonic flux returns again to the origin of the d_2-q_2 plane.
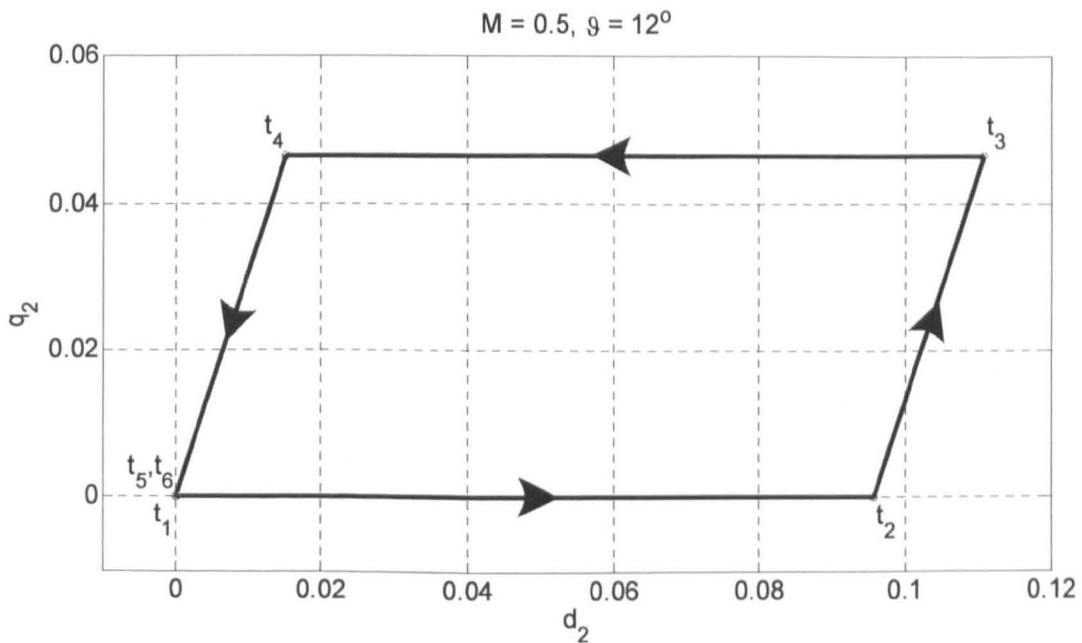
Fig. 7.3: Normalised harmonic flux trajectory in the d_2-q_2 plane during the first half of the switching period.

To further illustrate harmonic flux trajectories in the second plane, a set of simulations has been carried out for several values of the input reference space vector. The obtained trajectories are presented as multiple plots where the value of the modulation index is kept the same and angular position of the reference space vectors is changed stepwise. As it can be seen from Fig. 7.4, generated trajectories are of the same shape in all cases and only the scale changes in accordance with the value of *M*. All the results presented in Fig. 7.4 are valid for all the PWM methods analysed, except of the plot shown in Fig. 7.4d which is valid only for FHIPWM and SVPWM since SPWM cannot reach such a level of dc bus voltage utilisation.
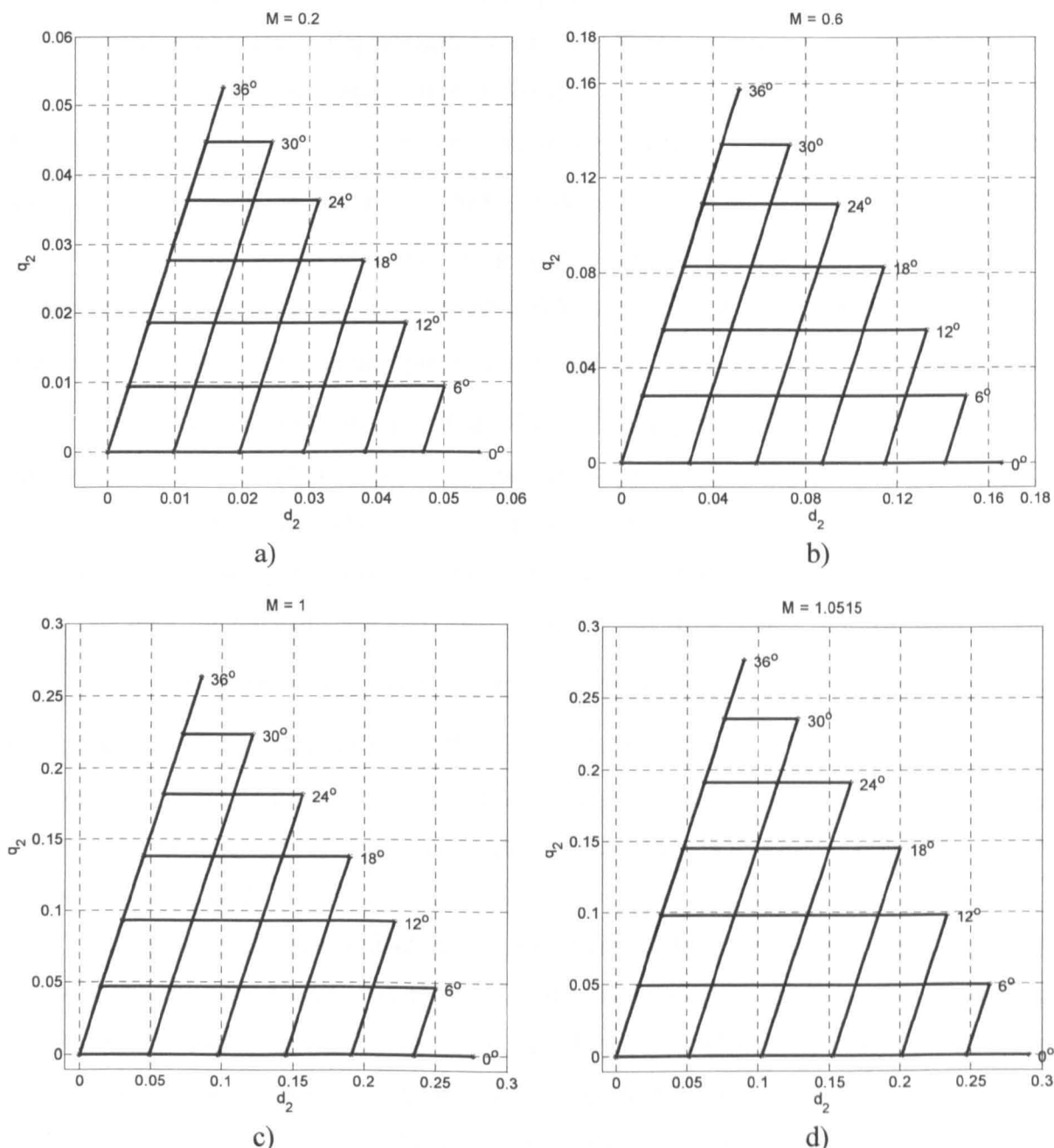
Fig. 7.4: Normalised harmonic flux trajectories in the d_2-q_2 plane during the first half of the switching period for various values of the modulation index: a) *M*=0.2, b) *M*=0.6, c) *M*=1 and d) *M*=1.0515.

7.4.2 HARMONIC FLUX TRAJECTORIES IN THE FIRST PLANE

Harmonic flux trajectories in the d_1-q_1 plane need to be analysed separately for each modulation scheme (it is again enough to consider only the first half of the switching period). Before presenting families of harmonic flux trajectories, one particular case is investigated first for illustration purposes. By evaluating (7.10) over the first half of the switching period, using the duty cycle distributions for SPWM, FHIPWM and SVPWM (Table 7.1), trajectories of harmonic flux are obtained and are illustrated in Figs. 7.5-7.7, respectively. The reference space vector is once more defined in the d_1-q_1 plane with $\bar{v}^* = 0.5e^{j\pi/15}$.

Although trajectories generated by all three PWM schemes appear similar in shape, there are differences associated with the distribution of the zero space vector duty cycles. During the sub-interval $(0 - t_1)$, zero space vector $(\bar{v}_0)$ is applied and since there is a reference space vector defined in the d_1-q_1 plane, error voltage is generated $(\bar{v}_0 - \bar{v}^*)$. Therefore harmonic flux moves in the direction $-\bar{v}^*$ proportionally to the product of the reference space vector and the duty cycle δ_0. Since every PWM scheme is with unique distribution of this duty cycle, position of harmonic flux at the instant defined with t_1 $(\Delta\bar{\lambda}_{dq1}(t_1))$ is different for every scheme. This is also visible in Figs. 7.5-7.7. During the application of the four active space vectors over the interval $(t_1 - t_5)$, generated harmonic flux trajectories are identical for all three schemes, since duty cycles of active space vectors are identical (Table 7.1). However, it should be pointed out here that, although trajectories during this interval are identical, they all have different starting point in the d_1-q_1 plane defined with $\Delta\bar{\lambda}_{dq1}(t_1)$. Therefore, at the instant defined with t_5, obtained trajectory positions $\Delta\bar{\lambda}_{dq1}(t_5)$ are different for every method. Finally, application of the zero space vector $(\bar{v}_{31})$ during the sub-interval $(t_5 - t_6)$ returns the harmonic flux to the origin of the d_1-q_1 plane. Trajectories during the second half of the switching period can be obtained by evaluating (7.10) in the reversed order than the one just explained.

Appearance of these trajectories is significantly different than in the case of three-phase PWM methods where, due to the use of only two active space vector per switching period, triangular-like trajectories are generated [Kolar et al (1990b), Blasko (1997), Hava et al (1999)]. Yet, like in the three-phase case, different distribution of the zero space vector duty cycles has influence on the shape of the generated trajectories. It can be seen that for a certain value of the reference space vector and by changing the distribution of the total zero space vector duty cycle between two zero space vectors, the common part of trajectories for

all schemes during the interval (t_1 - t_5) will slide along the line defined with the angular position of the reference space vector (line in between t_1 and t_5 in Figs. 7.5-7.7). This has an effect on the output current ripple as will be demonstrated shortly.
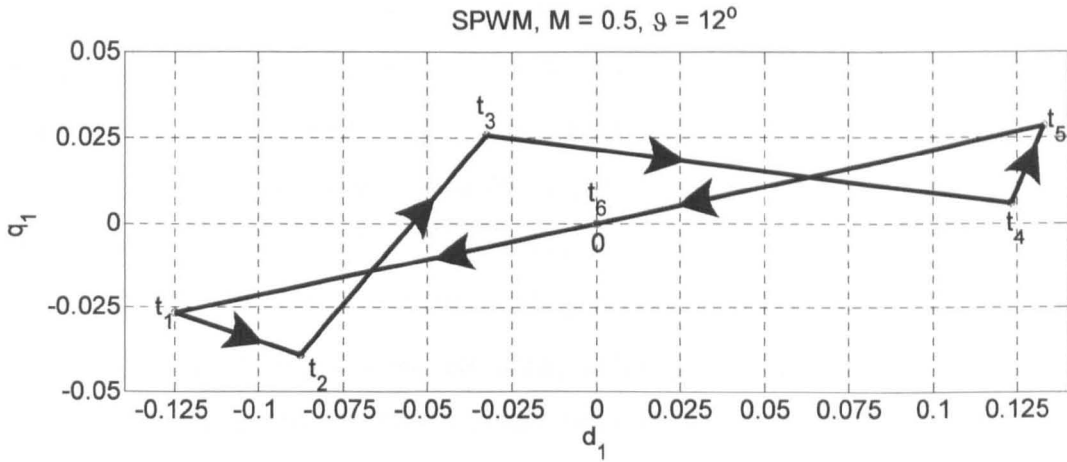

Fig. 7.5: SPWM normalised harmonic flux trajectory in the d_1-q_1 plane during the first half of the switching period.
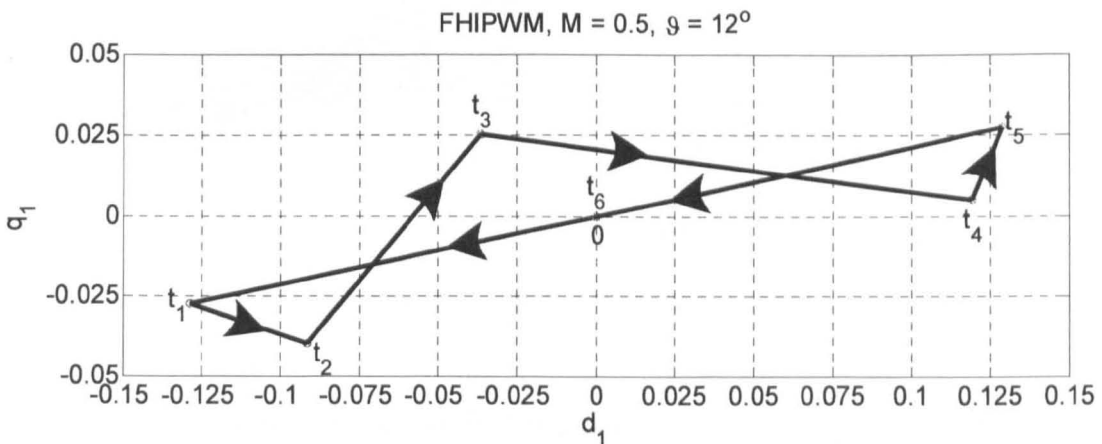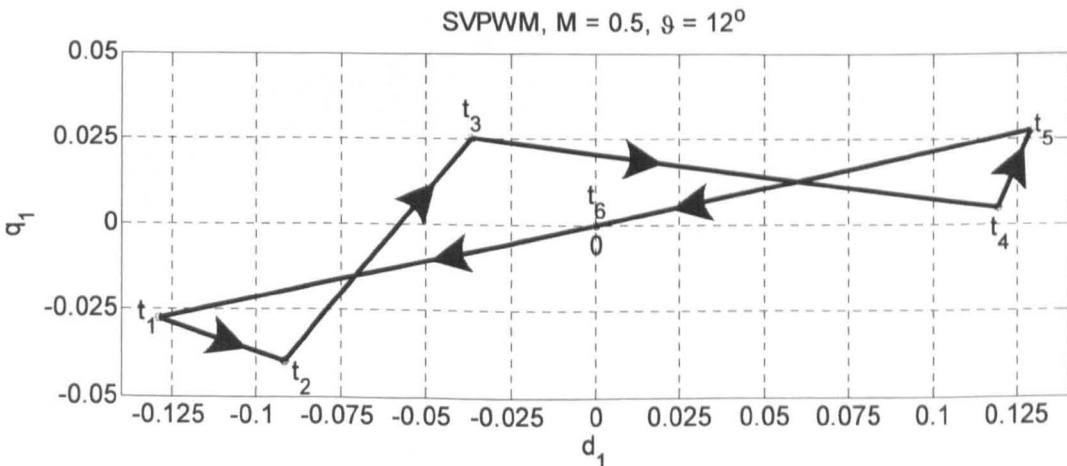

Fig. 7.6: FHIPWM normalised harmonic flux trajectory in the d_1-q_1 plane during the first half of the switching period.
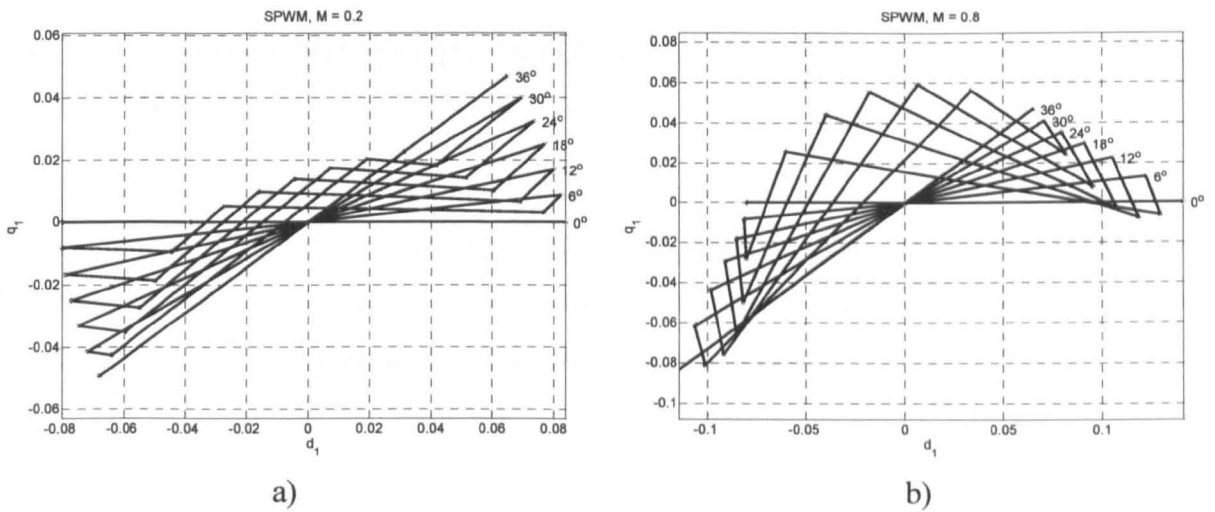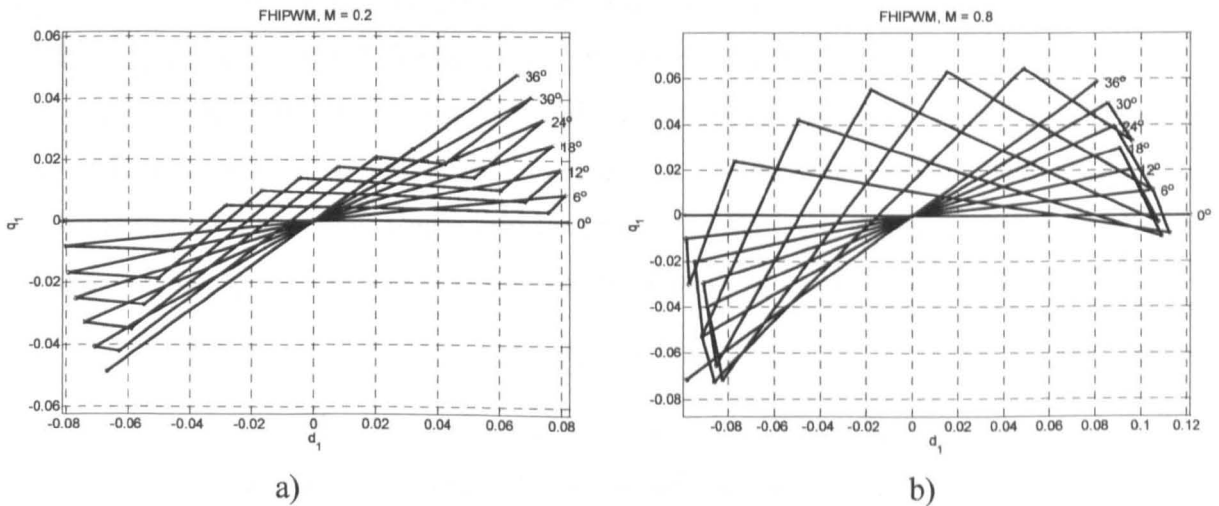

Fig. 7.7: SVPWM normalised harmonic flux trajectory in the d_1-q_1 plane during the first half of the switching period.
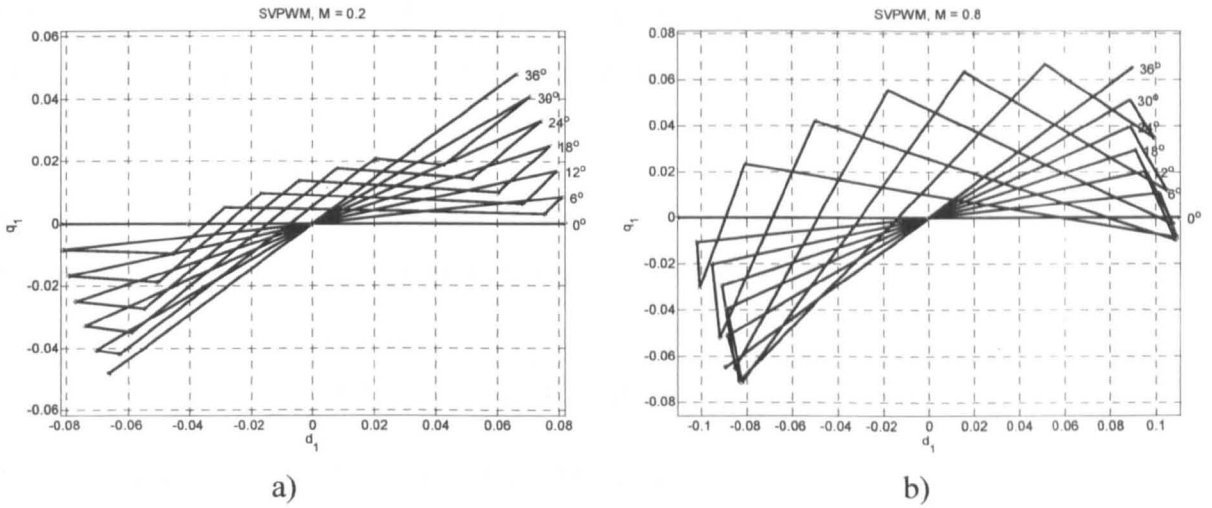
Families of harmonic flux trajectories, generated for two values of the input modulation index (M=0.2 and M=0.8) and several angular positions of the reference space vector, are shown in Figs. 7.8-7.10 for all three PWM methods, respectively. Differences in the obtained trajectories of the analysed PWM schemes are now more pronounced. Different distribution of the zero space vector duty cycles (Fig. 6.10 and Fig. 6.11) causes difference in the harmonic flux movement during sub-interval (0 - t_1), which effectively affects the remaining parts of the trajectories. Thus, by comparing distribution of δ_0 from Fig. 6.11a and the trajectories of SPWM in Fig. 7.8b, it can be seen that as the reference space vector progresses through the sector, increase of δ_0 pulls the harmonic flux more and more away from the origin (for different angular positions), although modulation index is fixed to M=0.8. Similar situation can be observed for the other two considered PWM schemes.

a)   b)

Fig. 7.8: SPWM normalised harmonic flux trajectories in the d_1-q_1 plane during the first half of the switching period for a) M=0.2 and b) M=0.8.

a)   b)

Fig. 7.9: FHIPWM normalised harmonic flux trajectories in the d_1-q_1 plane during the first half of the switching period for a) M=0.2 and b) M=0.8.

a)   b)

Fig. 7.10: SVPWM normalised harmonic flux trajectories in the d_1-q_1 plane during the first half of the switching period for a) $M=0.2$ and b) $M=0.8$.

7.5 MICROSCOPIC (PER-SWITCHING PERIOD) HARMONIC FLUX RMS

The second step involves an analysis of harmonic flux over the switching period (microscopic analysis). As a figure of merit, average squared value of the harmonic flux over the switching period can be used. To take into account all five phases of the load and to obtain per-phase solution, the following integral needs to be calculated:

$$\Delta\lambda^2_{abcde-RMS} = \frac{2}{T_s}\int_0^{\frac{T_s}{2}}\Delta\lambda^2_{abcde}\,dt \tag{7.13}$$

Here $\Delta\lambda^2_{abcde}$ represents phase deviations of the harmonic flux, which are obtained by formulating the sum of the squares of the harmonic flux deviations in each phase and transforming them into two 2-D planes using the decoupling transformation (3.15).

In general, after transforming the phase variables (voltages, currents) not only the mean value but ripple value will also be transformed into complex domain. Thus, considering transformation of the current ripple into complex domain, or, in particular, squares of phase currents, one has by analogy with the three-phase system [Kolar et al (1990b)]:

$$\left|\Delta\bar{i}_{dq1}\right|^2 + \left|\Delta\bar{i}_{dq2}\right|^2 = \frac{2}{5}[\Delta i_a^2 + \Delta i_b^2 + \Delta i_c^2 + \Delta i_d^2 + \Delta i_e^2] = \frac{2}{5}\Delta i^2_{abcde} \tag{7.14}$$

If complex current ripple components are decomposed into axis components, then it is possible to calculate phase squared value (rms) of the current ripple while staying in the complex planes:

$$\Delta i^2_{abcde} = [\Delta i_a^2 + \Delta i_b^2 + \Delta i_c^2 + \Delta i_d^2 + \Delta i_e^2] = \frac{5}{2}[\left|\Delta\bar{i}_{dq1}\right|^2 + \left|\Delta\bar{i}_{dq2}\right|^2] = \frac{5}{2}[\Delta i_{d1}^2 + \Delta i_{q1}^2 + \Delta i_{d2}^2 + \Delta i_{q2}^2] \tag{7.15}$$

Since current deviation is just different in scale from deviation of harmonic flux (here inductances need to be carefully chosen for scaling), then from (7.15):

$$\Delta \lambda^2_{abcde} = \frac{5}{2}[\Delta \lambda_{d1}^2 + \Delta \lambda_{q1}^2 + \Delta \lambda_{d2}^2 + \Delta \lambda_{q2}^2] \tag{7.16}$$

It should be noted here that all these expressions are actually functions of the time, but this dependency is not explicitly shown for the sake of brevity. Using (7.16) and (7.13) one gets:

$$\Delta \lambda^2_{abcde-RMS} = \frac{5}{2}\frac{2}{T_s} \int_0^{\frac{T_s}{2}} [|\Delta \bar{\lambda}_{dq1}|^2 + |\Delta \bar{\lambda}_{dq2}|^2]dt = \frac{5}{2}\frac{2}{T_s} \int_0^{\frac{T_s}{2}} [\Delta \lambda_{d1}^2 + \Delta \lambda_{q1}^2 + \Delta \lambda_{d2}^2 + \Delta \lambda_{q2}^2]dt \tag{7.17}$$

To evaluate (7.17) over the first half of the switching period, the time dependency of the function under the integral is necessary. However, from the previous step of the analysis, only values of the harmonic flux at the end of every sub-interval are obtained and time-dependent functions, which describe behaviour of the harmonic flux over the sub-intervals, are not defined (such an approach has been used by Hava et al (1999) and has been discarded at the beginning of this analysis). Solution for (7.17) can be obtained in an alternative way, based on the values of the harmonic flux ((7.10) and (7.12)) at the end of every sub-interval.

It is easy to prove that for linear change of harmonic flux (the assumption made in the very beginning and reflected in the obtained harmonic flux trajectories), instead of continuous integration (7.17) over the certain sub-interval (t_{n-1} - t_n), the solution can be obtained directly if the values of harmonic flux are known at the beginning and the end of the sub-interval [Kolar et al (1990b)], according to the following expression (proof is given in Appendix C):

$$\int_{t_{n-1}}^{t_n} \Delta \lambda(t)^2 \, dt = (t_n - t_{n-1})\frac{1}{3}[\Delta \lambda(t_{n-1})^2 + \Delta \lambda(t_{n-1})\Delta \lambda(t_n) + \Delta \lambda(t_n)^2] \tag{7.18}$$

Before applying (7.18), squared harmonic flux integral (7.17) can be separated into several integrals in accordance with the existing sub-intervals:

$$\Delta \lambda^2_{abcde-RMS} = \frac{5}{2}\frac{2}{T_s}
\begin{bmatrix}
\int_0^{t_1} [\Delta \lambda_{d1}^2 + \Delta \lambda_{q1}^2 + \Delta \lambda_{d2}^2 + \Delta \lambda_{q2}^2]dt + \int_{t_1}^{t_2} [\Delta \lambda_{d1}^2 + \Delta \lambda_{q1}^2 + \Delta \lambda_{d2}^2 + \Delta \lambda_{q2}^2]dt \\
+ \int_{t_2}^{t_3} [\Delta \lambda_{d1}^2 + \Delta \lambda_{q1}^2 + \Delta \lambda_{d2}^2 + \Delta \lambda_{q2}^2]dt + \int_{t_3}^{t_4} [\Delta \lambda_{d1}^2 + \Delta \lambda_{q1}^2 + \Delta \lambda_{d2}^2 + \Delta \lambda_{q2}^2]dt \\
+ \int_{t_4}^{t_5} [\Delta \lambda_{d1}^2 + \Delta \lambda_{q1}^2 + \Delta \lambda_{d2}^2 + \Delta \lambda_{q2}^2]dt + \int_{t_5}^{\frac{T_s}{2}} [\Delta \lambda_{d1}^2 + \Delta \lambda_{q1}^2 + \Delta \lambda_{d2}^2 + \Delta \lambda_{q2}^2]dt
\end{bmatrix} \tag{7.19}$$

A further partitioning can be done in order to perform analysis independently in the planes:

$$\Delta \lambda^2_{abcde-RMS} = \Delta \lambda^2_{abcde-RMS1} + \Delta \lambda^2_{abcde-RMS2} \tag{7.20}$$

Thus upon application of (7.20), squared harmonic flux in the d_1-q_1 plane can be found from:

$$\Delta\lambda^2{}_{abcde-RMS1} = \frac{5}{2}\frac{2}{T_s}\begin{bmatrix} \int_0^{t_1}[\Delta\lambda_{d1}{}^2 + \Delta\lambda_{q1}{}^2]dt + \int_{t_1}^{t_2}[\Delta\lambda_{d1}{}^2 + \Delta\lambda_{q1}{}^2]dt + \int_{t_2}^{t_3}[\Delta\lambda_{d1}{}^2 + \Delta\lambda_{q1}{}^2]dt \\ + \int_{t_3}^{t_4}[\Delta\lambda_{d1}{}^2 + \Delta\lambda_{q1}{}^2]dt + \int_{t_4}^{t_5}[\Delta\lambda_{d1}{}^2 + \Delta\lambda_{q1}{}^2]dt + \int_{t_5}^{\frac{T_s}{2}}[\Delta\lambda_{d1}{}^2 + \Delta\lambda_{q1}{}^2]dt \end{bmatrix} \quad (7.21)$$

In the d_2-q_2 plane one has:

$$\Delta\lambda^2{}_{abcde-RMS2} = \frac{5}{2}\frac{2}{T_s}\begin{bmatrix} \int_0^{t_1}[\Delta\lambda_{d2}{}^2 + \Delta\lambda_{q2}{}^2]dt + \int_{t_1}^{t_2}[\Delta\lambda_{d2}{}^2 + \Delta\lambda_{q2}{}^2]dt + \int_{t_2}^{t_3}[\Delta\lambda_{d2}{}^2 + \Delta\lambda_{q2}{}^2]dt \\ + \int_{t_3}^{t_4}[\Delta\lambda_{d2}{}^2 + \Delta\lambda_{q2}{}^2]dt + \int_{t_4}^{t_5}[\Delta\lambda_{d2}{}^2 + \Delta\lambda_{q2}{}^2]dt + \int_{t_5}^{\frac{T_s}{2}}[\Delta\lambda_{d2}{}^2 + \Delta\lambda_{q2}{}^2]dt \end{bmatrix} \quad (7.22)$$

Substituting now (7.18) into (7.21) and (7.22) and introducing duty cycles by means of expressions of the form $\delta = (t_n - t_{n-1})\frac{2}{T_s}$, the following is obtained for the d_1-q_1 plane:

$$\Delta\lambda^2{}_{abcde-RMS1} = \frac{5}{6}\begin{bmatrix} \delta_0[\Delta\lambda_{d1}{}^2(t_1) + \Delta\lambda_{q1}{}^2(t_1)] \\ + \delta_{am}[\Delta\lambda_{d1}{}^2(t_1) + \Delta\lambda_{d1}(t_1)\Delta\lambda_{d1}(t_2) + \Delta\lambda_{d1}{}^2(t_2) + \Delta\lambda_{q1}{}^2(t_1) + \Delta\lambda_{q1}(t_1)\Delta\lambda_{q1}(t_2) + \Delta\lambda_{q1}{}^2(t_2)] \\ + \delta_{bl}[\Delta\lambda_{d1}{}^2(t_2) + \Delta\lambda_{d1}(t_2)\Delta\lambda_{d1}(t_3) + \Delta\lambda_{d1}{}^2(t_3) + \Delta\lambda_{q1}{}^2(t_2) + \Delta\lambda_{q1}(t_2)\Delta\lambda_{q1}(t_3) + \Delta\lambda_{q1}{}^2(t_3)] \\ + \delta_{al}[\Delta\lambda_{d1}{}^2(t_3) + \Delta\lambda_{d1}(t_3)\Delta\lambda_{d1}(t_4) + \Delta\lambda_{d1}{}^2(t_4) + \Delta\lambda_{q1}{}^2(t_3) + \Delta\lambda_{q1}(t_3)\Delta\lambda_{q1}(t_4) + \Delta\lambda_{q1}{}^2(t_4)] \\ + \delta_{bm}[\Delta\lambda_{d1}{}^2(t_4) + \Delta\lambda_{d1}(t_4)\Delta\lambda_{d1}(t_5) + \Delta\lambda_{d1}{}^2(t_5) + \Delta\lambda_{q1}{}^2(t_4) + \Delta\lambda_{q1}(t_4)\Delta\lambda_{q1}(t_5) + \Delta\lambda_{q1}{}^2(t_5)] \\ + \delta_{31}[\Delta\lambda_{d1}{}^2(t_5) + \Delta\lambda_{q1}{}^2(t_5)] \end{bmatrix}$$

$$(7.23)$$

The same procedure for the d_2-q_2 plane yields:

$$\Delta\lambda^2{}_{abcde-RMS2} = \frac{5}{6}\begin{bmatrix} \delta_{am}[\Delta\lambda_{d2}{}^2(t_2) + \Delta\lambda_{q2}{}^2(t_2)] \\ + \delta_{bl}[\Delta\lambda_{d2}{}^2(t_2) + \Delta\lambda_{d2}(t_2)\Delta\lambda_{d2}(t_3) + \Delta\lambda_{d2}{}^2(t_3) + \Delta\lambda_{q2}{}^2(t_2) + \Delta\lambda_{q2}(t_2)\Delta\lambda_{q2}(t_3) + \Delta\lambda_{q2}{}^2(t_3)] \\ + \delta_{al}[\Delta\lambda_{d2}{}^2(t_3) + \Delta\lambda_{d2}(t_3)\Delta\lambda_{d2}(t_4) + \Delta\lambda_{d2}{}^2(t_4) + \Delta\lambda_{q2}{}^2(t_3) + \Delta\lambda_{q2}(t_3)\Delta\lambda_{q2}(t_4) + \Delta\lambda_{q2}{}^2(t_4)] \\ + \delta_{bm}[\Delta\lambda_{d2}{}^2(t_4) + \Delta\lambda_{q2}{}^2(t_4)] \end{bmatrix}$$

$$(7.24)$$

Expression (7.23) and (7.24) define squared harmonic flux over the switching period for all three analysed PWM schemes. For numerical evaluation, decomposition of complex values for harmonic flux deviations ((7.10) and (7.12)) into axis components is necessary.

The reference space vector $\vec{v}^* = Me^{j\vartheta} = v_{d1}{}^* + jv_{q1}{}^*$ is decomposed into components, which are defined as:

$$v_{d1}{}^* = M\cos(\vartheta); \qquad v_{q1}{}^* = M\sin(\vartheta) \quad (7.25)$$

The axis components of applied active space vectors in the d_1-q_1 and d_2-q_2 planes are available in Table 7.2. Contents of Table 7.2 fully correspond to the contents of Table 3.1, and the only difference is that an alternative writing style is used, based on trigonometric functions defined with (3.13). Decomposing now (7.10) into axis components and substituting (7.25) and corresponding data from the Table 7.2, one obtains for the axes of the d_1-q_1 plane:

$$\Delta\lambda_{d1}(t_1) = -2M\cos(\vartheta)\delta_0$$

$$\Delta\lambda_{d1}(t_2) = 2\left[\frac{4}{5}\delta_{am} - M\cos(\vartheta)[\delta_0 + \delta_{am}]\right]$$

$$\Delta\lambda_{d1}(t_3) = 2\left[\frac{4}{5}\delta_{am} + \frac{8}{5}L^2\delta_{bl} - M\cos(\vartheta)[\delta_0 + \delta_{am} + \delta_{bl}]\right] \tag{7.26}$$

$$\Delta\lambda_{d1}(t_4) = 2\left[\frac{4}{5}\delta_{am} + \frac{8}{5}L^2\delta_{bl} + \frac{8}{5}L\delta_{al} - M\cos(\vartheta)[\delta_0 + \delta_{am} + \delta_{bl} + \delta_{al}]\right]$$

$$\Delta\lambda_{d1}(t_5) = 2M\cos(\vartheta)\delta_{31}$$

and:

$$\Delta\lambda_{q1}(t_1) = -2M\sin(\vartheta)\delta_0$$

$$\Delta\lambda_{q1}(t_2) = -2M\sin(\vartheta)[\delta_0 + \delta_{am}]$$

$$\Delta\lambda_{q1}(t_3) = 2\left[\frac{8}{5}KL\delta_{bl} - M\sin(\vartheta)[\delta_0 + \delta_{am} + \delta_{bl}]\right] \tag{7.27}$$

$$\Delta\lambda_{q1}(t_4) = 2\left[\frac{8}{5}KL\delta_{bl} - M\sin(\vartheta)[\delta_0 + \delta_{am} + \delta_{bl} + \delta_{al}]\right]$$

$$\Delta\lambda_{q1}(t_5) = 2M\sin(\vartheta)\delta_{31}$$

Similarly, for the d_2-q_2 plane, using data from the Table 7.2, (7.12) gets decomposed into components as:

$$\Delta\lambda_{d2}(t_2) = 2\frac{4}{5}\delta_{am}$$

$$\Delta\lambda_{d2}(t_3) = 2\left[\frac{4}{5}\delta_{am} + \frac{8}{5}L_2{}^2\delta_{bl}\right] \tag{7.28}$$

$$\Delta\lambda_{d2}(t_4) = 2\left[\frac{4}{5}\delta_{am} + \frac{8}{5}L_2{}^2\delta_{bl} - \frac{8}{5}L_2\delta_{al}\right]$$

and:

$$\Delta\lambda_{q2}(t_3) = 2\frac{8}{5}K_2L_2\delta_{bl}$$

$$\Delta\lambda_{q2}(t_4) = 2\frac{8}{5}K_2L_2\delta_{bl} \tag{7.29}$$

In the set of expressions (7.26)-(7.29) only non-zero values are shown since they will directly contribute to the value of the squared harmonic flux. With all the parameters defined, numerical evaluation of the squared harmonic flux is done using MATLAB. Again, since the second plane characteristic is the same for all three PWM schemes (it can be seen from (7.28) and (7.29) that there is no dependency on the zero space vector duty cycles), this is analysed first.

7.5.1   SQUARED HARMONIC FLUX IN THE SECOND PLANE

Since $\Delta\lambda_{q2}(t_2) = 0$, (7.24) can be written in a slightly more compact form:

$$
\Delta\lambda^2_{abcde-RMS2} = \frac{5}{6}\begin{bmatrix} \delta_{am}[\Delta\lambda_{d2}{}^2(t_2)] \\ + \delta_{bl}[\Delta\lambda_{d2}{}^2(t_2) + \Delta\lambda_{d2}(t_2)\Delta\lambda_{d2}(t_3) + \Delta\lambda_{d2}{}^2(t_3) + \Delta\lambda_{q2}{}^2(t_3)] \\ + \delta_{al}[\Delta\lambda_{d2}{}^2(t_3) + \Delta\lambda_{d2}(t_3)\Delta\lambda_{d2}(t_4) + \Delta\lambda_{d2}{}^2(t_4) + \Delta\lambda_{q2}{}^2(t_3) + \Delta\lambda_{q2}(t_3)\Delta\lambda_{q2}(t_4) + \Delta\lambda_{q2}{}^2(t_4)] \\ + \delta_{bm}[\Delta\lambda_{d2}{}^2(t_4) + \Delta\lambda_{q2}{}^2(t_4)] \end{bmatrix}
$$

$$(7.30)$$

Evaluation is performed over the whole first sector for all possible values of the reference space vector. Thus a 3-D plot is obtained, which is shown in Fig. 7.11. It can be seen that, with an increase of the modulation index, squared value of the harmonic flux in the second plane increases as well. Thus the contribution of the harmonic flux from the second plane to the current ripple (obtained after scaling with the corresponding inductance) becomes more significant as the modulation index increases. The plot is given for values of the modulation index all the way up to $M=1.0515$, which is valid for the FHIPWM and SVPWM, while characteristic for the SPWM finishes at $M=1$. While the 3-D plot presents the complete solution for (7.30), it is hard to observe the angular position dependency of the squared harmonic flux over the first sector, since these variations are relatively small, compared to the effect of increase of the modulation index, which is dominant.
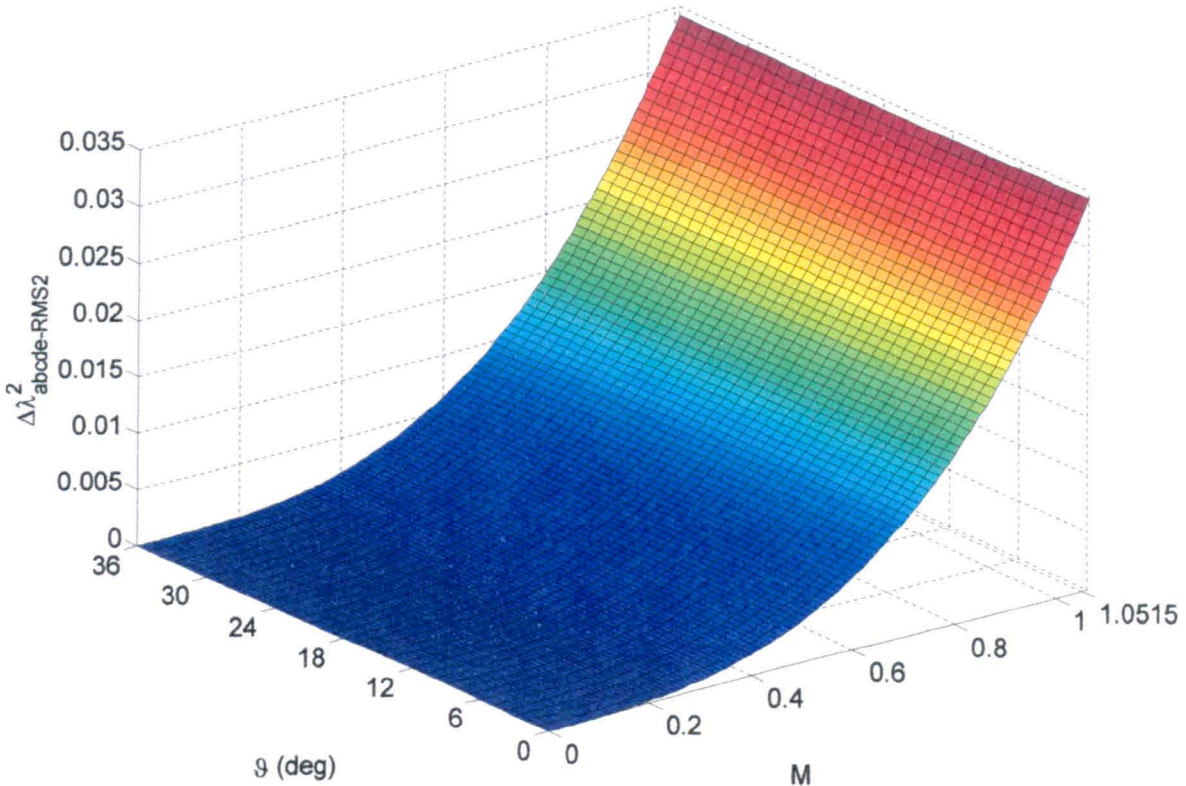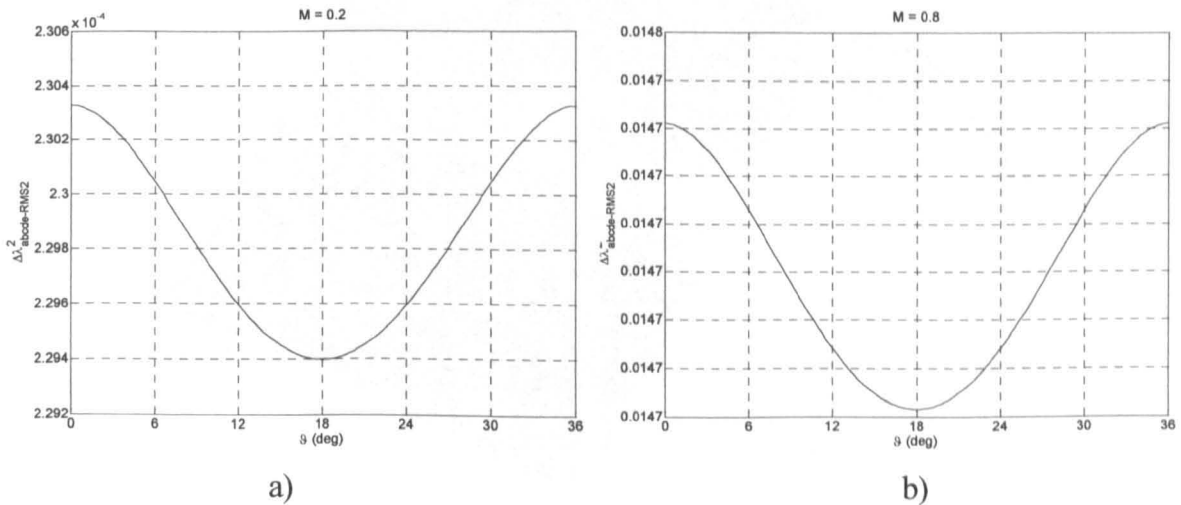

Fig. 7.11: Squared harmonic flux in the d_2-q_2 plane (the same for all PWM schemes).

Additional plots are therefore generated (Fig. 7.12) from where the reference position dependency of the squared harmonic flux is clearly visible. Thus, it can be observed that the value of the squared harmonic flux is the lowest in the middle of the sector, and with higher values at the beginning and at the end of the sector. Yet these variations are relatively small (note the Y-axis scale in Fig. 7.12b), especially for higher values of the modulation index. At the same time, squared harmonic flux is symmetrical with regard to the middle of the sector. This is a consequence of the shape of the trajectories of the harmonic flux in the second plane (Fig. 7.4), from where also certain symmetry with regard to the middle of the sector can be observed. Thus trajectories obtained for the reference space vector at angular position of 6° are similar to those at 30°, while situation at 12° is similar to the one at 24°. If one thinks about the surfaces enclosed by harmonic flux movement (Fig. 7.4) in the d_2-q_2 plane (for a particular angular position) as being solid objects with their own centres of mass, then certain analogy with the shape of the squared harmonic flux over the sector can be established.

If one considers movement of the centre of mass through the first sector, then it can be concluded that the minimum distance from the origin will appear in the middle of the sector. At the beginning and at the end of the sector the distance of the centre of mass of the imaginary solid object from the origin of the d_2-q_2 plane will be the longest. It is possible to establish deeper analogy with the concepts from the mechanics related to minimisation of the moment of inertia [Kolar et al (1990b)], but such an analysis is beyond the scope of the thesis.

Due to the zero reference space vector imposed in the second plane and the fact that it is realised only by means of active space vectors, there is no option to improve the squared harmonic flux in the second plane. The only degree of freedom (zero space vector duty cycles) does not have any impact on the harmonic flux in the d_2-q_2 plane.


a)   b)

Fig. 7.12: Angular position dependence of the squared harmonic flux in the d_2-q_2 plane for a) M=0.2 and b) M=0.8.
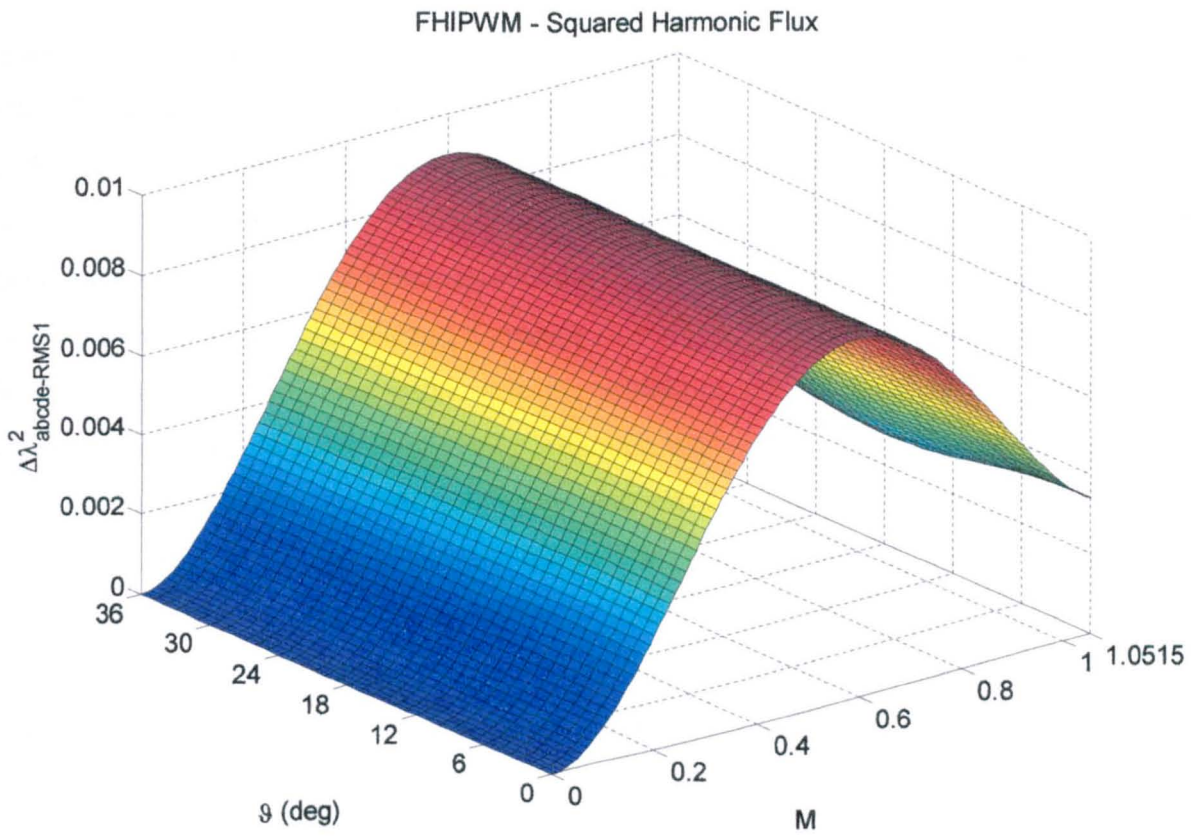
7.5.2   SQUARED HARMONIC FLUX IN THE FIRST PLANE

To obtain characteristics of the squared harmonic flux in the d_1-q_1 plane, (7.23) needs to be numerically evaluated, independently, for all three PWM schemes. The results are presented as 3-D plots separately for all three analysed PWM schemes in Figs. 7.13-7.15, respectively. Squared harmonic flux characteristics in the d_1-q_1 plane appear very similar to all three PWM schemes. In contrast to the common characteristic obtained in the d_2-q_2 plane (Fig. 7.11), dependence of the squared harmonic flux on the modulation index in the d_1-q_1 plane is completely different. Thus in the beginning squared harmonic flux increases with the increase of the modulation index and the maximum appears around M=0.6. With a further increase of the modulation index (up to M=1 for SPWM and up to M=1.0515 for FHIPWM and SVPWM), all three schemes show decrease in the value of the squared harmonic flux.

However, to perform a direct comparison of the squared harmonic flux of all three PWM schemes based on 3-D plots is not an easy task. Again, influence of the modulation index dominates over the influence of the angular position of the reference space vector and angular dependence is hardly observable. Thus, additional graphs are generated again for several values of the modulation index for all three PWM schemes, and are plotted together in order to investigate and compare angular position dependencies in the d_1-q_1 plane.
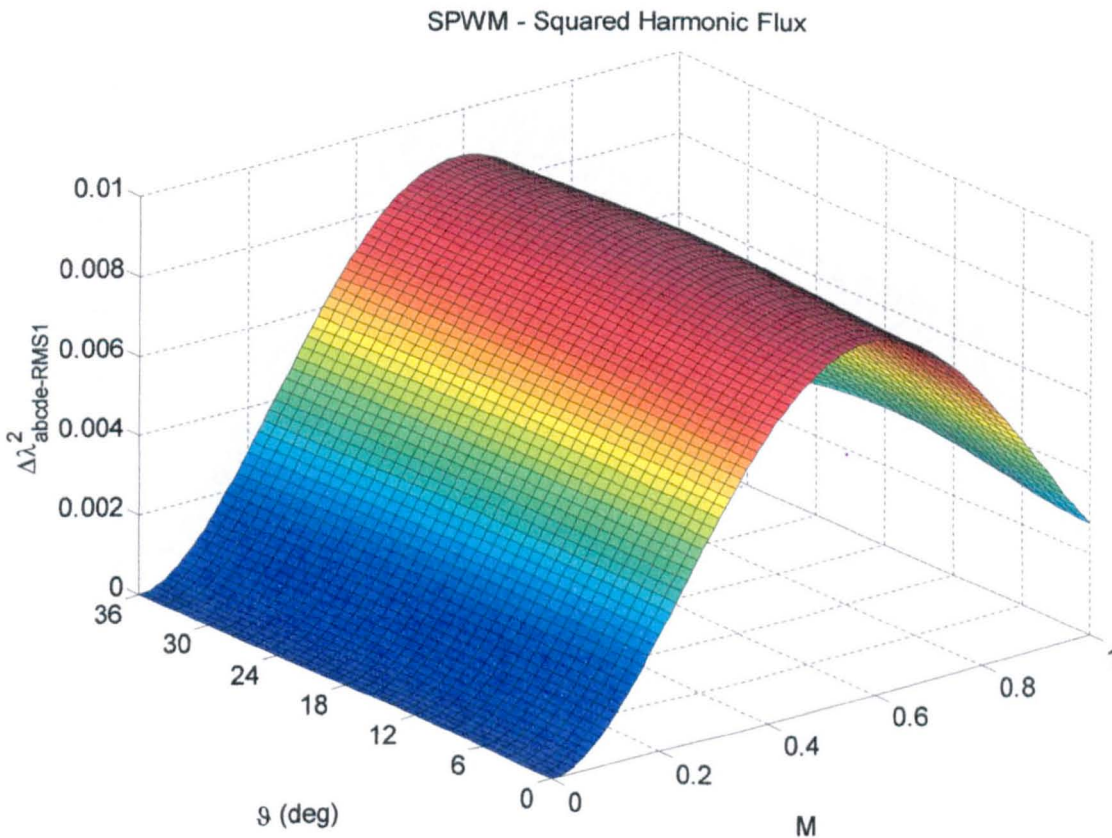
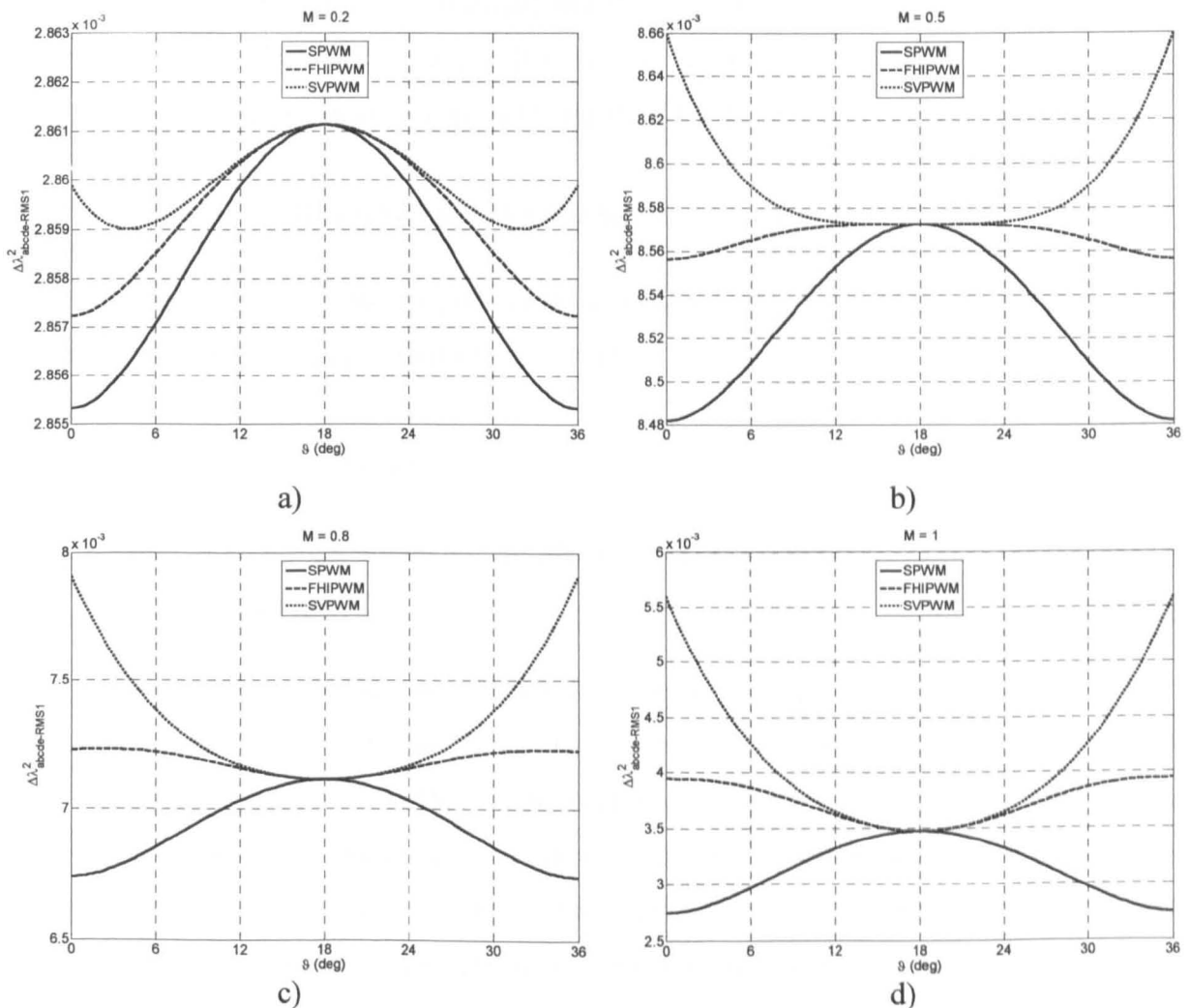**Fig. 7.13:** SPWM squared harmonic flux in the d_1-q_1 plane.

FHIPWM - Squared Harmonic Flux

Fig. 7.14: FHIPWM squared harmonic flux in the d_1-q_1 plane.

SVPWM - Squared Harmonic Flux
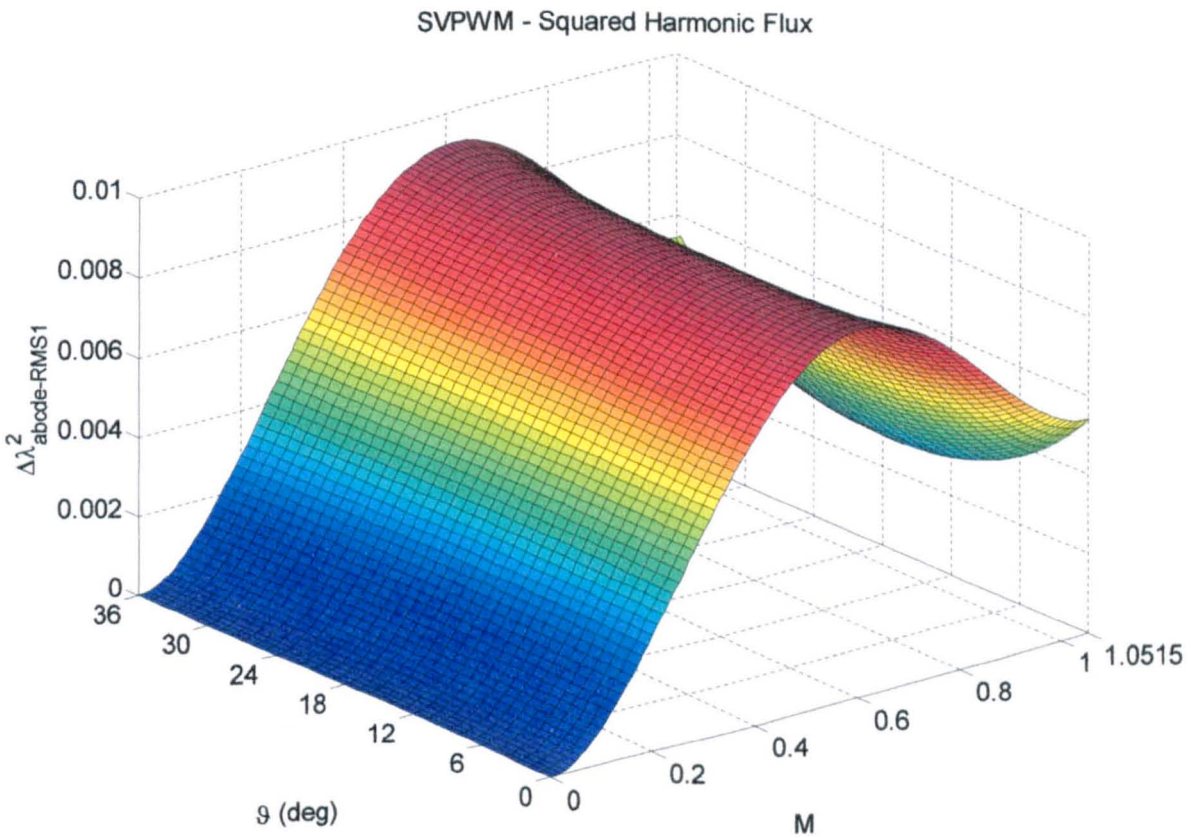
Fig. 7.15: SVPWM squared harmonic flux in the d_1-q_1 plane.

The results are shown in Fig. 7.16 from where it can be seen that SPWM (solid line) squared harmonic flux is the lowest among the three analysed PWM schemes. At the same time, the nature of the angular dependence does not change with an increase of the modulation index and maximum value always occurs in the middle of the sector. SVPWM (dotted line) exhibits the worst (highest) squared harmonic flux, having at the same time variations in the shape of the space dependency. Thus, for the higher values of the modulation index, the maximum of the squared harmonic flux occurs at the beginning and at the end of the sector, while the minimal value is in the middle of the sector. FHIPWM (dashed line) shows similar characteristics as SVPWM, although with slightly lower values, but yet higher than SPWM. Since these plots are nothing else but slices of the 3-D plots shown in Figs. 7.13-7.15 for certain value of the modulation index, it is clear that SPWM squared harmonic flux (Fig. 7.13) is lower than the one obtained with FHIPWM and SVPWM over the whole range of the modulation index. This indicates that the current ripple rms will be the lowest for the SPWM, which is an entirely different situation compared to the three-phase PWM schemes.

Fig. 7.16: Angular position dependencies of the squared harmonic flux in the d_1-q_1 plane for a) M=0.2, b) M=0.5 c) M=0.8, and d) M=1.

7.6 MACROSCOPIC (PER-FUNDAMENTAL PERIOD) HARMONIC FLUX RMS

As the third step of the analysis presented here and based on the complex approach, squared harmonic flux, obtained so far for each method, needs to be evaluated over the fundamental period (macroscopic analysis) in order to obtain a closed-form solution. Due to the symmetry in the five-phase system, the first sector is again sufficient for the analysis and one needs to find solution for the following integral:

$$\Delta\lambda^2_{abcde-RMSF} = \frac{5}{\pi}\int_0^{\frac{\pi}{5}} \Delta\lambda^2_{abcde-RMS}\, d\vartheta \qquad (7.31)$$

This can again be performed independently for each plane, by separating (7.31) as:

$$\Delta\lambda^2_{abcde-RMSF} = \frac{5}{\pi}\int_0^{\frac{\pi}{5}} \Delta\lambda^2_{abcde-RMS1}\, d\vartheta + \frac{5}{\pi}\int_0^{\frac{\pi}{5}} \Delta\lambda^2_{abcde-RMS2}\, d\vartheta \qquad (7.32)$$

As a result of this integration, polynomial functions of the modulation index can be obtained for each method, which are known as harmonic distortion factor (HDF) [Holmes and Lipo (2003)]. Thus the same notion is used here and HDF for the second plane is determined first.

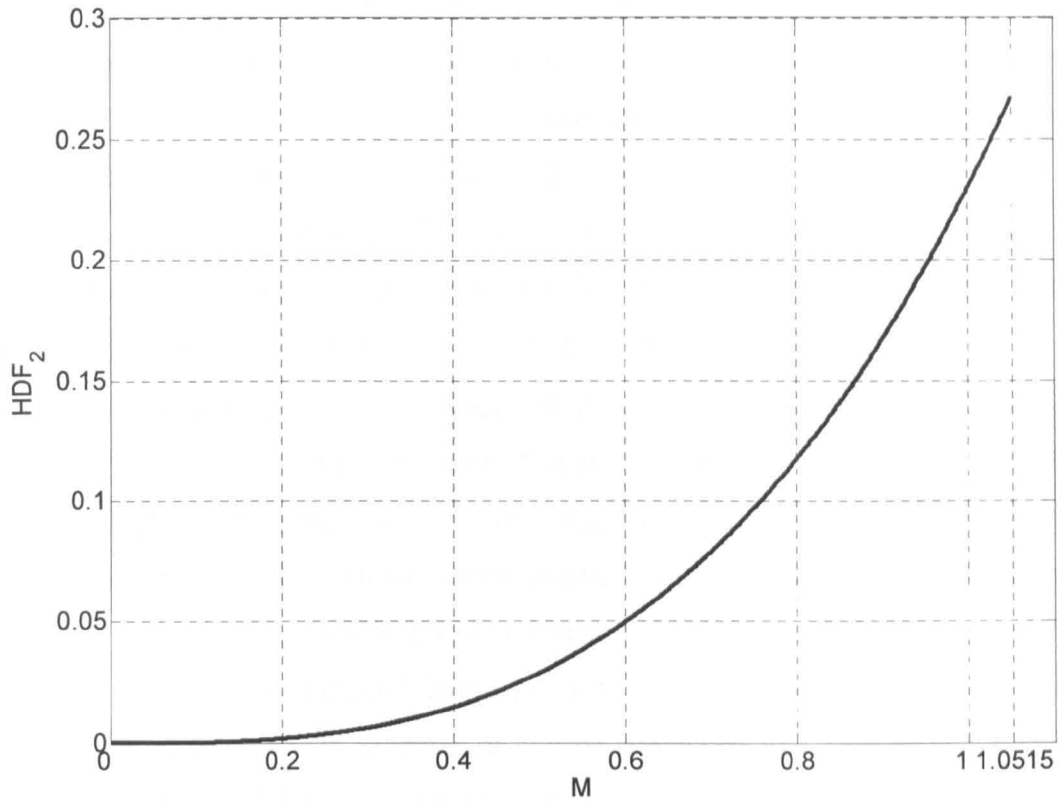### 7.6.1 HARMONIC DISTORTION FACTOR IN THE SECOND PLANE

Common HDF in the second plane is obtained after solving the following integral (function under the integral is defined with (7.30)):

$$HDF_2 = \frac{5}{\pi}\int_0^{\frac{\pi}{5}} \Delta\lambda^2_{abcde-RMS2}\, d\vartheta \qquad (7.33)$$

After some tedious manipulations, the following solution is obtained:

$$HDF_2 = \frac{1}{3}\frac{32}{3\pi}K^3 M^3 \qquad (7.34)$$

The result of plotting (7.34) over the whole range of the achievable modulation index is shown in Fig. 7.17. HDF is plotted all the way up to $M=1.0515$ and this is valid for FHIPWM and SVPWM, while for SPWM the validity is only up to $M=1$. It can be seen that the HDF in the second plane is a continuously increasing function, proportional to the value of the modulation index. Thus the impact of the second plane on the current ripple is more pronounced as the modulation index increases (a result already visible from the 3-D plot) and it is the common feature for all three analysed PWM schemes. Hence, for the purposes of the comparison of five-phase PWM schemes, HDFs in the first plane are sufficient.

Fig. 7.17: HDF in the second plane.

7.6.2 HARMONIC DISTORTION FACTORS IN THE FIRST PLANE

Similar to the second plane, HDF in the first plane can be determined by solving the following integral for each of the PWM schemes:

$$HDF_1 = \frac{5}{\pi} \int_0^{\frac{\pi}{5}} \Delta \lambda^2{}_{abcde-RMS1} d\vartheta \tag{7.35}$$

This involves a substantial amount of tedious manipulation with a number of integrals and, as a result, polynomial functions are obtained for all three PWM schemes. These are functions of the modulation index only, and, when expressed using the trigonometric constants (3.13), are in the form of:

$$HDF_{1-SPWM} = \frac{1}{3}\left[2(K^2 + K_2^2)M^2 - \frac{32}{3\pi}(2K^3 + K_2^3)M^3 + \frac{3}{2}(K^2 + K_2{}^2)M^4 \right] \tag{7.36}$$

$$HDF_{1-FHIPWM} = \frac{1}{3}\left[2(K^2 + K_2^2)M^2 - \frac{32}{3\pi}(2K^3 + K_2^3)M^3 + \frac{3}{2}(K^2 + K_2{}^2)(1 + 2b^2)M^4 \right] \tag{7.37}$$

$$HDF_{1-SVPWM} = \frac{1}{3}\left[\begin{array}{l} 2(K^2 + K_2{}^2)M^2 - \frac{32}{3\pi}(2K^3 + K_2^3)M^3 \\ \\ + \frac{3}{2}(K^2 + K_2{}^2)\left[\frac{7-\sqrt{5}}{4} - \frac{5}{8}\frac{\sqrt{50-22\sqrt{5}}}{\pi} \right]M^4 \end{array} \right] \tag{7.38}$$

166

It is possible to replace values for trigonometric constants and obtain a more compact solution, however the form of HDFs given with (7.36)-(7.38) will be useful for comparisons with the results obtained from the polygon approach (chapter 8). By comparing the final expressions of all three HDFs, one can notice that coefficients of the solution next to M^2 and M^3 are identical, while the differences occur regarding coefficients next to M^4. Solution for FHIPWM shows an additional dependence on the level of injection of the fifth harmonic, defined with parameter b (which is taken, for plots, as $b = -\sin(\pi/10)/5$).

Plots of HDF functions of all three PWM schemes, obtained for the first plane are given in Fig. 7.18. As can be seen, SPWM shows a better performance compared to the FHIPWM and SVPWM. In the lower region of the modulation index (up to M=0.5) all three PWM schemes show almost identical characteristic. For the values of the modulation index above M=0.5, HDFs diverge and it is visible that the SPWM characteristic is with the lowest value for the same value of the modulation index. Considering that HDF in the second plane is the same for all three PWM schemes, it can be concluded that SPWM yields the lowest current ripple among CPWM schemes (for sinusoidal output voltage generation) for five-phase drives. This is a completely different situation than the one valid for the three-phase PWM schemes, as reported in the literature survey in section 7.2. Before addressing in more detail this issue, the complete solutions for HDFs of all three PWM scheme are determined.
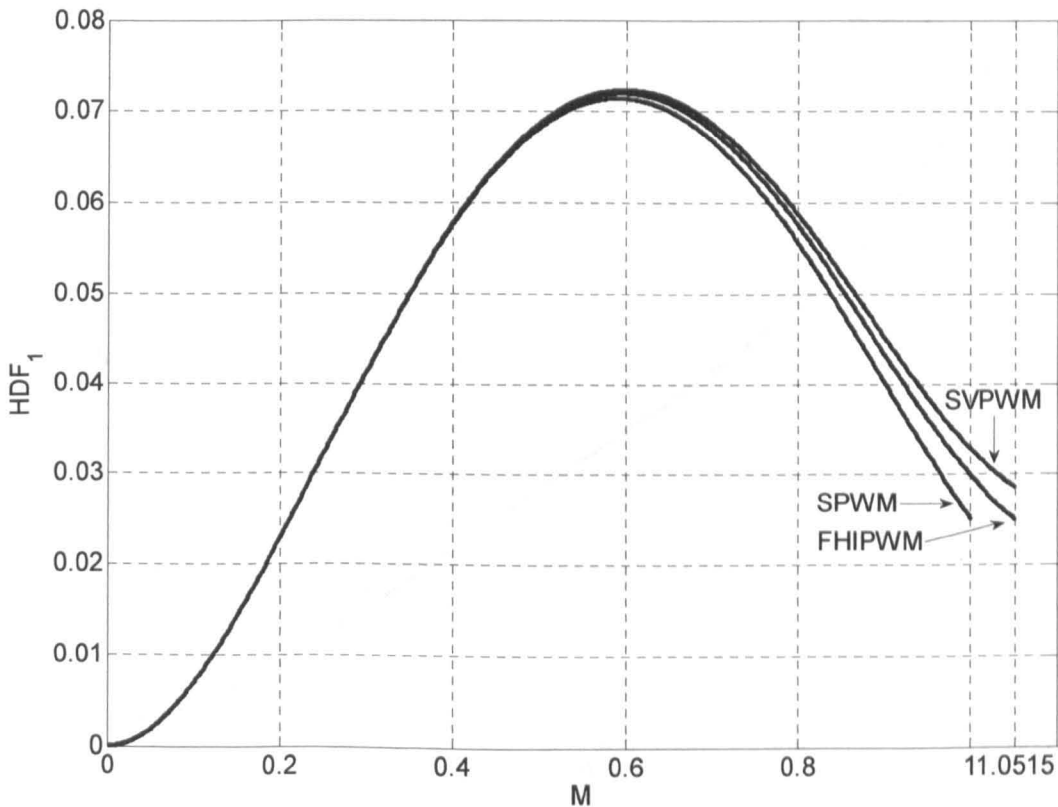

Fig. 7.18: HDF in the first plane.

7.6.3 HARMONIC DISTORTION FACTOR – COMPLETE SOLUTIONS

Since the analysis is based on the concept of harmonic flux, it allows for the complete HDF to be easily obtained for each PWM scheme. It is enough to add the common HDF obtained for the d_2-q_2 plane to the HDFs of each PWM scheme determined in the d_1-q_1 plane. Adding (7.34) to (7.36)-(7.38) changes only the coefficient of M^3 and the next is obtained:

$$HDF_{SPWM} = \frac{1}{3}\left[2(K^2 + K_2^2)M^2 - \frac{32}{3\pi}(K^3 + K_2^3)M^3 + \frac{3}{2}(K^2 + K_2^2)M^4 \right] \tag{7.39}$$

$$HDF_{FHIPWM} = \frac{1}{3}\left[2(K^2 + K_2^2)M^2 - \frac{32}{3\pi}(K^3 + K_2^3)M^3 + \frac{3}{2}(K^2 + K_2^2)(1 + 2b^2)M^4 \right] \tag{7.40}$$

$$HDF_{SVPWM} = \frac{1}{3}\left[\begin{array}{l} 2(K^2 + K_2^2)M^2 - \frac{32}{3\pi}(K^3 + K_2^3)M^3 \\[2mm] \quad + \frac{3}{2}(K^2 + K_2^2)\left[\frac{7 - \sqrt{5}}{4} - \frac{5}{8}\frac{\sqrt{50 - 22\sqrt{5}}}{\pi} \right]M^4 \end{array} \right] \tag{7.41}$$

The result of plotting the final HDF characteristics is shown in Fig. 7.19. As can be seen, contribution of the second plane dominates (it is visible, by comparing Y-axis scales in Figs. 7.17 and 7.18, that the HDF in the second plane is almost by one order of magnitude higher). The HDFs of the first plane slightly modify the characteristic of the second plane, so that mutual relation among HDFs of each scheme remains as in Fig. 7.18.
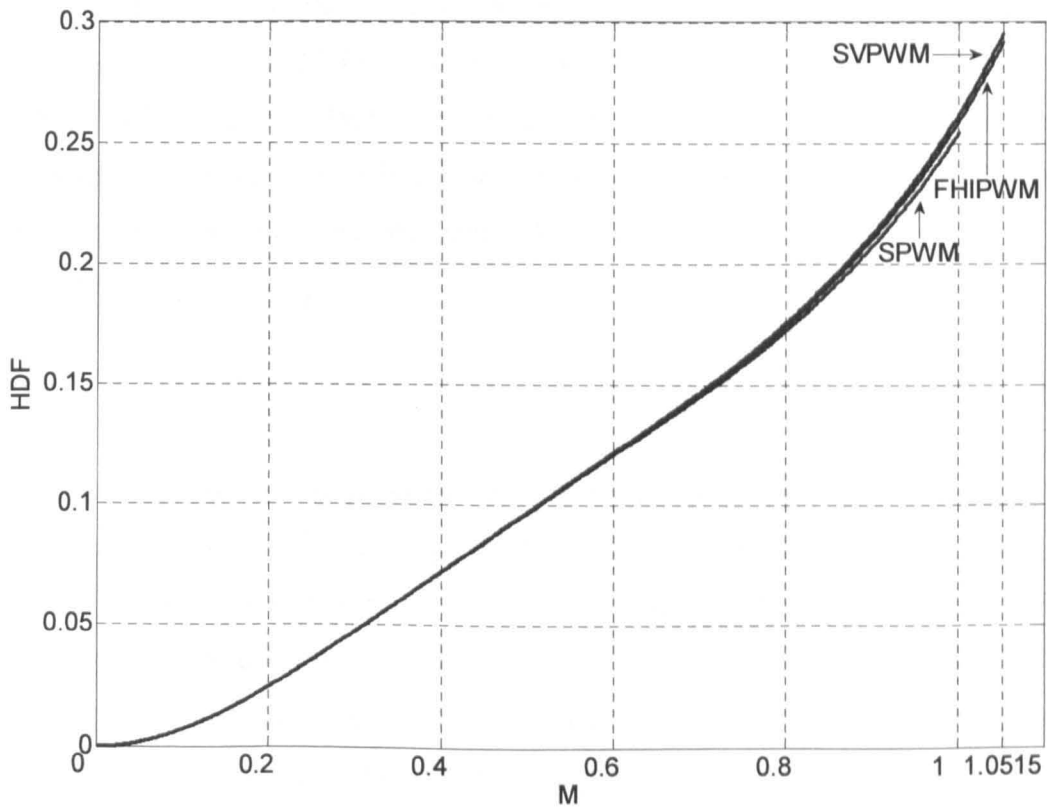

Fig. 7.19: HDF – complete solutions.

168

The final HDFs for each scheme have been obtained based on the harmonic flux concept. To get the current ripple HDF, scaling with corresponding inductances must be included. This requires a careful consideration with regard to the five-phase machine modelling aspects, as it will be demonstrated shortly.

7.7   DISCUSSION OF THE ANALYTICAL RESULTS

It is important to again emphasise the fact that, in the three-phase drives, the injection of the third harmonic can be used to both extend linear region of modulation and improve (minimise) the current ripple rms characteristic (HDF). Thus if the third harmonic is injected with $b = -1/6$, dc bus utilisation is maximised and the current ripple rms is improved compared to the levels offered by three-phase SPWM. However, injection with $b = -1/6$ is not optimal regarding the minimisation of the current ripple rms and it turns out that $b = -1/4$ is the optimal solution in this case. Yet, such an optimisation is accompanied by slightly lower dc bus utilisation (around 3% less) [Kolar et al (1990a), Kolar et al (1990b)].

The amount of injection of the fifth harmonic, used for FHIPWM during the preceding analysis, corresponds to the level defined with (6.20), which was determined as the optimal solution that maximises dc bus utilisation. Following the analogy with the three-phase case, it is natural to explore whether there is any other level of injection of the fifth harmonic that can be used to minimise the HDF in a five-phase system. According to (7.37), parameter b is present in the HDF of the FHIPWM in the d_1-q_1 plane and therefore it has an impact on it. To check if there is any other level of injection that is optimal and can minimise HDF, one needs to find for what b derivative of the obtained HDF is zero:

$$\frac{d(HDF_{1FHIPWM})}{db} = 0 = 2(K^2 + K_2^2)M^4 b \tag{7.42}$$

This is equal to zero only if:

$$b = 0 \tag{7.43}$$

This result is of paramount importance since it effectively means that five-phase CPWM schemes cannot be optimised regarding the HDF, which is effectively the current ripple rms characteristic that defines switching current harmonic losses. Thus, the injection of the fifth harmonic can not be used to improve HDF and bring it below the level offered by the SPWM. This is a completely different situation than the one for the three-phase PWM schemes.

Another important aspect that needs to be carefully addressed is related to the use of appropriate inductances, required to obtain current harmonic HDF from the harmonic flux HDF. Such a characteristic is especially of interest if results obtained for the five-phase case

are to be compared with results for some other phase number. Since harmonic flux is related to the error voltages, it was possible to sum the results obtained in two planes to produce final HDFs for each scheme. To obtain realistic values for the current ripple, per-phase equivalent circuits at switching frequencies of five-phase machines in the d_1-q_1 and d_2-q_2 planes need to be considered. Since the switching frequency (f_s) is assumed to be much higher than the fundamental frequency, only reduced per-phase equivalent schemes are shown in Fig. 7.20 for an induction machine, which are suitable for analysis. It is possible to neglect stator and rotor resistances since $2\pi f_s L_{\gamma s} \gg R_s$ and $2\pi f_s L'_{\gamma r} \gg R_r$. Thus, the equivalent inductance for the d_1-q_1 plane can be determined as:

$$L_{d_1-q_1} = L_\sigma = L_{\gamma s} + \frac{L'_{\gamma r} L_m}{L'_{\gamma r} + L_m} \qquad (7.44)$$

In the d_2-q_2 plane one has:

$$L_{d_2-q_2} = L_{\gamma s} \qquad (7.45)$$

To avoid dealing with two different values of inductances and to simplify further analysis, the following parameter is introduced as the ratio of the equivalent inductances of two planes:

$$\xi = \frac{L_\sigma}{L_{\gamma s}} \qquad (7.46)$$

If the equivalent inductance from the first plane is selected as a base value, then normalisation factor for the current ripple takes the form:

$$\Delta i_N = \frac{\Delta \lambda_N}{L_\sigma} = \frac{V_{dc} T_s}{8 L_\sigma} \qquad (7.47)$$

Using (7.47) and the results for the harmonic flux HDFs of each scheme, it is possible to obtain normalised current HDF for the harmonic current as:

$$HDF = HDF_1 + \xi^2 HDF_2 \qquad (7.48)$$

This can be easily evaluated based on the obtained results for HDFs (7.34), (7.36)-(7.38).
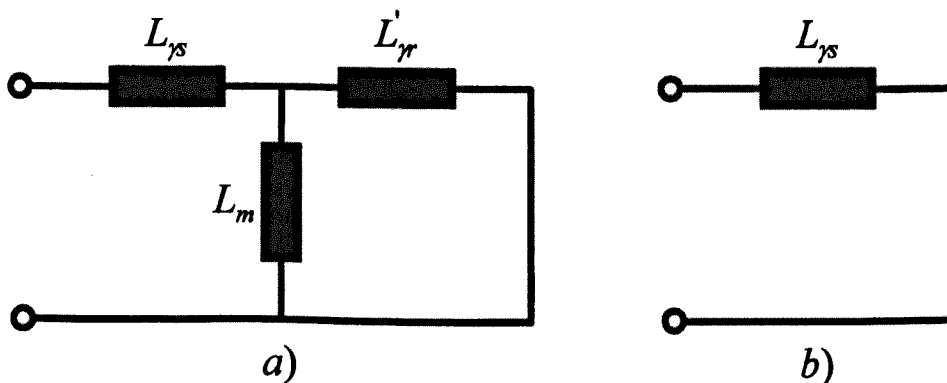

Fig. 7.20: Equivalent circuit of a five-phase induction machine in a) d_1-q_1 and b) d_2-q_2 plane.

Obviously, the parameter ξ plays an important role and influences the final current HDF. Based on Fig. 7.20, value of $\xi = 2$ can be taken as a pretty good approximation for the ratio of equivalent inductances for the induction machines. With this value selected, plots for all three current HDFs are obtained as shown in Fig. 7.21. A significant increase in the values of the HDFs is obvious, compared to results in Fig. 7.19, due to the smaller (realistic) value of the considered inductance in the second plane. However, differences between current HDFs of each scheme are practically undetectable.

Thus, although theoretically the output current ripple rms of a five-phase drive cannot be optimised by the injection of a proper zero-sequence signal, deterioration caused by the injection of the zero-sequence signal is relatively small. Considering that injection offers an increase in the dc bus utilisation of 5.15%, this advantage is very likely to prevail over the use of SPWM, which minimises the current ripple rms characteristic. Thus, the SVPWM, which theoretically has the worst HDF, is still a viable candidate for use in the five-phase induction motor drives.

To further verify theoretical results, characteristics of the output current ripple of a five-phase system are investigated by means of simulation using MATLAB model, as well as experimentally on a five-phase drive.
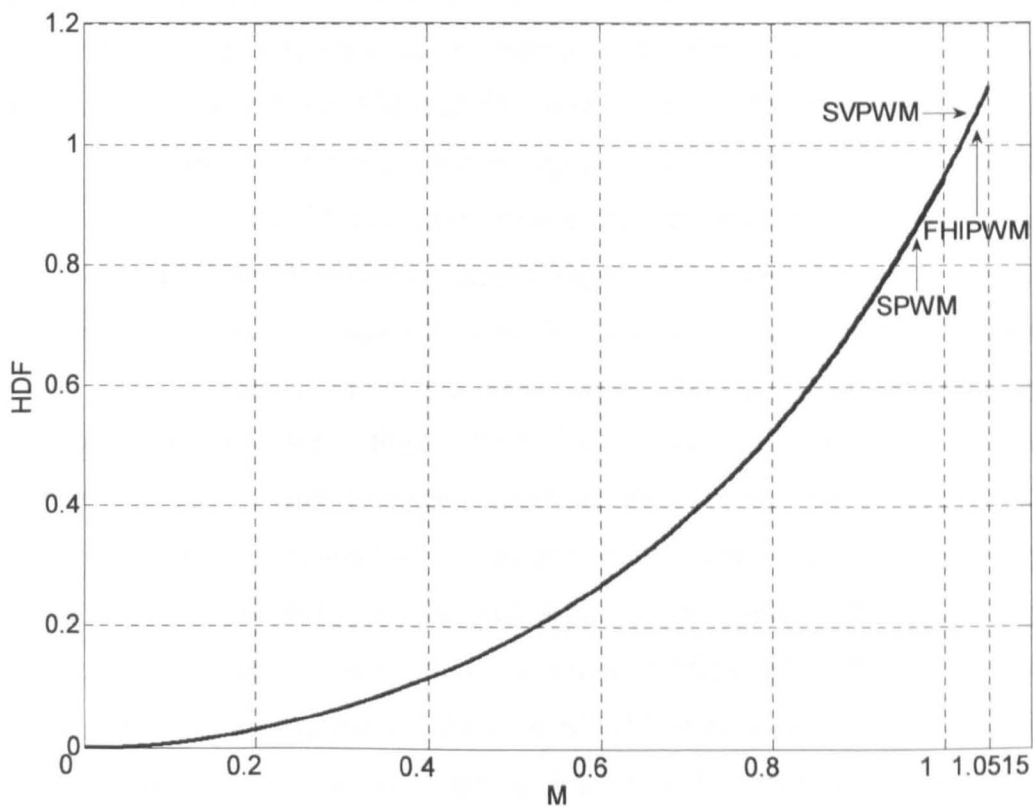

Fig. 7.21: Current HDF – complete solutions for $\xi = 2$.

7.8   SIMULATION AND EXPERIMENTAL RESULTS

To investigate differences in the current ripple of the analysed PWM schemes in some other way than analytically, both simulations and experiments are conducted. The results are presented in Figs. 7.22-7.27, for all three PWM schemes, respectively.

Simulation results (Figs. 7.22-7.24) show reference and switched voltage of one phase, from where error voltages are obtained and applied to a highly inductive (*R-L*) load in order to obtain the current ripple. In the simulations, fundamental frequency is set to 50 Hz, *M*=0.8 and switching frequency is lowered to 1 kHz, for illustration purposes. Shape of the current ripple is almost the same for all three schemes and eventually it is possible to observe slightly lower peak values with SPWM, compared to the other two schemes. However, a closer inspection of the high frequency portion of the current spectrum (which includes the first five carrier sideband harmonics), reveals that in the case of FHIPWM and SVPWM the spectrum is richer in the sideband harmonics when compared to the SPWM. These harmonics contribute to the total harmonic distortion (THD) and thus confirm theoretical analysis and verify that the SPWM is the optimal method regarding the current ripple.

Experimental results are collected from the star-connected five-phase induction motor (data are given in Appendix B). Switching frequency is set to 5 kHz and the motor operates in the open-loop with *V/f* profile set in such a way to obtain the same operating conditions for each scheme. Thus, since FHIPWM and SVPWM yield 5.15% higher dc bus utilisation, fundamental frequency in the *V/f* profile is adjusted in such a way that all three PWM schemes operate with *M*=1 at 50 Hz. Motor phase current is measured using Tektronix A6302 current probe and HP35665A dynamic signal analyser. Only high frequency portion of the current spectrum is shown. It includes the first three carrier sideband harmonics, obtained by means of 10 times averaging during the measurement. Several operating conditions were investigated and the two shown in Figs. 7.25-7.27 correspond to the operation with *M*=0.8 at 40 Hz and *M*=1 at 50 Hz. High frequency spectrum plots appear very similar to each other and visible differences in magnitudes of various harmonic components are relatively small. Yet, it can be seen that the most pronounced difference are the sideband harmonics around the first (5 kHz) and the second (10 kHz) carrier harmonics. Magnitudes of these harmonics are with slightly lower values around 5 kHz with SPWM than with FHIPWM and SVPWM schemes, while the situation is reversed in the 10 kHz sidebands. Also, the highest magnitudes measured in the spectrum are for the SVPWM, while FHIPWM results are in between SPWM and SVPWM, as predicted analytically.
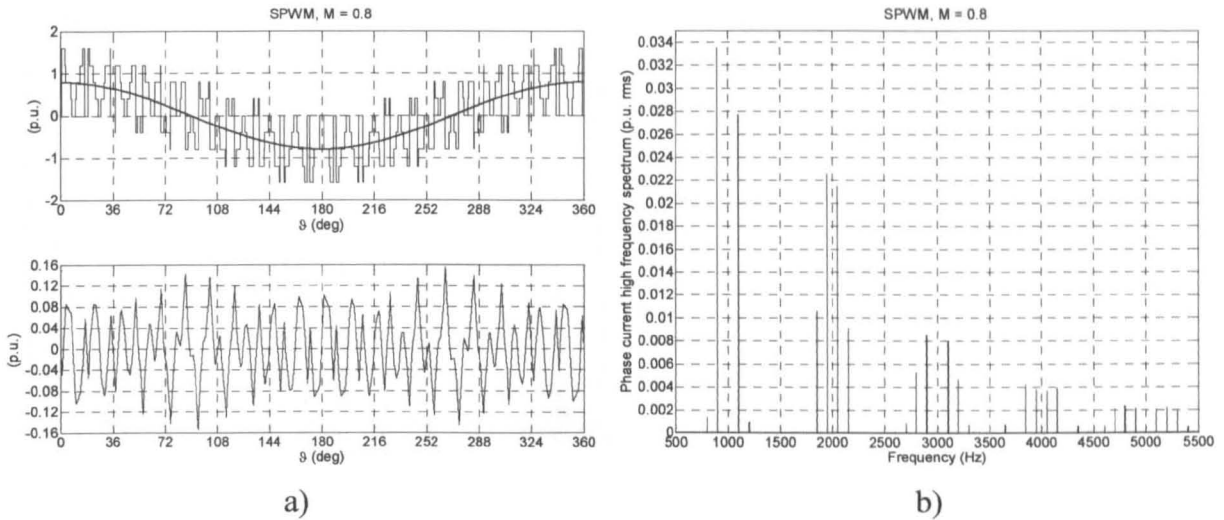
Fig. 7.22: SPWM: a) Simulated reference and switched voltage for one phase of a load (top) and harmonic current ripple (bottom); b) high frequency current spectrum.
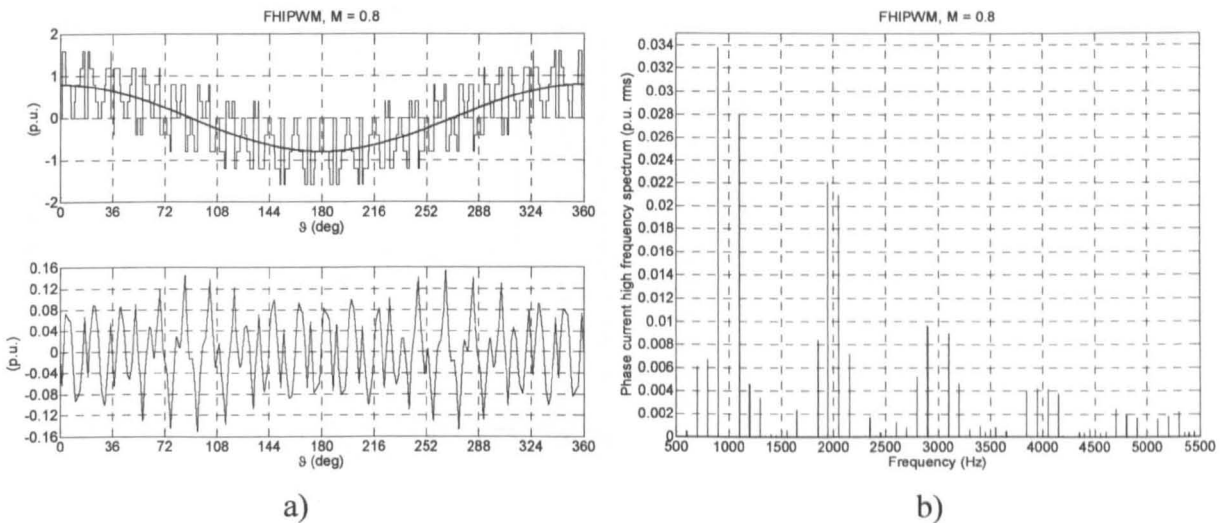
Fig. 7.23: FHIPWM: a) Simulated reference and switched voltage for one phase of a load (top) and harmonic current ripple (bottom); b) high frequency current spectrum.
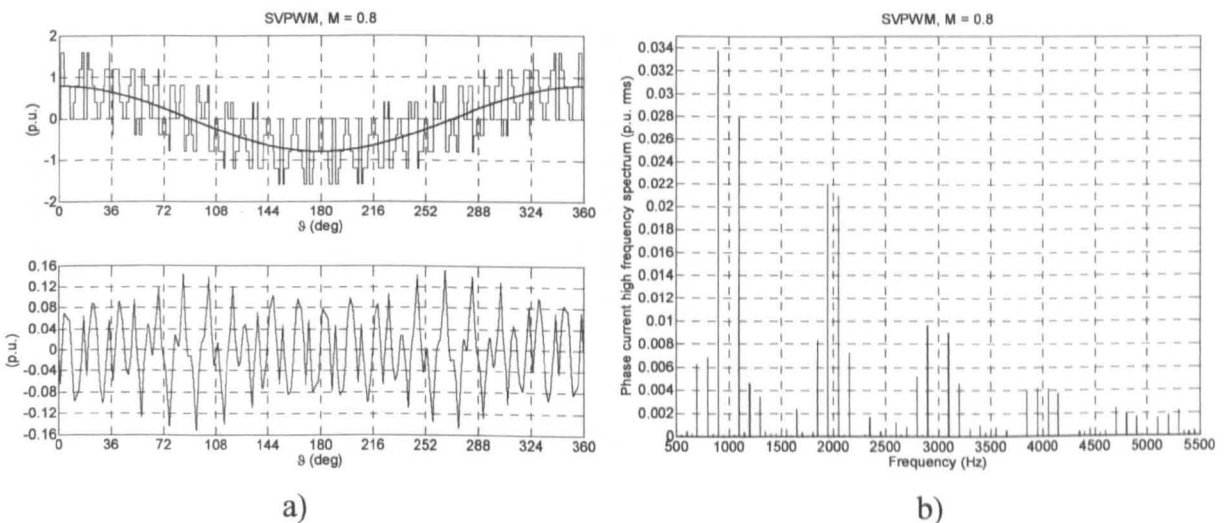
Fig. 7.24: SVPWM: a) Simulated reference and switched voltage for one phase of a load (top) and harmonic current ripple (bottom); b) high frequency current spectrum.
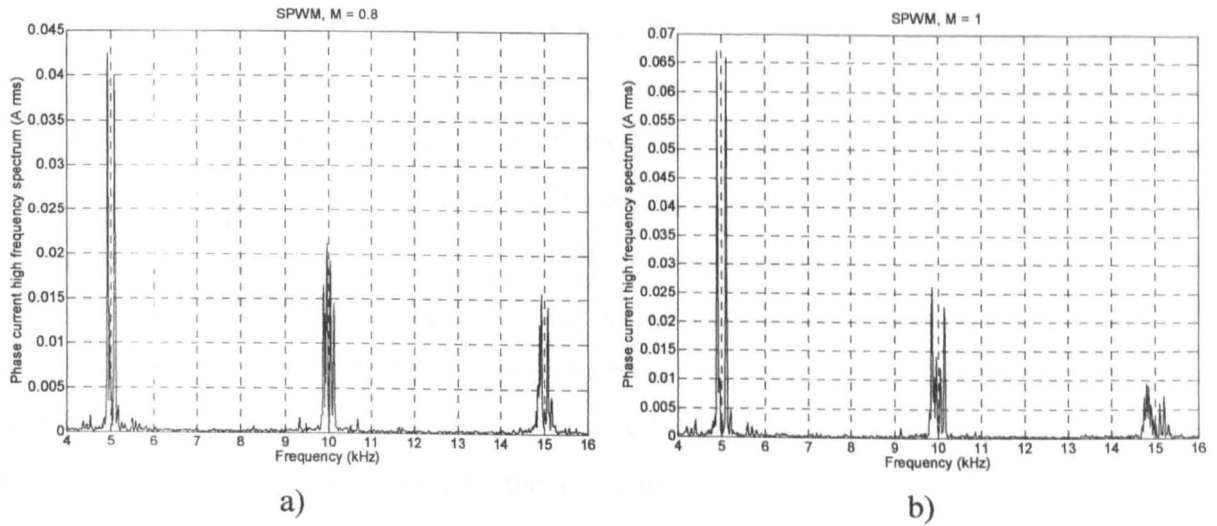
Fig. 7.25: SPWM: Experimentally recorded high frequency current spectrum,
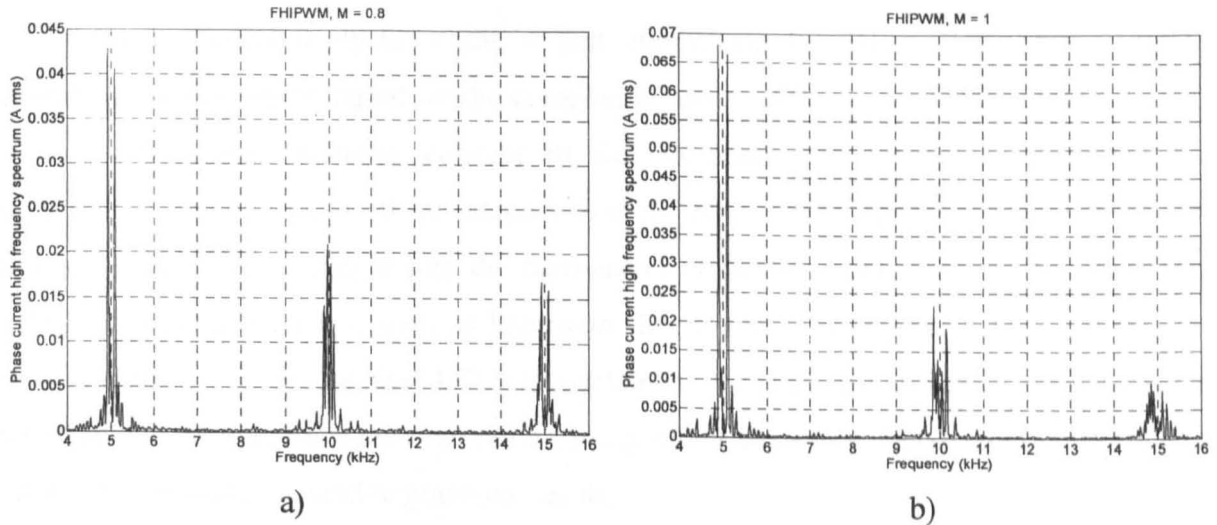a) *M*=0.8 at 40 Hz and, b) *M* = 1 at 50 Hz.

Fig. 7.26: FHIWM: Experimentally recorded high frequency current spectrum,
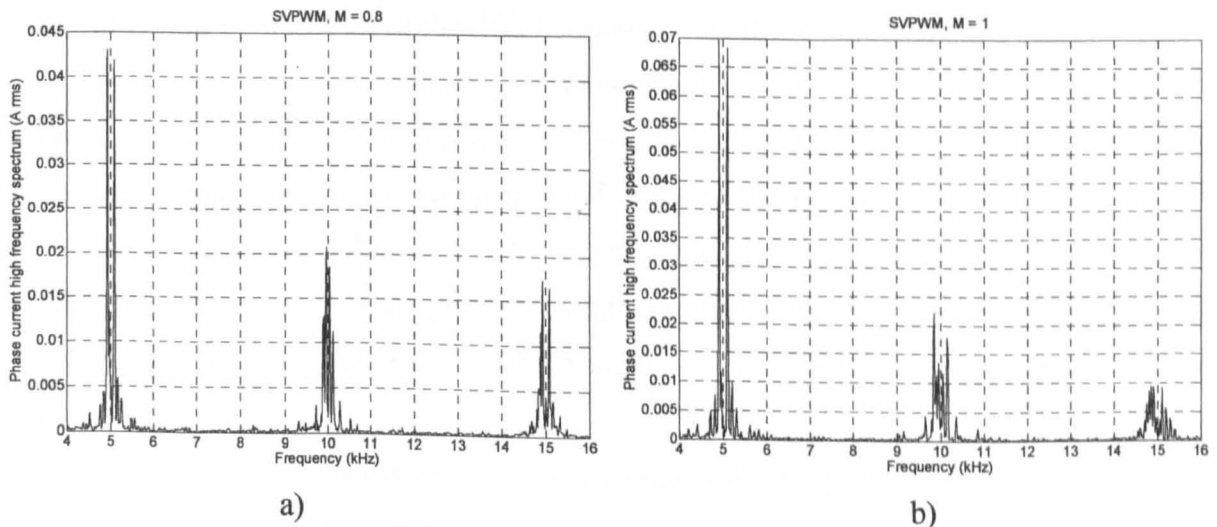a) *M*=0.8 at 40 Hz and, b) *M* = 1 at 50 Hz.

Fig. 7.27: SVPWM: Experimentally recorded high frequency current spectrum,
a) *M*=0.8 at 40 Hz and, b) *M* = 1 at 50 Hz.

Comparison of Figs. 7.22-7.24 with Figs. 7.25-7.27 shows a rather good agreement. However, based on the experimental results, differences in the current ripple of a five phase drive caused by the application of various PWM schemes are likely not to play an important role during selection of a PWM scheme. According to the experimental results, which are shown for the upper range of the modulation index where these differences are more pronounced, variation of the highest harmonic components in the spectrum is less than 3 mA for a fundamental current of 1.2 A (rms). Increased level of dc bus utilisation, offered by FHIPWM and SVPWM, is a feature that is very likely to be of higher importance than the slightly higher current ripple caused by the use of these two schemes, compared to SPWM.

7.9 SUMMARY

The analytical analysis of the output current ripple rms in five-phase drives is presented in this chapter, based on the complex approach. Due to the existence of two 2-D planes in five-phase systems, concept of the harmonic flux is used to mitigate the dependencies on the equivalent inductances in each plane, where current ripple occurs. Such an analysis offers deep insight into the mechanism of current ripple creation and generates various intermediate results, such as harmonic flux trajectories and harmonic flux angular position dependence, before final HDFs are obtained. Although the approach is analytical (a simple analytical solution is the final result), many of the steps of the analysis are numerically evaluated to provide illustrative graphical results.

Continuous SPWM, FHIPWM and SVPWM aimed for sinusoidal output voltage are directly compared and it is shown that, in the case of a five-phase system, current ripple can not be minimised by injection of the fifth harmonic. This is a completely different result than the one valid for three-phase drives. It is demonstrated that the second plane has a great impact on the output current ripple since the error voltages are restricted only by the stator leakage inductance. Yet, for the comparison of different PWM schemes, analysis in the first plane is sufficient, since all three PWM schemes are with the same characteristic in the second plane. However, from the practical point of view, differences in the current ripple are relatively small and may not have a strong impact on the PWM scheme selection during implementation.

Based on the presented results it is obvious that every multi-phase system would require separate analysis if complex approach is chosen. To further explore current ripple rms of multi-phase drives for an arbitrary number of phases and a possibility to perform analysis

in the original domain, a different approach is utilised in the next chapter. It is based on the use of polygon connection of multi-phase systems and is therefore termed 'polygon approach'.

<div style="text-align: center">

Chapter 8

ANALYTICAL ANALYSIS OF CURRENT RIPPLE RMS OF MULTI-PHASE DRIVES – POLYGON APPROACH

</div>

8.1 INTRODUCTION

In the previous chapter, output current ripple rms of the five-phase drives has been analysed using the complex approach. Such an analysis provided a great deal of the intermediate results, but it was exclusively conducted for the five-phase drives, and the results cannot be extrapolated to other multi-phase topologies. At the same time, the obtained results are already completely different than the corresponding ones for three-phase drives. Further investigation is therefore undertaken in order to clarify them. An alternative approach is presented in this chapter, based again on the existing analytical tools used for three-phase drives. To avoid difficulties of dealing with the zero-sequence component, current ripple of three-phase drives has been analysed considering delta connection of machine windings [Blasko (1997), Hava et al (1999), Holmes and Lipo (2003)]. The same approach is followed here and it is termed 'polygon approach'. A very general analysis is presented, which covers all multi-phase topologies, since it is not limited to any particular phase number.

This chapter is organised as follows. In section 8.2 some preliminary considerations are given and the polygon connections of the multi-phase systems are introduced. Analytical analysis of current ripple rms based on the polygon approach is conducted in section 8.3 and the same part of the solution of the HDF for all analysed PWM schemes is derived in section 8.4. Complete HDF for multi-phase SPWM schemes is given in section 8.5. Correlation with the results from the chapter 7, based on multiple polygon results, is also established. Possibilities to optimise HDF by the harmonic injection are analysed in section 8.6. Due to difficulties encountered in derivation of the general solution for SVPWM (TIPWM), only five-phase SVPWM is analysed in detail in section 8.7 using the polygon approach, in order to confirm the results obtained with the complex approach. Output current ripple of a half-bridge inverter and its relation to multi-phase topologies is outlined in section 8.8. Discussion

of obtained results and feasibility of the polygon approach are covered in section 8.9. Some simulation results are provided in section 8.10, while summary is given in section 8.11.

8.2 PRELIMINARY CONSIDERATIONS

Similar to the three-phase case where machine's windings can be connected either in star or delta connection, windings of multi-phase machines can be connected in polygon connections in addition to the star connection. However, polygon representation for a given phase number is not unique [Ferraris and Lazzari (1983)] and one can identify several ways to connect multi-phase machine's windings in polygons. Yet, it is easy to establish that number of different polygons of an *n*-phase machine (*n* is taken as an odd number) equals (*n*-1)/2, and is thus equal to the number of 2-D planes where representation is obtained after transformation from the original domain. Using windings of five-phase machines as an example. all three possible connections (including star connection) are shown in Fig. 8.1. As it can be seen, in the first polygon connection phases of a load are connected between adjacent legs of the inverter (denoted with capital letters), while non-adjacent legs are used in the second possible polygon connection. There is not any other possibility to connect windings of a five-phase machine. However, the star-connection is always considered, whenever practical considerations for five-phase machines are presented, while there is no reported practical use of polygon connections, with the exception of the work of [Ferraris and Lazzari (1983)].

Similar considerations apply to a seven-phase system where three different polygons exist, which again equals the number of 2-D planes of a seven-phase system, as well as the number of different line voltages. Nine-phase system has four different polygons, eleven-phase system five, etc.

a)   *b)*   *c)*
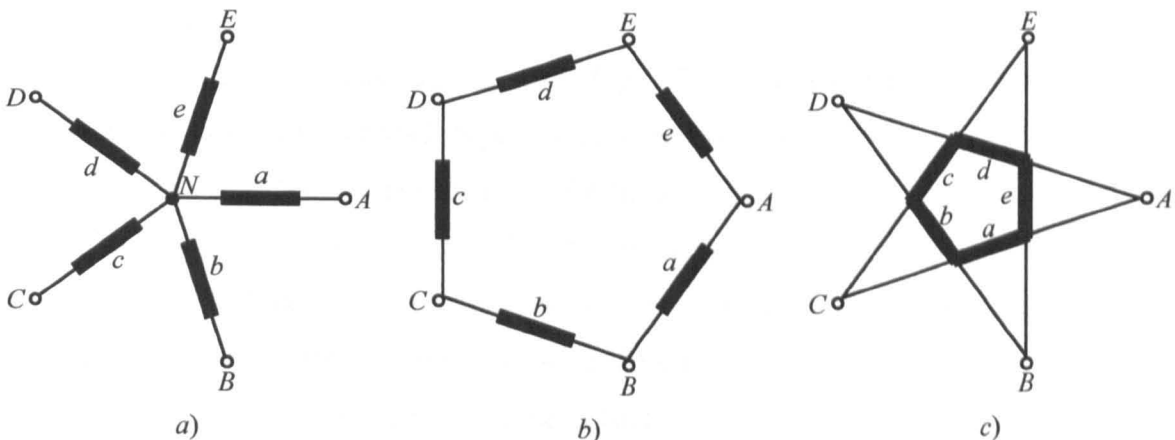
Fig. 8.1: Possible connections of five-phase machine windings, a) star connection, b) adjacent polygon, and c) non-adjacent polygon connection.
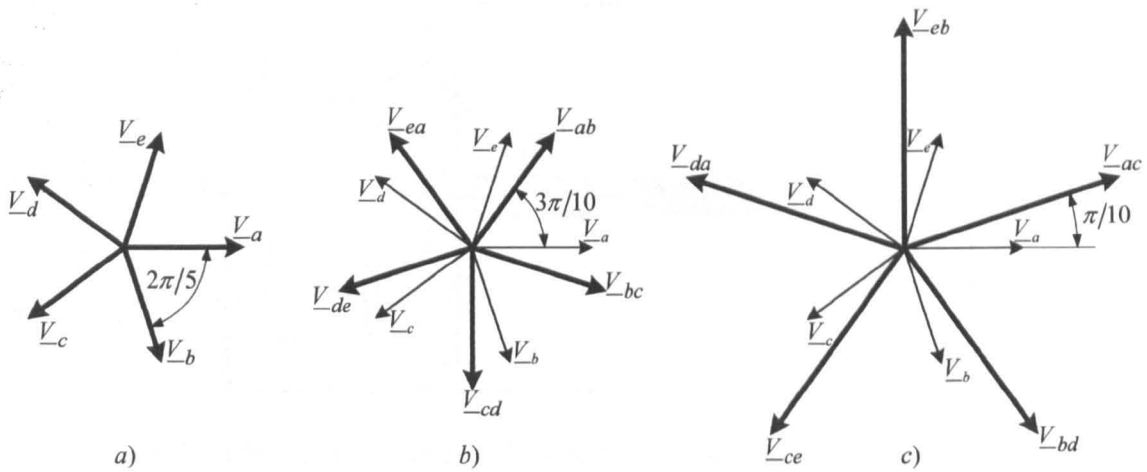
Fig. 8.2: Phase voltages of a five-phase machine in a) star connection, b) adjacent polygon and c) non-adjacent polygon connection.

An important thing to notice here is the fact that an increase in phase voltage is obtained with the use of polygon connections for the given dc bus voltage. Assuming that inverter generates balanced output voltages, in the adjacent polygon adjacent line voltage is applied over the phase of the load, while in the non-adjacent polygon non-adjacent line voltage appears across the phase of the load, as illustrated with the phasors in Fig. 8.2.

For the analysis of the current ripple rms, polygon connection greatly simplifies the procedure, since now one phase of the load is effectively connected in between two inverter legs. Thus, the phase current ripple rms can be directly obtained in the original domain, without the need to transfer the analysis into complex plane(s). Such an approach has been followed already by Blasko (1997), Hava et al (1999) and, Holmes and Lipo (2003) for a three-phase, and by Dahono (2006), Dahono and Deni (2006) and Deni et al (2007) for a five-phase system. However, in the latter case the existence of multiple polygons in multi-phase systems has not been recognised, and no general analysis has been done covering all multi-phase topologies.

Model used in the analysis is shown in Fig. 8.3. It consists of an H-bridge inverter that supplies the equivalent phase load, represented as an *R-L-e* load. Each leg of the inverter is simply identified with the number (1 and 2) for the sake of clarity. Constant dc bus voltage is provided at the input of the inverter and output of each leg is referenced with respect to the mid-point of dc the link. The same assumptions, given in chapter 7, are valid again and, due to the high switching frequency, the resistance (*R*) does not play an important role in current ripple rms analysis. At the same time, induced back emf can be regarded as constant over the switching period and equal to the reference line voltage. The same normalisation used so far is used in this chapter again, including the trigonometric constants of (3.13).
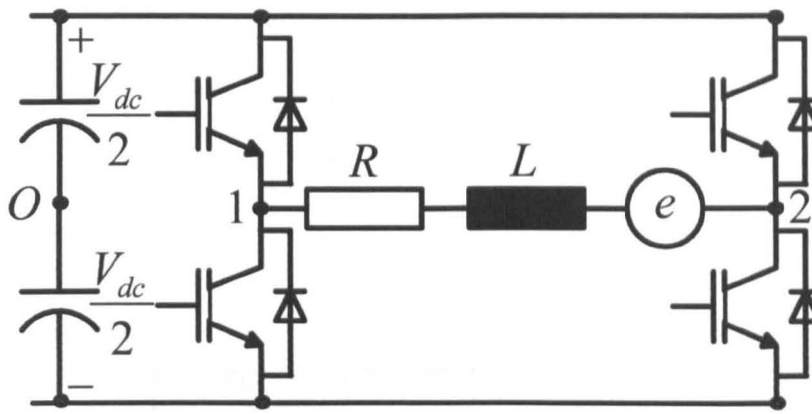
179

Fig. 8.3: H-bridge inverter and the equivalent load for the polygon analysis.

8.3 MULTI-PHASE CURRENT RIPPLE RMS ANALYSIS – POLYGON APPROACH

Based on Fig. 8.3, the switching pattern, sufficient for the analysis, is as shown in Fig. 8.4. Only two modulating signals are now of interest and these are defined in the same manner as in the chapter 6, with:

$$v_1 = M\cos(\vartheta) + v_{zs}$$
$$v_2 = M\cos(\vartheta - 2\alpha) + v_{zs} \tag{8.1}$$

The first part on the right-hand side of (8.1) describes the fundamental sinusoidal signals where angle α is defined as $\alpha = P\pi/n$ (n is the number of phases and $P = 1$ to $(n\text{-}1)/2$ is the polygon number). This eases the analysis of various polygon connections, since by varying the angle α modulating signals for a variety of topologies are generated.

During the sub-intervals $(0 - t_1)$ and $(t_2 - t_3)$, load is short circuited since the switching functions m_1 and m_2 of corresponding legs are the same. However, during the sub-interval $(t_1 - t_2)$ full dc bus voltage is applied to the load. Average back emf is assumed constant and it equals the reference line voltage $v_{12}{}^*$. Duty cycles are defined as before, and there are now three duty cycles that are of interest for the analysis, identified with sub-scripts 'x', 'y', and 'z'. Load current ripple (Δi) is shown in Fig. 8.4 and it is assumed that at the beginning and at the end of the first half of the switching period it has a value of zero. Difference between the applied voltage and internal back emf causes load current to rise and fall around its average value, thus resulting in the current ripple. Thus, for the purpose of analysis, deviation of the current (Δi), restricted by the equivalent phase inductance L, can be expressed as:

$$\Delta i = \frac{v - e_{12}}{L}\Delta t \tag{8.2}$$

Here, v is the applied voltage over the interval Δt, while $e_{12} = v_{12}{}^*$.
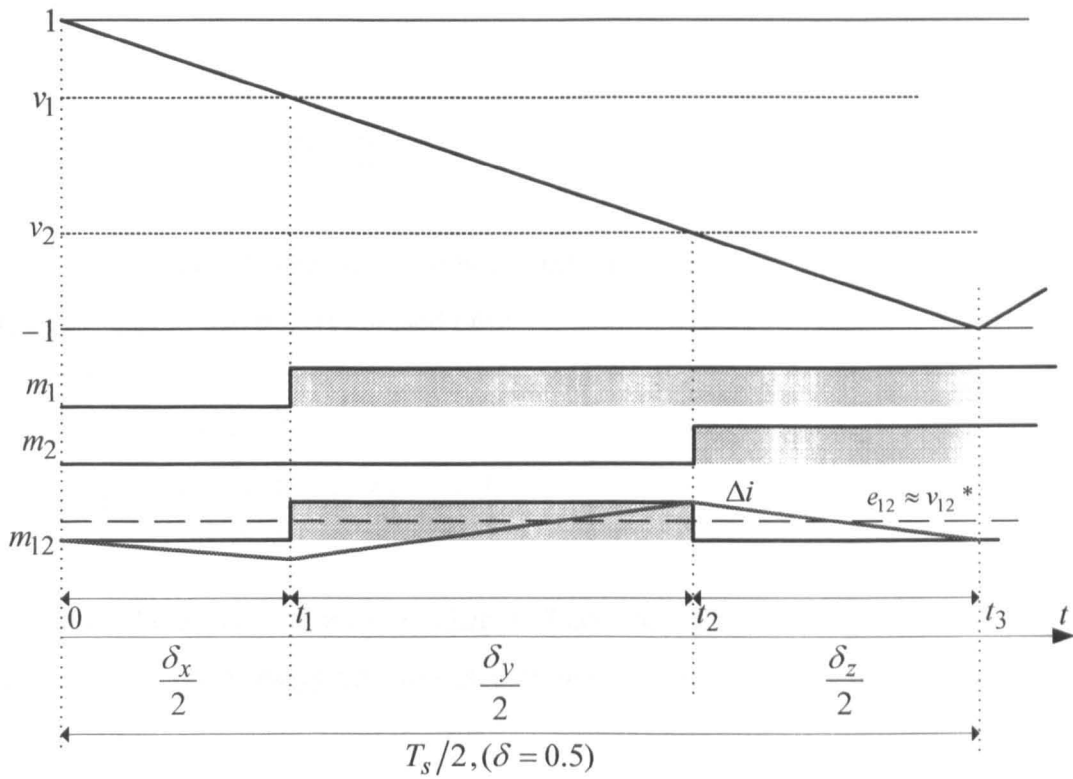
Fig. 8.4: Switching pattern over the first half of the switching period used for polygon approach analysis.

In what follows, current ripple is analysed from the beginning, in contrast to chapter 7 where the analysis commenced with harmonic flux. However, transition from current ripple to harmonic flux is on the basis of (8.2) straightforward, since $\Delta\lambda = L\Delta i$. Also, further on, an asterisk in the reference voltage (line voltage) notation is omitted in this chapter for the sake of simplicity.

The situation illustrated in Fig 8.4 applies to any multi-phase system. To perform a general analysis, angle α is used as the parameter. At first duty cycles of each of the inverter legs can be obtained from Fig. 8.4, by considering modulating signals, as:

$$\delta_1 = \frac{1}{2}[1 + v_1]; \qquad \delta_2 = \frac{1}{2}[1 + v_2] \qquad (8.3)$$

Based on (8.3) and Fig. 8.4, three characteristic duty cycles related to each sub-interval are determined as:

$$\delta_x = 1 - \delta_1; \qquad \delta_y = \delta_1 - \delta_2; \qquad \delta_z = \delta_2 \qquad (8.4)$$

This can be further expressed as:

$$\delta_x = \frac{1}{2}[1 - v_1]; \qquad \delta_y = \frac{1}{2}[v_1 - v_2]; \qquad \delta_z = \frac{1}{2}[1 + v_2] \qquad (8.5)$$

Using Fig. 8.4, one can write directly values of the current ripple at the end of every sub-interval as:

181

$$\Delta i(0) = 0$$

$$\Delta i(t_1) = \Delta i(0) + \frac{0 - e_{12}}{L} \delta_x \frac{T_s}{2}$$

$$\Delta i(t_2) = \Delta i(t_1) + \frac{V_{dc} - e_{12}}{L} \delta_y \frac{T_s}{2} \tag{8.6}$$

$$\Delta i(t_3) = 0$$

Under the assumption that the induced back emf equals the reference line voltage, after some manipulations (8.6) can be reorganised into:

$$\Delta i(0) = 0$$

$$\Delta i(t_1) = -\frac{v_{12}}{L} \delta_x \frac{V_{dc}}{2} \frac{T_s}{2}$$

$$\Delta i(t_2) = -\frac{v_{12}}{L} \delta_x \frac{V_{dc}}{2} \frac{T_s}{2} + \frac{2 - v_{12}}{L} \delta_y \frac{V_{dc}}{2} \frac{T_s}{2} \tag{8.7}$$

$$\Delta i(t_3) = 0$$

Normalisation factor is selected as in chapter 7 and the equivalent inductance now appears in the denominator, since analysis is not based on the harmonic flux any more:

$$\Delta i_N = \frac{V_{dc} T_s}{8L} \tag{8.8}$$

After normalisation (8.7) becomes (the same notation is used, although it is now in per-unit):

$$\Delta i(0) = 0$$

$$\Delta i(t_1) = -2 v_{12} \delta_x$$

$$\Delta i(t_2) = -2 v_{12} \delta_x + 2(2 - v_{12}) \delta_y \tag{8.9}$$

$$\Delta i(t_3) = 0$$

Substituting expressions for duty cycles (8.5) and using the relationship $-v_{12} = v_{21} = v_2 - v_1$, current ripple, as a function of the modulating signals, at the end of every sub-interval is obtained as:

$$\Delta i(0) = 0$$

$$\Delta i(t_1) = (v_2 - v_1)(1 - v_1)$$

$$\Delta i(t_2) = -(v_2 - v_1)(1 + v_2) \tag{8.10}$$

$$\Delta i(t_3) = 0$$

In further analysis, squared value of the current ripple (the second step of the complex approach) over the switching period (microscopic analysis) needs to be calculated. Due to the symmetry that exists, it is sufficient to perform calculation over the first half of the switching period:

$$\Delta i^2{}_{RMS} = \frac{2}{T_s} \int_0^{T_s/2} \Delta i^2(t) dt \tag{8.11}$$

Based on the knowledge of the current ripple at the end of every sub-interval, continuous integration can be replaced using the generic solution (Appendix C):

$$\int_{t_{n-1}}^{t_n} \Delta i^2(t)dt = (t_n - t_{n-1})\frac{1}{3}[\Delta i(t_{n-1})^2 + \Delta i(t_{n-1})\Delta i(t_n) + \Delta i(t_n)^2] \tag{8.12}$$

Considering defined sub-intervals from Fig. 8.4, integral (8.11) can be separated into three integrals:

$$\Delta i^2{}_{RMS} = \frac{2}{T_s}\left[\int_0^{t_1}\Delta i^2(t)dt + \int_{t_1}^{t_2}\Delta i^2(t)dt + \int_{t_2}^{T_s/2}\Delta i^2(t)dt\right] \tag{8.13}$$

Substituting (8.12) and taking into account duty cycles by means of the expressions that are of the form $\delta = (t_n - t_{n-1})\frac{2}{T_s}$, and making provision for $\Delta i(0) = 0$ and $\Delta i(t_3) = 0$, one has:

$$\Delta i^2{}_{RMS} = \frac{1}{3}\begin{bmatrix} \delta_x \Delta i^2(t_1) \\ + \delta_y[\Delta i^2(t_1) + \Delta i(t_1)\Delta i(t_2) + \Delta i^2(t_2)] \\ + \delta_z \Delta i^2(t_2) \end{bmatrix} \tag{8.14}$$

Duty cycles now re-appear in the solution and it is necessary to eliminate them from (8.14). After substitution of (8.5) and (8.10) into (8.14) and some manipulations, the following form of the solution for microscopic analysis is obtained:

$$\Delta i^2{}_{RMS} = \frac{1}{3}\left[(v_2 - v_1)^2 + (v_2 - v_1)^3 + (v_2 - v_1)(v_2{}^3 - v_1{}^3)\right] \tag{8.15}$$

Finally, to determine HDF (the third step of the complex approach), (8.15) needs to be evaluated over the fundamental period (macroscopic analysis). Since the load is exposed to the line voltage and induced back emf is assumed positive (Fig. 8.4), it is enough to do the integration only over the positive half of the line voltage fundamental period. By considering definitions for modulating signals it is easy to show that the line voltage (v_{12}) positive half period is always over the range ($\alpha - \pi + \alpha$), regardless of the phase number or the polygon selected.

Taking this into consideration, to obtain HDF, the following integral needs to be solved:

$$HDF = \Delta i^2{}_{RMSF} = \frac{1}{\pi}\int_{\alpha-\pi}^{\alpha}\Delta i^2{}_{RMS}d\vartheta \tag{8.16}$$

Substituting (8.15) into (8.16) and separating into three integrals yields a form that is suitable for the very general analysis followed in this chapter:

$$HDF = \frac{1}{\pi}\frac{1}{3}\left[\int_{\alpha-\pi}^{\alpha}(v_2 - v_1)^2 d\vartheta + \int_{\alpha-\pi}^{\alpha}(v_2 - v_1)^3 d\vartheta + \int_{\alpha-\pi}^{\alpha}(v_2 - v_1)(v_2{}^3 - v_1{}^3)d\vartheta\right] = \frac{1}{\pi}\frac{1}{3}[I_1 + I_2 + I_3] \tag{8.17}$$

It is important to note that the first two integrals are the same for all three PWM schemes analysed (SPWM, HIPWM and SVPWM (equivalent of the TIPWM)). Even if the zero-sequence signal is injected (HIPWM, SVPWM) it will get cancelled in the expressions of the form $(v_2 - v_1)$, thus leaving always the same function under the integral. The third integral is different for every PWM scheme due to the part $(v_2{}^3 - v_1{}^3)$, and needs to be calculated separately for each of the considered PWM schemes. Thus, this part of the solution will result in unique appearance of the final HDF for each of the PWM schemes.

At first however, common part of HDF, that is the same for all three PWM schemes, is determined by solving the first two integrals of (8.17).

8.4   HARMONIC DISTORTION FACTOR – COMMON PART OF THE SOLUTION

To obtain common part of HDF, the first two integrals of (8.17) are solved independently. The first integral, after substitution of (8.1) and taking M in front of the integral is:

$$I_1 = \int_{\alpha-\pi}^{\alpha} (v_2 - v_1)^2 \, d\vartheta = M^2 \int_{\alpha-\pi}^{\alpha} (\cos(\vartheta - 2\alpha) - \cos(\vartheta))^2 \, d\vartheta \tag{8.18}$$

Using the standard trigonometric relation, (8.18) is transformed into:

$$I_1 = M^2 \int_{\alpha-\pi}^{\alpha} (2\sin(\alpha)\sin(\vartheta - \alpha))^2 \, d\vartheta = 4K^2 M^2 \int_{\alpha-\pi}^{\alpha} \sin^2(\vartheta - \alpha) d\vartheta \tag{8.19}$$

Trigonometric constant defined with (3.13) is used in order to simplify appearance of the solution. Finally, after solving integral (8.19) one has:

$$I_1 = 2K^2 M^2 \pi \tag{8.20}$$

Similarly, the second integral can be developed into:

$$I_2 = \int_{\alpha-\pi}^{\alpha} (v_2 - v_1)^3 \, d\vartheta = 8K^3 M^3 \int_{\alpha-\pi}^{\alpha} \sin^3(\vartheta - \alpha) d\vartheta \tag{8.21}$$

Final solution is:

$$I_2 = -\frac{32}{3} K^3 M^3 \tag{8.22}$$

Based on the (8.20) and (8.22), the common part of HDF, which is the same for all three PWM schemes (sub-script 'C' stands for common), is of the form:

$$HDF_C = \frac{1}{3}\left[2K^2 M^2 - \frac{32}{3\pi} K^3 M^3 \right] \tag{8.23}$$

It is important to recall that solutions for HDFs of five-phase PWM schemes obtained in the previous chapter, by means of complex analysis, were also with the same coefficients next to M^2 and M^3 (which are however different from those in (8.23)). To determine the complete HDFs for SPWM, HIPWM and SVPWM, the third integral needs to be solved for each particular PWM scheme.

8.5 HARMONIC DISTORTION FACTOR OF THE SPWM

Sinusoidal PWM uses no zero-sequence signal and therefore the modulating signals are equal to the fundamental sinusoidal signals. Thus, the remaining integral is of the form:

$$I_{3-SPWM} = \int_{\alpha-\pi}^{\alpha} (v_2 - v_1)(v_2^3 - v_1^3)d\vartheta = M^4 \int_{\alpha-\pi}^{\alpha} [\cos(\vartheta - 2\alpha) - \cos(\vartheta)][\cos^3(\vartheta - 2\alpha) - \cos^3(\vartheta)]d\vartheta \quad (8.24)$$

Using standard trigonometric relations yields:

$$I_{3-SPWM} = 2KM^4 \int_{\alpha-\pi}^{\alpha} \sin(\vartheta - \alpha)[\cos^3(\vartheta - 2\alpha) - \cos^3(\vartheta)]d\vartheta \quad (8.25)$$

After some tedious manipulations the final solution is obtained as:

$$I_{3-SPWM} = \frac{3}{2}K^2 M^4 \pi \quad (8.26)$$

Combining this with the common part of solution (8.23) one has the HDF of the SPWM as:

$$HDF_{SPWM} = \frac{1}{3}\left[2K^2 M^2 - \frac{32}{3\pi}K^3 M^3 + \frac{3}{2}K^2 M^4\right] \quad (8.27)$$

Obtained result represents the general solution for HDF of the multi-phase SPWM and can be applied to any multi phase topology. If evaluated for all α and M of interest, a 3-D plot is obtained, which is shown in Fig. 8.5. While some value of α are unrealistic since $\alpha = P\pi/n$ is discrete, obtained 3-D plot actually encloses all possible HDF curves of the SPWM. To demonstrate the effectiveness of the obtained solution, it is enough to consider two-phase (H-bridge) and three-phase inverter topologies (solutions for HDFs of these two topologies are readily available in the literature [Holmes and Lipo (2003)]). Trigonometric constant K is now the key parameter that depends on the angle α, which is on the other hand firmly defined with the selected polygon used for the analysis. Values of the angle α and relations for various polygon connections of multi-phase systems are summarised in Table 8.1 (up to $n = 9$). Obviously, the first two topologies do not have multiple polygon representations (load in the case of H-bridge inverter can be connected in only one way, while in the three-phase case delta connection represents polygon (*P1*)). Substituting K values for the corresponding angles from Table 8.1 into (8.27), HDFs of SPWM for the first two topologies are obtained.
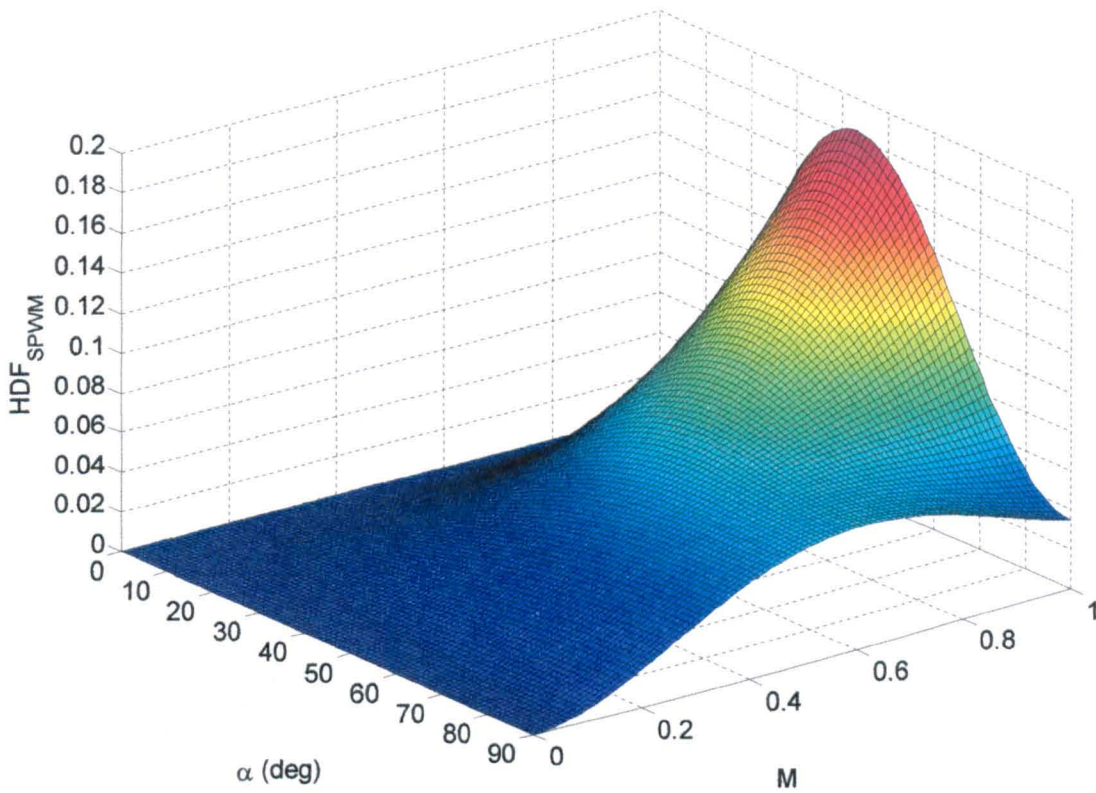
Fig. 8.5: Generalised multi-phase SPWM HDF as a function of α and M.

Thus, one has for the HDF of the H-bridge inverter, when SPWM is applied:

$$HDF_{2-SPWM} = \frac{1}{3}\left[2M^2 - \frac{32}{3\pi}M^3 + \frac{3}{2}M^4\right] \tag{8.28}$$
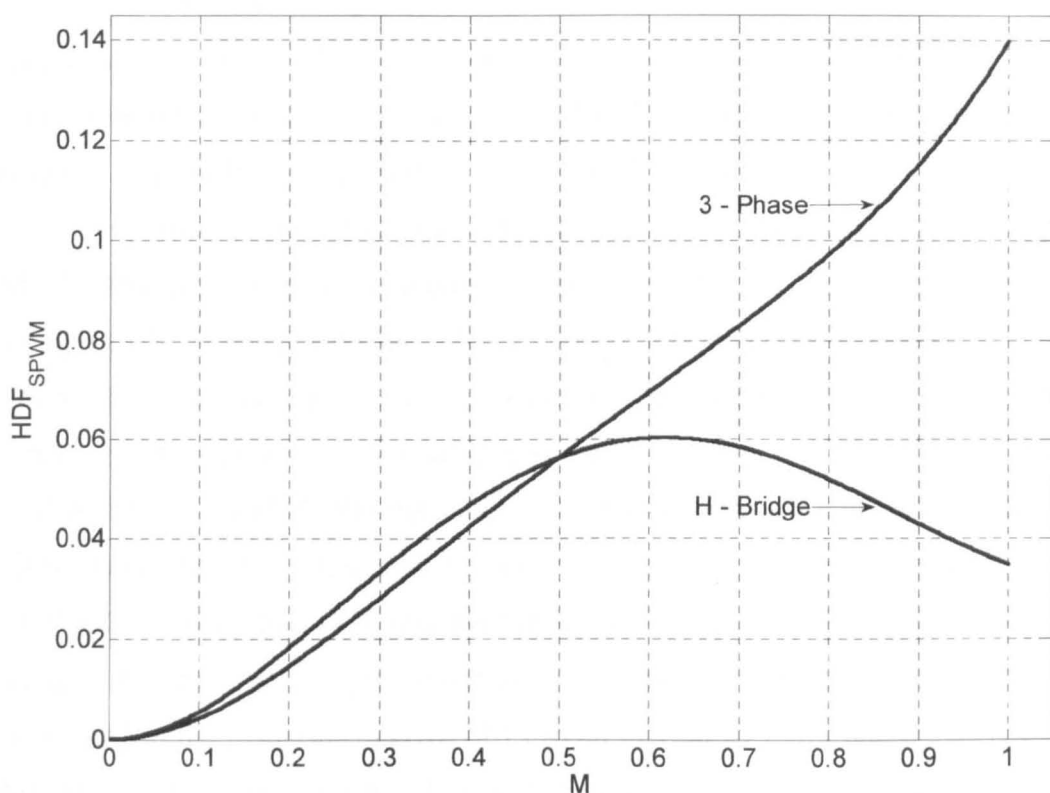
while HDF of SPWM of the three-phase inverter is:

$$HDF_{3-SPWM} = \frac{1}{3}\left[\frac{3}{2}M^2 - \frac{4\sqrt{3}}{\pi}M^3 + \frac{9}{8}M^4\right] \tag{8.29}$$

Plots of these two HDFs are shown in Fig. 8.6, from where it can be seen that H-bridge offers lower current ripple than a three-phase VSI [Holmes and Lipo (2003)].

Table 8.1: Values of the angle α for various polygon connections.

n | Polygon	P1	P2	P3	P4
2	$\alpha = \dfrac{\pi}{2}$	N/A	N/A	N/A
3	$\alpha = \dfrac{\pi}{3}$	N/A	N/A	N/A
5	$\alpha = \dfrac{\pi}{5}$	$\alpha = \dfrac{2\pi}{5}$	N/A	N/A
7	$\alpha = \dfrac{\pi}{7}$	$\alpha = \dfrac{2\pi}{7}$	$\alpha = \dfrac{3\pi}{7}$	N/A
9	$\alpha = \dfrac{\pi}{9}$	$\alpha = \dfrac{2\pi}{9}$	$\alpha = \dfrac{3\pi}{9}$	$\alpha = \dfrac{4\pi}{9}$

Fig. 8.6: SPWM HDF for H-bridge and three-phase inverter as a function of *M*.

However, the situation becomes more complicated as the number of phases increases. Considering a five-phase system as an example, there are two polygons to analyse. Based on the values of angle α one finds that solutions for the first (*P1*) and the second (*P2*) polygon differ only in trigonometric constants that appear in the solution:

$$HDF_{5-SPWM}^{P1} = \frac{1}{3}\left[2K^2M^2 - \frac{32}{3\pi}K^3M^3 + \frac{3}{2}K^2M^4\right] \tag{8.30}$$

$$HDF_{5-SPWM}^{P2} = \frac{1}{3}\left[2K_2^2M^2 - \frac{32}{3\pi}K_2^3M^3 + \frac{3}{2}K_2^2M^4\right] \tag{8.31}$$

This is the result of generalisation applied during the polygon analysis and it clearly shows the advantages of using the trigonometric constants of (3.13). However, only once when HDFs obtained for each polygon are summed, the same solution as the one given in the previous chapter under the assumption that equivalent inductances in all planes are equal (7.39) is obtained:

$$HDF_{5-SPWM} = \frac{1}{3}\left[2(K^2 + K_2^2)M^2 - \frac{32}{3\pi}(K^3 + K_2^3)M^3 + \frac{3}{2}(K^2 + K_2^2)M^4\right] \tag{8.32}$$

Plots of the HDFs of (8.30)-(8.32) are shown in Fig. 8.7. Polygon approach obviously cannot provide the exact solution for each of the planes of a five-phase system, as demonstrated with complex analysis in the chapter 7, but can be used to derive the complete solution for HDF.

Summing the HDFs for all polygons yields the same HDF as when the HDFs of the d_1-q_1 and d_2-q_2 planes are summed. While this result is a rather optimistic evaluation of the current ripple due to higher value of the equivalent inductance assumed for the second plane, it is still a valid figure of merit for the comparison of different PWM schemes.

It is important to note that exactly the same results are obtained for the HDF of the SPWM of a three-phase system using either the complex approach [Kolar et al (1990b)] or the polygon approach [Holmes and Lipo (2003)]. Yet, in a three-phase system there is only one plane as well as only one polygon (delta) to consider. At the same time, the equivalent inductance for both approaches is the same, given with (7.4).

This naturally leads to the question: if the results obtained by means of the complex analysis (chapter 7) are the actual HDFs of a star connected five-phase machine, do the results given in Fig. 8.7 suggest that HDF (current ripple) of a five-phase system can be optimised by connecting a machine into polygon rather than in a star connection? The difficulty with this claim is related to the increased degrees of freedom offered by multi-phase machines and the fact that, in the same way as one plane is not enough to describe the whole multi-phase machine, use of only one polygon does not provide the whole picture about the main properties of multi-phase systems. Thus, all polygons must be considered simultaneously, similar to the complex approach where all 2-D planes had to be considered together.
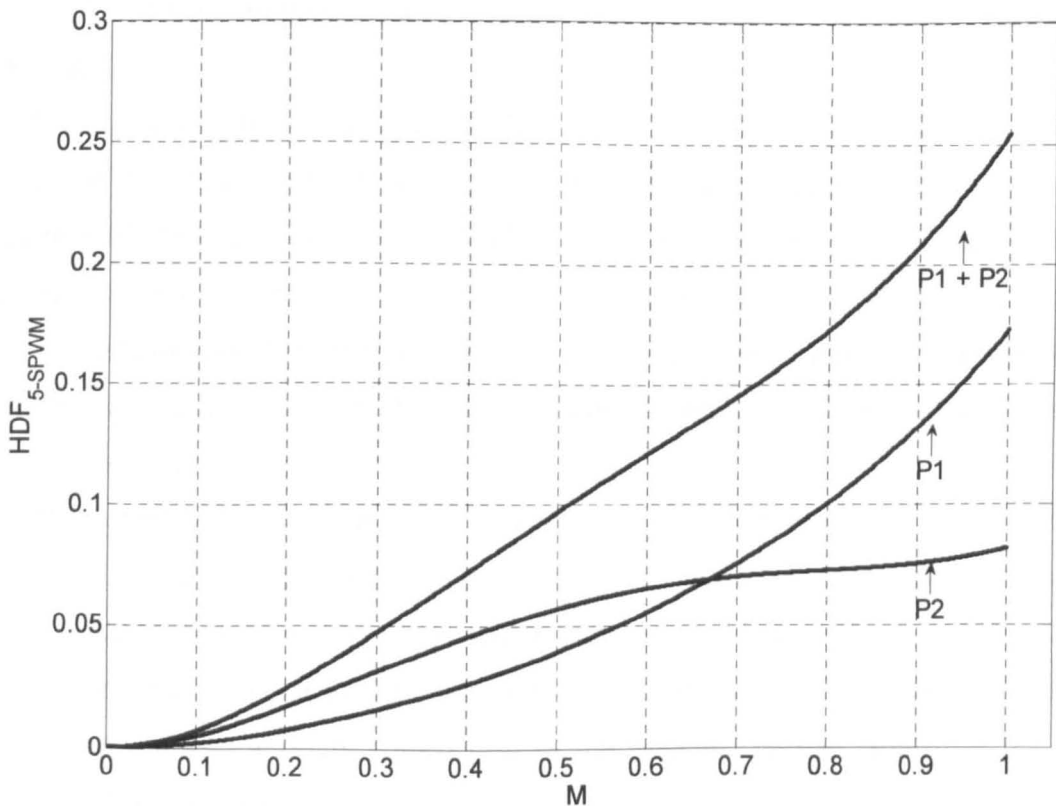

Fig. 8.7: SPWM HDF for five-phase polygons and the complete solution as a function of M.

Form of the solutions (8.30) and (8.31) for a five-phase system enables an extremely simple extrapolation for multi-phase systems with a higher number of phases. As it can be seen by comparing (8.30) and (8.31), the only difference is that constant K of (8.30) becomes constant K_2 of (8.31). If the phase number is higher than five, then for the third polygon constant of (8.30) will become constant K_3, for the fourth polygon K_4, and so on. Thus, for the case of a seven-phase system, where three polygon connections can be realised, the complete solution for HDF of a SPWM can be found, after summing solutions for individual polygons, as:

$$HDF_{7-SPWM} = \frac{1}{3}\left[2(K^2 + K_2^2 + K_3^2)M^2 - \frac{32}{3\pi}(K^3 + K_2^3 + K_3^3)M^3 + \frac{3}{2}(K^2 + K_2^2 + K_3^2)M^4\right] \quad (8.33)$$

Nine-phase system has four polygon connections. Individual polygon solutions, when summed, yield:

$$HDF_{9-SPWM} = \frac{1}{3}\begin{bmatrix} 2(K^2 + K_2^2 + K_3^2 + K_4^2)M^2 \\ -\frac{32}{3\pi}(K^3 + K_2^3 + K_3^3 + K_4^3)M^3 \\ +\frac{3}{2}(K^2 + K_2^2 + K_3^2 + K_4^2)M^4 \end{bmatrix} \quad (8.34)$$

The results of plotting the total HDF (and HDF of each polygon) for seven-phase and nine-phase system are shown in Fig. 8.8 and Fig. 8.9, respectively. As it can be seen, results for all polygons (for both seven-phase and nine-phase topology) are actually parts of the 3-D plot from Fig. 8. 5.

It is interesting to note that, due to the value of the angle α, solution for the *P3* of the nine-phase system is the same as for the three-phase system. This is in accordance with the organisation of the decoupling transformation matrix (3.21) and the third pair of the rows which defines the d_3-q_3 plane. At the same time, Jones et al (2003) have established that in the case of the series-connected nine-phase four-motor drive, three motors are nine-phase, while the fourth machine has to be three-phase. Polygon approach confirms these facts, in an alternative manner.

The complete solution for HDF attains higher and higher values as the number of phases increases, suggesting that the current ripple gets worse as more polygons/planes are available in the system. These complete solutions are obtained under the assumption of equal equivalent inductances in each of the polygons/planes, which is not realistic for multi-phase machines, but allows for rough comparison of the obtained current ripple for the case of different multi-phase systems.
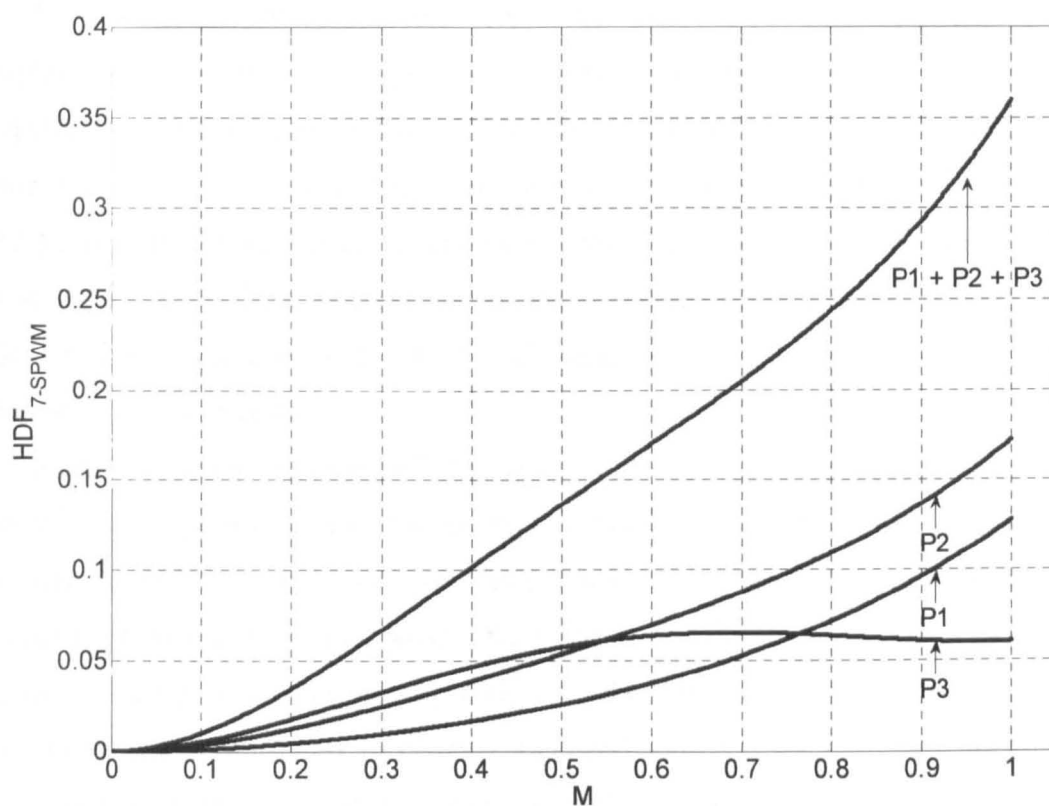
Fig. 8.8: SPWM HDF for seven-phase polygons and the complete solution as a function of M.
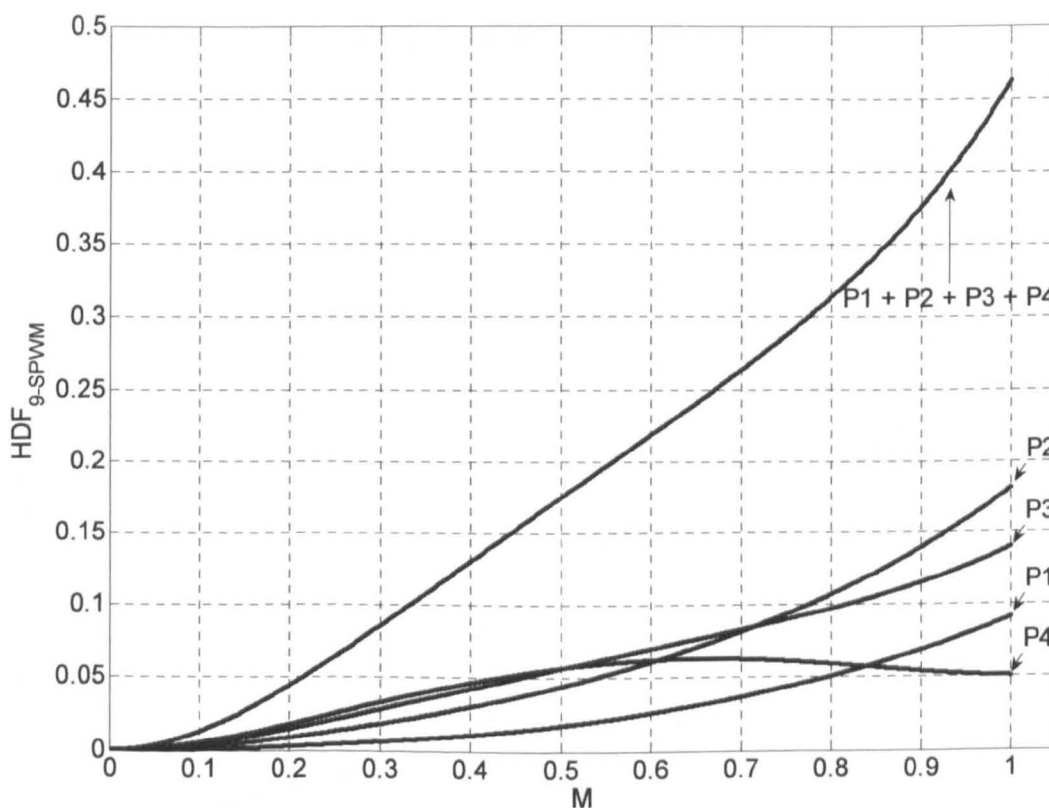
Fig. 8.9: SPWM HDF for nine-phase polygons and the complete solution as a function of M.

To provide an illustrative comparison, the total HDFs of three-phase, five-phase, seven-phase and nine-phase topologies, for the case of SPWM, are plotted together Fig. 8.10. It is visible that HDF of a multi-phase SPWM is of a similar shape over the whole range of the modulation index, yet higher values are obtained for higher numbers of phases. Thus, use of SPWM in a three-phase system offers lower current ripple than in all the other multi-phase systems. At the same time, as discussed in the literature [Kolar et al (1990a), Kolar et al (1990b), Holmes and Lipo (2003)], this characteristic can be further optimised by the injection of the third harmonic.

It has been shown in chapter 7 that similar optimisation is not possible in a five-phase system with the injection of the fifth harmonic. While the optimum level of injection that maximises dc bus utilisation can be determined easily, there is no such a level for optimisation of the current ripple, which effectively leaves the SPWM as the optimal method. However, to verify these findings by means of the polygon approach and to extend the analysis to all other multi-phase topologies, a general approach that considers the injection of the n-th harmonic into an n-phase system is analysed next. Since injected zero-sequence signal gets cancelled in the functions under the first two integrals, these remain as given by (8.20) and (8.22) and only the third integral needs to be solved, with the number of phases n and the level of injection b as new parameters.
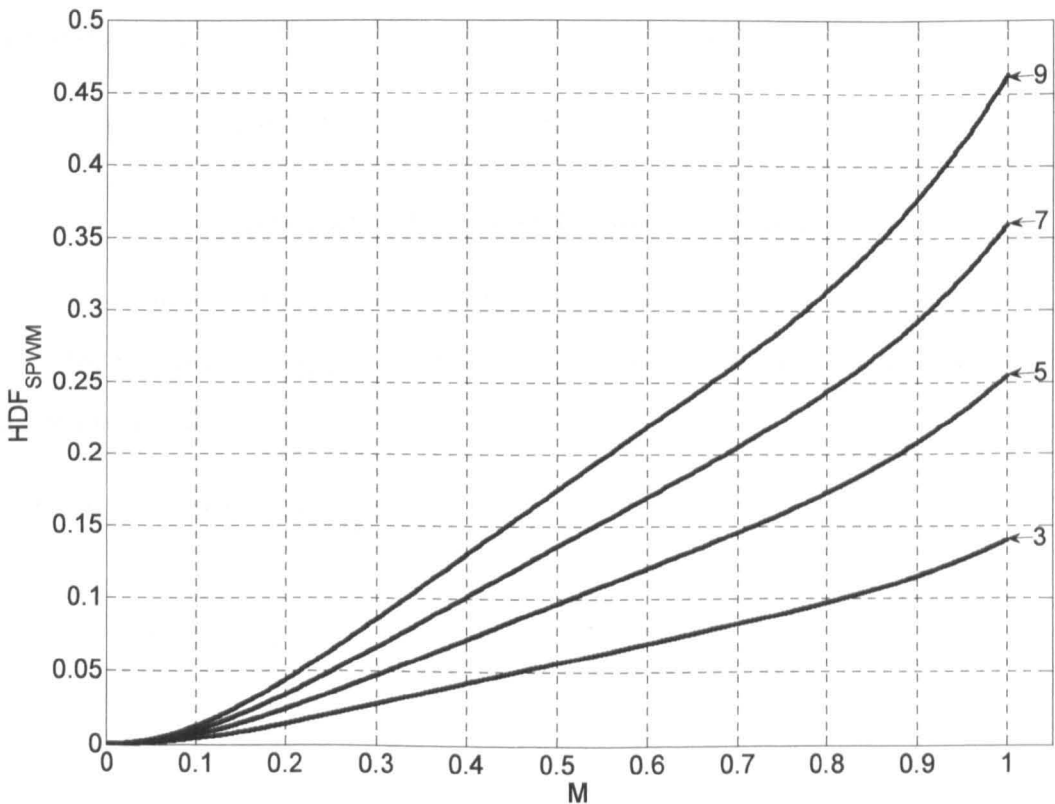
Fig. 8.10: SPWM HDF for the first four odd phase number topologies as a function of M.

8.6 HARMONIC DISTORTION FACTOR OF THE HIPWM

In the case of injection of the n-th harmonic, modulating signals for the legs of the H-bridge inverter are defined with:

$$
\begin{aligned}
v_1 &= M\cos(\vartheta) + bM\cos(n\vartheta) \\
v_2 &= M\cos(\vartheta - 2\alpha) + bM\cos(n\vartheta)
\end{aligned}
\tag{8.35}
$$

Parameter b defines the amount of injection of the n-th harmonic in the same way as in the preceding chapters. The only integral of (8.17) that needs to be solved is the third one:

$$
\begin{aligned}
I_{3-HIPWM} &= \int_{\alpha-\pi}^{\alpha} (v_2 - v_1)(v_2{}^3 - v_1{}^3)\,d\vartheta \\
&= M^4 \int_{\alpha-\pi}^{\alpha} [\cos(\vartheta - 2\alpha) - \cos(\vartheta)][[\cos(\vartheta - 2\alpha) + b\cos(n\vartheta)]^3 - [\cos(\vartheta) + b\cos(n\vartheta)]^3]\,d\vartheta
\end{aligned}
\tag{8.36}
$$

This can be simplified into:

$$
I_{3-HIPWM} = 2KM^4 \int_{\alpha-\pi}^{\alpha} [\sin(\vartheta - \alpha)][[\cos(\vartheta - 2\alpha) + b\cos(n\vartheta)]^3 - [\cos(\vartheta) + b\cos(n\vartheta)]^3]\,d\vartheta
\tag{8.37}
$$

Introducing the substitution of variables $x = \vartheta - \alpha, dx = d\vartheta$ and using the relationships:

$$
\begin{aligned}
K_n &= \sin(n\alpha) = \sin\!\left(n\frac{P}{n}\pi\right) = \sin(P\pi) = 0 \\
L_n &= \cos(n\alpha) = \cos\!\left(n\frac{P}{n}\pi\right) = \cos(P\pi) = \pm 1
\end{aligned}
\tag{8.38}
$$

after some tedious manipulation (8.37) can be developed into four simpler integrals:

$$
\begin{aligned}
I_{3-HIPWM} &= 6KL^2 \int_{-\pi}^{0} \cos^2(x)\sin^2(x)\,dx + 2K^3 \int_{-\pi}^{0} \sin^4(x)\,dx \\
&\quad + 6KLL_n b \int_{-\pi}^{0} \cos(nx)\sin(2x)\sin(x)\,dx + 6Kb^2 \int_{-\pi}^{0} \cos^2(nx)\sin^2(x)\,dx \\
&= 6KL^2 I_{3-1} + 2K^3 I_{3-2} + 6KLL_n b I_{3-3} + 6Kb^2 I_{3-4}
\end{aligned}
\tag{8.39}
$$

Solutions for the integrals I_{3-1}, I_{3-2} and I_{3-4} are independent from the number of phases n, and can be determined as:

$$
I_{3-1} = \int_{-\pi}^{0} \cos^2(x)\sin^2(x)\,dx = \frac{1}{8}\pi
\tag{8.40}
$$

$$
I_{3-2} = \int_{-\pi}^{0} \sin^4(x)\,dx = \frac{3}{8}\pi
\tag{8.41}
$$

$$
I_{3-4} = \int_{-\pi}^{0} \cos^2(nx)\sin^2(x)\,dx = \frac{1}{4}\pi
\tag{8.42}
$$

However, the solution of the integral I_{3-3} shows a dependence on the number of phases n and one finds that, for a three-phase case:

$$I_{3-3}(n=3) = \int_{-\pi}^{0} \cos(nx)\sin(2x)\sin(x)dx = -\frac{1}{4}\pi \qquad (8.43)$$

At the same time, in the case of $n=1$ one has that $I_{3-3}(n=1) = \pi/4$ (this particular case is not relevant for the analysis), while for all the other positive values of n the solution is:

$$I_{3-3}(n>0, n\neq 1, n\neq 3) = \int_{-\pi}^{0} \cos(nx)\sin(2x)\sin(x)dx = 0 \qquad (8.44)$$

The consequence of this is a different solution, obtained for the third integral, in the case of three-phase system and all the other multi-phase systems:

$$I_{3-HIPWM}(n=3) = 6KL^2\frac{1}{8}\pi + 2K^3\frac{3}{8}\pi - 6KLL_3b\frac{1}{4}\pi + 6Kb^2\frac{1}{4}\pi \qquad (8.45)$$

$$I_{3-HIPWM}(n>3) = 6KL^2\frac{1}{8}\pi + 2K^3\frac{3}{8}\pi + 6Kb^2\frac{1}{4}\pi \qquad (8.46)$$

Adding (8.45) to the common solution (8.23), HDF of the three-phase HIPWM is obtained as:

$$HDF_{3-HIPWM} = \frac{1}{3}\left[2K^2M^2 - \frac{32}{3\pi}K^3M^3 + \frac{3}{2}K^2M^4(1+b+2b^2)\right] \qquad (8.47)$$

For all the other higher odd phase numbers, HDF of n-phase HIPWM is of the form:

$$HDF_{n-HIPWM} = \frac{1}{3}\left[2K^2M^2 - \frac{32}{3\pi}K^3M^3 + \frac{3}{2}K^2M^4(1+2b^2)\right] \qquad (8.48)$$

Due to the differences in the solution of the integral I_{3-3}, HDFs differ in the part in the brackets related to the parameter b. Substituting the value of the trigonometric constants of the three-phase system into the general form of solution (8.47), the same solution as the one reported, for example, by Holmes and Lipo (2003), is generated:

$$HDF_{3-HIPWM} = \frac{1}{3}\left[\frac{3}{2}M^2 - \frac{4\sqrt{3}}{\pi}M^3 + \frac{9}{8}M^4(1+b+2b^2)\right] \qquad (8.49)$$

It is important to notice here that, in the case of a three-phase system, optimal solution for the injection of the third harmonic can be found from:

$$\frac{d(HDF_{3-HIPWM})}{db} = 0 = \frac{3}{8}M^4(1+4b) \qquad (8.50)$$

This is equal to zero only when

$$b = -\frac{1}{4} \qquad (8.51)$$

which is the well known level for the injection of the third harmonic in three-phase systems [Kolar et al (1990a), Kolar et al (1990b), Holmes and Lipo (2003)].

In the case of all other multi-phase systems one finds that the first derivative (minimum of the function (8.48)) equals zero only if:

$$b = 0 \tag{8.52}$$

Thus, the injection of the n-th harmonic in an n-phase system can not optimise the current ripple rms. The result, obtained in the chapter 7 for the five-phase system using the complex approach, is therefore confirmed.

For the illustration purposes, HDFs of the three-phase PWM with the third harmonic injection are plotted in Fig. 8.11. HDFs for both characteristic levels of injection are generated (dashed lines) and previously obtained HDF of a SPWM (solid line) is shown also to demonstrate improvements in HDF obtained by means of the injection. The injection of the third harmonic with the level of $b = -1/6$ optimises dc bus utilisation ($M_{max} = 1.1547$) and at the same time improves the current ripple when compared to the SPWM. Further improvement of HDF is obtained with the injection of the third harmonic with the level of $b = -1/4$. However, this yields slightly lower level of dc bus utilisation ($M_{max} = 1.1224$).

These results are readily available in the literature [Holmes and Lipo (2003)] and are presented here for the purpose of validation of the results obtained by means of the general polygon approach. To further verify the results of the polygon analysis, HDFs of the multi-phase HIPWM are compared for several other phase numbers next.
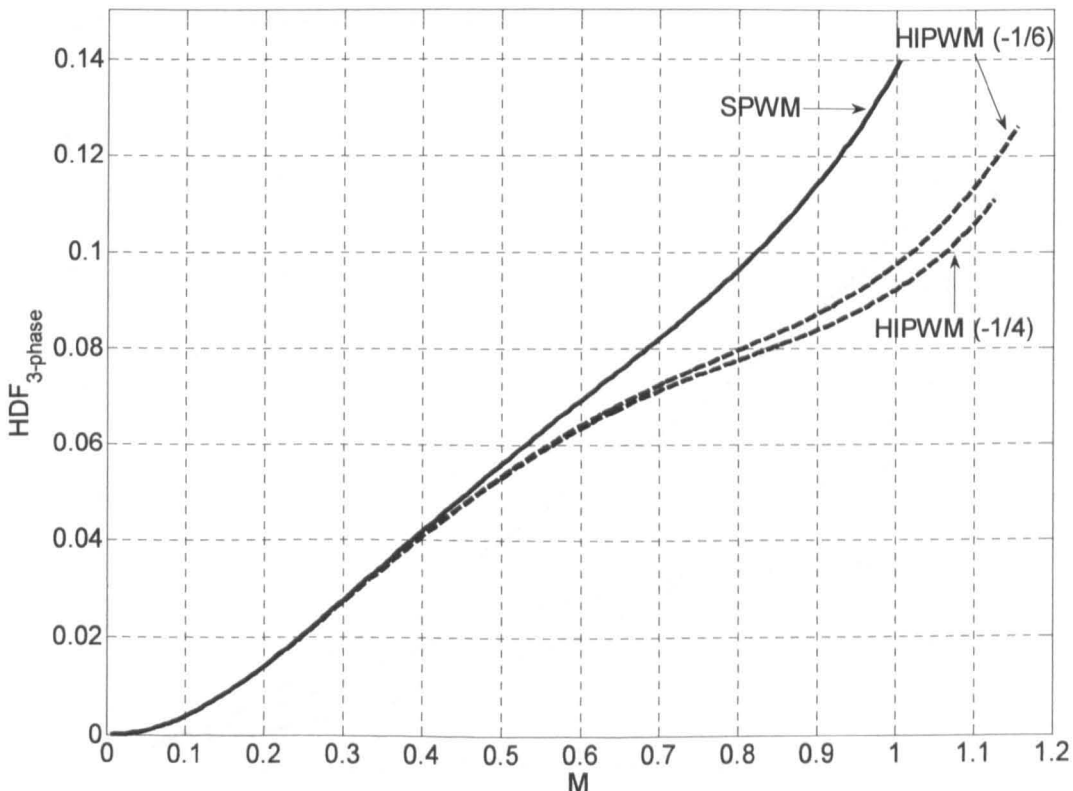

Fig. 8.11: HDF of the three-phase SPWM and HIPWM as a function of M.

Using again five-phase case as an example, to obtain solutions for HDF of each of the polygons, one needs to change the value of angle α in the initial step of analysis. This is reflected in the final HDF only through the value of trigonometric constants that appear in the solution. Thus, the fifth HIPWM (FHIPWM) HDFs for both polygons are of the form:

$$HDF_{5-HIPWM}^{P1} = \frac{1}{3}\left[2K^2M^2 - \frac{32}{3\pi}K^3M^3 + \frac{3}{2}K^2M^4(1+2b^2) \right] \tag{8.53}$$

$$HDF_{5-HIPWM}^{P2} = \frac{1}{3}\left[2K_2^2M^2 - \frac{32}{3\pi}K_2^3M^3 + \frac{3}{2}K_2^2M^4(1+2b^2) \right] \tag{8.54}$$

Again, like for the SPWM, direct summation of the HDFs of each polygon yields the same solution for the HDF of the FHIPWM as the one obtained in chapter 7 based on the harmonic flux analysis performed in two planes:

$$HDF_{FHIPWM} = \frac{1}{3}\left[2(K^2+K_2^2)M^2 - \frac{32}{3\pi}(K^3+K_2^3)M^3 + \frac{3}{2}(K^2+K_2^2)(1+2b^2)M^4 \right] \tag{8.55}$$

This is illustrated in Fig. 8.12, where HDFs based on (8.53)-(8.55) are shown (dashed line) together with results for SPWM (solid line) for the purposes of the comparison. As can be seen, both polygon HDFs of the FHIPWM are with higher values than corresponding HDFs of the SPWM. Thus, the complete solution is also worse than the one offered by SPWM, although modulation index can reach now higher value of $M_{max} = 1.0515$, compared to the unity value offered by the SPWM.
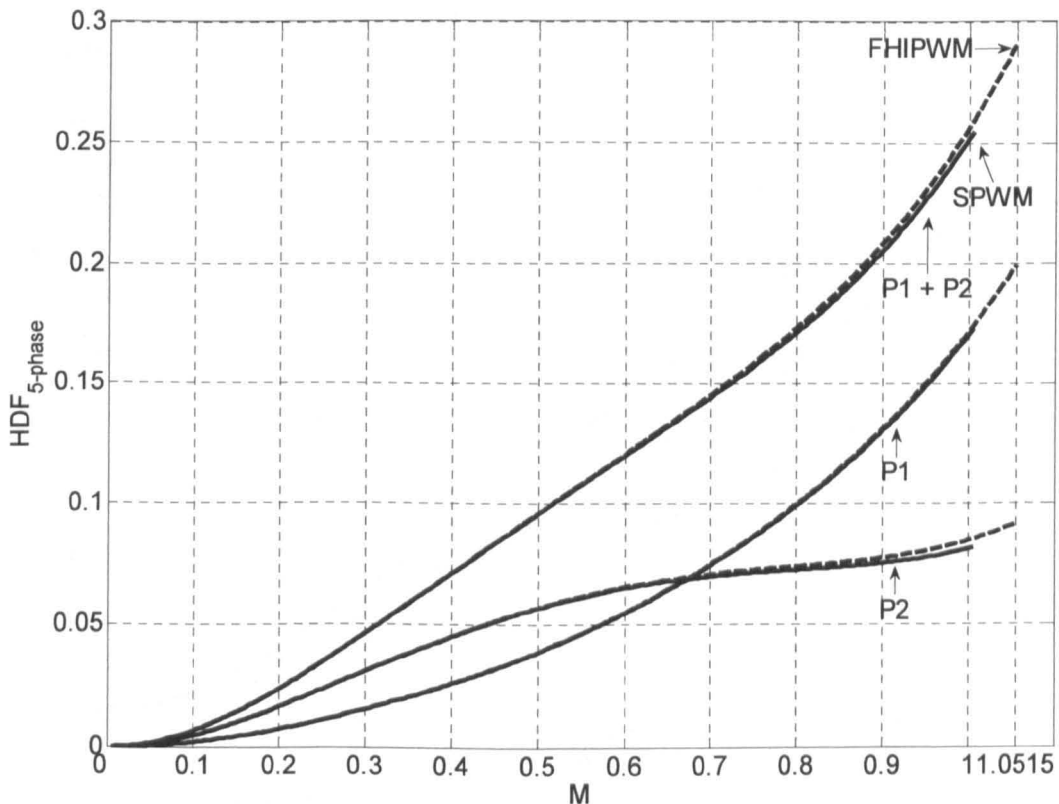

Fig. 8.12: HDF of the five-phase SPWM and the FHIPWM as a function of M.
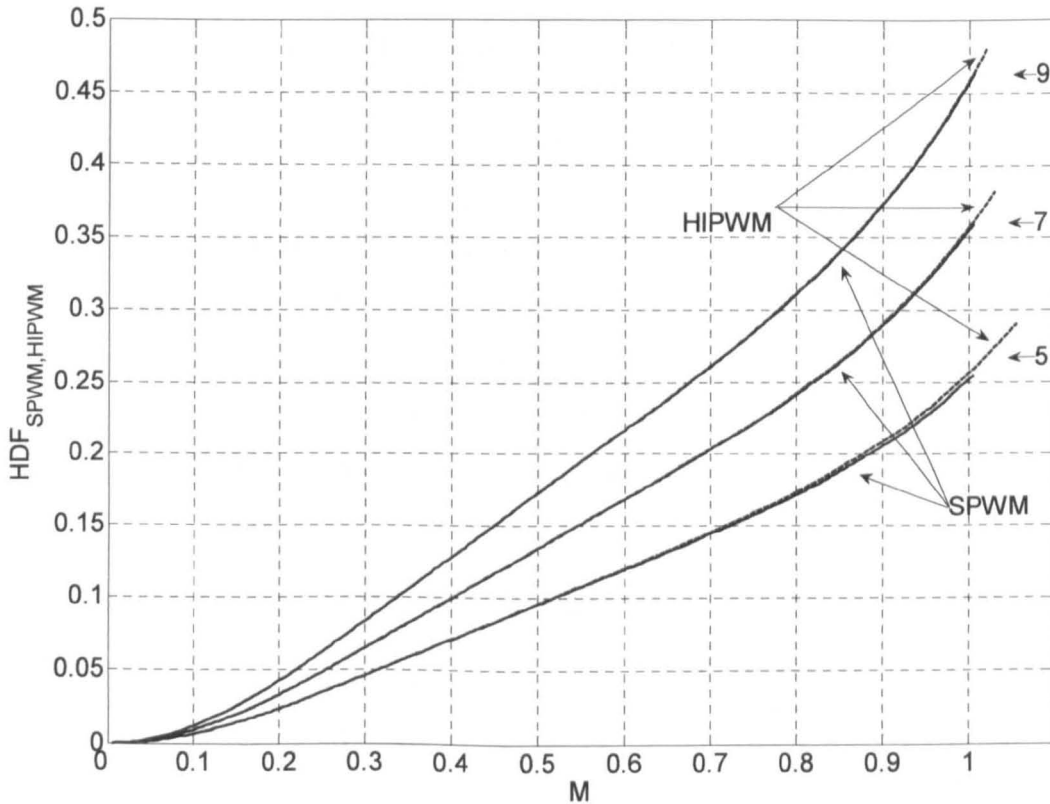
Similarly, for the seven-phase and nine-phase systems, one has that complete HDFs of HIPWM obtained after summations of each polygon HDFs are, respectively:

$$HDF_{7-HIPWM} = \frac{1}{3} \left[\begin{array}{l} 2(K^2 + K_2{}^2 + K_3{}^2)M^2 \\[2mm] -\frac{32}{3\pi}(K^3 + K_2{}^3 + K_3{}^3)M^3 \\[2mm] +\frac{3}{2}(K^2 + K_2{}^2 + K_3{}^2)(1+2b^2)M^4 \end{array} \right] \tag{8.56}$$

$$HDF_{9-HIPWM} = \frac{1}{3} \left[\begin{array}{l} 2(K^2 + K_2{}^2 + K_3{}^2 + K_4{}^2)M^2 \\[2mm] -\frac{32}{3\pi}(K^3 + K_2{}^3 + K_3{}^3 + K_4{}^3)M^3 \\[2mm] +\frac{3}{2}(K^2 + K_2{}^2 + K_3{}^2 + K_4{}^2)(1+2b^2)M^4 \end{array} \right] \tag{8.57}$$

Only total HDFs are shown in Fig. 8.13, including the HDF of the five-phase HIPWM for the sake of completeness. As the number of phases increases differences in HDFs become hardly observable although SPWM (solid line) has lower HDF than HIPWM (dashed line) for all the phase numbers greater than three.

Finally, HDF of a multi-phase SVPWM (TIPWM) has to be derived. Due to the difficulties in generalising the solution, only five-phase SVPWM is used as an example, in order to verify the results obtained in chapter 7.

Fig. 8.13: SPWM vs. HIPWM HDF of the five-phase, seven-phase and nine-phase topologies as a function of *M*.

8.7 HARMONIC DISTORTION FACTOR OF THE FIVE-PHASE SVPWM

To determine the HDF of a multi-phase SVPWM, similar approach as for SPWM and HIPWM is followed. In order to derive remaining part of the HDF, only the third integral of (8.17) needs to be evaluated. Yet, difficulties arise due to the fact that the zero-sequence signal, defined with:

$$v_{zs} = -0.5(v^*_{max} + v^*_{min}) \qquad (8.58)$$

is not the same over the whole positive fundamental half period of a line voltage. Zero-sequence signal changes in every sector, as the ordering of the fundamental signals changes and this defines the maximum and minimum values of (8.58). Therefore, for each particular phase number n, the integration of the third integral of (8.17) has to be performed over the n intervals/sectors enclosed by the positive half of the line voltage fundamental.

Using the five-phase SVPWM (TIPWM) as an example, Table 8.2 defines the zero-sequence signal through all ten sectors. Based on this and the value of $\alpha = \pi/5$, for the first polygon of a five-phase system, one has that the third integral of (8.17) can be expressed as:

$$
\begin{aligned}
I_3 &= \int_{\alpha-\pi}^{\alpha}(v_2 - v_1)(v_2^3 - v_1^3)d\vartheta = \int_{-4\pi/5}^{\pi/5}(v_2 - v_1)(v_2^3 - v_1^3)d\vartheta = \\
&= \int_{-4\pi/5}^{-3\pi/5}(v_2 - v_1)(v_2^3 - v_1^3)d\vartheta + \int_{-3\pi/5}^{-2\pi/5}(v_2 - v_1)(v_2^3 - v_1^3)d\vartheta + \int_{-2\pi/5}^{-\pi/5}(v_2 - v_1)(v_2^3 - v_1^3)d\vartheta \qquad (8.59) \\
&+ \int_{-\pi/5}^{0}(v_2 - v_1)(v_2^3 - v_1^3)d\vartheta + \int_{0}^{\pi/5}(v_2 - v_1)(v_2^3 - v_1^3)d\vartheta
\end{aligned}
$$

Modulating signals are defined as before with (8.1) and zero-sequence signal now takes the values in accordance with Table 8.2. For the *P1* of a five-phase system, sectors 7, 8, 9, 10 and 1 need to be considered, while for the *P2* borders of integrals are shifted by one sector (8, 9, 10, 1 and 2). However, it is enough to solve only the integral (8.59), developed for the *P1* and, based on that, by simple substitution of a trigonometric constant, to generate the solution for the HDF of *P2*.

Table 8.2: Zero-sequence signal through sectors of a five-phase system.

Sector	1	2	3	4	5	6	7	8	9	10
Range x $\pi/5$	$0 \div 1$	$1 \div 2$	$2 \div 3$	$3 \div 4$	$4 \div 5$	$5 \div 6$	$6 \div 7$	$7 \div 8$	$8 \div 9$	$9 \div 10$
v^*_{max}	v^*_a	v^*_b	v^*_b	v^*_c	v^*_c	v^*_d	v^*_d	v^*_e	v^*_e	v^*_a
v^*_{min}	v^*_d	v^*_d	v^*_e	v^*_e	v^*_a	v^*_a	v^*_b	v^*_b	v^*_c	v^*_c
v_{zs}					$-0.5(v^*_{max} + v^*_{min})$					

After some manipulations, HDF for the *P1* of a five-phase system in the case of SVPWM is obtained as:

$$HDF_{5-SVPWM}^{P1} = \frac{1}{3}\left[2K^2M^2 - \frac{32}{3\pi}K^3M^3 + \frac{3}{2}K^2\left[\frac{7-\sqrt{5}}{4} - \frac{5}{8}\frac{\sqrt{50-22\sqrt{5}}}{\pi}\right]M^4\right] \qquad (8.60)$$

Solution for the second polygon is of the same form and is obtained by simple replacement of the trigonometric constant *K* with K_2:

$$HDF_{5-SVPWM}^{P2} = \frac{1}{3}\left[2K_2^2M^2 - \frac{32}{3\pi}K_2^3M^3 + \frac{3}{2}K_2^2\left[\frac{7-\sqrt{5}}{4} - \frac{5}{8}\frac{\sqrt{50-22\sqrt{5}}}{\pi}\right]M^4\right] \qquad (8.61)$$

When directly summed, (8.60) and (8.61) yield the same solution as the one obtained for the five-phase SVPWM by means of the complex analysis performed in chapter 7 (see 7.41):

$$HDF_{5-SVPWM} = \frac{1}{3}\left[\begin{array}{l} 2(K^2+K_2^2)M^2 - \frac{32}{3\pi}(K^3+K_2^3)M^3 \\ \\ + \frac{3}{2}(K^2+K_2^2)\left[\frac{7-\sqrt{5}}{4} - \frac{5}{8}\frac{\sqrt{50-22\sqrt{5}}}{\pi}\right]M^4 \end{array}\right] \qquad (8.62)$$

These HDFs are not shown graphically, but one can check that both polygon HDFs are with higher values than corresponding solutions for the five-phase SPWM and HIPWM. Thus, total solution (8.62) is also with higher values than HDF of the other two methods, as demonstrated in chapter 7.

To derive HDF for other multi-phase topologies, the third integral of (8.17) needs to be solved independently for each topology. Thus, for example, in the case of a three-phase SVPWM, solution for HDF is of the form [Holmes and Lipo (2003)]:

$$HDF_{3-SVPWM} = \frac{1}{3}\left[2K^2M^2 - \frac{32}{3\pi}K^3M^3 + \frac{3}{2}K^2\left[\frac{3}{2} - \frac{9}{8}\frac{\sqrt{3}}{\pi}\right]M^4\right] \qquad (8.63)$$

When plotted, this curve fits in between two HDFs of the HIPWM, thus showing that three-phase SVPWM has lower current ripple than HIPWM with the level of injection of the third harmonic given with $b = -1/6$ [Holmes and Lipo (2003)] while dc bus utilisation is with the same level. The injection with $b = -1/4$ remains to be the optimal solution regarding the optimisation of the current ripple.

Before providing discussion of the results obtained so far and presenting some simulation results, it is interesting to analyse current ripple characteristic of a half-bridge inverter. This topology is a building-block for all the other multi-phase inverters and therefore, potentially, can be used to verify findings obtained so far with complex and polygon approaches, respectively. Such an analysis is briefly presented next.

8.8 HARMONIC DISTORTION FACTOR OF A HALF-BRIDGE INVERTER

Topology of a half-bridge inverter and the model of a load, necessary for the analysis, are shown in Fig. 8.14. There is now only one modulating signals that is defined with:

$$v = M \cos(\vartheta) \tag{8.64}$$

Characteristic switching diagram, used for the analysis, is shown in Fig. 8.15. Similar to the analysis from the beginning of the chapter, duty cycles that correspond to the 'off' and 'on' state of the upper switch can be determined as:

$$\delta_{off} = \frac{1}{2}[1-v]; \qquad \delta_{on} = \frac{1}{2}[1+v] \tag{8.65}$$

From Fig. 8.15 one can write values of the current ripple at the end of every sub-interval as:

$$\Delta i(0) = 0$$
$$\Delta i(t_1) = \Delta i(0) + \frac{-V_{dc}/2 - e}{L} \delta_{off} \frac{T_s}{2} \tag{8.66}$$
$$\Delta i(t_2) = 0$$

Using the assumption that induced back emf equals reference voltage, after substitution of (8.65) into (8.66) one has:

$$\Delta i(0) = 0$$
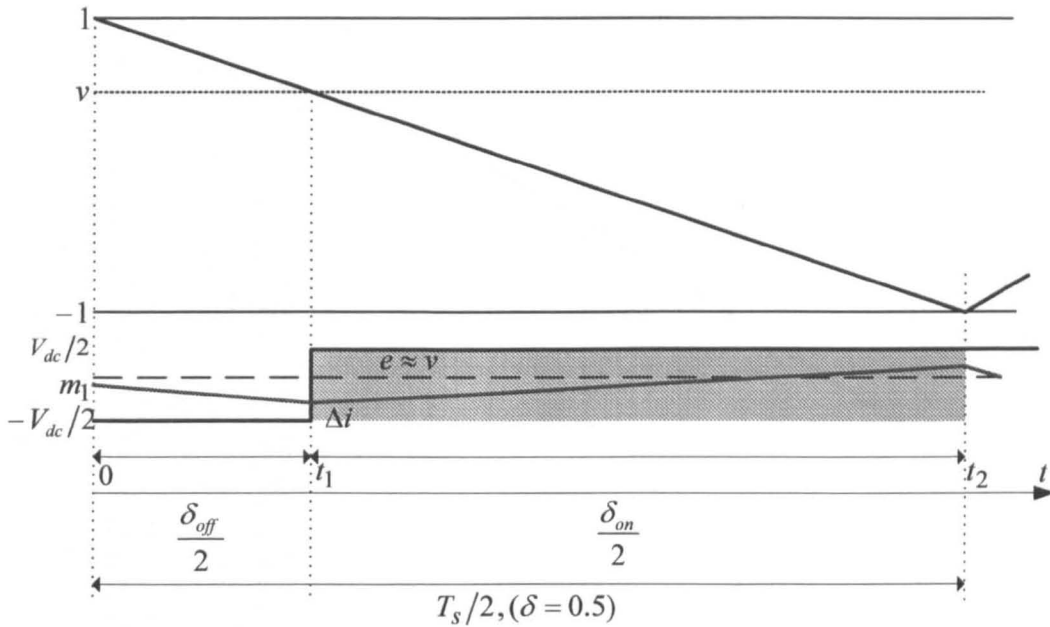$$\Delta i(t_1) = -\frac{V_{dc}T_s}{8L}(1-v^2) \tag{8.67}$$
$$\Delta i(t_2) = 0$$

Finally, the origin of the normalisation factor (8.8) used throughout chapters 7 and 8 becomes clear from (8.67). It represents the maximum value of the peak of the current ripple of a half-bridge inverter. After normalisation (8.67) becomes (in p.u.):

$$\Delta i(0) = 0$$
$$\Delta i(t_1) = -(1-v^2) \tag{8.68}$$
$$\Delta i(t_2) = 0$$
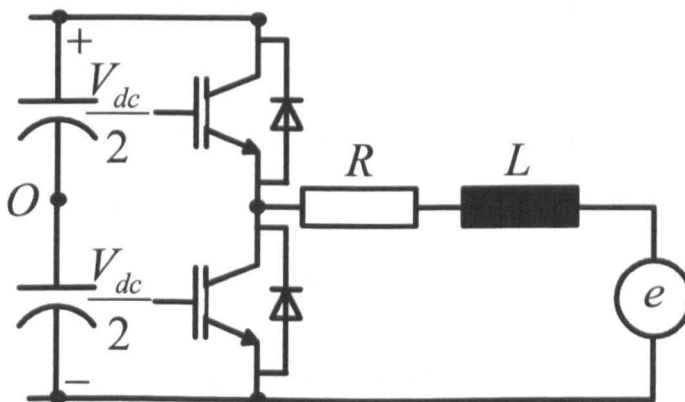
Fig. 8.14: Half-bridge inverter and the equivalent load for analysis.

Fig. 8.15: Switching pattern of the half-bridge inverter over the first half of the switching period.

For a microscopic analysis of the current ripple rms value, squared value of the current ripple over the switching period needs to be calculated. Again, it is sufficient to perform calculation over the first half of the switching period using (8.11). Based on the knowledge of the current ripple at the end of every sub-interval (only two exist now) continuous integration can be replaced again with the generic solution (8.12). Thus, based on two sub-intervals (Fig. 8.15), one has that squared value of the current ripple can be obtained from:

$$\Delta i^2{}_{RMS} = \frac{2}{T_s} \left[\int_0^{t_1} \Delta i^2(t)dt + \int_{t_1}^{T_s/2} \Delta i^2(t)dt \right] \tag{8.69}$$

Substituting (8.12) and taking into account that $\Delta i(0) = 0$ and $\Delta i(t_2) = 0$ one has:

$$\Delta i^2{}_{RMS} = \frac{1}{3} \left[\delta_{off} \Delta i^2(t_1) + \delta_{on} \Delta i^2(t_1) \right] \tag{8.70}$$

Introducing expressions (8.64), (8.65) and (8.68) into (8.70) yields:

$$\Delta i^2{}_{RMS} = \frac{1}{3} [1 - M^2 \cos^2(\vartheta)]^2 \tag{8.71}$$

Finally, to determine HDF, (8.71) needs to be evaluated over the fundamental period (macroscopic analysis). Therefore:

$$HDF_{Half-bridge} = \Delta i^2{}_{RMSF} = \frac{1}{2\pi} \int_0^{2\pi} \Delta i^2{}_{RMS} d\vartheta \tag{8.72}$$

After some manipulation, HDF of a half-bridge inverter is obtained as:

$$HDF_{Half-bridge} = \frac{1}{3} \left[1 - M^2 + \frac{3}{8} M^4 \right] \tag{8.73}$$
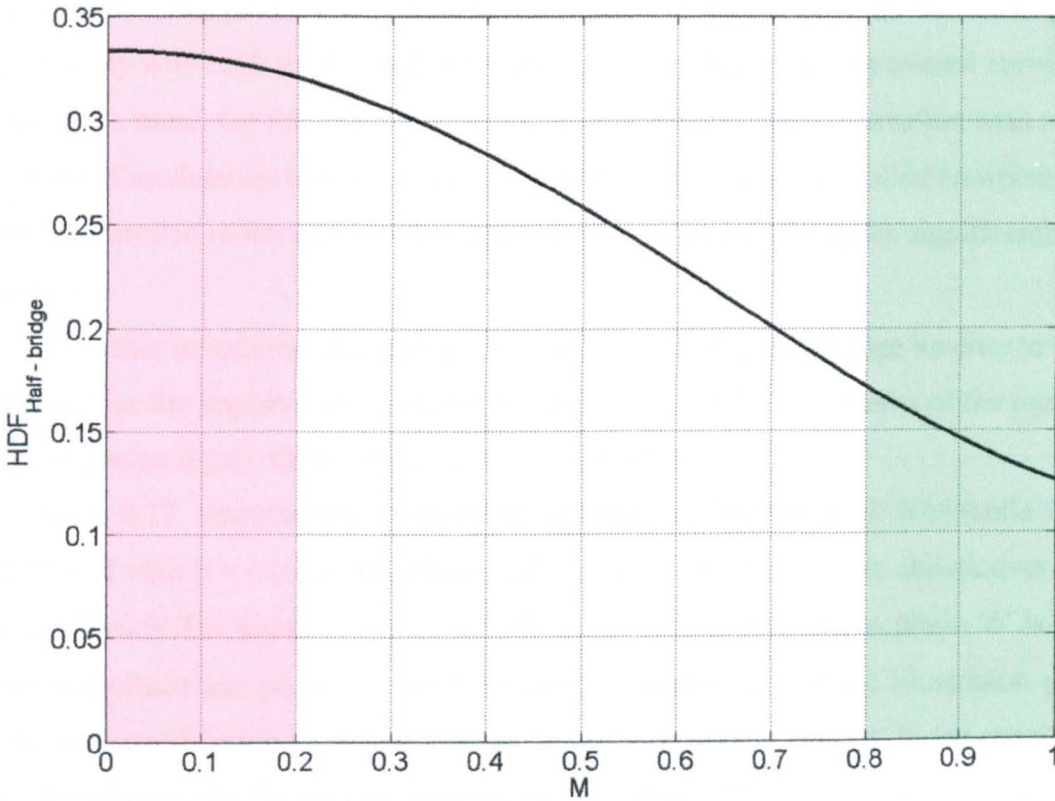
Fig. 8.16: HDF of a half-bridge inverter as a function of *M*.

This characteristic is plotted in Fig. 8.16 as a function of the modulation index *M*. The highest value of HDF is for the low values of the modulation index. For the illustration purposes, the low portion of the modulation index range is shaded to indicate the 'bad' zone of HDF where the current ripple is the highest. As the modulation index increases, HDF decreases, and the high portion of the modulation index range is differently shaded to indicate the 'good' zone of operation, where the current ripple is smaller. Depth of each zone is arbitrarily selected for the purpose of the following analysis.

Such an HDF characteristic appears very natural, considering that for the low values of *M* modulating signal is further away (considering scaling with $V_{dc}/2$) from discrete levels ±1 offered by the inverter during operation. Thus error voltage is relatively high at low value of *M*, resulting in a higher current ripple. With an increase of *M*, modulating signal gets closer to the voltage levels of ±1, thus resulting in lower error voltage that, when applied over the equivalent inductance, yields smaller current ripple.

Since the half-bridge inverter is the building-block for all the other multi-phase inverters, this observation can be used as a benchmark for the current ripple prediction in all other multi-phase topologies. It suggests that operation of the multi-phase inverter with modulating signals closer to the saturation levels of ±1 is preferable. In such operating regime, error voltage is smaller and should yield the lower current ripple. However, a

balanced set of multi-phase modulating signals obviously cannot have all modulating signals simultaneously with high values, and therefore impact of each phase on overall current ripple will not be the same. On the other hand, a regime that would require operation with relatively high values of modulation index is rather characteristic for PWM controlled rectifiers, but not for PWM controlled motor drives, where modulation index usually varies significantly during the operation.

To further investigate the possibility of using HDF of a half-bridge inverter to evaluate the potential for the improvement in the multi-phase PWM HDFs by means of the injection of the zero-sequence signal, three-phase case is analysed first.

In Fig 8.17, characteristic modulating signals of a three-phase SPWM (solid line), the third HIPWM with $b = -1/4$ (dashed line) and SVPWM (dotted line) are shown over the first sector, for $M=0.9$. The phase 'a' signal is with the maximum magnitude; phase 'b' is with the medium magnitude and phase 'c' is of the lowest magnitude. For the illustration purposes only, the same modulation index zones as in Fig. 8.16 are shown shaded. If one considers that each of the phases of a three-phase inverter has an equal effect on the overall HDF (current ripple), then the HDF of a half-bridge inverter can be considered as a benchmark for further evaluation, based on the analysis of the modulating signals before and after the injection.
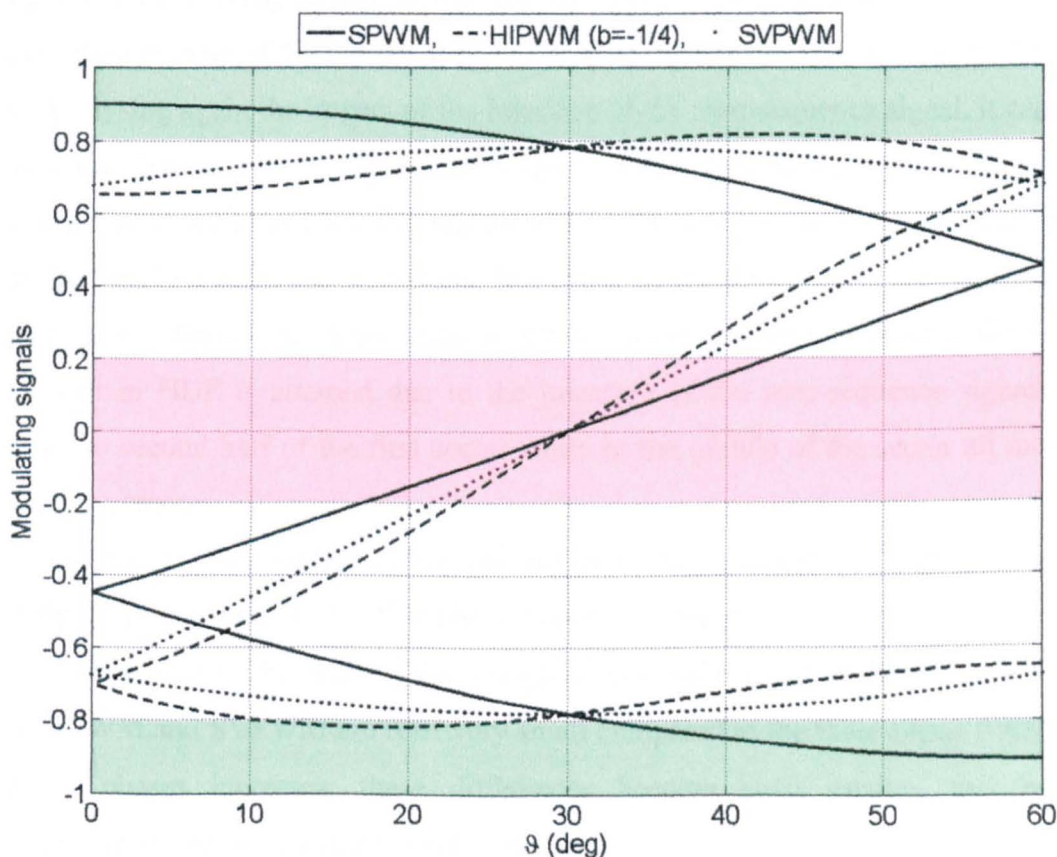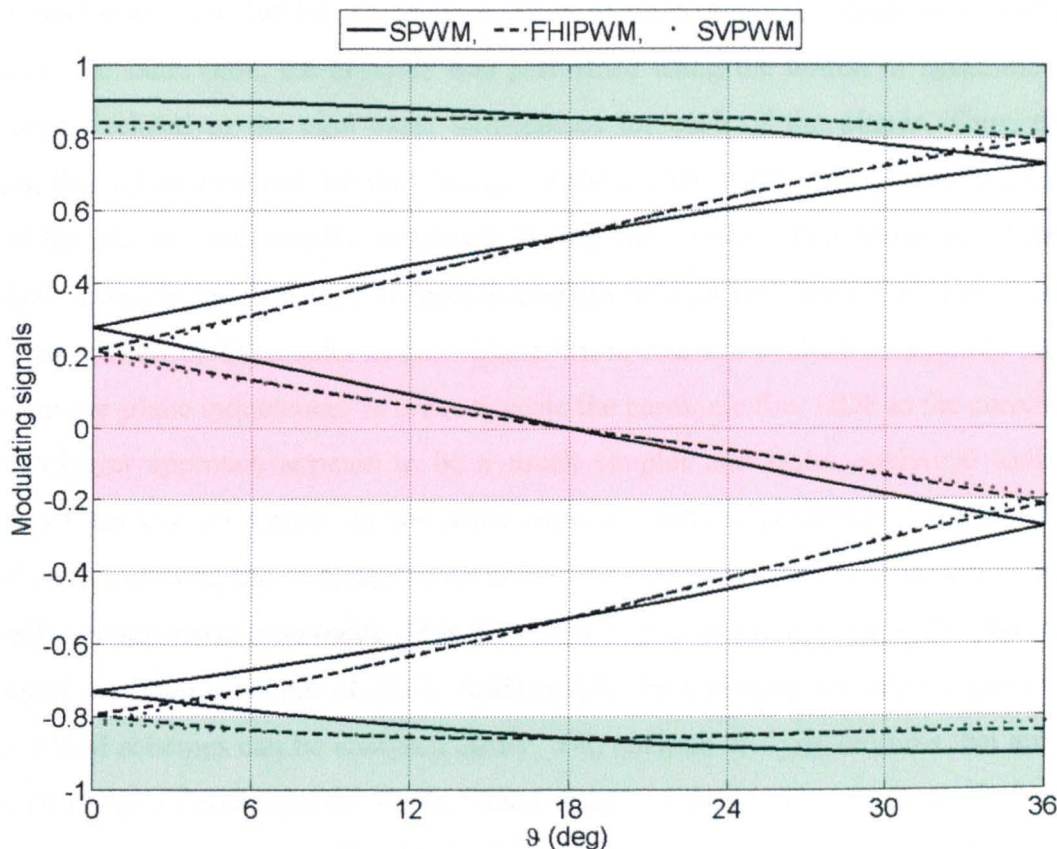

Fig. 8.17: Modulating signals of three-phase PWM schemes over the first sector ($M=0.9$).

Analysing the first half of the first sector, one can identify the effects of injection of the zero-sequence signals. Original SPWM modulating signal of phase '*a*' (the highest one in Fig. 8.17) that was in the 'good' zone of low HDF, gets pushed down towards the 'bad' zone of high HDF. Thus, overall, a negative action is applied to the phase '*a*' with injection of the zero-sequence signal. On the other hand, the other two phases receive positive actions with the injection, since new modulating signals of the HIPWM and SVPWM are pushed away from the 'bad' zone of high HDF (around zero), towards the 'good' zone of low HDF (closer to -1).

Therefore, in a three-phase system, one has two positive actions against one negative action as a result of the zero-sequence signal injection. While the injection worsens current ripple in phase '*a*', it actually improves current ripple in phases '*b*' and '*c*'. Therefore, based on this purely graphical analysis, zero-sequence signal injection in three-phase system can improve HDF over the level offered by the SPWM. A similar conclusion can be derived for any other instant over the second half of the first sector, while in the middle of the sector all three PWM schemes are with modulating signals of the same value.

The similar plot is shown in Fig. 8.18 for the analysed five-phase PWM schemes. Modulating signals of all three PWM schemes, are shown over the first sector for *M*=0.9. The ordering of the modulating signals is available in Table 6.1. It can be seen that differences in the modulating signals of FHIPWM and SVPWM are much smaller than in the three-phase system. Analysing again the impact of the injection of the zero-sequence signal, it can be seen that, over the first half of the first sector, three higher modulating signals of the SPWM receive negative actions (and become signals of FHIPWM or SVPWM) and are pushed down towards the 'bad' zone. At the same time, two lower modulating signals are pushed closer to the 'good' zone. Therefore, three negative actions overcome two positive actions, and no improvement in HDF is attained due to the injection of the zero-sequence signal. Similar applies to the second half of the first sector while in the middle of the sector all modulating signals are the same.

Thus this, rather simple, graphical analysis suggests that no improvement in the current ripple is possible in the five-phase system by means of the injection of the zero-sequence signal. It is visible that for the five-phase case differences in the modulating signals of the FHIPWM and SVPWM are relatively small compared to the three-phase PWM. As the number of phases increases, these differences become even smaller, this being the consequence of the reduced angular span of the sectors.

Fig. 8.18: Modulating signals of five-phase PWM schemes over the first sector (*M*=0.9).

8.9 DISCUSSION OF THE ANALYTICAL RESULTS

By comparing the results, obtained by means of the complex approach and the polygon approach, some findings need to be addressed in more detail. Complex approach, presented in chapter 7 and based on the space vector theory, is closely related to the principles of the modelling of electric machines. Using the five-phase system as an example, decoupling transformation is of the form given with (3.15).

$$\underline{C}_5 = \frac{2}{5}\begin{bmatrix} 1 & \cos(\alpha) & \cos(2\alpha) & \cos(3\alpha) & \cos(4\alpha) \\ 0 & \sin(\alpha) & \sin(2\alpha) & \sin(3\alpha) & \sin(4\alpha) \\ 1 & \cos(2\alpha) & \cos(4\alpha) & \cos(\alpha) & \cos(3\alpha) \\ 0 & \sin(2\alpha) & \sin(4\alpha) & \sin(\alpha) & \sin(3\alpha) \\ 1/2 & 1/2 & 1/2 & 1/2 & 1/2 \end{bmatrix} \tag{3.15}$$

Here, the angle *α* within brackets is defined as before with $\alpha = 2\pi/5$, and is not related to angle *α* used in polygon analysis. During the complex analysis, variables from the original domain (squares of phase currents) have been transformed into complex domain and their representation in the d_1-q_1 and d_2-q_2 planes has been obtained. The first two rows of (3.15) correspond to the d_1-q_1 plane, while the second two rows are related to the d_2-q_2 plane. This

204

transformation allowed for the complex analysis to be performed separately in each of the planes. At the same time, the analysis was performed using the notion of harmonic flux, to avoid issues related to the equivalent inductances for each of the planes. Thus, the error voltages, that are responsible for the creation of the current ripple, were actually analysed in each of the planes. The results, produced in this way, were independent from the actual equivalent inductances in each of the planes, and allowed for the final HDF to be obtained by simple summation of the results in each plane. More realistic evaluation requires use of the equivalent per-plane inductances in order to scale the harmonic flux HDF to the current HDF.

Polygon approach appears to be a much simpler and faster analytical tool for the analysis of the current ripple. At the same time, it offers a possibility to perform a very general analysis, using the H-bridge inverter and the equivalent load representation, covering all possible multi-phase topologies. This is achieved by a simple change of the phase shift of the second modulating signal of (8.1). Additionally, by changing the zero-sequence signal, various PWM schemes can be analysed easily. Yet, such an analysis requires that an n-phase system (n being an odd number) is connected in one of its $(n-1)/2$ polygons. Each polygon yields its own solution for the HDF for a particular PWM scheme. Thanks to the generalisation introduced with angle $\alpha = P\pi/n$, these solutions differ only in the trigonometric constant that appears in each of the particular HDFs. On the other hand, an immediate difficulty with polygon approach, when applied to a multi-phase case, is the identification of the equivalent inductance. Based on the analysis presented in this chapter, it appears that whatever polygon is selected, the equivalent inductance is the same, since one phase of the load is directly exposed to the relevant line voltage. This inductance is however neither equal to the one of (7.44) nor the one of the (7.45), since these values result after decomposition into 2-D planes.

Considering a five-phase system again, the HDFs obtained for each polygon are completely different from the solutions obtained for each of the planes with the complex approach (irrespectively of the PWM scheme considered). However, a closer inspection of the way how decoupling transformation (3.15) is organised and Fig. 8.1, where polygon connections are shown, reveals an analogy. The connection of the *P1* (Fig. 8.1b) corresponds to the first two rows of (3.15), while the *P2* (Fig. 8.1c) is in accordance with the second two rows of (3.15). Yet, as emphasised already, HDFs of the polygons are not the same as HDFs of the planes. However, when summed (HDFs of two polygons, and HDFs of two planes), both complex and polygon approach produce exactly the same final current HDF. This is valid for all PWM scheme analysed in the thesis, as long as the equivalent inductances are

assumed equal, for either planes or polygons. Since all the results are normalised, this does not represents a problem, as long as precise numerical evaluation is not a goal. However if an exact evaluation of the current HDF for a multi-phase motor drive is required, it appears that the complex approach has to be used since it naturally leads to definition of different inductances in 2-D planes ((7.44) and (7.45)). The equivalent phase inductance of (8.2) in polygon approach is obviously the same regardless of which polygon is analysed, while in essence the machine behaves as having very different inductances for different harmonics (in different planes).

The use of the concept of harmonic flux for the analysis of current ripple alleviates the problems of selection of the equivalent inductance per plane. This is achieved by simple replacement of the analysis of the current deviation by the analysis of the deviation of the error voltage. Since these error voltages are created in the same way in each of the planes, this allows for the summation of the final results (harmonic flux HDFs of each plane). The dependence on the equivalent inductances is thus effectively disguised by the introduced normalisation, and direct comparison of HDFs of different PWM schemes for the same phase number is possible. However, if these results are used to compare certain PWM schemes of different multi-phase systems, then these HDFs are very optimistic predictions of current ripple (giving lower values than the actual ones), since they assume unrealistically high values for the equivalent inductances in the planes other than the first plane.

Thus, the polygon approach produces a valid result. It yields the solution comprising several parts (the number of parts equals the number of polygons of a system), which must be all summed together to obtain the final HDF. It is important to note that mutual relations between the HDFs obtained for particular PWM schemes stay the same for each polygon. This is illustrated in Fig. 8.19 where HDFs of all three PWM schemes are shown for both polygons and for the complete solution as well. As can be seen, HDFs obtained for each of the polygons show that SPWM is with the lower HDF than FHIPWM and SVPWM, and that HDF of the SVPWM is with the highest values (these differences are visible in the upper range of the modulation index). Thus, the use of just one of the polygons is sufficient only for the purposes of a quantitative comparison of the PWM schemes for a particular multi-phase topology. This mean that the results presented by Dahono (2006), Dahono and Deni (2006) and Deni et al (2007) are correct at least to some extent (regarding the comparison of different PWM scheme based on the results for the *P1*). Yet, the use of the HDF of only one of the polygons does not represent a complete solution for the HDF of a particular multi-phase system and selected PWM scheme.
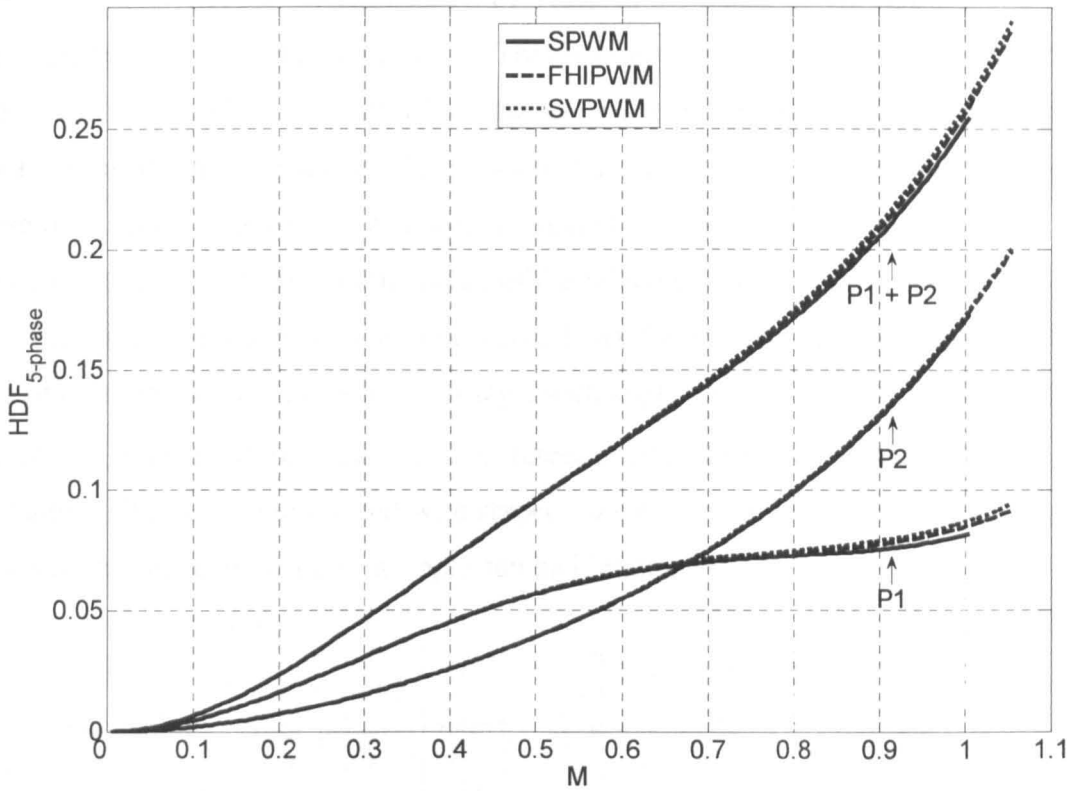
Fig. 8.19: HDF of the five-phase SPWM, FHIPWM and the SVPWM as a function of *M*.

8.9   SIMULATION RESULTS

A similar set of simulations, as for the complex approach, has been carried out in order to determine the current ripple of various polygon connections of multi-phase systems. In all the cases analysed, switching frequency is set to 1 kHz while the fundamental frequency is set to 50 Hz (since only highly inductive (*R-L*) load is considered as being connected to the H-bridge inverter). Only the plots of the switched voltage and the reference voltage (bold traces) are shown, together with the shape of the generated harmonic current ripple. Spectrum plots are not shown here, since polygon analysis applies line voltage across the equivalent load, which is of different value for each polygon connection (for the same phase number). Thus, to avoid the difficulties associated with normalisation to the same level, only the shape of the current ripple is analysed. At first, results are presented for the cases of half-bridge and H-bridge inverters, in order to verify the validity of the developed MATLAB model, since these results are available in the literature [Holmes and Lipo (2003)].

Fig. 8.20 shows one fundamental period of the reference and switched voltage, and the shape of the current ripple for the case of the half-bridge inverter. Sinusoidal modulating signal is applied and two cases are illustrated that correspond to the operation with *M*=0.1 and

207

M=0.9, respectively. It can be seen that a decrease in the peaks of the ripple current occurs with the increase of the modulation index. This is in accordance with the HDF characteristic from Fig. 8.16. Around the instants where the reference voltage is close to the zero (and thus far away from the discrete levels ±1), peaks of the ripple current are the highest. With the increase of the modulation index a significant reduction in the peak excursions of the current ripple happens (especially around the peaks of the reference voltage).

The same simulations have been carried out for the H-bridge inverter. Modulating signals of (8.1) are applied to the inverter legs, with angle α set as $\alpha = \pi/2$, for the modulation index of the values M=0.1 and M=0.9, respectively. Switched voltage is now of the magnitudes of 0 and ±2 (normalised with respect to the $V_{dc}/2$). This is illustrated in Fig. 8.21, from where the shape of the current ripple can be identified.
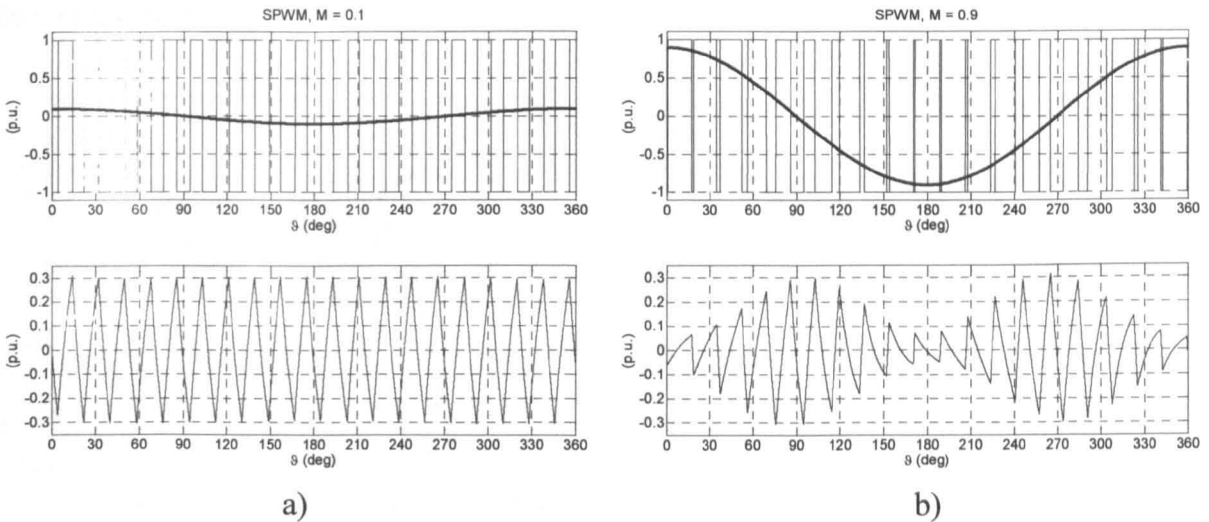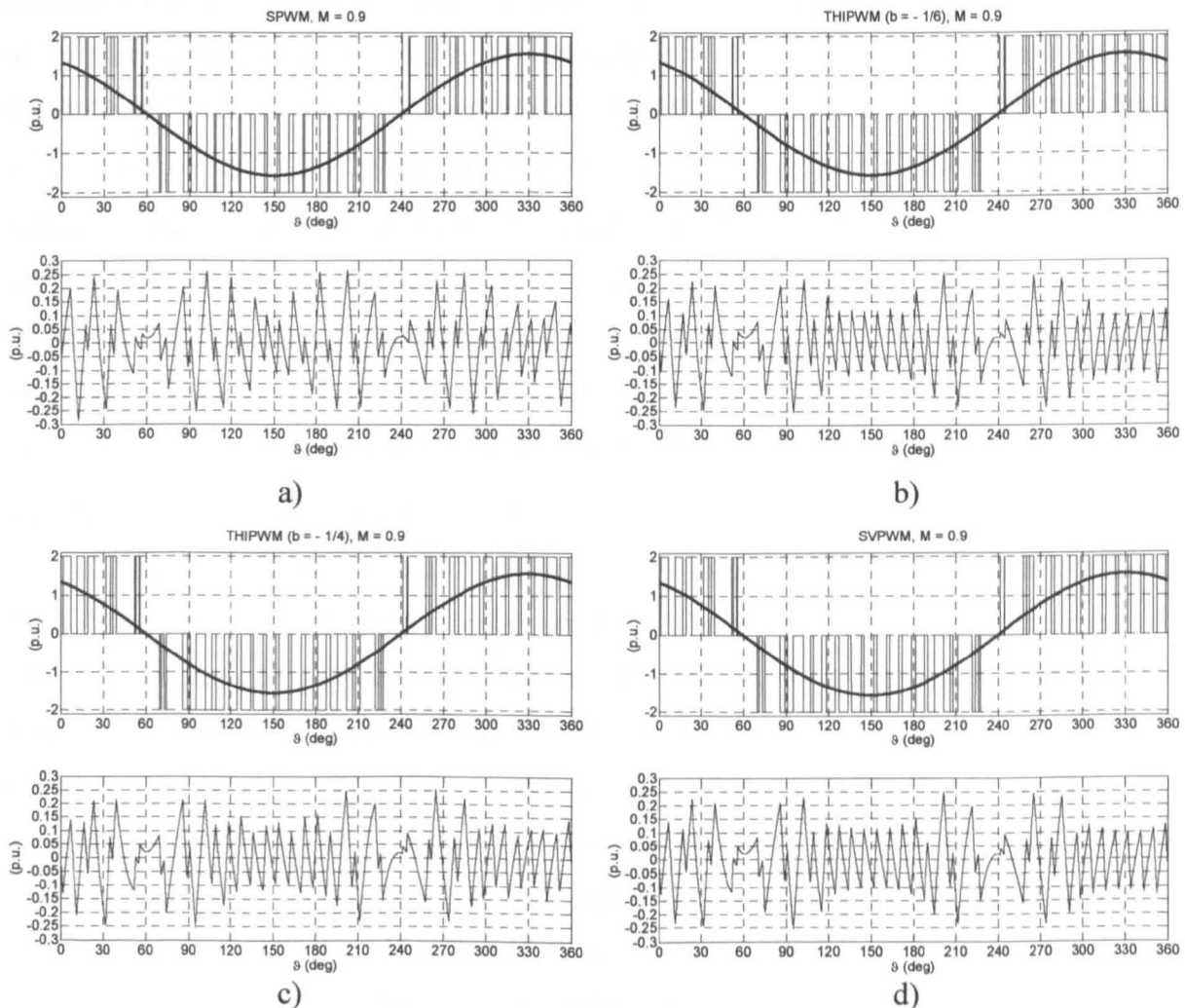

Fig. 8.20: Half-bridge SPWM: Simulated reference and switched voltage for half-bridge inverter (top) and harmonic current ripple (bottom) at: a) M=0.1 and b) M=0.9.
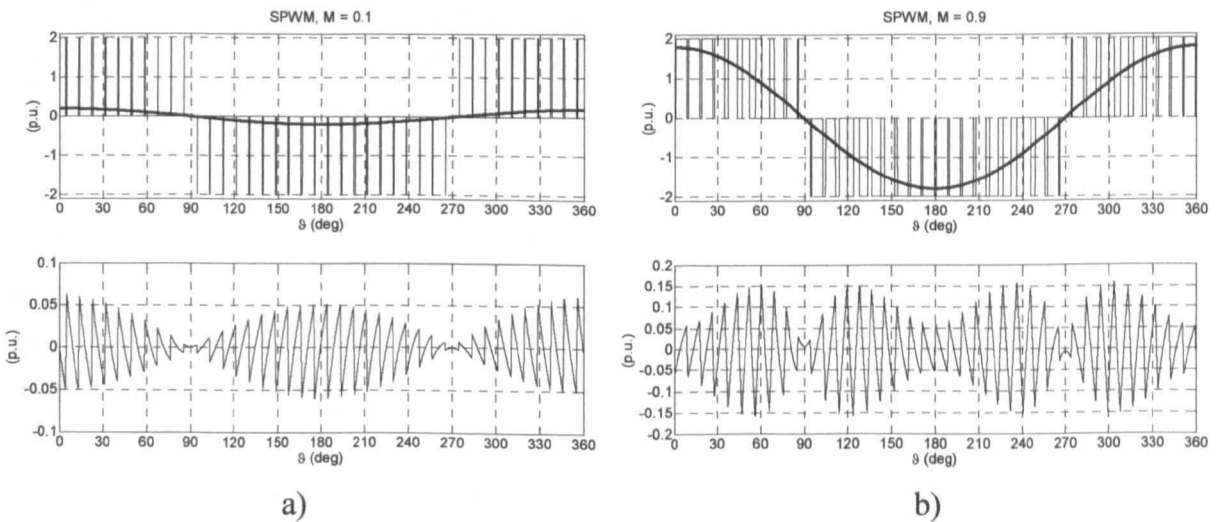
Fig. 8.21: H-bridge SPWM: Simulated reference and switched voltage for H-bridge inverter (top) and harmonic current ripple (bottom) at: a) M=0.1 and b) M=0.9.

It can be seen from Fig. 8.21b that the ripple frequency is doubled, compared to the case of the half-bridge inverter. At the same time, a reduction in the magnitude is obtained, which is in accordance with the HDF characteristics shown in Fig. 8.6 (H-bridge inverter) and Fig. 8.16 (half-bridge inverter).

Three-phase case is investigated next. Angle α is set as $\alpha = \pi/3$, which corresponds to the three-phase load being in the delta connection. Like in previous two cases, simulations are performed over one fundamental period of the modulating signals (8.1) and the reference line voltage is of the $\sqrt{3}$ higher magnitude. Current ripple, created by the application of three PWM schemes, is analysed for the case of $M=0.9$, since at higher range of the modulation index differences in the obtained HDFs are more pronounced. These results are shown in Fig. 8.22 from where it can be seen that the shape of the current ripple appears very similar in all four cases illustrated.
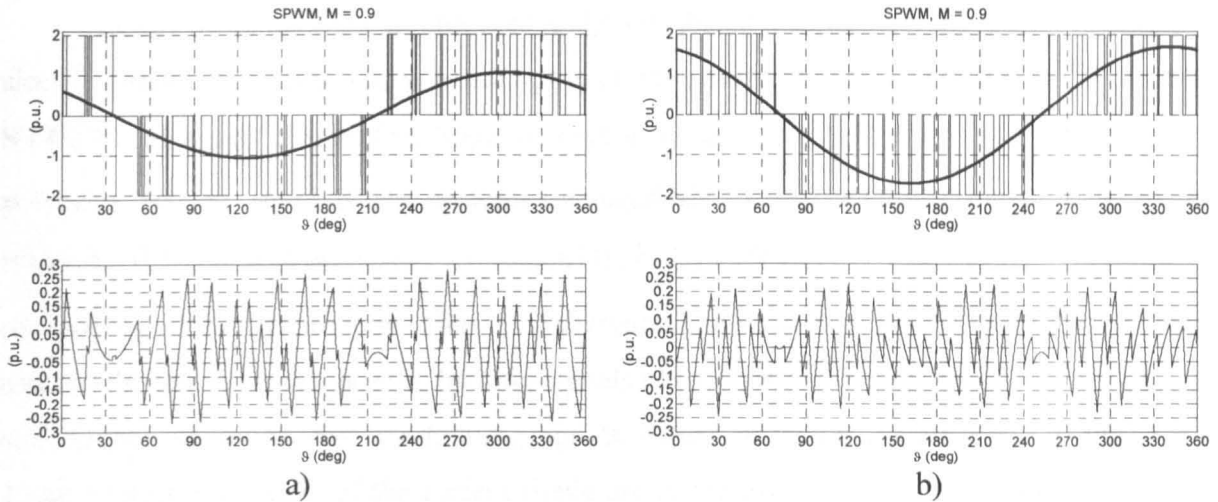

Fig. 8.22: Three-phase PWM: Simulated reference and switched voltage for one phase of a load in delta connection (top) and harmonic current ripple (bottom) at $M=0.9$ for: a) SPWM, b) THIPWM ($b = -1/6$), c) THIPWM ($b = -1/4$) and, d) SVPWM.

However, it can be seen that the peak excursions are reduced with the use of the third HIPWM (THIPWM) with level of the third harmonic defined with $b = -1/4$ (Fig. 8.22c), compared to the other three cases illustrated. At the same time, peaks of the current ripple caused by the application of SPWM, are of the highest values. These observations are in accordance with the mutual relations of the HDFs of the SPWM, HIPWM (both levels of the injection) and the SVPWM in a three-phase system. Similar results can be found in Holmes and Lipo (2003), where more detailed considerations are given for three-phase PWM schemes.

Both polygon connections of a five-phase system are analysed next, including all three PWM schemes, namely: SPWM, FHIPWM (with the level of injection set to optimise dc bus utilisation; $b = -\sin(\pi/10)/5$) and SVPWM (equivalent of the TIPWM). These results are shown in Figs. 8.23-8.25, respectively, for the operation, in the higher range of the modulation index, with $M=0.9$. The X-axis in all plots corresponds to one fundamental period of the modulating signals (8.1) and the appearance of the reference line voltage (shown in bold) depends on the value of the angle α. The value of this angle is for the *P1* equal to $\alpha = \pi/5$ and for *P2* is $\alpha = 2\pi/5$ (in accordance with the data given in Table 8.1). Therefore, reference line voltages (shown in bold) appear with different phase shift for each polygon, although the same range applies for the X-axis. At the same time, the magnitude of the reference line voltage of both polygons is higher than the magnitude of the reference modulating signals of (8.1). Thus for the *P1*, magnitude of the reference line voltage is $|v_{12}|_{P1} = 2M\cos(3\pi/10)$, while for the *P2*, the magnitude is $|v_{12}|_{P2} = 2M\cos(\pi/10)$. This is visible for all cases illustrated in Figs. 8.23-8.25.

Comparing at first the results obtained for two polygons, it can be seen that for all three PWM schemes peaks of the ripple current of *P2* are lower than those in the case of *P1*. This is in accordance with the results presented in Fig. 8.19, where it can be seen that for operation with $M=0.9$ *P2* has lower HDF than the *P1*. It is also visible from Fig. 8.19, that situation is reversed for the values of M below approximately 0.67. These operating points have not been investigated by means of simulations. Further investigation reveals that peaks of the ripple current of the SPWM are with slightly lower values than those of FHIPWM and SVPWM, for both polygons. Yet, these differences are relatively small, and not immediately obvious. This is also in accordance with the HDFs of Fig. 8.19, from where it can be seen that all the HDFs practically overlap and only relatively small separation occurs for high values of M.

Fig. 8.23: Five-phase SPWM: Simulated reference and switched voltage for one phase of a load in polygon connection (top) and harmonic current ripple (bottom) at *M*=0.9 for: a) adjacent polygon (*P1*) and b) non-adjacent polygon (*P2*).
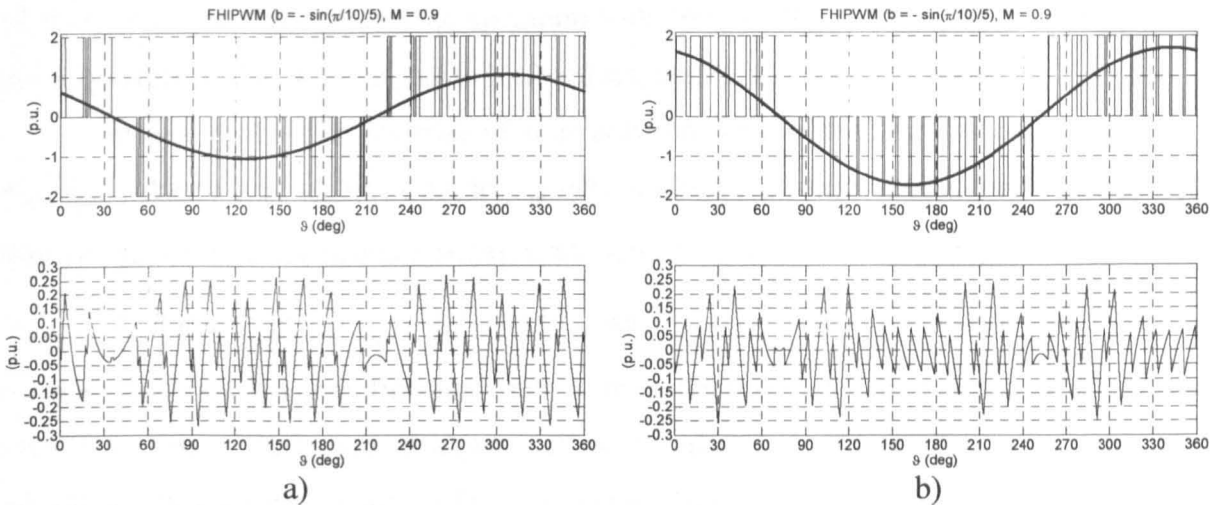
Fig. 8.24: Five-phase FHIPWM: Simulated reference and switched voltage for one phase of a load in polygon connection (top) and harmonic current ripple (bottom) at *M*=0.9 for: a) adjacent polygon (*P1*) and b) non-adjacent polygon (*P2*).
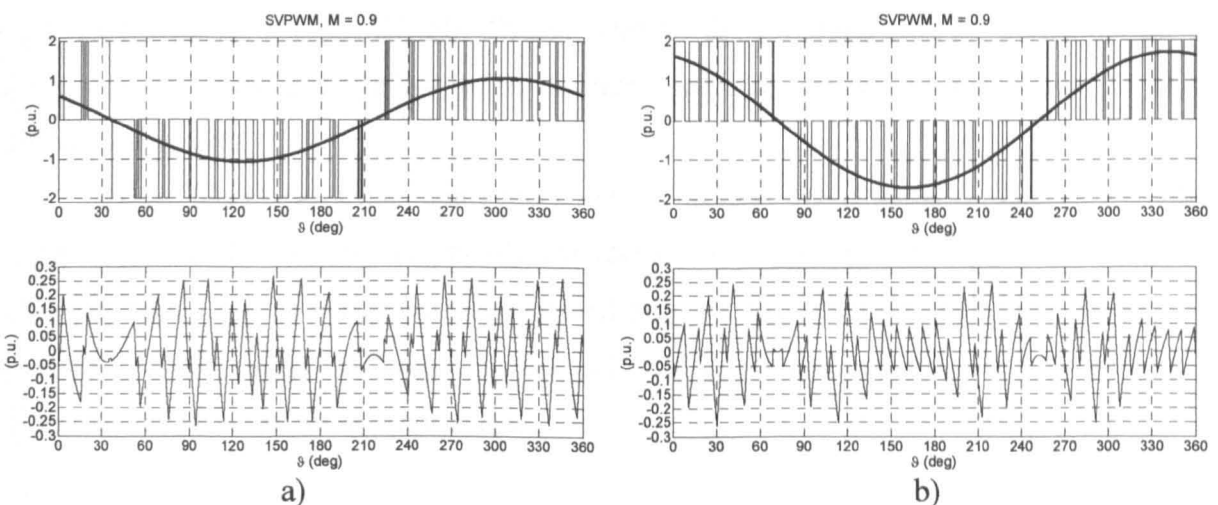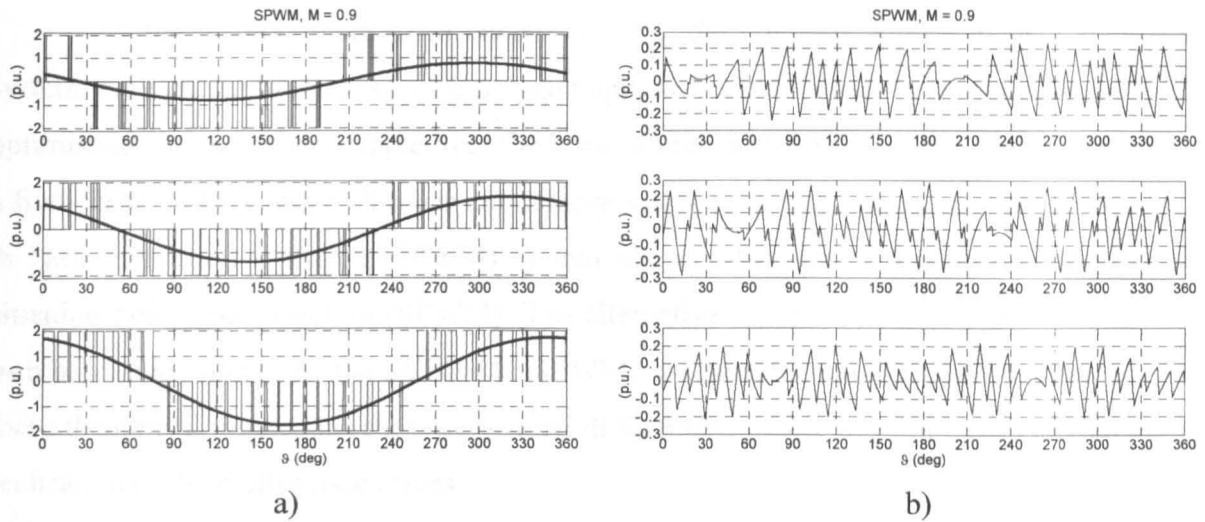

Fig. 8.25: Five-phase SVPWM: Simulated reference and switched voltage for one phase of a load in polygon connection (top) and harmonic current ripple (bottom) at *M*=0.9 for: a) adjacent polygon (*P1*) and b) non-adjacent polygon (*P2*).

211

Seven-phase system is analysed only for the application of the SPWM, since, as already emphasised, differences in the ripple current caused by the use of the HIPWM or the SVPWM are hardly observable. Angle a is set to $\alpha = \pi/7$, $\alpha = 2\pi/7$ and $\alpha = 3\pi/7$ for the three polygons of the seven-phase systems, respectively. Corresponding, magnitudes of the reference line voltages are $|v_{12}|_{P1} = 2M\cos(5\pi/14)$, $|v_{12}|_{P2} = 2M\cos(3\pi/14)$ and $|v_{12}|_{P3} = 2M\cos(\pi/14)$, respectively, for each polygon. Thus, the reference line voltage of the *P1* is actually of lower magnitude than the reference modulating signals of (8.1), while the other two line voltages are with higher magnitude than modulating signals. Based on the results presented in Fig. 8.26b, it can be seen that peaks of the current ripple are of the lowest value in the case of *P3*, while *P2* current ripple is with the highest peaks excursions. Thus, the results obtained by means of the simulation confirm validity of the already given HDFs of each polygon of a seven-phase SPWM, shown in Fig. 8.8. For the operation with *M*=0.9, HDFs of the polygons organised in the descending order, with respect to their values, are *P2, P1, P3*.

Similar results, for the case of four polygons of a nine-phase system, are shown in Fig. 8.27. Angle a is set this time to $\alpha = \pi/9$, $\alpha = 2\pi/9$, $\alpha = 3\pi/9$ and $\alpha = 4\pi/9$, respectively. Magnitudes of the reference line voltages are now: $|v_{12}|_{P1} = 2M\cos(7\pi/18)$, $|v_{12}|_{P2} = 2M\cos(5\pi/18)$, $|v_{12}|_{P3} = 2M\cos(3\pi/18)$ and $|v_{12}|_{P4} = 2M\cos(\pi/18)$, respectively. Again, the magnitude of the line voltage of *P1* is lower than the magnitude of the reference modulating signals of (8.1), while remaining line voltages are of higher values. Similar to the seven-phase case, one easily establishes that results shown in Fig. 8.9, where HDFs for each polygon are given, are in agreement with the results obtained by means of simulation and shown in Fig. 8.27b. The ordering of current ripple peaks of different polygons, from the one with the highest to the one with the lowest, is: *P2, P3, P1, P4*. This is valid for the operation with *M*=0.9, while for the lower values of the modulation index different ordering applies, in accordance to HDFs shown in Fig. 8.9.

Thus, based on these simulation results, it can be concluded that an excellent agreement is achieved with analytically calculated HDFs for various polygons of the multi-phase systems. The investigation is conducted only for the operation with high value of the modulation index, where differences between HDFs (or the current ripple peak excursions) of different polygons are more pronounced.

Fig. 8.26: Seven-phase SPWM: Simulated reference and switched voltage for one phase of a load (a)) and harmonic current ripple (b)) at *M*=0.9 for polygon connections: *P1* (top), *P2* (middle) and *P3* (bottom).
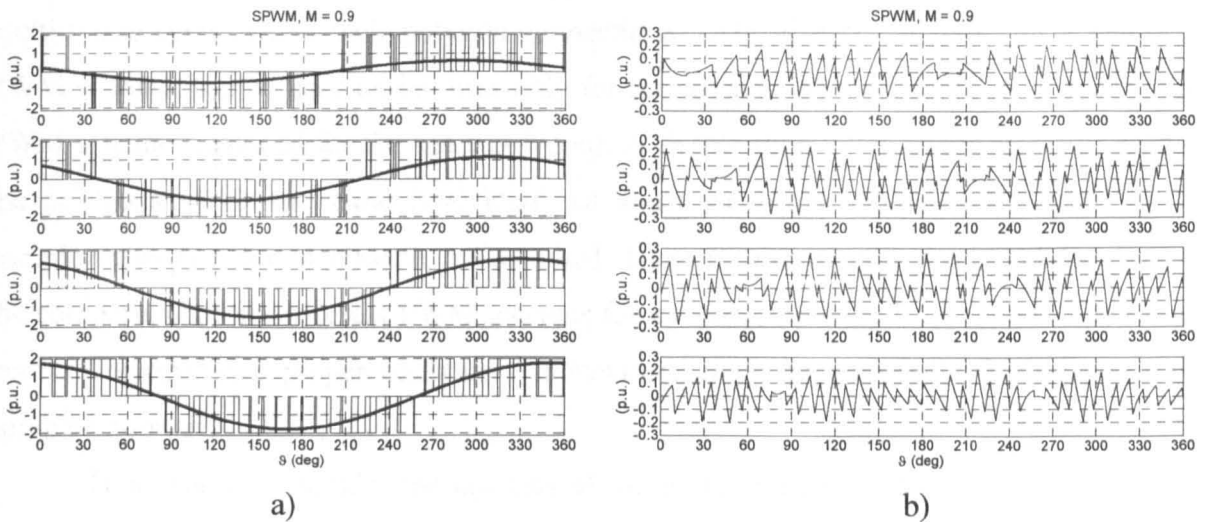
Fig. 8.27: Nine-phase SPWM: Simulated reference and switched voltage for one phase of a load (a)) and harmonic current ripple (b)) at *M*=0.9 for polygon connections, (from top to bottom): *P1, P2, P3* and *P4*.

8.10 SUMMARY

The use of polygon approach, for the analytical analysis of the output current ripple rms in multi-phase drives, has been presented in this chapter. A very general analysis is given, and generated results include those, already known, for the half-bridge, H-bridge and three-phase inverter topologies. The results obtained for the higher phase number topologies show different characteristics than those of a three-phase system, with respect to the application of different PWM schemes and their influence on the output current ripple.

All the results, obtained in chapter 7 using the complex approach for a five-phase system, are verified by means of the polygon approach. Additionally, it is established that the optimisation of the current ripple over the level offered by SPWM in not possible not only in a five-phase system, but in all other multi-phase systems, as well. Thus, the injection of the n-th harmonic in an n-phase (HIPWM) system worsens the current ripple, compared to the situation before the injection (SPWM). The alternative injection of all the odd multiples of n-th harmonic, offered by the SVPWM (TIPWM), worsens the current ripple even more. Yet, these theoretical predictions show very small differences, which may not be of concern during realisation of the multi-phase drives.

In contrast to the complex approach, the polygon approach does not offer intermediate results, although final HDFs are obtained in a simpler fashion. Additionally, HDFs are of the general form (at least for the SPWM and HIPWM) and can be directly applied to all other multi-phase systems and their polygon connections. HDF of each polygon, for a particular PWM scheme, can be used on its own, only for the comparison with the HDF of some other PWM scheme (obtained for the same polygon). A simple summation of the HDFs of each of the polygons yields the same final HDF, as when the HDFs, obtained by means of the complex approach for each plane, are summed. These results are completely valid as long as the comparison of the different PWM schemes for the same topology is of interest. For a more realistic comparison, proper equivalent inductances must be included, which favours the complex approach.

This chapter concludes the analysis of the basic properties of the multi-phase PWM modulation methods, aimed at sinusoidal output voltage generation for single-motor drives. In the next two chapters, development of the PWM schemes, which are able to generate multi-frequency output voltage necessary for multi-motor drives, is presented. PWM methods for series-connected multi-phase multi-motor drives are elaborated in the next chapter.

<center>Chapter 9</center>

PWM METHODS FOR MULTI-FREQUENCY OUTPUT VOLTAGE GENERATION WITH MULTI-PHASE VOLTAGE SOURCE INVERTERS

9.1   INTRODUCTION

In the preceding chapters, the analysis has been focused on the development of PWM schemes and identification of the main characteristics of multi-phase VSIs for multi-phase single-motor drives. For all the considered numbers of phases, sinusoidal output voltage generation was aimed at, suitable for multi-phase machines with distributed windings (near-sinusoidal mmf distribution). Such PWM schemes generate inverter output voltages based on the non-zero reference in the first plane, with zero reference setting in the all other planes.

As discussed in chapters 1 and 2, available degrees of freedom of a multi-phase machine with distributed windings allows for connection of several other multi-phase machines in an appropriate series connection. In such a topology, the multi-phase VSI has to generate output voltages that can effectively control flux and torque production of each of the machines. Therefore, multi-frequency output voltage is necessary, which requires an appropriate PWM scheme. Development of such a scheme, based on both carrier-based PWM and SVPWM is presented in this chapter, and is verified experimentally on a five-phase series-connected two-motor drive.

This chapter is organised as follows. In section 9.2, series-connected multi-phase multi-motor drives are briefly addressed and requirements for the PWM scheme are set forth. Problems of voltage limits (dc bus utilisation) imposed to such drive topologies are analysed in section 9.3 and a simple analytical method is devised that characterises dc bus utilisation in the linear region of modulation. Detailed development of multi-frequency SVPWM scheme is presented in section 9.4, using the five-phase series-connected two-motor drive as an example. Principles of extension to higher phase numbers are also given. Section 9.5 deals with the carrier-based approach to multi-frequency output voltage generation. DSP related

<div align="right">215</div>

implementation issues are addressed in section 9.6, while the experimental results are provided in section 9.7. Summary of the chapter is given in section 9.7.

The main original results of this chapter have been presented in Dujić et al (2008a), Dujić et al (2008b), Levi et al (2008), and Casadei et al (2008).

## 9.2   SERIES-CONNECTED MULTI-PHASE MULTI-MOTOR DRIVES

The basic operating principles of series-connected multi-phase drives have already been reviewed in chapters 1 and 2. Therefore, only requirements imposed on the multi-phase VSI are addressed in this section.

The number of phases n of the machine/VSI is further assumed to be a prime number. Such a multi-phase machine (VSI) can be modelled using VSD approach [Zhao and Lipo (1995)]. Assuming star connected stator winding with isolated neutral, modelling leads to the representation of the machine/inverter in $(n-1)/2$ mutually orthogonal and decoupled 2-D planes. This situation, which arises in machines with near-sinusoidal mmf distribution, means that only the first plane (d_1-q_1) of $(n-1)/2$ planes is excited, while the inverter output voltage reference is zero in all the other planes (neglecting switching harmonics). The situation however changes substantially if a machine has a concentrated stator winding. In such a case all odd supply harmonics of the order lower than the phase number n can be utilised for torque production (for example, the first and the third in a five-phase machine, the first, the third and the fifth in a seven-phase machine, etc.). As far as the VSI is concerned, this means that it has to generate a multi-frequency output voltage, with, in principle one voltage component (harmonic) per each of the $(n-1)/2$ 2-D planes $(d_1-q_1, d_2-q_2, d_3-q_3...)$. Appropriate PWM control schemes for such output voltage generation with VSIs have already been developed, for example for five-phase VSIs [Ojo and Dong (2005), Ryu et al (2005), Ojo et al (2006)].

The third situation that may arise is the use of multi-phase machines with an appropriate series-connection of stator windings and the supply coming from a single multi-phase VSI [Levi et al (2004a), Levi et al (2004b)]. Phase transposition, introduced in the series connection, essentially leads to independent control of, in general, $(n-1)/2$ multi-phase machines. This requires that the inverter generates at the output again one voltage component per each of the $(n-1)/2$ planes. The only, but important, difference, compared to the case of a single multi-phase machine with concentrated winding, is that in this case required voltage components in different planes are completely unrelated. Some PWM schemes for series-

connected multi-phase machines, that enable multi-frequency output voltage generation, have been developed in [Iqbal and Levi (2006b), Iqbal et al (2006b)].

On the basis of the explanations given above it is obvious that, from the inverter point of view, supply of a machine with concentrated stator winding is the same as the supply of a series-connected multi-phase multi-motor drive system. In both cases the VSI has to generate an output voltage that contains $(n-1)/2$ voltage components (harmonics), which belong to different planes (one per each of the $(n-1)/2$ 2-D planes). A consequence of the physical phase transposition, introduced in the series connection of stator windings, is that fundamentals of $(n-1)/2$ machines are mapped into $(n-1)/2$ 2-D planes, respectively. This is illustrated in Figs. 9.1 and 9.2 for the five-phase and seven-phase case, respectively. It is important to realise that the two cases shown are only equivalent from the inverter output voltage generation point of view. While for series-connected multi-motor drives Figs. 9.1 and 9.2 include representation of physical stator windings, it is not so for concentrated winding machines. in which case these are fictitious windings that do not exist as separate entities in reality.
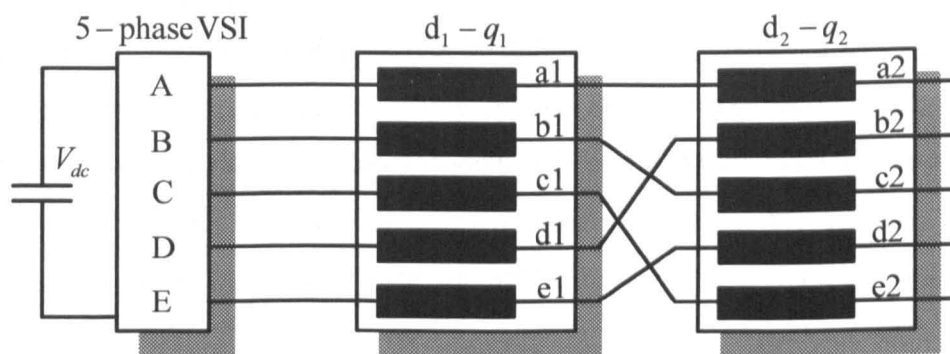
Fig. 9.1: Illustration of the required VSI output voltage generation in two planes of the five-phase system (two-motor series-connected drive system or concentrated winding machine with the third harmonic injection).
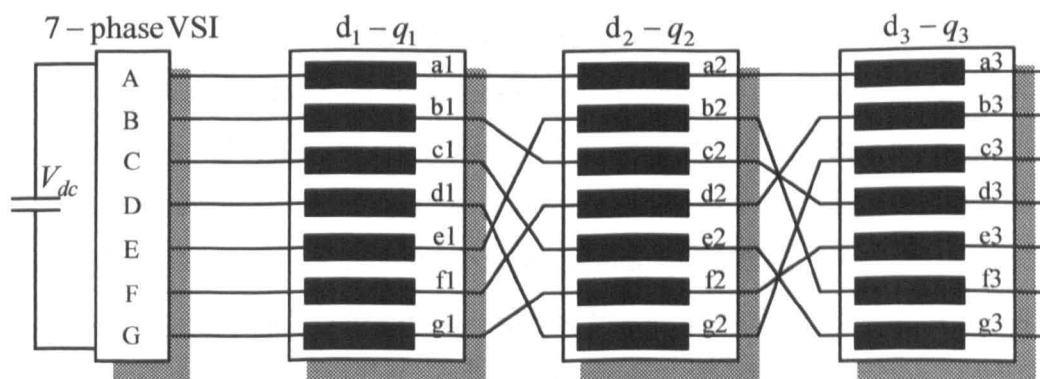
Fig. 9.2: Illustration of the required VSI output voltage generation in three planes of the seven-phase system (three-motor series-connected drive system or concentrated winding machine with the fifth and the third harmonic injection).

Taking two-motor five-phase drive system (Fig. 9.1) as an example, the situation may arise where magnitude of the reference in the d_2-q_2 plane (reference voltage of the second machine) is considerably larger than the reference in the d_1-q_1 plane (reference voltage of the first machine). The existing space vector PWM methods [Ryu et al (2005), Ojo et al (2006)], with vector selection based on the reference in the d_1-q_1 plane, are unable to cope with such a situation. Hence the experimental studies on two-motor series-connected five-phase and six-phase drive systems with a single VSI supply [Iqbal et al (2005), Levi et al (2005), Mohapatra et al (2005), Levi et al (2007a)] have all utilised carrier-based PWM, where desired inverter modulating signals are generated in a straightforward manner [Iqbal et al (2006b)].

The only attempt to develop a SVPWM method for the five-phase two-motor structure, using the concept of multiple 2-D planes, has been described in [Iqbal and Levi (2006b)]. It was suggested to select in each of the two planes, completely independently, a set of four active space vectors neighbouring the corresponding reference. Then it becomes possible to create two voltage space vector references independently, using the same approach and the same analytical expressions as for the case of purely sinusoidal output voltage generation. However, the application of the selected vectors was done in such a way that d_1-q_1 plane reference voltage was applied in one switching period, while the d_2-q_2 plane voltage references was applied in the next switching period. Such an approach to realisation of the two space vector voltage references has automatically restricted the available fundamental for each of the two machines to only 50% of its maximum value for the given dc bus voltage (since only every second period is used for application of the voltage to any of the two machines).

In any inverter-fed drive it is of utmost importance to determine the limit(s) of the dc bus voltage utilisation in the linear modulation region. For example, if the inverter dc bus voltage is of a certain value, it is crucial to understand how much of the available dc bus voltage can be allocated to the third harmonic injection for a given fundamental in a concentrated winding machine, or how much can be allocated to the second machine in a series-connected five-phase two-motor drive for a given fundamental of the first machine. However, regardless of the previous work surveyed in this section, that has been done regarding PWM techniques for multi-frequency output voltage generation, there is no indication that dc bus utilisation has been explored in a systematic manner. Importance of this issue is obvious if one considers that, for both topologies shown in Figs. 9.1 and 9.2, dc bus voltage is set as being of the value required for single multi-phase drives (1 p.u.).

Therefore, before development of a multi-frequency PWM scheme that overcomes the shortcomings of the existing schemes, a simple analytical method is presented, which enables determination of boundaries of the linear modulation region for any multi-phase VSI with an odd (prime) number of phases. Since series-connected multi-phase machines can have completely arbitrary voltage requirements, only magnitudes of phase voltages of the machines are considered (frequencies and phase shifts are disregarded) and appropriate relations with the dc bus voltage are established. Detailed considerations are given for the five-phase and the seven-phase case, with subsequent generalisation to higher phase numbers. An important characteristic of the presented method is its complete independence from the applied PWM technique.

9.3 VOLTAGE LIMITS OF MULTI-PHASE VOLTAGE SOURCE INVERTERS

It has been already established in chapter 5 that, for the sinusoidal output voltage generation, dc bus utilisation as a function of the number of phases is governed with the following rule:

$$M_{max}(n) = \frac{1}{K_{(n-1)/2}} = \frac{1}{\sin(\frac{n-1}{2}\frac{\pi}{n})} \tag{9.1}$$

This result was obtained during development of PWM schemes for single multi-phase drives. For the sake of clarity, dc bus utilisation in three-phase system is briefly reviewed first, since subsequent analysis relies on the same principles.

Maximum level of the dc bus voltage utilisation is customarily determined for a three-phase VSI by an analysis of the line voltage of the machine. Using already established definition for the modulation index, phase and line voltages of a machine can be expressed as functions of the modulation index. For a three-phase system, maximum utilisation of the dc bus voltage (i.e. limit of the linear modulation region) is reached when peak value of the line voltage becomes equal to the dc bus voltage. Since in a three phase system all line voltages are of the same magnitude (phasor diagram is shown in Fig. 9.3a), it is sufficient to consider only one line voltage, referenced to phase 'a'. From Fig. 9.3a, simple trigonometry yields:

$$|\underline{V}_{ab}| = 2M\,0.5V_{dc}\cos(\pi/6) = V_{dc} \tag{9.2}$$

From (9.2), the maximum value of the modulation index is:

$$M_{max} = \frac{1}{\cos(\pi/6)} = 1.1547 \tag{9.3}$$

This is the well known maximum value of the modulation index for continuous three-phase PWM methods. This basic principle, which relies on analysis of line voltages, is now extended to multi-phase systems. In a five-phase system there are two different groups of line voltages, with regard to their magnitudes (Fig. 9.3b). The first group are the adjacent line voltages. Their magnitude, as a function of the modulation index, is given with:

$$\left|\underline{V}_{ab}\right| = 2M\,0.5V_{dc}\cos(3\pi/10) \tag{9.4}$$

Similarly, magnitude of non-adjacent line voltages can be expressed as (Fig. 9.3b):

$$\left|\underline{V}_{ac}\right| = 2M\,0.5V_{dc}\cos(\pi/10) \tag{9.5}$$

As with a three-phase system, limit of the linear modulation region is obtained when peak value of the largest line voltage reaches value of the dc bus voltage. Thus, by equating (9.5) to the value of the dc bus voltage one finds that the maximum value of the modulation index in a five-phase system is:

$$M_{\max} = \frac{1}{\cos(\pi/10)} = 1.0515 \tag{9.6}$$

This value has already been established in chapter 4. Finally, in a seven-phase system (Fig. 9.3c) there are three different groups of line voltages and their magnitudes (in ascending order) can be expressed from Fig. 9.3c as:

$$\begin{aligned}
\left|V_{ab}\right| &= 2M\,0.5V_{dc}\cos(5\pi/14) \\
\left|\underline{V}_{ac}\right| &= 2M\,0.5V_{dc}\cos(3\pi/14) \\
\left|\underline{V}_{ad}\right| &= 2M\,0.5V_{dc}\cos(\pi/14)
\end{aligned} \tag{9.7}$$

In the same manner as before, the maximum value of the modulation index in the linear modulation region is obtained as equal to $M_{\max} = 1/\cos(\pi/14) = 1.0257$. The values of the maximum modulation index in the limit of the linear modulation region, established here through analysis of line voltages, are valid as long as the inverters are required to operate with sinusoidal output voltage (i.e. reference voltages are zero in all the planes other than d_1–q_1).
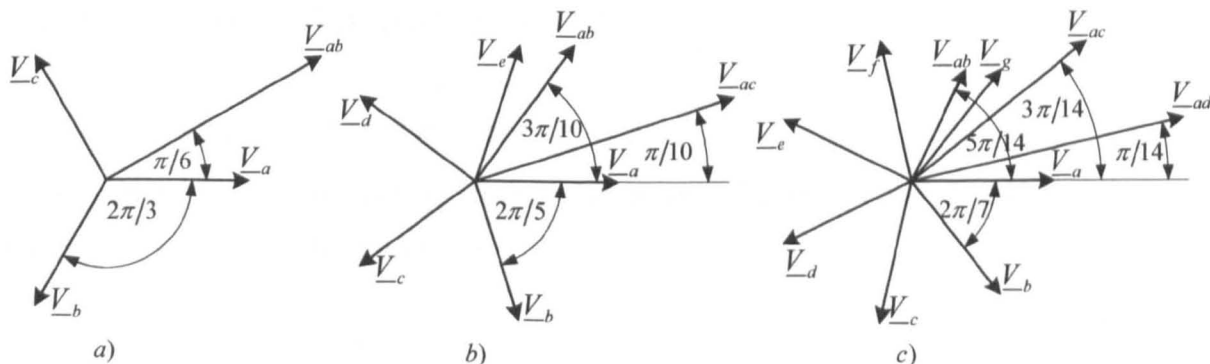
Fig. 9.3: Phase and line voltage phasors: a) three-phase system, b) five-phase system, c) seven-phase system.

Finally, values of the maximum modulation index are related to the phase number n through the following relationship:

$$M_{max}(n) = \frac{1}{\cos(\frac{\pi}{2n})} \qquad (9.8)$$

This is just an alternative way of writing the solution already given with (9.1). The machine's line voltages are, in the case of a single motor drive, at the same time inverter line voltages. Therefore, limits of operation in the linear region of modulation are reached when peak value of the inverter line voltage becomes equal to the dc bus voltage. The same criterion is applied to multi-phase series-connected multi-motor drives next.

9.3.1 FIVE-PHASE VOLTAGE SOURCE INVERTER VOLTAGE LIMITS

In this case the inverter has to generate a voltage component in both planes of Fig. 9.1. Dc bus voltage utilisation is therefore not function of a single modulation index any more. Let the modulation indices in the two planes of Fig. 9.1 be denoted as M_1 and M_2, respectively. Here M_2 is either firmly tied to the M_1 (concentrated winding machine) or is completely independent of M_1 (series-connected two-motor drive). By analysing Fig. 9.1, one establishes that all inverter line voltages are a sum of an adjacent (resp. non-adjacent) line voltage in the d_1-q_1 plane and a non-adjacent (resp. adjacent) line voltage in the d_2-q_2 plane. For example, inverter v_{AB} and v_{AC} voltages can be expressed as:

$$\begin{aligned} v_{AB} &= v_A - v_B = (v_{a1} + v_{a2}) - (v_{b1} + v_{c2}) = v_{ab1} + v_{ac2} \\ v_{AC} &= v_A - v_C = (v_{a1} + v_{a2}) - (v_{c1} + v_{e2}) = v_{ac1} + v_{ae2} \end{aligned} \qquad (9.9)$$

The worst-case scenario is considered further on. Since two individual line voltages in planes d_1-q_1 and d_2-q_2 (right-hand side in (9.9)) are in general unrelated and of arbitrary frequencies, magnitudes and phase-shifts, the worst possible situation arises when these voltages reach the peak values in the same time instant. Hence, to establish limits of the dc bus utilisation, one substitutes expressions (9.4) and (9.5) into (9.9):

$$\begin{aligned} |v_{AB}| &= M_1 V_{dc} \cos(3\pi/10) + M_2 V_{dc} \cos(\pi/10) \le V_{dc} \\ |v_{AC}| &= M_1 V_{dc} \cos(\pi/10) + M_2 V_{dc} \cos(3\pi/10) \le V_{dc} \end{aligned} \qquad (9.10)$$

Re-arranging (9.10) gives the constraints that have to be satisfied if PWM operation is to remain in the linear modulation region:

$$\begin{aligned} M_1 \cos(\frac{3\pi}{10}) + M_2 \cos(\frac{\pi}{10}) \le 1 \\ M_1 \cos(\frac{\pi}{10}) + M_2 \cos(\frac{3\pi}{10}) \le 1 \end{aligned} \qquad (9.11)$$
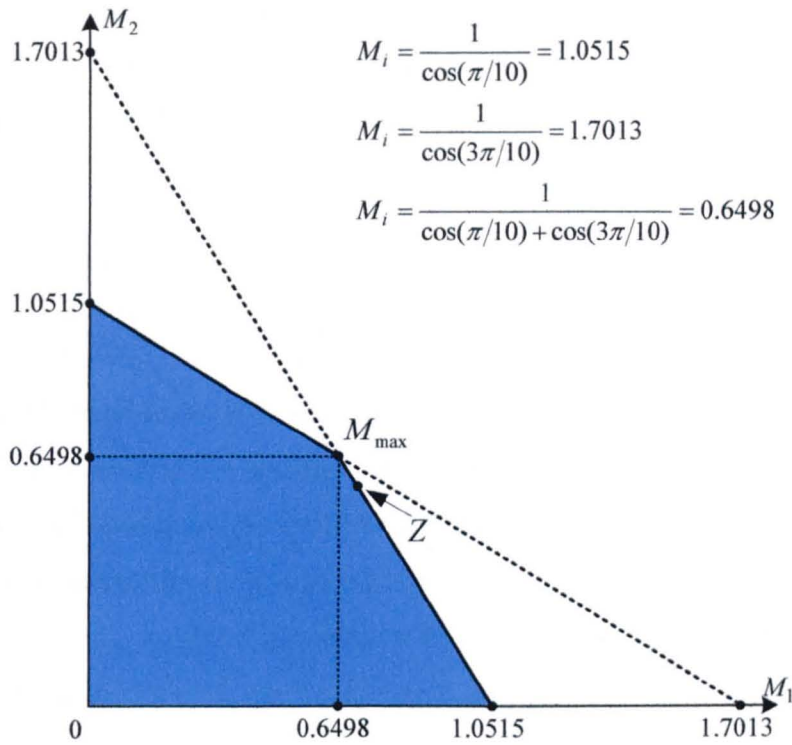
Fig. 9.4: Combination of modulation indices that yield operation in the linear modulation region for a five-phase VSI (shaded area).

These two equations define an area when plotted in a co-ordinate system with modulation indices M_1 and M_2 as axes. Graphical representation of (9.11) is shown in Fig. 9.4. Any operating point (i.e. any combination of the two modulation indices) within the shaded area is available in the linear modulation region. In the special case when modulation indices in the two planes are equal ($M_1 = M_2 = M_{max}$) one finds from (9.11) that $M_{max} = 0.6498$. This is a considerably larger value than the one that would have resulted had the planes in Fig. 9.1 not been transposed (i.e. $1.0515/2 = 0.52575$).

9.3.2   SEVEN-PHASE VOLTAGE SOURCE INVERTER VOLTAGE LIMITS

It is possible to establish relations between permissible values of the modulation indices and the available dc bus voltage for a seven-phase VSI using the same procedure as in the previous sub-section. Due to the transposition between the three planes of Fig. 9.2, each inverter line voltage is a sum of three different line voltages defined in (9.7). Thus the inverter line voltages are of the form:

$$v_{AB} = v_A - v_B = v_{ab1} + v_{ac2} + v_{ad3}$$
$$v_{AC} = v_A - v_C = v_{ac1} + v_{ae2} + v_{ag3} \qquad (9.12)$$
$$v_{AD} = v_A - v_D = v_{ad1} + v_{ag2} + v_{ac3}$$

Once more the worst-case scenario is explored, by assuming that all line voltages in each plane may reach peak values in the same time instant. The following constrains then result by combining (9.7) and (9.12):

$$M_1 \cos(\frac{5\pi}{14}) + M_2 \cos(\frac{3\pi}{14}) + M_3 \cos(\frac{\pi}{14}) \le 1$$

$$M_1 \cos(\frac{3\pi}{14}) + M_2 \cos(\frac{\pi}{14}) + M_3 \cos(\frac{5\pi}{14}) \le 1 \qquad (9.13)$$

$$M_1 \cos(\frac{\pi}{14}) + M_2 \cos(\frac{5\pi}{14}) + M_3 \cos(\frac{3\pi}{14}) \le 1$$

Here M_1, M_2, and M_3 stand for modulation indices of the three planes of Fig. 9.2. Since (9.13) consists of three inequalities, the possible combinations of the modulation indices can be visualised in a three-dimensional space where each modulation index is assigned to one of the axes. However, it is interesting to at first explore the availability of the dc bus voltage under the condition that one of the three modulation indices (in any of the three planes) is zero. Assuming for example that $M_3 = 0$, system (9.13) reduces to:

$$M_1 \cos(\frac{5\pi}{14}) + M_2 \cos(\frac{3\pi}{14}) \le 1$$

$$M_1 \cos(\frac{3\pi}{14}) + M_2 \cos(\frac{\pi}{14}) \le 1 \qquad (9.14)$$

$$M_1 \cos(\frac{\pi}{14}) + M_2 \cos(\frac{5\pi}{14}) \le 1$$

Solving (9.14) for this particular case and (9.13) for other two cases (when either $M_1 = 0$ or $M_2 = 0$), an area in 2-D plane is obtained, which determines boundaries of the available modulation indices of a seven-phase VSI when only two (out of three) planes of Fig. 9.2 are excited. The solution is the same regardless of which modulation index is set to zero and is shown in Fig. 9.5, where the pair of axes (M_x, M_y) corresponds to combinations (M_1, M_2), (M_2, M_3) or (M_3, M_1). It can be noted that there is an inherent asymmetry in the relations among any two of the modulation indices of the planes. The reason is the existence of three different line voltages in each plane and the way in which these voltages are summed due to the transposition between planes. When one plane is not excited, the inverter line voltages are not all the same (in the sense of (9.12)) any more. It can be observed in Fig. 9.5 that one of the dotted lines (solution of the first row of (9.14)) does not play any role in the determination of the dc bus utilisation.

To illustrate the complete solution when all three planes of a seven-phase VSI are excited, three planes determined with (9.13) are plotted in the 3-D space using modulation indices of the three $d-q$ planes as axes. This is illustrated in Fig. 9.6 where volume that defines dc bus utilisation is shown.
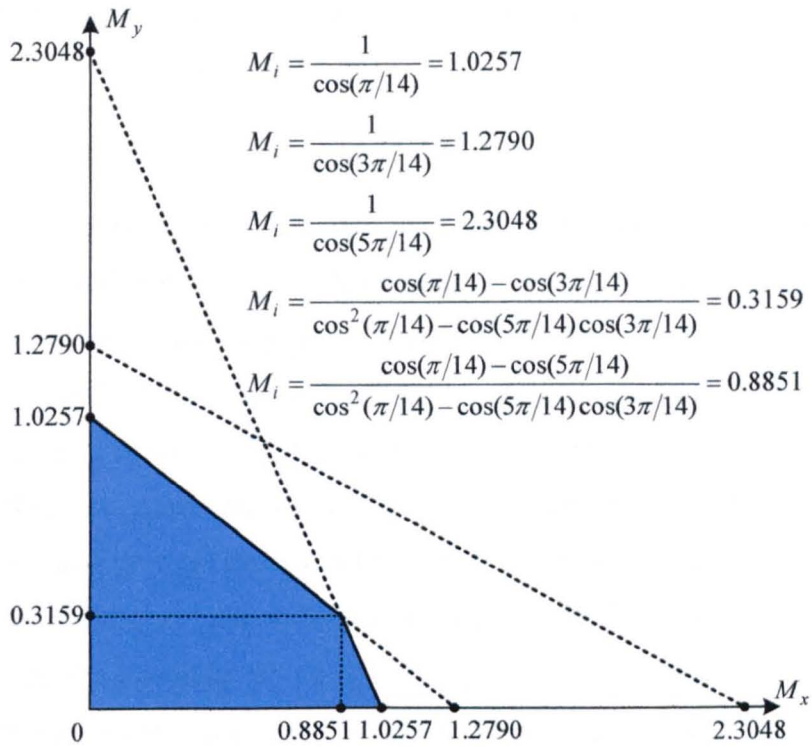
Fig. 9.5: Combination of modulation indices that yield operation in the linear modulation region for a seven-phase VSI when only two planes are excited (shaded area).
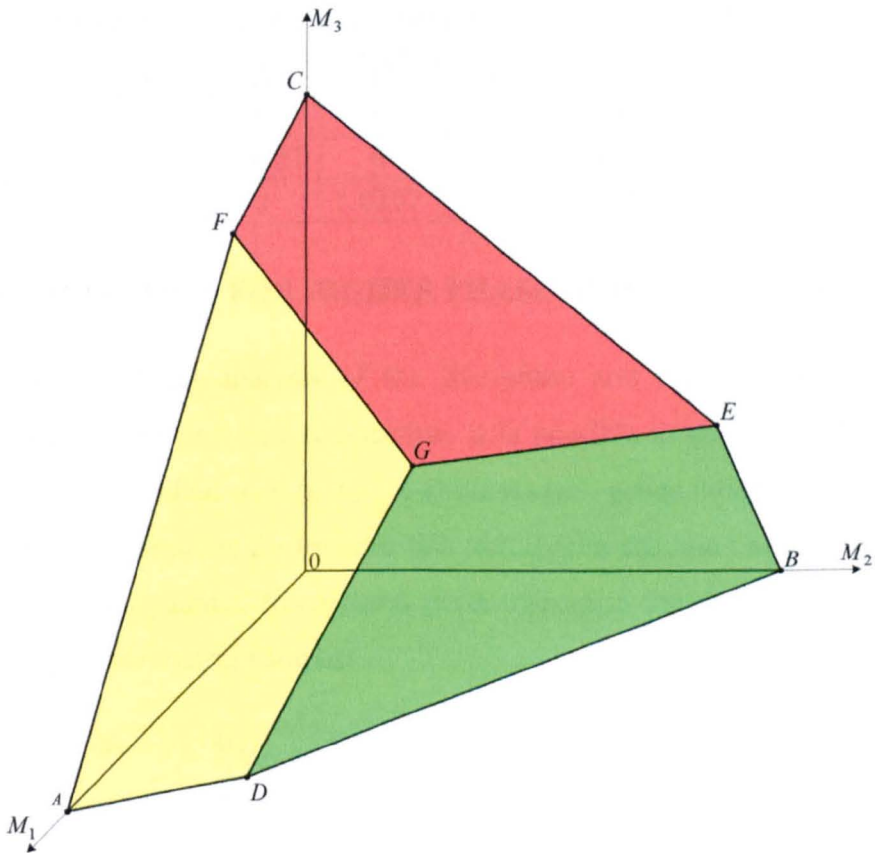
Fig. 9.6: Volume that defines dc bus utilisation for a seven-phase VSI with excitation in all three planes.

The characteristic point obtained when all three modulation indices are mutually equal ($M_1 = M_2 = M_3 = M_{max}$) is found from (9.13):

$$M_{max} = \frac{1}{\cos(\pi/14) + \cos(5\pi/14) + \cos(3\pi/14)} = 0.4565 \tag{9.15}$$

The value in (9.15) is considerably higher than the value that would have been obtained without phase transposition between the three planes of Fig. 9.2 ($1.0257/3 = 0.342$).

Six different four-sided polygons, which bound the volume in the 3-D space and therefore characterise dc bus voltage utilisation, can be identified in Fig. 9.6. Three of them correspond to the one shown in Fig. 9.5, valid when one of the modulation indices is zero. The remaining three polygons are the result of the intersections of three different planes defined with (9.13) and they are shown in Fig. 9.6 in different colour. The volume in Fig. 9.6 effectively relates modulation indices of all three planes with the available value of the dc bus voltage. As long as the operating point, defined by three modulation indices in M_1, M_2, M_3 space, is inside the enclosed volume, it is possible to generate required voltages in each plane while keeping the modulator operation in the linear region. Coordinates of characteristic points, labelled with capital letters in Fig. 9.6, are summarised in Table 9.1.

Table 9.1: Characteristic operating points shown in Fig. 9.6.

	A	B	C	D	E	F	G
M_1	1.0257	0	0	0.8851	0	0.3159	0.4565
M_2	0	1.0257	0	0.3159	0.8851	0	0.4565
M_3	0	0	1.0257	0	0.3159	0.8851	0.4565

9.3.1 GENERALISATION FOR HIGHER PHASE ORDER NUMBERS

On the basis of the analysis of the five-phase and the seven-phase VSI dc bus utilisation, detailed in the previous sub-section, it is possible to generalise the approach for any n-phase system, described with $(n-1)/2$ 2-D planes (n = prime number). This comes down to determination of expressions for inverter line voltages in the same manner as for the five-phase and seven-phase systems. Normalised (with respect to the dc-bus voltage) constraints can be given in a general matrix form as:

$$\begin{bmatrix} M_1 & M_2 & M_3 & \cdots & M_{\frac{n-1}{2}} \\ M_{\frac{n-1}{2}} & M_1 & M_2 & \cdots & M_{\frac{n-1}{2}-1} \\ \vdots & \vdots & \vdots & \cdots & \vdots \\ M_3 & M_4 & M_5 & \cdots & M_2 \\ M_2 & M_3 & M_4 & \cdots & M_1 \end{bmatrix} \begin{bmatrix} \cos(\frac{n-2}{2n}\pi) \\ \cos(\frac{n-4}{2n}\pi) \\ \vdots \\ \cos(\frac{3}{2n}\pi) \\ \cos(\frac{1}{2n}\pi) \end{bmatrix} \leq \begin{bmatrix} 1 \\ 1 \\ \vdots \\ 1 \\ 1 \end{bmatrix} \tag{9.16}$$

By extracting rows of (9.16) for any given phase number n of a multi-phase system, set of $(n\text{-}1)/2$ inequalities can be obtained, that define boundaries of the dc bus voltage utilisation in the linear PWM region. An obvious difficulty is a lack of means for graphical visualisation of the complete solution for any phase number greater than seven, since one deals with more than three modulation indices (more than three d–q planes). It can be easily verified that (9.16) reduces to (9.11) and (9.13) for the five-phase and the seven-phase system, respectively.

Using (9.16), the coordinates of the point in which M_{max} results (that are all the same) can be expressed as

$$M_{max}(n) = \cfrac{1}{\displaystyle\sum_{j=1}^{(n-1)/2} \cos(\frac{2j-1}{2n}\pi)} \tag{9.17}$$

Application of (9.17) in conjunction with eleven-phase and thirteen-phase systems yields the values of 0.2876 and 0.2428, respectively. Table 9.2 illustrates numerical values for odd prime phase numbers up to 13. The first row shows maximum value of the modulation index for purely sinusoidal (single-frequency) output, which corresponds to (9.1) or (9.8) and is denoted as M_{max}^{*}. The second row illustrates the maximum value of the modulation index M_{max} that can be reached simultaneously in all planes, when all planes are excited (multi-frequency output). Finally, the third row shows the product of the number of planes (machines) and the second row. A graphical illustration of the data in Table 9.2 is shown in Fig. 9.7. On the basis of numerical values in Table 9.2 and Fig. 9.7 it can be concluded that:

- Value of the maximum modulation index approaches unity as the number of phases increases for purely sinusoidal output voltages.

- With simultaneous and equal amplitude excitation in all planes, the value of the maximum modulation index M_{max} decreases as the phase number increases.

- The product of the number of 2-D planes $(n-1)/2$ and the maximum modulation index M_{max} increases as the number of phases increases and is in the 13-phase systems 45% higher than with single-frequency excitation.

This is the direct consequence of the phase transposition in the connection of the planes.

Table 9.2: Modulation index values against the phase number.

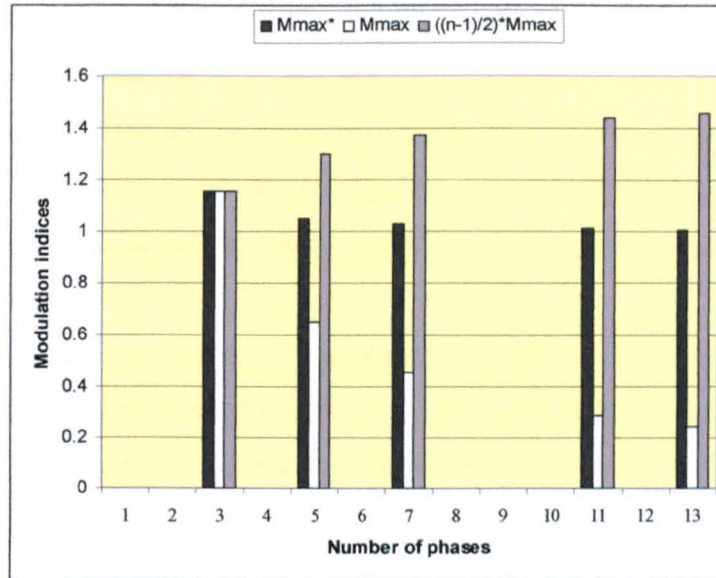| Phase number n	3	5	7	11	13
M_{max}^{*}	1.1547	1.0515	1.0257	1.0103	1.0073
M_{max}	1.1547	0.6498	0.4565	0.2876	0.2428
$[(n-1)/2]M_{max}$	1.1547	1.2996	1.3695	1.438	1.4568

Fig. 9.7: Graphical illustration of the data given in Table 9.2.

9.4   MULTI-FREQUENCY SPACE VECTOR PWM

The main characteristics of the SVPWM for a sinusoidal output voltage generation with multi-phase VSIs have been presented in chapters 4 and 5. These results are directly used for development of a multi-frequency SVPWM scheme. For the sake of simplicity five-phase series-connected two-motor drive is used as an example. Principles of extension to other phase numbers are addressed as well.

As established already, application of decoupling transformation (3.12) leads to representation of a multi-phase system (machine) in multiple 2-D planes. In a five-phase case, the second plane is usually used to control injection of the third harmonic voltage component when a five-phase VSI supplies a single machine with concentrated stator winding, since output voltage harmonics of the order $10k\pm1$ map into the d_1-q_1 plane, while harmonics of the order $10k\pm3$ belong to the d_2-q_2 plane ($k = 0,1,2,3\ldots$). However, the second plane can also be used to control the second five-phase machine in the drive system with two series-connected machines supplied from a single VSI (Fig. 9.1). In this case both machines are with near-sinusoidal mmf distribution and the phase transposition in connection corresponds to phase shifting in decoupling transformation for a five-phase system given with (3.15). Using VSD into two planes, the resulting equivalent circuit representation of the two-motor drive of Fig. 9.1 is, from the VSI point of view (but not from the machines' point of view), identical to the one obtained for concentrated winding single-motor drive: the inverter has to generate non-zero voltage references in both planes. The important difference is however that for a

concentrated winding machine the reference voltage in the second plane has a frequency and the phase shift firmly determined with the first plane reference; also, the second reference magnitude is only a small fraction of the first reference magnitude in steady state operation [Ryu et al (2005)]. In the drive system of Fig. 9.1 two voltage references are completely independent one from the other and can be of any magnitude [Levi et al (2004a), Levi et al (2007a)].

Therefore, there are two reference space vectors (one per plane/machine) that need to be simultaneously satisfied (averaged over the switching period with corresponding set of active space vectors) if decoupled control of both machine is to be achieved. If a concentrated winding machine is supplied, reference in the d_2-q_2 plane, is also of non-zero value [Ryu et al (2005)]. In this case, a set of four active space vectors $\bar{v}_i, \bar{v}_j, \bar{v}_h, \bar{v}_k$ should be properly selected from the set of available thirty ($\bar{v}_1, \bar{v}_2, ..., \bar{v}_{30}$). Due to the fixed relation between fundamental in the d_1-q_1 plane and the third harmonic in the d_2-q_2 plane, the same selection of active space vectors as the one presented in chapter 4 is sufficient. The corresponding application times are now found by solving on-line the set of equations:

$$
\begin{aligned}
v_{id_1} T_i + v_{jd_1} T_j + v_{hd_1} T_h + v_{kd_1} T_k &= v_{d_1}^* T_s \\
v_{iq_1} T_i + v_{jq_1} T_j + v_{hq_1} T_h + v_{kq_1} T_k &= v_{q_1}^* T_s \\
v_{id_2} T_i + v_{jd_2} T_j + v_{hd_2} T_h + v_{kd_2} T_k &= v_{d_2}^* T_s \\
v_{iq_2} T_i + v_{jq_2} T_j + v_{hq_2} T_h + v_{kq_2} T_k &= v_{q_2}^* T_s
\end{aligned}
\tag{9.18}
$$

where i, j, h, k are in the range $1 \div 30$, and the total time of application of zero space vectors $T_O = T_s - (T_i + T_j + T_h + T_k)$ can be shared by zero space vectors $\bar{v}_0$ and $\bar{v}_{31}$. Indices d_1, q_1, d_2, q_2 stand for projections of the space vectors along the four axes of the 4-D space (Fig. 9.8).
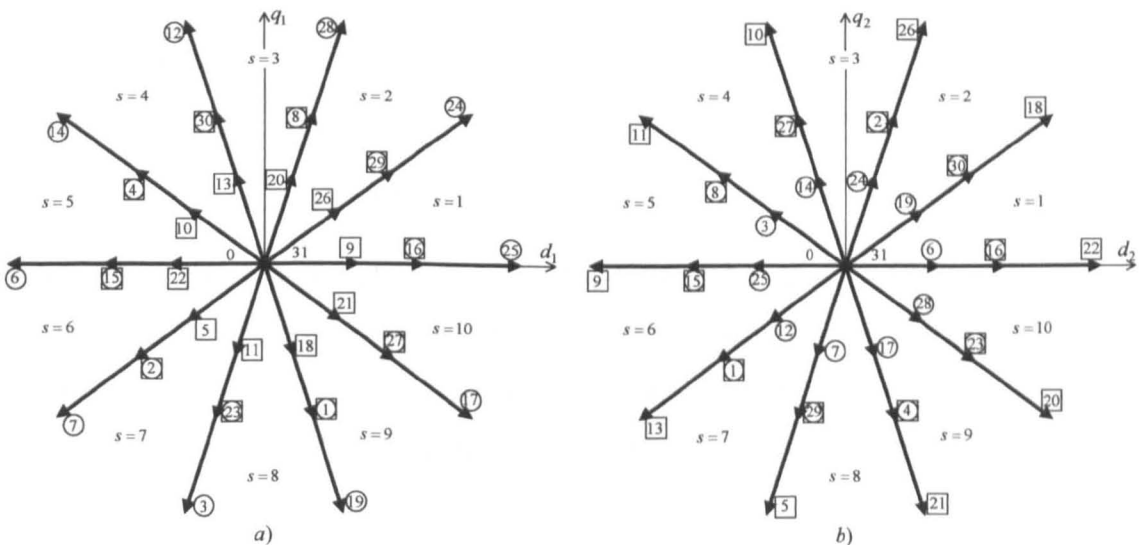

Fig. 9.8: Space vectors of a five-phase VSI in the: a) d_1-q_1 plane and, b) d_2-q_2 plane.

As far as the two-motor drive of Fig. 9.1 is concerned, application of this very general approach (9.18) is also feasible, provided that the most appropriate four active space vectors are selected. However, active space vector selection based on the reference in the d_1-q_1 plane is now inappropriate since references in the two planes are unrelated, can be anywhere in the planes, can have an arbitrary ratio of magnitudes and both magnitudes can be large. A general method to determine the proper four space vectors has not been found yet, and the calculations based on (9.18) could be very time consuming for on-line implementation.

9.4.1 MULTI-FREQUENCY SVPWM FOR FIVE-PHASE TWO-MOTOR DRIVE

The SVPWM method of Iqbal and Levi (2006b) is reviewed first (Method 1), since the initial active space vector selection, considered in this work, is based on the same approach. Since there are two independent voltage references in two planes, it is suggested in Iqbal and Levi (2006b) to select for each of the two references four neighbouring active space vectors (Figs. 9.9a and 9.9b), in the same manner as it has been done in chapter 4 for a single-motor drive. Two medium and two large vectors are selected in each plane. This means that, in general, there are eight active space vectors that need to be imposed. In terms of the d_1-q_1 plane there are four medium, two large and two small space vectors. However, one of the medium space vectors selected in the two planes may be the same. This depends on the two space vector references and means that the total number of selected different active space vectors is either seven or eight.

Two independent space vector modulators are further utilised to realise required two voltage space vector references, with dwell times calculated independently in the two planes using:

$$T_{am} = K M_k \sin(s^k \frac{\pi}{5} - \vartheta_{d_k - q_k}) T_s; \qquad T_{bm} = K M_k \sin(\vartheta_{d_k - q_k} - (s^k - 1)\frac{\pi}{5}) T_s$$

$$T_{al} = K_2 M_k \sin(s^k \frac{\pi}{5} - \vartheta_{d_k - q_k}) T_s; \qquad T_{bl} = K_2 M_k \sin(\vartheta_{d_k - q_k} - (s^k - 1)\frac{\pi}{5}) T_s \qquad (9.19)$$

$$T_0 = T_{31} = \frac{1}{2}[1 - K_2 M_k \cos((2s^k - 1)\frac{\pi}{10} - \vartheta_{d_k - q_k})] T_s$$

Here, sub-script and superscript, used with modulation index M and sector s, respectively, is $k = 1, 2$, and defines the plane where the calculation is placed. The modulators impose the required references in a sequential manner, as illustrated in Fig. 9.10 where switching pattern is shown for two consecutive switching periods for the references positioned as in Figs. 9.9a and 9.9b.

a)

b)
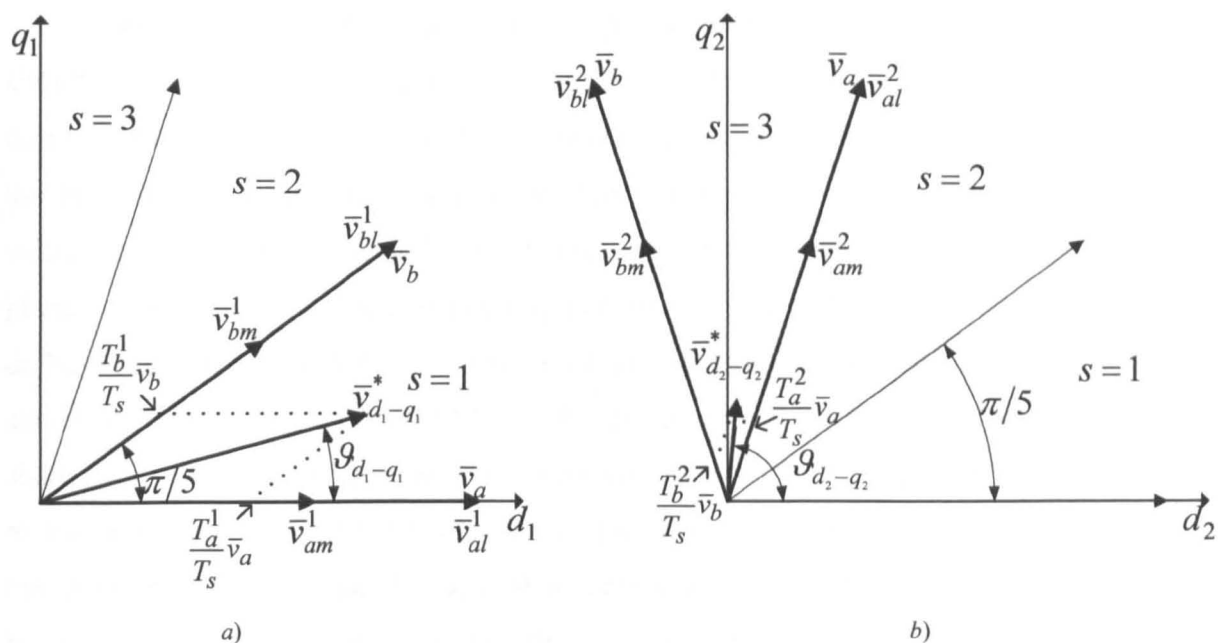
Fig. 9.9: SVPWM for five-phase series-connected two-motor drive: two independent voltage space vector references in two planes and associated active space vector selection done independently in each of the planes, a) d_1-q_1 plane and b) d_2-q_2 plane.

Space vectors that are included in the switching pattern are those shown in Fig. 9.8, where numbers inside a circle/square correspond to the active space vector from the first/second plane responsible for voltage generation for the first/second machine. Fig. 9.10 is drawn to scale for one particular pair of the voltage space vector references in the two planes in one instant in time (this pair of references is used further on in all considered PWM schemes for illustrative purposes): $\left| \bar{v}_{d_1-q_1}^* \right| = 0.6, \vartheta_{d_1-q_1} = 15°$ (i.e. in the first sector) and $\left| \bar{v}_{d_2-q_2}^* \right| = 0.2, \vartheta_{d_2-q_2} = 85°$ (i.e. in the third sector).
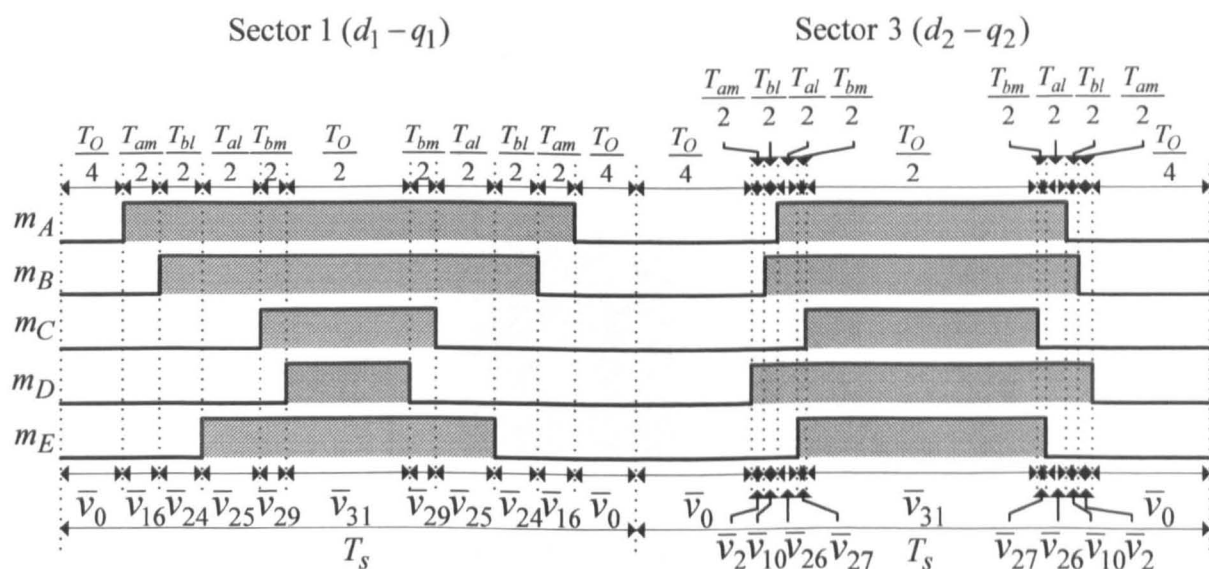
Fig. 9.10: Switching pattern obtained with SVPWM – Method 1.

However, since in each switching period only one reference is imposed while simultaneously zeroing the applied voltage in the other plane, the effective values of the output voltages will be one half of the given reference values. This simultaneously means that the effective realisable reference in both planes is restricted to only 50% of the maximum value obtainable for the given dc bus voltage, regardless of the reference value in the other plane. Thus, even if the first machine requires zero voltage and there is potentially the whole dc bus voltage available for the control of the second machine, only half of the full dc voltage can be applied due to the SVPWM Method 1 nature. This is illustrated in Fig. 9.11 where the shaded area represents realisable pairs of references in the two *d-q* planes. Each reference is restricted to at most $M=0.5257$ (i.e. 50% of the maximum value), regardless of the value of the other reference. It can be seen that, compared to analytically determined operating boundaries for the operation in the linear region, Method 1 significantly underutilises available dc bus voltage. An additional disadvantage is that, since the switching pattern repeats every two periods, the first harmonic sideband appears around one half of the switching frequency.

Further development aims at removing the limitations of the sequential approach of Iqbal and Levi (2006b) (multi-frequency SVPWM Method 1). The idea is to provide full dc bus utilisation by respecting the operating conditions of the two machines in the SVPWM scheme. In other words, the aim is to expand the operating region in Fig. 9.11 to the one analytically determined and shown in Fig. 9.4, and thus improve substantially dc bus utilisation for all operating conditions.
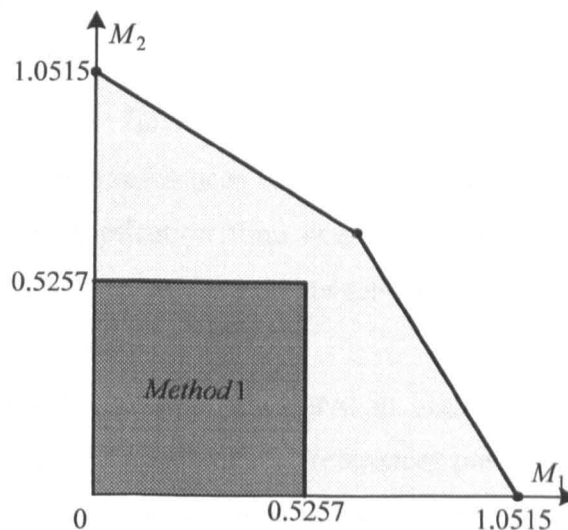
Fig. 9.11: Dc bus utilisation offered with SVPWM Method 1, compared to theoretically determined dc bus utilisation for a five-phase two-motor drive.

To alleviate drawbacks of the Method 1, some changes are introduced first and SVPWM scheme is termed Method 2. In the Method 1, each reference is created in one switching period using four active vectors in the given plane. However, it is observed that, from the point of view of the application of any of the two space vector voltage references, application of the other reference is identical to the zero space vector application, since (9.19) zeroes the average voltage in the other plane. This opens up a possibility of replacing zero space vectors with active space vectors from the other plane. Therefore, instead of using two consecutive periods for voltage control in the two planes, only one switching period can be used. It can be considered as consisting of two sub-periods T_s^1, T_s^2 $(T_s = T_s^1 + T_s^2)$ that are proportional to the magnitudes of reference space vectors in the two planes, according to:

$$T_s^1 = \frac{|\vec{v}_{d_1-q_1}^*|}{|\vec{v}_{d_1-q_1}^*| + |\vec{v}_{d_2-q_2}^*|} T_s; \qquad T_s^2 = \frac{|\vec{v}_{d_2-q_2}^*|}{|\vec{v}_{d_1-q_1}^*| + |\vec{v}_{d_2-q_2}^*|} T_s \qquad (9.20)$$

Superscripts 1 and 2 are used to distinguish the sub-periods. Application times for both sets of four active vectors are still calculated individually for two references using (9.19):

$$T_{am}^1 = KM_1 \sin(s^1 \frac{\pi}{5} - \vartheta_{d_1-q_1}) T_s; \qquad T_{bm}^1 = KM_1 \sin(\vartheta_{d_1-q_1} - (s^1-1)\frac{\pi}{5}) T_s$$

$$T_{al}^1 = K_2 M_1 \sin(s^1 \frac{\pi}{5} - \vartheta_{d_1-q_1}) T_s; \qquad T_{bl}^1 = K_2 M_1 \sin(\vartheta_{d_1-q_1} - (s^1-1)\frac{\pi}{5}) T_s \qquad (9.21)$$

$$T_{am}^2 = KM_2 \sin(s^2 \frac{\pi}{5} - \vartheta_{d_2-q_2}) T_s; \qquad T_{bm}^2 = KM_2 \sin(\vartheta_{d_2-q_2} - (s^2-1)\frac{\pi}{5}) T_s$$

$$T_{al}^2 = K_2 M_2 \sin(s^2 \frac{\pi}{5} - \vartheta_{d_2-q_2}) T_s; \qquad T_{bl}^2 = K_2 M_2 \sin(\vartheta_{d_2-q_2} - (s^2-1)\frac{\pi}{5}) T_s \qquad (9.22)$$

The zero space vector dwell times now become

$$T_O^1 = T_s^1 - \left(T_{al}^1 + T_{am}^1 + T_{bl}^1 + T_{bm}^1\right) \qquad (9.23)$$

$$T_O^2 = T_s^2 - \left(T_{al}^2 + T_{am}^2 + T_{bl}^2 + T_{bm}^2\right) \qquad (9.24)$$

$$T_O = T_o^1 + T_o^2 = T_s - \left(T_{al}^1 + T_{am}^1 + T_{bl}^1 + T_{bm}^1\right) - \left(T_{al}^2 + T_{am}^2 + T_{bl}^2 + T_{bm}^2\right) \qquad (9.25)$$

It follows from (9.25) that the two references can be created within one switching period as long as the zero space vector application time does not become negative. Total time of application of zero space vectors can be shared between two sub-periods in accordance with the reference space vector magnitudes.

Switching pattern now becomes as illustrated in Fig. 9.12. It should be noted that although the illustration in Fig. 9.12 applies to the references positioned in sectors 1 and 3 of the d_1-q_1 and d_2-q_2 planes, respectively, it can be shown that the same kind of the switching pattern can be obtained for all possible combinations of the sectors s^1, s^2 in which the two references are (10x10=100 sector combinations).
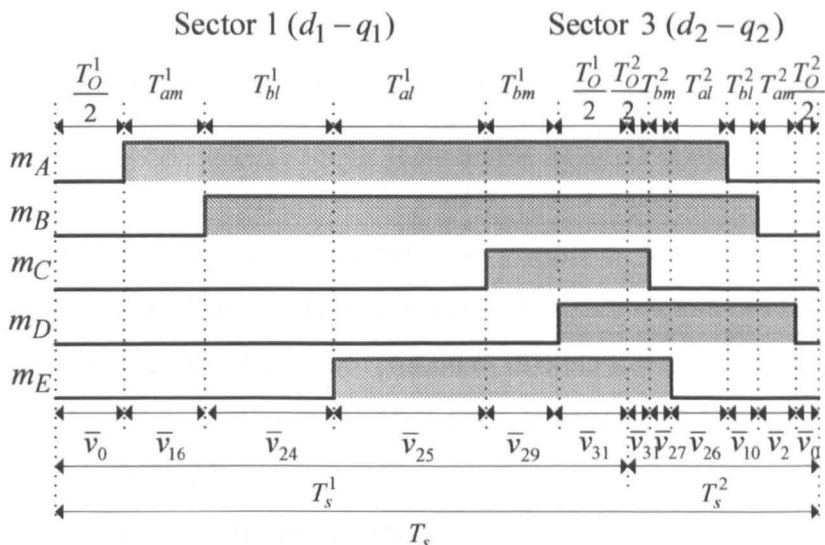
Fig. 9.12: Switching pattern obtained with SVPWM – Method 2.

This approach to SVPWM (Fig. 9.12) is easy to understand and it also clearly shows the application of eight active space vectors in one switching period, while avoiding the voltage harmonics around one half of the switching frequency and preserving the same switching frequency as in Fig. 9.10. Control over both machines is now performed over one switching period, in contrast to Method 1 where two consecutive periods were used.

By introducing variable sub-periods as functions of the individual voltage reference magnitudes in the two planes, dc bus utilisation is significantly improved. In the context of the series connected two-motor drive this means that one machine may receive full voltage (i.e., run at rated speed) if the other machine is at standstill (i.e., with voltage requirement close to zero), and vice versa. Finally, gain in the dc bus utilisation with respect to the Method 1 is obvious from the illustration given in Fig. 9.13.
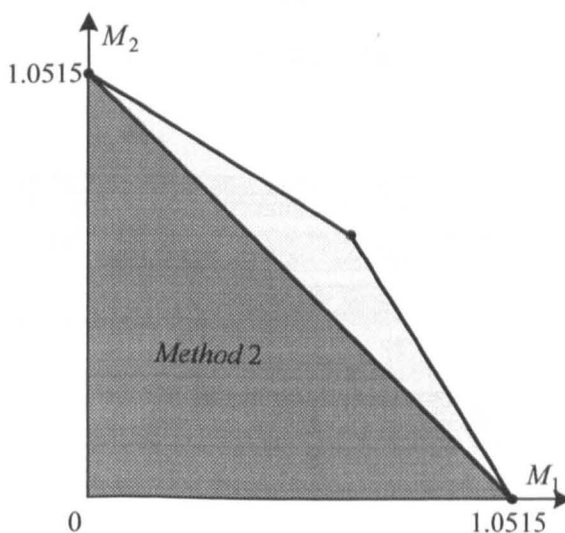

Fig. 9.13: Dc bus utilisation offered with SVPWM Method 2, compared to theoretically determined dc bus utilisation for a five-phase two-motor drive.

As just shown, introduction of two sub-periods of variable durations enables operation with any two voltage references that satisfy condition (9.25). The use is made of the fact that each of the two voltage space vector references is applied in such a manner that the average voltage in the other plane is kept at zero. Hence active space vectors used to generate reference in one plane can be used to replace zero vectors in the other plane. There are all together eight active vectors that are applied in a switching period and the switching pattern is asymmetrical, thus being the cause of potential difficulties in implementation (this is explained in more details in section 9.6). Therefore, the SVPWM Method 2 is modified as follows and is termed Method 3.

The average voltage of an inverter leg over the switching period is a function of only the duty cycle applied to that leg. Thus, if switching pattern of Fig. 9.12 is centered with respect to the midpoint of the switching period, while keeping the on/off ratio (duty cycles) the same for each leg, the average voltage of each inverter leg will stay the same. However, this will result in symmetrical PWM pattern that is easy to implement using standard DSP PWM units. Hence, the following modifications are introduced.

To preserve the same values of the average leg voltages as in Fig. 9.12, the application times of active space vectors from both planes, determined independently by the two modulators, are summed on per-leg basis. Calculation of application times of active space vectors is the same as before and relies on (9.21) and (9.22). Since sub-periods do not exist any more, calculations (9.20), (9.23) and (9.24) are omitted. Finally, total application time of zero space vectors is shared equally between two zero space vectors, thus taking care of the centering and providing a symmetrical PWM. Switching pattern, obtained with Method 2 (Fig. 9.12), becomes after described modifications as shown in Fig. 9.14. The appearance of the switching pattern is the same as for all the CPWM schemes analysed experimentally so far in the thesis.
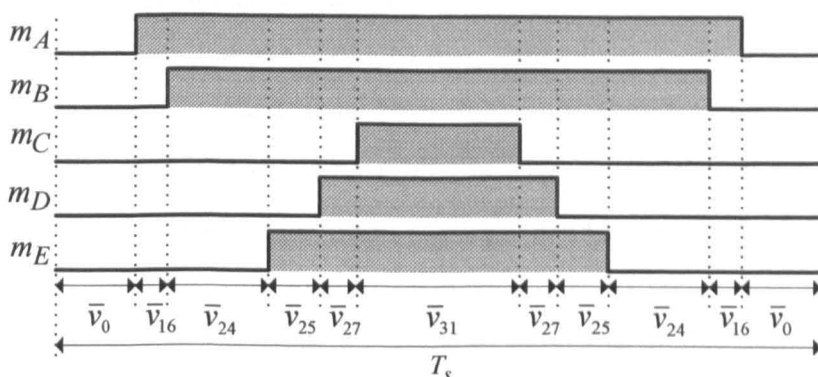

Fig. 9.14: Switching pattern obtained with SVPWM – Method 3.

It can be observed from Fig. 9.14 that, after centering, only four instead of eight active space vectors are applied. The four vectors are in this case a sub-set of the original eight vectors in Fig. 9.12. In general, however, this is not necessarily the case and this is a property of the SVPWM scheme introduced by the centering operation. A detailed study has shown that the applied set of four active vectors will always contain two medium length vectors. Referencing the vector lengths with respect to the d_1-q_1 plane, the other two can however be both large (in principle, if reference in d_1-q_1 is larger than the reference in the d_2-q_2 plane), both small (in principle, if reference in d_2-q_2 is larger than the reference in the d_1-q_1 plane) or there may be one large and one small (in principle, when both references are of similar/same magnitudes and in different positions in the planes).

As an example, Table 9.3 illustrates resulting four active space vectors that will be applied for various combinations of magnitudes and phases of the two reference space vectors. For all cases illustrated, two reference space vectors are in the first and the third sector of the two planes (Fig. 9.9), respectively. The initially selected eight active space vectors, in accordance with Fig. 9.12, are always the same and are 16, 24, 25, 29 and 2, 10, 26, 27. Depending on the magnitude and phase of reference space vectors in the two planes, resulting four active space vectors, applied after the centering, will differ although input set of eight active space vectors is always the same since reference vectors are always in same sectors. Space vectors in bold font are those that will be ultimately applied as one of the four final active vectors, although they were not present at all in the set of the initial eight vectors.

Another very important difference, brought in by the centering operation, is the change in the total time of zero vector application. Although the switching patterns in Figs. 9.12 and 9.14 apply to exactly the same pair of references, it is easy to see that the total application time of zero vectors (vectors 0 and 31) in Fig. 9.14 is considerably longer than in Fig. 9.12. This enables a further improvement in the dc bus voltage utilisation in the linear modulation region, when compared to the limit of the Method 2, illustrated in Fig. 9.13. It has already been established in Iqbal et al (2006b) that, with carrier-based PWM, the limit of the linear modulation region is reached when both references simultaneously take the value of M=0.6498. Exactly the same value has been obtained by analytical analysis presented in the sub-section 9.3.1 of this chapter. Therefore, multi-frequency SVPWM Method 3 is able to provide a level of dc bus utilisation equal to the one analytically determined in section 9.3 and graphically illustrated in Fig. 9.4. Since the limits of the linear modulation region are now as shown in Fig. 9.4, the applied motor control scheme (vector control, for example) should ensure operation in the linear PWM region without saturation of the VSI.

Table 9.3: Active space vectors utilised in switching pattern of Fig. 9.14 for a few reference pairs (second row illustrated in Fig. 9.14).

$d_1 - q_1$ reference		$d_2 - q_2$ reference		Active vectors
magnitude	phase	magnitude	phase	
1	15°	0	-	16, 24, 25, 29
0.6	15°	0.2	85°	16, 24, 25, 27
0.4	15°	0.4	85°	8, 24, 26, 27
0.4	5°	0.4	110°	8, 24, 25, 27
0.4	30°	0.4	75°	16, 24, 26, 27
0.2	15°	0.6	85°	8, 10, 26, 27
0	-	1	85°	2, 10, 26, 27

It is important to stress here once more that voltage references in the two planes are in general mutually independent in the case of a five-phase series-connected two-motor drive. However, SVPWM Method 3 can also be used for output voltage generation in the case of five-phase VSI fed five-phase concentrated winding machine. Yet, in that case, voltage references in the two planes are mutually dependant, and in accordance with the discussion presented in chapter 5 (section 5.4 and Fig. 5.17), dc bus utilisation is different from the one presented here (Fig. 9.4.). The reason for this is the fixed relation of the third harmonic from the second plane to the fundamental, and the impacts the peaks of the modulating signals.

## 9.4.2 EXTENSION OF MULTI-FREQUENCY SVPWM TO HIGHER PHASE NUMBERS

The SVPWM methods presented in the previous sub-section for the multi-frequency output voltage generation of a five-phase VSI can be extended to higher phase numbers. For example, if a seven-phase VSI is considered ($n=7$), there are three independent voltage vector references, since there are $(n-1)/2 = 3$ d-q planes. The number of active space vectors selected, using the sinusoidal SVPWM principles [Dujić et al (2007b)], is $n-1=6$ in each of the three d-q planes. Hence the initial selection will involve $(n-1)^2/2 = 18$ active space vectors. The switching period would further be subdivided into three (rather than two) sub-periods, and one would have 18 expressions of the type shown in (9.21) and (9.22) (rather than 8). Subsequent modifications of the Method 2, described in the previous sub-section, would again produce a symmetrical switching pattern of the type illustrated in Fig. 9.14 (for seven rather than five inverter legs) and six active space vectors would ultimately be applied (where again some of them may be vector(s) that were not at all initially selected). Thus, multi-frequency SVPWM Method 3 for the seven-phase VSI could be developed. The implementation

principle, that will be addressed later, remains the same, except that there would be three voltage vector references (rather than two) at the input of, now, three (rather than two) space vector modulators.

9.5 MULTI-FREQUENCY CARRIER-BASED PWM

Similar to the multi-phase single-motor drives, principles of carrier-based PWM appear to be much simpler than the SVPWM approach. General layout of a multi-frequency carrier-based modulator for an n-phase VSI is shown in Fig. 9.15. On the left-hand side of Fig. 9.15 one has the fundamental sinusoidal references for each plane, defined by means of the magnitude (i.e. modulation index) and frequency for each plane (M_k, f_k). Set of these sinusoidal references is then summed using phase transposition, illustrated in Figs. 9.1 and 9.2 for the five-phase and seven-phase systems, for example. Compared to the layout shown in Fig. 6.1 for a single-motor drive, there are now (n-1)/2 sets of n-phase sinusoidal references in accordance with the number of planes (machines in series connection). This was not the case with the layout in Fig. 6.1, since, for sinusoidal output voltage generation, references in all the planes other than the d_1-q_1 were zero.

To explain the need for zero-sequence signal injection, two sets of sinusoidal references are provided at the input of the modulator in Fig. 9.15. The sets correspond to an operating point in the limit of the linear modulation region in Fig. 9.4 (five-phase system, point denoted as Z) and are such that $M_1 = 0.7$ (at 33 Hz) and $M_2 = 0.5687$ (at 27 Hz).
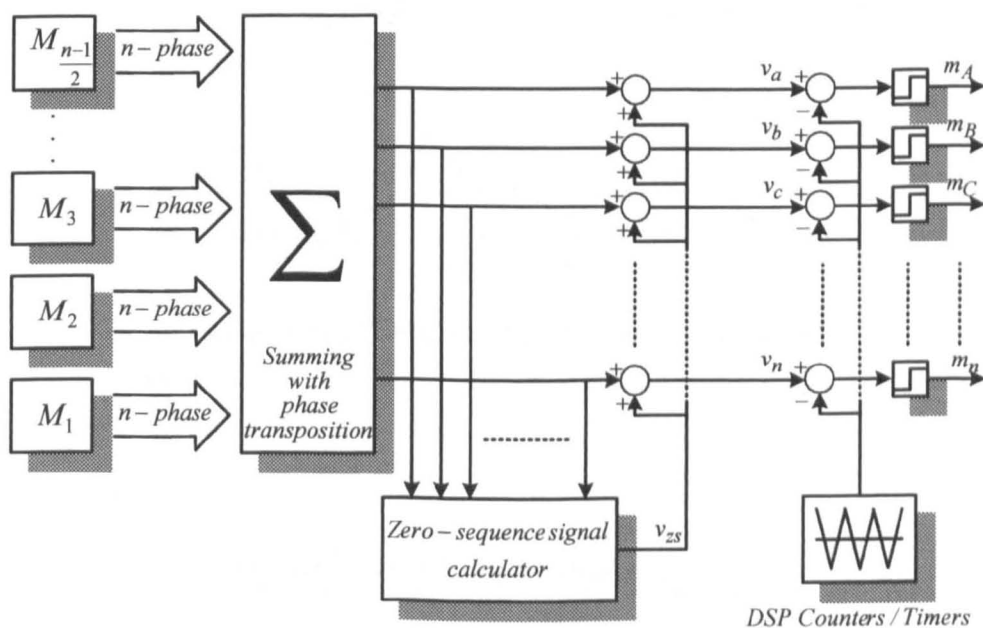

Fig. 9.15: Principle of the carrier-based PWM for multi-frequency output voltage generation with an n-phase VSI.

Fig. 9.16 (upper part) illustrates the resulting modulating signals after the 'Summing with phase transposition' block of Fig. 9.15. It is evident that the modulating signals are highly asymmetrical and that they exceed the range of the carrier (i.e., over-modulation takes place). However, the instants of clamping to the upper dc bus rail and to the lower dc bus rail do not coincide, meaning that clamping occurs in only one of the inverter legs. To alleviate this problem and enable full dc bus voltage utilisation in the linear region, it is necessary to modify the modulating signals by centering positive and negative peaks with respect to the mid-point of the range that they span (around zero in Fig. 9.16). To perform the centering, the zero-sequence signal, determined by maximum and minimum values of the modulating signal, is injected:

$$v_{zs} = -0.5(v_{max}^* + v_{min}^*) \tag{9.26}$$

Addition of the zero-sequence signal modifies modulating signals, as shown in the bottom part of Fig. 9.16, and thus enables full dc bus utilisation in accordance to the analytically established limits given in Fig. 9.4.

It can be seen that after adding zero-sequence signal, envelopes (shown as bold trace in both parts of Fig. 9.16) that correspond to positive and negative peak values of the modulating signals appear as mirrored images. This will guarantee that dc bus utilisation is maximised and that clamping occurs simultaneously in two inverter legs when the limit of the linear modulation region is reached.
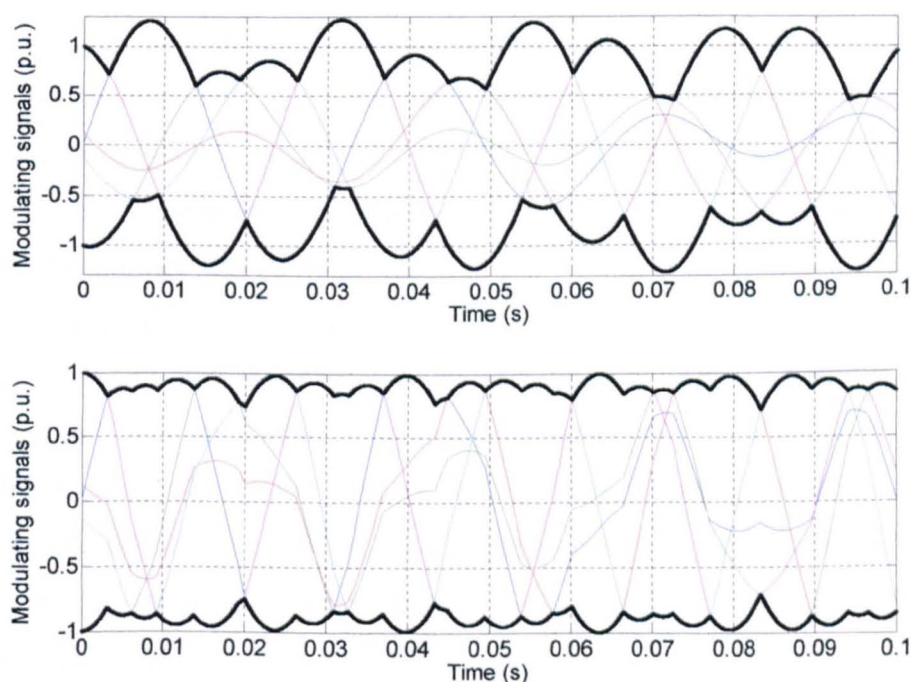
Fig. 9.16: Resulting modulating signals for five-phase VSI: before (top) and after (bottom) zero-sequence signal injection (simulation).
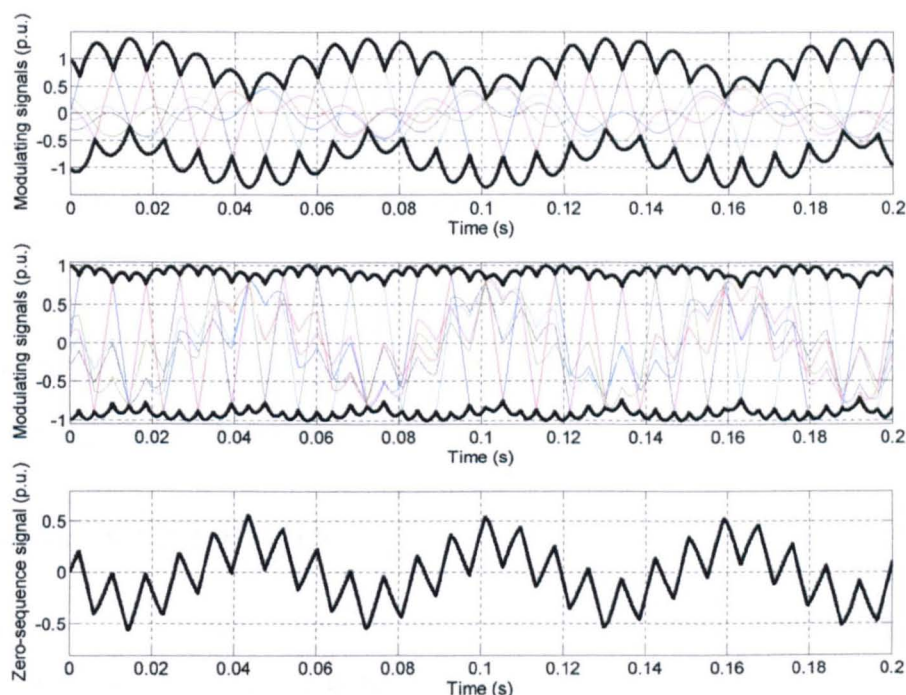
Fig. 9.17: Resulting modulating signals for seven-phase VSI: before (top) and after (middle) zero-sequence signal injection, and zero-sequence signal (bottom), (simulation).

Results shown in Fig. 9.16 further confirm that the zero-sequence signal (9.26), widely used in three-phase systems, is also valid for higher phase numbers (as already established), as well as for multi-frequency output voltage generation in multi-phase systems. Results similar to those of Fig. 9.16 but for a seven-phase system are shown in Fig. 9.17, which further confirm validity of (9.26) for higher phase numbers with multi-frequency output voltage generation. For the seven-phase system modulation indices are selected as $M_1 = M_2 = M_3 = 0.4565$ at frequencies of 27, 37 and 47 Hz, respectively. Resulting modulating signals before and after zero-sequence injection are shown in Fig. 9.17. As can be seen from the results, application of the zero-sequence injection according to (9.26) has again the effect of returning modulating signals into the region (-1,1).

The zero-sequence signal obtained by means of (9.26) is also shown in Fig. 9.17. Due to the modulating signals that contain three sinusoidal components of different frequency, zero-sequence signal is a rather complicated function. Expression (9.26) is valid regardless of the phase number and regardless of the form of the original modulating functions.

To prove this statement, consider a set of modulating signals of any form, for any phase number. In any particular instant in time it is possible to find the maximum and minimum values within this set, v_{max}^* and v_{min}^*. The role of the zero-sequence injection is to alter these values, so that they become after zero-sequence injection $v_{max}^{'}, v_{min}^{'}$, where:

$$v'_{max} = v^*_{max} + v_{zs}$$
$$v'_{min} = v^*_{min} + v_{zs}$$

(9.27)

Since the zero-sequence injection needs to perform the centering within the interval (-1;1), then after zero-sequence injection one has the equal values for new positive and negative maximums:

$$v'_{max} = -v'_{min}$$

(9.28)

By substituting (9.27) into (9.28), one obtains (9.26), which is the zero-sequence that needs to be injected in order to perform the centering.

9.6 DSP IMPLEMENTATION

Multi-frequency SVPWM Methods 2 and 3 have been implemented in a TMS3230F2812 DSP, which is used to control custom-built multi-phase VSI supplying two five-phase machines in series connection. Since there are five inverter legs to control, both event managers (A and B) of the DSP are utilised and proper synchronisation of the DSP timers is performed. At the implementation stage, two independent SVPWM modulators are developed (one in each of the two planes), based on the theoretical considerations presented in the preceding part of the chapter. Due to the use of standard DSP PWM hardware units that operate based on carrier-comparison principle, outputs of each modulator can be considered as modulating signals that will be loaded into compare registers of the DSP. Value of these signals is subsequently compared with the DSP timer values (carrier) in order to define shape of the output PWM signals. Therefore, although the introduced PWM methods are based on the space vector theory, notions like modulating and carrier signal (characteristic for carrier-based approach) play an important role with regard to implementation using DSPs.

Although Method 2 makes the full dc bus voltage available to one machine if the other one does not require voltage (and vice versa), it is not convenient for practical DSP-based implementation, since it involves two variable time sub-periods, one of which may approach zero value. Problems arise due to the need to handle very low sub-period values, since the resolution of the DSP counters/timers is limited, and due to the inability to use the existing DSP PWM units in a standard way (since different carrier up/down slopes are required). The need to calculate variable sub-periods also increases computational complexity.

Setting the DSP counters/timers to count in continuous 'up' mode generates saw-tooth shaped carrier, period of which is controlled alternatively by calculated sub-periods. Further action on DSP PWM unit output polarity and additional software modifications make the

implementation of Method 2 possible using standard DSPs, at the expense of an increased computational complexity. Resulting PWM pattern, generated by the DSP for the same conditions used throughout the chapter, is shown in Fig. 9.18a. Effect of two different sub-periods, separated by the dashed vertical line in Fig. 9.18a, is clearly visible, as is the application of different active space vectors at the beginning of the PWM pattern (vectors from the first plane) and at the end of the PWM pattern (vectors from the second plane). It should be noted that the experimental result in Fig. 9.18a is identical to the theoretical study displayed in Fig. 9.12 (both apply to the same voltage space vector reference values).

The above-mentioned implementation-related difficulties are eliminated if Method 3 is utilised. Centering of pulses generated with Method 2 is obtained by re-setting DSP counters/timers to operate in continuous up/down mode, thus creating triangular carrier signal. Resulting modulating signals for each inverter leg are obtained based on the output of each modulator and considering equal zero space vector placements. This effectively places active parts of PWM pulses from Fig. 9.18a in the middle of the switching period, as shown in Fig. 9.18b. At the same time original eight active vectors are replaced with the four most appropriate active space vectors that will satisfy required average voltage generation in each of the two planes.

A schematic illustration of the implementation process is shown in Fig. 9.19, where the segments within the dotted-line box represent actual software implementation of multi-frequency SVPWM Method 3 based on two SVPWM modulators (one per each 2-D plane), while the rest of the figure corresponds to the principle of operation of the DSP PWM units.

Voltage requirement of any of the two machines is in this manner analysed in 10 sectors in the relevant (d_1-q_1 or d_2-q_2) plane. Since the two references are mutually independent and can be positioned in any sector of the relevant plane, one in this manner avoids the need to deal with all $10 \times 10 = 100$ combinations of 2-D sectors that can take place. Experimental results, presented in the following section, prove that new sequences of four active vectors, created in the described manner, effectively synthesise commanded voltage references for both machines.

Last but not least, it is worth noting that the PWM signal sequence, illustrated in Figs. 9.12 and 9.14, utilises both available zero space vectors. This is so, first of all, because the goal was here to realise CPWM (although DPWM could be easily realised). Secondly, such a sequence is also a result of the desire to achieve simple DSP implementation, yielding a PWM pattern that can be obtained with the existing DSP PWM units. Thus, the simplest way to realise centering of PWM pulses is to allow the DSP timer/counter units to perform this task.

a)   b)
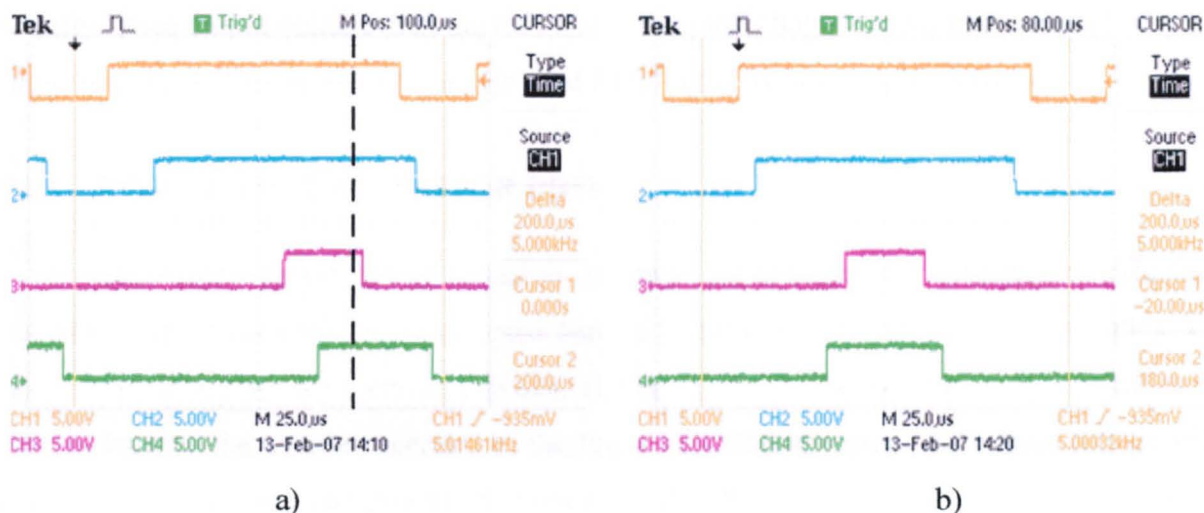
Fig. 9.18: PWM signals for inverter legs A, B, C and D: a) SVPWM Method 2, and b) SVPWM Method 3.

DSP Counters / Timers
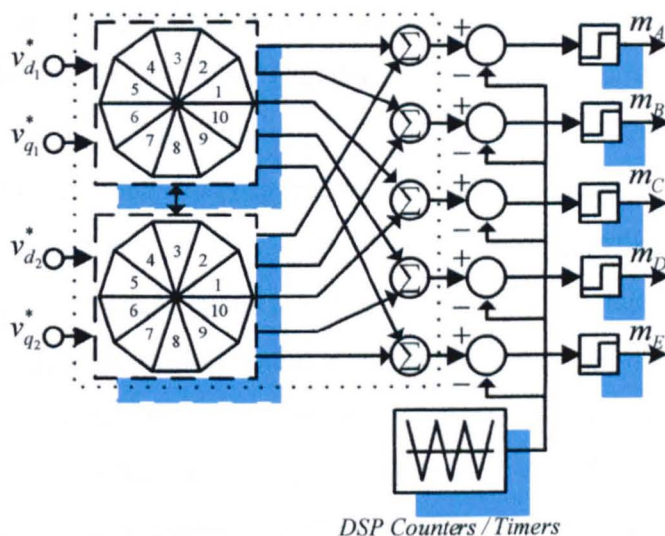
Fig. 9.19: Signal flow in DSP-based implementation of the developed SVPWM Method 3.

9.7   EXPERIMENTAL RESULTS

Experiments were carried out with two aims in mind. In order to experimentally verify the established boundaries, which govern dc bus utilisation in five-phase and seven-phase VSIs, a multi-frequency carrier-based PWM scheme is used to create switching functions for multi-phase inverter legs. On the other hand, multi-frequency SVPWM Method 3 is tested also, in order to experimentally verify theoretical development.

Modulators have been implemented in TMS320F2812 DSP. Value of the dc bus voltage is in all experiments around 600 V and the switching frequency is set to 5 kHz. There is no compensation of inverter dead-time and semiconductor voltage drops, since these are irrelevant for the purposes of verification of PWM schemes (their main consequence is

slightly lower output voltage than the reference). Output voltage is measured using a low-pass filter (with cut-off frequency of 1.6 kHz) and HP35665A dynamic signal analyser.

9.7.1 FIVE-PHASE TWO-MOTOR DRIVE

The experimental set-up consists of two series-connected five-phase induction machines and a nine-phase inverter (used here in five-phase configuration). The simplest V/f control law is applied for control purposes. The basic idea in the experimental verification is that, as long as the inverter operates in the linear modulation region, the output voltage will contain only frequency components that correspond to the references. Since the machines are identical and V/f control law is therefore the same (set V/f profile includes boost voltage of 3.2 V at 0 Hz), operation in the point M_{max} in Fig. 9.4 means operation with the same frequencies. As this would appear as a single frequency component in the spectrum, operation in the very vicinity of the already utilised point Z of Fig. 9.4, in the limit of the linear modulation region, is examined experimentally instead. Hence, $M_1 = 0.699$ at 33 Hz and $M_2 = 0.553$ at 26 Hz.

Experimentally recorded inverter phase 'A' voltage (across the windings of both machines) and its spectrum are shown in Fig. 9.20a for this operating condition. As can be seen from Fig. 9.20a, the inverter generates required two fundamentals at required frequencies without any low order harmonics, indicating that operation is in the linear modulation region. The two fundamentals, which appear in the two different planes of Fig. 9.1, are just a few percent below the corresponding reference values (148.3 V and 117.5 V rms), due to the uncompensated inverter non-linearities. In the second test the settings are changed to $M_1 = 0.636$ at 30 Hz and $M_2 = 0.553$ at 25 Hz. Since $M_1 + M_2 = 1.1902 > 1.0515$ operation is again in a point of Fig. 9.4 where overmodulation would have resulted had there not been phase transposition in connection of the planes in Fig. 9.1. Results for this operating condition of the two-motor drive are shown in Fig. 9.20b. Once more, spectrum is practically perfectly clean, with only two fundamentals of just slightly lower values than the references (135.1 at 30 Hz and 117.4 V at 25 Hz). Thus the inverter operates again in the linear PWM region.

Next, operating point is pushed outside the shaded region of Fig. 9.4, by selecting $M_1 = 0.636$ at 30 Hz and $M_2 = 0.844$ at 40 Hz. Spectrum of the inverter voltage, shown in Fig. 9.21, now contains a whole range of low order harmonics (including sub-harmonics), thus confirming that the inverter operates outside the linear modulation region. Also, achieved values of the two fundamentals in the inverter output voltage are now substantially bellow the corresponding references (135.1 and 179.1 V rms), since the dc bus voltage is now too low.
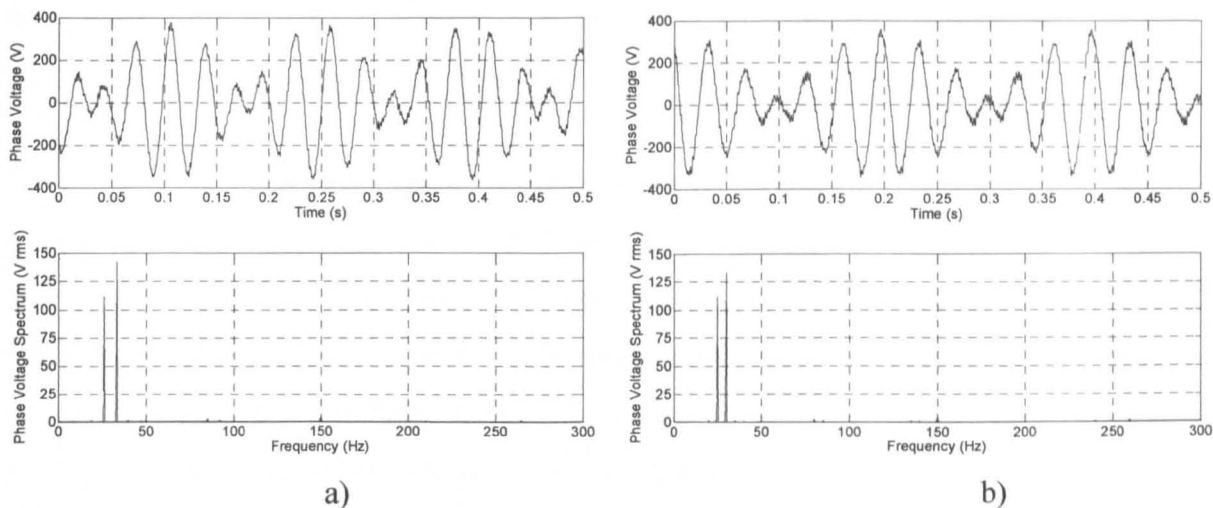
Fig. 9.20: Experimentally recorded inverter phase voltage and its spectrum for operation with: a) $M_1 = 0.699$ at 33 Hz and $M_2 = 0.553$ at 26 Hz (immediate vicinity of point Z in Fig. 9.4) and, b) $M_1 = 0.6369$ at 30 Hz and $M_2 = 0.5533$ at 25 Hz (within the shaded area in Fig. 9.4).
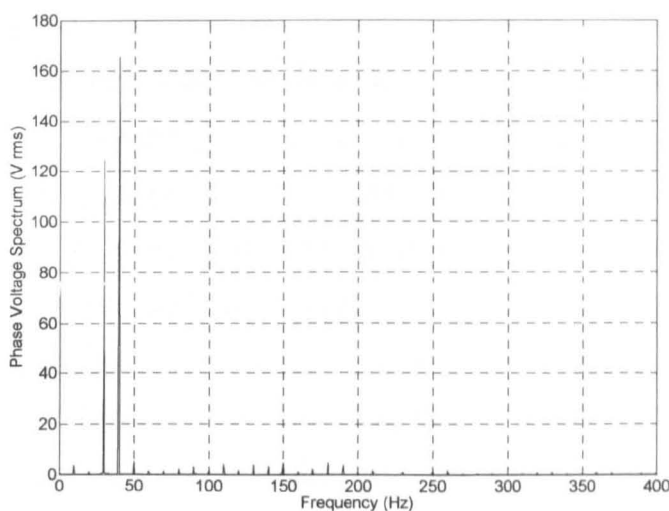
Fig. 9.21: Experimentally recorded inverter phase voltage spectrum for operation with: $M_1 = 0.636$ at 30 Hz and $M_2 = 0.844$ at 40 Hz (outside the shaded area of Fig. 9.4)

Multi-frequency SVPWM is tested next. The measured quantities are the inverter phase voltage (across the windings of both machines), and the second machine (M2) phase voltage. Reference voltage of M1 is of frequency f_1 and is in the d_1-q_1 plane, while reference voltage of M2 is of frequency f_2 and it appears in the d_2-q_2 plane.

In accordance with the steady state equivalent circuit representation for this drive configuration [Levi et al (2006b)], measured inverter phase voltage will contain two different frequency components that will correspond to the two sets of references in terms of both magnitude and frequency. On the other hand, phase voltage of M2 will contain a component at frequency f_2 that will be slightly smaller than the corresponding component in the inverter phase voltage, due to the additional voltage drop at M1 at frequency f_2. M2 voltage will also

have a small component at frequency f_1, this being the additional voltage drop at M2 (on stator leakage impedance) due to the flow of the currents of frequency f_1 through M2 [Levi et al (2006b)].

The first set of measured voltages is shown in Fig. 9.22. The voltage reference magnitudes of the two machines are governed with frequencies $f_1 = 33$ Hz and $f_2 = 16$ Hz at the input of the related V/f profiles. The inverter voltage spectrum contains two corresponding components of app. 80 V and 40 V, respectively. Most of the 16 Hz component also appears in the spectrum of M2 voltage, while the component at 33 Hz is 6 V, since most of this frequency component is the voltage at M1. Operating conditions of Fig. 9.22 correspond to the case when the voltage reference magnitude in the d_1-q_1 plane is twice the voltage reference magnitude in the d_2-q_2 plane. Hence the applied four active space vectors are dominated by the vectors neighbouring the reference in the d_1-q_1 plane, as discussed in conjunction with Table 9.3.

In the second operating condition, illustrated in Fig. 9.23, situation is different. The frequencies are now $f_1 = 20$ Hz and $f_2 = 25$ Hz, which means that the magnitudes of the two voltage space vector references are close one to the other. Under these conditions the applied four active space vectors are never from the same plane and may involve a vector that is not neighbouring any of the two references (middle portion of Table 9.3). The components at 20 Hz and 25 Hz are now app. 50 V and 60 V, respectively, in the inverter voltage. Most of the 60 V appears on M2 (operating at 25 Hz) while most of the 20 Hz component appears on M1 (and the 20 Hz component at M2 is small, around 2.5 V).

The last operating point, shown in Fig. 9.24, applies to the frequency pair $f_1 = 10$ Hz and $f_2 = 40$ Hz. Since the voltage reference in the d_2-q_2 plane is now four times larger than the reference in the d_1-q_1 plane, applied four active space vectors are dominated by the vectors neighbouring the reference in the d_2-q_2 plane. This is from the point of view of the applied four active space vectors the situation inverse to the one depicted in Fig. 9.22. The magnitudes of two frequency components in Fig. 9.24 are in full agreement with the applied $V/f =$ const. control law and the values already observed in Figs. 9.22 and 9.23.

Inverter phase currents under all operating conditions contain two components at two different frequencies, where the component at f_1 creates flux and torque in M1, while the component at f_2 yields flux and torque in M2. The waveform of inverter current is similar to the inverter phase voltage. For this reason, measured phase currents are not included in set of the results presented here.
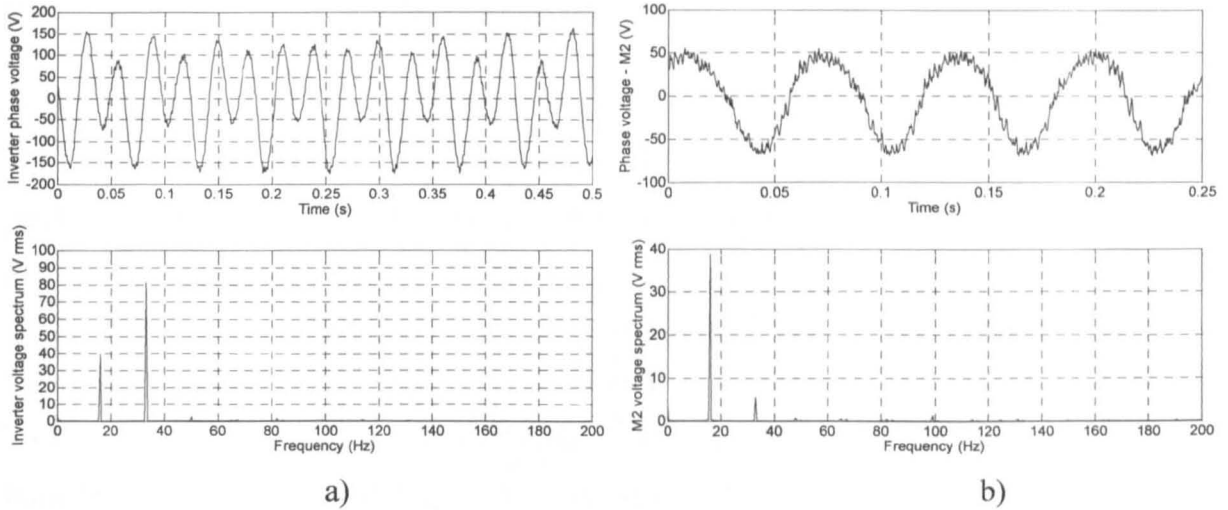
Fig. 9.22: Experimentally recorded: a) inverter phase voltage and its spectrum and, b) M2 phase voltage and its spectrum for the frequency pair $f_1 = 33$ Hz and $f_2 = 16$ Hz.
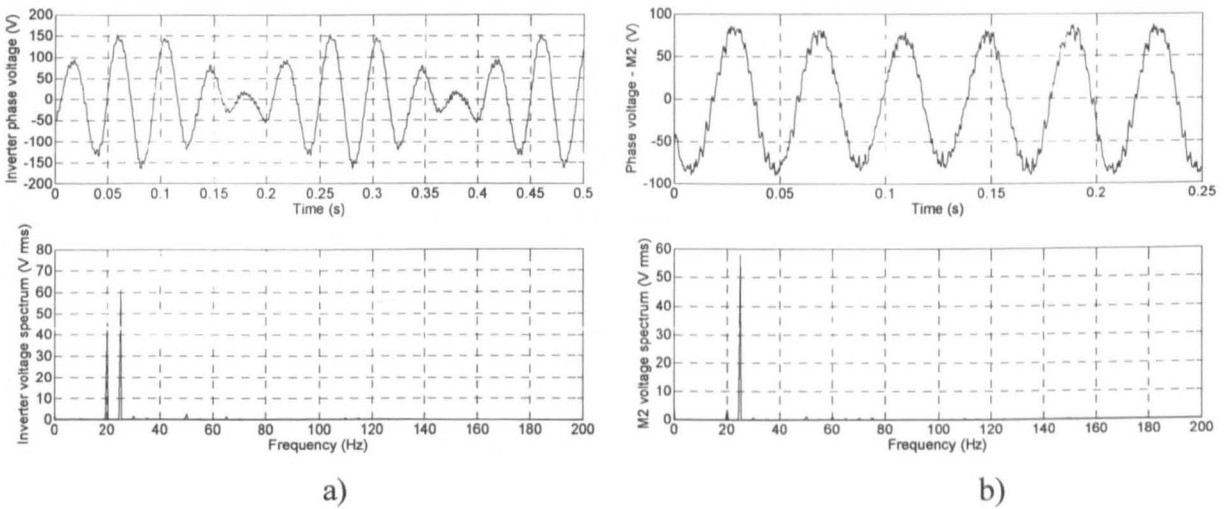
Fig. 9.23: Experimentally recorded: a) inverter phase voltage and its spectrum and, b) M2 phase voltage and its spectrum for the frequency pair $f_1 = 20$ Hz and $f_2 = 25$ Hz..
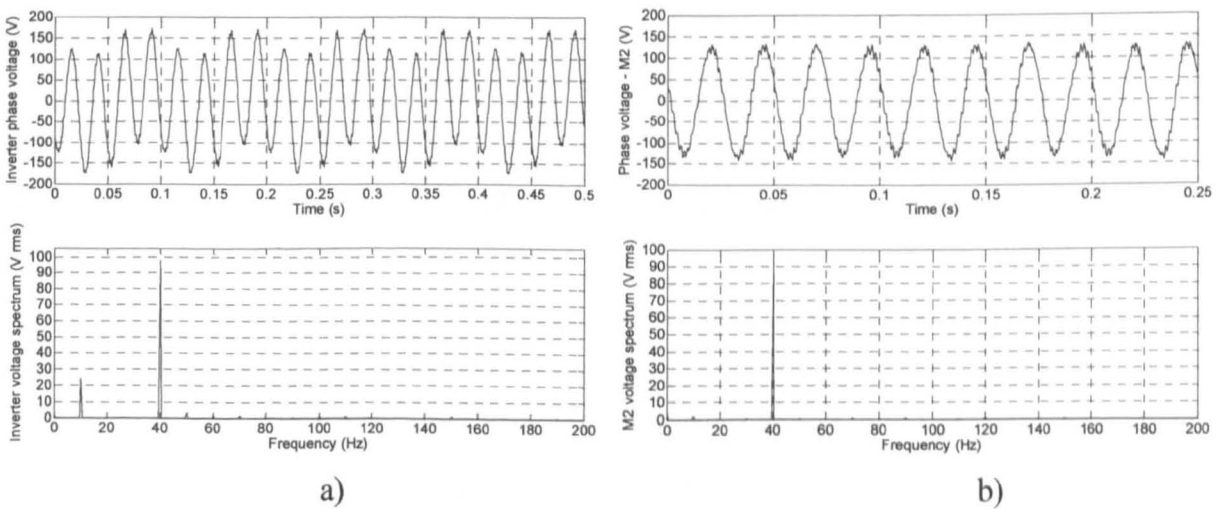
Fig. 9.24: Experimentally recorded: a) inverter phase voltage and its spectrum and, b) M2 phase voltage and its spectrum for the frequency pair $f_1 = 10$ Hz and $f_2 = 40$ Hz..

9.7.1 SEVEN-PHASE THREE-MOTOR DRIVE

The same multi-phase inverter is now configured as a seven-phase one. The load is however now static star-connected *R-L* and is the same one used in chapter 5. Only multi-frequency carrier-based PWM scheme of Fig. 9.15 is tested in order to verify boundaries that determine dc bus utilisation in the linear region of modulation. Reference frequencies and values for the modulation indices are selected arbitrarily now (since *R-L* load is used) and three different operating conditions are examined experimentally. Phase voltage of the *R-L* load is measured, and such a measurement is sufficient to confirm the validity of the multi-frequency PWM scheme and determined voltage limits. Since only PWM scheme is under investigation, *R-L* load is sufficient as replacement for three seven-phase machines in series connection to the seven-phase VSI.

Modulation index and frequency for the plane d_3-q_3 are at first set to zero and the limits illustrated in Fig. 9.5 are explored. Modulation indices in the first two planes are therefore set to $M_1 = 0.885$ (at 43 Hz) and $M_2 = 0.315$ (at 15 Hz). This corresponds to the point *D* in Fig. 9.6. Measured inverter phase voltage and its spectrum are illustrated in Fig. 9.25. It can be seen that the spectrum contains only two components at frequencies of the references, without any other low order harmonics. Hence the inverter does operate in the linear modulation region, as predicted in Fig. 9.6 for this operating point. The rms values in the spectrum of Fig. 9.25 are a couple of percent lower that the corresponding rms references (187.7 V and 66.8 V).

In the second experiment operation in point *G* of Fig. 9.6 is examined. Modulation indices are therefore set to the same value $M_1 = M_2 = M_3 = 0.456$ and frequencies are arbitrarily selected as 27, 37 and 47 Hz, respectively, in the three planes. Experimental results are shown in Fig. 9.25b. As can be seen, all three fundamentals are correctly generated, are of almost the same rms value (again slightly below the reference, which is 96.8 V rms), and the spectrum does not show existence of any other low order harmonics, thus confirming that the inverter operates in the linear modulation region.

To illustrate the operation in the overmodulation, an operating point outside the volume of Fig. 9.6 is considered in the third experiment. The frequencies of three sets of references are kept the same as in the previous case but modulation indices are increased to $M_1 = M_2 = M_3 = 0.65$. Phase voltage and its spectrum are now as shown in Fig. 9.26. It is obvious that the inverter now operates in the overmodulation region, since the spectrum contains a whole range of low-order harmonics (including sub-harmonics).
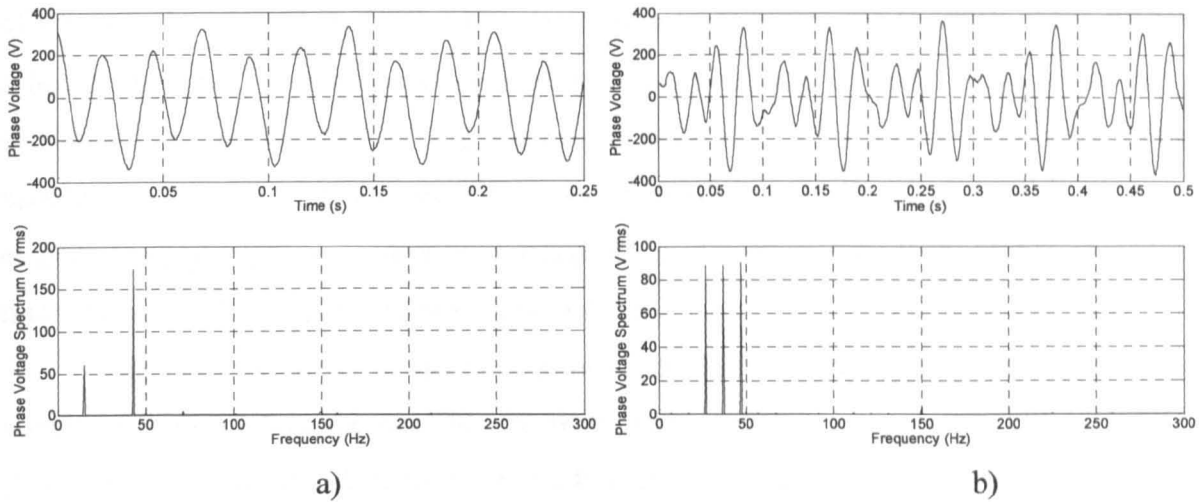
Fig. 9.25: Experimentally recorded inverter phase voltage and its spectrum for operation with:
a) $M_1 = 0.885$ at 43 Hz and $M_2 = 0.315$ at 15 Hz; point D in Fig. 9.6 and,
b) $M_1 = M_2 = M_3 = 0.456$ at 27, 37 and 47 Hz; point G in Fig.9.6.
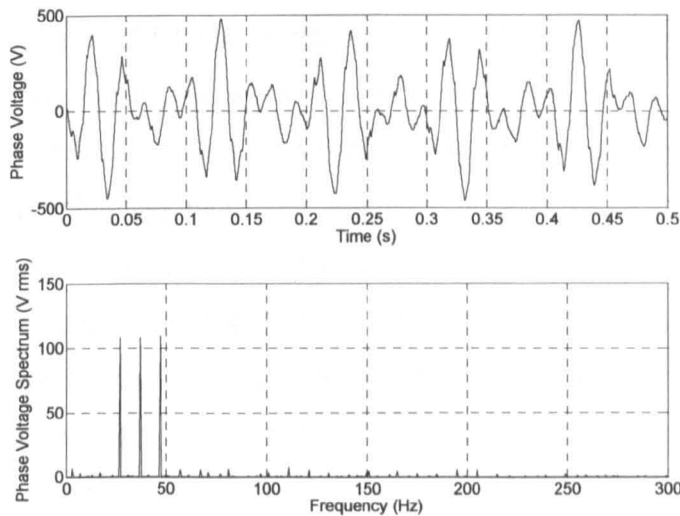
Fig. 9.26: Experimentally recorded inverter phase voltage and its spectrum for the operation
of the seven-phase VSI in the overmodulation region ($M_1 = M_2 = M_3 = 0.65$
at 27, 37 and 47 Hz; operating point outside the volume of Fig. 9.6).

9.8   SUMMARY

In this chapter a SVPWM method for multi-phase VSIs is developed, that is capable of generating required voltage references in all 2-D planes without restricting *a-priori* achievable reference magnitudes in planes other than d_1-q_1. This is achieved by selecting initially $(n-1)^2/2$ active space vectors within a switching period, instead of the customary $n-1$ active vectors. More specifically, a set of $(n-1)$ active vectors are selected in each of the $(n-1)/2$ planes, in a manner that follows previously established rules for single-frequency output voltage generation with multi-phase VSIs. It is shown that, by a suitable manipulation

of the initially selected $(n-1)^2/2$ active space vectors, it is possible to arrive at the SVPWM scheme where only $n-1$ active vectors are eventually applied. However, the vectors that are finally utilised are not known in advance and some may even not be among the initially selected set of $(n-1)^2/2$ vectors. The same SVPWM principles developed here can be extended to higher phase numbers in a straightforward manner. Simplicity of the carrier-based multi-frequency PWM has also been demonstrated.

The basic principle of determination of the limits of the linear modulation region, widely utilised for three-phase VSIs, is extended to multi-phase inverters with an arbitrary prime number of phases. Due to the phase transposition that exists between the multitude of the planes, dc bus utilisation in the linear modulation region is better than it would have been had all the required voltage components belonged to the same plane. It is shown that the dc bus voltage utilisation of a five-phase VSI is governed with an area in the (M_1, M_2) plane. In the case of a seven-phase VSI linear PWM is obtainable as long as the three modulation indices determine a point that belongs to the volume in the (M_1, M_2, M_3) 3-D space. The principle is further extended to higher prime phase numbers, where a corresponding graphical representation is not possible any more.

Developed method is entirely independent of the applied method of pulse width modulation and is equally applicable to both space vector and carrier-based PWM. Theoretical considerations are verified experimentally using a series-connected two-motor five-phase induction motor drive and a static load supplied from a seven-phase VSI.

The basic idea of this chapter, development of a multi-frequency output PWM scheme, is explored further in the next chapter. However, instead of a multi-phase VSI, a multi-leg VSI aimed at supplying a group of three-phase machines is addressed.

Chapter 10

PWM METHODS FOR MULTI-FREQUENCY OUTPUT VOLTAGE GENERATION WITH MULTI-LEG VOLTAGE SOURCE INVERTERS

10.1 INTRODUCTION

In contrast to preceding chapters, where the PWM schemes have been developed for multi-phase machines, in this chapter PWM for three-phase machines is considered. A multi-leg VSI is used to supply a group of three-phase machines connected to the inverter in accordance to the principle shown in Fig. 1.3. Thus, all three-phase machines share one of the inverter legs, offering the reduction in the number of power semiconductors necessary to control such a multi-motor drive, compared to the standard industrial solution based on utilisation of independent converter-machine units.

Since the independent control of each of the machines is the goal, multi-leg VSI must generate multi-frequency output voltage, in accordance with the voltage requirements of each machine. Thus, development of an improved PWM scheme that, overcomes drawbacks of the existing solutions (section 2.4), is presented in this chapter. Viability of the novel PWM scheme is demonstrated through extensive experimentation on several multi-leg topologies. Multi-leg VSI fed multi-motor drive topology suffers from some inherent drawbacks, which are also addressed in this chapter, as well as are some solutions for their alleviation. Similar to the series-connected multi-phase multi-motor drives, value of dc bus voltage imposes restrictions on the operational range of multi-leg VSI fed multi-motor drives. The method for determination of the voltage limits, developed in chapter 9, is here extended to the multi-leg VSI topology.

This chapter is organised as follows. Section 10.2 presents the general topology of the multi-leg VSI fed multi-motor drives and corresponding requirements imposed on the PWM. Dc bus utilisation limits are determined in section 10.3, and the operational range for the case of CPWM is defined. Development of the carrier-based PWM scheme for multi-leg VSI is

given in section 10.4, using the well known principles of the zero-sequence injection. Multi-frequency SVPWM scheme is presented in section 10.5. Experimental results, obtained from five-leg VSI fed two-motor, seven-leg VSI fed three-motor and nine-leg VSI fed four-motor drive, are shown in section 10.6. Discussion of the results is given in section 10.7, while summary in section 10.8 concludes the chapter.

The main original results of this chapter have been presented in: Dujić et al (2007e), Jones et al (2007a), Dujić et al (2008b), Jones et al (2008a), Vukosavić et al (2008), Jones et al (2008b), Jones et al (2008c) and Dujić et al (2008c).

10.2 MULTI-LEG VOLTAGE SOURCE INVERTER FED MULTI-MOTOR DRIVES

Principal layout of a multi-leg VSI fed multi-motor drive topology is shown in Fig. 10.1. A nine-leg VSI fed four-motor drive is used as an example (since experimental investigation covers topologies up to this one), although the principles of connection can be applied to both lower and higher leg number inverters. Leg *A* of the inverter is selected as the common leg for the phase '*a*' of each of the three-phase machines. Such a selection is purely for illustration purposes and any inverter leg can be selected as the common one. Similar to the series-connected multi-phase multi-motor drives, discussed in chapter 9, an *n*-leg inverter can be used to supply (*n*-1)/2 machines. Yet, this time all machines are three-phase ones and only the number of the inverter legs varies.
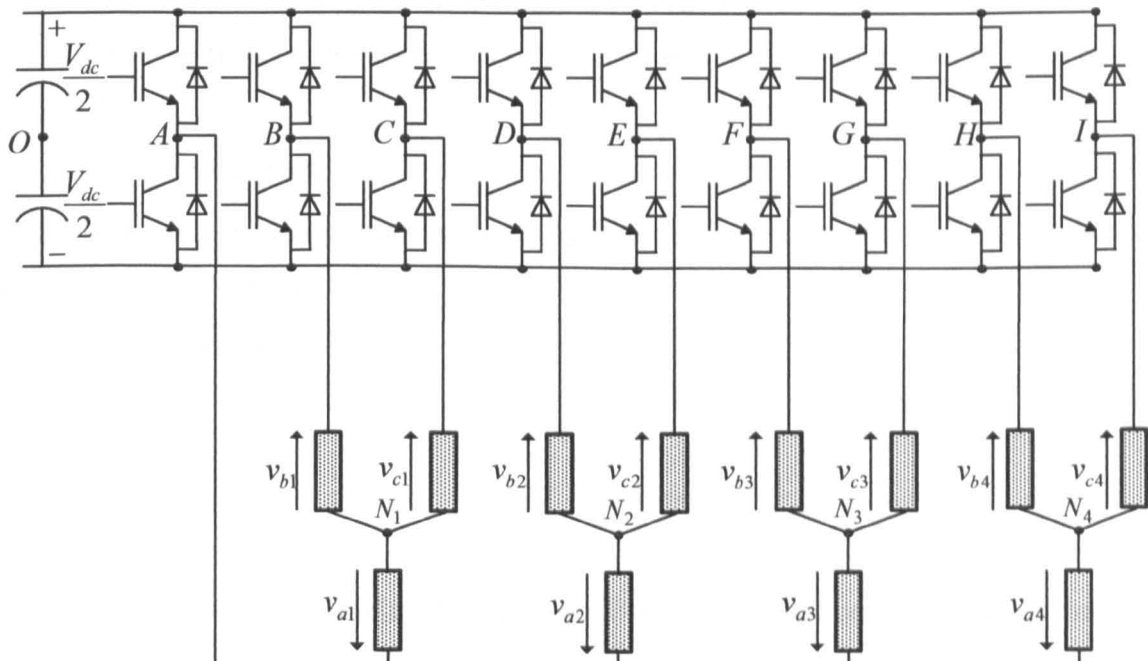

Fig. 10.1: Nine-leg VSI fed four-motor drive.

Dc bus voltage is assumed to be of the rated value required in the case of a three-phase single-motor drive. This imposes restrictions on the operational range of each machine in this topology. Therefore, before development of PWM schemes suitable for independent control of each of the three-phase machines, voltage limits are determined first. For this purpose, the same principles established in chapter 9 are followed, and permissible values for modulation indices that correspond to the operation of a multi-leg VSI fed multi-motor drive in the region of the linear modulation are determined. Analysis of operation in the overmodulation is beyond the scope of the thesis.

10.3 VOLTAGE LIMITS OF MULTI-LEG VOLTAGE SOURCE INVERTERS

Having a value of the dc bus voltage restricted to the level that corresponds to a single-motor drive places restrictions on the operational range of the analysed topologies. It is therefore important to define correlations between permissible values of the modulation indices and the available dc bus voltage. By restricting the analysis to the area of linear modulation only, the simplest way is to analyse again inverter line voltages. It is known that the maximum value of the modulation index in the linear modulation region corresponds to the case when peak value of the machine's fundamental line voltage equals dc bus voltage. This is, at the same time, inverter line voltage, and that fact is used to determine boundaries of the operation in the linear modulation. To perform such analysis topology from Fig. 10.1 is sufficient, as it will be demonstrated shortly.

In a three-phase system, there is only one line voltage (with respect to the magnitude) given with:

$$\left| \underline{V}_l \right| = 2M0.5V_{dc} \cos(\pi/6) \tag{10.1}$$

Considering the line voltages of the multi-leg inverter, based on Fig. 10.1 and referenced to the inverter leg A, one has:

$$
\begin{aligned}
v_{AB} &= v_A - v_B = v_{ab1} \\
v_{AC} &= v_A - v_C = v_{ac1} \\
v_{AD} &= v_A - v_D = v_{ab2} \\
v_{AE} &= v_A - v_E = v_{ac2} \\
v_{AF} &= v_A - v_F = v_{ab3} \\
v_{AG} &= v_A - v_G = v_{ac3}
\end{aligned}
\tag{10.2}
$$

Thus, with respect to the common leg, inverter line voltages are defined with machine's line voltages. At the same time none of the inverter line voltages are related to the line voltages of

two or more machines. However, referencing the inverter line voltages with respect to some other (not common) inverter leg, one can obtain relationships that are more suitable for the determination of the limits of the dc bus utilisation. Thus, with respect to the inverter leg B, inverter line voltages are:

$$
\begin{aligned}
v_{BA} &= v_B - v_A = v_{ba1} \\
v_{BC} &= v_B - v_C = v_{bc1} \\
v_{BD} &= v_B - v_D = v_{b1} - v_{a1} + v_{a2} - v_{b2} = v_{ba1} + v_{ab2} \\
v_{BE} &= v_B - v_E = v_{b1} - v_{a1} + v_{a2} - v_{c2} = v_{ba1} + v_{ac2} \\
v_{BF} &= v_B - v_F = v_{b1} - v_{a1} + v_{a3} - v_{b3} = v_{ba1} + v_{ab3} \\
v_{BG} &= v_B - v_G = v_{b1} - v_{a1} + v_{a3} - v_{c3} = v_{ba1} + v_{ac3}
\end{aligned}
\tag{10.3}
$$

It can be seen that line voltages of (10.3) are now functions of either one line voltage of a particular machine or line voltages of two machines. Yet, it is easy to check by further inspection of the inverter line voltages that there is not any inverter voltage that is a function of three or more line voltages of different machines.

Thus, the relevant constraint is obtained by analysing the inverter line voltages for the worst-case scenario (when peaks of any two machine's line voltages reach their maximum at the same time). Thus, for any two machines with their corresponding modulation indices M_x and M_y, one has:

$$
|v_{INV}| = M_x V_{dc} \cos(\pi/6) + M_y V_{dc} \cos(\pi/6) \le V_{dc}
\tag{10.4}
$$

Constraint (10.4) applies directly to the inverter line voltages that appear between inverter legs connected to a phase of any two machines (e.g. *BD, BE, BF, DE...*). Having $M_x = 0$ or $M_y = 0$ reduces (10.4) to the constraint that applies to the case when both inverter legs supply the same machine (e.g. *AB, BC, DE...*). At the same time, this is the same constraint that yields the maximum value of the modulation index for a three-phase system, $M_{max} = 1/\cos(\pi/6) = 1.1547$.

Re-arranging (10.4) yields the operational area for the multi-leg VSI in the linear modulation region that relates the modulation indices of any two machines as:

$$
M_x \cos(\pi/6) + M_y \cos(\pi/6) \le 1
\tag{10.5}
$$

This is illustrated in Fig. 10.2 where shaded region shows permissible values of modulation indices. Since this area relates only two of a multitude of three-phase machines that can be connected to the multi-leg VSI, it offers limited information about permissible area of the operation in the linear modulation region when there are more than two machines. For example, in the case of a nine-leg VSI fed four-motor drive, there are four modulation indices that are different from zero, if all four machines operate at the same time.
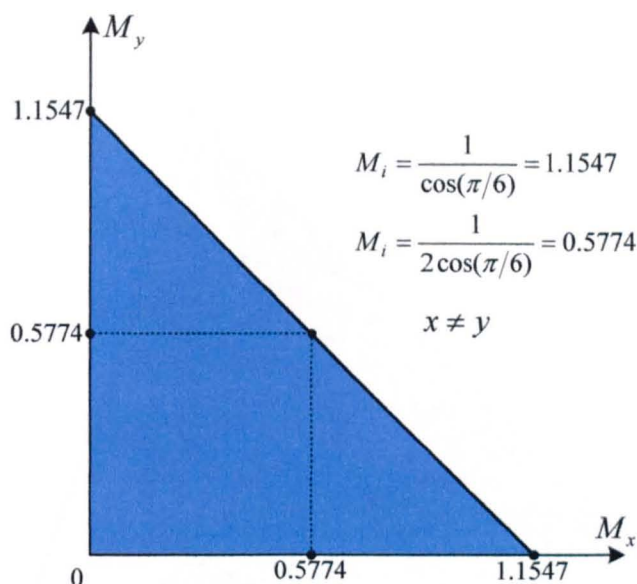
Fig. 10.2: Combination of modulation indices of any two machines that yield operation in the linear modulation region for a multi-leg VSI (five-leg VSI fed two-motor drive).

At the same time, shaded area of Fig. 10.2 actually corresponds to the operational range of a five-leg VSI fed two-motor drive. As can be seen, full dc bus voltage is available to one machine if the second machine is at standstill (zero value of the reference modulation index). In contrast to the characteristic of a series-connected five-phase two-motor drive, the characteristic appears now as a straight line, connecting two maximum values of the modulation indices. Thus, both machines are able to operate only at a maximum of $M_{max} = 0.5774$ simultaneously, which, assuming the simplest V/f profile (for rated frequency of 50 Hz), corresponds to the operation at 25 Hz for both machines. If one of the machines requires more than 25 Hz, the other one must operate with a lower frequency, if the operation is to remain in the linear region of the modulation.

Since this characteristic applies to any two machines, and all the machines within a multi-leg drive are regarded as being of the same voltage ratings, a further extension of the solution for the dc bus utilisation is possible. Thus, using the 2-D solution from Fig. 10.2, the complete solution in the case of three machines can be represented in a 3-D system of axis defined with the modulation indices M_x, M_y and M_z, respectively. This is shown in Fig. 10.3, where given volume represents possible values of the modulation indices that yield the operation in the linear region of modulation. Volume, shown in Fig. 10.3, defines the boundaries of the linear modulation for the case of seven-leg VSI fed three-motor drive. Coordinates of all characteristic points in the 3-D space are summarised in Table 10.1.
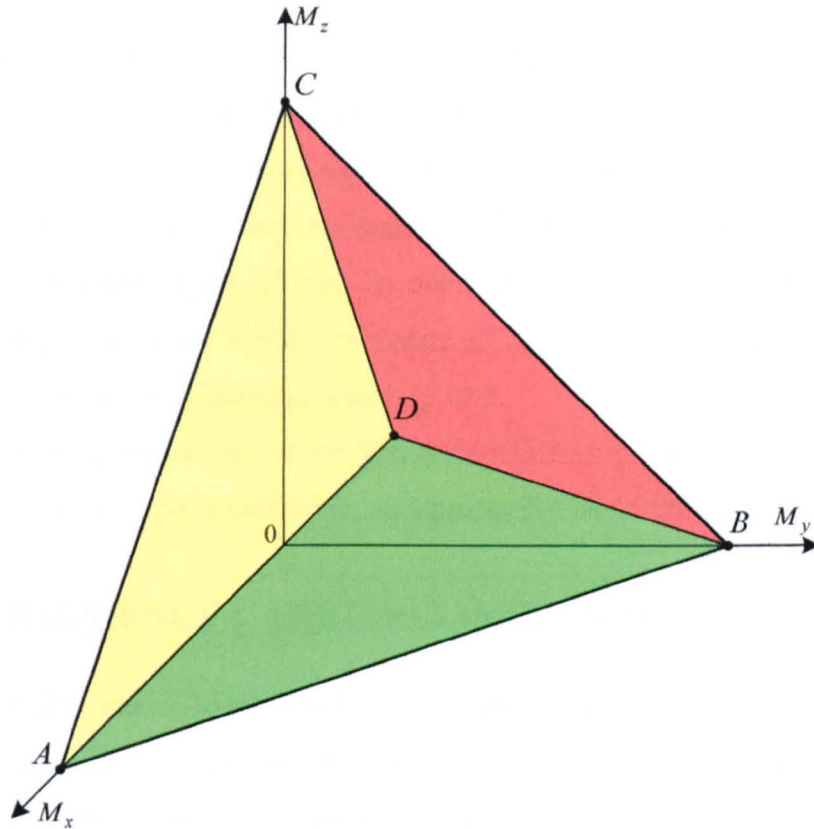
Fig. 10.3: Combination of modulation indices of any three machines that yield operation in the linear modulation region for a multi-leg VSI (seven-leg VSI fed three-motor drive).

It can be seen that it is possible to achieve operation of all three machines simultaneously at half of the rated speed (point D, value of all three modulation indices equal to 0.5744). The enclosed volume encompasses all combinations of the modulation indices that create an operating point in the (M_x, M_y, M_z) space. As long as the operating point defined in this way is inside the enclosed volume, operation of the multi-leg multi-motor drive in the linear region of modulation is possible. Similar to the situation in chapter 9, it is not possible to graphically illustrate solution for higher leg numbers. However, based on the results presented it is obvious that the machine with the highest value of the modulation index will automatically define the maximum value allowable for the modulation indices of all the other machines. Therefore, the solutions shown in Figs. 10.2 and 10.3 provide good guidelines for understanding the complete solutions for any leg number.

Table 10.1: Characteristic operating points shown in Fig. 10.3.

|	*A*	*B*	*C*	*D*
M_x	1.1547	0	0	0.5744
M_y	0	1.1547	0	0.5744
M_z	0	0	1.1547	0.5744

By considering Figs. 10.2 and 10.3, it can be established that all the $(n$-$1)/2$ three-phase machines supplied from an n-leg VSI are able to reach simultaneously half of their rated speed. For the 50 Hz machines, this corresponds to simultaneous operation at 25 Hz. Further increase of the reference frequency (and correspondingly the value of the modulation index) for one three-phase machine, requires that, for all the other machines, the frequency (modulation index) is reduced below 25 Hz. To maintain operation in the linear region of modulation, it is therefore necessary that at any instant all possible machine pairs operate with the modulation indices within the shaded area of Fig. 10.2.

This general rule applies to any n-leg VSI fed $(n$-$1)/2$-motor drive. Yet, to utilise dc bus voltage up to this theoretically predicted level, a proper PWM scheme must be developed.

10.4 MULTI-FREQUENCY CARRIER-BASED PWM

Principles of the carrier-based PWM for multi-leg VSI fed multi-motor drives, developed in this chapter, heavily rely on the principle of the zero-sequence injection, already used in chapter 6. Principal layout of a carrier-based three-phase modulator is shown in Fig. 10.4. A set of fundamental reference signals (denoted with superscripts '*') are modified by proper zero-sequence signal injection into final modulating signals before comparison with the high frequency carrier signal. As the result, switching functions for the inverter legs are generated (m_A, m_B, and m_C).

As demonstrated in chapter 6, zero-sequence signal represents a degree of freedom that is normally used to improve the dc bus utilisation of the carrier-based PWM method. At the same time, in three-phase systems output current ripple rms can be improved, in contrast to the other multi-phase systems. Different selections of the zero-sequence signal lead to different carrier-based PWM methods [Zhou and Wang (2002)]. Yet, the zero-sequence signal is always related to the input set of the fundamental signals. Thus, HIPWM uses the n-th harmonic (the third harmonic in this case) as the zero-sequence signal, which can be determined even without the use of the block 'zero-sequence calculator'. The TIPWM injects all the odd multiple of the n-the harmonic, and the corresponding zero-sequence signal is determined by means of manipulations with minimum and maximum values of the input set of the fundamental signals. Similarly, DPWM schemes can be developed as well, by properly setting the block 'zero-sequence signal calculator' in Fig 10.4 [Zhou and Wang (2002)].
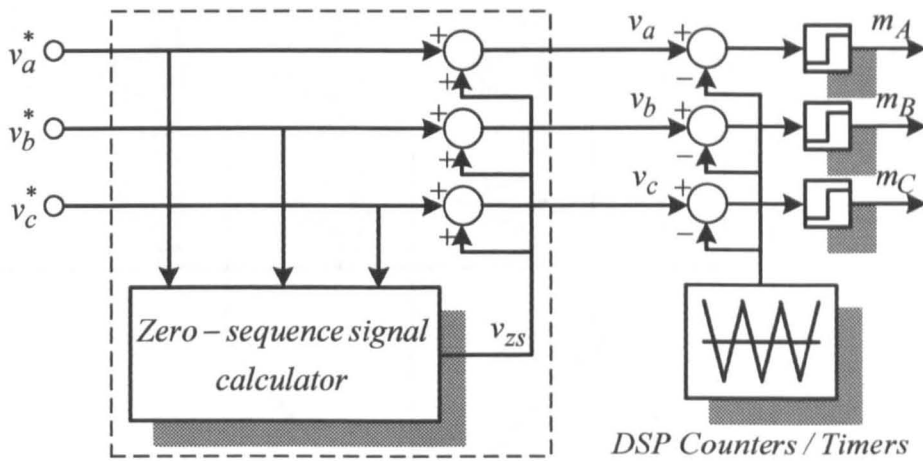
**Fig. 10.4:** Principle of carrier-based PWM for a three-phase VSI.

An important aspect of the zero-sequence signal injection is that the zero-sequence signal does not appear in either line or phase voltages of the three-phase machine. This offers a possibility to utilise the principle of zero-sequence signal injection in a very different manner for a multi-leg VSI supplied variable speed multi-motor drive. For the sake of clarity, a five-leg VSI fed two-motor drive is used as an example in the development of the multi-frequency carrier-based PWM scheme.

10.4.1 CARRIER-BASED PWM FOR A FIVE-LEG VOLTAGE SOURCE INVERTER

A five-leg VSI fed two-motor drive is illustrated in Fig. 10.5. This time, inverter leg C is taken as the common leg for the phase 'c' of the machine 1 (M1) and the phase 'a' of the machine 2 (M2). As noted, this selection is arbitrary. Additional sub-scripts (1 and 2) are used to distinguish the stator windings of the M1 and M2, respectively. Inverter legs are labelled with capital letters, while corresponding modulating signals are denoted with lower case letters, as indicated in Fig. 10.5.

To start with, it is assumed that only M1 is connected to the first three legs of the five-leg VSI of Fig. 10.5. To control M1, generalised structure of the carrier-based three-phase modulator from Fig. 10.4 is sufficient. Modulating signals for M1 can be obtained based on the set of fundamental reference signals and the injection of an opportune zero-sequence signal, in general, as ($\vartheta_1 = 2\pi f_1 t$):

$$
\begin{aligned}
v_{a_1} &= v_{a_1}^* + v_{zs_1} = M_1 \cos(\vartheta_1) + v_{zs_1} \\
v_{b_1} &= v_{b_1}^* + v_{zs_1} = M_1 \cos(\vartheta_1 - 2\pi/3) + v_{zs_1} \\
v_{c_1} &= v_{c_1}^* + v_{zs_1} = M_1 \cos(\vartheta_1 - 4\pi/3) + v_{zs_1}
\end{aligned}
\tag{10.6}
$$
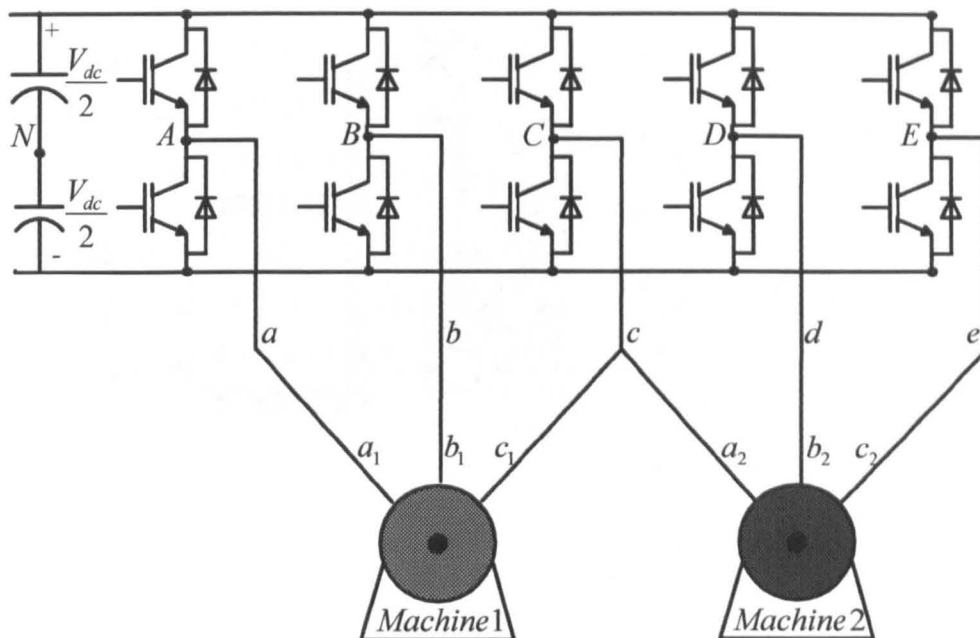
Fig. 10.5: Five-leg VSI fed two-motor drive.

A certain zero-sequence signal is added to the fundamental sinusoidal signals. Its exact nature is irrelevant for the analysis presented here. What matters is that the zero-sequence signal will not appear in either phase or line voltages of the M1, since it gets cancelled in the case of the star connected three-phase machine with isolated neutral.

Consider now the case of having the second machine connected in accordance to the layout shown in Fig. 10.5. Fundamental sinusoidal signals for the M2 can be of arbitrary magnitude and frequency with respect to the signals of the M1. Thus one has ($\vartheta_2 = 2\pi f_2 t$):

$$
\begin{aligned}
v_{a_2} &= v_{a_2}^* + v_{zs_2} = M_2 \cos(\vartheta_2) + v_{zs_2} \\
v_{b_2} &= v_{b_2}^* + v_{zs_2} = M_2 \cos(\vartheta_2 - 2\pi/3) + v_{zs_2} \\
v_{c_2} &= v_{c_2}^* + v_{zs_2} = M_2 \cos(\vartheta_2 - 4\pi/3) + v_{zs_2}
\end{aligned}
\tag{10.7}
$$

An appropriate zero-sequence signal is added to modify signals of (10.7) during creation of the resulting set of modulating signals. It follows that, in total, there are six modulating signals (three per machine) while there are only five legs of the inverter. Thus, to reduce the number of modulating signals from six to five, the idea of the zero-sequence signal injection is applied to the multi-leg VSI in a unique manner. Five modulating signals are created as:

$$
\begin{aligned}
v_a &= v_{a_1} + v_{a_2} \\
v_b &= v_{b_1} + v_{a_2} \\
v_c &= v_{c_1} + v_{a_2} \\
v_d &= v_{b_2} + v_{c_1} \\
v_e &= v_{c_2} + v_{c_1}
\end{aligned}
\tag{10.8}
$$

The principal layout of the carrier-based PWM for a five-leg VSI is shown in Fig. 10.6.
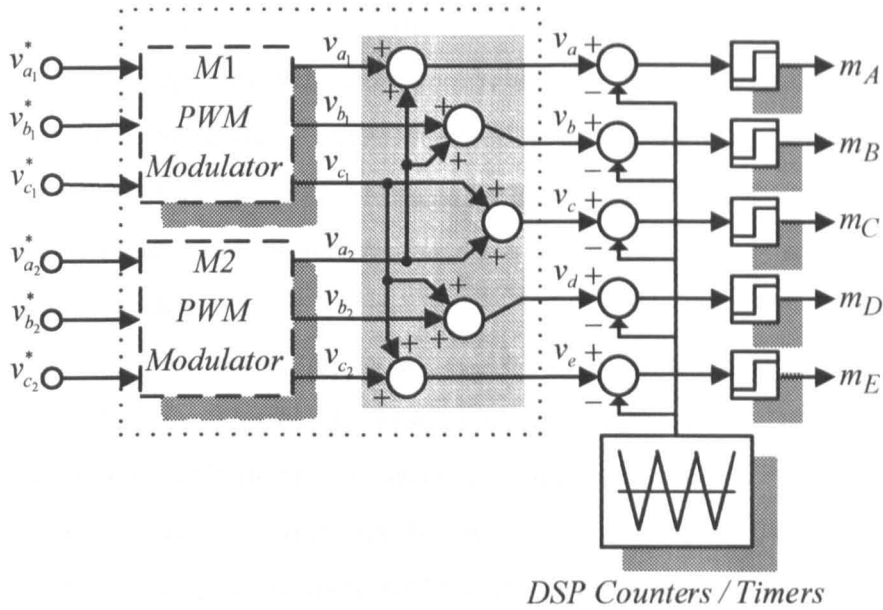
Fig. 10.6: Principle of the carrier-based PWM for a five-leg VSI based on double zero-sequence signal injection (DZSI).

It follows from (10.8) and Fig. 10.6 that, as far as the M1, connected to inverter legs *A, B* and *C*, is concerned, the same signal v_{a_2} is added to the modulating signals coming from the modulator of the M1. Therefore this signal has no effect on the reference voltages of the M1 since it appears as a zero-sequence component and it gets cancelled in line voltages of the M1. Similarly, signal v_{c_1} is added to the outputs of the modulator of the M2. It does not affect operation of the M2, connected to legs *C, D* and *E*. The highlighted part of Fig. 10.6 summarises the principle of (10.8), which allows the reduction in the number of modulating signals. All five modulating signals, necessary to control the five-leg VSI, are generated in this way. Only two standard three-phase carrier-based PWM modulators are utilised. At the same time, initial zero-sequence injection, described with (10.6) and (10.7) and shown in Fig. 10.4, is retained. It thus follows that there are two zero-sequence injections (one per modulator) and the PWM scheme is therefore termed double zero-sequence signal injection (DZSI). Although the highlighted block from Fig. 10.6 is in essence another zero-sequence signal injection, the main task of this injection is the reduction of the number of modulating signals.

Taking into consideration defined magnitudes of modulating signals and the carrier, restrictions of the proposed PWM scheme with regard to the combined voltage requirements of two machines are clearly visible. As long as the combined modulating signals generated by the modulator (outputs of the dotted-line box in Fig. 10.6) do not exceed the magnitude of the carrier signal, both machines will operate in linear region of the modulation with CPWM as

though they are supplied from their own independent three-phase inverters. In other words, the available dc bus voltage will get automatically sub-divided between the two machines, in accordance with their respective reference signal magnitudes. For example, if M1 is at standstill, there is the full dc bus voltage available to supply the M2 since the modulator will at all times provide the same switching functions for the M1, thus keeping the effective voltage applied to it at zero.

The implementation principle, shown in Fig. 10.6, assumes utilisation of two three-phase modulators of the form within the dashed-line box in Fig. 10.4. Thus, as noted already, two initial zero-sequence calculators are necessary (one per machine) before reduction of the number of modulating signals from six to five. This can be simplified, if two sets of fundamental signal for M1 and M2 are at first summed in accordance with:

$$
\begin{aligned}
v_a^* &= v_{a_1}^* + v_{a_2}^* \\
v_b^* &= v_{b_1}^* + v_{a_2}^* \\
v_c^* &= v_{c_1}^* + v_{a_2}^* \\
v_d^* &= v_{b_2}^* + v_{c_1}^* \\
v_e^* &= v_{c_2}^* + v_{c_1}^*
\end{aligned}
\tag{10.9}
$$

Here, individual modulating signals of (10.6) and (10.7) used to create (10.9), do not include the initial zero-sequence signals. A single zero-sequence signal calculator is then applied to five modulating signals on the left-hand side of (10.9) as shown in Fig. 10.7. Highlighted block in Fig. 10.7, which corresponds to the application of (10.9), is the same as before with a difference that zero-sequence signal injection now happens only once. This simplifies the DSP implementation and reduces the number of calculations. This approach to the multi-frequency PWM for multi-leg VSI fed multi-motor drives is termed single zero-sequence signal injection (SZSI). The feasibility of using the zero-sequence signal,

$$
v_{zs} = -0.5(v_{max}^* + v_{min}^*)
\tag{10.10}
$$

already utilised in chapters 6 and 9, is demonstrated next, by means of simulations.

Modulation indices are set as $M_1 = M_2 = 0.5774$ and frequencies are arbitrarily selected as $f_1 = 20$ Hz and $f_2 = 30$ Hz. This operating point corresponds to the operation in the limit of the linear modulation, according to Fig. 10.2. Therefore, resulting modulating signals should stay within the carrier range (± 1), without excursions outside this range. However it is easy to establish that, if no injection of the initial zero-sequence signal is applied, both DZSI and SZSI modulators produce the same set of modulating signals in accordance with (10.9).
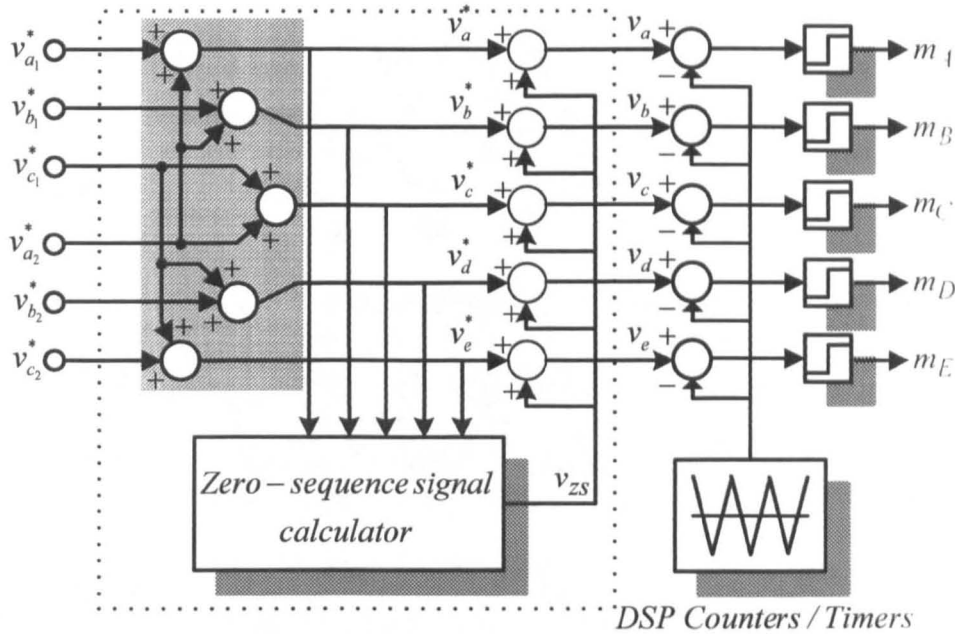
Fig. 10.7: Principle of carrier-based PWM for a five-leg VSI based on single zero-sequence signal injection (SZSI).

These signals are shown in the top part of the Fig. 10.8. As can be seen, there are instants when some of the modulating signals are above the carrier range (± 1), which effectively means that overmodulation takes place. Envelopes of minimum and maximum signals are shown in bold, and it can be observed that when overmodulation takes place, only one of the inverter legs is clamped either to the upper of lower dc bus rail. This is not in accordance to Fig. 10.2 and boundaries for the operation in the linear region of PWM.

Further two parts of Fig. 10.8 illustrate the resulting modulating signals of the DZSI (middle) and the SZSI (bottom), when corresponding zero-sequence calculators are activated. For DZSI, this means that zero-sequence signals defined with (10.10) are added to the fundamental modulating signals of M1 and M2, as in (10.6) and (10.7), before summation defined with (10.8) is applied. On the other hand, in the case of SZSI, (10.10) is added to the signals of (10.9) in order to produce final modulating signals. Irrespectively of the modulator applied, resulting modulating signals in both cases remain now within the range of the carrier signal. However, it can be seen that differences in the generated modulating signals do exist.

The SZSI performs better centering of the resulting modulating signals (envelopes, shown in bold in Fig. 10.8, illustrate the maximum and minimum of all modulating signals). In the case of SZSI, if overmodulation were to take place, clamping would appear simultaneously in two inverter legs. On the other hand, DZSI would enter into overmodulation by clamping only one of the inverter legs. Yet, both methods provide operation in the linear region of modulation in accordance with the limits shown in Fig. 10.2.
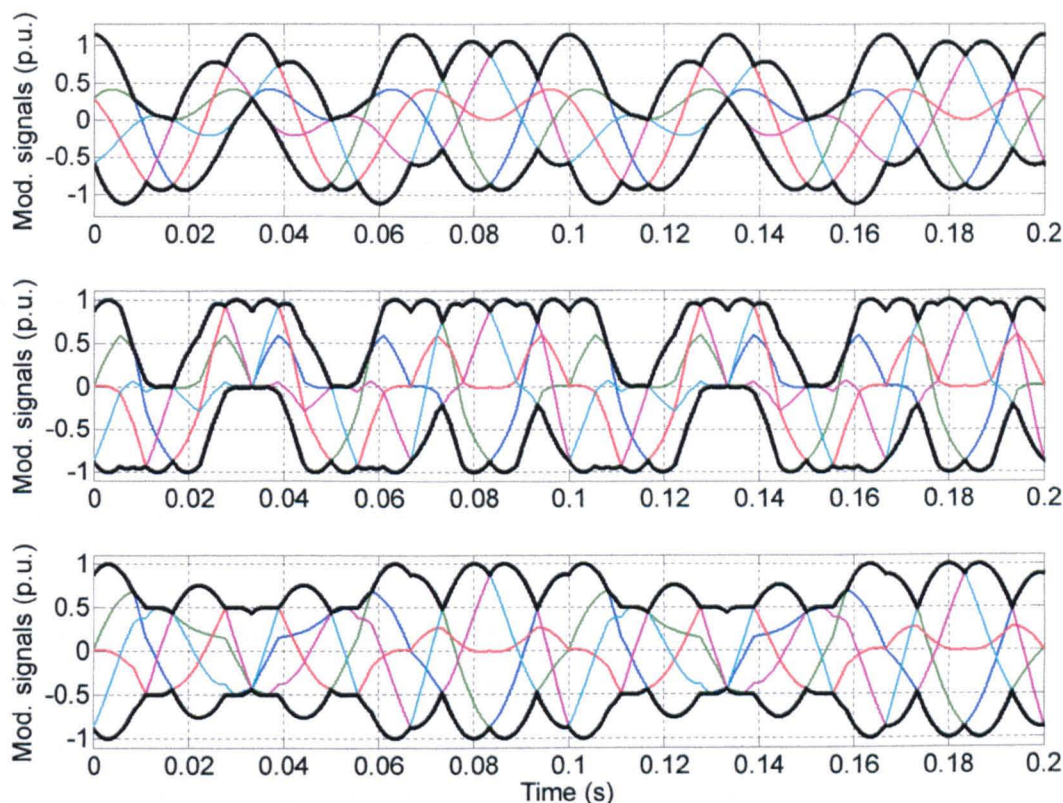
Fig. 10.8: Resulting modulating signals of the five-leg VSI PWM modulators: both DZSI and SZSI when no initial injection takes place (top), DZSI (middle), and SZSI (bottom).

By considering the results given in chapters 7 and 8, regarding the impact of the zero-sequence signal on the output current ripple rms, it is clear that DZSI and SZSI modulators will have different HDF characteristics. Such an analysis is however beyond the scope of the thesis.

The extension of the multi-frequency carrier-based PWM to other multi-leg VSI fed multi-motor drives, with higher number of the legs, is given next.

10.4.2 EXTENSION TO INVERTERS WITH HIGHER LEG NUMBERS

To demonstrate the basic rule for the creation of the resulting modulating signal for other multi-leg VSIs, particular cases of the seven-leg and nine-leg VSI are considered. These two cases are used as examples how reduction from initial $3(n-1)/2$ modulating signals to final n modulating signals can be done, by an extension of the principle (highlighted block in Figs. 10.6 and 10.7) presented for the five-leg case. This time the layout from Fig. 10.1 is used and thus leg A is common for all the machines. Using, for example, the SZSI modulator, resulting modulating signals for the seven-leg VSI fed three-motor drive, before the injection of the zero-sequence signal (10.10), can be obtained as:

$$v_a^* = v_{a_1}^* + v_{a_2}^* + v_{a_3}^*$$

$$v_b^* = v_{b_1}^* + v_{a_2}^* + v_{a_3}^*; \qquad v_c^* = v_{c_1}^* + v_{a_2}^* + v_{a_3}^*$$

$$v_d^* = v_{b_2}^* + v_{a_1}^* + v_{a_3}^*; \qquad v_e^* = v_{c_2}^* + v_{a_1}^* + v_{a_3}^* \qquad (10.11)$$

$$v_f^* = v_{b_3}^* + v_{a_1}^* + v_{a_2}^*; \qquad v_g^* = v_{c_3}^* + v_{a_1}^* + v_{a_2}^*$$

Resulting seven modulating signals are further centred by means of (10.10). Similarly, in the case of a nine-leg VSI fed four-motor drive, one has:

$$v_a^* = v_{a_1}^* + v_{a_2}^* + v_{a_3}^* + v_{a_4}^*$$

$$v_b^* = v_{b_1}^* + v_{a_2}^* + v_{a_3}^* + v_{a_4}^*; \qquad v_c^* = v_{c_1}^* + v_{a_2}^* + v_{a_3}^* + v_{a_4}^*$$

$$v_d^* = v_{b_2}^* + v_{a_1}^* + v_{a_3}^* + v_{a_4}^*; \qquad v_e^* = v_{c_2}^* + v_{a_1}^* + v_{a_3}^* + v_{a_4}^* \qquad (10.12)$$

$$v_f^* = v_{b_3}^* + v_{a_1}^* + v_{a_2}^* + v_{a_4}^*; \qquad v_g^* = v_{c_3}^* + v_{a_1}^* + v_{a_2}^* + v_{a_4}^*$$

$$v_h^* = v_{b_4}^* + v_{a_1}^* + v_{a_2}^* + v_{a_3}^*; \qquad v_i^* = v_{c_4}^* + v_{a_1}^* + v_{a_2}^* + v_{a_3}^*$$

Magnitudes and frequencies of the fundamental reference signals are completely unrelated, except for the requirements imposed for the operation in the linear region of the modulation, as discussed in section 10.3. The approach can be extended further on to any other higher leg numbers and used to reduce initial $3(n-1)/2$ modulating signals to final n modulating signals.

10.5 MULTI-FREQUENCY SPACE VECTOR PWM

As with the series-connected multi-phase multi-motor drives of chapter 9, multi-frequency PWM can be developed using the space vector approach. To demonstrate the development, a five-leg VSI is used again as an example. Extensions to other VSIs with higher leg numbers are addressed briefly later on. Since the principles of the multi-frequency SVPWM for multi-leg VSI rely on the use of the standard three-phase modulator blocks, a synthesis of the three-phase SVPWM is illustrated first. For this purpose, the generalised approach presented in section 5.5 is applied with the aim of verifying the idea of SVPWM which does not require analysis of the voltage space vectors of a three-phase system.

10.5.1 THREE-PHASE SVPWM

Following the guidelines given in section 5.5, a three-phase SVPWM scheme can be developed easily. The common feature of n-phase sinusoidal SVPWM schemes is the need to use $n-1$ active space vectors per switching period. Therefore, in a three-phase system, there are two active space vectors per switching period. In addition two zero space vectors are applied as well.

Based on (5.27), a generic solution for duty cycles of two active space vectors (valid for any sector $s = 1$ to 6) used for the three-phase SVPWM, for sinusoidal output voltage generation, can be written as:

$$\delta_a = KM \sin(s\frac{\pi}{3} - \vartheta); \qquad \delta_b = KM \sin(\vartheta - (s-1)\frac{\pi}{3}) \qquad (10.13)$$

Similar to the development of the SVPWM for other multi-phase VSIs, 'a' and 'b' active space vectors are those that separate the sectors. It can be seen that all active space vectors, used for the SVPWM are of the same magnitude. Trigonometric constant K of (3.13) is now of the value $K = \sin(\pi/3)$.

Under the assumption of the equal distribution of the total zero space vector duty cycle among two zero space vectors one has (based on (5.28)):

$$\delta_0 = \delta_7 = \frac{1}{2}\delta_O = \frac{1}{2}[1 - KM \cos((2s-1)\frac{\pi}{6} - \vartheta)] \qquad (10.14)$$

In the next step, per-leg duty cycles need to be calculated based on the knowledge of the switching pattern in every sector. It is easy to establish based on Fig. 5.18, that switching pattern in all odd sectors is $\bar{v}_0, \bar{v}_a, \bar{v}_b, \bar{v}_7, \bar{v}_b, \bar{v}_a, \bar{v}_0$, while in even sectors it is $\bar{v}_0, \bar{v}_b, \bar{v}_a, \bar{v}_7, \bar{v}_a, \bar{v}_b, \bar{v}_0$. Therefore, per-leg duty cycles are determined based on (5.29) and (5.30) as:

$$\delta_1 = \frac{\delta_O}{2}$$
$$\delta_2^O = \frac{\delta_O}{2} + \delta_b; \qquad \delta_2^E = \frac{\delta_O}{2} + \delta_a \qquad (10.15)$$
$$\delta_3 = \frac{\delta_O}{2} + \delta_a + \delta_b$$

Here, superscripts 'O' and 'E' stand again for odd and even, respectively. Once when per-leg duty cycles are calculated, they need to be distributed properly through all six sectors. This is summarised in Table 10.2.

With this, the feasibility of the developed generalised structure of the multi-phase SVPWM for sinusoidal output voltage generation is demonstrated for a three-phase system. The same type of modulator is used further on for the development of the multi-frequency SVPWM for a five-leg VSI fed two-motor drive.

Table 10.2: Duty cycle disposition through six sectors of the three-phase SVPWM.

Leg | Sector	1	2	3	4	5	6
A	δ_3	δ_2^E	δ_1	δ_1	δ_2^O	δ_3
B	δ_2^O	δ_3	δ_3	δ_2^E	δ_1	δ_1
C	δ_1	δ_1	δ_2^O	δ_3	δ_3	δ_2^E

## 10.5.2 SVPWM FOR A FIVE-LEG VOLTAGE SOURCE INVERTER

The principle of the developed SVPWM for a five-leg VSI is shown in Fig. 10.9. Two separate three-phase space vector modulators (that operate independently) are used to control the machines. The modulation scheme based on the SVPWM is entirely based on manipulation of the placement of zero space vectors within the switching pattern, generated independently by two modulators. References for each machine are the vectors in the corresponding d-q planes with a completely arbitrary mutual position, situated in any of the six sectors in their respective planes. Assuming that both modulators operate in the standard manner where total time of application of zero space vectors is equally shared among zero space vectors $\bar{v}_0$ (000) and $\bar{v}_7$ (111), each reference space vector will be realised on average over the switching period by means of two adjacent active space vectors. The set of equations necessary for implementation has already been given in sub-section 10.5.1. Outputs, generated from each of the three-phase SVPWM modulators, are duty cycles, which are within the range of (0÷1). Thus value of the $\delta = 1$ defines the switching period, and any duty cycle with a value higher than one will lead to clamping of the corresponding inverter leg.

In a similar way as with the carrier-based PWM, a simple summing of the duty cycles generated from each modulator can be used to determine initially the resulting five duty cycles for the five-leg VSI. That is,

$$
\begin{aligned}
\delta_a &= \delta_{a_1} + \delta_{a_2} \\
\delta_b &= \delta_{b_1} + \delta_{a_2} \\
\delta_c &= \delta_{c_1} + \delta_{a_2} \\
\delta_d &= \delta_{b_2} + \delta_{c_1} \\
\delta_e &= \delta_{c_2} + \delta_{c_1}
\end{aligned}
\tag{10.16}
$$

However, due to the placement of the zero space vector (111) in the middle of the switching pattern, generated duty cycles will have values equal to 0.5 when the input reference is zero. After summation defined with (10.16), the resulting duty cycles get shifted into the range (0.5÷1.5), which does not fit with the value of the switching period ($\delta = 1$). Therefore, the value of 0.5 has to be continuously subtracted from the resulting duty cycles, calculated using (10.16).

This is shown in Fig. 10.9, where the described principle of SVPWM for a five-leg VSI supplying a two-motor drive is illustrated. Highlighted block again represents the key feature of the method that allows for the reduction of number of generated duty cycles to the number that equals the number of inverter legs. The principle is almost identical to the one used for carrier-based PWM scheme in section 10.4.
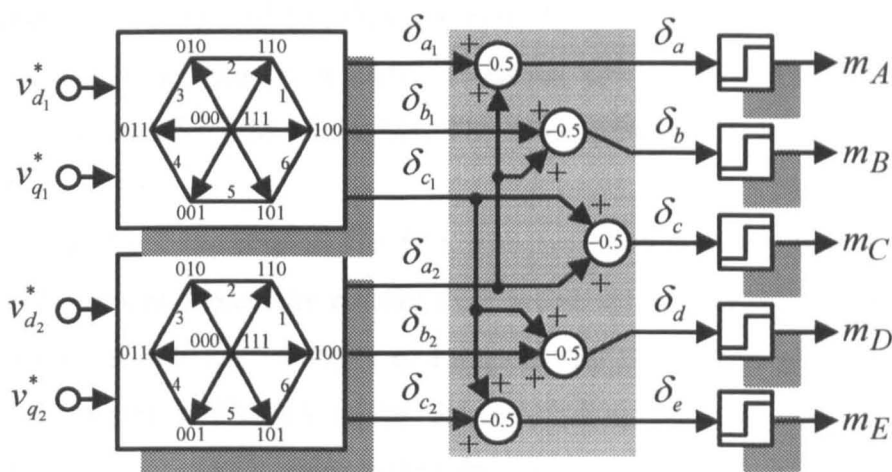
**Fig. 10.9:** Principle of SVPWM for a five-leg VSI.

The net effect of the duty cycle summation is the redistribution of the application times of the zero space vectors. From the first three equations of (10.16) it is visible that the addition of the value of the duty cycle δ_{a_2} increases all three duty cycles, originally generated by the first SV modulator, in the same manner. Thus, the application time of the zero space vector (111) is effectively increased (and the application time of the zero space vector 000 is decreased) without affecting the application times of two active space vectors. The same explanations apply to M2 on the basis of the last three equations of (10.6). Further subtraction of 0.5 will alter this value and provide operation in the linear modulation as along as modulation indices of two machines are within the shaded area of Fig. 10.2.

Also, it can be seen that principle of the SVPWM shown in Fig. 10.9, fully corresponds to the carrier-based DZSI PWM from Fig. 10.6. Both methods inject the zero-sequence signal (10.10) into fundamental sinusoidal signals (SVPWM is the equivalent of TIPWM, as discussed in chapter 6). It is also possible to implement a multi-frequency SVPWM equivalent of the carrier-based SZSI, simply by leaving distribution of the zero space vector duty cycles to be determined after summation with (10.16). Yet, this scheme is not analysed since the only differences compared to the carrier-based SZSI are related to the implementation stage, which favours the carrier-based approach.

An illustration of the modulator operation is shown in Fig. 10.10 (drawn to scale). It applies to the reference space vectors given with $\vec{v}^*_{d_1-q_1} = 0.6\angle 45°$ (for M1) and $\vec{v}^*_{d_2-q_2} = 0.4\angle 100°$ (for M2) (references in sectors 1 and 2, respectively). Sequences and duty cycles of active space vectors are shown in different colour for the easiness of understanding, at first individually for the two machines in Fig. 10.10 (parts a and b). It is visible that, after the application of the SVPWM principle given in Fig. 10.9, these active sequences (and their duty

cycles) stay preserved in the final five duty cycles of the five-leg VSI (Fig. 10.10c). Thus, M1 connected to the inverter legs *A, B* and *C*, receives the voltage in accordance with the requirements set to the SVPWM of the M1. The same applies to the M2, connected to the inverter legs *C, D* and *E.*

It is also visible from Fig. 10.10c that there are instants within the switching period when both machines simultaneously receive their active space vectors (overlapped coloured parts). This contrasts with the SVPWM of Francois and Bouscayrol (1999), Delarue et al (2001), and Delarue et al (2003a) where these switching configurations were forbidden switching states. This is exactly what makes the multi-frequency SVPWM developed here capable of fully utilising the dc bus voltage under all operating conditions. What this means is that all $2^5 = 32$ switching states of a five-leg VSI are utilised and there are no restrictions regarding the use of any of them (in contrast to only 14 states that were used in Francois and Bouscayrol (1999), Delarue et al (2001) and Delarue et al (2003a) or 31 switching state used in Delarue et al (2003b)). The resulting PWM pattern is symmetrical with two commutations per inverter leg and is therefore easy to implement using standard DSP PWM units. A more detailed comparison of the developed multi-frequency SVPWM with the existing solutions is available in Jones et al (2008b).
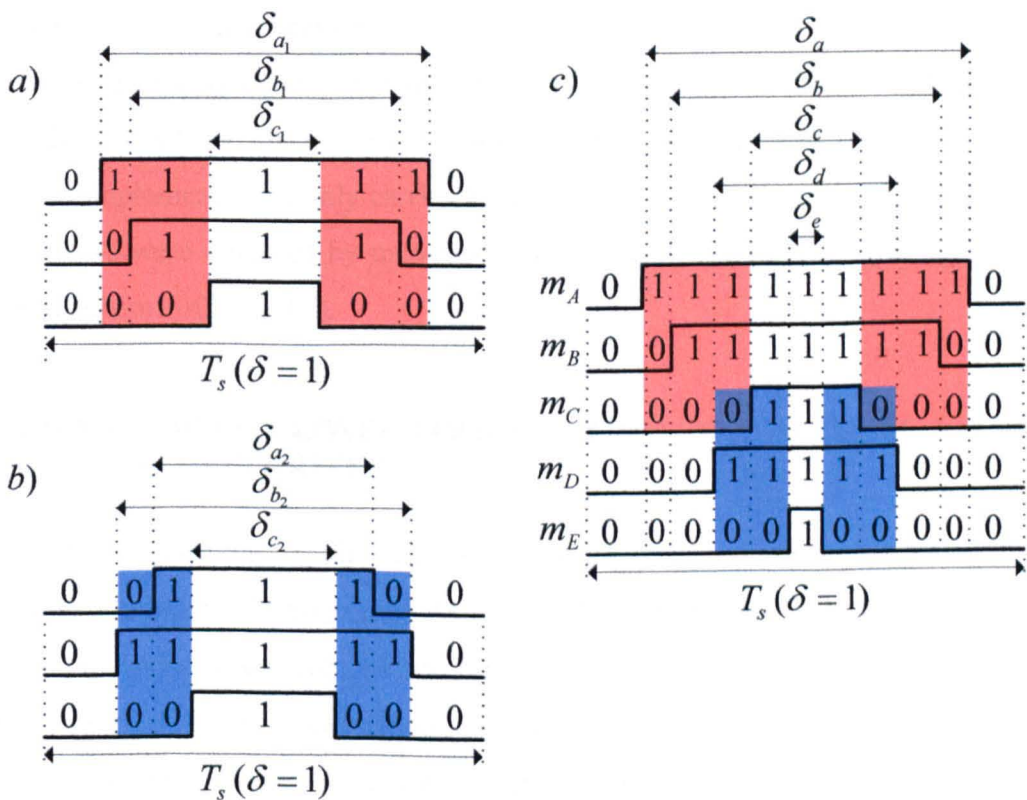
Fig. 10.10: Developed SVPWM: a) SVPWM for M1, b) SVPWM for M2, and c) SVPWM for five-leg VSI fed two-motor drive.

Similar to the carrier-based approach, an extension to the other multi-leg VSI fed multi-motor topologies is possible, based on the layout shown in Fig. 10.9. Thus, for a seven-leg inverter, three three-phase SVPWM need to be used, and summation of the similar type to (10.16) would be executed. In this case the value of 1 should be continuously subtracted to return the duty cycles within the range of (0÷1). Nine-leg inverter requires four three-phase modulators and subtraction of the value of 1.5, after corresponding summation, etc.

10.6 EXPERIMENTAL RESULTS

To verify developed multi-frequency PWM schemes for multi-leg VSI fed multi-motor drives, experiments have been carried out using all possible topologies that can be realised with the custom-built nine-leg inverter. Thus, five-leg VSI fed two-motor, seven-leg VSI fed three-motor and nine-leg VSI fed four motor drives are tested. Open-loop operation, with V/f profiles set independently for each machine, was analysed, as well as the operation in the closed-loop mode with current controllers placed in the rotational reference frame. In this mode the inverter operates in closed-loop current-controlled V/f mode. A pair of synchronous current controllers is used for each machine and the reference frame is synchronised with the reference current frequency. Additionally, behaviour of the five-leg VSI fed two-motor drive was also tested under vector control.

All the necessary control software (except for the vector control) was implemented on TMS320F2812 DSP and data of used machines are available in Appendix B. Due to the simplicity in implementation, only carrier-based PWM was tested and all the results presented in what follows were obtained by means of application of the multi-frequency carrier-based SZSI PWM scheme of Fig. 10.7.

10.6.1 OPEN-LOOP VS. CLOSED-LOOP CONTROL OF MULTI-LEG VSI FED MULTI-MOTOR DRIVES

All three multi-leg topologies, namely five-leg, seven-leg and nine-leg, are tested under similar conditions. Behaviour of these multi-leg VSI fed drives has been investigated at first in open-loop operation with V/f control of three-phase machines and carrier-based SZSI PWM scheme. Dead-time compensation has not been implemented and inverter operates with 3.25 µs blanking time, implemented within IGBTs drivers. The operation under V/f control is sufficient to verify validity of the developed modulation schemes. Only phase currents of the machines are measured, together with their spectra. As shown shortly, it was observed that

during operation of the multi-leg VSI fed drives in open-loop, there are some interactions between machines, visible in the corresponding phase currents and their spectra. This is the reason why current control in the rotational reference frame has also been implemented, and the experiments then repeated under the same conditions as for *V/f* control.

Fig. 10.11 shows phase currents of M1 and M2 of a five-leg VSI fed two-motor drive, for the operation of M1 at $f_1 = 10$ Hz and M2 at $f_2 = 0$ Hz (at standstill). It can be seen from Fig. 10.11a that under *V/f* control machine operates with no-load current of around 1.6 A, and that phase current is slightly distorted. At the same time (Fig. 10.11c) phase current of M2 is present, although it should theoretically be of the zero value. The frequency of the M2 phase current is equal to the frequency of the M1, although of significantly lower value. When current control is applied, situation is significantly improved. The results are shown in Fig. 10.11b for the M1 phase current and in Fig. 10.11d for the M2 phase current.
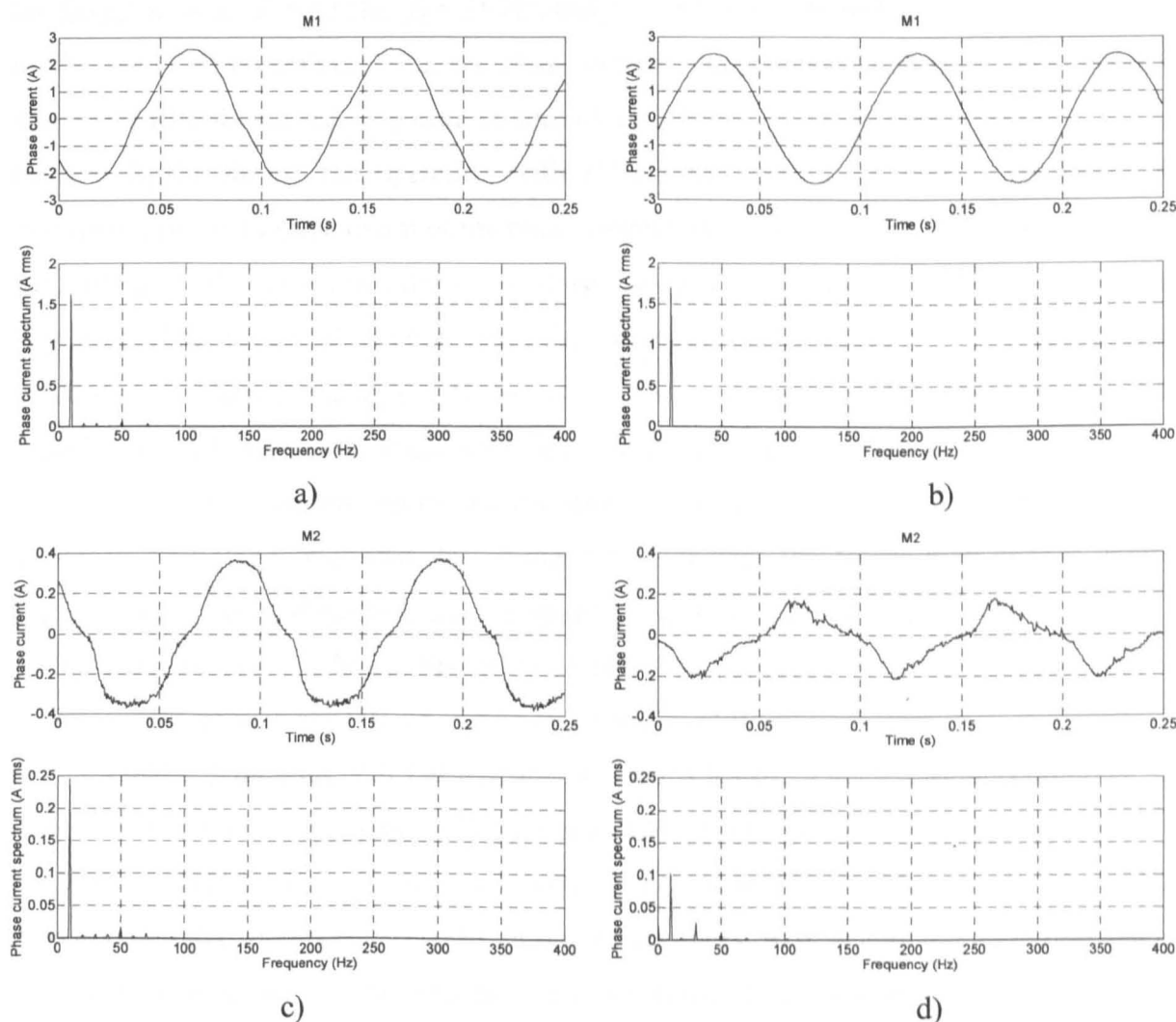
Fig. 10.11: Five-leg VSI fed two-motor drive, experimentally recorded phase currents and their spectra for operation of M1 at 10 Hz and M2 at 0 Hz: M1, open-loop *V/f* (a)) and closed-loop current control (b)); M2, open-loop *V/f* (c)) and closed-loop current control (d)).

It can be seen that the waveform of the M1 phase current is now almost perfectly sinusoidal (current reference is set as 1.6 A), as well as that M2 phase current is suppressed and is of substantially lower magnitude. Further improvements are subject to better tuning of the current regulators, which are, for all the cases illustrated, with the same parameters for all machines. Independent sets of current controller parameters could further improve and eventually suppress even more M2 phase current, but such an objective is beyond the scope of these experiments.

More detailed considerations, regarding the origins of the interactions in open-loop V/f mode, are given in section 10.7. It is important to note that similar current interactions have been observed in the work of Kominami and Fujimoto (2007) for a different nine-switch inverter topology, used also to supply two three-phase motors.

The seven-leg VSI fed three-motor drive is tested next. Induction machines operate at the frequencies of $f_1 = 10$ Hz, $f_2 = 25$ Hz, and $f_3 = 18$ Hz, respectively. The results are shown in Fig. 10.12. The differences in the phase currents, during operation in the open-loop V/f mode and with the closed-loop current control, are clearly visible in both waveforms and the spectra. Again, during the operation with V/f control, significant interactions among the machines exist and deterioration of the phase current waveforms occurs. This is also visible in the spectra. At the same time, due to the lower rating of M3 compared to M1 and M2, phase current is of the lower value. Once when the current control is added, current waveforms are improved, and corresponding spectra are cleaned from the unwanted components. For these experiments, the same value of the reference currents has been set (1.6 A).

In addition, the waveform and the spectrum of the inverter common leg current are shown in Fig. 10.13, recorded during the operation with the closed-loop current control. Current waveform is of multi-frequency appearance, since common leg carriers the current of all three three-phase machines. Spectrum clearly shows all three components, in accordance with the input frequencies (10, 25 and 18 Hz, respectively).

Finally, a nine-leg VSI fed four-motor drive is tested, under the same conditions. The frequency references are set as 10, 25, 20 and 15 Hz, respectively. Only the phase current of the M1 is shown for the operation in open-loop V/f mode (Fig. 10.14a) and the closed-loop current controlled mode (Fig. 10.14b). Improvements are visible in both the waveform and the spectrum. Similar can be observed from the spectrum of the inverter common leg current, shown in Figs. 10.14c and 10.14d, respectively. During the operation with V/f, the spectrum contains all kinds of low frequency components, associated with already mentioned interactions that exist among the machines' phase currents. Yet, when in closed-loop current

controlled mode of operation, current spectrum of the inverter common leg clearly shows only four frequency components, in accordance with the input current references (1.3 A for M3).
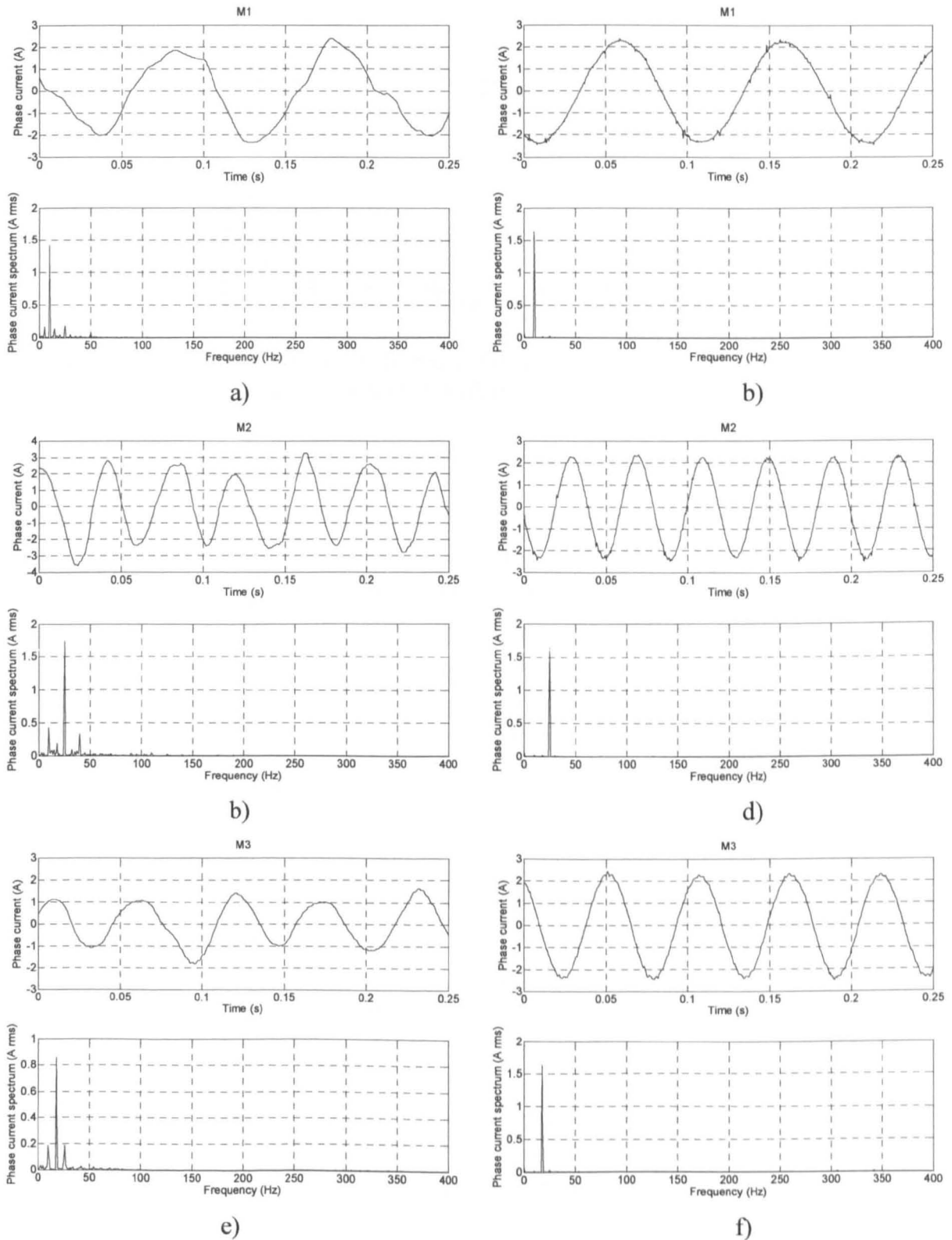
Fig. 10.12: Seven-leg VSI fed three-motor drive, experimentally recorded phase currents and their spectra for operation of M1 at 10 Hz, M2 at 25 Hz and M3 at 18 Hz: M1, open-loop *V/f* (a)) and closed-loop current control (b)); M2, open-loop *V/f* (c)) and closed-loop current control (d)); M3, open-loop *V/f* (e)) and closed-loop current control (f)).
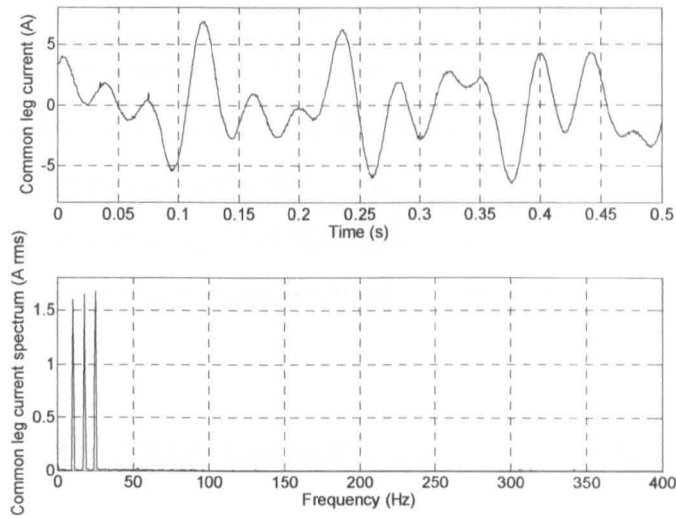
Fig. 10.13: Seven-leg VSI fed three-motor drive: experimentally recorded common leg current and its spectrum with closed-loop current control.

a)

b)

c)

d)
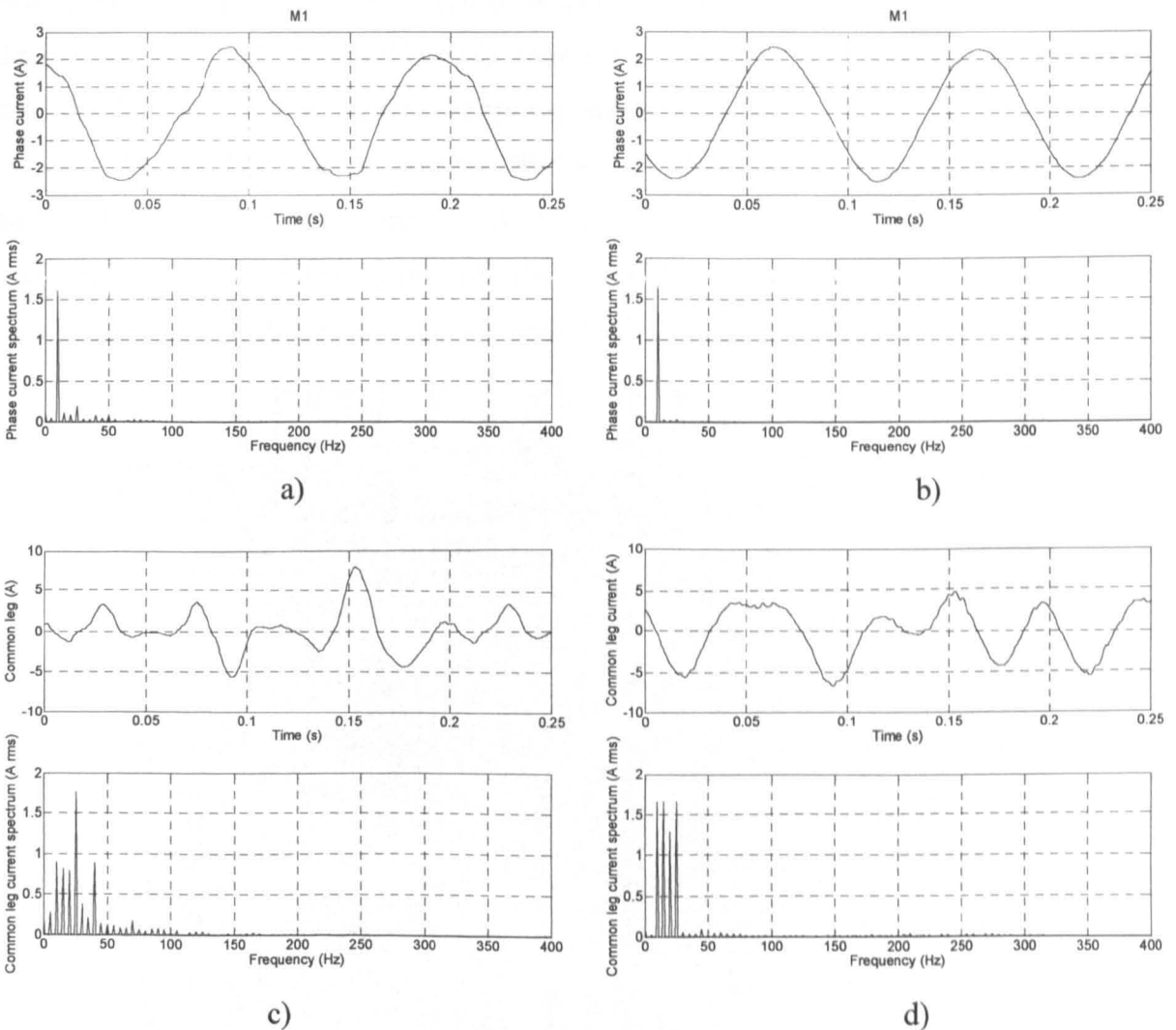
Fig. 10.14: Nine-leg VSI fed four-motor drive, experimentally recorded phase current and its spectrum for operation of M1 at 10 Hz, M2 at 25 Hz, M3 at 20 Hz and M4 at 15 Hz: M1, open-loop *V/f* (a)) and closed-loop current control (b)); common leg current, open-loop V/f (c)) and closed-loop current control (d)).

With this, the viability of the developed multi-frequency PWM for multi-leg VSI fed multi-motor drives is demonstrated. It is shown that the problem of current interactions, observed during operation in the open-loop *V/f* mode, can be alleviated and suppressed by implementation of the closed-loop current control. To further demonstrate, the viability of the developed PWM scheme, a five-leg VSI fed two-motor drive under vector control is tested and some results obtained during transients are shown to illustrate the achieved decoupling of control.

10.6.2 VECTOR CONTROLLED FIVE-LEG VSI FED TWO-MOTOR DRIVE

Experimental results are collected from a vector controlled two-motor drive, consisting of two 2.2 kW, 4-pole, 50 Hz three-phase induction machines (IM1 and IM2, respectively) connected to five legs of a multi-leg inverter, according to the connection diagram in Fig. 10.5. Standard indirect rotor flux oriented control is implemented, together with the developed PWM method. Experimental set-up is illustrated in Fig. 10.15. It consists of two industrial frequency converters DS2000 from MOOG connected to the same dc bus, and TMS320F2407 DSP control board, where the vector control is implemented. All the protection features, offered by the industrial converters, are preserved, and only the control algorithm is now implemented using the additional DSP board, outside the converters.
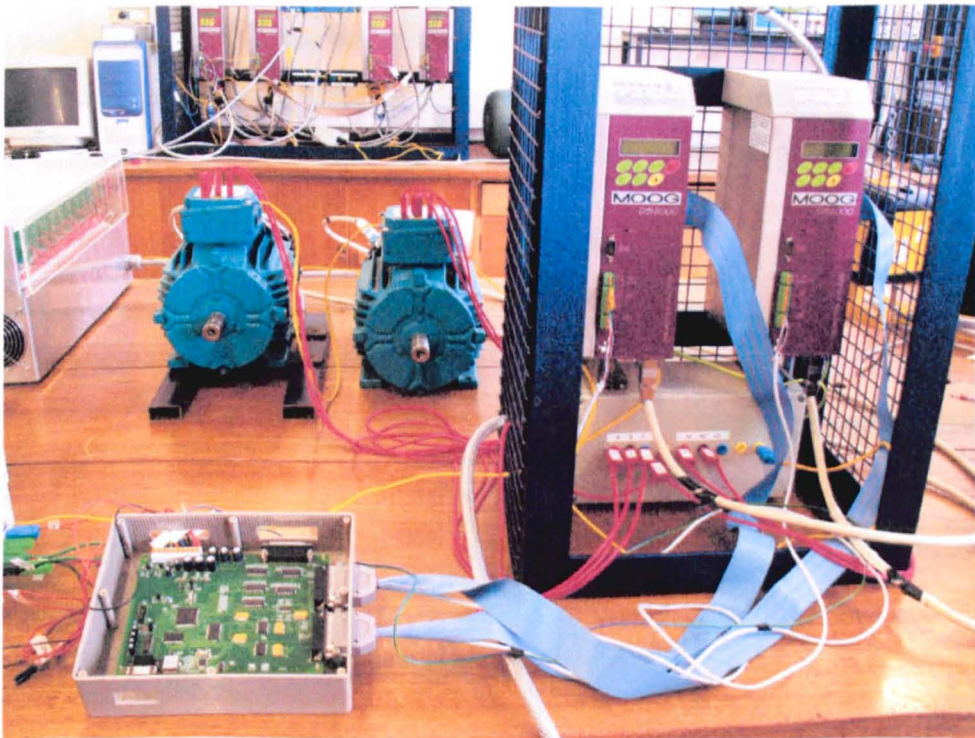
Fig. 10.15: Experimental set-up.

Speed transient of IM1 from standstill up to 1000 rpm is shown in Fig. 10.16a. During transient IM2 operates with constant speed reference of 300 rpm. As can be seen from Fig. 10.16a, IM2 is not affected by the speed transient of IM1 at all. This is also evident from the examination of the *q*-axis current references of the two machines, shown for the same conditions in Fig. 10.16b.

Modulating signals for the first two inverter legs are shown in Fig. 10.17. From here the principle of operation of the developed modulator is clearly visible. Initially, up to the start of the transient for IM1, only IM2 receives the ac voltages since it runs at 300 rpm. This machine is connected to the inverter legs *C, D* and *E*. Therefore, modulating signal of the inverter common leg *C* is the same as modulating signals for the legs *A* and *B*. These signals are identical as long as IM1 is at standstill, which is clearly visible from Fig. 10.17 (up to the instant when acceleration starts). Once when speed command for IM1 is given, these modulating signals become complex function (and in general different from each other) in order to satisfy voltage requirements of both machines. At the same time it can be seen that no overmodulation occurs and the modulating signals stay within the range of the carrier signal (±1). Similar results are shown in Figs. 10.18 and 10.19. This time IM1 reverses from -1000 rpm to 1000 rpm, while IM2 is kept at 400 rpm all the time. Speeds of both machines are shown in Fig. 10.18a, while the corresponding *q*-axis current references are in Fig. 10.18b. Two phase currents of IM1, which correspond to the inverter legs *A* and *B,* are shown in Fig. 10.19. As can be seen from these results, under the vector controlled operation five-leg VSI fed two-motor drive shows very good performance. Completely decoupled control is possible, and proper selections of the controller gains mitigate completely the problems detected during the operation in open-loop *V/f* mode.
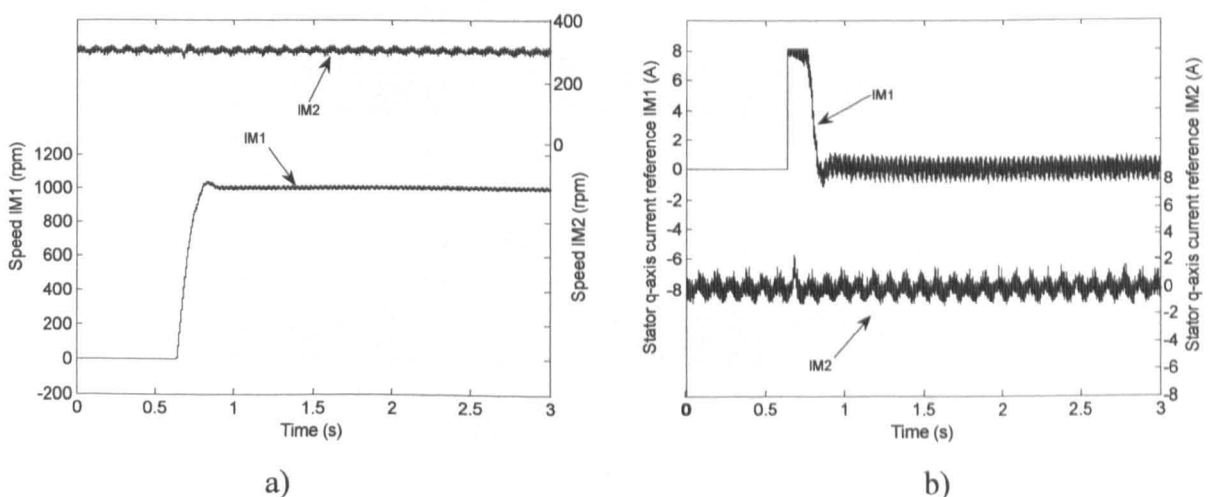
Fig. 10.16: Experimentally recorded acceleration of IM1 from 0 to 1000 rpm with IM2 held at 300 rpm (a)) and stator *q*-axis current references (b)).
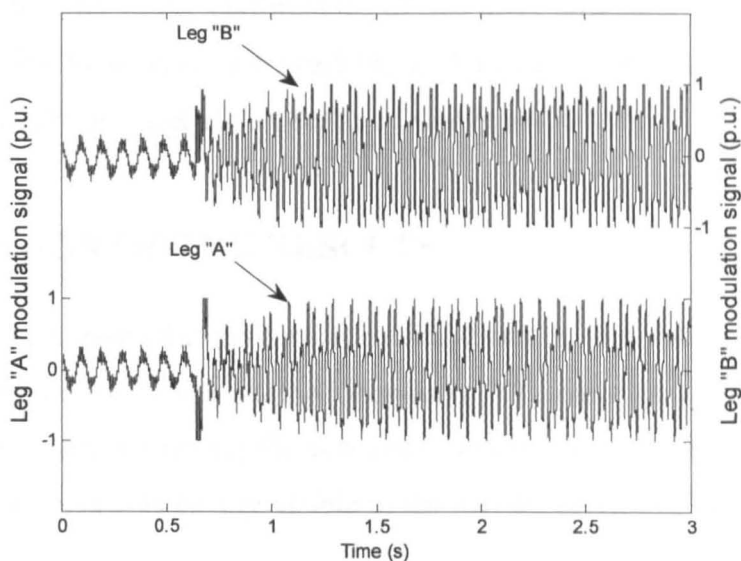
Fig. 10.17: Experimentally recorded modulating signals of inverter legs '*A*' and '*B*'.
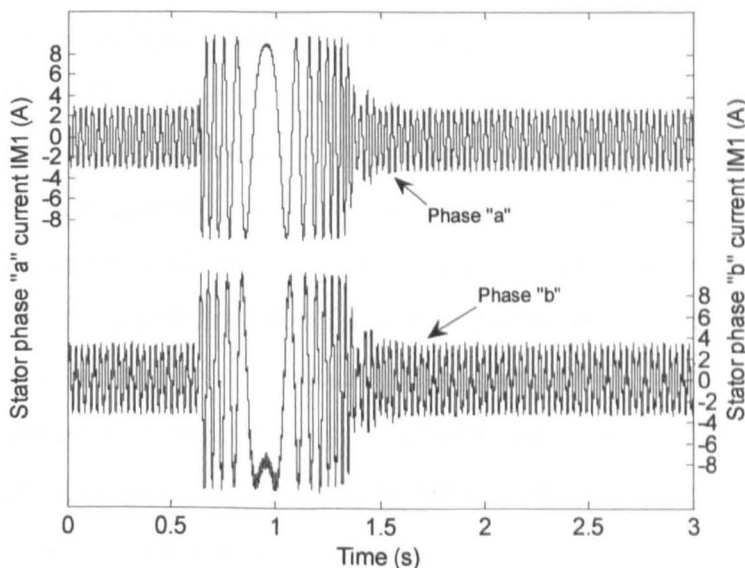

a)

b)
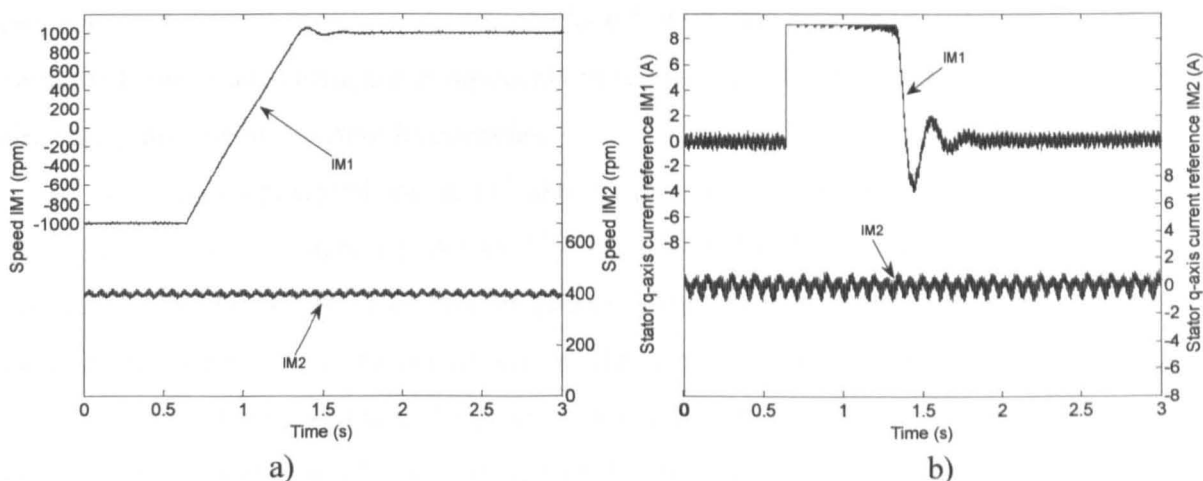
Fig. 10.18: Experimentally recorded reversing transient of IM1 from -1000 to 1000 rpm with IM2 held at 400 rpm (a)) and stator *q*-axis current references (b)).

Fig. 10.19: Experimentally recorded IM1 phase currents '*a*' and '*b*'.

Further details regarding performance of this drive structure, based on the utilisation of the developed PWM scheme, are available in Jones et al (2007a), Jones et al (2008a), Vukosavić et al (2008), Jones et al (2008c) and Dujić et al (2008c).

10.7 DISCUSSION OF THE RESULTS

Based on the presented experimental results, it can be seen that operation of the multi-leg VSI fed multi-motor drives in the open-loop *V/f* control mode suffers from some drawbacks. The interactions among the machines appear and are reflected through parasitic current harmonic components clearly visible in the current spectrum. The reasons for this are two-fold.

The first one is related to the effects caused by the dead-time, which is not compensated during the experiments conducted with the open-loop *V/f* control. Thus, the generated low order harmonic components may circulate through both machines, especially since they operate at different frequencies.

The second potential source is linked to the variations of the IGBT parameters during operation. If one considers the five-leg VSI fed two-motor drive structure shown in Fig. 10.5 and the operation of M1 at certain frequency with M2 at standstill, then it is possible to explain the origin of the current in M2, as the one recorded and shown in Fig. 10.11c, as follows. During the operation of M1, the modulating signals generated for the inverter legs *C*, *D* and *E* are the same. Ideally, this should lead to the same leg voltages of latter three legs of the inverter. In such a situation, there should be no current flowing through M2, connected to those legs. However, at the same time, common inverter leg *C* needs to carry phase current of M1. Therefore there is an in/out current flow through the common leg *C*. As a consequence, voltage drops on the IGBTs in the leg *C* are different than voltage drops in legs *D* and *E*. This introduces an unbalance in the voltages of legs where the M2 is connected (although the same modulating signals are applied), and results in the flow of currents through M2. The frequency of these currents fully corresponds to the current of the common leg (phase current of M1). Yet, the magnitudes of these non flux/torque producing parasitic currents are small.

Thus, these effects are the result of the topology itself, and are not related to the developed PWM schemes. Closed-loop current control with properly determined PI controller gains can alleviate this problem, which has been demonstrated for all three multi-leg topologies investigated experimentally.

10.8 SUMMARY

Development and experimental verification of multi-frequency PWM schemes for a multi-leg VSI fed multi-motor drive is presented in this chapter. Both carrier-based and space vector PWM approaches are addressed and schemes capable of utilisation of all the available switching states of a multi-leg VSI are devised. The principles of the PWM can be easily applied to any n-leg VSI fed $(n\text{-}1)/2$-motor drive. Developed PWM schemes rely on the use of standard three-phase modulators, which offers possibility to use standard building-blocks during implementation of control. Thus, a multitude of three-phase machines can be supplied from the reduced switch-count inverter, which can offer an overall reduction in the cost of a system.

Dc bus voltage, taken as being of the rated value for a single-motor drive, greatly affects the operational range of the multi-leg VSI. Investigation of the voltage limits reveals that any operating point is always defined by the two maximum modulation indices of any two machines. Any multi-leg VSI line voltage is always the function of only two machines, irrespectively of the inverter leg number. Thus, for 50 Hz rated machines, it is possible to simultaneously reach operation at one half of the rated speed for all the machines.

Based on the experimental results presented, the operation of multi-leg VSI fed multi-motor drives in the open-loop V/f mode may not be a preferred choice. Problems caused by the inverter non-linearities can increase the losses, due to the interactions between phase currents of different machines. Closed-loop current control can alleviate these problems, as it was demonstrated experimentally.

Chapter 11

CONCLUSION

11.1 SUMMARY AND CONCLUSIONS

This thesis deals with analysis, development, implementation and experimental verification of various PWM techniques for multi-phase/multi-leg VSI fed single/multi-motor drives. Both carrier-based PWM and SVPWM approaches, restricted to continuous modulation in the linear region, are considered. All these schemes are aimed at sinusoidal output voltage generation, necessary whenever single multi-phase machine with distributed windings (near-sinusoidal mmf distribution) is connected to the multi-phase VSI. In particular, five-phase, seven-phase and nine-phase topologies are used to illustrate theoretical findings which are in general applicable to all multi-phase systems. Output current ripple characteristics, as influenced by the selected modulation method, are also determined. Increased number of degrees of freedom, offered by multi-phase machines, allows for connection of several multi-phase machines into an appropriate series connection and independent control of each of the machines. Development of a suitable PWM scheme for this type of drives is demonstrated, in which case a multi-frequency output voltage is generated by the multi-phase VSI.

A similar kind of multi-frequency output voltage is necessary if, instead of several multi-phase machines, a multitude of three-phase machines is connected, in an appropriate manner, to the multi-leg VSI. In addition, characterisation of multi-leg VSIs is performed regarding the voltage limits.

Based on the literature survey, presented in chapter 2, a lack of systematic analysis and development in the area of PWM methods for multi-phase VSIs is apparent. While multi-phase motor drives have been known for half a century, an increased pace of development is evident during the last ten-fifteen years or so. This is primarily driven by the search for new solutions in some areas where three-phase drives do not represent a satisfactory solution. Thus, for example, in high power applications, where limited power ratings of the currently

available power semiconductors are an obstacle, ability of the multi-phase drives to spread the power through an increased number of phases is an advantage of great potential. Similar applies to the fault tolerant applications (irrespectively of the power level) where multi-phase machines are considered as a viable solution.

Yet, whatever the application where a multi-phase drive will found its place is, an appropriate PWM scheme is a necessary part of the control system. For development of such PWM schemes, properties of multi-phase drives need to be considered carefully, since these are different from the well established industrial three-phase drives. Modelling of the multi-phase VSIs, presented in chapter 3, was based on the general notions that are also applicable to three-phase VSIs. However, space vector representation of an n-phase VSI needs to take into account existence of $(n-1)/2$ 2-D planes, in order to fully describe an n-phase system. An advantage, obtained by using the vector space decomposition, is a clear harmonic mapping into different planes, which is of paramount importance during the synthesis of the SVPWM strategies. This is, on the other hand, closely related to the type of multi-phase machine windings, which has an impact on the treatment of each of the planes, within the modulator. As the number of phases increases, the number of the space vectors increases as 2^n, thus making the analysis more and more complicated, while at the same time offering the flexibility during the selection of the final set of active space vectors.

The multi-phase PWM schemes, analysed in the thesis in conjunction with single-motor drives, are all aimed at multi-phase machines with distributed windings, in which case generation of purely sinusoidal output voltage from the inverter is necessary. To achieve this, output voltage must be synthesised in the first plane (irrespectively of the number of the phases of a system) with simultaneous zeroing of the voltages in all the other planes. This is demonstrated in detail in chapter 4, for a five-phase VSI. It is also shown that simple extension of the three-phase SVPWM (use of only two largest active space vectors per sector) does not produce sinusoidal output voltage. In addition, harmonics that are characteristic of the second plane are generated (primarily the third and the seventh). While this modulation scheme offers a significant increase in the dc bus utilisation (M_{max}=1.2311) compared to the three-phase case (M_{max}=1.1547), it leads to appearance of large harmonic currents if machine is with distributed windings (since these are restricted only by the stator leakage impedance). However, this rather simple PWM scheme is suitable for a multi-phase machines with concentrated windings, where an enhancement in torque production may be achieved by low order stator current harmonic injection.

To avoid these harmonic currents, the number of active space vectors is increased to four and the second plane is included into development of the SVPWM. Five-phase SVPWM, obtained in this way, yields sinusoidal output voltage, yet with lower dc bus utilisation (M_{max}=1.0515). Switching pattern is symmetrical with two commutations per switching period and can be easily implemented using standard DSP PWM units. The same sinusoidal output voltage can be obtained by an alternative selection of four active space vectors per sector, however an uneven number of commutations in inverter legs causes difficulties in the implementation. Therefore only SVPWM based on the use of two medium and two large active space vectors from the first plane of the five-phase system has been experimentally verified.

SVPWM schemes for seven-phase and nine-phase systems, developed in chapter 5, are based on the same principles. In order to produce sinusoidal output voltage, fundamental needs to be synthesised in the first plane with zero reference voltages imposed in all other planes. Similar to the five-phase case, simple extension of the three-phase SVPWM, if applied, generates, in addition to the fundamental, low order harmonics characteristic for other planes. For multi-phase machines with concentrated windings, this approach offers, again, an increase in the dc bus utilisation (M_{max}=1.2518 for a seven-phase VSI, and M_{max}=1.2603 for a nine-phase VSI), with simultaneous torque enhancement. Yet, for machines with distributed windings, dc bus utilisation drops towards the unity value as the number of phases increases and is M_{max}=1.0257 for a seven-phase VSI, and M_{max}=1.0154 for a nine-phase VSI.

All these n-phase SVPWM schemes for sinusoidal output voltage apply n-1 active space vectors over the switching period. Further generalisation is performed based on the appearance of the solutions for duty cycles of applied space vectors, and the appearance of the switching pattern. Thus, a general SVPWM scheme (general with respect to the phase number of the system) is devised, to speed up the implementation, since the tedious analysis of 2^n space vectors of an n-phase system in (n-1)/2 2-D planes can be completely avoided. It is demonstrated also that the three-phase SVPWM is just a special case of this general SVPWM.

Established generalisation is further verified through the analysis of multi-phase carrier-based PWM schemes. It has been shown in chapter 6 that, similar to the three-phase PWM, a full correlation exists between multi-phase SVPWM and multi-phase carrier-based PWM. It has been demonstrated that injection of the zero-sequence signal, based on the offset calculation that uses minimum and maximum of fundamental signals, is actually an equivalent of the SVPWM with equal sharing of the total zero space vector time. The main

differences among carrier-based methods are related to the distribution of the zero space vector duty cycles. All three PWM schemes (SPWM, HIPWM and TIPWM) apply the same set of active space vectors, with equal durations over the switching period (for the given reference), the same as the developed SVPWM scheme. At the same time n-phase carrier-based PWM schemes naturally apply the set of n-1 active space vectors (by means of comparison of n modulating signal with the carrier signal) per switching period (defined by the carrier signal). However, different distributions of the zero space vector duty cycles position these active parts of PWM pulses differently within a switching period. The impact of this is not immediately obvious and requires further analysis.

This is examined in chapter 7, where output current ripple rms of a five-phase VSI is analysed. The method used is termed 'complex approach' and it included an indirect analysis of the current ripple using the notion of the 'harmonic flux'. This eases the analysis, since dependence on the equivalent inductance in each of the planes of a five-phase system is initially avoided. Obtained results clearly demonstrate the negative impact of the second plane on the output current ripple, in synthesis of the sinusoidal output voltage. However, HDF characteristic in the second plane is the same for all three analysed PWM schemes (SPWM, HIPWM and SVPWM), which allows use of only HDFs from the first plane for the comparison of different schemes. In contrast to three-phase PWM schemes, five-phase SPWM yields the best performance of all analysed PWM schemes. It is proved further on that injection of the fifth harmonic cannot optimise output current ripple. Consequently, the injection of all odd multiples of the fifth harmonic (which takes place by the application of the SVPWM) deteriorates even further HDF characteristic. However, the differences are relatively small and may not have a strong impact on the selection of the PWM scheme for five-phase drives. This is so since both HIPWM and SVPWM offer an increase of 5.15 % in dc bus utilisation, compared to the SPWM.

These findings have been further verified following an alternative, more general, method for output current ripple analysis termed 'polygon approach' in chapter 8. By considering the polygon connections of a multi-phase system, the analysis is effectively simplified to the analysis of a current ripple of an H-bridge inverter. However, by properly setting the modulating signals for each of the legs, various polygon connections of multi-phase topologies can be analysed. Compared to the complex approach, results obtained for a particular polygon of a particular multi-phase system reveal only a part of the solution. When solutions for all polygons are superimposed, the complete harmonic distortion factor is obtained, similar to the analysis based on the complex approach and summation of the HDFs

of each plane. With this, the feasibility of the polygon approach for this type of theoretical analysis has been demonstrated, producing at the same time very general results that are easily extendable to other multi-phase topologies. Thus, various solutions regarding the output current ripple analysis, available in the existing literature, are just special cases of the developed general solution.

This concludes the analysis of the basic properties of multi-phase PWM schemes for sinusoidal output voltage generation for single-motor drives. While great similarities and close correlation between carrier-based PWM and SVPWM exist, deeper analysis reveals that mutual relations between different PWM schemes are not the same as for three-phase drives. This is primarily related to the output current ripple rms analysis, where multi-phase SPWM offers the best performances that cannot be further optimised (at least not for the continuous PWM). At the same time, carrier-based PWM schemes are much simpler to implement, as long as DSPs with PWM units that operate on the carrier-based comparison principles are used.

Multi-motor drives supplied from a single multi-phase/multi-leg inverter are further analysed, focusing on the development of appropriate PWM schemes, which are able to generate multi-frequency output voltage. Two different topologies are elaborated, and yet, many similar results are obtained, regardless of the use of machines with completely different number of phases, in considered topologies.

In chapter 9, multi-frequency PWM scheme for series-connected multi-phase multi-motor drives is presented. The phase transposition, introduced in the series connection of two five-phase machines, places the fundamental voltage of each machine into one of the available 2-D planes. Since multi-phase machines considered for this topology are with distributed windings, PWM scheme need to synthesise only these two fundamentals, without any low order harmonic components. The existing method of the SVPWM type for series-connected five-phase two-motor drive led to significant dc bus underutilisation, as well as the necessity to use two switching periods to apply voltage references for both machines. The novel PWM method, developed in the thesis, is able to simultaneously provide voltages for all the multi-phase machines in series connection, using the optimal set of active space vector within a switching period. This set of space vectors, although not known in advance, appears to be the optimal one that leads to symmetrical switching pattern with two commutations per inverter leg. The only restriction, available level of dc bus voltage, has been investigated in detail and a simple analytical method has been devised to determine boundaries of the operation in the linear region. The method is independent of the applied PWM scheme and it

yields natural characteristic of the dc bus utilisation in a multi-phase VSI, as long as multi-frequency output voltage generation (with independent arbitrary references in each of the planes) is of concern. Harmonic injection PWM schemes, suitable for multi-phase machines with concentrated windings, are with different dc bus utilisation characteristic, which is not encompassed by the developed analytical method. Developed multi-frequency PWM schemes (both carrier-based PWM and SVPWM) are experimentally verified, confirming the theoretical developments, and showing excellent performance. The viability of use of the zero-sequence (offset based) signal is also demonstrated for multi-frequency PWM. Centering of the multi-frequency modulating signals is obtained in this way, in a simple manner, in order to achieve maximum possible utilisation of the dc bus voltage.

Finally, replacing the multi-phase machines with an equal number of three-phase machines, and using an alternative connection layout, multi-leg VSI fed multi-motor drives are obtained, which are analysed in chapter 10. Compared to standard independent converter-machine units, savings in the number of necessary inverter legs (power semiconductors) are obtained. Thus, for example, a nine-leg VSI fed four-motor drive could be realised based on three three-phase inverters sharing the same dc bus, with one of the inverter legs common for all four machines, rather than with four independent three-phase inverters. However, operational range is again greatly affected by the level of the available dc bus voltage. The boundaries for the operation in the linear region of modulation are determined, in a similar fashion as for series-connected multi-phase drives. To use fully the available voltage, a simple PWM scheme has been developed, based on the well known principles of the zero-sequence signal injection. With this PWM scheme all the available switching states of a multi-leg VSI are utilised and an arbitrary dc bus voltage allocation (similar to multi-phase multi-motor drives) is achieved. Open-loop *V/f* operation of multi-leg VSI fed multi-motor drives suffers from some drawbacks, related to the inverter non-linearities, which are reflected through interactions among phase currents of different machines. This problem is greatly suppressed by operation in the closed-loop current mode, as experimentally verified in the thesis. It is believed that these drives (for example, a five-leg VSI fed two-motor drive) could find a place in certain types of constant-power applications. One example is a two-motor centre-driven winder, where voltage requirements during operation are rather different. Thus, when one machine operates at high speed the other one is at low speed and vice versa, which is the characteristic well suited to the voltage limit boundaries of the five-leg VSI fed two-motor drive. More detailed considerations of this particular application are beyond the scope of this thesis, since the focus has been here on the PWM schemes.

By comparing the work described in this thesis and the research objectives listed in section 1.3, it can be concluded that all the set goals have been achieved successfully.

11.2 FUTURE WORK

The material presented in this thesis, although characterised by considerable new knowledge, leaves a lot of scope for further research. Since the analysis presented in the thesis has been narrowed to the continuous PWM schemes, operating in the linear region of modulation, there are plenty of ways to continue further on. Some of them are listed here as possible directions for future work:

- Analysis of multi-phase discontinuous PWM schemes.

- Investigation of the operation of the multi-phase PWM in the overmodulation.

- Development of harmonic injection PWM schemes, with controllable injection of the low order harmonics, suitable for multi-phase machines with concentrated windings.

- Investigation of possibilities for output current ripple reduction by means of different space vector selection and organisation within a switching period.

- Detailed characterisation of the switching losses caused by application of various PWM schemes.

- Research on the impact of dead-time in multi-phase single-motor drives and multi-phase/multi-leg VSI fed multi-motor drives.

- Investigation of the dc link harmonics as a function of the phase number and the applied PWM schemes.

- Application of the 'complex approach' to current ripple rms determination for other multi-phase topologies not covered in the thesis.

Chapter 12

REFERENCES

Abbas, M.A., Christen, R., Jahns, T.M., (1984), Six-phase voltage source inverter driven induction motor, *IEEE Trans. on Industry Applications*, vol. IA-20, no. 5, pp. 1251-1259.

Accardo, L., Fioretto, M., Giannini, G., Marino P., (2006), Techniques of PWM space vector modulation for the reduction of magnetic acoustic noise in traction motors, *Proc. Int. Symposium on Power Electronics, Electric Drives, Automation and Motion SPEEDAM,* Taormina, Italy, pp. S2-1-S2-6.

Alger, P.L., Freiburghouse, E.H., Chase, D.D., (1930), Double windings for turbine alternators, *AIEE Trans.*, vol. 49, pp. 226-244.

Andersen, E., Bienek, K., (1981), 6-phase induction motors for current source inverter drives, *Proc. IEEE Industry Applications Society Annual Meeting IAS*, Philadelphia, PA, pp. 607-618.

Apsley, J.M., Williamson, S., Smith, A.C., Barnes, M., (2006), Induction motor performance as a function of phase number, *IEE Proc. - Electric Power Applications*, vol. 153, no. 6, pp. 898-904.

Bakhshai, A.R., Joos, G., Jin, H., (1998), Space vector PWM control of a split-phase induction machine using the vector classification technique, *Proc. IEEE Applied Power Electronics Conf. APEC*, Anaheim, CA, pp. 802-808.

Barnard, J.M., Van Wyk, J.D., Dunford, W.G., (1994), Battery operated wheelchairs using three-phase cage rotor induction machines and PWM inverters, *EPE Journal*, vol. 4, no. 1, pp. 15-19.

Belhadj, J., Belkhodja, I., Fornel, B., Pietrzak-David, M., (2001), DTC strategy for multi-machine multi-inverter industrial system, *Proc. European Power Electronics and Applications Conf. EPE*, Graz, Austria, CD-ROM paper PP01002.

Benatmane, M., McCoy, T., (1998), Development of a 19 MW PWM converter for U.S. Navy surface ships, *Proc. Int. Conf. on Electric Ship ELECSHIP*, Istanbul, Turkey, pp. 109-113.

Blaabjerg, F., Freysson, S., Hansen, H.H., Hansen, S., (1995), Comparison of a space-vector modulation strategy for a three phase standard and component minimized voltage source inverter, *Proc. European Power Electronics and Applications Conf. EPE*, Sevilla, Spain, pp. 1806-1813.

Blasko, V., (1997), Analysis of a hybrid PWM based on modified space-vector and triangle-comparison methods, *IEEE Trans. on Industry Applications*, vol. 33, no. 3, pp. 756-764.

Bojoi, R., Lazzari, M., Profumo, F., Tenconi, A., (2002a), Digital field oriented control for dual three-phase induction motor drives, *Proc. IEEE Industry Applications Society Annual Meeting IAS*, Pittsburgh, PA, CD-ROM paper 22P1.

Bojoi, R., Tenconi, A., Profumo, F., Griva, G., Martinello, D., (2002b), Complete analysis and comparative study of digital modulation techniques for dual three-phase AC motor drives, *Proc. IEEE Power Electronics Specialists Conf. PESC*, Cairns, Australia, CD-ROM paper 10159.

Bojoi, R., Profumo, F., Tenconi, A., (2003), Digital synchronous frame current regulation for dual three-phase induction motor drives, *Proc. IEEE Power Electronics Specialists Conf. PESC*, Acapulco, Mexico, pp. 1475-1480.

Bojoi, R., Farina, F., Profumo, F., Tenconi, A., (2006a), Dual three-phase induction machine drives control - a survey, *IEEJ Trans. on Industry Applications*, vol. 126, no. 4, pp. 420-429.

Bojoi, R., Levi, E., Farina, F., Tenconi, A., Profumo, F., (2006b), Dual-three phase induction motor drive with digital current control in the stationary reference frame, *IEE Proc. – Electric Power Applications*, vol. 153, no. 1, pp.129-139.

Bojoi, R., Tenconi, A., Griva, G., Profumo, F., (2006c), Vector control of dual-three-phase induction-motor drives using two current sensors, *IEEE Trans. on Industry Applications*, vol. 42, no. 5, pp. 1284-1292.

Bouscayrol, A., Pietrzak-David, M., De Fornel, B., (1996), Comparative studies on inverter structures for a mobile robot asynchronous motorisation, *Proc. IEEE Int. Symposium on Industrial Electronics ISIE*, Warsaw, Poland, pp. 15-19.

Bowes, S.R., Clements, R.R., (1982), Computer-aided design of PWM inverter systems, *IEE Proc.*, vol. 129, Pt. B, no. 1, pp. 1-17.

Buja, G., Indri, G., (1975), Improvement of pulse width modulation techniques, *Archiv für Elektrotechnik*, vol. 57, pp. 281-289.

Casadei, D., Serra, G., Tani, A., Zarri, L., (2004), Theoretical and experimental analysis for the RMS current ripple minimization in induction motor drives controlled by SVM technique, *IEEE Trans. on Industrial Electronics*, vol. 51, no. 5, pp. 1056-1065.

Casadei, D., Serra, G., Tani, A., Zarri, L., (2005), Multi-phase inverter modulation strategies based on duty-cycle space vector approach, *Proc. Ship Propulsion and Railway Traction Systems Conf. SPRTS*, Bologna, Italy, pp. 222-229.

Casadei, D., Serra, G., Tani, A., Zarri, L., (2007), General inverter modulation strategy for multi-phase motor drives, *Proc. IEEE Int. Symposium on Industrial Electronic ISIE*, Vigo, Spain, pp. 1131-1137.

Casadei, D., Dujić, D., Levi, E., Serra, G., Tani, A., Zarri, L., (2008), General modulation strategy for seven-phase inverters with independent control of multiple voltage space vectors, *IEEE Trans. on Industrial Electronics*, vol. 55, no. 5, pp. 1921-1932.

Coates, C.E., Platt, D., Gosbell, V.J., (2001), Performance evaluation of a nine-phase synchronous reluctance drive, *Proc. IEEE Industry Applications Society Annual Meeting IAS*, Chicago, IL, pp. 2041-2047.

Correa, M.B.R., Jacobina, C.B., da Silva, C.R., Lima, A.M.N., da Silva, E.R.C., (2003a), Six-phase AC drive system with reduced common-mode voltage, *Proc. IEEE Int. Electrical Machines and Drives Conf. IEMDC*, Madison, WI, pp. 1852-1858.

Correa, M.B.R., Jacobina, C.B., da Silva, C.R., Lima, A.M.N., da Silva, E.R.C., (2003b), Vector modulation for six-phase voltage source inverters, *Proc. European Power Electronics and Applications Conf. EPE*, Toulouse, France, CD-ROM paper 1084.

Correa, M.B.R., Jacobina, C.B., da Silva, C.R., Lima, A.M.N., da Silva, E.R.C., (2003c), Vector and scalar modulation for six-phase voltage source inverters, *Proc. IEEE Power Electronics Specialists Conf. PESC*, Acapulco, Mexico, pp. 562-567.

Corzine, K.A., Sudhoff, S.D., Lewis, E.A., Schmucker, D.H., Youngs, R.A., Hegner, H.J., (1998), Use of multi-level converters in ship propulsion drives, *Proc. All Electric Ship Conf.*, London, UK, pp. 155-163.

Dahono, P.A., Sato, Y., Kataoka, T., (1996), Analysis and minimization of ripple components of input current and voltage of PWM inverters, *IEEE Trans. on Industry Applications*, vol. 32, no. 4, pp. 945-950.

Dahono, P.A., (2006), Analysis and minimization of output current ripple of multiphase PWM inverters, *Proc. IEEE Power Electronics Specialists Conf. PESC*, Jeju, Korea, pp. 3024-3029.

Dahono, P.A., Deni (2006), Analysis and minimization of output current ripple of five-phase PWM inverters, *Proc. Int. Conf. on Electrical Machines ICEM*, Chania, Crete, CD-ROM paper 670.

Delarue, Ph., Bouscayrol, A., Semail, E., Francois, B., (2001), Control method for multileg voltage source inverter, *Proc. European Power Electronics and Applications Conf. EPE*, Graz, Austria, CD-ROM paper 636.

Delarue, Ph., Bouscayrol, A., Francois, B., (2003a), Control implementation of a five-leg voltage-source-inverter supplying two three-phase induction machines, *Proc. IEEE Int. Electric Machines and Drives Conf. IEMDC*, Madison, WI, pp. 1909-1915.

Delarue, Ph., Bouscayrol, A., Semail, E., (2003b), Generic control method of multileg voltage-source-inverter for fast practical implementation, *IEEE Trans. on Power Electronics*, vol. 18, no. 2, pp. 517-526.

Deni, Supriatna, E.G., Dahono, P.A., (2007), Output current ripple analysis of five-phase PWM inverters, *Proc. IEEE Int. Conf. on Power Electronics and Drive Systems PEDS,* Bangkok, Thailand, pp. 1074-1080.

Dente, J., Labrique, F., (1985), Induction motor current-source inverter systems with phase number greater than 3, *Proc. European Power Electronics and Applications Conf. EPE,* Brussels, Belgium, pp. 3.143-3.147.

Dujić, D., (2005), Space vector pulse width modulator for a six phase voltage source inverter, *M.Sc. Thesis,* University of Novi Sad, Novi Sad, Serbia.

Dujić, D., Iqbal, A., Levi, E., Vasić, V., (2006), Analysis of space vector pulse width modulation for a symmetrical six-phase voltage source inverter, *Proc. Int. Power Conversion and Intelligent Motion Conf. PCIM,* Nürnberg, Germany, CD-ROM paper 154_S6b-04_Dujic.

Dujić, D., Iqbal, A., Levi, E., (2007a), A space vector PWM technique for symmetrical six-phase voltage source inverters, *EPE Journal,* vol. 17, no. 1, pp. 24-32.

Dujić, D., Levi, E., Jones, M., Grandi, G., Serra, G., Tani, A., (2007b), Continuous PWM techniques for sinusoidal voltage generation with seven-phase voltage source inverters, *Proc. IEEE Power Electronics Specialists Conference PESC,* Orlando, FL, pp. 47-52.

Dujić, D., Jones, M., Levi, E., (2007c), Continuous carrier based vs. space vector PWM for five phase VSI, *The Int. Conf. on "Computer as a tool" EUROCON,* Warsaw, Poland, pp. 1772-1779.

Dujić, D., Jones, M., Levi, M., (2007d), Space vector PWM for nine-phase VSI with sinusoidal output voltage generation: analysis and implementation, *Proc. IEEE Industrial Electronics Society Annual Meeting IECON,* Taipei, Taiwan, pp. 1524-1529.

Dujić, D., Jones, M., Levi, M., (2007e), A PWM scheme for five-leg VSI supplying two three-phase induction motors with a common inverter leg, *Int. Power Conversion and Intelligent Motion Conf. PCIM,* Nürnberg, Germany, CD-ROM paper: S6d-1.

Dujić, D., Grandi, G., Jones, M., Levi, E., (2008a), A space vector PWM scheme for multifrequency output voltage generation with multiphase voltage source inverters, *IEEE Trans. on Industrial Electronics,* vol. 55, no. 5, pp. 1943-1955.

Dujić, D., Jones, M., Levi, E., (2008b), Features of two multi-motor drive schemes supplied from five-phase/five-leg voltage source inverters, *Proc. Int. Power Conversion and Intelligent Motion Conf. PCIM,* Nürnberg, Germany, CD-ROM paper: S2d-2.

Dujić, D., Jones, M., Levi, E., Vukosavić, S.N., (2008c), A two-motor centre-driven winder drive with a reduced switch count, *Proc. IEEE Industrial Electronic Society Annual Meeting IECON,* Orlando, FL, (in press).

Duran, M.J., Levi, E., (2006), Multi-dimensional approach to multi-phase space vector pulse width modulation, *Proc. IEEE Industrial Electronics Society Annual Meeting IECON*, Paris, France, pp. 2103-2108.

Duran, M.J., Toral, S., Barrero, F., Levi, E., (2007a), Real-time implementation of multi-dimensional five-phase space vector pulse-width modulation," *Electronics Letters*, vol. 43, no. 17, pp. 949-950.

Duran, M.J., Barrero, F., Toral, S., Levi, E., (2007b), Multi-dimensional space vector pulse width modulation scheme for five-phase series connected two-motor drive, *Proc. IEEE Int. Electric Machines and Drives Conf. IEMDC*, Antalya, Turkey, pp. 1208-1214.

Enjeti, P.N., Rahman, A., (1993), A new single-phase to three-phase converter with active input current shaping for low cost ac motor drives, *IEEE Trans. on Industry Applications*, vol. 29, no. 4, pp. 806-813.

Enjeti, P.N., Rahman, A., Jakkli, R., (1993), Economic single-phase to three-phase converter topologies for fixed and variable frequency output, *IEEE Trans. on Power Electronics*, vol. 8, no. 3, pp. 329-335.

Ertugrul, N., Soong, W., Dostal, G. and Saxon, D., (2002), Fault tolerant motor drive system with redundancy for critical applications, *Proc. IEEE Power Electronics Specialists Conf. PESC*, Cairns, Australia, CD-ROM paper 10499.

Ferraris, P., Lazzari, M., (1983), Phase numbers and their related effects on the characteristics of inverter fed induction motor drives, *Proc. IEEE Industry Applications Society Annual Meeting IAS*, Mexico City, Mexico, pp. 494-502.

Francois, B., Bouscayrol, A., (1999), Design and modelling of a five-phase voltage-source inverter for two induction motors, *Proc. European Power Electronics and Applications Conf. EPE*, Lausanne, Switzerland, CD-ROM paper 626.

Fukuda, S., Suzuki, K., (1997), Harmonic evaluation of carrier-based PWM methods using harmonic distortion determining factor, *Proc. Power Conversion Conf. PCC*, Nagaoka, Japan, pp. 259-264.

Gataric, S., (2000), A polyphase Cartesian vector approach to control of polyphase ac machines, *Proc. IEEE Industry Applications Society Annual Meeting IAS*, Rome, Italy, CD-ROM paper 38_02.

Golubev, A.N., Ignatenko, S.V., (2000), Influence of number of stator-winding phases on the noise characteristics of an asynchronous motor, *Russian Electrical Engineering*, vol. 71, pp. 41-46.

Gopakumar, K., Sathiakumar, S., Biswas, S.K., Vithayathil, J., (1984), Modified current source inverter fed induction motor drive with reduced torque pulsations, *IEE Proc., Pt. B*, vol. 131, no. 4, pp. 159-164.

Gopakumar, K., Ranganthan, V.T., Bhat, S.R., (1993a), Split-phase induction motor operation from PWM voltage source inverter, *IEEE Trans. on Industry Applications*, vol. 29, no. 5, pp. 927-932.

Gopakumar. K., Ranganthan, V.T., Bhat, S.R., (1993b), An efficient PWM technique for split phase induction motor operation using dual voltage source inverters, *Proc. IEEE Industry Applications Society Annual Meeting IAS*, Toronto, Canada, pp. 582-587.

Grandi, G., Serra, G., Tani, A., (2006a), General analysis of multi-phase systems based on space vector approach, *Proc. Int. Power Electronics and Motion Control Conference EPE-PEMC*, Portorož, Slovenia, pp. 834-840.

Grandi, G., Serra, G., Tani, A., (2006b), Space vector modulation of a seven-phase voltage source inverter, *Proc. Int. Symposium on Power Electronics, Electric Drives, Automation and Motion SPEEDAM*, Taormina, Italy, CD-ROM paper S8-6.

Grandi, G., Serra, G., Tani, A., (2007a), Space vector modulation of a nine-phase voltage source inverter, *Proc. IEEE Int. Symposium on Industrial Electronic ISIE*, Vigo, Spain, pp. 431-436.

Grandi, G., Serra, G., Tani, A., (2007b), Space vector modulation of nine-phase voltage source inverters based on three-phase decomposition, *Proc. European Power Electronics and Applications Conf. EPE*, Aalborg, Denmark, CD-ROM paper 0286.

Gritter, D., Kalsi, S.S., Henderson, N., (2005), Variable speed electric drive options for electric ships, *Proc. IEEE Electric Ship Technologies Symposium ESTS*, Philadelphia, PA, pp. 347-354.

Hadiouche, D., Razik, H., Rezzoug, A., (2000), Modeling of a double-star induction motor with an arbitrary shift angle between its three phase windings, *Proc. Int. Conf. on Power Electronics and Motion Control PEMC*, Kosice, Slovakia, pp. 5.125-5.130.

Hadiouche, D., Baghli, L., Rezzoug, A., (2006), Space vector PWM techniques for dual three-phase AC machine: Analysis, performance evaluation and DSP implementation, *IEEE Trans. on Industry Applications*, vol. 42, no. 4, pp. 1112-1122.

Hava, A.M., (1998), Carrier based PWM-VSI overmodulation strategies, *PhD thesis*, UW-Madison, WI.

Hava, A.M., Kerkman, R., Lipo, T.A., (1998a), A high performance generalized discontinuous PWM algorithm, *IEEE Trans. on Industry Applications*, vol. 33, no. 5, pp. 1059-1071.

Hava, A.M., Kerkman, R., Lipo, T.A., (1998b), Carrier-based PWM-VSI overmodulation strategies: analysis, comparison, and design, *IEEE Trans. on Power Electronics*, vol. 13, no. 4, pp. 674-689.

Hava, A.M., Kerkman, R., Lipo, T.A., (1999), Simple analytical and graphical methods for carrier-based PWM-VSI drives, *IEEE Trans. on Power Electronics*, vol. 14, no. 1, pp. 49-61.

Hodge, C., Williamson, S., Smith, A.C., (2002), Direct drive marine propulsion motors, *Proc. Int. Conf. on Electrical Machines ICEM*, Bruges, Belgium, CD-ROM paper 087.

Hodge, C., Williamson, S., Smith, A.C., (2004), Marine propulsion direct drive multi phase induction motors, *Proc. Institute of Marine Engineering, Science & Technology - Journal of Marine Design and Operations*, Part B., no. B5, pp 33-37.

Hofmann, W., Zitzelsberger, J., (2006), PWM-Control Methods for common mode voltage minimization – a survey, *Proc. Int. Symposium on Power Electronics, Electric Drives, Automation and Motion SPEEDAM*, Taormina, Italy, CD-ROM paper S8-30.

Holmes, D.G., (1996), The significance of zero space vector placement for carrier-based PWM schemes, *IEEE Trans. on Industry Applications*, vol. 32, no. 5, pp. 1122-1129.

Holmes, D.G., Lipo, T.A., (2003), *Pulse Width Modulation for Power Converters - Principles and Practice*, IEEE Press Series on Power Engineering, Piscataway, NJ.

Hua, L., Yunping, Z., Bi, H. (2006), The vector control strategies for multiphase synchronous motor drive systems, *Proc. IEEE Int. Symposium on Industrial Electronics ISIE*, Montreal, Canada, pp. 2205-2209.

Iqbal, A., (2005), Modelling and control of series-connected five-phase and six-phase two-motor drives, *PhD Thesis*, Liverpool John Moores University, Liverpool, UK.

Iqbal A., Levi, E., (2005), Space vector modulation schemes for a five-phase voltage source inverter, *Proc. European Power Electronics and Applications Conf. EPE*, Dresden, Germany, CD-ROM paper 0006.

Iqbal, A., Vukosavić, S.N., Levi, E., Jones, M., Toliyat, H.A., (2005), Dynamics of a series-connected two-motor five-phase drive system with a single-inverter supply, *Proc. IEEE Industry Applications Society Annual Meeting IAS*, Hong Kong, pp. 1081-1088.

Iqbal A., Levi, E., (2006a), Space vector PWM techniques for sinusoidal output voltage generation with a five-phase voltage source inverter, *Electric Power Components and Systems*, vol. 34, no. 2, pp.119-140.

Iqbal, A., Levi, E., (2006b), Space vector PWM for a five-phase VSI supplying two five-phase series-connected machines, *Proc. Int. Power Electronics and Motion Control Conf. EPE-PEMC*, Portoroz, Slovenia, pp. 222-227.

Iqbal, A., Levi, E., Jones, M., Vukosavić, S.N., (2006a), Generalised sinusoidal PWM with harmonic injection for multi-phase VSIs, *Proc. IEEE Power Electronics Specialists Conf. PESC*, Jeju, Korea, pp. 2871-2877.

Iqbal, A., Levi, L., Jones, M., Vukosavić, S.N., (2006b), A PWM scheme for a five-phase VSI supplying a five-phase two-motor drive, *Proc. IEEE Industrial Electronics Society Annual Meeting IECON*, Paris, France, pp. 2575-2580.

Jacobina, C.B., Oliveira, T.M., Correa, M.B.de.R., Lima, A.M.N., da Silva, E.R.C., (2002), Component minimized drive systems for multi-machine applications, *Proc. IEEE Power Electronics Specialists Conf. PESC*, Cairns, Australia, CD-ROM paper 10028.

Jacobina, C.B., Silva, O.I., dos Santos Jr, E.C., Lima, A.M.N., (2005), Dual AC drives with five-leg converter, *Proc. IEEE Power Electronics Specialists Conf. PESC*, Recife, Brazil, pp. 1800-1806.

Jahns, T.M., (1980), Improved reliability in solid state AC drives by means of multiple independent phase drive units, *IEEE Trans. on Industry Applications.*, vol. 16, no. 3, pp. 321-331.

Jones, M., Levi, E., (2002), A literature survey of state-of-art in multiphase AC drives, *Proc. Universities Power Engineering Conference UPEC*, Stafford, UK, pp. 505-510.

Jones, M., Levi, E., Vukosavić, S.N., Toliyat, H.A., (2003a), Independent vector control of a seven-phase three-motor drive system supplied from a single voltage source inverter, *Proc. IEEE Power Electronics Specialists Conf. PESC*, Acapulco, Mexico, pp. 1865-1870.

Jones, M., Levi, E., Vukosavić, S.N., Toliyat, H.A., (2003b), A novel nine-phase four-motor drive system with completely decoupled dynamic control, *Proc. IEEE Industrial Electronics Society Annual Meeting IECON*, Roanoke, VA, pp. 637-642.

Jones, M., Levi, E., Iqbal, A., (2004a), A five-phase series-connected two-motor drive with current control in the rotating reference frame, *Proc. IEEE Power Electronics Specialists Conf. PESC*, Aachen, Germany, pp. 3278-3284.

Jones, M., Vukosavić, S.N., Levi, E., Iqbal, A., (2004b), A novel six-phase series-connected drive with decoupled dynamic control, *Proc. IEEE Industry Applications Society Annual Meeting IAS*, Seattle, WA, pp. 639-646.

Jones, M., (2005), A novel concept of a multi-phase, multi-motor vector controlled drive system, *PhD Thesis*, Liverpool John Moores University, Liverpool, UK.

Jones, M., Vukosavić,, S.N., Levi, E., Iqbal, A., (2005a), A six-phase series-connected two-motor drive with decoupled dynamic control, *IEEE Trans. on Industry Applications*, vol. 41, no. 4, pp. 1056-1066.

Jones, M., Levi, E., Iqbal, A., (2005b), Vector control of a five-phase series connected two-motor drive using synchronous current controllers, *Electric Power Components and Systems*, vol. 33, no. 4, pp. 411-430.

Jones, M., Levi, E., Vukosavić, S.N., (2006a), A parallel-connected vector-controlled five-phase two-motor drive, *Proc. Int. Conf. on Electrical Machines ICEM*, Chania, Greece, CD-ROM paper PMA2-19.

Jones, M., Levi, E., Vukosavić, S.N., (2006b), Independent control of two five-phase induction machines connected in parallel to a single inverter supply, *Proc. IEEE Industrial Electronics Society Annual Meeting IECON*, Paris, France, pp. 1257-1262.

Jones, M., Dujić, D., Levi, E., Batako, A., Mgaloblishvili, O., (2007a), A novel five-leg PWM technique for two-motor centre-driven winders *Proc. International Electric Machines and Drives Conference IEMDC*, Antalya, Turkey, pp. 254-259.

Jones, M., Dujić, D., Levi, E., (2008a), A PWM method for seven-leg inverters supplying three three-phase motors, *Proc. IEEE Power Electronics Specialists Conf. PESC*, Rhodes, Greece, pp. 2902-2908.

Jones, M., Dujić, D., Levi, E., (2008b), A performance comparison of PWM techniques for five-leg VSIs supplying two-motor drives, *Proc. IEEE Industrial Electronics Society Annual Meeting IECON*, Orlando, FL, (in press).

Jones, M., Vukosavić, S.N., Dujić, D., Levi, E., Wright, P., (2008c), A five-leg inverter PWM technique for reduced switch count two-motor constant power applications, *IET – Electric Power Applications*, vol. 2, no. 5, pp. 275-287.

Kelly, J.W., Strangas, E.G., Miller, J.M., (2003), Multi-phase space vector pulse width modulation, *IEEE Trans. on Energy Conversion*, vol. 18, no. 2, pp. 259-264.

Kianinezhad, R., Nahid, B., Betin, F., Capolino, G.A., (2005), Multi-vector SVM: A new approach to space vector modulation for six-phase induction machines, *Proc. IEEE Industrial Electronics Society Annual Meeting IECON*, Raleigh, NC, pp. 1359-1364.

Kim, G.T., Lipo, T.A., (1996), VSI-PWM rectifier/inverter system with a reduced switch count, *IEEE Trans on Industry Applications*, vol. 32, no. 6, pp. 1331-1337.

Kimura, Y., Hizume, M., Matsuse, K., (2005), Independent vector control of two PM motors with five-leg inverter by expanded two arm modulation, *Proc. European Power Electronics and Applications Conf. EPE*, Dresden, Germany, CD-ROM paper 0345.

King, K.G., (1974), A three phase transistor class-b inverter with sinewave output and high efficiency, *IEE Conf. Publ.*, no. 123, pp. 204-209.

Kolar, J.W., Ertl, H., Zach, F.C., (1989), Calculation of the passive and active components stress of three phase PWM converter system with high pulse rate, *Proc. European Power Electronics and Applications Conf. EPE*, Aachen, Germany, pp. 1303-1311.

Kolar, J.W., Ertl, H., Zach, F.C., (1990a), Minimization of the harmonic RMS contents of the mains current of a PWM converter system based on the solution of an extreme value problem, *Proc. Int. Conf on Harmonics in Power Systems ICHPS*, Budapest, Hungary, pp. 234-243.

Kolar, J.W., Ertl, H., Zach, F.C., (1990b), Analytically closed optimization of the modulation method of a PWM rectifier system with a high pulse rate, *Proc. Int. Power Conversion and Intelligent Motion Conf. PCIM*, Munich, Germany, pp. 209-223.

Kolar, J.W., Ertl, H., Zach, F.C., (1991a), Influence of the modulation method on the conduction and switching losses of a PWM converter system, *IEEE Trans. on Industry Applications*, vol. 27, no. 6, pp. 1063-1075.

Kolar, J.W., Ertl, H., Zach, F.C., (1991b), Minimising the current harmonic RMS value of three-phase PWM converter system by optimal and sub-optimal transition between continuous and discontinuous modulation, *Proc. IEEE Power Electronics Specialists Conf. PESC*, Boston, MA, pp. 372-381.

Kolar, J.W., Wolbank, T.M., Schrödl, M., (1999), Analytical calculation of the RMS currnet stress on the DC link capacitor of voltage DC link PWM converter system, *Proc. Int. Conf. on Electrical Machines and Drives EMD*, Canterbury, UK, pp. 81-89.

Kominami, T., Fujimoto, Y., (2007), A novel nine-switch inverter for independent control of two three-phase loads, *Proc. IEEE Industrial Electronics Society Annual Meeting IECON*, Taipei, Taiwan, pp. 1559-1564.

Ledezma, E., McGrath, B., Munoz, A., Lipo, T.A., (2001), Dual ac-drive system with a reduced switch count, *IEEE Trans. on Industry Applications*, vol. 37, no. 5, pp. 1325-1333.

Lee, B., Fahimi, B., Ehsani, M., (2001), Overview of reduced parts converter topologies for ac motor drives, *Proc. IEEE Power Electronics Specialists Conf. PESC*, Vancouver, Canada, pp. 2019-2024.

Levi, E., Jones, M., Vukosavić, S.N., (2003a), Even-phase multi-motor vector controlled drive with single inverter supply and series connection of stator windings, *IEE Proc. – Electric Power Applications,* vol. 150, no. 4, pp. 580-590.

Levi, E., Jones, M., Vukosavić, S.N., Toliyat, H.A., (2003b), A five-phase two-machine vector controlled induction motor drive supplied from a single inverter, *Proc. European Power Electronics and Applications Conf. EPE,* Toulouse, France, CD-ROM paper 0001.

Levi, E., Jones, M., Vukosavić, S.N., Toliyat, H.A., (2004a), Operating principles of a novel multiphase multimotor vector-controlled drive, *IEEE Trans. on Energy Conversion,* vol. 19, no. 3, pp. 508-517.

Levi, E., Jones, M., Vukosavić, S.N., Toliyat, H.A., (2004b), A novel concept of a multi-phase multi-motor vector controlled drive system supplied from a single voltage source inverter, *IEEE Trans. on Power Electronics,* vol. 19, no. 2, pp. 320-335.

Levi, E., Vukosavić, S.N., Jones, M., (2005), Vector control schemes for series-connected six-phase two-motor drive systems, *IEE Proc. - Electric Power Applications,* vol. 152, no. 2, pp. 226-238.

Levi, E., Jones, M., Vukosavić, S. N., (2006a), A series-connected two-motor six-phase drive with induction and permanent magnet machines, *IEEE Trans. on Energy Conversion,* vol. 21, no. 1, pp. 121-129.

Levi, E., Jones, M., Vukosavić, S.N., Toliyat, H.A, (2006b), Steady state modelling of series-connected five-phase and six-phase two-motor drives, *Proc. IEEE Industry Applications Society Annual Meeting IAS,* Tampa, FL, pp. 415-422.

Levi, E., Jones, M., Vukosavić, S.N., Iqbal, A., Toliyat, H.A., (2007a), Modelling, control and experimental investigation of a five-phase series-connected two-motor drive with single inverter supply, *IEEE Trans. on Industrial Electronics,* vol. 54, no. 3, pp. 1504-1516.

Levi, E., Bojoi, R., Profumo, F., Toliyat, H.A., Williamson, S., (2007b), Multiphase induction motor drives – a technology status review, *IET Electric Power Applications,* vol. 1, no. 4, pp. 489-516.

Levi, E., Dujić, D., Jones, M., Grandi, G., (2008), Analytical determination of DC-bus utilization limits in multi-phase VSI supplied AC drives, *IEEE Trans. on Energy Conversion,* vol. 23, no. 2, pp. 433-443.

Lipo, T.A., (1980), A d-q model for six-phase induction machines, *Proc. Int. Conf. on Electrical Machines ICEM,* Athens, Greece, pp. 860-867.

Locment, F., Semail, E., Kestelyn, X., Bouscayrol, A., (2006), Control of a seven-phase axial flux machine designed for fault operation, *Proc. IEEE Industrial Electronics Society Annual Meeting IECON,* Paris, France, pp. 1101-1107.

Lu, S., Corzine, K., (2005), Multilevel multi-phase propulsion drives, *Proc. IEEE Electric Ship Technologies Symposium ESTS,* Philadelphia, PA, pp. 363-370.

Lyra, R.O.C., Lipo, T.A., (2002), Torque density improvement in a six-phase induction motor with third harmonic current injection, *IEEE Trans. on Industry Applications,* vol. 38, no. 5, pp. 1351-1360.

Matsumoto, Y., Ozaki, S. and Kawamura, A., (2001), A novel vector control of single-inverter multiple-induction motors drives for Shinkansen traction system, *Proc. IEEE Applied Power Electronics Conf. APEC,* Anaheim, CA, pp. 608-614.

McCoy, T., Benatmane, M., (1998), The all-electric warship; an overview of the U.S. Navy's integrated power system development programme, *Proc. Int. Conf. on Electric Ship ELECSHIP,* Istanbul, Turkey, pp. 1-4.

Mohapatra, K.K., Kanchan, R.S., Baiju, M.R., Tekwani, P.N., Gopakumar, K., (2005), Independent field-oriented control of two split-phase induction motors from a single six-phase inverter, *IEEE Trans. on Industrial Electronics,* vol. 52, no. 5, pp. 1372-1382.

Narayanan, G., Ranganathan, V.T., (2005), Analytical evaluation of harmonic distortion in PWM AC drives using the notion of stator flux ripple, *IEEE Trans. on Power Electronics,* vol. 20, no. 2, pp. 466-474.

Nelson, R.H., Krause, P.C., (1974), Induction machine analysis for arbitrary displacement between multiple winding sets, *IEEE Trans. on Power Apparatus and Systems,* vol. PAS-93, no. 3, pp. 841-848.

Nozawa, Y., Oka, K., Omata, R., Matsuse, K., (2006), Performance for position control of two permanent magnet synchronous motors with the five-leg inverter, *Proc. IEEE Industrial Electronics Society Annual Meeting IECON,* Paris, France, pp. 1182-1186.

Ojo, O., Dong, G., (2005), Generalized discontinuous carrier-based PWM modulation scheme for multi-phase converter machine system, *Proc. IEEE Industry Applications Society Annual Meeting IAS,* Hong Kong, CD-ROM paper 38P3.

Ojo, O., Dong, G., Wu, Z., (2006), Pulse-width modulation for five-phase converters based on device turn-on times, *Proc. IEEE Industry Applications Society Annual Meeting IAS,* Tampa, FL, pp. 627-634.

Oka, K., Matsuse, K., (2006), A performance analysis of a four-leg inverter in two ac motor drives with independent control, *IEEJ Trans. on Electrical and Electronic Engineering,* vol. 1, pp. 104-107.

Oka, K., Nozawa, Y., Matsuse, K., (2006), Improved method of voltage utility factor for PWM control method of five-leg inverter, *Proc. IEEE Power Electronics Specialists Conf. PESC,* Jeju, Korea, pp. 531-535.

Oriti, G., Julian, L., Lipo, T.A, (1997a), An inverter/motor drive with common mode voltage elimination, *Proc. IEEE Industry Applications Society Annual Meeting IAS,* New Orleans, LA, pp. 587-592.

Oriti, G., Julian, A.L., Lipo, T.A., (1997b), A new space vector modulation strategy for common mode voltage reduction in PWM invertors, *Proc. IEEE Power Electronics Specialists Conf. PESC,* St Louis, MO, pp. 1541-1546.

Osama, M., Lipo, T.A., (1999), A magnetic relief scheme for four pole induction motors, *Proc. ElectrIMACS,* Lisbon, Portugal, pp. 115-121.

Pavithran, K.N., Parimelalagan, R., Krishnamurthy, M.R., (1988), Studies on inverter-fed five-phase induction motor drive, *IEEE Trans. on Power Electronics,* vol. 3, no. 2, pp. 224-235.

Pena-Eguiluz R., Pietrzak-David, M., Fornel, B., (2001), Observation strategy in a mean control structure for parallel connected dual induction motors in a railway traction drive system, *Proc. European Power Electronics and Applications Conf. EPE,* Graz, Austria, CD-ROM paper PP01016.

Qiang, Y., Kerkman, R.J., Nondahl, T.A., Lu, H., (2005), Analytical investigation of the switching frequency harmonic characteristic for common mode reduction modulator, *Proc. IEEE Industry Applications Society Annual Meeting IAS,* Hong Kong, pp. 1398-1405.

Razik, H., Rezzoug, A., Hadiouche, D., (2005), Modeling and analysis of dual-stator induction motor drives, *IEEJ Trans. on Industry Applications,* vol. 125, no. 12, pp. 1093-1104.

Ryu, H.M., Kim, J.H., Sul, S.K., (2005), Analysis of multi-phase space vector pulse width modulation based on multiple d-q spaces concept, *IEEE Trans. on Power Electronics*, vol. 20, no. 6, pp. 1364-1371.

Silva, P.S.N. de, Fletcher, J.E., Williams, B.W., (2004), Development of space vector modulation strategies for five phase voltage source inverters, *Proc. IEE Power Electronic, Machines and Drives Conf. PEMD*, Edinburgh, UK, pp. 650-655.

Singh, G.K., (2002), Multi-phase induction machine drive research – a survey, *Electric Power Systems Research*, vol. 61, no. 2, pp. 139-147.

Shi, R., Toliyat, H.A., (2002), Vector control of five-phase synchronous reluctance motor with space vector pulse width modulation for minimum switching losses, *Proc. IEEE Applied Power Electronics Conf. APEC*, Dallas, TX, pp. 57-63.

Shibata, M., Hoshi, N., (2007), Novel inverter topologies for two-wheel drive electric vehicles with two permanent magnet synchronous motors, *Proc. European Power Electronics and Applications Conf. EPE*, Aalborg, Denmark, CD-ROM paper 0743.

Steiner. M., Deplazes, R., Stemmler, H., (2000), A new transformerless topology for AC-fed traction vehicles using multi-star induction motors, *EPE Journal*, vol. 10, no. 3-4, pp. 45-53.

Stefanović, V.R., Vukosavić, S.N., (1992), Space vector PWM voltage control with optimised switching sequence, *Proc. IEEE Industry Applications Society Annual Meeting IAS*, Houston, TX, pp. 1025-1033.

Su, G.J., Tang, L., Huang, X., (2006), Control of two permanent magnet machines using a five-leg inverter for automotive applications, *Proc. IEEE Industry Applications Society Annual Meeting IAS*, Tampa, FL, pp. 1606-1612.

Toliyat, H.A., Lipo, T.A., Coleman, J., (1991), Analysis of a concentrated winding induction machine for adjustable speed drive applications - part 1 (Motor analysis), *IEEE Trans. on Energy Conversion*, vol. 6, no. 4, pp. 679-683.

Toliyat, H.A., Xu, L., Lipo, T.A., (1992), A five-phase reluctance motor with high specific torque, *IEEE Trans. on Industry Applications*, vol. 28, no. 3, pp. 659-667.

Toliyat, H.A., Waikar, S.P., Lipo, T.A., (1998), Analysis and simulation of five-phase synchronous reluctance machines including third harmonic of airgap mmf, *IEEE Trans. on Industry Applications*, vol. 34, no. 2, pp. 332-339.

Toliyat, H.A., Shi, R., Xu, H., (2000), A DSP based vector control of five-phase synchronous reluctance motor, *Proc. IEEE Industry Applications Society Annual Meeting IAS*, Rome, Italy, pp. 1759-1765.

van der Broeck, H.W., van Wyk, J.D., (1984), A comparative investigation of three-phase induction machine drive with a component minimized voltage-fed inverter under different control options, *IEEE Trans. on Industry Applications*, vol. 20, no. 1, pp. 309-320.

van der Broeck, H.W., Skudelny, H.C., (1988), Analytical analysis of the harmonic effects of a PWM ac drive, *IEEE Trans. on Power Electronics*, vol. 3, no. 2, pp. 216-223.

van der Broeck, H.W., Skudelny, H.C., Stanke, G.V., (1988), Analysis and realization of a pulsewidth modulator based on voltage space vectors, *IEEE Trans. on Industry Applications*, vol. 24, no. 1, pp. 142-150.

Vukosavić, S.N., Jones, M., Levi, E., Varga, J., (2005), Rotor flux oriented control of a symmetrical six-phase induction machine, *Electric Power Systems Research*, vol. 75, no. 2-3, pp. 142-152.

Vukosavić, S.N., Jones, M., Levi, E., Dujić, D., (2008), An improved PWM method for a five-leg inverter supplying two three-phase motors, *Proc. IEEE International Symposium on Industrial Electronics ISIE*, Cambridge, UK, pp. 160-165.

Wang, Y., Xuhui, W., Xue, S., (2007), Space vector PWM control of multi-phase induction motor drives based on orthogonal vector spaces concept, *Proc. IEEE Power Electronics Specialists Conf. PESC*, Orlando, FL, pp. 553-558

Ward, E.E., Härer, H., (1969), Preliminary investigation of an inverter-fed 5-phase induction motor, *Proc. IEE*, vol. 116, no. 6, pp. 980-984.

Williamson, S., Smith, A.C., (2003), Pulsating torque and losses in multiphase induction machines, *IEEE Trans. on Industry Applications*, vol. 39, no. 4, pp. 986-993.

White, D.C., Woodson, H.H., (1959), *Electromechanical energy conversion*, New York, Willey.

Xu, H., Toliyat, H.A., Petersen, L.J., (2001), Rotor field oriented control of five-phase induction motor with the combined fundamental and third harmonic currents, *Proc. IEEE Applied Power Electronics Conf. APEC*, Anaheim, CA, pp. 392-398.

Xu, L., Fu, W., (2002), Evaluation of third harmonic component effects in five-phase synchronous reluctance motor drives using time-stepping finite-element method, *IEEE Trans. on Industry Applications*, vol. 38, no. 3, pp. 638-644.

Xue, S., Wen, X., (2005), Simulation analysis of two novel multiphase SVPWM strategies, *Proc. IEEE Int. Conf. on Industrial Technology ICIT*, Hong Kong, pp. 1401-1406.

Xue, S., Wen, X., Feng, Z., (2006), A novel multi-dimensional SVPWM strategy of multiphase motor drives, *Proc. Int. Power Electronics and Motion Control Conference EPE-PEMC*, Portoroz, Slovenia, pp. 931-935.

Zhao, Y., Lipo, T.A., (1995), Space vector PWM control of dual three-phase induction machine using vector space decomposition, *IEEE Trans. on Industry Applications*, vol. 31, no. 5, pp. 1100-1109.

Zhang, X.F., Yu, F., Li, H.S., Song, Q.G., (2006), A novel discontinuous space vector PWM control for multiphase inverter, *Proc. Int. Symposium on Power Electronics, Electric Drives, Automation and Motion SPEEDAM*, Taormina, Italy, CD-ROM paper S8-14.

Zhou, K., Wang, D., (2002), Relationship between space-vector modulation and three-phase carrier-based PWM: a comprehensive analysis, *IEEE Trans. on Industrial Electronics*, vol. 49, no. 1, pp. 186-196.

Ziogas, P.D., Photiadis, P.N.D., (1983), An exact input current analysis of ideal static PWM inverters, *IEEE Trans. on Industry Applications*, vol. IA-19, no. 2, pp. 281-295.

Ziogas, P.D., Wiechmann, E.P., Stefanović, V.R., (1985), A computer-aided analysis and design approach for static voltage source inverters, *IEEE Trans. on Industry Applications*, vol. IA-21, no. 5, pp. 1234-1241.

Appendix A

DESCRIPTION OF THE REALISED NINE-PHASE VSI AND ACCOMPANYING TMS320F2812 DSP-BASED CONTROL SYSTEM

A.1 EXPERIMENTAL SET-UP

For the purpose of flexible and efficient experimental verification of the theoretical findings of the thesis, most of the hardware has been custom designed and built. Thus, nine-phase VSI is designed and description of the main electronic circuits is presented here. This includes description of the topology, selection of power semiconductors, their characteristics and ratings, functional connections and user interface. Control system is designed based on commercially available eZDSP development system with TMS320F2812 DSP. An additional electronic daughter-board is designed for the purpose of control of the inverter, which incorporates electronic circuits for various I/O signals, PWM signals, analog-to-digital (ADC) conditioning, encoder signals, CAN and RS232 interface. Communication between DSP control system and nine-phase inverter is established through 5 MBd optical link.

A.1.1 NINE-PHASE VOLTAGE SOURCE INVERTER

Nowadays, the most popular topology of power electronic converters for electric motor drives is realised as two-stage ac/dc - dc/ac converters. In accordance with the power electronics terminology, such a converter consists of a rectifier and an inverter, coupled usually through a dc link. The whole structure is very often termed as a frequency converter, due to the ability to transform fixed input voltage and frequency into arbitrary multi-phase output voltage and frequency. General block-diagram of a frequency converter, with a three-phase diode bridge rectifier at the input stage and nine-phase VSI at the output stage, realised for the purpose of experimental investigation of PWM methods for multi-phase VSIs, is shown in Fig. A.1.
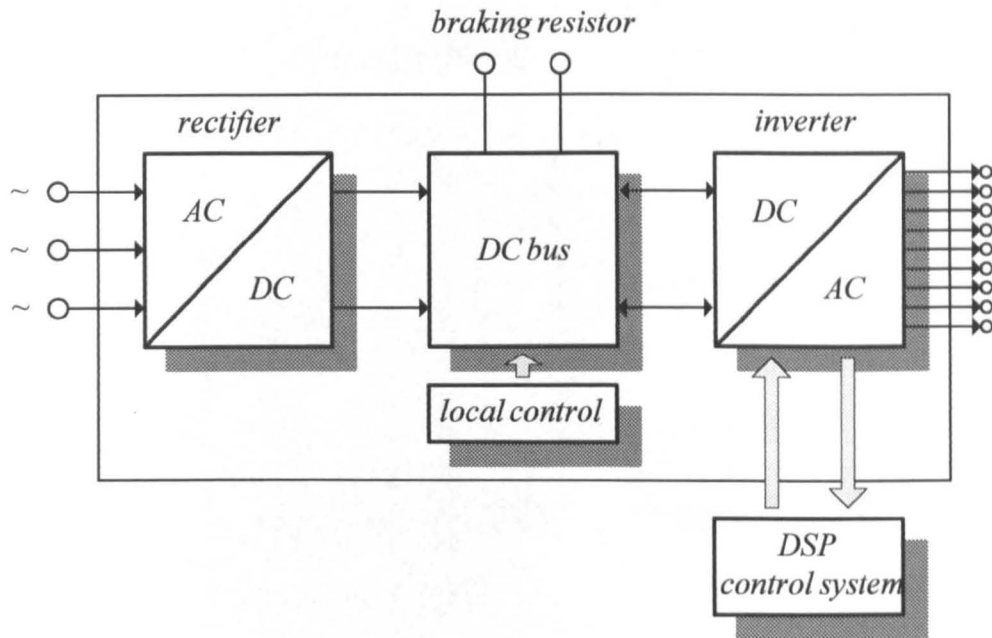
Fig. A.1: Block-diagram of the realised frequency converter.

The whole topology can be divided into three main parts. Input stage consists of the rectifier that converts mains ac voltages into dc voltage. Middle stage stabilises dc bus voltage provided from the rectifier and has some additional functions that will be detailed shortly. Output stage contains the nine-phase inverter that transforms dc voltage into variable ac voltage/frequency by means of a proper PWM control scheme. Relevant control in connection with the first two stages is realised locally, within the converter, by using electronic circuits, while control system for the nine-phase inverter is realised outside the frequency converter and is based on the above mentioned DSP control system. This offers a great flexibility, since the frequency converter is independent of the technologies used for implementation of control algorithms (microcontrollers, DSP, dSPACE,...).

Due to the medium power rating of the frequency converter, the input stage is realised with a three-phase diode rectifier (no provision for the energy flow towards the mains). Used module is SKD51 (Semikron) with switch ratings of 1200 V / 50 A. Obtained dc bus voltage is therefore around 600 V, considering 415 V, 50 Hz three-phase mains.

Although the main purpose of the dc bus is to provide ripple filtering and smoothing of dc voltage obtained from the rectifier, there are also some other electronic circuits, which are necessary for the proper operation of the converter and are related to the dc bus (Fig. A.2). Thus, there are inrush current control circuit, braking chopper with associated control circuit, measurement sensors for the dc bus current and voltage, as well as a dc bus voltage monitoring circuit. These circuits are realised locally within the converter.
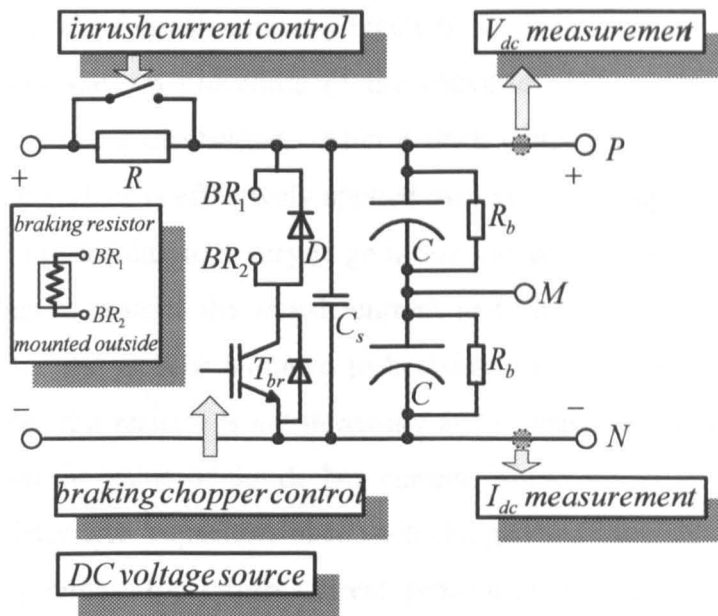
Fig. A.2: Dc bus and other related electronic circuits.

Main parts of the dc bus are two identical filtering capacitors (*C*), connected between points *P* (plus rail of dc bus) and *N* (negative rail of dc bus). Each capacitor is with capacitance of 4700 μF and rated for 400V. They are connected in series, thus creating the equivalent capacitance of 2350 μF, but now with 800V withstanding capability, this being in accordance with the rated value of the dc bus voltage (around 600V). Theoretically, dc bus voltage should be shared equally by two series connected capacitors. However, in practice this is not the case due to the variations of dielectric resistance of each capacitor, although they can be of the same type. Effects are different leakage currents of each capacitor, which leads to unequal dc bus voltage sharing among two series connected capacitors and eventual destruction of one of them if the voltage exceeds rated voltage of the capacitor. To prevent this eventual failure and provide equal dc bus voltage allocation over two capacitors in series connection, balancing resistors (*R_b*) are connected in parallel to each of the capacitors. Ratings of each resistor are 47 kΩ / 10 W. All three characteristic points (*P*, *M* and *N*) of the dc bus are taken out from the converter and provided to user for connection of some other inverter modules to the same dc bus (between *P* and *N*), while point *M* is purely for the purposes of measurements.

Other important parts of the dc bus that are summarised in four shaded boxes in Fig. A.2 are: inrush current protection, braking chopper and its control circuit, dc bus voltage/current measurement circuits and dc voltage source necessary for supply of incorporated electronics inside the converter.

Main purpose of the inrush current protection circuit is to prevent appearance of large inrush current during start-up procedure of the converter. When converter is not in use, capacitors in the dc bus are discharged. After sudden connection to the three-phase mains voltages, rectified dc voltage is effectively applied over very low impedance of the equivalent capacitor in the dc bus, leading to a very large inrush current. To prevent this, resistor (R) is added in the dc bus to restrict the inrush current and slow down the initial charging of capacitors. Ratings of the resistor mounted to heatsink are 460 Ω / 200 W. During normal operation of the converter resistor is not necessary and it causes variable voltage drop in the dc bus depending on the value of the dc bus current. Therefore, relay contacts are used to short circuit the resistor after capacitors have been charged and rated dc bus voltage has been established. Control circuit for inrush current protection is realised internally inside the converter and is activated immediately after providing mains supply to the rectifier. Once capacitors are charged to 95% of the rated dc bus voltage relay contacts are short-circuited and associated light emitting diode (LED) on the front panel will be lit, indicating that the converter is ready for use. Dc bus voltage is constantly monitored and two additional LEDs on the front panel provide indication in the case of under-voltage (UV) and over-voltage (OV).

Braking chopper protects the converter in case of an increase of the dc bus voltage over the value that is considered as the maximum allowed. This increase in the dc bus voltage will typically appear during braking of the machine. Since diode rectifier is used at the front end of the converter, energy coming from the machine cannot be delivered to the mains, thus leading to an increase of the dc bus voltage over the rated value. This can cause destruction of the capacitors in the dc bus if voltage exceeds their rated voltage, and hence total failure of the converter. Role of the braking chopper is to decrease dc bus voltage by dissipating excess energy on the braking resistor. Thus, constant monitoring of the dc bus voltage is necessary for proper operation of the braking chopper. Braking chopper is realised with the module SKM50GAL123D (Semikron) which incorporates insulated gate bipolar transistor (IGBT) (T_{br}) and freewheeling diode (D) parallel to the load. Load is braking resistor, which has to be mounted outside the converter between points BR_1 and BR_2. Braking chopper module is rated at 1200 V / 50 A. Control circuit, used for control of braking chopper and realised internally inside the converter, is based on the use of a hysteresis comparator with high and low threshold values determined in accordance with the values of the dc bus voltage when braking starts and stops, respectively. Internal control of braking chopper contains dc bus voltage sensing circuit, hysteresis comparator circuit with adjustable thresholds and IGBT driver

circuit IR2117 (International Rectifier), which controls braking transistor T_{br}. Incorporated LED on the front panel of the converter will lit whenever braking transistor is in the 'on' state. This means that as long as the braking chopper is active, associated LED will flash in the rhythm of discharge/charge of the dc bus. It is important to note that lower hysteresis threshold should be adjusted to be of a higher value than the rated dc bus voltage; otherwise braking chopper will short-circuit rectifier output, which effectively means short-circuit of the mains.

Measurement of the dc bus voltage, in order to provide information to the control system, is realised with closed loop voltage transducer LV25-P (LEM). In essence, voltage transducer is composed of a current transducer assembly and external primary resistance. Total value of the external resistance of 60 kΩ (3 x 20 kΩ / 7 W) defines rated input current of 10 mA for rated 600V DC bus voltage. Under these conditions rated output current equals 25 mA. By connecting an additional sensing resistor at the output of the sensor, output current is transformed into voltage and can be used for control purposes. Sensing resistor is not mounted in electronic board inside the converter, thus current signal is transferred all the way to the control system, where it is transformed into voltage and sampled with ADC circuit of the control system.

Although dc supply voltages for electronic circuits inside the converter are usually realised by means of switching mode power supply converters, a simpler solution is implemented here. Two transformers are used to step down ac voltage from the mains, which is rectified and further stabilised and regulated with linear voltage regulators. Thus, low dc voltages are provided to all necessary parts of the converter. These include voltage levels of ±15 V for current/voltage transducer circuits, 15 V for inrush current control circuit and braking chopper circuit, 15 V for IGBT drivers, and additional ±5 V.

Finally, the output stage of the converter is the nine-phase VSI. Fig. A.3 shows detailed layout of the important electronic circuits for one of the inverter legs. The same applies to all nine inverter legs. Each leg is realised using half-bridge IGBT module SKM50GB123D (Semikron) (shown inside dashed box) that is with ratings of 1200 V / 50 A. All nine IGBT modules are mounted on the same heatsink and connected between P and N rails of the dc bus. Decoupling capacitor C_s (0.68 μF / 1000 V) is mounted directly on each module. Its role is to protect each module against voltage spikes during commutation. This solution is found to be sufficient for protection of the modules, considering medium power rating of the converter. Hence there is no need to use more advanced snubber circuits.
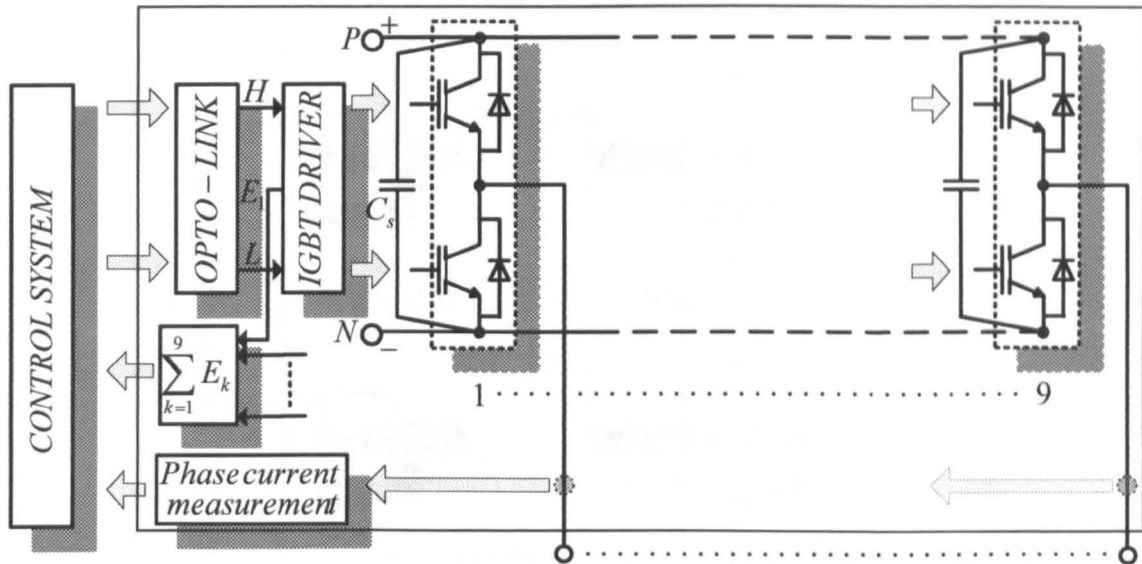
Fig. A.3: Inverter modules and associated electronic circuits.

Each IGBT module is controlled with PWM signals coming from the control system through the optical link to the half-bridge IGBT driver SKHI22-AH4 (Semikron), connected to each module. Drivers are mounted directly above IGBT modules, thus allowing the shortest possible wiring. All electronic circuits for driving, voltage supply, error monitoring, dead-time control, short pulse suppression, pulse shaping and galvanic isolations are integrated in the drivers. Only a few external components are required in between drivers and modules for proper operation. Dead-time of 3.25 μs is implemented inside the driver and therefore complementary PWM signals can be brought all the way to the input of each driver. Dedicated error circuit of drivers is triggered by under-voltage or short-circuit of the IGBTs. On appearance of any fault, power driver will turn 'off' IGBTs providing at the same time error signal at the output of the driver. Error signal, generated by any of the IGBT drivers, is fed back to the control system, also through the optical link.

Output currents of each phase of the inverter are measured with current transducer LA55 (LEM), and low power current signal is provided to the control system where it is transformed into an equivalent voltage signal for ADC circuits.

PWM signals from the control system are transferred to the converter through the fiber optical link realised with the use of transmitter/receiver components from HFBR-0501 series (Agilent Technologies). Link consists of HFBR-1521 transmitter and HFBR-2521 receiver optimised for use with 1 mm diameter plastic optical fiber cable. Selected components offer 5 MBd high performance fiber optical link. Principal layout is shown in Fig. A.4. For each leg of the inverter there are 2 receiver/transmitter pairs of component. An additional line is provided for the common error signal generated in the case of an error on any of the drivers.
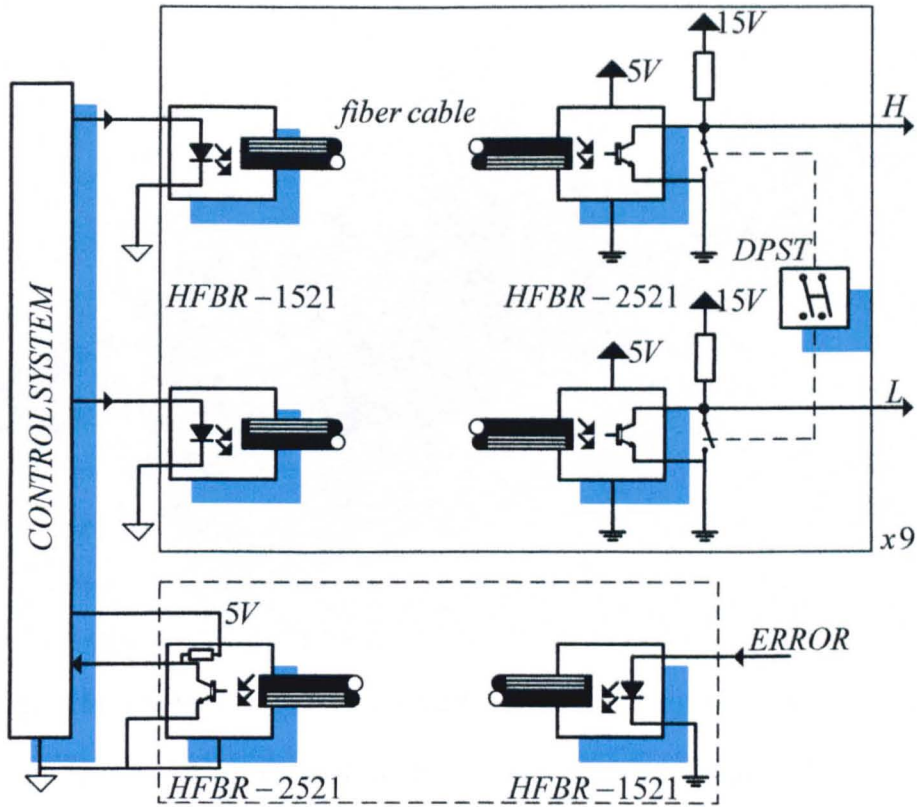
Fig. A.4: Optical fiber link layout.

In addition, PWM signals at the input of each driver can be also forced to low level with double-pole single-throw (DPST) switches provided outside the converter for each leg. This safety feature allows that unused legs of the inverter can be turned 'off' during operation.

Realised frequency converter is shown in Figs. A.5 and A.6.
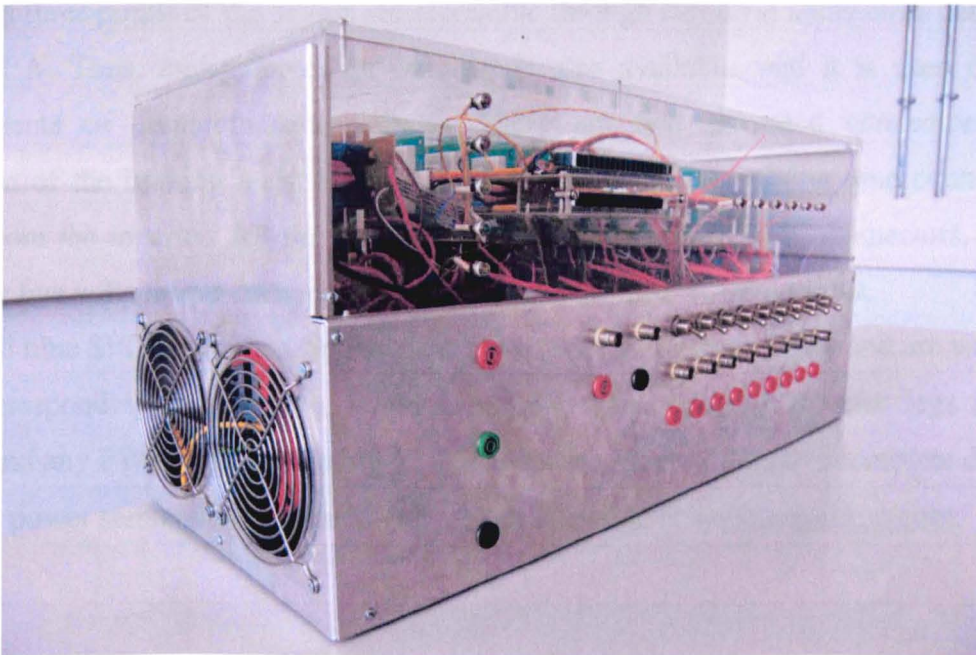
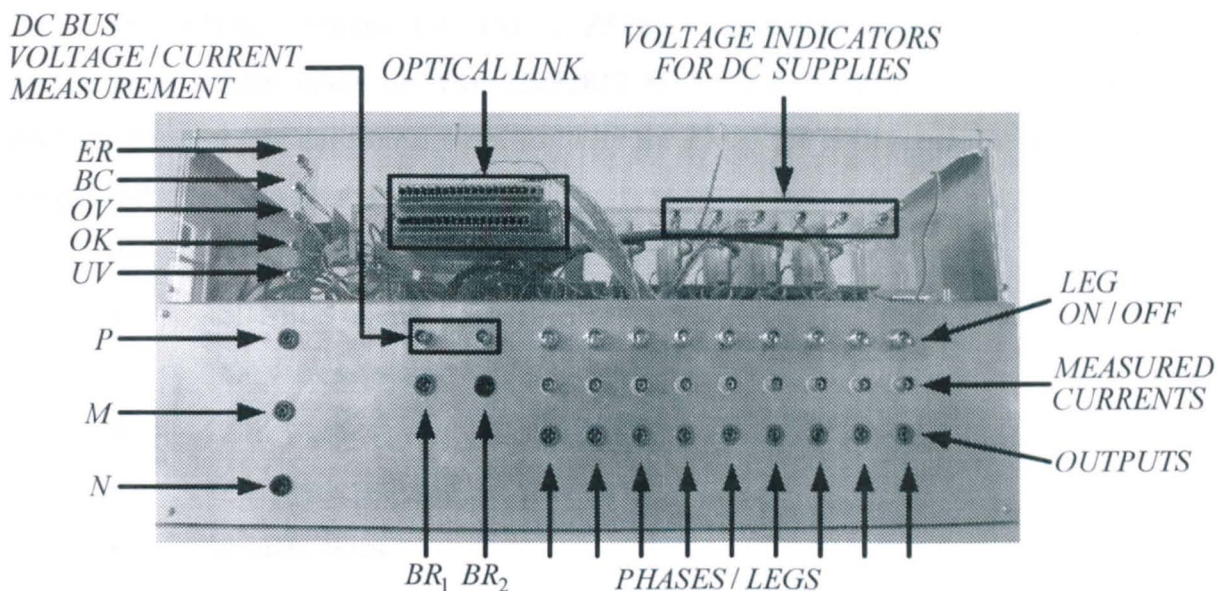**Fig. A.5:** Realised frequency converter with nine-phase VSI at the output.
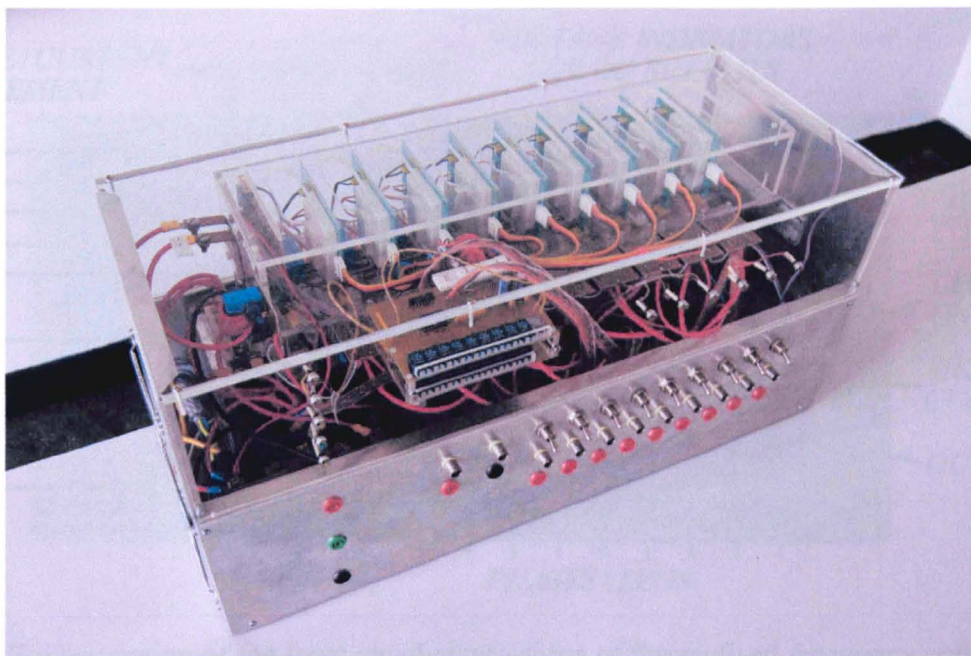
Fig. A.6: Realised frequency converter with nine-phase VSI at the output.

A more detailed description of the front panel is given in Fig. A.7. The LEDs, located in the upper left part of the front panel, are used for indication of under-voltage (*UV*), over-voltage (*OV*), dc bus charged (*OK*), braking in progress (*BC*) and presence of the error signal coming from drivers (*ER*). The other set of LEDs, located in the upper right part of the front panel, indicates the presence of the dc voltages from the associated dc supplies within the inverter. Finally, in the upper middle part, connectors for the optical cables of the optical link are located.

All three points of the dc bus are accessible through shrouded connectors denoted with *P*, *M* and *N*. Thus, mid-point of dc bus (*M*) is also available, and it is used during the measurements of common-mode voltage. There are two shrouded connectors for the connection of the braking resistor (*BR$_1$* and *BR$_2$*), while the remaining nine connectors are outputs from the inverter. All the measurement outputs are with BNC connectors, and these include dc bus voltage and current measurement, and all nine phase currents.

All nine SPDT switches, on the front panel, operate independently and are used to shut down corresponding inverter leg, when necessary. Thus, unused inverter legs are easily blocked and any PWM signals coming to these legs are ignored. Finally, complete data sheets for all the power semiconductor modules used are available at www.semikron.com.

Fig. A.7: Description of the front panel connections of the realised frequency converter.

A.1.2 TMS320F2812 DSP-BASED CONTROL SYSTEM

For the purpose of flexible implementation of different control algorithms, additional electronic daughter-board is designed for the commercially available eZDSP development system based on TMS320F2812 DSP. Main features, characteristic for whole C2000 series of these processors from Texas Instruments that are optimised for motor control purposes, can be summarised as:

- High-performance static CMOS technology
- JTAG boundary scan support
- High-performance 32-Bit fixed-point CPU
- On-chip memory
- Boot ROM
- External interface and external interrupts
- Motor control peripherals
- Serial port peripherals: SPI, SCI, eCAN, McBSP
- 12-bit ADC
- Up to 56 general purpose I/O lines
- Two dedicated event managers

A more detailed summary of features of the TMS320F2812 chip can be found at www.ti.com.

The eZDSP system kit TMDSEZS2812 (Spectrum Digital) is a stand-alone development system based on TMS320F2812 DSP from Texas Instruments. It represents platform necessary to develop and run software for TMS320F2812 processor. Key features of the eZDSP kit can be summarised as:

- TMS320F2812 digital signal processor
- 150 MIPS operating speed
- 18K words on-chip RAM
- 128K words on-chip Flash memory
- 64K words off-chip SRAM memory
- 30 MHz clock
- 2 expansion connectors (analog, I/O)
- On board IEEE 1149.1 JTAG controller
- 5-volt only operation with supplied AC adapter
- TI F28xx 'Code Composer Studio' tools driver
- On board IEEE 1149.1 JTAG emulation connector

Detailed description and complete schematics can be found at www.ti.com. To allow further connection and distributions of signals coming from and to eZDSP board, additional electronic daughter-board is designed and adapted for easy connection to the existing expansion connector of the eZDSP board.

Principal layout of the daughter-board with main electronic circuits is shown in Fig. A.8. The board incorporates necessary electronics and driver circuits in order to provide correct signal levels coming out of and to the DSP. Since all DSP pins are 3.3V (not 5V tolerant), proper buffering and voltage level manipulations are implemented in order to prevent destruction of the DSP chip. Daughter-board requires bipolar supply voltage in the range $\pm(10...15)$V, which is on-board stabilised to ±5 V necessary for electronic circuits.
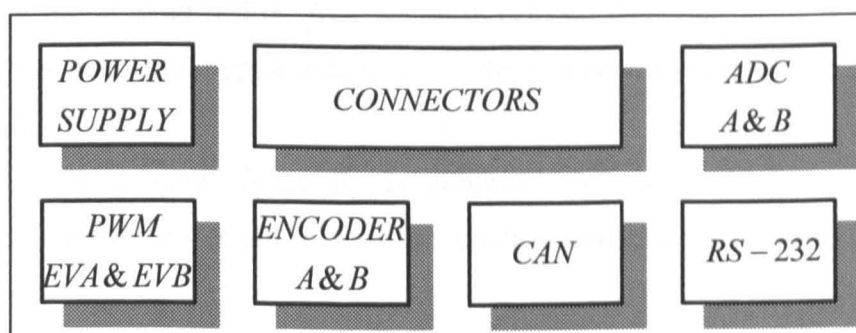
Fig. A.8: Layout of the eZDSP daughter-board.

There are two event-managers (EVA & EVB) on TMS320F2812 chip that include general purpose (GP) timers, full-compare/PWM units, capture units and quadrature-encoder pulse (QEP) circuits. Each event-manager has two GP timers and is responsible for control of eight PWM output pins. Thus, there are GP timers 1 and 2 for EVA and GP timers 3 and 4 for EVB. Out of the eight PWM pins per event-managers, three pairs of PWM pins (PWM1-6 for EVA and PWM7-12 for EVB) are aimed for control of standard three-phase VSI, thus having option to control dead-time through DSP associate registers. Therefore, signals coming from these pins are just buffered with fast-TTL circuit which is CMOS compatible at the input (3.3V) and has standard TLL outputs (5V). Additional two PWM output pins per event-manager (T1PWM, T2PWM for EVA and T3PWM, T4PWM for EVB) are single pin outputs. Therefore signals coming from these pins are separated through fast-TTL buffer/inverter circuit to obtain complementary pair of PWM signals. There is not any option to implement dead-time control into these signals and that is left to be done externally with the use of IGBT drivers (in this case SKHI22 AH4). These signals are transferred to the inverter through optical link.

Among others, remaining parts of daughter-board incorporate a circuit for conditioning of the signals coming from the voltage/current transducers from the inverter. All 16 channels are made available to the user for bringing the bipolar signals, which are expected to be in the range of ±1.5 V. In addition, the first three inputs of each connector (A0-A2 and B0-B1) can be modified, by proper jumper settings, to receive signals in the range 0-3V.

There is support for connection of two incremental encoders, Controller Area Network (CAN) protocol as well as for RS-232 communication. All the remaining (unused) pins from the eZDSP board are brought out from the daughter-board to the additional set of connectors, and can be used if necessary.

Dc voltages provided as a supply to the daughter-board can supply the eZDSP board at the same time, or the supply provided with the eZDSP system kit can be used. All the above mentioned parts are marked in Fig. A.9, where developed daughter-board is shown without eZDSP board attached. Final appearance of the system, once when two boards are attached, is shown in Fig. A.10.

In this way, a great flexibility is achieved, which allowed for fast and easy reconfiguration of the experimental set-up in accordance with the objectives of the thesis.
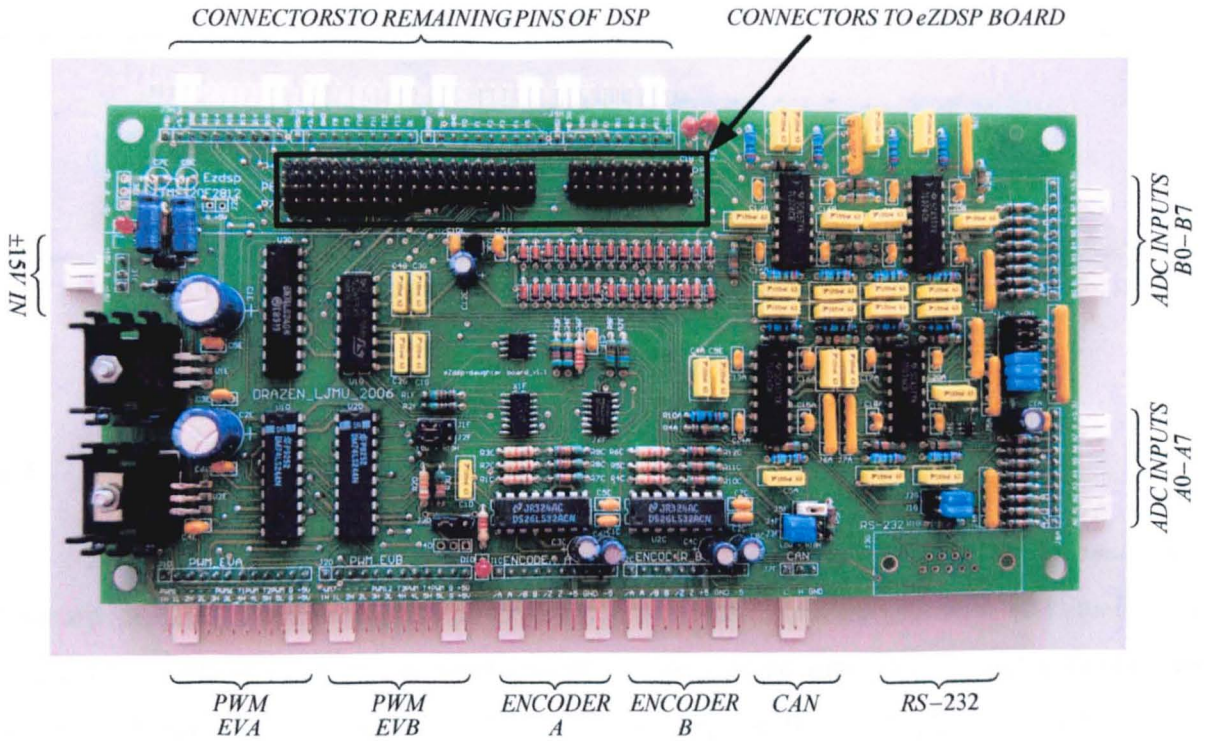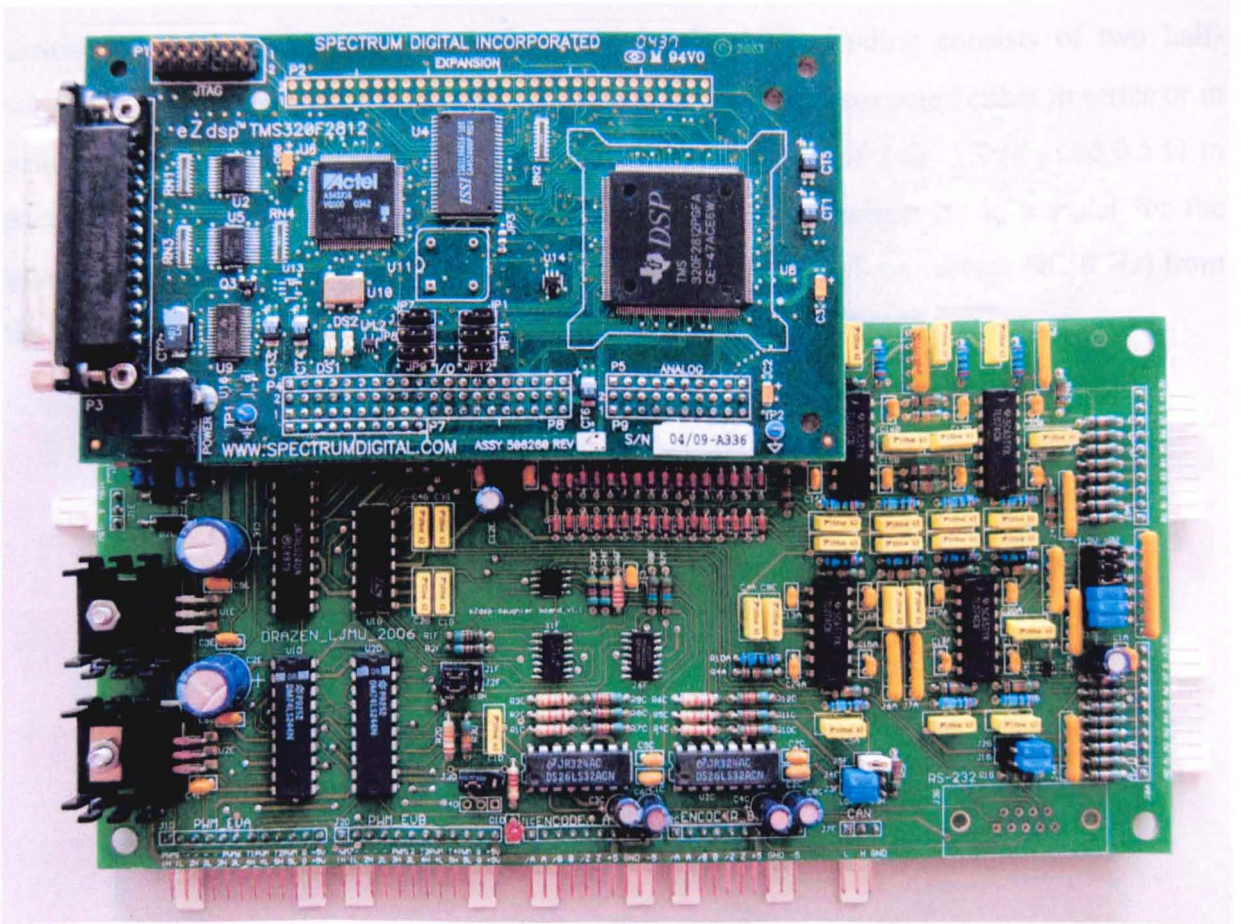
CONNECTORS TO REMAINING PINS OF DSP   CONNECTORS TO eZDSP BOARD

Fig. A.9: Developed eZDSP daughter-board.

Fig. A.10: eZDSP board mounted on the daughter-board.

Appendix B

DATA OF MACHINES AND STATIC LOAD

B.1   FIVE-PHASE MACHINES

Two five-phase machines that are used within series-connected five-phase two-motor drive are identical. They were obtained by cutting new stator laminations with 40 slots for two identical three-phase machines. Precise data for the five-phase machines are not available and Fig. B.1 shows original nameplate from the housing of the three-phase machine. After manufacturing of new stator laminations and rewinding, each five-phase machine is with 4 poles. The winding is single-layer and the winding pitch is 9 slots. The winding is therefore distributed, with 2 slots per phase, per pole. Each phase winding consists of two half-windings, with resistance of around 1 Ω. Half-windings can be connected either in series or in parallel. This gives the value of the per phase stator resistance of 2 Ω in series and 0.5 Ω in parallel connection. Machines were used with half-windings connected in parallel for the experiments with *V/f* profiles set to provide maximum available phase voltage (at 50 Hz) from the available dc bus (around 600 V).
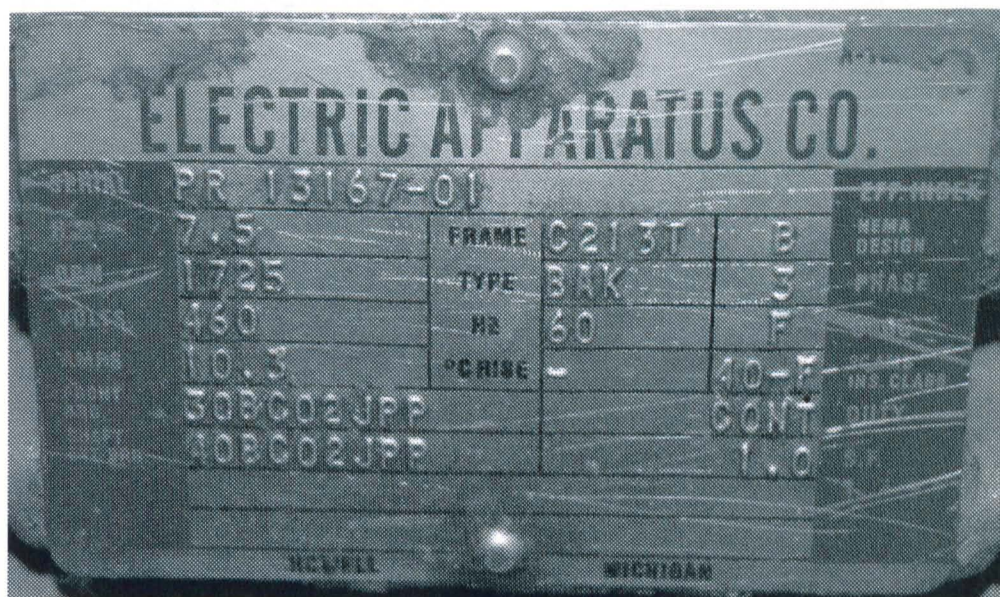

Fig B.1: Nameplate of the original three-phase machines.

B.2 THREE-PHASE MACHINES

Four different three-phase machines (M1, M2, M3 and M4, respectively) are used during experimental investigation of the multi-leg VSI fed multi-motor drives. Nameplates of these machines are given in Figs. B.2 and B.3, respectively.
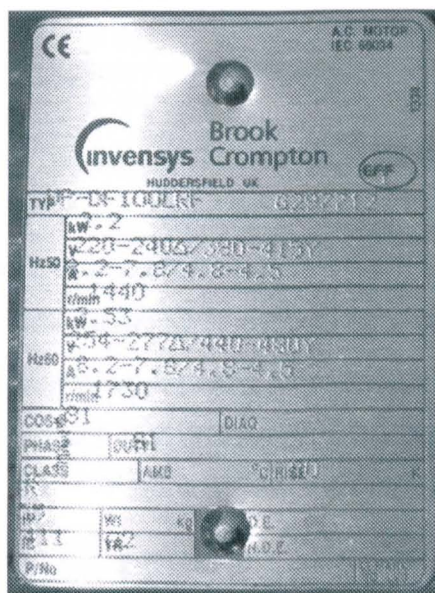

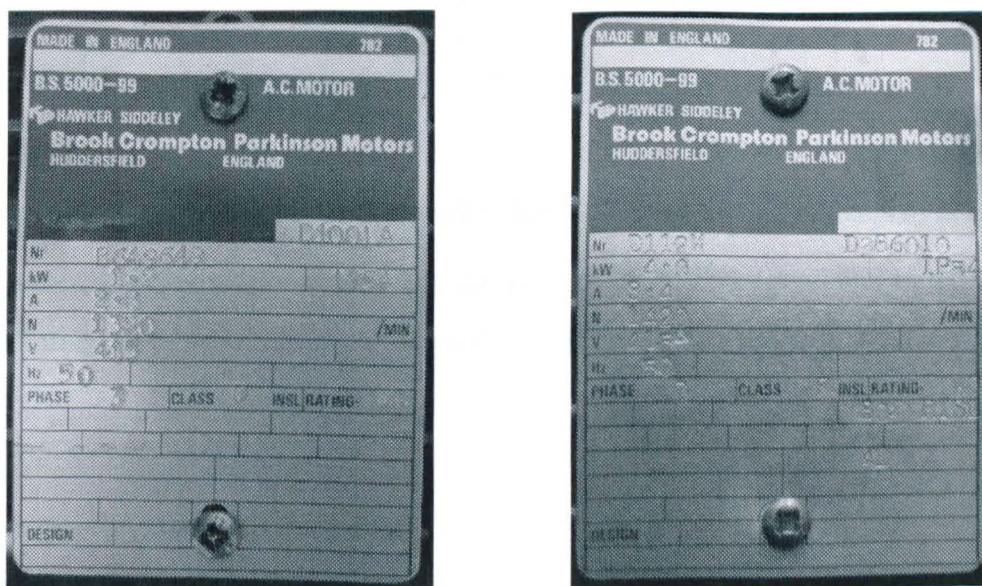**Fig B.2:** Nameplate of the three-phase machines M1 and M2.

Fig B.3: Nameplates of the three-phase machines M3 (left) and M4 (right).

B.3 STATIC *R-L* LOAD

The per-phase parameters of the static star-connected *R-L* load are:

R ≈ 150 Ω and L ≈ 200 mH

Appendix C

DERIVATION OF (7.18)

The following example illustrates the solution used for the determination of the integral of squared piece-wise linear function over a predefined period, based on the knowledge of values of the function at certain time instants.

One can consider a simple case of ripple analysis with only two sub-intervals, as shown in Figure C.1. Inductance L is exposed to a change of voltage as defined, where different levels of voltage are denoted with different sub-scripts.
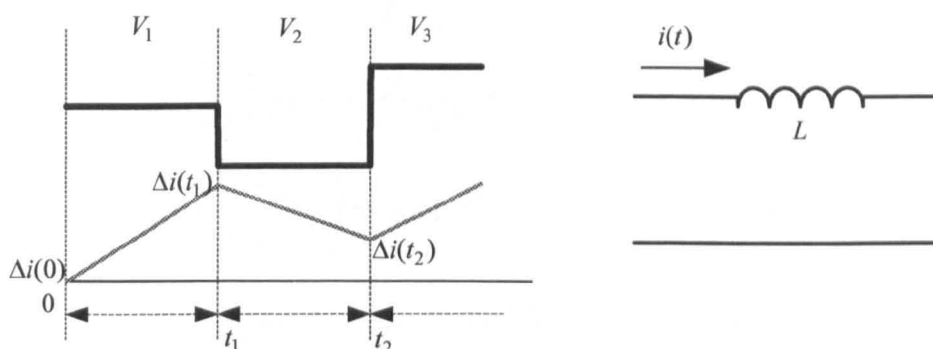
Fig. C.1: Current ripple caused by the application of different voltage levels over an L load.

Assuming linear rate of change of current over each sub-interval and initial zero value at the beginning, one can write following equations for the behaviour of the current ripple:

$$
\begin{aligned}
t = 0 \rightarrow & \quad \Delta i(0) = 0 \\
0 < t < t_1 \rightarrow & \quad \Delta i(t) = \frac{V_1}{L} t \\
t_1 < t < t_2 \rightarrow & \quad \Delta i(t) = \Delta i(t_1) + \frac{V_2}{L}(t - t_1) \\
t_2 < t < t_3 \rightarrow & \quad \Delta i(t) = \Delta i(t_2) + \frac{V_3}{L}(t_3 - t_2) \\
& \quad \ldots\ldots\ldots\ldots \\
t_{n-1} < t < t_n \rightarrow & \quad \Delta i(t) = \Delta i(t_{n-1}) + \frac{V_n}{L}(t_n - t_{n-1})
\end{aligned}
\tag{C.1}
$$

At the end of every sub-interval one has:

$$\Delta i(0) = 0$$

$$\Delta i(t_1) = \frac{V_1}{L}t_1$$

$$\Delta i(t_2) = \Delta i(t_1) + \frac{V_2}{L}(t_2 - t_1) \qquad\qquad (C.2)$$

....

$$\Delta i(t_n) = \Delta i(t_{n-1}) + \frac{V_n}{L}(t_n - t_{n-1})$$

In order to determine the square value of the current ripple over every sub-interval one can find the solution over the first sub-interval as:

$$0 < t < t_1 \to \Delta i^2 = \frac{1}{t_1 - 0}\int_0^{t_1}\Delta i(t)^2\, dt = \frac{1}{t_1}\int_0^{t_1}(\frac{V_1}{L}t)^2\, dt = \frac{1}{t_1}(\frac{V_1}{L})^2\int_0^{t_1} t^2\, dt$$

$$= \frac{1}{t_1}(\frac{V_1}{L})^2\frac{t_1^3}{3} = (\frac{V_1}{L})^2\frac{t_1^2}{3} = \frac{1}{3}(\frac{V_1}{L}t_1)^2 = \frac{1}{3}\Delta i(t_1)^2 \qquad (C.3)$$

Similarly, for the next sub-interval:

$$t_1 < t < t_2 \to \Delta i^2 = \frac{1}{t_2 - t_1}\int_{t_1}^{t_2}\Delta i(t)^2\, dt = \frac{1}{t_2 - t_1}\int_{t_1}^{t_2}(\Delta i(t_1) + \frac{V_2}{L}(t - t_1))^2\, dt =$$

$$= \frac{1}{t_2 - t_1}\int_{t_1}^{t_2}(\Delta i(t_1)^2 + 2\Delta i(t_1)\frac{V_2}{L}(t - t_1) + (\frac{V_2}{L}(t - t_1))^2)\, dt =$$

$$= \frac{1}{t_2 - t_1}\left[\Delta i(t_1)^2\int_{t_1}^{t_2} dt + 2\Delta i(t_1)\frac{V_2}{L}\int_{t_1}^{t_2}(t - t_1)\, dt + (\frac{V_2}{L})^2\int_{t_1}^{t_2}(t - t_1)^2\, dt\right] =$$

$$= \frac{1}{t_2 - t_1}\left[\Delta i(t_1)^2(t_2 - t_1) + 2\Delta i(t_1)\frac{V_2}{L}\int_0^{t_2 - t_1} x\, dx + (\frac{V_2}{L})^2\int_0^{t_2 - t_1} x^2\, dx\right] = \qquad (C.4)$$

$$= \Delta i(t_1)^2 + \frac{1}{t_2 - t_1}\left[2\Delta i(t_1)\frac{V_2}{L}\frac{(t_2 - t_1)^2}{2} + (\frac{V_2}{L})^2\frac{(t_2 - t_1)^3}{3}\right] =$$

$$= \Delta i(t_1)^2 + \Delta i(t_1)\frac{V_2}{L}(t_2 - t_1) + \frac{1}{3}[\frac{V_2}{L}(t_2 - t_1)]^2$$

Recognising that:

$$\frac{V_2}{L}(t_2 - t_1) = \Delta i(t_2) - \Delta i(t_1) \qquad\qquad (C.5)$$

the following is further obtained for (C.4):

$$t_1 < t < t_2 \to \Delta i^2 = \Delta i(t_1)^2 + \Delta i(t_1)[\Delta i(t_2) - \Delta i(t_1)] + \frac{1}{3}[\Delta i(t_2) - \Delta i(t_1)]^2 =$$

$$= \Delta i(t_1)^2 + \Delta i(t_1)\Delta i(t_2) - \Delta i(t_1)^2 + \frac{1}{3}[\Delta i(t_1)^2 - 2\Delta i(t_1)\Delta i(t_2) + \Delta i(t_2)^2] = \qquad (C.6)$$

$$= \Delta i(t_1)\Delta i(t_2) + \frac{1}{3}\Delta i(t_1)^2 - \frac{2}{3}\Delta i(t_1)\Delta i(t_2) + \frac{1}{3}\Delta i(t_2)^2 =$$

$$= \frac{1}{3}\Delta i(t_1)^2 + \frac{1}{3}\Delta i(t_1)\Delta i(t_2) + \frac{1}{3}\Delta i(t_2)^2$$

Finally, (C.6) can be written as:

$$t_1 < t < t_2 \rightarrow \Delta i^2 = \frac{1}{3}[\Delta i(t_1)^2 + \Delta i(t_1)\Delta i(t_2) + \Delta i(t_2)^2] \tag{C.7}$$

Following the same approach, it can be shown that in general:

$$t_{n-1} < t < t_n \rightarrow \Delta i^2 = \frac{1}{t_n - t_{n-1}} \int_{t_{n-1}}^{t_n} \Delta i(t)^2 \, dt = \frac{1}{3}[\Delta i(t_{n-1})^2 + \Delta i(t_{n-1})\Delta i(t_n) + \Delta i(t_n)^2] \tag{C.8}$$

Thus, instead of continuous integration over the defined period of time, one can use (C.8) if the values of the function under the integral are known at the end of every sub-interval. The same applies for harmonic flux, since it is different only in scale from the current ripple:

$$t_{n-1} < t < t_n \rightarrow \Delta \lambda^2 = \frac{1}{t_n - t_{n-1}} \int_{t_{n-1}}^{t_n} \Delta \lambda(t)^2 \, dt = \frac{1}{3}[\Delta \lambda(t_{n-1})^2 + \Delta \lambda(t_{n-1})\Delta \lambda(t_n) + \Delta \lambda(t_n)^2] \tag{C.9}$$

Alternatively, (C.9) can be written as:

$$\int_{t_{n-1}}^{t_n} \Delta \lambda(t)^2 \, dt = (t_n - t_{n-1})\frac{1}{3}[\Delta \lambda(t_{n-1})^2 + \Delta \lambda(t_{n-1})\Delta \lambda(t_n) + \Delta \lambda(t_n)^2] \tag{C.10}$$

Appendix D

PUBLICATIONS FROM THE THESIS

D.1 JOURNAL PAPERS

Dujić, D., Grandi, G., Jones, M., Levi, E., (2008), A space vector PWM scheme for multifrequency output voltage generation with multiphase voltage source inverters, *IEEE Trans. on Industrial Electronics*, vol. 55, no. 5, pp. 1943-1955.

Levi, E., Dujić, D., Jones, M., Grandi, G., (2008), Analytical determination of DC-bus utilization limits in multi-phase VSI supplied AC drives, *IEEE Trans. on Energy Conversion*, vol. 23, no. 2, pp. 433-443.

Casadei, D., Dujić, D., Levi, E., Serra, G., Tani, A., Zarri, L., (2008), General modulation strategy for seven-phase inverters with independent control of multiple voltage space vectors, *IEEE Trans. on Industrial Electronics*, vol. 55, no. 5, pp. 1921-1932.

Jones, M., Vukosavić, S.N., Dujić, D., Levi, E., Wright, P., (2008), A five-leg inverter PWM technique for reduced switch count two-motor constant power applications, *IET – Electric Power Applications*, vol. 2, no. 5, pp. 275-287.

D.2 CONFERENCE PAPERS

Dujić, D., Jones, M., Levi, E., Vukosavić, S.N., (2008), A two-motor centre-driven winder drive with a reduced switch count, *Proc. IEEE Industrial Electronics Society Annual Meeting IECON*, Orlando, FL, (in press).

Jones, M., Dujić, D., Levi, E., (2008), A performance comparison of PWM techniques for five-leg VSIs supplying two-motor drives, *Proc. IEEE Industrial Electronics Society Annual Meeting IECON*, Orlando, FL, (in press).

Vukosavić, S.N., Jones, M., Levi, E., Dujić, D., (2008), An improved PWM method for a five-leg inverter supplying two three-phase motors, *Proc. IEEE International Symposium on Industrial Electronics ISIE*, Cambridge, UK, pp. 160-165.

Jones, M., Dujić, D., Levi, E., (2008), A PWM method for seven-leg inverters supplying three three-phase motors, *Proc. IEEE Power Electronics Specialists Conf. PESC*, Rhodes, Greece, pp. 2902-2908.

Dujić, D., Jones, M., Levi, E., (2008), Features of two multi-motor drive schemes supplied from five-phase/five-leg voltage source inverters, *Proc. Int. Power Conversion and Intelligent Motion Conf. PCIM*, Nürnberg, Germany, CD-ROM paper: S2d-2.

Dujić, D., Jones, M., Levi, E., (2007), Continuous carrier based vs. space vector PWM for five phase VSI, *The Int. Conf. on "Computer as a tool" EUROCON*, Warsaw, Poland, pp. 1772-1779.

Dujić, D., Jones, M., Levi, M., (2007), Space vector PWM for nine-phase VSI with sinusoidal output voltage generation: analysis and implementation, *Proc. IEEE Industrial Electronics Society Annual Meeting IECON*, Taipei, Taiwan, pp. 1524-1529.

Dujić, D., Levi, E., Jones, M., Grandi, G., Serra, G., Tani, A., (2007), Continuous PWM techniques for sinusoidal voltage generation with seven-phase voltage source inverters, *Proc. IEEE Power Electronics Specialists Conference PESC*, Orlando, FL, pp. 47-52.

Dujić, D., Jones, M., Levi, M., (2007), A PWM scheme for five-leg VSI supplying two three-phase induction motors with a common inverter leg, *Int. Power Conversion and Intelligent Motion Conf. PCIM*, Nürnberg, Germany, CD-ROM paper: S6d-1.

Jones, M., Dujić, D., Levi, E., Batako, A., Mgaloblishvili, O., (2007), A novel five-leg PWM technique for two-motor centre-driven winders, *Proc. International Electric Machines and Drives Conference IEMDC*, Antalya, Turkey, pp. 254-259.